

# Optical and material properties of varnishes for paintings

Samuel J. Lawman

A thesis submitted in partial fulfilment of the requirements of  
Nottingham Trent University for the degree of Doctor of Philosophy

This research programme was carried out  
in collaboration with the National Gallery, London

August 2011

© This work is the intellectual property of the author, and may also be owned by the research sponsor(s) and/or Nottingham Trent University. You may copy up to 5% of this work for private study, or personal, non-commercial research. Any re-use of the information contained within this document should be fully referenced, quoting the author, title, university, degree level and pagination. Queries or requests for any other use, or if a more substantial copy is required, should be directed in the first instance to the author.

## Acknowledgements

To Rachel, who was there all the way.

This work could only happen because of the funding provided by EPSRC and the National Gallery, London.

Thanks go to the supervisory team of Dr Haida Liang, Dr Mike Newton and Dr Martin Bencsik who provided guidance, knowledge and knowhow throughout the project.

Thanks go to Marika Spring and the conservators at the National Gallery, who provided their knowledge and experience to the project. They also provided samples and their time.

Thanks go to Dr René de la Rie, Dr John Delaney and Kathryn Morales of the National Gallery of Art, Washington, and Dr Mady Elias of Institut des Nanoscience de Paris, who provided useful discussion, information and advice on equipment, and the samples that got the project underway.

Thanks go to Dr David Fairhurst, Dr Rob Morris, Dr Neil Shirtcliffe, Dr Carl Evans, Prof. Carl Brown, Rachel Bolton-King, Dr Gary Wells, Dr Hans Adriaensen, Dr Sammy Cheung, Dr David Willmer and Dr Gabriel Boutaud, at Nottingham Trent University for knowledge, suggestions, advice, instruction on equipment, instruction on MATLAB, lend of samples and endless lend of equipment.

Finally thanks go to everyone else who I have shared a lab and a 5 a-side football pitch with in my four years at Nottingham Trent University.

# Contents

Abstract.....	1
1. Introduction.....	3
1.1 History and chemistry of varnishes.....	4
1.1.1 Ancient and oil varnishes.....	4
1.1.2 Traditional solvent varnishes.....	6
1.1.3 Varnish degradation.....	9
1.1.4 Synthetic solvent varnishes.....	10
1.1.5 Coating additives.....	14
1.1.6 Current varnishes preferred by conservators.....	14
1.2 Optical properties of varnish.....	15
1.3 Material properties and processes.....	20
1.3.1 Physical description and thermodynamics of solutions.....	21
1.3.2 Diffusion coefficients.....	22
1.3.3 Rheology.....	23
1.3.4 Film drying theory.....	24
1.3.5 Surface levelling.....	27
1.3.6 Other factors that influence appearance.....	33
1.3.7 Glass transition.....	35
1.3.8 Solvent effects on final film.....	36
1.4 Summary.....	37
1.5 References.....	39
2. OCT multi-interface profilometry.....	49
2.1 Introduction.....	49
2.1.1 Interface profiles and roughness quantification.....	49
2.1.2 Review of available techniques.....	52
2.1.3 OCT for multi-interface measurement.....	58
2.2 Instrument and methods.....	64
2.2.1 Instrument.....	64
2.2.2 Interface identification.....	68

2.2.3 Measurement of instrument Point Spread Function.....	68
2.2.4 Evaluation of methods to find centre of PSF.....	71
2.3 Sources of error and correctable distortions.....	80
2.3.1 Vibration.....	80
2.3.2 Instrument optics, speckle and diffraction.....	83
2.3.3 Optical path length distortion across OCT image and measurement of telecentricity .....	88
2.4 Results.....	92
2.4.1 Regular surfaces.....	92
2.4.2 Random rough surfaces .....	99
2.4.3 Random rough second interface.....	106
2.5 Conclusion.....	108
2.6 References .....	109
3. OCT multi-interface profilometry for dynamic refractive index measurements of drying droplets.....	114
3.1 Introduction.....	114
3.2 Method.....	120
3.3 Validation and distortion.....	123
3.4 Drying varnish results.....	130
3.5 Conclusion.....	132
3.6 References .....	133
4. NMR for measurements of varnish.....	136
4.1 Introduction.....	136
4.1.1 NMR, and properties thereof... ..	138
4.1.2 NMR MOUSE.. ..	143
4.2 NMR MOUSE self-diffusion measurements of solvent varnishes.....	146
4.2.1 Methods .....	146
4.2.2 Calibrations.....	147
4.2.3 Diffusion results of a polymer varnish.....	151
4.2.4 Diffusion results of a low molecular weight varnish... ..	155
4.3 NMR $T_1$ and $T_2$ times of varnish solutions.....	160
4.3.1 $T_2$ .....	161

4.3.1.1 Method.....	161
4.3.1.2 AYAT Results.....	161
4.3.1.3 Regalrez results.....	165
4.3.2 T <sub>1</sub> .....	169
4.4 Molecular description, of high and low molecular weight varnish solutions, from NMR evidence.....	171
4.5 Welled Drying.....	173
4.5.1 Method.....	174
4.5.2 Mass balance results.....	175
4.5.3 OCT.....	177
4.5.4 NMR Imaging (MRI).....	181
4.5.4.1 Mean amplitude (intensity) images.....	181
4.5.4.2 NetT <sub>2</sub> images.....	185
4.5.4.3 Net T <sub>1</sub> imaging and measurement.....	186
4.5.5 Welled drying discussion.....	189
4.6 Measurement of drying varnish coatings with NMR/MRI.....	189
4.7 Conclusion.....	192
4.8 References.....	194
5. Rheology of varnish solutions.....	197
5.1 Introduction.....	197
5.2 Methods.....	199
5.3 Results.....	204
5.3.1 Rheological characterisation of varnish solutions.....	204
5.3.2 Viscosity-concentration function: dependence on resin.....	206
5.3.3 Viscosity-concentration function: dependence on solvent.....	212
5.4 Conclusion.....	213
5.5 References.....	214
6. Development of surface roughness of drying varnish.....	216
6.1 Introduction.....	216
6.2 Dimensions of real painting systems.....	221
6.2.1 Paint and varnish roughness.....	221
6.2.2 Varnish thickness.....	224

6.3 Experimental method.....	225
6.3.1 Substrate preparation... ..	225
6.3.2 Application.....	226
6.3.3 OCT measurement.....	227
6.4 Experimental results.....	229
6.4.1 Laser cut trench substrate.....	229
6.4.2 Ground substrates: different resins.....	231
6.4.3 Ground substrates: different thicknesses (dry and initial)...	242
6.4.4 Discussion.....	246
6.5 Modelling the formation of roughness.....	247
6.5.1 Numerical differential lubrication approximation.....	247
6.5.2 Evaporation function measurement.....	249
6.5.3 Modelling results: different resins.....	256
6.5.3 Modelling results: different thicknesses.....	269
6.6 Conclusion.....	271
6.7 References.....	272
7. Optical properties of conservator applied and aged coatings.....	274
7.1 Introduction.....	274
7.1.1 Wetting, penetration and adhesion.....	275
7.1.2 Volume scattering.....	280
7.1.3 OCT for other optical measurement.....	281
7.2 Conservator applied coatings: ground glass plates.....	282
7.2.1 Methods: applied coatings.....	282
7.2.2 Methods: measurement of plates.....	284
7.2.3 Results: uncoated ground glass reference.....	285
7.2.4 Results: dammar coated plate... ..	287
7.2.5 Results: Paraloid B72 and MS2A coated plate.....	290
7.2.6 Results: Regalrez and MS2A coated plate.....	294
7.2.7 Discussion: all conservator coated glass plates .....	298
7.3 Conservator coated painted canvas samples.....	299
7.3.1 Method.....	299
7.3.2 Results.....	300
7.4 Volume scattering measurements .....	303

7.4.1 Method..	303
7.4.2 Results.....	304
7.4.3 Discussion.....	308
7.5 Conclusion.....	309
7.6 References .....	310
8. Conclusion.....	312
Appendix 1: Fourier transform.....	316
Appendix 2: Additional NMR data.....	318
A2.1 Additional Hahn echo data for molecular liquids.....	318
A2.2 Additional CPMG data for molecular liquids.....	320
A2.3 Hahn echo data for AYAT and toluene solutions.....	322
A2.4 AYAT diffusion results comparison between Hahn echo and CPMG method.....	324
A2.5 AYAT $T_2$ measurements.....	325
A2.6 Regalrez $T_2$ measurements.....	327
Appendix 3: Flow rheology of various varnish resins dissolved in toluene.....	329
Appendix 4: Substrate preparation.....	333
A4.1 Ground glass.....	333
A4.2 Laser cut trench.....	334
Appendix 5: viscoelastic models.....	336
Appendix 6: published papers .....	338

## Abstract

Clear varnish coatings are applied to the surface of historic paintings to provide a protective barrier layer and/or change their appearance. The natural varnishes used by the original artist would have given the painting its original finished appearance. Over a period of years these varnish layers degrade with age, which changes the appearance. Then it becomes necessary to remove and replace the coating. This removal and replacement is undesirable as it can lead to damage of the painting. Synthetic alternatives can provide a much longer life coating but may not give the same appearance. This thesis details research into the soft matter physics and fluid mechanisms that determine the relationships between the material properties of varnishes and their effect on the appearance of paintings.

The mobility (self diffusion coefficient) of a high molecular weight varnish resin (AYAT) was measured with Nuclear Magnetic Resonance (NMR) to be up to three orders of magnitude lower than the solvent (Toluene) and a low molecular weight resin (Regalrez 1094). The similarity of the low and high molecular weight resins NMR relaxation times,  $T_1$  and  $T_2$ , showed the important difference was the size of the molecules. A unilateral NMR imaging system (using a CPMG sequence with a  $T_E$  time of 100 $\mu$ s) was able to resolve a signal from the varnish coatings until the solvent content was approximately 10%. The use of a NMR system, capable of shorter  $T_E$  times, could allow the non-invasive measurement of solvent content of varnish coatings until completely solvent free.

To measure the formation of substrate induced roughness of  $\mu$ m and nm amplitudes, a new method was developed using Optical Coherence Tomography (OCT) to simultaneously measure the air-varnish and varnish-substrate profiles. The potential accuracy of this technique was shown to be the same as any other White Light Interferometry method (<10nm for smooth surfaces but decreases with surface roughness). The experimental accuracy achieved for smooth surfaces, without significant vibration suppression, was 50nm. The high sensitivity of OCT allowed the otherwise unachievable measurement of extremely faint varnish-ground glass interfaces.

The development of varnish surface profiles and power spectral densities inherited from a substrate (crucial to varnish appearance) were accurately modelled using the lubrication approximation of the Navier-Stokes equation. Though for better levelling varnish coatings, a different process dominated low spatial frequencies. Viscosity, as a function of concentration, was shown to be the crucial variable determining surface roughness. The viscosity functions of high molecular weight polymer resins (AYAT and Paraloid B72) were shown to be considerably different to low molecular weight resins (Dammar, Laropal A81, MS2A, Regalrez 1094 and Regalrez 1126). The differences in the viscosity between low molecular weight resins (including natural resins) are less substantial and other factors, such as choice of solvent, are of increased importance.

In conservator applied coatings, the amount of varnish applied was shown to be a key variable along with choice of resin in the final surface roughness. OCT measurements of these provided strong evidence that some coatings completely wetted substrate pores, while others showed different fractions of wetting. This showed dependencies on the resin and variations in the conservators' application. The assumption that the surface state is the only dominant factor in the appearance of coatings is not necessarily true.

The thesis concludes that, to understand the difference in appearance between different coatings, the material properties of the varnish solution should be directly measured. With these the surface roughness, hence appearance, of a coating can be accurately predicted. This will allow the prediction of how a varnish solution can be manipulated, by a conservator, to get precisely the desired surface state.

## 1 Introduction

A varnish coating is an optically transparent layer applied to a surface of a material. The purposes of a varnish coating is well defined by Theophilus Presbyter around 1100 CE, who recorded<sup>1</sup> about them

“Every painting that is coated with this gluten (varnish) is made bright, beautiful, and completely lasting.”

The first purpose “made bright, beautiful” refers to the change in the appearance of colour of a surface, that the varnish is applied to. The second purpose “completely lasting” refers to the protection (preservation) qualities of varnish coatings. Though not necessarily the oldest reference to both purposes it is certainly one of the most eloquent and reliable references. It predates most works of art that are likely to be encountered in an art rather than archaeological context, for example the oldest work of art in The National Gallery in London is from the 13<sup>th</sup> Century. The view of modern researchers has always backed this dual purpose<sup>2,3</sup>.

This project is only interested in varnish coatings for paintings, though varnish coatings are used for other materials, in particular wood. The field of wood varnishes includes the conservation of wooden artefacts, with the demands and varnishes used similar to those for paintings. It also includes industrial produced coatings for indoor and outdoor use, these coating demands are different to painting varnishes and the varnishes used are different.

Multiple varnish coatings may be applied to a surface.

This project is focused on solvent type varnishes, which involves a solid inert material (resin) being dissolved in a solvent to give a liquid solution. It is then applied to form a film on the material to be coated. The methods of application are by brushing or spraying of the solution. The volatile solvent then evaporates and leaves the inert solid (resin) as the dry coating. The resin is chemically unchanged in the application process but material properties of the final film may be influenced by

retained solvent<sup>2</sup> and arrangement of resin molecules in the dry coating, due to their behaviour in solution<sup>4</sup>.

Varnish coatings can also be formed by the use of chemical reactions to produce a solid layer from an applied liquid film. Oil varnishes consist of drying oils such as linseed. After the application of the film the components of the oil undergo polymerisation leading to a change of physical state to a solid. Similar to oil varnishes are modern epoxy resins<sup>5</sup> which are used for highly resistant coatings of wood, such as in a marine environment. In epoxy varnishes two components are mixed together then applied to as a film onto the material, the components of the film chemically react, leading to the change of state. The inability to safely remove drying oil and epoxy varnish coatings means that they can not be considered for conservation applications.

A varnish coating provides a physical barrier for the paint layers. It prevents particles from reaching the paint surface and becoming engrained or doing other damage. However, a varnish layer is unlikely to restrict the diffusion of gaseous molecules, such as oxygen, to the paint<sup>2</sup>. When the painting is being handled the varnish prevents the paint from being touched. The absorption of UV light by varnish acts as a filter, preventing UV induced photochemical reactions of the paint, though in most galleries this will be a redundant feature as the UV component of the lighting will be limited. Away from the conservation of paintings, a main purpose of varnish is to prevent the impregnation of liquid water into wood.

## 1.1 History and chemistry of varnishes

### 1.1.1 Ancient and oil varnishes

The archaeological evidence for varnish coatings dates back to before 2000BCE in Egypt<sup>6,7</sup> and China<sup>8</sup>. The composition and method of application of ancient Egyptian varnishes is interesting. The main component has been identified as resin extracted from *pistacia atlantica*<sup>9</sup>, which is of the same genus as mastic (*pistacia lentiscus*) that is widely used as a solvent varnish (Sections 1.1.2 and 1.1.6). The

method of application of these varnishes is uncertain, but may have been applied like a solvent varnish.

Sources from the medieval period in Western Europe, such as the Lucca manuscripts<sup>6, 10</sup> and Theophilus Presbyter's on Divers Arts<sup>1</sup>, up till the late 16<sup>th</sup> century<sup>6</sup> give recipes for varnish coatings involving drying oils. The content of these varnishes are natural resins, such as sandarac and mastic, dissolved in a drying oil, such as linseed or cypress oil. Figure 1.1.1.1 shows the molecular structure of drying oils<sup>11,12</sup> which are esters of glycerol and unsaturated fatty acids. R is representative of the residual fatty acid chains. An example of such a chain is for Oleic acid where R is given by figure 1.1.1.2. The other fatty acid groups found in drying oils include linolenic, linoleic, eleosteric, lincanic and ricinoleic acids. The R groups in a single molecule are not usually identical but a random combination of fatty acids. The probability distribution of the fatty acids is determined by the specific oil used. When the film is exposed to the atmosphere, the drying oil undergoes polymerisation of the double bonds within the fatty acid chains through an oxidation process<sup>11</sup>. This causes the varnish solution to solidify. All the varnish recipes of this type also contain inert resin dissolved in the drying oil, which will also solidify as its solvent (the drying oil) solidifies.

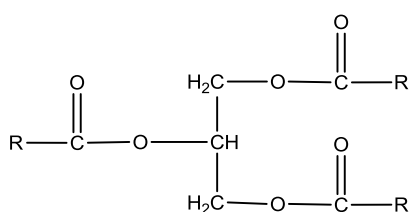


Figure 1.1.1.1  
General molecular structure of drying oils where the R groups are fatty acid chains, such as in figure 1.1.1.2.

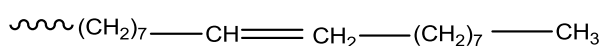


Figure 1.1.1.2  
Example fatty acid chain (Oleic acid) found in drying oils.

The use of drying oil as a painting medium (oil paint) did not develop as a main practice for fine art until after van Eyck in the early 15<sup>th</sup> C<sup>13</sup>. The main paint medium before this period was egg tempera, which was also occasionally used as a varnish<sup>6, 14</sup> (or additional component<sup>6</sup>). This dries by denaturation of proteins within the egg<sup>15</sup>.

## 1.1.2 Traditional solvent varnishes

Varnishes not containing any drying oils, that is only resins dissolved in a volatile solvent, were first recorded in the 16<sup>th</sup> century and were widely used by the 17<sup>th</sup> C<sup>3, 6</sup>. The resins used in these varnishes were no different from what had been used as components of the oil varnishes that preceded them. The resins in use all came from natural sources (usually the secretions of different trees) and will be referred to as the genre of natural resins. The main chemical components of these resins are various terpene or terpenoid products<sup>16</sup>. Figure 1.1.2.1 shows the building block of these molecules, isoprene. These are assembled into chains or rings and various functional groups are added and the structure modified to give a wide variety of molecules. Figure 1.1.2.2 shows an example of a terpenoid present in dammar resin, dammardienone. Chapter 3 in de la Rie<sup>17</sup> provides a much more detailed summary of the terpenoid molecules present in dammar resin. The identification of the terpenoid molecules present in mastic has also been carried out<sup>18</sup>. As well as a mix of terpenoid molecules, natural resins also contain varying amounts of naturally occurring polymers. This polymer content is an important part of the broad range of molecular sizes present in natural resins. Figure 1.1.2.3 gives the chemical structure of a polymer identified in mastic resin<sup>19</sup>. If there was a technological driving force of the uptake of solvent varnishes in the 16<sup>th</sup> and 17<sup>th</sup> centuries (instead of drying oil varnishes) it was likely be the developments in solvent production at the time.

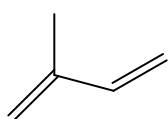


Figure 1.1.2.1  
Molecular structure of isoprene, a chemical building block of natural resins.

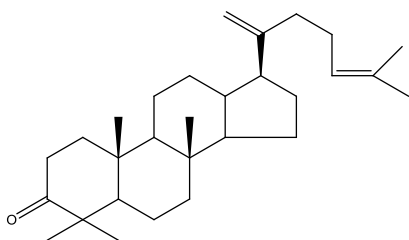


Figure 1.1.2.2  
Molecular structure of dammardienone, one of many chemical components of dammar resin

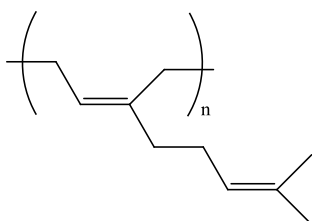


Figure 1.1.2.3  
Molecular structure of cis-1,4-poly- $\beta$ -myrcene, a naturally occurring polymer in mastic resin

The key advantage in the use of solvent varnishes is that as they do not involve any chemical change (ideally) of the coating, they can always be removed with the solvent they were applied with. The resins used are amorphous solids (glasses) when pure at room temperature, rather than crystalline. As they do not crystallise, they do not precipitate out of solution (form crystals with solvent forced out) as the concentration increases but remains homogenous at all concentrations. As a varnish coating dries by the evaporation of solvent, the concentration of resin increases without discontinuities and the physical state of the coating changes gradually.

Dammar and Mastic<sup>6, 20</sup> are the most important two natural resins in current use for the conservation of paintings. Mastic is the secretion of *pistacia lentiscus*, a tree native to the Mediterranean, but the supply of it is mostly associated with the *chia* variety from the island of Chois<sup>16</sup>. The results of a survey of the varnish material found upon a range of paintings<sup>20</sup> shows that mastic has probably been artists and conservators most favoured resin. The main reason given by its users for the preference of it over dammar is that it is easier to manipulate when applying<sup>21</sup>. This ease of manipulation may be due the higher amount of high molecular weight component<sup>22</sup>, giving it higher viscosities at lower concentration. However there are several drawbacks to the use of mastic, the one of most concern for conservators is the fast rate of degradation. Mastic varnish coatings are well documented to yellow faster than Dammar coatings<sup>23</sup>. Other defects include tendency to bloom and possible poorer mechanical wearing qualities<sup>21</sup>.

Whereas mastic resin is defined as being from a particular species, indeed for the most part a specified variety grown in a single location, the definition of dammar resin is not as specific. Dammar resin comes primarily from several species of two genera (*shorea* and *hopea*) from the *dipterocarpaceae* family of trees<sup>2, 16, 21</sup>. The geographic location of the collection of dammar resin is limited to an area presently covered by the nations of Malaysia and Indonesia. The location of the source of the resin meant that it did not become used as a varnish in Europe until much later than most other natural resins. The literature consensus on the first use of dammar appears to be the early 19<sup>th</sup> C. Due to its ageing advantages over mastic it is the currently preferred natural resin.

There is a wide variety of other natural resins that have been used as varnishes or components of varnish recipes<sup>6, 20</sup>. Here two more will be briefly introduced. African sandarac is the secretion from the conifer tree *Tetraclinis articulate* native to Algeria and Morocco<sup>16</sup>. The varnish coating is brittle and it ages less well than mastic<sup>2, 21</sup>. Shellac is the natural secretion of the insect *kerria lacca*<sup>16</sup>. As a result of being from a source other than tree secretion, the composition of the resin is much different to other natural resins. The composition of shellac also contains wax and colouring matter as well as the resin. The resin is not terpene or terpenoid derived but is a naturally occurring oligomer<sup>15</sup> (like a polymer but with only a small (rather than large) number of monomers per molecule) soluble in alcohol but not turpentine. Copal and amber<sup>24</sup> can refer to secretions of various trees with varying degrees of polymerisation/fossilisation after the secretion. Fir balsam, larch resin and pine resin<sup>20</sup> are other examples of tree secretions that have been used as varnishes.

A survey of the varnish composition and individual conservator practice between 1850 and the introduction of synthetic resins<sup>20</sup>, provides an overview of varnishing practices at the end of the natural resin era. In the UK in 1850 the use of dammar as a varnish resin appears scarce at best. Though its use does become more prevalent, it does not overtake mastic as the most common varnish component in the paintings surveyed by White and Kirby. The use of dammar may have been more common outside the United Kingdom<sup>25</sup>. Mastic was preferred as the superior resin in the absence of dammar, though was certainly not uniform in its use. Mastic was often blended with small amounts of a drying oil, preferably pre polymerised by boiling. The reasoning of this method was to change the application properties and mechanical resistance of the coating. However, as it is a form of meglip<sup>21, i</sup> the degradation of the coating would have been increased. The mastic was also often blended with other natural resins in solvent varnish solutions. The blending of the resins seemed more successful in incorporating the properties desired, especially the addition of dammar which seemed to inhibit the degradation of the mastic resin. Varnishes of copal, fir balsam and larch were also popular. A few of the coatings are

---

<sup>i</sup> A mixture of mastic and linseed oil. If prepared correctly (oil cooked with lead), it can give a “gelatinous” material that was used “extensively”. However, its use was “disastrous to the life of paintings”. As a result the use of mastic is described as “only safe to use in simple-solution picture varnishes which contain no linseed, poppy or other drying oils”.

identified as polyterpene<sup>26</sup> only, this natural polymer could come from a variety of coatings such as spike of lavender oil.

A review of painting instruction books during the 19<sup>th</sup> century<sup>14</sup> identified three other areas of interest in this period. Firstly the use of aqueous varnishes (including egg white) as a temporary coating to the drying oil paints. Secondly for final varnish the use of separate layers of different resins, the bottom layer is a permanent protective coating while the top layer is the sacrificial coating to be replaced when it discolours. Thirdly the choice of varnish may have been dependent on the paint vehicle (binder) it is being applied to. The conservator/artist could select a varnish material to be similar to the material of the paint, so to limit cracking due to different mechanical stresses. Alternatively the conservator/artist could choose the varnish material to be much different from the paint material, in order to ease varnish removal without damage to the paint by ensuring the varnish is soluble in solvents that the paint is not.

### 1.1.3 Varnish degradation

The material that forms the varnish layer can be prone to chemical changes with time (degradation). This generally leads to yellowing and physical changes that ruin the appearance of the picture. It also leads to solubility changes which become a danger when trying to remove the varnish coating. There may be several mechanisms for this change, especially with the complex content of natural resins. For dammar<sup>27</sup> three different mechanisms were identified: (i) A light induced auto-oxidation of functional groups within the resin, resulting in a change in solubility parameters, (ii) a Cross linking mechanisms producing higher molecular weight components and (iii) a yellowing mechanism, which was not light induced. The degradation mechanisms are similar for other natural and synthetic resins. As well as the usual mass spectrometry, the degradation of varnish coatings has also been measured using FT-IR and FT-Raman spectroscopy and a Quartz Crystal Microbalance system<sup>28</sup>.

The changes in appearance of varnishes as they degrade are undesirable for viewing the painting. This means that the degraded varnish coating must be removed, and

replaced with a new varnish coating. To remove the old varnish coating requires the use of solvents and mechanical action by the conservator<sup>29</sup>. The main danger lies in the fact that components of the paint layer beneath may be soluble<sup>2, 30, 31</sup>, leading to leaching of these components out of the paint layers or permanent effects on the surface of these layers<sup>32</sup>. The change in the solubility parameters of the aged varnish can make the problem worse. If a different solvent is used to remove the varnish than that used to apply it, the paint layer is being exposed to solvents of different characteristics leading to more potential for leaching.

As a result of the potential damage to a painting, whenever the varnish coating is removed and replaced, it is desirable for the lifetime of varnish coatings to be as long as possible. This does not necessarily mean that the varnish resin remains completely chemically unaltered as it ages, but it does maintain the same optical and solubility properties.

#### 1.1.4 Synthetic solvent varnishes

By the early 20<sup>th</sup> century developments in synthetic chemistry allowed polymer resins to be produced for the first time<sup>33</sup>. Some of these proved to be highly resistant to degradation with age making them an attractive option for longer life varnish coatings. The two synthetic polymers of interest to conservators in the present day are polyvinyl acetate (used as a varnish since the 1930s<sup>34</sup>) and acrylate polymers. Figure 1.1.4.1 shows a monomer of polyvinyl acetate. For use as a varnish this polymer comes in the grades designated AYA(x), where (x) is a letter determined by molecular weight distribution.

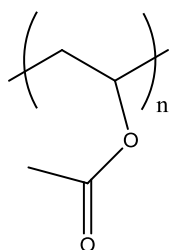


Figure 1.1.4.1  
Monomer structure of polyvinyl acetate

Figure 1.1.4.2 shows the two co-monomers of the acrylate polymer B72, methyl acrylate and ethyl methacrylate<sup>35</sup>. The advantage of synthetic resins over natural resins is that their content is a single molecular species. This means that their

degradation properties are easy to characterise and understand. The complex mix of molecular species in natural resins makes it much more difficult to understand all the degradation processes and with many molecular species some of them are likely to be unstable. The single molecular species in synthetic resins can be chosen for their stability. Though Paraloid B72 coatings do undergo chemical reactions during their life, the net effect of these reactions does not lead to changes in the films properties. As a result the coating can be regarded as stable<sup>36</sup>.

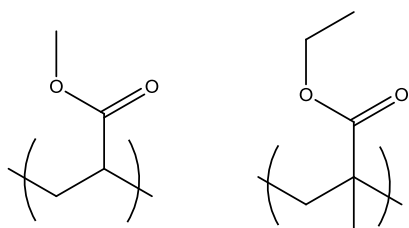


Figure 1.1.4.2  
Monomer structures methyl acrylate and ethyl methacrylate. Co-monomers in Paraloid B72 varnish.

The polymer chain length of these varnish resins are relatively long, this gives them a high molecular mass ( $\overline{M}_n \sim 9000\text{u}$ ) compared to the average molecules within mastic or dammar ( $\overline{M}_n \sim 500\text{u}$ )<sup>22</sup>. The polymer chain lengths are not uniform but are polydisperse, however the polydispersity of the synthetic resins are still much smaller than the natural resins. The larger molecular size of these polymer resins make it much more difficult for them to flow past each other when in solution<sup>37</sup>, which leads to high viscosities previously shown<sup>2</sup>. It was rapidly realised that these high molecular weight polymer varnishes did not produce the same optical appearance as natural resins<sup>24</sup>.

Lower molecular weight synthetic resins suitable for varnishing became available for conservators in the 1930's<sup>38</sup> with the introduction of ketone or polycyclohexanone resins AW2 and MS2. These were in use as picture varnishes by the 1950's<sup>23</sup>. Figure 1.1.4.3 shows the constituent feedstock<sup>39</sup> for these resins, cyclohexanone (a) and methyl cyclohexanone (b). Rather than being a true polymer these resins are oligomers (small number of monomers per molecule). The literature seen by the author<sup>39</sup> about the chemical structures of these resins seems inconclusive. The name polycyclohexanone is probably misleading as that would suggest a structure such as shown in figure 1.1.4.3 (c)<sup>40</sup>. Figure 1.1.4.3 (d) shows how the real molecular structure is more likely to be composed<sup>39</sup>. The presence of ketone groups

in these resins limited the life of these coatings. In the late 1950's the reduction of these ketone groups to alcohols in the manufacturing process<sup>38, 39</sup> was developed to produce the reduced ketone resins MS2A and MS2B. Figure 1.1.4.3 (e) shows this reduced form of the presumed structure. These low molecular weight synthetic varnishes give a more similar appearance to the natural resins than polymer coatings. However, they do not have the same life expectancy as polymer coatings and the mechanical properties are not ideal, forming brittle films<sup>38</sup>.

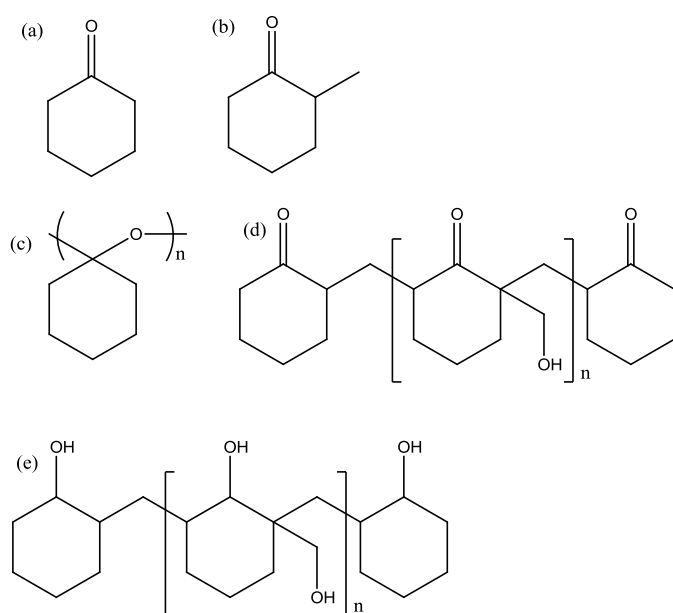


Figure 1.1.4.3  
 (a) Cyclohexone  
 (b) Methyl cyclohexone  
 (c) Polycyclohexone<sup>40</sup> (d)  
 Ketone resin  
 (e) Reduced ketone resin

By the 1990's<sup>41, 42</sup> two new synthetic resin types, hydrogenated hydrocarbon and urea-aldehyde, were available for painting varnishes. These are currently at the forefront of the field combining low molecular weight with long coating life. Fully hydrogenated (all CC double bonds replaced with hydrogen to create single bonds) hydrocarbon (with no other function groups) resins are extremely inert due to their alkane structure. Arcon and Escorez resins fit into this category<sup>41</sup>, but the most important resin for conservation use is Regalrez (particularly Regalrez 1094 and Regalrez 1126). Regalrez is produced from the oligomerisation of styrene (Figure 1.1.4.4 (a)) and alpha-methyl styrene (Figure 1.1.4.4 (b)) feed stock<sup>43</sup>. The resultant oligomer will be a short chain polystyrene molecule and the hydrogenation of this to form the final product will result in the benzene rings being converted to cyclohexane rings (Figure 1.1.1.4 (c) and (d)). Regalrez is highly resistant to photochemical degradation<sup>44</sup> and can be expected to give a coating life on a par with

the most stable polymer resins such as Paraloid B72. Regalrez 1094 is generally the grade used by conservators but this suffers from the problem of becoming tacky when handled<sup>45</sup>. This tackiness is not the result of the incomplete drying of the solvent but may be related to uncertainty in the glass temperature of the resin<sup>44</sup>. The values of  $T_g$  reported for this resin are highly varied, as low as 33°C. In a recent study into the effect of solvents on the physical properties of a film, all the final glass transition temperatures for Regalrez 1094 were measured between 20.9 and 24.9 °C<sup>46</sup>. For the varnish coating to truly be solid it needs to be below glass transition temperature<sup>47</sup>. If the relatively small, uniform sized and with weak intermolecular bonding, molecules of the surface of the Regalrez coating are raised above their glass transition, such as by a human finger, it will become tacky. Glass transition temperature is dependent on molecular size<sup>48</sup>, the use of higher molecular weight grade of Regalrez 1126 does not show the tackiness of 1094<sup>45</sup>.

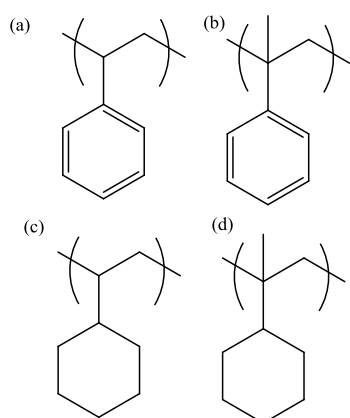


Figure 1.1.4.4

- (a) Styrene monomer
- (b) Alpha-methyl styrene monomer
- (c) Hydrogenated styrene monomer
- (d) Hydrogenated alpha-methyl styrene monomer

Urea-aldehyde resins (such as Laropal A81) are produced from low weight aldehyde molecules (Figure 1.1.4.5 (a)) and urea (Figure 1.1.4.5 (b)). These molecules react together to produce long chains, however there are several reaction processes that can happen leading to complex and branched chains<sup>49,50</sup>. De la Rie et al<sup>51</sup> provide a complex theoretical structure for the resulting resin. Like the hydrogenated hydrocarbon resins, these also have good stability<sup>51</sup> with low molecular weight, providing an alternative choice for conservators.

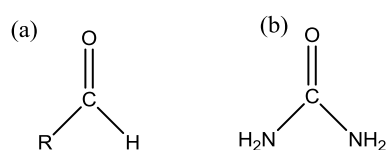


Figure 1.1.4.5

- Chemical feedstock of urea aldehyde resins.
- (a) Ketone where R is short alkane chain
  - (b) Urea

### 1.1.5 Coating additives

In the coatings industry additives to the varnish are often used to modify the behaviour of films to get the desired effect<sup>52</sup>. Small amounts of drying oil or wax, to change the mechanical properties of the final film, or agents, to induce a matte finish, added to a solvent varnish can be considered additives. In art conservation the main additives of importance are stabilisers<sup>53, 54</sup>, such as Tinuvin. These stabilisers inhibit the chemical reactions that occur when films degrade. Addition of stabilisers is an attractive method to increase the life of natural resin coatings but also improves the life of all synthetic resins as well<sup>44</sup>. Though these additives can give an improvement in the life of coatings the addition of extra chemical components onto the surface of the painting may not be desirable and the longest life coatings will still be formed with the resin that is the most inherently stable. The National Gallery London has the policy that it will not add stabilisers into conservation varnishes<sup>55</sup>. This project does not consider the addition of additives into varnishes.

### 1.1.6 Current varnishes preferred by conservators

The range of varnishes in use for conservation in the present time<sup>56</sup> encompasses various solvent resins identified in sections 1.1.2 and 1.1.4. Conversation with conservators at the National Gallery in London<sup>55</sup> identified that the choice of a varnish for a particular painting depended on the conservator's preference. The conservator's confidence in materials and their ability to use them effectively is dependent on their experience. With the use of a material the experience gained means they are more likely to use it in the future, while with material which they do not use they are not gaining the experience and the incentive to use again. A conservator's work can be identified by the constituent parts of a coating, provided there is previous knowledge of their work<sup>20</sup>.

Regalrez 1094 is particularly popular of the recent low molecular weight synthetic resins. It is capable of producing extremely glossy finishes<sup>57, 58</sup> and is extremely resistant to degradation<sup>44</sup>. Conservators who by trend use natural resins rather than Regalrez cite handling property differences as a reason for not switching, as Regalrez has lower viscosity when applying. The natural resin dammar is the first

choice for many conservators, while mastic is only used as a last resort by some conservators for varnishing particular surfaces<sup>55</sup>. Due to the stability of Paraloid B72 it is a popular choice if a matte coating is required or as a layer in a multiple layer coating with a glossier varnish. The reduced ketone resin MS2A became popular in the UK (place of manufacture) as it was the first low weight synthetic resin that gave a significant improvement in life span over natural resins, though this benefit has now been superseded. Laropal A81 is the most recent addition to the market. With low molecular weight and high stability it has the potential to become the main rival to Regalrez as the highest performing resin.

## 1.2 Optical properties of varnish

A varnish coating causes visual changes of the material it is applied to. Colour<sup>59</sup> is the detection and interpretation of a light spectrum returned from within a lateral resolution element by the eye. The eye (normally) consists of three (cone) types of receptors (plus rod receptors that don't have a role in colour vision) that have different relative sensitivity spectrums. The interpretation of these channels by the brain provides colour vision. For an object such as a painting the spectrum that is being interpreted is dependent on the illumination spectrum and the filtering by the reflectance of the object. To understand the source of the colour of a paint surface, and how it is modified by varnishes, two types of reflection of light need to be considered. These are surface scattering/reflections and volume scattering.

When light is initially travelling in a single direction and is incident on an optically smooth surface, the light is reflected in a defined (specular) direction dependent on the initial direction of travel of light and the direction of the normal of the surface. The fraction of light incident that is reflected is given by the Fresnel equations

$$R_s = \left( \frac{n_1 \cos \theta - n_2 \cos \phi}{n_1 \cos \theta + n_2 \cos \phi} \right)^2 \quad (1.2.1)$$

and

$$R_p = \left( \frac{n_2 \cos \theta - n_1 \cos \phi}{n_2 \cos \theta + n_1 \cos \phi} \right)^2, \quad (1.2.2)$$

$R_s$  is the fraction of energy reflected (reflection coefficient) of the incident light with electric field polarised in the plane of the surface.  $R_p$  is the reflection coefficient of light with electric field polarised perpendicular to  $R_s$  and direction of travel.  $n_1$  and  $n_2$  are the refractive indices of the two materials,  $\theta$  is the angle of incidence and  $\phi$  is resultant direction of travel through the second material, this is given by Snell's law

$$n_2 \sin \phi = n_1 \sin \theta. \quad (1.2.3)$$

The total reflected power fraction can be approximated (for any polarisation at near normal angles of incidence) by

$$R = \left( \frac{n_2 - n_1}{n_2 + n_1} \right)^2. \quad (1.2.4)$$

The intensity of reflected light from an interface is seen to be dependent on the refractive index difference between the two mediums (top term), which can vary over many orders of magnitude. The dependence on the bottom term is of less importance, as it can never be less (after squaring) than 4 and will rarely be higher than 12, limiting its maximum effect to a factor of 3.

If light is incident on an optically rough surface it can be reflected (or scattered) in any direction. The fraction of incident light intensity observed reflected from a surface, as a function of observation and illuminating angle, is the Bidirectional Reflectance Distribution Function (BRDF). Light reflected well away from the specular direction is considered the diffuse reflection. As the optical roughness of a surface increases, the ratio of diffuse to specular reflected light increases. Though it may be possible that the total reflected light is affected by the optically matte surface, this difference is not important to derive the difference in the optical properties<sup>60</sup> of varnishes and is not considered here. The important difference in the reflections, at interfaces with different roughnesses, is the fraction of light reflected/scattered diffusely.

The colour of paints comes from scattering and absorption of light by pigment particles within its volume<sup>61</sup>. The direction of scatter of light by these particles is independent of the direction of illumination. The modelling of the scattering and

absorption of light within the paint volume is beyond the scope of this thesis. The returned light, from the volume, is filtered by the wavelength dependent on absorption of the pigment, giving the coloured spectrum.

A varnished surface can be considered as an optical system. Figure 1.2.1 shows (a) an unvarnished and (b) a varnished rough painted surface, which are each illuminated by a single white light source and viewed by an observer. In figure 1.2.1 (a) the light is first incident on the paint – air interface. The typical refractive index difference at this interface will be 0.5 ( $n_{\text{air}} \approx 1$  and  $n_{\text{material}} \approx 1.5$ ), resulting in 4% of the light being reflected (from equation 1.2.4). As the interface is rough this light is diffusely scattered. The rest of the light enters the volume of the paint where it is adsorbed and scattered by the pigment particles. The coloured reflected light from the volume is also diffuse. The observer of the painting surface sees both the diffusively scattered coloured light from the volume of the paint and the diffusely reflected white light from the surface. The white light, from the surface, is an addition to the coloured spectrum, from the paint volume scattering. The resulting (sum of) spectrum observed (colour) is hence lighter and less chromatic.

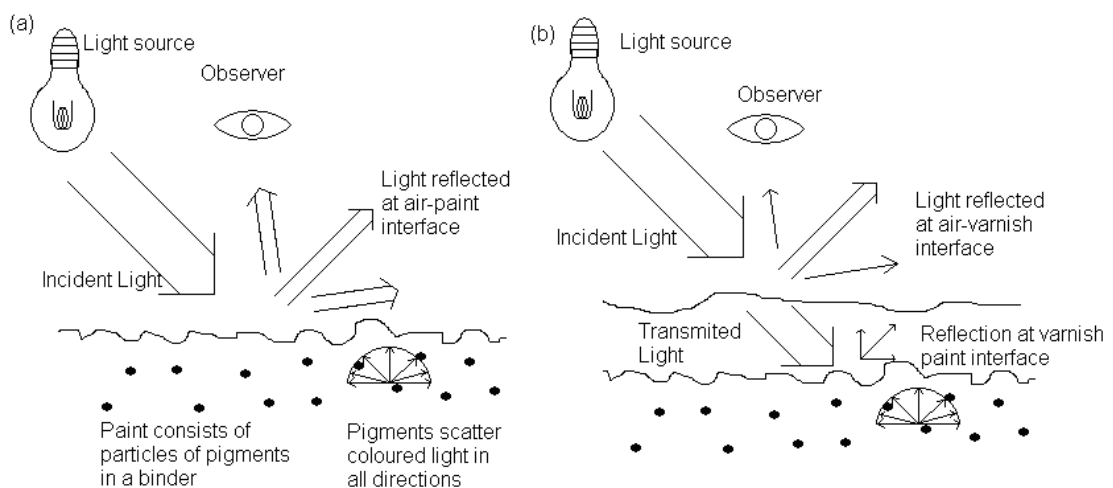


Figure 1.2.1  
Diagram of optical systems of observing (a)  
unvarnished and (b) varnished paint surfaces.

For a varnished painting surface (Figure 1.2.1 (b)), the light is first incident on the surface of the varnish. This is generally much smoother than the paint substrate<sup>58</sup>, meaning that a higher proportion of the light is specula reflected, though the total

amount of light is similar to the air – paint interface in the unvarnished sample as the refractive index difference is similar. The light is then incident on the varnish – paint interface, the maximum refractive index difference that would be expected here would only be 0.05. This would result in the maximum reflected amount of light being approximately 0.027 % of light incident (from equation 1.2.2.4), which is 150 times smaller than the uncoated painting interface. Though the reflection at this interface is still diffuse the total amount of light reflected is no longer significant to the observer. The light scattered from the volume of the paint is unchanged. The observer in the non-specular direction still observes the colour spectrum of light from the volume of paint, but the addition of diffusely reflected light from the surface has been reduced as this has now been reflected in the specular direction instead. The lack of addition of the white light means that the colour appears more chromatic (closer to the pigment transmission spectrum). The surface roughness of the varnish will determine how much diffusely reflected light comes from the surface so determines the final appearance.

The BRDFs of surfaces are more complicated functions, dependent on the properties of the surface roughness, than just a changing ratio of specular and diffusely reflected light. Gloss is the observed properties of surface reflection due to surfaces BRDF. Gloss can be characterised into six different quasi-subjective types<sup>62</sup>, they are

- specular gloss – total amount of light reflected in specular direction at low angles of incidence,
- sheen – as specular gloss but at grazing angles of incidence,
- distinction of image gloss – image clarity on reflection or transmission,
- contrast gloss (lustre) – contrast between reflections at random non-specular angles,
- haze – intensity of light reflected at small angular displacement from specular angle,
- macroscopic surface properties – features of lateral spatial frequency sufficiently large to be resolved directly by eye.

The perceived colour differences of a material due to change in gloss can be accurately modelled<sup>60</sup>.

The reflection of light from rough surfaces can be modelled in several ways, dependent on the roughness of the surface<sup>63, 64</sup>. For this project the precise scattering due to surface roughness is not considered, just the most generalised solution that diffuse scattering is dependent on spatial frequency of roughness and the amplitude of that frequency. The closer a spatial frequency component of roughness to the wavelength of light, and the greater the amplitude of that roughness component, the greater the diffuse scattering of light by that component will be. The total diffuse scattering will be the sum of the scattering due to all frequency components. Modelling of the change in the reflected spectra from an object due to the addition of surface roughness has been carried out<sup>65</sup> using a Kirchhoff (physical optics) derived approximation for the surface reflection<sup>66</sup>. The modelling was tailored to the backscattering geometry of the “goniospectrophotometer” instrument they used in their measurements. With the assumption of Gaussian surface statistics the variable of dependence within this model was  $h/l$ , where  $h$  is *rms* roughness and  $l$  is the auto correlation length of the surface. There was no dependence on the wavelength of light for this model. In comparison to the Fourier description, which will be used here, the increase in roughness amplitude is the same while the decrease in correlation length corresponds to net increase (towards the wavelength of light) in the spatial frequency of the roughness components.

Modelling of the transmission through varnish layers was originally attempted by a transparent layer on a diffusely reflecting background representing the paint<sup>67, 68</sup>, where the effect of the internal reflections and refractions dependent on the refractive index differences between the layers were modelled. In these two papers the interfaces are treated as planar with no inclusion of specific interface roughness terms. The inclusion of surface roughness into such models<sup>69, 70</sup> showed that it had much more impact on the reflected spectrum and resultant colour than variations in the refractive indices of the layers. These models provide the strong proof of the dominance of surface roughness effects over refractive index in the appearance of varnishes. However this modelling only considers varnish layers that are in complete optical contact (complete wetting) with the paint, to the authors knowledge no attempt has been made to include incomplete wetting into such

models. The relative effects of incomplete wetting in the appearance of a varnished paint layer are currently unknown.

A painting by definition is a visual object. It would have been constructed by the artist to look a certain way. The fact that the varnish coating affects the visual appearance makes it an integral part of the work. When a fresh varnish coating is applied by a conservator to a painting, the intended appearance of the work by the artist is an important factor in what material and application method is chosen. The precise debate on how to balance the desire for an authentic appearance with factors such as the best preservation of the object is a contentious issue<sup>71</sup>. The change in the optical appearance of other components, such as the paint, with degradation complicates the issue further. Should the closest material to the varnish used by the artist still be used, or should the degradation be compensated for to achieve the closest appearance desired by the artist<sup>72</sup>.

The purpose of this project is to develop and test the understanding of the physical processes that occur during the application and drying of varnish coatings that determine the final appearance. The better these processes are understood then the better a conservator is able to tailor their choice of materials and method to get the appearance they desired, while limiting drawbacks of the coating. This includes the selection of synthetic (stable) materials to mimic the appearance of natural resins (unstable).

### 1.3 Material properties and processes

To understand the processes which affect the final surface roughness of a varnish coating this section starts from a description of what a solvent varnish solution is at molecular level and the behaviour of the molecules at this level. It then introduces rheology and the process of evaporation. After the introduction of these crucial factors, the current knowledge of the levelling of drying varnish coatings is reviewed. Next other processes that may influence the appearance of a varnish coating are discussed. Finally the glass transition and dependence of physical properties of dry film on the solvent are discussed.

### 1.3.1 Physical description and thermodynamics of solutions

Figure 1.3.1.1 shows the behaviour of the solvent and solute (resin) molecules before and after mixing. The figure shows molecular movement and the intermolecular interactions (bonds). Before mixing the solvent (a liquid) molecules are free to move while the resin (a solid) molecules are not. After the resin is dissolved in the solvent both resin and solvent molecules are free to move. The ease of movement of the molecules is dependent on concentration. The total energy of the bonds contribute to the enthalpy,  $H$ , of the system, so the relative energies of the solvent-solvent, solute-solute and solvent-solute bonds are important to the formation of solutions.

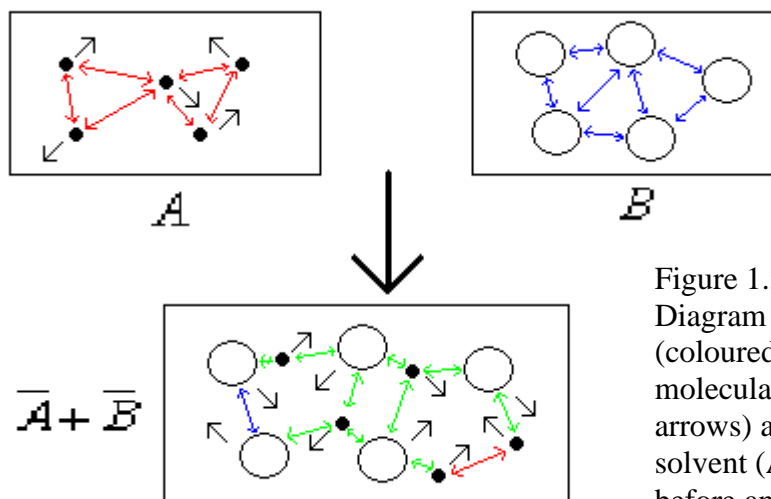


Figure 1.3.1.1  
Diagram of the molecular forces (coloured double ended arrows), molecular movement (black arrows) and total volume of a solvent (A) and solute (B), before and after mixing

The interaction of the solution can be considered and solved as a thermodynamics problem<sup>73</sup>. From figure 1.3.1.1, the temperature and pressure is constant in the system, the volume occupied in A is  $n_A V_{m,A}$ , where  $n_A$  is the moles of A and  $V_{m,A}$  is the volume occupied by one mole of pure A. Likewise the volume of B is  $n_B V_{m,B}$ . Upon mixing the total volume becomes  $n_A \bar{V}_A + n_B \bar{V}_B$  where  $\bar{V}_i$  is now the partial molar volumes. Note as pressure and temperature must be conserved, volume is not necessarily conserved. The volume change on mixing,  $\Delta V_{mix}$ , is defined by

$$\Delta_{mix} V = V(\text{after}) - V(\text{before}) = n_A (\bar{V}_A - V_A) + n_B (\bar{V}_B - V_B). \quad (1.3.1.1)$$

The molar volume of mixing is then given by

$$\Delta_{mix} V_m = \frac{\Delta_{mix} V}{n_A + n_B} = x_A \Delta_{mix} \bar{V}_A + x_B \Delta_{mix} \bar{V}_B, \quad (1.3.1.2)$$

where  $x_i$  is the molar fraction of each component.

Likewise the molar change on mixing for other thermodynamic properties, including enthalpy,  $H$ , entropy,  $S$ , and Gibbs,  $G$ , free energy, can also be defined. The molar change in Gibbs free energy of mixing is given by

$$\Delta_{mix} G_m = \Delta_{mix} H_m - T \Delta_{mix} S_m. \quad (1.3.1.3)$$

The decrease of Gibbs free energy drives the formation of the solution.

Where the interactions (bonds) between solvent-solvent, solute-solute and solvent-solute molecules are identical, the enthalpy change of mixing is zero (the mixing of the solution is driven entirely by entropy). This is known as an ideal solution where, in this case only, the volume change of solution is 0 and volume is conserved on mixing.

### 1.3.2 Diffusion coefficients

Diffusion<sup>74</sup> defines the mobility of a molecule. In a homogenous varnish solution the molecules are moving around in random walk paths, as time progresses they will travel an average distance away from the original position. The speed of this travel is the self diffusion coefficient,  $D_0$ , of the molecule. Knowledge of the self diffusion coefficients within a solution provides important information about the freedom of the individual molecules. If there is a gradient in concentration, the speed of inter-diffusion of the two molecular species into one another is determined by the mutual diffusion coefficient,  $D_{12}$ . The relationship between self diffusion and mutual diffusion can be complex. For a drying varnish film the mutual diffusion is important for the transport of the solvent to the surface as the solvent flux,  $J$ , is determined by Fick's first law<sup>74</sup>

$$J = -D_{12} \frac{dc}{dz}, \quad (1.3.2.1)$$

where  $dc/dz$  is the concentration ( $c$ ) ( $\text{mol/m}^3$ ) gradient across spatial dimension ( $z$ ).

The modelling of diffusion coefficients for polymer and solvent systems can be carried out<sup>75, 76, 77, 78</sup>. Molecular size and shape are important variables in the final values<sup>79</sup>. Self-diffusion is often inversely proportional to the macroscopic viscosity of the solutions. An example of this is the Stokes-Einstein equation for the Brownian diffusion of spherical particles within a liquid.

### 1.3.3 Rheology

Figure 1.3.3.1 is a diagram of a differential cross section of a liquid between two parallel planes, A and B, separated by distance,  $dz$ , and subject to a shear stress between the two plane,  $\sigma$ . The system is in a steady state with a velocity difference between the planes of  $dv$ . The relationship between the shear rate,  $dv/dz$ , and shear stress is

$$\frac{dv}{dz} = \frac{\sigma}{\eta}, \quad (1.3.3.1)$$

where  $\eta$  here is instantaneous viscosity. The most basic rheological behaviour of a liquid is Newtonian, where the instantaneous viscosity is constant at all times and all shear rates/stresses.

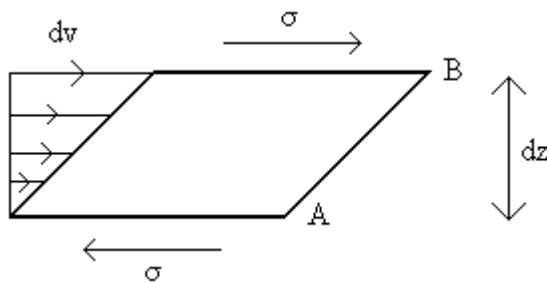


Figure 1.3.3.1  
Diagram to define  
instantaneous viscosity. See  
text for definitions.

Many liquids, including polymer solutions, can have a Rheology more complex than Newtonian under common conditions. Under certain extreme conditions it could be expected that any materials will show non-Newtonian properties (for example water is expected to show non-Newtonian behaviour at shear rates of  $10^{12} \text{ s}^{-1}$ <sup>80</sup>). Deviation from Newtonian behaviour can be shown in three different physical frames. Firstly in a steady state scenario shown in Figure 1.3.3.1 the instantaneous viscosity,  $\eta$ , can be dependent on the shear stress,  $\sigma$ . This can lead to behaviours such as shear

thickening, shear thinning and Bingham plastics. Away from a steady state scenario the viscosity can undergo temporal hysteresis with stress, for example thixotropic liquids are reduced in viscosity at a lower shear stress after the application of a large shear stress. Finally an oscillating shear stress can be applied to the liquid. For a Newtonian liquid the shear stress will always be proportional to velocity. However many liquids will behave viscoelastically in that the shear stress also contains an elastic (solid behaviour) component proportional to displacement. This leads to a phase displacement between the velocity and shear stress magnitude oscillations.

### 1.3.4 Film drying theory

This section briefly reviews the theory of how solvents evaporate from a varnish film. For a molecule of solvent to be removed from the varnish three processes must occur. These are illustrated in figure 1.3.4.1 (a – c). First the solvent molecule has to get from the volume of the varnish to the surface. As solvent is lost from the surface there must be a difference created between the surface concentration and the concentration within the volume. The system will tend back to a homogenous state by the diffusion of the solvent molecules. The evaporation and diffusion are both continuous processes and a concentration gradient will be set up within the film. The rate of transfer of the solvent through the volume is then determined by Fick's first law (equation 1.3.2.1).

When a solvent molecule reaches the surface it then has to evaporate, this is a thermodynamic process where the vaporisation pressure of the liquid solvent has to be in equilibrium with the solvent partial pressure in the adjacent atmosphere. The vaporisation pressure of a pure liquid is given by<sup>81</sup>

$$p_0 = BT \exp\left(\frac{-L}{RT}\right) \quad (1.3.4.1)$$

where B is a constant, L is the energy of vaporisation per mole (energy required to break intermolecular bonds of the solvent molecules), T is absolute temperature and R is the universal gas constant. This partial pressure for a solution is also dependent on the concentration. The simplest relationship is Raoult's law

$$p = C_{mol} p_0 \quad (1.3.4.2)$$

where  $C_{mol}$  is molar fraction of solvent, though for most solutions the relationship will deviate substantially from this. If there is a substantial flux of solvent evaporating from the surface, the energy required for this,  $L$ , will result in the lowering of the local temperature reducing the vapour pressure (equation 1.3.4.1). As a result of this the flow of heat to the surface also becomes an important parameter.

As the evaporation is dependent on the solvent partial pressure in the gas adjacent to the film, the rate of drying is also limited by the rate of removal of solvent molecules from the atmosphere adjacent to the coating. This transport mechanism is influenced by factors such as air flow over the surface and the use of vacuum chambers for drying.

The relationship of these three processes (diffusion of solvent to surface, evaporation of solvent and the gas transport of solvent away from the surface) in controlling the drying rate is analogous to electrical resistors in series. This is shown in Figure 1.3.4.1 (d). The flux of solvent is analogous to current (must be equal in the three processes when in steady state), the potential across the diffusion is the concentration gradient, the potential across evaporation is the energy required and the potential across removal is the slowness of gas transport. The resistance to drying of each step is proportional to the potential. The step with the highest resistance will have the highest resulting potential. For example if transport away from the surface is the main limiting factor then the concentration gradient in the film will be small.

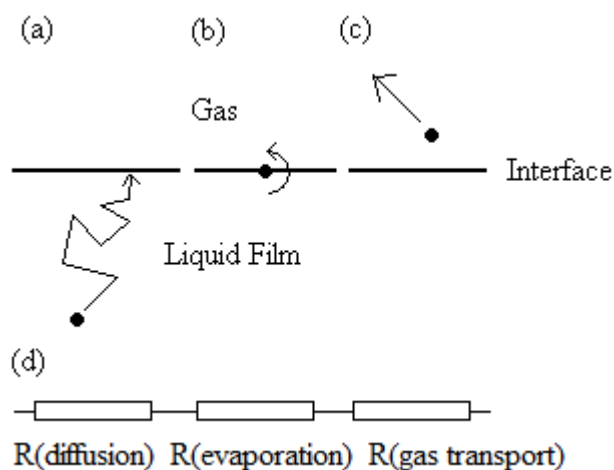


Figure 1.3.4.1  
Diagram of the three steps required by a solvent molecule to evaporate, (a) the diffusion to the surface, (b) Evaporation and (c) transport away. (d) Process analogy as an electrical circuit.

There has been previous studies<sup>82, 83, 84, 85, 86, 87, 88</sup> into the physics and modelling of the drying of glassy polymer films, including polymer varnishes. The glass transition within the material has a substantial effect on the diffusion of the solvent. This can lead to effects such as glass skinning trapping<sup>89</sup>, where a driven concentration gradient results in a glass skin to the film reducing the evaporation rate. The non-Newtonian rheology of the high molecular weight polymer films has to be taken into account when modelling the diffusion<sup>86</sup>. Most varnish resins in contrast to polymers are generally of lower molecular weight, the theoretical modelling of such solution may be simplified in comparison to polymers with the reduction of non-Newtonian dependencies. The author is not aware of any theoretical studies specific to the drying of low molecular weight resins.

In this context the physical state of a varnish over all concentrations (as it dries) can be considered. For high-weight polymer solutions the physical states passed through will be similar to the states of the polymer at different temperatures<sup>81</sup>. At low concentrations it may be regarded as viscous (Newtonian) liquid, at higher concentrations it will pass through viscoelastic liquids (rubbery) and viscoelastic solid before entering a glassy state. For a low molecular weight varnish the difference between the concentration above which the rheology is significantly non-Newtonian and the concentration above which the varnish is in a glass state, is presumably less than for polymer solutions. This is due to the smaller molecule being less like chains needed for viscoelastic behaviour of polymers.

### 1.3.5 Surface levelling

The early synthetic polymer resins (PVAes and acrylates, Section 1.1.4) provided coatings that were much more stable than natural resins, but did not produce the same optical appearance. As discussed in section 1.2 the difference in surface roughness of varnish coatings is the most favoured theory, from modelling, for this low chromatic appearance. Here the previous experimental work measuring the difference in roughness between different varnishes and previous models of the formations mechanisms of varnish surface roughness will be reviewed. The levelling of drying films has been more carefully considered in other areas of soft matter physics, such as for paint and spin coated polymers, than it has for varnish. The physical mechanism for the formation of roughness and methods of modelling it mathematically will be reviewed.

The reasoning for the formation of varnish roughness has previously been developed upon on a single “no-flow” point<sup>2,90</sup>. Here the varnish film is considered to be self levelling and remains flat and homogenous up until the “no-flow” point. Figure 1.3.5.1 (a) and (b), shows this initial evaporation of solvent that reduces the films volume. After the “no-flow” point each lateral point of the film is considered an independent column. These columns reduce in height as the remaining volume of solvent evaporates. Figure 1.3.5.1 (c) shows the result of this, which leads to the surface profile becoming a scaled version of the substrate profile, reducing the roughness. The greater the concentration when the “no flow” point occurs the lower the roughness. The concentration of the no flow point would be expected to be dependent on the viscosity of the solutions. The shrinkage of the drying film is assumed to occur in the vertical dimension only. This is fine within two limits. Firstly the lateral extent of the film is much greater than the film thickness and the edge of the film is pinned, this ensures there is no lateral contraction of the film. Secondly the substrate roughness is much less than the film thickness, ensuring the local vertical direction (the shortest distance from top to bottom interface) does not differ from the global vertical direction (the normal to the plane of the surface) significantly.

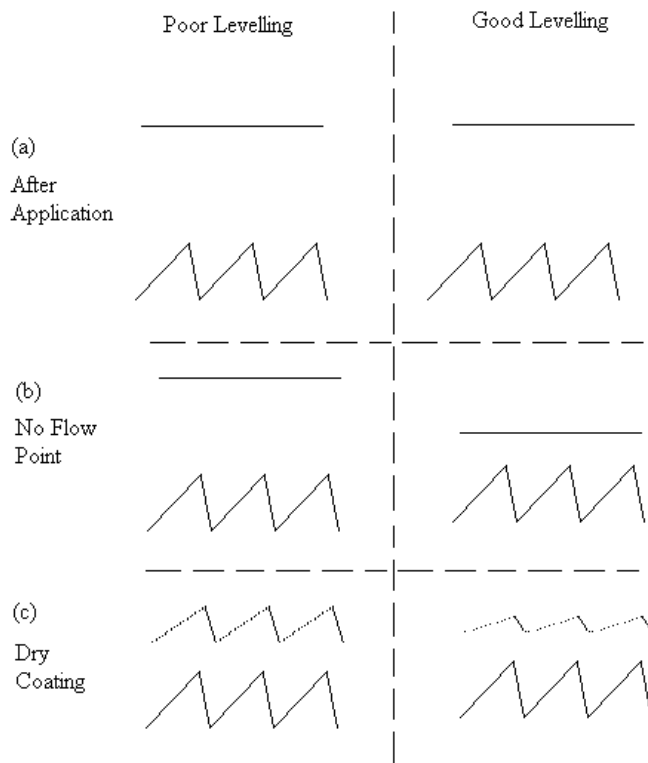


Figure 1.3.5.1  
 No flow point model for a poor and good levelling varnish.  
 (a) Starting conditions for both varnishes identical.  
 (b) No flow point for two varnishes, both still homogenous and flat surfaced but at different concentrations and hence thicknesses.  
 (c) After the no flow point the coating shrinks vertically with no flow or diffusion laterally until all solvent is gone.

The failings of this over simplified approach is highlighted when comparing the Power Spectrum Densities (amplitudes of the different Fourier components, see chapter 2 for definition) (PSD) of different varnish coatings and the substrates to which they are applied<sup>57</sup>. The single “no-flow point” model leads to just a scaled version of the substrate profile, likewise the PSD of this is also a scaled version. In reality all varnishes reduce the higher frequencies of roughness better than they reduce the low frequency roughness. The high molecular weight and low molecular weight varnishes differed in their levelling abilities across a range of spatial frequencies.

To explain the development of substrate dependent roughness in a drying varnish film a much more rigorous approach to the physics of the films is required. In other soft matter areas the behaviour of liquid films is well understood<sup>91, 92, 93</sup>. The shape inherited by a drying film from its substrate, such as varnish on a paint surface, is determined by the film’s levelling properties. Levelling properties are determined by the interplay of the process by which the film is shrinking to the surface and the process by which the film levels itself.

The reason why the varnish surface (or any liquid surface) tries to remain smooth is considered next. Surface tension/energy is the special case of interfacial tension/energy when the neighbouring material is a vacuum or the atmosphere. The classical explanation of interfacial tension and energy<sup>94</sup> considers the comparison of molecules within the volume of a liquid (or solid) and those at its interface. This is shown in figure 1.3.5.2. Within a volume of a liquid, a molecule's interactions with its neighbours are energetically favourable and hence each interaction can be described as a bond with energy. Across an interface the bonds between molecules are less strong (otherwise solvation would occur and it would not be an interface). Where this bonding is reduced at the interface it leads to an increase in energy of the system, the interface energy. Interface energy and tension are identical, but differ in how they are defined. When an interface is curved, the forces generated by interfacial tension create pressure. This is known as the Laplace pressure and is given by<sup>94</sup>

$$\Delta p = \frac{2\gamma}{R} \quad (1.3.5.1)$$

for a spherical interface, where  $\gamma$  is surface tension and  $R$  is the radius of curvature. The direction of curvature determines whether this is a negative or positive pressure. This pressure is the driving force of levelling flow. It can be seen that a surface, with lateral points with decreased radii of curvature, will undergo increased levelling flow. For Fourier components of the same amplitude, the higher frequency component will have the smaller *rms* curvature along its profile.

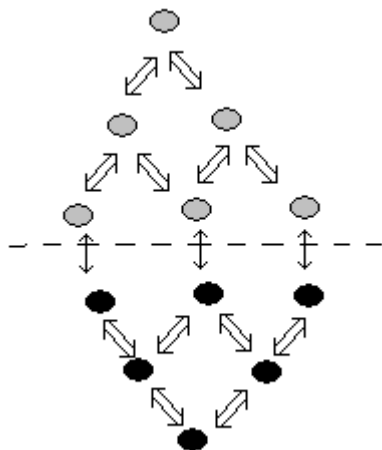


Figure 1.3.5.2  
Relative strength of  
intermolecular interactions at a  
material interface.

Gravity also acts upon the varnish coating. Conservator applied coatings are usually less than a few hundred microns thick. The vertical scale at which the effect of gravity becomes significant can be defined as being above the capillary length<sup>94</sup>

$$G = \sqrt{\frac{\gamma}{\rho g}}, \quad (1.3.5.2)$$

where  $\rho$  is density and  $g$  is local gravitational field ( $9.8\text{m/s}^2$ ). For most fluids this value is around the magnitude of a few mm (toluene = 1.8mm), therefore the effect of gravity can be ignored.

As the surface roughness of the varnish increases due to shrinkage with evaporation of solvent, the total surface area of the varnish increases. This increases the total surface energy of the system, which is not favoured. The Laplace pressures drive the levelling flow in the film to reduce the surface area. For Fourier components of roughness with high spatial frequency the radius of curvature is smaller and the total displacement of material needed to completely level the surface is less, so the effect of levelling is expected to be increased compared to low spatial frequencies.

The flow at any point in a fluid is calculable by resolving forces and momentum through the system. As compression of a drying varnish system is going to be negligible, so the resolution of these forces can be carried out by solving the incompressible Navier-Stokes equation<sup>95</sup>

$$\frac{dv}{dt} \rho + \rho.v.\nabla v + \nabla p = \eta \nabla^2 v, \quad (1.3.5.3)$$

where  $v$  is velocity,  $t$  is time,  $\rho$  is density,  $p$  is pressure and  $\eta$  is viscosity. The first term is the change of momentum with time, second term is change of momentum with position, third term is change of pressure with position and fourth term is resistance to flow due to viscosity. A lubrication approximation assumes that, as the velocities (momentum) within the drying film is small, so the first two terms of equation 1.3.5.3 can be ignored. The levelling flow is driven by the differential of the Laplace pressure and the resistance to the flow is proportional to the viscosity of the solution.

Analytical solutions of the rate of levelling of individual Fourier components (specific spatial frequencies) of roughness can be found dependent of viscosity<sup>96</sup> and the resultant functions have been used to explain the frequency dependent levelling of different varnishes<sup>58</sup>. However, the surface profile and properties of surface roughness of drying varnish films have not previously been modelled and compared with experimental results. Such work is needed to evaluate the accuracy of the theoretical derivations. The ability to model the final surface of a coating would be an important tool in developing and using synthetic varnishes to achieve desired appearances.

The levelling of coatings on textured substrates is also of interest in other fields. These include when films are spin coated<sup>97</sup> and how many polymer coatings are required to remove substrate defects in polymer mirrors<sup>98</sup>.

The main varnish parameter differentiating poor and good levelling varnishes has been identified as molecular weight<sup>22, 57</sup>. As can be seen from above, the viscosity of varnish solutions is expected to have a large influence on the levelling. A link can be made between the molecular weight of the varnish resin and the viscosity of the varnish solution. Away from art conservation the dynamic behaviour of polymers molecules in solution is an important part of the polymer field<sup>99</sup>, with implications to all industrial practices which handle these solutions. The general relationship between the resin molecular weight and viscosity is that viscosity increases with molecular weight, though molecular weight is by no means the only factor.

For infinitely dilute solutions of a specific solution of a polymer and solvent the relationship between molecular weight,  $M_v$  (viscosity average), and intrinsic viscosity,  $[\eta]$  is given by the Mark-Houwink equation<sup>100</sup>

$$[\eta] = KM_v^a, \quad (1.3.5.4)$$

where  $K$  and  $a$  are constants specific to the polymer-solvent combination. Some physical interpretation of these constants can be made<sup>100, 101</sup>. Intrinsic viscosity is defined by

$$[\eta] = \lim_{C_m \rightarrow 0} \frac{\eta(C_m) - \eta_0}{\eta_0 C_m}, \quad (1.3.5.5)$$

where  $C_m$  is mass concentration,  $\eta$  is viscosity of solution and  $\eta_0$  is the viscosity of the pure solvent. The intrinsic viscosity determines the viscosity contribution of the polymer for dilute solutions.

Molecular weight is not the only physical parameter of a polymer chain. Polymer chains are not necessarily linear but may branch. A polymer that is branched will have a different intrinsic viscosity of the same polymer that is not<sup>102</sup>.

Away from infinite dilution, the relationship of viscosity with molecular mass and concentration becomes more complex<sup>103, 104, 105</sup>. Large polymers can be thought of behaving like an elastic chain. With increased the concentrations these chains can entangle restricting their free movement. Then increasing concentration further the polymer chains will get to a point where they can only move by Reptation<sup>106</sup>, where a chain can not move side ways due to the presence of adjacent chains but the ends of the chain have a small enough cross section to pass through the gaps, pulling the rest of the chain through space it already occupies. These effects lead to high viscosity and viscoelastic properties of the solution, rather than it being a Newtonian liquid. Most varnish resins used are of low molecular weight so entanglement effects can be expected to be negligible.

Varnish resins molecules are not of uniform mass but instead the resins have a molecular mass distribution. A histogram of the molecular mass distribution provides qualitative information, but to get quantitative comparable values four different weighted averages are used

$$M_n = \frac{\sum M_i N_i}{\sum N_i}, M_w = \frac{\sum M_i^2 N_i}{\sum N_i M_i}, M_z = \frac{\sum M_i^3 N_i}{\sum N_i M_i^2}, M_v = \left[ \frac{\sum M_i^{1+a} N_i}{\sum N_i M_i} \right]^{\frac{1}{a}} \quad (1.3.5.6)$$

where  $M_n$  is number average,  $M_w$  is weight averaged,  $M_z$  is z averaged and  $M_v$  is viscosity averaged molecular masses, with  $a$  being the constant from equation 1.3.5.4. For a monodisperse material all these values are the same. Polydispersity

(spread of molecular mass distribution) is usually quantified as  $M_w/M_n$ . Importantly polydispersity has an influence on viscosity<sup>107</sup>. The measurement of molecular weight distribution of various varnish resins in current use has recently been carried out<sup>22, 44</sup>. The viscosity-concentration functions are crucial to the levelling properties of varnishes. Research to establish the relationship between the statistics of the resin molecular mass and properties of the viscosity-concentration function is important. This will allow the future tailoring of molecular mass distribution of synthetic resins in order to achieve the desired levelling and handling properties.

### 1.3.6 Other factors that influence appearance

Though surface levelling is likely to be the main process that differentiates varnish appearance, there are other material properties and processes that may be important. Here these properties and processes are briefly reviewed.

From the consideration of the varnish as an optical system, in section 1.2, refractive index is an important part of the system, however it has been shown that the refractive index differences between varnishes are insignificant compared to surface roughness<sup>69, 70</sup>. The refractive index of various paint media, including varnishes, has previously been experimentally measured for a selection of 19<sup>th</sup> C paintings<sup>108</sup>. This provides an overview of the refractive indices of oil painting material, including the change of refractive indices with degradation.

All current modelling of varnishes as an optical system assume that the varnish perfectly wets the paint substrate to which it is applied. The possibility that this may not always be the case has been recognised for a long time<sup>23, 109</sup>, though no evidence has previously been found and the possibility has been ignored. If air pockets do exist at the varnish-paint interface, this may have a significant effect on appearance. The topic of the wetting of the complex rough substrate by the varnish is also closely related to its continued adhesion<sup>110</sup> throughout the life of the coating.

In addition to limited levelling there are other causes of surface texture in drying coatings. These lead to defects in the appearance, often descriptively labelled as orange peel, which are undesirable in industrial coatings. As a result there already

exists a large body of work covering the physical processes<sup>52, 111, 112</sup>. The two main physical processes are convection (Bénard<sup>113</sup>) cells and flow driven by surface tension gradients across the surface (Marangoni effect). In a drying film Bénard convection cells can form (see Figure 1.3.6.1 (a)) as the solvent evaporates from the surface causing axial inhomogeneities. These convection cells result in lateral inhomogeneities in the system. Lateral in-homogeneities at a liquid surface result in surface tension differences and gradients. These surface tension gradient results in a force driving flow from areas of low surface tension to areas of high surface tension. This is shown in figure 1.3.6.1 (b).

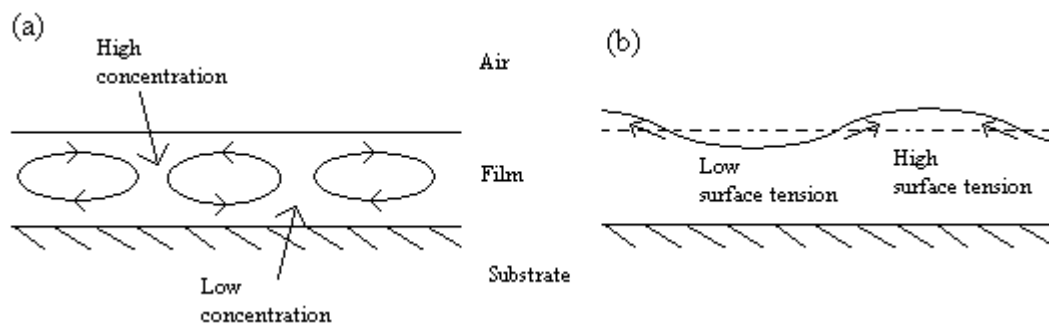


Figure 1.3.6.1  
Diagrams of  
(a) Bénard convection cell  
and (b) Marangoni flow  
within drying films.

These two effects in coatings are now usually considered together as Marangoni-Bénard convection. The pattern formed by the effect is dependent on the components of the film<sup>114</sup>. Like the levelling of drying film on rough substrates, these effect can also be modelled by the lubrication approximation to the Navier-Stokes equation<sup>115, 116</sup>. The formation of craters in coatings is an extreme example of such effects and is modelled in a similar way<sup>117</sup>. The spatial wavelengths of these Marangoni-Bénard defects are generally at mm or higher. These are too long to contribute to scattering roughness (may be considered a smooth wavy surface rather than rough) and as a result the Marangoni-Bénard effect is not of direct interest to this project.

Bloom is a defect that occurs during the drying of coatings that leads to a hazy appearance. The likely cause in most cases of this defect appears to be the condensation of contaminants and water at the surface during drying or after,

leading to a roughening of the surface. This defect is most prevalent in humid conditions or where there is a change in temperature. Though research into this effect has been identified as important<sup>2</sup> the author is not aware of a large amount of recent research specific to the effect. Though this defect will impact on the optical appearance that this project is working on, it is regarded as an independent problem (with independent solutions) and is not considered.

The final appearance consideration is that a drying varnish film is a liquid body. Hence some magnitude of capillary waves (ripples) will be present<sup>118</sup>. The expected size of these waves and the impact that they would have on the varnish surface after it has past through the glass transition temperature is negligible. No experimental work has contradicted this expectation.

### 1.3.7 Glass transition

The evaporation of solvent leaves behind the final coating of resin. Solvent varnish resins are amorphous glasses, rather than crystalline solids. The reason that varnishes are not made of crystalline materials is simply that the crystallisation of a coating during drying would lead to a fractured structure and rough surface (consider a salt solution as it dries) which would not give the desired optical properties.

The arrangement of molecules in glasses is essentially the same random arrangement that would be found at single point in time in a liquid<sup>119</sup>. The transition from a non-solid state to the solid glass state is generally considered by decreasing the material through the glass transition temperature,  $T_g$ . At  $T_g$  the material undergoes a thermodynamic phase transition. Below this temperature the material can not undergo viscous deformation (of significant magnitude over realistic timescales) when a shear stress is applied, but will fracture instead if the material is overloaded. The glass state is a true solid, while above  $T_g$  materials can be categorised by their Rheological behaviour.

The resins used as solvent varnishes all have their  $T_g$  just above room temperature<sup>44</sup>. The reasoning for these values is a balance of the properties of the final coating. If a

varnish is above its glass transition temperature then it cannot be described as being truly dry (solid). Dirt which lands on the surface of such a coating can become imbedded inside the material<sup>2</sup> and the coating may be tacky to the touch<sup>45</sup>. However a mechanical property of glasses is high brittleness, which is not ideal for a physical protective coating. The glass transition temperatures of the varnish resins are not necessarily completely discrete, meaning that some modification of the material properties towards a less brittle state may be present close to the glass transition temperature.

The varnish coating does not undergo thermal glass transition as it solidifies but must undergo an equivalent transition as the concentration changes by solvent evaporation. As the concentration of resin increases within a varnish film, the rate of evaporation of solvent decreases. At high concentrations the evaporation of solvent becomes slow. Small amount of solvent may remain within the film for long periods of time<sup>2</sup> or trace amount even indefinitely. If the varnish film is in a glass state the solvent molecules maybe considered trapped between the stationary resin molecules. After undergoing a glass transition the molecules in a material are not necessarily static, but their position can relax into lower energy states leading to changes in physical properties<sup>120, 121</sup>, this is known as physical ageing.

### 1.3.8 Solvent effects on final film

The retention of amounts of solvent in a dry varnish film has been introduced above. Any amount of solvent in a film may be assumed to affect the properties of a varnish film. However backwards interpretation of observation to this assumption comes with a warning, the author's discussions with conservators and conservation scientists revealed that they are under the impression that Regalrez's affinity to some solvents, meaning that solvent is retained longer, is the reason why it remains sticky for a long time (slow drying). However the stickiness of Regalrez 1094 has been shown to exist when there is absolutely no solvent present<sup>45</sup> so is of a more direct cause of the resin rather than slowness in drying.

However there is another solvent mechanism that can influence the mechanical properties of a varnish film after there is absolutely no solvent remaining. For large

polymers in solution the radius of gyration (*rms* spread of monomers from the centre of the molecule) is dependent on solvent<sup>33</sup>. The energetic favourability between solvent-monomer and monomer-monomer intermolecular bonding determines how much polymer molecules spread (open out) in solution. For the case of an ideal solution, between the solvent and monomer molecules, the solvent for the polymer is known as a theta solvent. If the solvent-monomer interaction is energetically favourable the solvent is classed as good and the polymer will open up. If the solvent-monomer interaction is unfavoured the polymer will coil up more and the solvent is classed as poor. The radius of gyration of polymer molecules in a glassy film will be expected to be retained after the solvent has evaporated, this can affect material properties of dry film. These effects have been studied for polymer varnish films<sup>4, 46</sup>.

## 1.4 Summary

So far in this chapter the context and content of this project have been introduced. The research aims of this project were:

- Measure the properties of varnish solutions at macroscopic and molecular levels and be able to relate them to the varnish solutions molecular composition.
- Develop an OCT multi-interface profilometry method to dynamically measure the surface profile development of a drying varnish, and the profile of the substrate directly underneath in the same measurement.
- Model the dynamic profile of a drying varnish from the starting conditions and material properties only. The modelling accuracy is to be confirmed with the experimental results of the multi-interface profilometry method.
- The agreement of the modelling and measured dynamic surface profiles (point above) will confirm that surface roughness development in varnish (and other films) coatings match the assumed theoretical model.

- Evaluate the importance of different factors of varnish coating (thickness, initial concentration, resin and solvent) in the development of surface roughness.
- Evaluate whether the trends found in controlled experiments match with trends found for real conservator applied coatings.
- Produce and evaluate evidence for other causes of light scattering, which will affect relative appearance between varnish coatings.

To present the research undertaken, to achieve these aims, this thesis is divided into the following chapters.

**Chapter 2** shows the selection and development of OCT for multi-interface profilometry. The accuracy of this technique was analysed for many different interfaces, and comparison to other broadband interferometry profilometer techniques is made. This included determining the accuracy of the technique for measuring the rough varnish-substrate interfaces crucial to this study.

To provide the refractive index values, needed for the correction of internal interfaces (*i.e.* varnish-substrate interface), in **Chapter 3** the measurements of the dynamic refractive index of drying materials is presented. This measurement was carried out utilising the multi-interface OCT profilometry technique.

**Chapter 4** presents the use of NMR for the study of the molecular behaviour within varnish solutions and evaluates the technique for the measurement of solvent content within drying varnish films. The molecular behaviour measured was firstly the mobility (self-diffusion) of the resin and solvent molecules, within varnish solutions as they dry. Secondly it was used to provide some information on the molecular interactions of the solvent and resin molecules. Thirdly the potential use of NMR/MRI for the non-invasive measurement of remaining solvent content in real varnish coatings was evaluated.

**Chapter 5** presents the measurement of the rheology of different varnish solutions. This examines the effect of the choice of resin and solvent on the rheology across the measurable range of concentrations.

**Chapter 6** measures (with multi-interface OCT profilometry) and models (using the viscosity-concentration functions measured in chapter 5) the levelling of different varnish coatings on rough substrates. A comparison of these is made. The effect of choice of resin, applied and final thickness, and choice of solvent is made.

**Chapter 7** examines the optical properties of conservator applied coatings. The surface roughness of the different coatings is measured, and these results are compared to the previous findings of the thesis. This was done to see how well the results from controlled scientific setups matched reality. In this section, the significance of two other scattering sources within a varnish system was examined. Firstly differences in the wetting/penetration of conservator applied coating was serendipitously found. Secondly the magnitudes of scattering from within the volume of aged varnishes were measured.

## 1.5 References

---

<sup>1</sup> Presbyter Theophilus, *On Divers Arts : the foremost medieval treatise on painting, glassmaking and metalwork / Theophilus ; translated from the Latin with introduction and notes by John G. Hawthorne and Cyril Stanley Smith*, Dover (1979).

<sup>2</sup> Feller Robert L., Stowlow Nathan and Jones Elizabeth H., *On Picture Varnishes and their Solvents*, National Gallery of Art, Washington (1985).

<sup>3</sup> De la Rie E. Rene, "The Influence of Varnishes on the Appearance of Paintings", *Studies in Conservation*, 32 (1), 1-13 (1987).

<sup>4</sup> Hansen Eric F., Derrick Michele R., Schilling Michael R. and Garcia Raphael, "The effects of solution application on some mechanical and physical properties of thermoplastic amorphous polymers used in conservation: Poly(vinyl acetate)s", *JAIC*, 30 (2), pp. 203-213 (1991).

<sup>5</sup> Bauer Roland S., Marx Edward J. and Watkins Michael J., Ed. Koleske Joseph V., "Epoxy Resins in Coatings" in *Paint and coating testing manual: fourteenth edition of the Gardner-Sward*, American society for testing and materials (1995).

---

<sup>6</sup> Caley Tom, "Aspects of Varnishes and the cleaning of oil paintings before 1700", Cleaning, retouching and coatings: Contributions to the 1990 IIC Congress, Brussels pp 70-72 (1990).

<sup>7</sup> Lucas A., "Ancient Egyptian Materials and Industries", Third Edition, The St Annes Press (1948).

<sup>8</sup> Reference to Chang Chien, General Chinese History, Vol. I, p. 194, Commercial Press, Shanghai (1934). in TIAO-HSIN WANG, "THE CHINESE VARNISH OF THE SUNG DYNASTY", *Artibus Asiae*, 11 (1/2), pp111-114 (1948). Original reference not found.

<sup>9</sup> Nicholson Paul T. and Shaw Ian, *Ancient Egyptian Materials and Technology*, Cambridge University Press (2000).

<sup>10</sup> Eastlake Charles Lock, *Methods and Materials of the Great Schools and Masters*, Dover Publications inc (2001).

<sup>11</sup> Koleske Joseph V, "Drying Oils" in *Paint and Coating testing manual*, 14<sup>th</sup> Edition, American Society for testing and materials (1995).

<sup>12</sup> Wheeler D. H., "The Chemistry of Drying Oils", *The Journal of the American Oil Chemists' Society*, 27 (11), pp 440-445 (1950).

<sup>13</sup> Mérimée Jean-François-Léonor and Taylor William Benjamin Sarsfield, *The art of painting in oil and in fresco*, Gilbert and Rivington Printers London (1839).

<sup>14</sup> Carlyle Leslie, "British Nineteenth-Century Oil Painting Instruction Books: A Survey of Their Recommendations for Vehicles, Varnishes and Methods of Paint Application." *Cleaning, Retouching, and Coatings, Preprints of the Contributions to the IIC Brussels Congress, 3-7 September 1990*, pp. 76-80 (1990).

<sup>15</sup> Mills John S. and White Raymond, *The organic chemistry of museum objects*, Second edition, Butterworth and Heinmann, (1994).

<sup>16</sup> Langenheim Jean H., "Plant resins: chemistry, evolution, ecology, and ethnobotany", Timber Press inc (2003).

<sup>17</sup> De la Rie E. René, *Stable varnishes for old master paintings*, PhD Thesis, University of Amsterdam (1988).

<sup>18</sup> Papageorgioua V.P, Bakola-Christianopouloua M.N, Apazidoua K.K and Psarrosb E.E, "Gas chromatographic–mass spectroscopic analysis of the acidic triterpenic fraction of mastic gum", *Journal of Chromatography A*, 769 (2), pp 263-267 (1997).

<sup>19</sup> Van de Berg Class Jan, van de Horst Jerre, Boon Jaap J and Sudeijer Olof O., "Cis-1,4-poly- $\beta$ -myrcene; the structure of the polymeric fraction of mastic resin

---

(*Pistacia lentiscus* L.) elucidated”, *Tetrahedron Letters*, 39 (17), pp 2645-2648 (1998).

<sup>20</sup> White Raymond and Kirby Jo, “A survey of nineteenth-and early twentieth-century varnish compositions found on a selection of paintings in the National Gallery Collection”, *The National Gallery Technical Bulletin*, 22, pp 64 – 84 (2001).

<sup>21</sup> Mayer Ralf, *The artists handbook of materials and techniques*, Fourth Edition, faber and faber (1987).

<sup>22</sup> de la Rie E. René, Delaney John K., Morales Kathryn M., Maines Christopher A. and Li-Piin Sung, “Modification of Surface Roughness by Various Varnishes and Effect on Light reflection”, *Studies in Conservation*, 55 (2), pp. 134-143 (2010).

<sup>23</sup> Thomson Garry, “Some Picture Varnishes”, *Studies in Conservation*, 3 (2), pp 64 - 67 (1957).

<sup>24</sup> Gettens George, Rutherford John and Stout Leslie, “*Painting materials: a short encyclopaedia*”, Dover Publications (1966).

<sup>25</sup> Mayer Lance and Myers Gay, “A Note on the Early Use of Dammar Varnish”, *Studies in Conservation*, 47, pp. 134-138 (2002).

<sup>26</sup> Silvestre Armando J. D. and Gandini Alessandro, *Terpenes: Major Sources, Properties and Applications*, in *Monomers, polymers and composites from renewable resources*, Eds. Belgacem Mohamed Naceur and Gandini Alessandro, Elsevier (2008).

<sup>27</sup> De la Rie E. René, “Photochemical and Thermal Degradation of Films of Dammar Resin”, *Studies in Conservation*, 33 (2), pp. 53-70 (1988).

<sup>28</sup> Cavicchioli Andrea and de Faria Dalva L.A., “Impedance analysis of varnish-modified crystal quartz resonators coupled with FT-IR and FT-Raman: Assesment of the environmental impact on artistic materials in conservation sites”, *Sensors and Actuators B*, 115, pp. 656-665 (2006).

<sup>29</sup> Michalski Stefan, “A physical model of the cleaning of oil paint”, *Cleaning, retouching and coatings: Contributions to the 1990 IIC Congress, Brussels* pp 85-92 (1990).

<sup>30</sup> Erhardt David and Tsang Jia-sun, “The extractable components of oil paint films”, *Cleaning, retouching and coatings: Contributions to the 1990 IIC Congress, Brussels*, pp. 93-97 (1990).

<sup>31</sup> Sutherland Ken, “Measurements of Solvent Cleaning Effects on Oil Paintings”, *Journal of the American Institute for Conservation*, 45 (3), pp. 211-226 (2006).

<sup>32</sup> Hedley G., Odlyha M., Burnstock A., Tillinghast J. and Husband C., “A study of the mechanical and surface properties of oil paint films treated with organic solvents

---

and water”, *Journal of Thermal Analysis and Calorimetry*, 37 (9), pp. 2067-2088 (1991).

<sup>33</sup> Geede Ulf W., *Polymer Physics*, Kluwer Academic Publishers (1999).

<sup>34</sup> Gettens Rutherford J., “Polymerized vinyl acetate and related compounds in the restoration of objects of art”, *Technical Studies in the Field of the Fine Arts*, 4, pp 15-27 (1935).

<sup>35</sup> Feller Robert L., “New Solvent-type varnishes”, *Recent advances in conservation contributions to the IIC Rome conference 1961*, pp 171 -175 (1963).

<sup>36</sup> Chiantore O. and Lazzari M., “Photo-oxidative stability of paraloid acrylic protective polymers”, *Polymer*, 42, pp 17-21 (2001).

<sup>37</sup> Flory Paul J., *Principles of Polymer Chemistry*, Cornell University Press (1953).

<sup>38</sup> Routledge Vincent, “The Development of MS2A Reduced Ketone Resin in Painting Conservation”, *WAAC Newsletter*, 22 (2), (2000).

<sup>39</sup> De la Rie E. René and Shedrinsky Alexander M., “The Chemistry of Ketone Resins and the Synthesis of a Derivative with Increased Stability and Flexibility”, *Studies in Conservation*, 34 (1), pp 9-18 (1989).

<sup>40</sup> Sigma-Aldrich Catalogue, Product number 468541, polycyclohexanone, [http://www.sigmaaldrich.com/catalog/ProductDetail.do?D7=0&N5=Product%20No.%7CBRAND\\_KEY&N4=468541%7CALDRICH&N25=0&QS=ON&F=SPEC](http://www.sigmaaldrich.com/catalog/ProductDetail.do?D7=0&N5=Product%20No.%7CBRAND_KEY&N4=468541%7CALDRICH&N25=0&QS=ON&F=SPEC), Accessed 22/03/11.

<sup>41</sup> De la Rie E. René and McGlinchey, Christopher W., “New synthetic resins for picture varnishes”, *Cleaning, retouching and coatings: Contributions to the 1990 IIC Congress, Brussels*, pp 168-173 (1990).

<sup>42</sup> Leonard Mark, “Some observations on the use and appearance of two new synthetic resins for picture varnishes”, *Cleaning, retouching and coatings: Contributions to the 1990 IIC Congress, Brussels* pp 174-176 (1990).

<sup>43</sup> Whitten Jill, “Regalrez 1094: Properties and uses”, *WAAC Newsletter*, 17 (1), (1995).

<sup>44</sup> Maines Christopher M. and de la Rie E. Rene, “Size-exclusion chromatography and differential scanning calorimetry of low molecular weight resins used as varnishes for paintings”, *Progress in Organic Coatings*, 52, pp. 39-45 (2005).

<sup>45</sup> Piena Hans, “Regalrez in Furniture Conservation”, *Journal of the American Institute for Conservation*, 40 (1) pp 59-68 (2001).

- 
- <sup>46</sup> Opena Mareike and Jagers Elisabeth, “Effects of Solvents on the Physical Properties of Polymeric Films”, Poster given at Cleaning 2010: new insights into the cleaning of paintings, (2010).
- <sup>47</sup> Donth Ernst-Joachim, *The glass transition: relaxation dynamics in liquids and disordered materials*, Springer (2001).
- <sup>48</sup> Fox Thomas G. and Flory Paul J., “Second-Order Transition Temperatures and Related Properties of Polystyrene. I. Influence of Molecular Weight”, *J. Appl. Phys.* 21 (6), pp 581-592 (1950).
- <sup>49</sup> Obichukwu Mathew, “Comparative Study of Synthesis Procedures for Urea – Formaldehyde Resins (Part I)”, *Leonardo Electronic Journal of Practices and Technologies*, 9, pp 63-80 (2006).
- <sup>50</sup> Christjansona Peep, Pehkb Tõnis, and Siimera Kadri, “Structure formation in urea-formaldehyde resin synthesis”, *Proc. Estonian Acad. Sci. Chem.*, 55 (4), pp 212-225 (2006).
- <sup>51</sup> de la Rie E. René, Lomax Suzanne Quillen, Palmer Michael R. and Maines Christopher A.. "An Investigation of the Photochemical Stability of Films of the Urea-Aldehyde Resins Laropal® A 81 and Laropal® A 101." In 13th Triennial Meeting of the ICOM Committee for Conservation, Rio de Janeiro, September 2002, vol. 2, edited by Roy Vontobel, 881–887. London: James and James (Science Publishers) Ltd., 2002.
- <sup>52</sup> Orr Edward W., *Performance enhancement in coatings*, Carl Hanser Verlag (1998).
- <sup>53</sup> De la Rie, E. René and McGlinchey Christopher W., “Stabilized dammar picture varnish”, *Studies in Conservation*, 34 (3), pp 137 – 146 (1989).
- <sup>54</sup> Bourdeau James, “A further examination of the barrier properties of tinuvin 327 ultraviolet absorber in the protection of dammar films”, *Cleaning, retouching and coatings: Contributions to the 1990 IIC Congress, Brussels*, pp 165-167 (1990).
- <sup>55</sup> Tomlinson Hayley, Spring Marika and Other Conservators, *Private Communication*, National Gallery, London.
- <sup>56</sup> American Institute for Conservation of Historic and Artistic Works and Samet Wendy, *Painting Conservation Catalog: Varnishes and surface coatings*, AIC (1998).
- <sup>57</sup> Elias Mady, de la Rie E. René, Delaney John K., Charron Eric and Morales Kathryn M., “Modification of the surface state of rough substrates by two different varnishes and influence on the reflected light”, *Optics Communications*, 266 (2), pp. 586-591 (2006).

- 
- <sup>58</sup> Delaney John K., de la Rie E. René, Elias Mady, Sung Li-Piin and Morales Kathryn M., “The Role of Varnishes in Modifying Light Reflection from Rough Surfaces”, *Studies in Conservation*, 53 (3), pp. 170-186 (2008).
- <sup>59</sup> Berns Roy S., Billmeyer and Saltzman’s *Principles of color technology*, Third Edition, John Wiley & Sons inc (2000).
- <sup>60</sup> Dalal Edul N. and Natale-Hoffman Kristen M., “The Effect of Gloss on Color”, *COLOR research and application*, 24 (5), pp. 369-376 (1999).
- <sup>61</sup> Bentley J. and Turner G. P. A., *Introduction to paint chemistry and principles of paint technology*, Chapman and Hall (1998).
- <sup>62</sup> O’Donnell Francis X. D. and Billmeyer Fred W. Jr., Eds. Rennilson Jay J. and Hale W. N., “Psychometric Scaling of Gloss” in *Review of Evaluation and Appearance Methods and Techniques*, American Society for Testing and Materials (1986).
- <sup>63</sup> Ogilvy J. A., *Theory of wave scattering from random rough surfaces*, IOP Publishing Ltd (1991).
- <sup>64</sup> Beckmann Petr and Spizzichino, *The scattering of electromagnetic waves from rough surfaces*, Artech House inc (1987).
- <sup>65</sup> Simonot Lionel and Elias Mady, “Color Change Due to Surface State Modification”, *COLOR research and application*, 28 (1), pp. 45-49 (2003).
- <sup>66</sup> Elias Mady and Menu Michel, “Experimental characterization of a random metallic rough surface by spectrophotometric measurements in the visible range”, *Optics Communications*, 180 (4-6), pp. 191-198 (2000).
- <sup>67</sup> Elias Mady, Simonot Lionel and Menu Michel, “Bidirectional reflectance of a diffuse background covered by a partly absorbing layer”, *Optics Communications*, 191, pp. 1-7 (2001).
- <sup>68</sup> Simonot Lionel and Elias Mady, “Color Change Due to a Varnish Layer”, *COLOR research and application*, 29 (3), pp. 45-49 (2004).
- <sup>69</sup> Berns Roy S. and de la Rie E. Rene, “The Effect of the Refractive Index of a Varnish on the Appearance of Oil Paintings”, *Studies in Conservation*, 48 (4), pp. 251-262 (2003).
- <sup>70</sup> Elias Mady, Simonot Lionel, Thoury Mathieu and Frigerio Jean Marc, “Bi-directional reflectance of a varnished painting Part 2: Comparison between the effects of the refractive indices, of the surface states and of the absorption of the varnish – experiments and simulations”, *Optics Communications*, 231, pp. 25-33 (2004).

- 
- <sup>71</sup> Dykstra S. W., "The artists intentions and the Intentional Fallacy in Fine Arts Conservation", *Journal of the American Institute for Conservation*, 35 (3), 197-218 (1996).
- <sup>72</sup> Katz Kenneth B., "The artist's intention and the varnishing of German Expressionist paintings: two case studies", *Cleaning, retouching and coatings: Contributions to the 1990 IIC Congress, Brussels*, pp. 158-159 (1990).
- <sup>73</sup> Stølen Svien and Grande Tor, *Chemical Thermodynamics of Materials*, John Wiley and sons (2004).
- <sup>74</sup> Tyrrell H. J. V. and Harris K. R., *Diffusion in Liquids*, Butterworth & Co (1984).
- <sup>75</sup> Vrentas J. S. and Duda J. L., "Reexamination of the Free-Volume Theory", *Journal of Polymer Science*, 15, pp. 403-416 (1977).
- <sup>76</sup> Vrentas J. S. and Duda J. L., "Diffusion in Polymer-Solvent System. II. A Predictive Theory for the Dependence of Diffusion Coefficients on Temperature, Concentration, and Molecular Weight", *Journal of Polymer Science*, 15, pp. 417-439 (1977).
- <sup>77</sup> Duda, J. L., Vrentas J. S., Ju S. T. and Liu H. T., "Prediction of Diffusion Coefficients for Polymer-Solvent Systems", *AIChE Journal*, 28 (2), pp. 279-285 (1982).
- <sup>78</sup> Zielinski John M. and Duda J. L., "Predicting Polymer/Solvent Diffusion Coefficients Using Free-Volume Theory", *AIChE Journal*, 38 (3), pp. 405-415 (1992).
- <sup>79</sup> Iwahashi Makio and Kasahara Yasutoshi, "Effects of Molecular Size and Structure on Self-Diffusion Coefficient and Viscosity for Saturated Hydrocarbons Having Six Carbon Atoms", *Journal of Oleo Science*, 56 (8), pp. 443-448 (2007).
- <sup>80</sup> Lieberman Norman P. and Lieberman Elizabeth T., *Working guide to process equipment*, second edition, McGraw-Hill (2003).
- <sup>81</sup> Tabor D., *Gases, liquids and solids and other states of matter*, Third Edition, pp. 343-345, Cambridge University Press (1991).
- <sup>82</sup> Errede L. A., "Polymer Drying. IV. A molecular Interpretation of Polymer Drying", *Journal of Polymer Science: Part A*, 28, pp. 857-870 (1990).
- <sup>83</sup> Errede L. A., Henrich P. J. and Tiers George V. D., "Polymer Drying. X. A Reconsideration of the Kinetics of Evaporation from Polymer-Liquid Systems During the Interval of Transition from the Rubbery to a Glassy State", *Journal of Applied Polymer Science*, 54, pp. 669-696 (1994).
- <sup>84</sup> Alsoy Sacide and Duda J. L., "Drying of Solvent Coated Polymer Films", *Drying Technology*, 16, pp.15-44 (1998).

- 
- <sup>85</sup> Alsoy Sacide and Duda J. Larry, "Modeling of Multicomponent Drying of Polymer Films", *AIChE Journal*, 45 (4), pp. 896-905 (1999).
- <sup>86</sup> Cairncross Richard A. and Durning Christopher J., "A Model of Drying of Viscoelastic Polymer Coatings", *AIChE Journal*, 42 (9), pp. 2415-2425 (1996).
- <sup>87</sup> Dubreuil A.C., Doumenc B., Guerrier B. and Allain C., "Drying of polymer varnishes: Solvent diffusion in glassy polymer films", 12<sup>th</sup> Int. Heat and Mass Transfer Conf., (2002).
- <sup>88</sup> Tsige Mesfin and Gest Gary S., "Solvent evaporation and interdiffusion in polymer films", *J. Phys.: Condens. Matter*, 17, pp. S4119-S4132 (2005).
- <sup>89</sup> Edwards David A., "An asymptotic analysis of polymer sorption and skinning", *Macromol. Theory Simul.*, 8, pp. 10-14 (1999).
- <sup>90</sup> Bruxelles G. N. and Mahlman B. H., "Glossiness of Nitrocellulose Lacquer Coatings", *Official digest – Federation of Paint and Varnish Production Clubs*, 351, pp. 299-314 (1954).
- <sup>91</sup> Quach A. "Polymer Coatings. Physics and Mechanics of Leveling", *Ind. Eng. Chem. Prod. Res. Develop.*, 12 (2), pp. 110-116 (1973).
- <sup>92</sup> Myers T. G., "Thin Films with High Surface Tension", *SIAM Rev.*, 40 (3), pp. 441-462 (1998).
- <sup>93</sup> Weinstein Steven J. and Ruschak Kenneth J., "Coating Flows", *Annu. Rev. Fluid Mech.*, 36, pp. 29-53 (2004).
- <sup>94</sup> de Gennes Pierre-Gilles, Brochard-Wyart Françoise and Quéré David, *Capillarity and Wetting Phenomena*, Springer (2004).
- <sup>95</sup> Doering Charles R. and Gibbon J. D., *Applied analysis of the Navier-Stokes Equations*, Cambridge University Press (1995).
- <sup>96</sup> Orchard S. E., "On surface levelling in viscous liquids and gels", *Appl. Sci. Res.*, 11 (A), pp. 451-464 (1962).
- <sup>97</sup> Gu J., Bullwinkle M. D. and Campbell G. A., "Spin Coating on Substrate with Topography", *J. Electrochem. Soc.*, 142 (3), pp. 907-913 (1995).
- <sup>98</sup> Mollenhauer David and Camping John, "Multilayered Polymer Mirror Experiment", *Journal of Spacecraft and Rockets*, 39 (5), pp. 691-694 (2002).
- <sup>99</sup> Yamakawa Hiromi, *Modern theory of polymer solutions*, Harper & Row (1971).
- <sup>100</sup> Sperling L. H., *Introduction to Physical Polymer Science*, Fourth Edition, John Wiley and Sons (2006).

- 
- <sup>101</sup> Munk Petr and Halbrook Micheal E., “Intrinsic Viscosity of Polymers in Good Solvents”, *Macromolecules*, 9 (3), pp. 441 – 446 (1976).
- <sup>102</sup> Bohdanecký M., “A Semiempirical Formulation of the Effect of Random Branching on Intrinsic Viscosity”, *Macromolecules*, 10 (5), pp. 971 – 975 (1977).
- <sup>103</sup> Doolittle Arthur K., “Studies in Newtonian Flow. IV. Viscosity vs Molecular Weight in Liquids; Viscosity vs Concentration in Polymer Solutions”, *Journal of Applied Physics*, 23 (4), pp. 418-426 (1952).
- <sup>104</sup> Freed F. Karl and Edwards S. F., “Polymer viscosity in concentrated solutions”, *The journal of chemical physics*, 61 (9), pp. 3626-3633 (1974).
- <sup>105</sup> Muthukumar M, “Viscosity of polymer solutions”, *J. Phys. A: Math. Gen.*, 14, pp. 2129-2148 (1981).
- <sup>106</sup> Hess Walter, “Generalized Rouse Theory for Entangled Polymeric Liquids”, *Macromolecules*, 21, pp. 2620-2632 (1988).
- <sup>107</sup> Rubinstein Micheal, Helfand Eugene and Pearson Dale S., “Theory of Polydispersity Effects on Polymer Rheology. Binary Distribution of Molecular Weights”, *Macromolecules*, 20, pp. 822-829 (1987).
- <sup>108</sup> Townsend Joyce H., “The Refractive Index of 19<sup>th</sup>-Century Paint Media: A Preliminary Study”, *ICOM Committee for Conservation 1993, Vol II*, pp. 586-592 (1993).
- <sup>109</sup> Feller Robert L., “Factors affecting the appearance of picture varnish”, *Science*, 125 (3258), pp. 1143-1144 (1957).
- <sup>110</sup> Packham D. E., “Surface energy, surface topography and adhesion”, *International Journal of Adhesion & Adhesives*”, 23, pp. 437-448 (2003).
- <sup>111</sup> Patton Temple C., *Paint Flow and Pigment Dispersion*, 2nd Edition, John Wiley & Sons inc (1979).
- <sup>112</sup> Kornum L. O. and Nielsen H. K. R., “Surface defects in drying paint films”, *Progress in Organic Coatings*, 8, 275-324 (1980).
- <sup>113</sup> Bénard H., *Rev. Gen. Sci. Pure Appl.* 11, 1261 (1900).
- <sup>114</sup> Abbasian A., Ghaffarian S. R., Mohammadi N., Khosroshani M. R. and Fathollahi, “Study on different planforms of paint’s solvents and the effect of surfactants (on them)”, *Progress in Organic Coatings*, 49, pp. 229-235 (2004).
- <sup>115</sup> Howison S. D., Moriarty J. A., Ockendon J. R., Terrill E. L. and Wilson S. K., “A mathematical model for drying paint layers”, *Journal of Engineering Mathematics*, 32, pp. 377-394 (1997).

---

<sup>116</sup> Eres M. H., Weidner D. E. and Schwartz L. W., “Three-Dimensional Direct Numerical Simulation of Surface-Tension-Gradient Effects on the Leveling of an Evaporating Multicomponent Fluid”, *Langmuir*, 15, pp. 1859-1871 (1999).

<sup>117</sup> Evans P. L., Schwartz L. W. and Roy R. V., “A Mathematical Model for Crater Defect Formation in a Drying Paint Layer”, *Journal of Colloid and Interface Science*, 227, pp. 191-205 (2000).

<sup>118</sup> Kim Hyunjung, Ruhm A., Lurio L. B., Basu J. K., Lal J., Lumma D., Mochrie S. G. J. and Sinha S. K., “Surface Dynamics of Polymer Films”, *Physical Review Letters*, 90 (6), 068302 (2003).

<sup>119</sup> Zarzycki J., *Glasses and the vitreous state*, Cambridge University Press (1991).

<sup>120</sup> Hodge Ian M., “Physical Aging in Polymer Glasses”, *Science*, 267, pp. 1945-1947 (1995).

<sup>121</sup> Mahajana Dhiraj K., Estevezb Rafael and Basu Sumit, “Ageing and rejuvenation in glassy amorphous polymers”, *Journal of the Mechanics and Physics of Solids*, 58 (10), pp. 1474-1488 (2010).

## 2. OCT multi-interface profilometry

### 2.1 Introduction

The aim of this project was the understanding, and the ability to predict, differences in optical properties between different varnish coatings. A major part of this was the formation of substrate induced surface roughness during drying. There are a large number of techniques that are used for the measurement of surface profiles and roughness. For the measurement and comparative modelling (of the development of roughness during drying) carried out in this project, it was necessary to be able to measure both the varnish-air and varnish-substrate profiles simultaneously through the drying process, with suitable accuracy.

#### 2.1.1 Interface profiles and roughness quantification

Profilometry is the measurement of profiles and the acquisition of statistical values of roughness from these profiles<sup>1,2</sup>. A 2 dimensional (2D) interface profile is the measurement of the axial position ( $z$ ) of an interface as a function of a single lateral dimension,  $z(x)$ , while a 3 dimensional (3D) interface profile is a function of both lateral dimensions,  $z(x,y)$ . In this work generally only 2D measurements are taken and likewise modelling systems are only 2D. One important aspect of this definition of the interface profiles is that there is only one interface position at any lateral coordinate which may not match reality (further discussion given in chapter 7.1). To compare different profile measurements, it is necessary to extract comparable numerical value from the profiles. The first processing step is the subtraction of the plane of the surface from the profile. With the profile level several approaches can be used to “measure” the roughness. To extract a single value to quantify the roughness of the profile, an average modulus distance of displacement of the profile positions from the plane of the surface can be taken. There are several mathematical methods of doing this including average roughness

$$R_a = \frac{1}{N} \sum_{i=1}^N |z_i|, \quad (2.1.1.1)$$

*rms* roughness

$$R = \sqrt{\frac{1}{N} \sum_{i=1}^N z_i^2} \quad (2.1.1.2)$$

and the peak to peak roughness (highest - lowest positions). In this project *rms* roughness is used as the quantified value.

The problem with average roughness values is that they do not provide any information on the lateral spacing of features in the profile. For example take two sinusoidal surfaces of different periods, one 1mm and the other 1 $\mu$ m, but same peak to peak amplitude. As long as the profiles measured are much greater than the period of the lowest frequency surface, the average roughness values of these surfaces will be identical even though the profiles and optical properties are much different. Alternative methods exist to characterise the roughness of the surface profile dependent on spatial roughness. The first of these is the auto-covariance, *G*, (or auto-correlation if normalised), this is given by<sup>2</sup>

$$G(l) = \frac{1}{N} \sum_{i=1}^{N-l} z_i z_{i-l} , \quad (2.1.1.3)$$

where *l* is the amount of lagged points (lagged length is *l* times the distance between adjacent points) and *N* is the total amount of points on the profile. This function takes two copies of the profile, lags the position between them and takes the product. Figure 2.1.1.1 shows an example lagged profile (to show definition of *l*) and the example profiles auto-covariance function. The lag length that the auto-covariance function falls to 1/e of its value at *l*=0 is the correlation length of the surface, and can be regarded as the intrinsic period of the surface. The discrete Fourier Transform (Appendix 1) of the auto-covariance function (symmetric, from  $-Nl$  to  $Nl$ ) is mathematically the same as the PSD (see below). However note that in the calculation of the auto-covariance an effective window is being applied to the surface (as the sum of the product is being divided by the original profile length rather than the amount of profile points in the calculation at that lag length). Hence the calculation of PSD via auto-covariance produces fewer artefacts than direct calculation via an un-windowed discrete Fourier transform of the surface profile<sup>2</sup>.

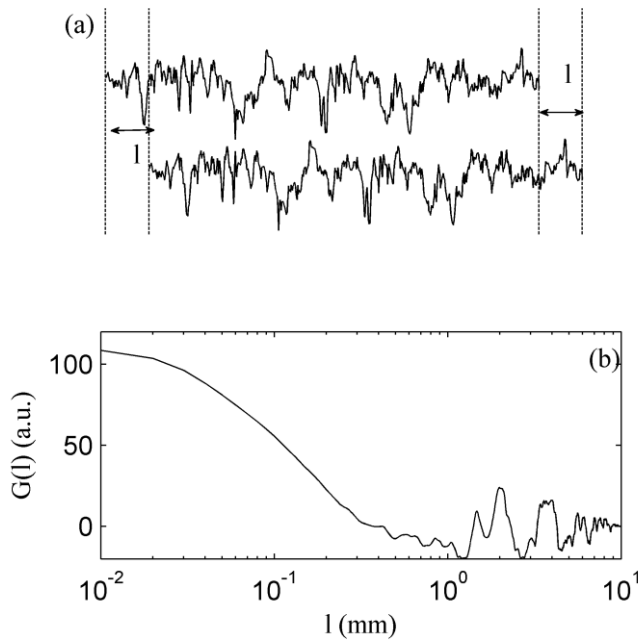


Figure 2.1.1.1  
 (a) Diagram of two copies of a surface profile (axially displaced for viewing) displaced by a lag distance ( $l$ ) for calculation of the auto-covariance function.  
 (b) The calculated auto-covariance function ( $G(l)$ ) for the example surface profile.

Power Spectral Density (PSD) uses the fact that a discrete function can be constructed by the sum of a series of discrete sinusoids (discrete Fourier transform) with different frequencies, amplitudes and phases. The definition of PSD comes from the signal processing field, where the electric field of a wave times by its complex conjugate give its total power. The definition of the PSD,  $P$ , of a surface profile is given by

$$P(u) = DFT(z(x)).DFT(z(x))^* = |DFT(z(x))|^2, \quad (2.1.1.4)$$

where  $u$  is spatial frequency and DFT is the discrete Fourier transform. The result is the power (magnitude) of the roughness at each spatial frequency. Differences in magnitude and spatial properties between rough surfaces will both be highlighted when comparing PSDs. In this project MATLAB is used to carry out the discrete Fourier transform using a fast Fourier transform (FFT) algorithm. To overcome sectioning artefacts within the PSD, a Gaussian window is used on the profiles before calculation (Appendix 1).

The final method, which is used in this project to quantify roughness at different spatial frequency, is the use of FFTs to apply spatial frequency band pass filters. After Fourier transforming the profile, unwanted spatial frequencies were set to 0

and the data inverse Fourier transformed back into the profile. The *rms* roughness of this profile, containing only the selected spatial frequencies, was then taken.

## 2.1.2 Review of available techniques

Most techniques that measure surface profiles can be split into two classes. Firstly contact mechanical profilometry methods and secondly a variety of non-contact optical techniques. Mechanical profilometry is a standard way of measuring roughness. Figure 2.1.2.1 is a diagram of a mechanical (or stylus) profiler. It consists of a stylus, with a tip fine which is kept in contact with the surface by a small force while being scanned across the surface. The vertical displacement of the stylus is measured by a linear variable differential transformer (LVDT) or optical transducer<sup>1</sup>. The height accuracy of the system is determined by the accuracy of the sensor and vibrational stability of the system. In a measurement of varnished surfaces this was  $10\text{nm}^3$ .

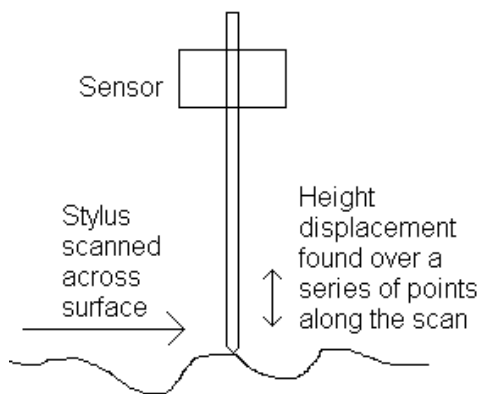


Figure 2.1.2.1  
A diagram of a mechanical profiler.

The relative size and shape of the stylus tip, to the real surface profile, determines the path of the stylus over the surface and hence measured profile. The effect of the stylus size on measured profiles has been measured<sup>4</sup> and can be modelled<sup>5</sup>. Features of smaller lateral dimensions than the stylus tip will be filtered out. The size of stylus profilometer tips vary from radii between  $20\text{nm}^6$  and  $25\mu\text{m}$ . In this project there was access to a Veeco Dektak 6M with a stylus tip size of  $12.5\mu\text{m}$  radius. There were two main disadvantages for the use of mechanical profilometry in this project. Both of these are due to being a contact method. Firstly there is always the potential to damage the sample that is being measured and secondly the technique has no potential to be used at any interface other than the top surface.

Though Atomic Force Microscopy (AFM) <sup>7</sup> was developed from Scanning Tunnelling Microscopy (STM), for profilometry it can be regarded as a highly refined mechanical profiler, with a very small stylus tip and high axial sensitivity due to measurement by laser deflection. As a result, it is often used as the reference technique for studies in the performance of convention mechanical profilometry and optical techniques<sup>4</sup>. For the measurement of varnish roughness, this technique was not used as the lateral range of measurements (of the available instrument) was not sufficient. As well as profilometry, the adaptability of AFM technique means that it can be used to measure the mechanical properties of dry films as well<sup>8</sup>.

The first category of optical profilometry is focus detection, where the axial position of a surface is measured, at a lateral position, by measuring where the reflection from the surface is in focus. Of these techniques confocal microscopy<sup>9</sup> is the most common and powerful. Figure 2.1.2.2 shows an example of a confocal system. The pinhole apertures in the system significantly reduce the amount of unfocused light reaching the detector. This means that the majority of light being detected only comes from within the instrument resolution of the point in three dimension space being measured. This three dimensional resolution element can be described as a voxel. The position of this voxel can be scanned through a sample to produce three dimensional tomographic imaging. To measure the position of a surface, fitting can be carried out to the axial point spread function of the surface in the same manner as is done for this project with OCT.

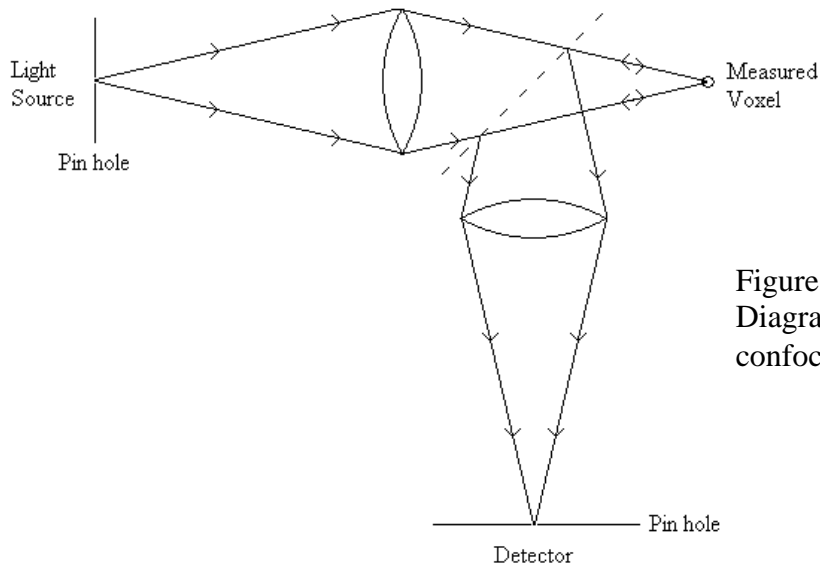


Figure 2.1.2.2  
Diagram of a typical  
confocal setup.

Confocal microscopy is a potential alternative method for carrying out the multi-interface profilometry work carried out by OCT (or any other broadband interferometric method) in this project. However there are some important differences in capabilities of the two methods. OCT has much greater sensitivity than confocal microscopy<sup>10</sup>. The multi-layer profilometry of a polymer coating on a substrate has previously been done with confocal microscopy<sup>11</sup>, however the substrate used was metal with a reflection coefficient approaching unity (100%), giving easy identification of the signal. Compare this with the expected  $\sim 0.027\%$  Fresnel reflection for a varnish - paint binder interface. The amplitude of reflection from a glass-varnish interface will be similar. For the experimental work carried out in this thesis, where varnishes are applied to a ground glass substrate, the amplitude of reflection from the Fresnel reflection, at the varnish-glass interface, is much smaller than has previously been used to measure an interface with confocal microscopy.

The second group in optical profilometry is the use of interferometry to achieve axial ranging. Figure 2.1.2.3 shows a diagram of a generic Michelson type interferometer. In this work Michelson type will refer to any optical interferometer with separate sample and reference paths where their return paths are quasi-identical to the forward path. As such includes Michelson, Linnik and Mirau setups but does not include Mach-Zander and Fabry-Perot.

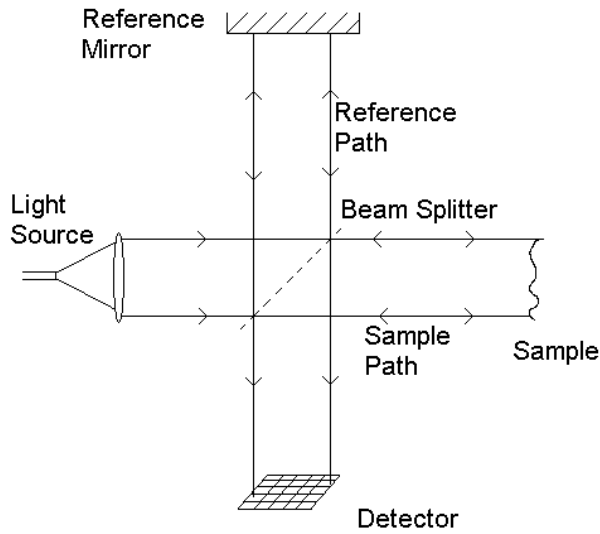


Figure 2.1.2.3  
Principle of  
generic Michelson  
type interferometer

Phase Shifting Interferometry<sup>12</sup> (PSI) is a highly precise method (commercial accuracies are as good as  $0.1\text{nm}^{13}$ ) that recovers relative axial positions from the phase of the interferogram. A Michelson type interferometer (Figure 2.1.2.3) is used with a monochromatic light source. The detector records the intensity,  $I$ , of the signal (this is usually done with a 2D CCD or CMOS camera with full field optics to measure all the 3D surface profile at once). The relative path length difference between the sample and reference path are changed by a fraction,  $1/N$ , of the wave length of the light,  $\lambda$ . From these intensities the relative phase of the interferogram can be calculated. An example of such an equation for four quarter wavelength step measurements is given by

$$\phi = -\tan^{-1} \left[ \frac{I_4 - I_2}{I_1 - I_3} \right]. \quad (2.1.2.1)$$

The difference of the phase, between adjacent lateral points, can then be equated to the difference between the path lengths, hence the surface height. However this is only a relative measurement. If the surface height difference of two adjacent measured points is greater than a quarter of the wavelength of the light, the absolute displacement between them is lost. In these cases PSI will be unable to distinguish the surface heights correctly. The resulting errors are called phase ambiguities. These errors mean that the technique is unable to measure surfaces with significant roughness, slopes or discontinuities.

To overcome the problems of PSI measurements there is a different interferometric approach that can be used. White Light (or broadband) Interferometry (WLI)<sup>14, 15, 16</sup> uses light with a broad bandwidth, hence low temporal coherence. In an interferometer, interference is only measurable when the path length difference of light is within the coherence length of the measured light. To achieve axial ranging in a Michelson type interferometer (figure 2.1.2.3) the relative path difference between the reference mirror and sample arm is scanned. When the reference path is within the coherence length of the reflection from the sample an interferogram will be formed. Figure 2.1.2.4 gives a simulated interferogram from a reflection from a surface. The centre of the coherence envelope corresponds to the position of the surface. In WLI profilometry this position is found with high accuracy and the value returned to the user.

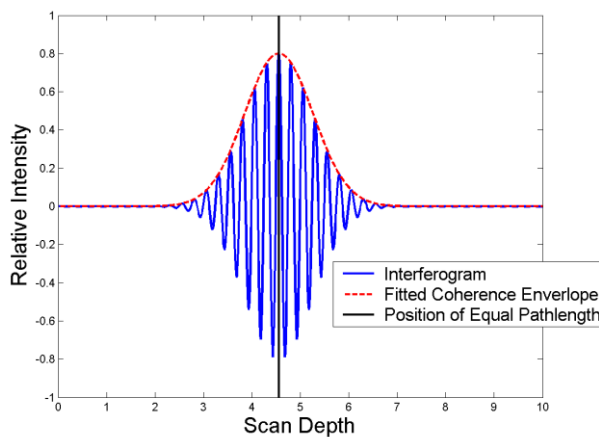


Figure 2.1.2.4  
Simulated TD  
white light  
interferogram.

The acquisition of the ranging information by changing the relative path lengths of the arms of the interferometer is known as Time Domain (TD). Axial ranging information can be recovered, without displacement of the path lengths, by measuring the spectrum of the returned light. This is known as Fourier (or Frequency) Domain (FD). The mathematical derivation of how this works is given in the OCT introduction below (section 2.1.3). Profilometry with FD instruments has only seen recent limited use<sup>17, 18</sup>.

WLI can distinguish between reflections separated by axial differences greater than the coherence length of the instrument. This means that it is capable of measuring multi-interface profiles<sup>19</sup>. Away from profilometry, the same instrument can be used to return to the user the amount of coherence signal as a function of 3D position to

produce tomographic images. When WLI instruments are optimised for the purpose of imaging, it is known as Optical Coherence Tomography (OCT)<sup>20</sup>. This optimisation also improves its potential for multi-interface profilometry. OCT is introduced below (section 2.1.3).

WLI does not have as good as accuracy as PSI, a typical quoted accuracy of a commercial system is  $3\text{nm}^{13}$ . When measuring rough surfaces with multiple sample path lengths within the resolution voxel of the instrument, the technique is subject to profile artefacts<sup>21, 22</sup>. If the surface in question is a regular rough surface these errors can be described as diffraction<sup>22</sup> related, while if the surface is randomly rough then the description would be speckle<sup>23</sup> error. The accuracy and reduction of artefacts of WLI can be improved by the incorporation of phase measurement<sup>24</sup>.

A Veeco Inc. Wyko NT1100 has been used in this project (mainly for validation and comparison of the OCT profilometry method developed). This instrument can be set up to undertake WLI or PSI measurements. It uses a thermal halogen lamp source (filtered for PSI). The result of using this light source was that the instrument not sensitive enough (requires 1 % reflection) to detect most interfaces that were to be measured in this project.

The third class of optical profilometry is the projection of a known pattern upon the object. The surface profile is then reconstructed from the measured distortions of the pattern. There are a wide variety of methods of pattern projection and reconstruction of the surface. These methods have been widely applied for the measurement of works of art and archaeological objects<sup>25, 26, 27, 28, 29, 30, 31, 32</sup>. These techniques are generally used to measure objects of scales greater than is measured in this work. The accuracy of these technique ranges from 100s of microns<sup>31</sup> to an axial precision of  $1\mu\text{m}^{30}$ , though in this case lateral resolution is 0.5mm. As a result of the poor lateral resolution and axial precision of these techniques they are not suitable for the work of this project.

Surface roughness statistics can be measured without the measurement of the profile itself. The bidirectional reflectance distribution function (BRDF) of the surface contains the information on the surface properties. This is exploited to measure

roughness statistics in gloss meters, Total Intergrated Scattering (TIS), Angle Resolved Scattering (ARS) and diffractometers (optical Fourier transform of surface reflection)<sup>2,33</sup>.

In the field of thin films<sup>34</sup> (in this context a solvent deposited varnish film would be regarded as a “thick” film), ellipsometry<sup>35</sup> is a powerful technique to deduce multiple properties of films from their reflection of polarised light. The ideal conditions for this technique are uniform films with little interface roughness, which is not the case for real varnish coatings and measurement of surface roughness development. As a result the technique has not been used in this project. It has been used previously to measure varnish coatings in a laboratory environment<sup>36</sup>.

The majority of conventional profilometry instruments are only able (and designed) to measure the surface of samples. A major requirement for this project is the measurement of weakly reflecting internal interfaces. Though confocal microscopy<sup>11</sup> and (non OCT system based) WLI<sup>19</sup> do have the potential for measuring multiple interfaces near simultaneously, the lack of sensitivity of the available instruments meant they were unable to meet the needs of the project. To provide the required capability, a multi-interface profilometry method, using a commercial FD OCT, system was developed.

### 2.1.3 Optical Coherence Tomography (OCT) for multi-interface measurement

OCT is broadband interferometry that has been optimised for tomographic imaging. The main purpose of the technique<sup>37,38,39</sup> has been to give video rate images for bio-medical use, particularly in vivo. As a result of this purpose the focus of development of the technique has been on sensitivity. The choice of light sources, of OCT systems, is an important criterion to achieve this sensitivity. The high sensitivity allows the weak scattering within a bio-medical sample to be distinguished from noise and artefacts in very rapid measurements. This high sensitivity of the method allows reflections of many orders of magnitude to be measured (high dynamic range). Like WLI profilometry, the early OCT systems were Time Domain. However the desire for faster sensitive systems has meant that

the use of Fourier Domain<sup>40</sup> methods, including with a spectrometer or swept source laser, have taken a large part of the market, unlike for WLI profilometry.

Though OCT is primarily a bio-medical imaging technique, its use in different fields has been established<sup>10</sup>, including in art conservation and archaeology<sup>41, 42</sup>. Qualitative imaging of dried<sup>41</sup> and drying<sup>43</sup> has previously been carried out. The high sensitivity of OCT allows faint interfaces, such as the matte glass-varnish interfaces used in this project, to be seen. All visible interface (with strong and consistent (along its profile) enough signal) within an OCT image can be processed in the same generic manner as the raw signal within a WLI profilometer. This will give the profile of those interfaces with high accuracy. This ability allows the measurement of varnish-ground glass interfaces while simultaneously measuring the profile of the varnish surface directly above. These two profiles can then be directly compared dynamically, to show how the two are related during drying.

The potential of the use of OCT instruments for profilometry is only starting to be realised. Recently the use of a time domain ultra high resolution OCT to measure the topography of glossy paper<sup>44</sup> produced a standard deviation of 60nm of the position of peak signal, but went no further in exploring the error of the profilometry for different surfaces. The use of FD OCT for profiles of canvas paintings and measuring varnish thickness has previously been published<sup>41</sup> but without a focus on achieving sub-resolution accuracy. This project is the first work exploiting OCT to measure the profiles of two interfaces simultaneously with the highest accuracy.

Figure 2.1.3.1 shows the three main setups used in OCT systems. The original design of OCT systems was a Time Domain (TD) setup like most WLI profilometry methods, with a scanning reference mirror to get the depth information (Figure 2.1.3.1 A). Though this is still a popular OCT set up, alternatively, a Fourier Domain (FD) interferometric setup can be used to retrieve the same axial information<sup>37</sup>. The reference mirror is fixed and the light returned is measured with a spectrometer (Figure 2.1.3.1 B). The Fourier transform of this spectrum contains the axial structural information of the sample. FD OCT is a popular method due to the need for rapid video rate measurement as a biomedicine imaging technique. This is due to the inherent improvement in signal to noise over the time domain method<sup>45</sup>.

A variation on the Fourier domain principle is the use of a Swept Source (SS) laser as the light source (Figure 2.1.3.1 C), which removes the need for the spectrometer as the wavelength of light is scanned temporally.

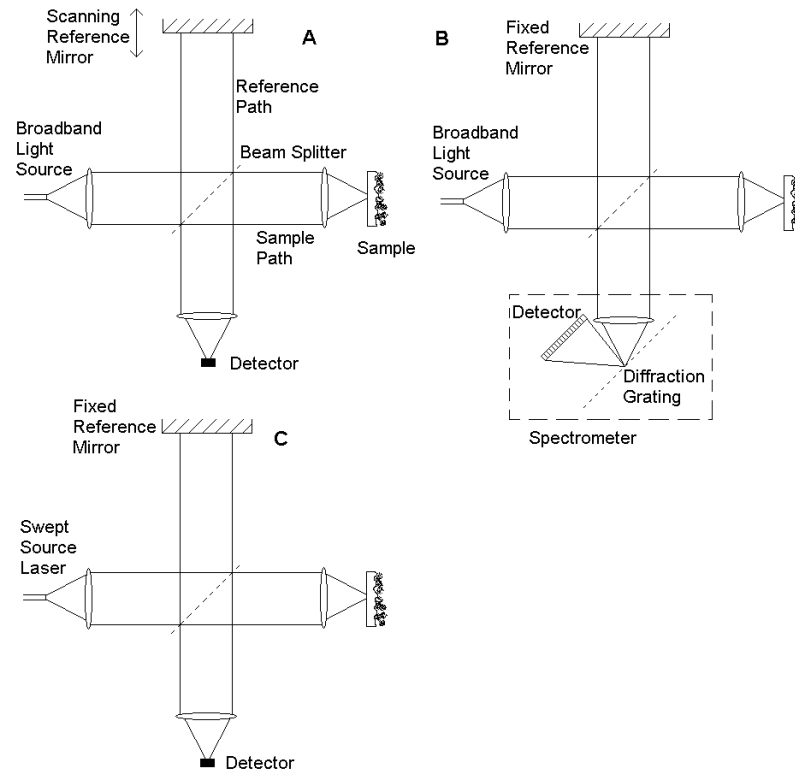


Figure 2.1.3.1  
 Diagrams of the three most common implementations of  
 Optical Coherence Tomography (OCT).  
 A – Time Domain (TD), B – Fourier Domain (FD) and C –  
 Swept Source (SS) (Variant of FD).

OCT uses interferometry to achieve axial ranging in the instrument. In an interferometer light from a light source is sent down two physical paths before being recombined. After the recombination, the classically described Electro-Magnetic (EM) waves returned from both paths will superimpose. The resultant intensity from this superposition is dependent on the relative phase difference between the two paths. The resultant intensity at any point,  $I$ , by the superposition of these coherent waves,  $I_1$  and  $I_2$  is given by<sup>46</sup>

$$I = I_1 + I_2 + 2\sqrt{I_1 I_2} \cos \delta. \quad (2.1.3.1)$$

Where  $\delta$  is the phase difference between the two waves. As the intensity of an EM wave is proportional to the electric field squared,  $I \propto E^2$ , this can also be expressed as

$$E^2 = E_1^2 + E_2^2 + 2E_1E_2 \cos \delta. \quad (2.1.3.2)$$

The phase difference of interest is that due to the relative time delay between the light paths to the detector. This phase difference between two paths of a single monochromatic wave is given by

$$\delta = \Delta t_{2-1} \cdot f \cdot 2\pi + \Delta\Phi_{2-1} = \Delta t_{2-1} \cdot \omega + \Delta\Phi_{2-1}, \quad (2.1.3.3)$$

where  $\Delta t_{2-1}$  is the time difference between the two paths,  $f$  is the frequency and  $\omega$  is the angular frequency of light. There are other sources of phase differences,  $\Delta\Phi$ , between the paths. These include phase change on reflection and dispersion (group and phase velocities being different). The dependence on frequency of light of these phase differences is taken to be negligible and hence a constant.

Considering an FD OCT system (Figure 2.1.3.1 B) with a sample with  $N$  reflections at different depths, the signal at the spectrometer is described as

$$I(\omega) = T \cdot R^2 \cdot S(\omega) + T \cdot S(\omega) \cdot \sum_{j=1}^N \sum_{k=1}^N h_j h_k \cos(\omega \Delta t_{j-k} + \Delta\Phi_{j-k}) + 2T \cdot R \cdot S(\omega) \cdot \sum_{j=1}^N h_j \cos(\omega \Delta t_j + \Delta\Phi_j) \quad (2.1.3.4)$$

where  $I$  is intensity,  $T$  is the transmission coefficient of the interferometer (beam splitter energy transmission coefficient multiplied by its energy reflection coefficient),  $R$  is the field reflection coefficient of the reference path,  $S(\omega)$  is the source intensity spectrum,  $h_j$  is the field reflection coefficient back into the instrument of reflection  $j$ , likewise for  $k$ ,  $\Delta t_{j-k}$  is the time of flight difference between reflections  $j$  and  $k$  and  $\Delta t_j$  is the time of flight difference between the reflection  $j$  and the reference path. The definitions of the constant phase differences ( $\Phi$ ) subscripts are the same as the time of flight subscripts. It should be noted that this has approximated the superposition by only considering the superposition of two fields (paths) at a time, rather than all the fields together. The intensity of the paired interference calculations is then summated together as if incoherent to each other.

An example measured spectrum, with one strong reflection in the sample, is shown in figure 2.1.3.2 (a).

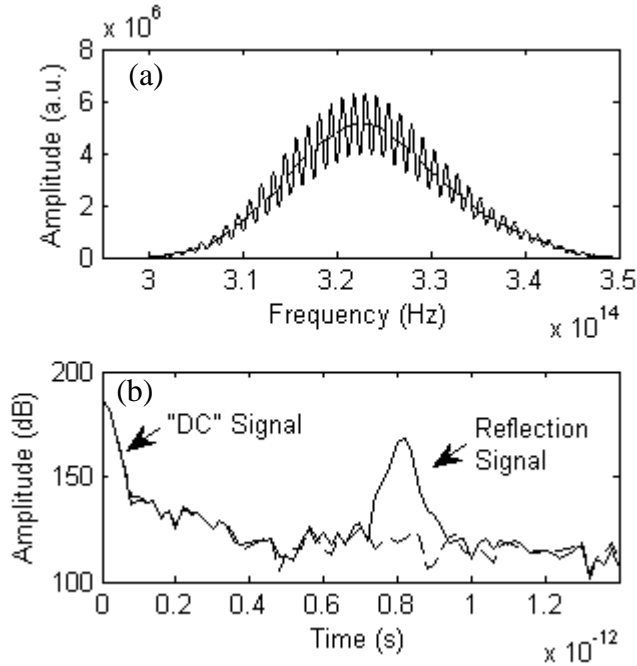


Figure 2.1.3.2  
 (a) Spectrometer signal with no sample in the sample arm (dashed line) and single high reflection surface in sample arm (solid line).  
 (b) Modulus of the Fourier Transform of both signals.

Taking the modulus of the discrete Fourier transform of the spectrometer signal (equation 2.1.3.4) gives

$$\begin{aligned}
 I(t) = & \left| DFT(I(\omega)) \right| = T.R^2 \left| DFT(S(\omega)) \right| + T \left| DFT \left( S(\omega) \cdot \sum_{j=1}^N \sum_{k=1}^N h_j h_k \cos(\omega \Delta t_{j-k} + \Delta \Phi_{j-k}) \right) \right| \\
 & + 2.T.R \left| DFT \left( S(\omega) \cdot \sum_{j=1}^N h_j \cos(\omega \Delta t_j + \Delta \Phi_j) \right) \right|
 \end{aligned}
 \tag{2.1.3.5}$$

Figure 2.1.3.2 (b) shows the result of the discrete Fourier transform for the example data. The first term is the "DC" component from the reference arm, and the component of the second term where  $j=k$  is the "DC" component from the sample arm. These components do not contain spatial information and appear after the Fourier transform as a strong signal at zero path length difference. This "DC" signal has to be subtracted from the final image.

When  $j \neq k$  in the second term (of equation 2.1.3.5), the multiple reflections in the sample arm also superimpose on each other, this leads to common path interference. Usually, due to the reflections in the sample being small in magnitude compared to

the reference mirror, these are usually of insignificant magnitude. However, if the sample contains a strong reflection, this can act in the same way as the reference mirror creating partial static artefact images, which do not move with the sample's axial position but does change in magnitude (and clarity) as the sample moves through the focus. This is classified as common path interference.

The third term (of equation 2.1.3.5), containing the intended spatial information can be resolved by convolution theorem<sup>47</sup>, giving

$$I'(t) = 2.T.R|DFT(S(\omega)) \otimes \sum_{j=1}^N h_j \delta_{t,\Delta x_j} \cdot \quad (2.1.3.6)$$

The final signal is seen to be the convolution of the axial information (relative path times and intensities of reflections) of the sample with a Point Spread Function (PSF) of the instrument, which is the Fourier transform of the source spectrum. Hence the broader the spectrum (frequency not wavelength) of the source the smaller the PSF and higher the axial image resolution of the system.

So far, during the mathematical derivation of axial OCT signal, the path length differences in the interferometer have been purposefully kept as time. Usually time delays within an interferometer are converted rapidly into length, which is the quantity of interest. If the medium of the sample is a vacuum, then the conversion to distance is simply  $\Delta x = \frac{\Delta t.c}{2}$ , where  $c$  is the speed of light and factor 2 comes from the light travelling the path twice, forward and back. However most samples, including varnish layers, do not approximate vacuums as the speed of light through the material is significantly reduced.

In most materials the speed energy and information is carried, through it by light, is determined by the group refractive index,  $n_g$ , of the material at the frequency of the light. The speed of light through a material is hence given as  $c_m(\omega) = \frac{c_v}{n_g(\omega)}$ . If the sample being measured consists of several layers of different materials, then the conversion of the reflection by the back interfaces ( $j$ ) of the layers to distances is then given by

$$\Delta x_j = \frac{c_v}{2} \cdot \sum_{k=1}^{k=j} \frac{\Delta t_k}{n_{gk}}, \quad (2.1.3.7)$$

where  $\Delta t_k$  is the time taken to travel through layer  $k$  and  $n_{gk}$  is the group refractive index of that layer.

## 2.2 Instrument and methods

### 2.2.1 Instrument

For this work, a commercial “spectral radar” FD OCT (SROCT) from Thorlabs HL (OCT930SR<sup>48</sup>) was used. Figure 2.2.1.1 is a schematic diagram of the instrument. It consisted of a unit, containing the light source and spectrometer, connected to the probe, with the interferometer, by a single fibre optic cable. The instrument is controlled and measured data is then processed to form the images by a PC. The light source of the instrument was a Super Luminescent Diode (SLD) with a central wavelength of 930nm and a band width of 100nm.

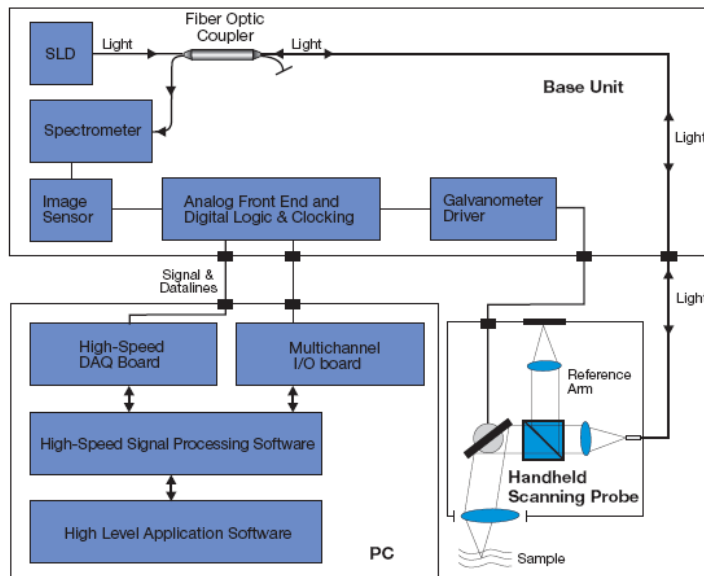


Figure 2.2.1.1  
Schematic diagram  
of Thorlabs HL  
OCT930SR.  
© Thorlabs HL.

The optics of an OCT instrument is as important as the interferometer, as it provide the lateral resolution of the image. In the Thorlabs SROCT instrument a probe beam/spot is scanned laterally across the sample by the optics. At each lateral position the axial data is recovered by the interferometry. Two sets of optics were used during this work, first the standard “hand held” probe and secondly a larger

probe with a longer working distance. The hand held probe was used for the majority of the work. During measurements the probes were attached to a motorised three axial micrometer stage. In both probes the probe beam was scanned across the sample by the use of a galvanometer in the sample arm. To construct a two dimensional optical section, the axial data sets (image columns) are put together for evenly spaced lateral positions. Often terminology from ultra sound is used to describe this process, with the individual depth signals being called “AScans” and the resulting 2D optical sections being known as “BScans”. In this work the terms axial data and images are used instead.

For the processing of the axial data, though the mathematics of calculating the axial signal from the spectrum of light is straight forward, a few addition steps need to be carried out on the raw data before the final image is produced. These are needed to ensure optimum image quality and overcome practical aspects. A (CCD or CMOS) detector, used by an OCT system, will have a thermal signal present when no light is incident on it (dark current). This dark current is measured before (with equal integration time as measurements), with no light incident on the detector, and subtracted from the raw data.

The discrete Fourier transform requires the data to have uniform frequency separation ( $k$  space). However the majority of spectrometers are designed to have uniform spacing in wavelength ( $\lambda$  space), though it is possible to design a spectrometer with uniform spacing in  $k$  space and use within an OCT system<sup>49</sup>. The third stage is to convert from  $\lambda$  (wavelength) space to  $k$  (frequency) space. The equal  $\lambda$  space data from the detector is converted into equal  $k$  space by use of a spline. Along with sensor non linearity this will be a contributory factor in the distortion of the sinusoidal signal leading to harmonic ghost images from strong signals. A recent alternative method, which overcomes the limitations of splining, is the use of a non-uniform Fourier transform of the uneven  $k$ -spaced sampled raw data<sup>50</sup>.

As the point spread function of the instrument is determined by the Fourier transform of the (effective) measured spectrum, consideration needs to be given to the spectrum shape measured by the detector. This is dependent on two factors that

lead to a non-optimum shape of the spectrum, hence PSF. Though separate problems, their effect on the spectrum is corrected for in one step. Firstly the light source spectrum will not be identical to an optimum mathematical function, with low high frequency Fourier components. The real spectrum shape will have increased high frequency components, leading to a broader PSF and image artefacts from the high frequency structure of the DC component. Secondly, the detector in the spectrometer measures a finite top hat window of the spectrum. The Fourier transform of a top hat function is a sinc function, so this discrete sampling of a spectrum results in ringing artefacts in the image. To overcome these two effects a weighting function ( $W(\omega)$ ) is applied to the raw data, before the Fourier transform, to change the raw source spectrum ( $S(\omega)$ ) into a more optimum (the desired) shape ( $S'(\omega)$ ). Figure 2.2.1.2 (a) shows a measured spectrum from the Thorlabs SROCT instrument, along with an example desired (optimum) function. To achieve the optimum/desired image properties there are three separate factors this function needs to balance. The first is that the function should taper to zero at each end of the measured window, to minimise ringing due to finite sampling. Secondly the Fourier transform of the function should be narrow (also with no high frequency components, which would give image artefacts) to give the maximum axial imaging resolution. Thirdly, assuming noise variation over the spectrum is negligible, the higher the increase in weighting of parts of the spectrum, compared to the average weighting value, the more signal to noise is decreased, *i.e.* more the spectrum shape is changed the lower the resulting signal to noise. The desired function will be chosen to balance these factors. For OCT signal to noise is not crucial issue in the choice of function, as the raw function already closely approximates function that meet the criteria the other two factors. The choice of an OCT desired function is made to balance with width of the PSF and ringing artefacts. In this project a Hann (erroneously called Hanning by the instrument manufacturers) function was chosen, which is shown with the raw spectrum in figure 2.2.1.2 (a). From these two functions, the weighting function, that is to be applied to all the data, can be calculated by

$$W(\omega) = \frac{S'(\omega)}{S(\omega)}. \quad (2.2.1.1)$$

This function is shown in figure 2.2.1.2 (b).

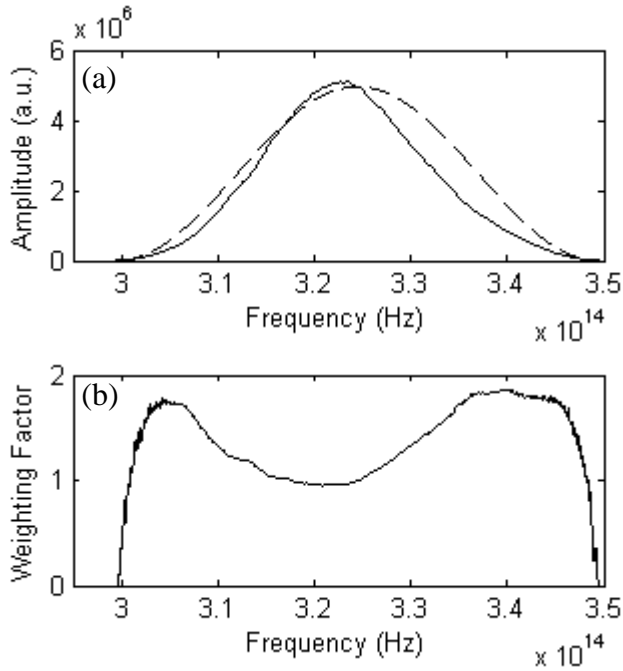


Figure 2.2.1.2  
 (a) Measured spectrum from detector ( $S(\omega)$ , solid line) and desired spectra shape (Hann function in this case,  $S'(\omega)$ , dashed line).  
 (b) Weighting function ( $W(\omega)$ ) multiplied to the measured spectrum to achieve the desired function.

This process makes use of the fact that digitally weighting the measured data is mathematically the same as physically filtering the raw light source. This is important to profilometry as the shape of the PSF, for a reflection from a single axial depth only, is the discrete Fourier transform of the chosen function ( $S'(\omega)$ ). However for most real surfaces there is going to be a variation of the axial position of the surface within the three dimensional resolution element of the instrument.

The next stage in the processing of the data is performing the Fourier transform. The discrete Fourier transform is carried out by use of a fast Fourier transform (FFT) algorithm and the modulus of the result is taken. In the Thorlabs OCT the penultimate stage appears to be the subtraction of the DC components of the signal from around the zero path length difference. The output is then converted in to decibels (dB)

$$dB = 20\log_{10} I'(t) \quad (2.2.1.2)$$

to produce the images. The conversion to dB is crucial for the presentation of the images, as it allows the viewer to see reflections of very different magnitudes on one image, utilising the dynamic range of OCT. The Thorlabs FD OCT used in this work returns the dB images as the output. This is the only data with which interface

positions were calculated. When processing the outputted dB images they were usually converted back to linear units.

The signal, from the instrument, of an interface is given by the convolution of the instrument PSF with the position of the interface

$$I'(t) = 2.T.R.h_j \cdot |DFT(S'(\omega))| \otimes \delta_{t,\Delta_j} \cdot \quad (2.2.1.3)$$

The accuracy of the position of the interface is determined by how accurately you can determine the centre of the PSF, like traditional WLI profilometry methods.

### 2.2.2 Interface identification

Before the position of an interface can be fitted to a PSF, the PSF was detected automatically. Erroneous identifications were a large source of error. To overcome this, automatic search algorithms were developed for each scenario. For surface profilometry (the majority of samples) it was only needed to take the brightest pixel, in each axial data set, as the centre of the surfaces PSF. The measurement of applicator applied varnish coatings, on ground glass substrates, was an example of a scenario where a number of steps were required to recover both interfaces reliably. First an axial search range was set manually, which included both interfaces but excluded image artefacts. Second the highest value pixel in the range was found automatically, this position usually corresponded to the surface reflection. Third the highest pixel is automatically found within a set range of pixels behind the identified surface pixel, this was to exclude the sides (and ringing) of the surface PSF from the searched pixels. This pixel should correspond to the substrate profile. In a case such as this erroneous identifications can be common, so post processing algorithms were often applied to final profiles to remove remaining (obvious) anomalous points.

### 2.2.3 Measurement of instrument Point Spread Function (PSF)

To determine the best method of finding the centre of the axial point spread function, hence the axial position of an interface at that lateral position, an experimental approach was used. This approach was taken, rather than directly fitting a theoretical derived PSF (Fourier transform of the effective source spectrum), as

experimental factors, such as dispersion and combination of lateral resolution, surface slope and texture, would act to distort the PSF from the theoretical solution. Here an experimental method and results of the measurement of the instruments PSF, for a flat interface, are presented.

The point spread function, of an interface by the OCT system, can be taken from the measurement of that interface. However the axial data sampling, 3.1µm per pixel, is far too low for a single data set to give a detailed image of PSF. To measure the detailed PSF the axial sampling needs to be increased. This is done by a simple experimental method.

The OCT probe was attached to the 3 axis micrometer stage, with a standard flat surface placed on the bench underneath the probe. While the OCT system took streamed measurements of the surface, the computer controlled micrometer stage was used to move the OCT probe towards or away from the target at a constant small velocity. This gave a small, fraction of a pixel, axial shift between temporally adjacent OCT images. These series of images were then combined into to one image with much greater axial sampling. To reduce noise in the measurements, such as due vibration, the raw data was smoothed by boxcar averaging.

Figure 2.2.3.1 shows an example of an axial intensity profile, taken from the standard flat interface, by this shifting method. Many distributions are often well approximated by a Gaussian (or statistically normal) function,

$$A = A_0 e^{-C(x_0-x)^2} . \tag{2.2.3.1}$$

A Gaussian function was fitted to the smoothed PSF data to see how good this approximation is. The function was found to be good for the central part of the PSF but deviation increased away from the centre.

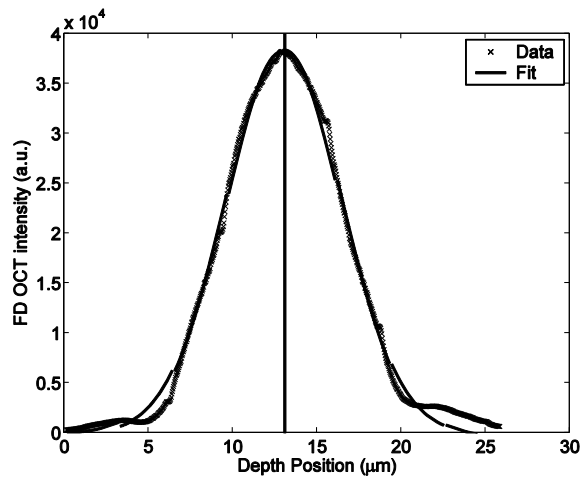


Figure 2.2.3.1  
The system axial point spread function measured by “shifting” the position of the surface by sub pixel amounts between measurements. A Gaussian fit to the data is shown as a solid curve. The vertical line marks the centre of the PSF found by this fit.

The intensity of signal from an interface is dependent on its axial position within the image. This is due to two reasons. Firstly the focus of the optics of the sample beam is at a fixed position within the image (neglecting refraction). As the position of the interface moves away from the focus, the amount of light returned back into the interferometer is reduced, lowering the signal. Secondly the resolution of the spectrometer (including finite detector pixels) is limited, which leads to some loss of signal with distance away from the reference path length<sup>51</sup>.

With the degradation of signal with axial position, it was possible that this may change the PSF dependent on the interface position in the image. The PSF of a smooth interface was again measured by the shifting technique, this time at three different heights in the image, the top, middle and bottom. Smoothing was not applied to these data sets but they were rescaled so that they have the same amplitude and central position to aid visual comparison. This is shown in figure 2.2.3.2. It can be seen that the measured PSFs from the top and middle of the image are similar. However the PSF of the weakest of the signals from the bottom of the image is different in shape and significantly broader away from the centre of the peak. This is a relatively benign example, showing that for a flat interface the PSF does not show significant variation if the bottom of the image is avoided. However, as will be shown later, the measurement of textured surface does have a significant impact on the PSF shape, due to speckle/diffraction effects. Also the PSF on an interface will be broadened (change of shape) if it is imaged through a (significant thickness of) dispersive material.

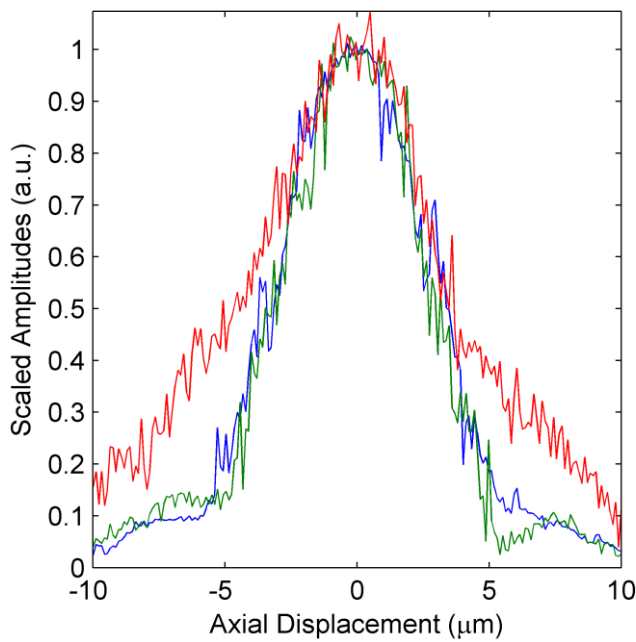


Figure 2.2.3.2  
Scaled PSF  
measurements, by shifting,  
at 0.26mm (blue), 0.76mm  
(green) and 1.4mm (red)  
from the top of an OCT  
image.

## 2.2.4 Evaluation of methods to find centre of PSF

To determine the best method to accurately find interface positions from their OCT axial PSF, several methods were initially evaluated. In this evaluation the accuracy of the method was the main criteria, though the computational speed of the method and potential for stability were also considered. In order to measure the difference in error between each method, the same image data sets were used for each method allowing direct comparison of measured profiles. The surface measured was a Veeco standard flat surface used to calibrate optical profilometers, it was measured to be flat to <10nm by use of Phase Shifting Interferometry (PSI) (with the Veeco instrument) (Figure 2.2.4.1).

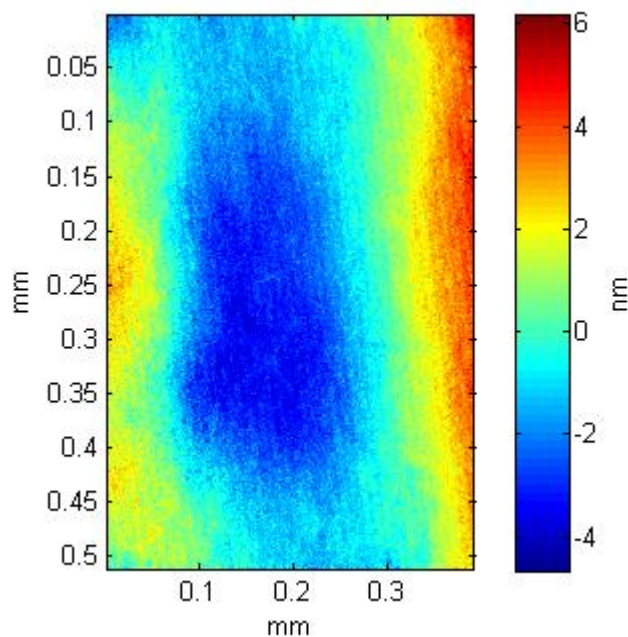


Figure 2.2.4.1  
PSI surface profile of  
standard flat surface used  
to evaluate error of  
different methods of  
finding the centre of an  
OCT PSF for  
profilometry.

For the measurement of the surface with OCT, the large (long working distance) optics was used. Due to the instrument optics of the OCT, the optical path length across the image is not uniform, leading to curvature of the image and profiles. This curvature can be measured by the measurement of the standard flat surface. This can then be subtracted from any other measured profile (as long as the optics of the instrument are not altered in-between), removing this artefact. So in order to measure the surface correctly, two separate measurements were needed. The first measurement acting as the measurement of curvature was carried out with the shifting technique to give increased sampling and signal to noise, this aimed to ensure the best accuracy of the measurement.

Then in a separate measurement at a separate location on the standard flat surface, a single static image measurement of the surface was made to simulate the taking of data in a real situation. In both cases the calculation of position was done with pixels within  $\sim 6\mu\text{m}$  axially of highest value pixel. With each technique, the interface profiles were measured from the single and shifted data sets and then the two profiles were subtracted together. The mean and slope of the resulting profile were subtracted, leaving only the residual (error). It is likely the errors in the measurement add as the root mean square, hence the difference in standard deviation of the final residual profiles are attributed to the difference in the error of the fitting, as all the other sources of error will be the same for each measurement.

The effect the different methods have on the “structure” of the residual profiles can also be compared by their plots.

The OCT system returns to the user the image intensity in decibels. If the PSF is Gaussian, then in dB the central part of the PSF, where the noise floor value is insignificant, should approximate a quadratic function

$$I_{dB} = 20\log_{10} I_0 - 20C(x - x_0)^2 \log_{10} e, \quad (2.2.4.1)$$

where  $I_{dB}(x)$  is the dB amplitude as function of axial position  $x$  and  $I_{dB}(x)$  is the linear peak amplitude of the PSF. This multiplies out to

$$I_{dB} = I_{0dB} - C_{dB}x_0^2 + 2C_{dB}x_0x - C_{dB}x^2 \quad (2.2.4.2)$$

where  $C_{dB} = 20.C.\log(e)$ . A quadratic function was fitted to the PSF of the dB data with the use of MatLAB’s polyfit function. The centre of the PSF,  $x_0$ , can then be calculated from the values of the fit. Figure 2.2.4.2 shows an example fit.

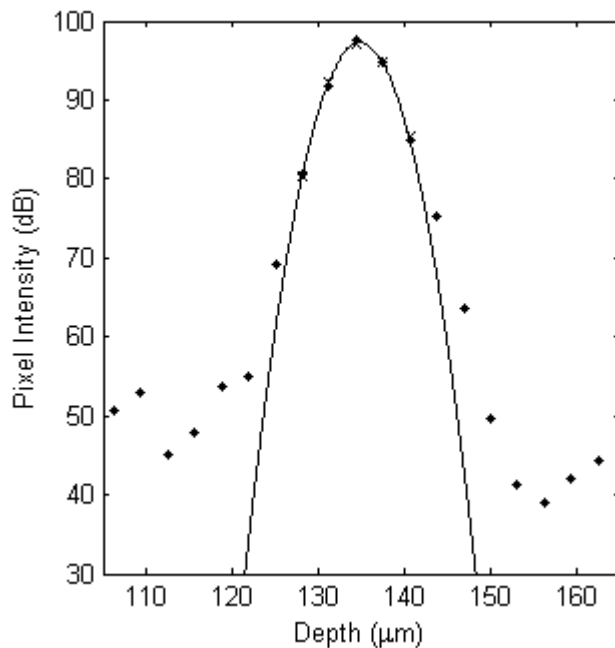


Fig 2.2.4.2  
Quadratic fit to PSF in dB. Showing measured pixel intensities (dots), fitted pixel intensities (crosses) and the fitted function (line).

Finding the centre of symmetric PSF is the same as finding its centre of mass or centroid. This principle can be turned around so that if you find the centroid of the

points of the PSF you find its centre. For discrete amplitudes in one dimension ( $I(x)$ ), the centre of mass of those amplitudes is calculated by

$$x_0 = \frac{\sum x.I(x)}{\sum I(x)} . \quad (2.2.4.3)$$

Finding the centroid has been used in WLI profilometry, with pre-processed highly sampled time domain data<sup>52</sup>. This routine is effective for a densely and completely sampled axial PSF. However with the low density axial sampling and the use of the central part only of the PSF, in the OCT method, this method is not effective. Figure 2.2.4.3 shows the actual shape of the function that equation 2.2.4.3 gives the centre of mass of, for the example axial data. This is a poor and biased approximation of the real PSF.

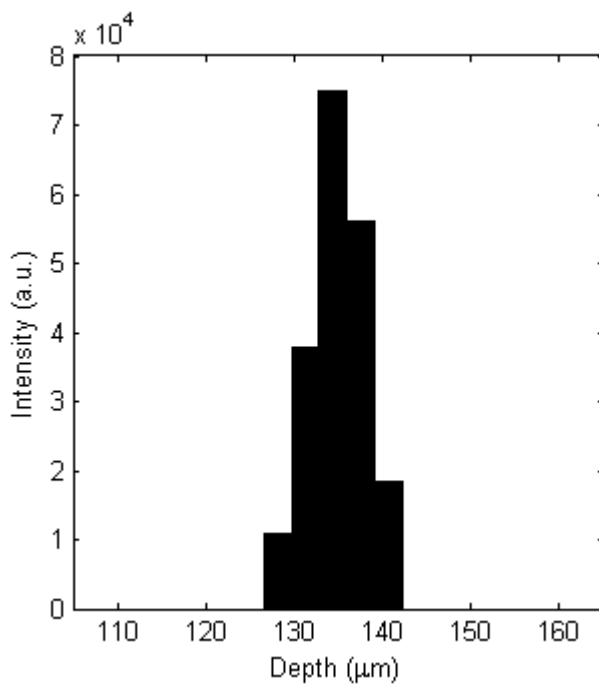


Figure 2.2.4.3  
The shape, from the example measured axial data points, that the centroid is calculated from.

It has been shown that the centre of the PSF, of the OCT system used, is approximated by a Gaussian function. After converting the image intensity back to linear units, fitting a Gaussian function to the PSF should return its centre with high accuracy. In order to fit a Gaussian to the intensity data, the MATLAB minimisation function `fminsearch` was used. This is an iterative algorithm to find input values to the function that result in the smallest output. This was used to iterate variables in

the fitted function,  $f(x)$ , in order to minimise the sum squared difference with the intensity data ( $I(x)$ )

$$Y = \sum \{ [f(x) - I(x)]^2 \}. \quad (2.2.4.4)$$

For the free width Gaussian, the Gaussian function (previous equation 2.2.3.1) was fitted with  $A_0$ ,  $C$  and  $x_0$  being varied to achieve a minimum value. Figure 2.2.4.4 shows this Gaussian fit to the example axial data. A main limitation of this method was that the iterative process of fitting was computationally heavy.

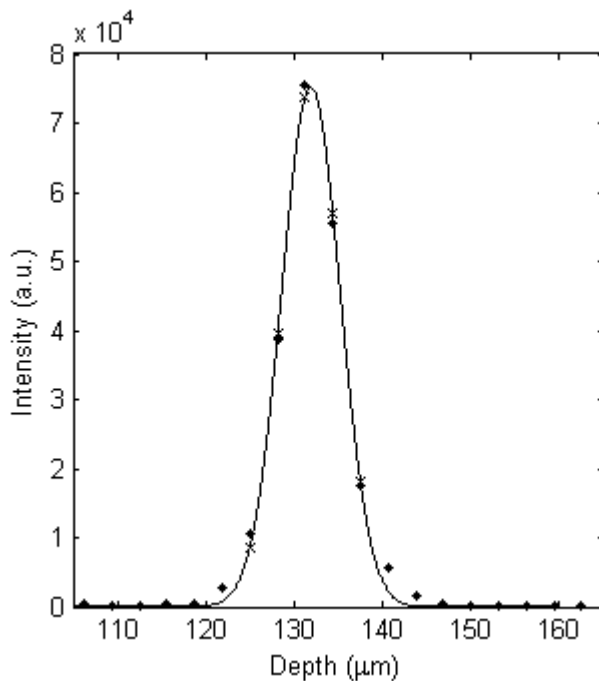


Figure 2.2.4.4  
Free width Gaussian  
fit to PSF in linear  
intensity units.  
Showing measured  
pixel intensities (dots),  
fitted pixel intensities  
(crosses) and the fitted  
function (line).

If the shape controlling parameter of fitted Gaussian,  $C$ , is allowed vary, in certain situations, such as low signal-noise data or two interfaces closer than the FWHM resolution of the PSF functions, a meaningless function may be fitted to the data. A solution to this is fixing the value  $C$ , at a pre measured value, to keep the shape of the Gaussian constant. If the PSFs are constant in shape, then this would have minimum impact of the accuracy. However, as has previously been discussed (section 2.2.3) the point spread function is not always uniform in shape. With the reduction of fitted parameters by a third, the computational demand on the fitting process should be reduced. Figure 2.2.4.5 shows the example fit of the fixed width Gaussian.

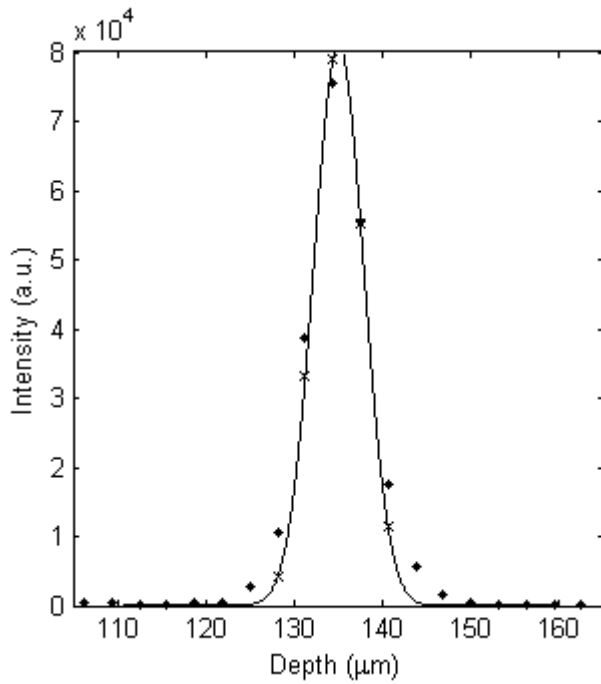


Figure 2.2.4.5  
Fixed width Gaussian  
fit to PSF in linear  
intensity units.  
Showing measured  
pixel intensities (dots),  
fitted pixel intensities  
(crosses) and the fitted  
function (line).

In section 2.2.3 it was shown that the point spread function could be measured experimentally and the noise smoothed. This Measured PSF (MPSF) was fitted to the experimental data by the same method as the Gaussian fits. A cubic spline was used to calculate (from the discrete points of the MPSF) the fitted function values for each iteration of the fit. Figure 2.2.4.6 shows the fit of the MPSF to the axial data.

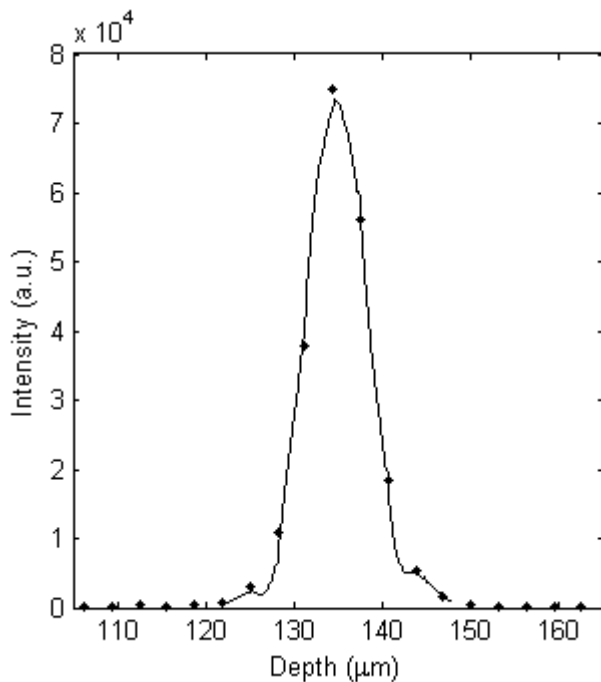


Figure 2.2.4.6  
MSPF fit to PSF in  
linear intensity units.  
Showing measured  
pixel intensities (dots),  
fitted pixel intensities  
(crosses) and the fitted  
function (line).

Three main problems existed with this method. Firstly the calculation of a cubic spline at each iteration of the fit leads to this method to be computationally the slowest. Some improvement may be made in this method, such as by use of a reference table system instead, with only one computation of the spline. Secondly, the quality of the shifted MPSF measurement was not sufficient to achieve improvements in accuracy over other methods. This again is an implementation problem, and may be overcome. Thirdly this method also depends on the PSF being consistent between measurements, which will not always be the case.

Figure 2.2.4.7 (a) shows the measured residual profiles for the fitting methods and figure 2.2.4.7 (b) shows the PSD of these profiles. It can be seen from the profiles that the majority of the residual is independent of the processing method. This data noise has a spatial frequency of  $10\text{mm}^{-1}$ . Later this is shown to be due to vibration in the system. The PSD of each method, away from the vibration spatial frequency, are much different. Here the errors in the fitting methods are dominating.

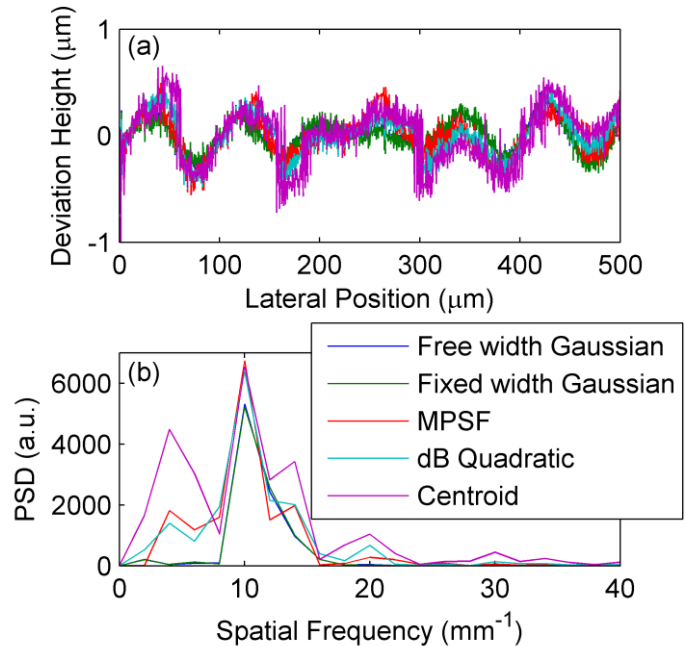


Figure 2.2.4.7  
For the different fitting  
methods the  
(a) residual profiles  
(b) PSD of the residual  
profiles

The standard deviations of the residual for each method are given in table 2.2.4.1. The free width Gaussian is seen to have the lowest standard deviation, though the value for the fixed width Gaussian fit is only slightly higher. The MPSF had a significantly worse standard deviation, though this is not necessarily indicative of its

potential. The quadratic fit performed slightly worse than the MPSF. The worst value of standard deviation was for the centroid.

<b>Method</b>	<b>Standard Deviation (<math>\mu\text{m}</math>)</b>
Quadratic (dB)	0.2054
Centroid (Linear)	0.2686
Free Width Gaussian (Linear)	0.1576
Fixed Width Gaussian (Linear)	0.1585
Measured PSF(Linear)	0.2005

Table 2.2.4.1  
The standard deviations of the residuals of each fitting method.

The free width Gaussian fitting had the lowest measured standard deviation of residual of the initially tested methods. As a result, it was the method that was chosen for use in the project.

However, since the completion of this work, it has become apparent that taking the differential of the middle three points of the PSF is an alternative way to find the centre<sup>53</sup>. If the data is left in decibels, as long as the noise is negligible to the signal, and the PSF is Gaussian over the three points the PSF is a square function. If the differential is taken it is thus a linear function, with the x-axis intercept being the centre. So if a straight line is drawn between the two differential points this intercept can be calculated by

$$x_c = x_{1.5} + \frac{\Delta S_{2-1}}{\Delta S_{3-2} - \Delta S_{2-1}} \cdot (\Delta x), \quad (2.2.4.4)$$

where  $x_c$  is the central position,  $x_{1.5}$  is the distance half way between pixel 1 and 2,  $\Delta S$  is the difference in pixel values and  $\Delta x$  is the pixel spacing.

The use of the shifted data set, for one of the profiles in the residual calculation, is unsuitable for this measurement. So the shifted measurement profile used was that of the best accuracy previously found, the free width Gaussian. As the total standard deviation, of the residual profile, is likely to be the root of the quadratic sum of the error in both measured profiles, the difference in the final standard deviation will be determined by the non shifted profile. As well as this “edge detection” method, a

couple of related techniques were also evaluated with the same procedure. The differential method was applied to the linear data, which does not mathematically give the centre of the PSF, so should lead to higher error. The Gaussian fit to the central three points (rather than central 5) of the linear data should give exactly the same result as the differential of dB values method. This is because the Gaussian fitted should be the same (exact) solution for the three points.

Figure 2.2.4.8 and table 2.2.4.2 show the residuals for the methods. It can be seen that in this high signal regime, the dB differential method has less error than the standard Gaussian fitting. The residual profile of the 3 point Gaussian fit matches the dB differential profile exactly. The better performance of the 3 point fits can be explained with the high signal to noise compared to the deviation of the Point spread function from a Gaussian. As has previously been shown (Figure 2.2.3.1) the PSF approximates a Gaussian function much better in the centre. Already at two pixels away (6.2 $\mu\text{m}$ ) from the centre it is distorted significantly. The use of these points in the fit in this case distorts the results. An important comparison can be made with Quadratic fitting, the distortions in dB have a much greater effect than for the linear data in the 5 point Gaussian fit. As the method does not compute the centre of the PSF, the differential of the linear data method proved to have a higher residual.

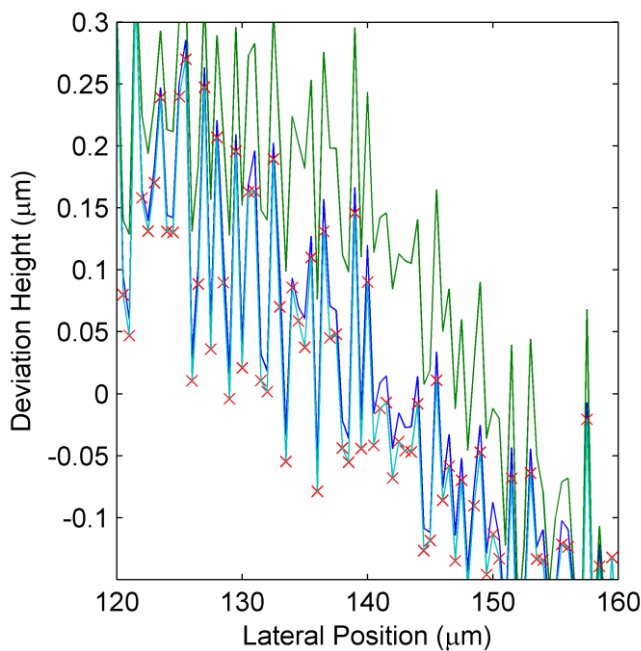


Figure 2.2.4.8  
Part of the residual profiles for the additional fitting methods (differential dB method (red crosses), 3 point Gaussian fit (cyan line) and differential of linear data method (green line)) and 5 point free width Gaussian fit (dark blue line).

Method	Standard Deviation
(5 Point) Gaussian Fit	0.1576
(3 point) Differential dB	0.1570
(3 point) Differential linear	0.1749
(3 Point) Gaussian Fit	0.1570

Table 2.2.4.2

The standard deviations of the residuals of the additional fitting methods and the 5 point free width Gaussian method.

It has been shown that the dB differential is more accurate, when there is high signal to noise, than the 5 point Gaussian fit due to the PSF distortion from a Gaussian shape. However, the performance in a low signal-to-noise/distortion (diffraction/speckle) system has not been evaluated. The fitting of 5 points rather than 3 has the potential to increase the signal-to-noise/distortion of the fitted data. The effect of the number of fitted points on measured surface profiles for low signal-to-noise/distortion data is a recommendation for future work.

## 2.3 Sources of profile error and correctable distortion

### 2.3.1 Vibration

It has been noted in the previous section that the majority of the structure in the residual profiles is independent of the method of finding the PSF centre and centred on a single spatial frequency. The source of this “noise” can be shown to be vibrations in the instrument and/or sample, rather than intrinsic fitting errors common to all methods.

The software for the spectral radar OCT was modified to return the raw spectral data and a reflective smooth surface was measured. When the consecutive Fourier images were viewed as a video they were seen to be moving. The movement of the Fourier image was caused by phase changes in the interferogram. Figure 2.3.1.1 shows consecutive sets of spectra, taken from the same lateral position, highlighting this phase change. The cause of this change in phase is a change in the path length difference between the reflection and the reference arm,  $\Delta t_j$  (in equation 2.1.3.4). Almost certainly, this will be caused by a physical change in the path length in one

of the arms of the interferometer due to movement (vibration) of instrument components or sample.

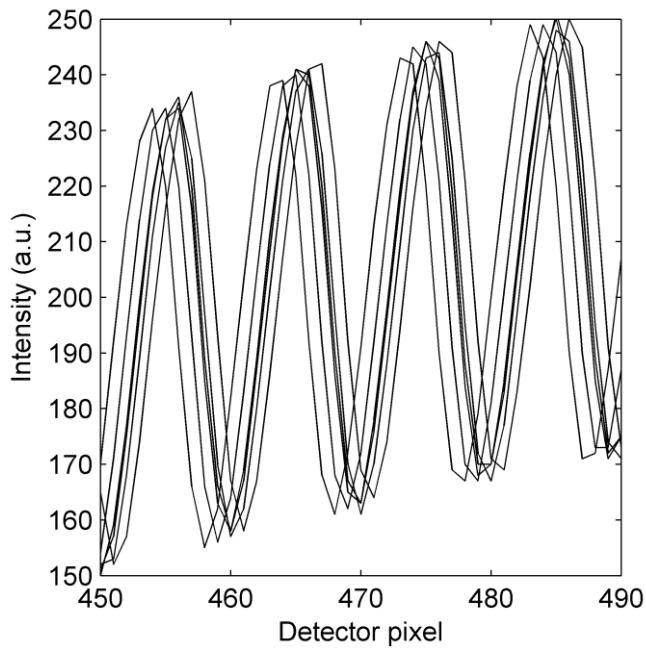


Figure 2.3.1.1  
Part of consecutive  
measured spectrums  
for single lateral point.

This change is also seen in the image data, where in a series of measurements the pixel intensity of the PSF do “rock” as the PSF moves slightly. From the spatial frequency of the distortions the vibrational frequency was roughly estimated to be of the order of 25Hz.

The hand held probe was used to take a series of static OCT images of the standard flat surface, over a profile length of 0.5mm. The surface profile for each consecutive image was measured, shown in figure 2.3.1.2. The vibration in the consecutive profiles is very apparent, though they may not be entirely uncorrelated.

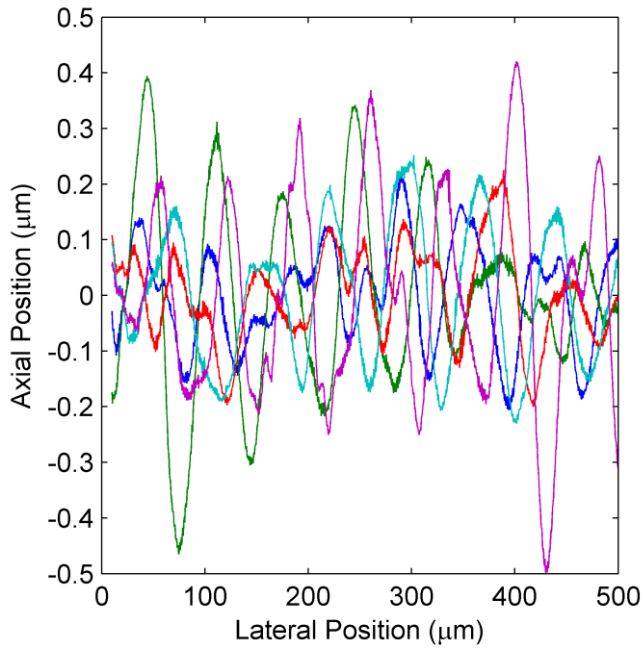


Figure 2.3.1.2  
Measured profiles of standard flat surface from five consecutive OCT images, showing vibrational noise.

If these deviations of the measured surface profiles are caused by uncorrelated vibration, the averaging of the (linear intensity units) image data of the consecutive measurements, before the finding of the interface profile, should average out the movement of the PSFs. This is an alternative to the averaging of the measured profiles of each data set, as multiple measurements of the profile would consume far more computing time. Figure 2.3.1.3 shows the measured profile (a) after averaging 11 and (b) 61 images. There is seen to be an increase in reduction in the vibrational component of the profile with the increased averaging of the data sets.

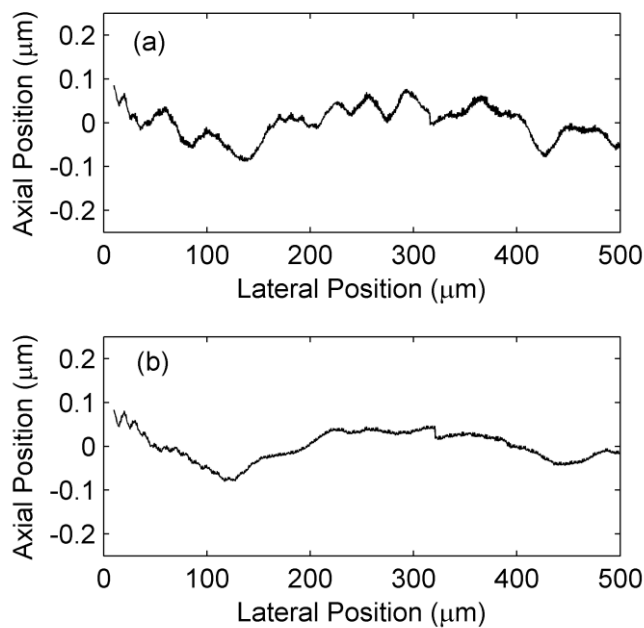


Figure 2.3.1.3  
 (a) Measured profile of standard flat surface from the average of 11 consecutive OCT images.  
 (b) Measured profile of standard flat surface from the average of 61 consecutive OCT images.

In conclusion it has been shown that the major cause of the error the surface profile of a smooth surface, with the OCT system, is due to vibration. The instrument set up did not have any special anti-vibrational features incorporated in its design and was used upon a lab bench rather than an anti-vibrational table. For high precision profilometers, manufactures go to long lengths to reduce vibration in their instruments<sup>54</sup>. Therefore it is not unexpected that vibration is a limiting factor for our system. However, averaging images before calculating the profile, the effect of these vibrations can be reduced.

### 2.3.2 Instrument optics, speckle and diffraction

Though the interferometer gives the OCT system its axial ranging capabilities, it is only with the optics in the sample arm of the interferometer that the instrument focus spot/probe beam is scanned laterally across the sample, allowing the construction of images. The optics used directly determines the lateral resolution, depth of field, the relative optical path length laterally across image and the axial direction travelled by the light. For many interfaces, affects dependent on/interlinked with the optics of an OCT instrument will be a dominant source of error.

The optics in the sample arm of the Thorlabs SROCT, used in this project, was telecentric (measured below). Figure 2.3.2.1 is a ray diagram showing the path of light in and out of the optics for different lateral focus positions. The light in the interferometer side of the sample arm optics is focused at infinity (collimated). The direction of travel of this light is changed by the movement of the galvanometer scanning mirror, before the optics. After passing through the optics the chief rays (central) of each illumination direction are parallel, with the light through the focus approximating a narrow (collimated) beam through the sample at a single lateral position.

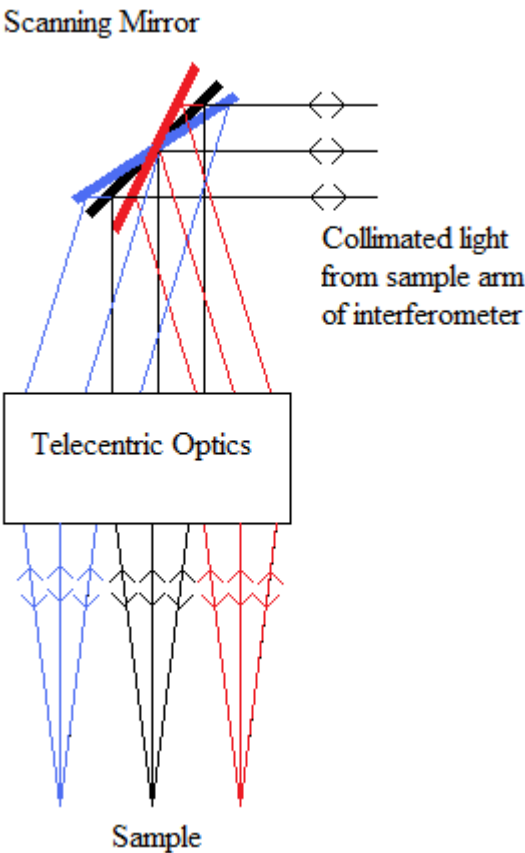


Figure 2.3.2.1  
A ray diagram of how the light in the sample arm of the OCT system is focused at different lateral positions (blue, black, red) by the scanning mirror and telecentric optics.

The OCT image is constructed by placing the axial data, of each lateral beam position, together in a rectangular image. Each axial column is placed parallel and at equal heights. If the optics of an OCT is not telecentric, the chief rays (beams) are not parallel, then the real shape of the constructed image would be fan like, leading to fan beam distortions<sup>55</sup>. Though an OCT optics maybe telecentric, the plane of equal optical distance through the optics is not necessarily flat in space or perpendicular to the optical axis. This means that the OCT image may still be

distorted. The measurement and corrections for this is detailed in the next section (2.3.3).

When measuring textured surfaces, their shape leads to intrinsic errors in broadband interferometry profilometry methods due to superposition effects within the imaging resolution of the system. These effects can be described as either speckle or diffraction dependant on the surface, though they are essentially the same process. Speckle<sup>23</sup> is diffraction under a broader case of limits in the same way that diffraction is interference under a broader case of limits<sup>56</sup>. Interference refers to the superposition of two pathways, diffraction to the superposition of infinite (or a large number of) pathways but with defined regular pattern (including top hat and delta functions) and speckle to the superposition of infinite (or a large number of) (quasi-) random pathways. In terms of WLI profilometry, the distortion of the measured profiles of regular rough surfaces has been identified as due to an effect of diffraction on the resultant interferogram<sup>57</sup>. The resultant errors from the same process with a random rough surface is defined here as speckle error.

The lateral resolution of an OCT system (or any other optical system) is finitely big. Figure 2.3.2.2 shows a light wave front in the lateral resolution spot incident on a textured surface. Here the wave front is approximated to a collimated beam for illustrative purposes. As wave front is incident on the textured surface, at each point of the surface reflection occurs. These reflections must obey Huygens principle, with each point on the surface acting as hemi-spherical sources of waves with phase dependent on the height of the surface. These hemi-spherical Huygens sources produced the reflected wave front by their superposition on each other. However, for an OCT (or any other interferometer) system the superposition of these Huygens points do not need to be resolved here but at the detector. As was modelled by Harasaki and Wynatt for a stepped surface<sup>22</sup>, the resultant PSF is dependent of the optics as well as the surface and light source.

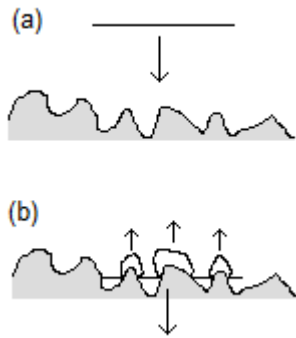


Figure 2.3.2.2  
 Sketch of wave front incident upon textured surface considered by Huygens principle.  
 (a) Before the wave front is incident.  
 (b) As the wave front is incident

When measuring the profile of a textured sample with a broadband interferometry profilometry method (including OCT), the speckle/diffraction error will remain constant if the system is static. However if part of the system is changed, such as a change in the optics, with time the speckle/diffraction error will also change. Under some circumstances, the speckle/diffraction error may become decorrelated from its previous values. Then with sufficient temporal averaging, of these speckle/diffraction error decorrelated measurements, the speckle/diffraction error will be averaged out. This is the same principle as most speckle suppression techniques.

One difference, between Fourier Domain and Time Domain OCT systems, is that FD OCT collects the axial information from all depths simultaneously. In TD OCT (and TD WLI profilometry) the need to scan the relative path length difference between the two arms of the interferometer, gives the opportunity to also change the position of the focus simultaneously. This allows the axial position being measured to be kept in the best focus all the time<sup>58</sup>. This is not possible with FD OCT, generally the optimal focus position is at a single axial position and the focus will deteriorate with distance from this depth. The use of bifocal optics has been demonstrated for the measurement of refractive index<sup>59</sup>, giving two axial focus depths rather than one. The depth of field of the optics will determine how quickly the focus deteriorates with distance from the focal point. In the design of FD OCT optics, the need of the large depth of field needs to be compromised with the desire for high lateral resolution.

The distortion of the optical field, with distance from the focus, when measuring a textured surface will affect the speckle/diffraction error. In early experimental work

for the project, the degradation of the accuracy of profile measurements were noted with increased distance from the focus. The large optics were used to measure a profile of a Rubert sinusoidal surface 528X (1.5 $\mu\text{m}$  peak to peak and 50 $\mu\text{m}$  period) at different axial positions in the image, hence from focus. Each measurement was made with an average of 60 images. Figure 2.3.2.3 shows part of the surface profiles of two measurements of the sinusoidal surface. One has its axial position close to the focus while the other is displaced axially by 300 $\mu\text{m}$ . The profile measurement away from the focus position has significantly increased distortions, than the measurement closer to the focus.

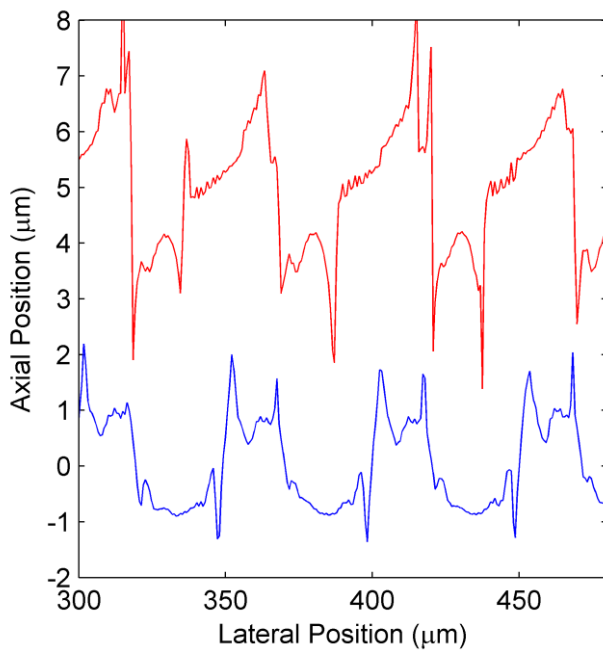


Figure 2.3.2.3  
Measured surface profile of a sinusoidal surface measured at two different heights within FD OCT image, closer to focus (blue) and further from focus (red). Profiles have been axial positioned for viewing.

Speckle/diffraction is required to explain the increase of profile error due to focus. Moving away from the axial focal position will increase the spot size of illumination and accepted returned light. If this light superimposed at the detector incoherently, then the defocusing would lead to just smoothing of the image by the increased lateral PSF. The measured profiles are not smoothed, away from the focus, the coherent interaction of the light leads to increased distortions in the measured profile. When measuring the standard flat surface at different distances from the focus, no increase in error was found. Hence surface texture is needed for the error.

The addition of error to profile measurements by distance from the focus is of importance when measuring multiple interfaces simultaneously. If the sample is

thicker than several hundred microns, then it is not possible that both interfaces are in focus. Also, materials with refractive index greater than one are going to change the focus position and lateral spot size (aberrations).

### 2.3.3 Optical path length distortion across OCT image and measurement of telecentricity

When measuring a lateral range 1mm or greater with the handheld probe (the effect on the larger optics was greater still) the OCT image was noticeably curved. By the measurement of the profile of a standard flat surface the curvature of the image can be measured. The measurement of this curvature also provides a method to measure the telecentricity of the optics. If the optics is not telecentric, then the probe beam for each axial set of data will not be parallel but convergent or divergent. From trigonometry, then the measured profile would be different at different distances from the instrument.

The profile of the standard flat surface was measured over a lateral range of 10mm at different axial distances from the probe (different heights in the OCT image). This was done by moving the probe with the motorised 3-axis micrometer stage. Figure 2.3.3.1 shows (a) the profile measurements and (b) the difference between one of the profile measurements and the rest. The most significant distortion of the curvature profile happens when the surface is placed at the top of the image. This is possibly due to how the “DC” signal is removed from the OCT data. In producing the images, the Thor Labs OCT somehow removes the strong “DC” component of signal that will always be present around zero depth in the image. The effect of this removal could be seen in all the OCT images, with strong drop off of signals and noise within the top 200 $\mu\text{m}$  of the images. This distortion of pixel values will distort the measured PSFs near the top of the image, distorting the measured profiles. When placed entirely below 300  $\mu\text{m}$  in the image, the profiles showed no systematic position dependent distortions, above vibrational noise. It is concluded that the optics were telecentric within experimental error.

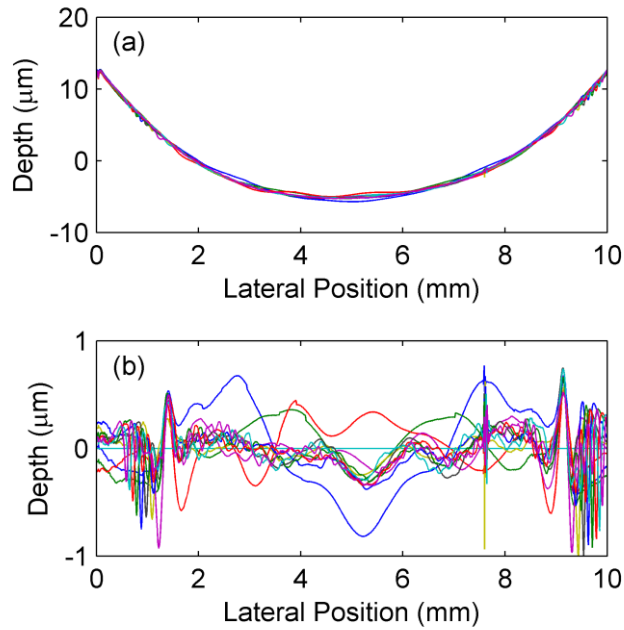


Figure 2.3.3.1  
 (a) Profile measurements of a standard flat surface at different height with OCT image.  
 (b) Differences between one profile and the others.

Two other experiments were also carried out to determine the factors affecting the image curvature. Like the axial position, the angle of the standard flat surface with respect to the axial direction of the measurement should also have no effect on the curvature of the profiles. The angle of the standard flat surface was controlled by a goniometer. Figure 2.3.3.2 (a) shows the measured curvature of profiles at three different angles. There are increased distortions in the profiles compared to the measurements at different heights. As the angled profiles cover a larger axial range than individual height measurements, these slight distortions may be due to minor distortions of the PSF with axial position, due to factors like the axial position of the focus across the image and again “DC” subtraction distortion.

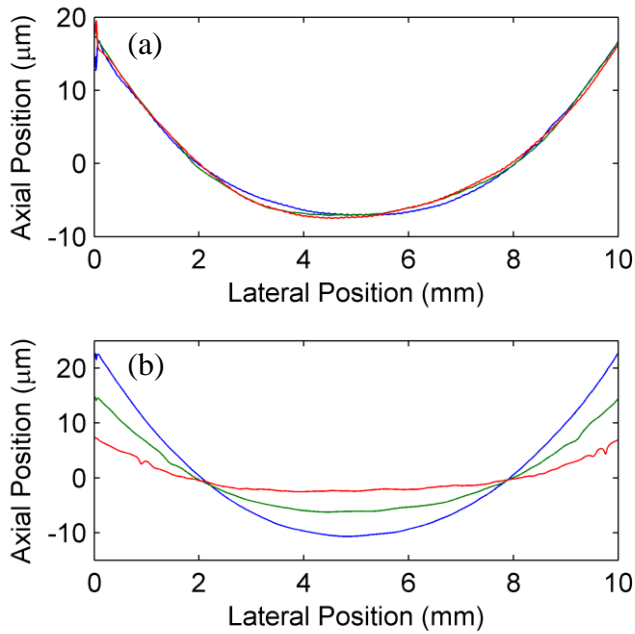


Figure 2.3.3.2  
 (a) Profile measurements of a standard flat surface at different angles within OCT image.  
 (b) Profile measurements of a standard flat surface with different focus adjustments.

The handheld OCT probe had a mechanism to adjust the focus position by the user. The focus was changed for three measurements of the curvature profile (Fig 2.3.3.2 (b)). It is seen that the curvature profile is dependent on the focus adjustment.

The curvature of the measured OCT profiles can be corrected for by measuring a standard flat surface before or after the measurement and ensuring that no adjustment of the probe is done between.

Take a plane normal to the optical axis of the probe beam/lateral spot, at an arbitrary depth. Consider the axial depth of this plane at each lateral position in the OCT image as a measured profile. This measured profile is distorted due to the difference in the relative optical path lengths through the optics. This profile distortion can be split into two components by considering it as a polynomial function. The measurement of the profile of a standard flat surface, at an arbitrary angle to the optical axis, gives the non-linear components of the polynomial function. However, as the angle between the flat surface and the optical axis is unknown, the linear polynomial component of the distortion cannot be calculated from this measurement. For the correction of surface profiles, this is not a problem as it is only the curvature (non-linear components) that needs to be corrected for, as the surface profile will be levelled anyway for any analysis. However, to correct for refraction the precise angle upon which the optical axis is incident on an interface needs to be known (to

correct by Snell's law). To measure the linear component of distortion needed for this, the properties of the cone of collection and illumination of the optics can be exploited.

The cone of illumination and collection of the instrument must be identical, as the light returned through the instrument must enter the same optical fibre from which it entered interferometer. Given a symmetric illumination, with a ray tracing approximation, it can be easily seen that the maximum light returned from a smooth surface will occur when that surface is normal to the optical axis. By measuring at what angle, within the OCT image, an interface gives the most intense reflection, this linear distortion is measured.

To measure this angle, two methods were used. Firstly the standard flat surface was measured over a range of angles using a goniometer. The intensity was taken from the amplitude of the Gaussian fit, taking the raw maximum pixel value gave near identical results. The angle was measured by a linear polynomial fit to the measured profile. Figure 2.3.3.3 (a) shows an example result by this method. The linear distortion in this measurement is  $1.5 \pm 0.5^\circ$ . When correcting for refraction when measuring refractive index by the droplet method described in the next chapter, knowledge of this value is necessary. Measurement of droplets provides a method to directly measure this linear distortion from the data taken for the RI measurement. The curvature of the droplet surface provides a range of slope/angle values, that can be measured with a linear fit with the adjacent lateral points of the profile. Figure 2.3.3.3 (b) shows an example measurement for a drying distilled water droplet. In this case the linear distortion is approximately  $1^\circ$ . The difference in the measured linear distortion between the two example measurements may be due to differences in the focus adjustment. It has been shown that this adjustment has a large impact on the nonlinear components of this distortion, so is likely to affect the linear component as well.

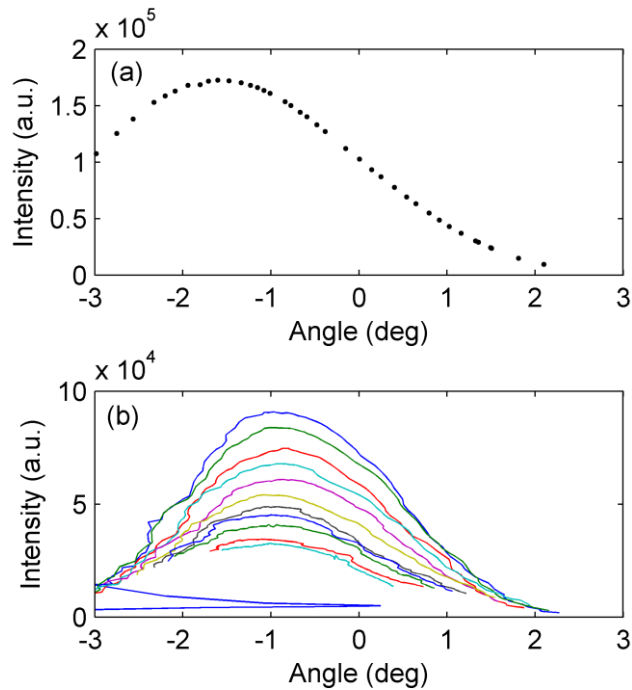


Figure 2.3.3.3  
Intensity of the PSF  
measured as function of  
lateral slope of interface  
within OCT image.  
(a) With a standard flat  
surface.  
(b) With a drying distilled  
water droplet.

## 2.4 Results

### 2.4.1 Regular surfaces

The first stage of quantitatively assessing the performance of the OCT profilometry technique was the measurement of standard references manufactured to a known profile. Distortions, in the measurements, away from the known profiles were identified and quantified. To overcome the problem of the curvature of the image, the handheld optics was chosen for use instead of the larger optics. This was because the curvature within the handheld probe was lower. The profile length used for the measurements was  $500\mu\text{m}$ . Over this length the measured curvature was negligible, meaning that correction was not needed.

A main source of error in the measurement of a smooth surface profile has been shown to be vibration in the system, which can be reduced by taking time domain averages of the cross-section images.

To quantify the accuracy on smooth surfaces and the improvement in accuracy with time domain data averaging, consecutive OCT images were taken of the standard flat surface. The fits for the surface profile were then carried out for different amount of images averaged. The surface tilt was removed from the fitted surface

profiles and the standard deviations of the profiles were measured. Figure 2.4.1.1 shows the decrease in the standard deviation with increased number of averaged frames. Little further improvement was seen after the averaging of 20 frames. The standard deviation of the surface measurement after averaging is shown, in this case, to level out at 55nm. The accuracy of the measurement depends on the level of vibration and the value quoted is typical of a measurement during the day on a lab bench without special anti-vibration devices.

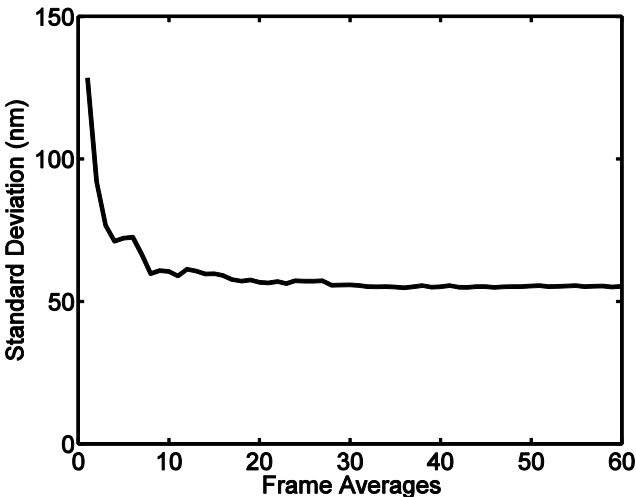


Figure 2.4.1.1  
Standard deviation of the surface profile measurement, of a standard flat surface, as a function of the number of frames averaged.

The accuracy of axial ranging is of key importance to any profilometry technique. The verification of correct ranging, by the technique, was carried out with a Veeco standard step surface of  $9.932\mu\text{m}$  in step height. This is a standard surface that is used to calibrate the Veeco VSI profilometer. The OCT cross-section image of the surface is shown in figure 2.4.1.2 (a). The surface profile and step height is then extracted from the mean of 60 OCT images (figure 2.4.1.2 (b)). The step height was measured at 6 separate locations on the surface with the FD-OCT which gave a mean  $\pm$  standard deviation of  $9.944 \pm 0.043\mu\text{m}$  consistent with the quoted reference value. The uncertainty in this measurement is similar in magnitude to that of the measurement of the standard flat surface.

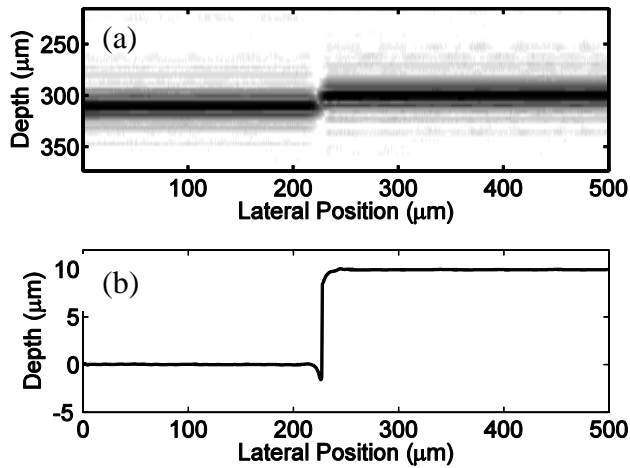


Figure 2.4.1.2  
 (a) FD-OCT image of a standard step surface in cross-section  
 (b) Surface profile measured from the FD-OCT image of the standard step.

Further evaluation of the performance of the technique, on a stepped surface, was carried out with the use of a square cut groove of  $1\mu\text{m}$  depth and  $100\mu\text{m}$  width (Rubert and Co Ltd precision reference specimen – 511). This surface was also measured with the Veeco VSI commercial system, with low magnification optics, for comparison of performance. Figure 2.4.1.3 shows measured surface profiles of the groove for both techniques. It can be seen that the commercial WLI profilometry system produced a less noisy profile than OCT. The added vibrational stability of the Veeco instrument gives smoother profiles on the flat surfaces. Also, in this measurement, OCT appears to have greater bat-winging artefacts. Bat wing effects can be explained by the diffraction caused by the discontinuity<sup>22</sup>. The low magnification optics used with the Veeco system measurement is likely to be a contributing factor in its reduced bat wings. The combination of the PSI principle into WLI is able to remove this effect<sup>24</sup>.

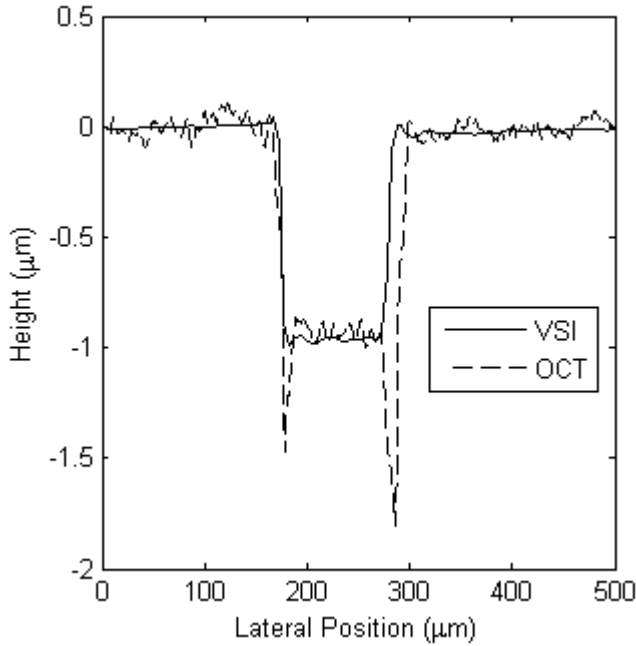


Figure 2.4.1.3  
Commercial WLI  
profilometer (Veeco inc  
Wyko NT1100) and the OCT  
measured profiles of 1µm  
deep trench (Rubert and Co  
surface 511).

Sinusoidal surfaces can be regarded as a regular rough surface with only one component of spatial frequency. It is well known that commercial WLI profilometers are susceptible to artefacts when measuring sinusoidal surfaces<sup>60</sup>, OCT will also be susceptible to the same artefacts. Two sinusoidal reference surfaces were measured with the Thorlabs OCT and the Veeco WLI instruments to compare the performance.

The first sinusoidal surface measured was Rubert and Co. surface 527. This can be considered relatively easy to map, with a large period of 100 µm and peak to peak height of 10 µm. Figure 2.4.1.4 (a) shows the OCT image of the surface. The surface profile was measured by Gaussian fits to an average of the images. To quantify the errors in the measurement the sinusoidal profile can be fitted to the result (figure 2.4.1.4 (b)). It is assumed that the incident light in the measurements are normal to the plane of the surface, if this were not the case the profile measured would be distorted. The reference surface is sinusoidal in one direction,  $\mathbf{x}$ , and planar perpendicular,  $\mathbf{y}$ . The lateral measurement direction of the profiles,  $\mathbf{r}$ , is likely to be distorted from the  $\mathbf{x}$  direction by angle  $\theta$ . By trigonometry distance travelled in  $\mathbf{x}$  is given by  $\frac{r}{\cos \theta}$ , hence the measured period is also scaled by  $\frac{1}{\cos \theta}$ . The phase of the sinusoidal profile is dependent on the starting position of the profile. Hence, for the sinusoidal fit; the amplitude was fixed to the reference value,

but period and phase were fitted. The fitting was carried out by the same method as the Gaussian fits for profile measurement, with least square fit using of MATLAB's `fminsearch` function.

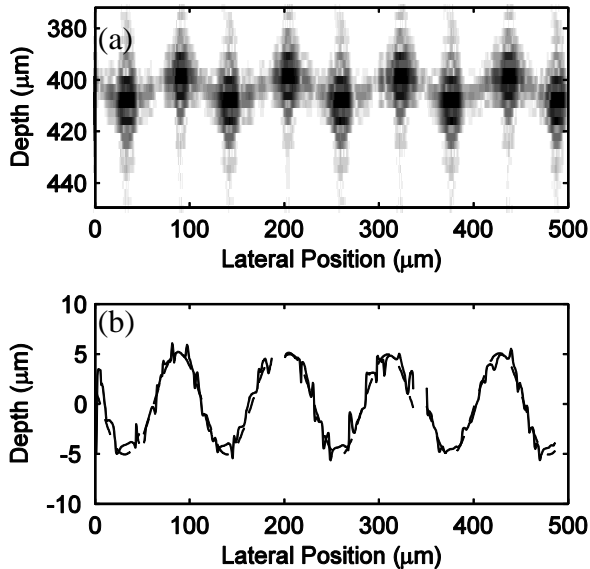


Figure 2.4.1.4  
(a) SROCT image of a sinusoidal surface;  
(b) Surface profile measured from the SROCT data (solid line) with the sinusoidal surface profile fitted to the result (dashed line).

The Veeco VSI (WLI) method on this surface proved problematic. Due to technical reasons the objective lens used was of low NA (low magnification – large working distance) and it could not be changed. As shown in the OCT image (figure 2.4.1.4 (a)), due to the relative slope of the surface the signal from the sides of the sinusoid are much lower than at the top and bottom. This is due to the sloped sides reflecting the light away from the return path of the optics (geometric optics regime). In this measurement the Veeco system did not return a result due to lack of signal from the sides of the sinusoid, only giving the height of the troughs and peaks. This result is shown compared to the OCT result in Figure 2.4.1.5. Larger NA objective optics for the Veeco instrument is expected to improve this result by increasing the size of the cone of acceptance for the reflected light. It can also be noted that by design, the NA of the OCT system will also be low, but the high sensitivity to the weak signal, from the sides of the sinusoid, compensates for this issue.

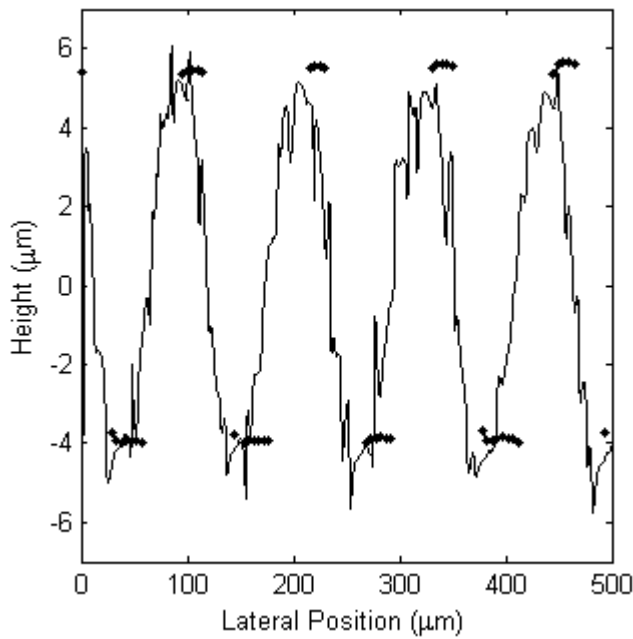


Figure 2.4.1.5  
Surface profile measured from the SROCT data (solid line) compared with the measured points by the Veeco WLI profilometer (points).

The second sinusoidal surface measured was Rubert and Co surface 528. This has peak-to-peak amplitude of  $1.5\mu\text{m}$  and period of  $50\mu\text{m}$ . To verify the quality of the surface independently the PSI method was used with the Veeco instrument to measure the surface (figure 2.4.1.6). The result showed the sinusoid to be smooth. However phase ambiguity errors, associated with PSI, are very apparent.

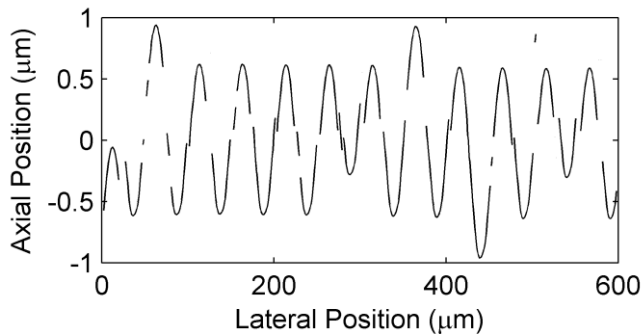


Figure 2.4.1.6  
Surface profile of Rubert and Co surface 528 (sinusoid) surface measured with PSI.

The surface was again measured with the Veeco VSI (WLI) and Thorlabs OCT methods. The sinusoidal profile shape was fitted to the results. The measured profiles, fits and deviation from the fits are shown for measurements with the Thorlabs OCT (figure 2.4.1.7 (a) and (b)) and the Veeco WLI (figure 2.4.1.7 (c) and (d)). The *rms* of the residual from the fit for the Thorlabs OCT is  $0.2733\mu\text{m}$  and for the Veeco WLI is  $0.2594\mu\text{m}$ , showing that the magnitude of errors are similar.

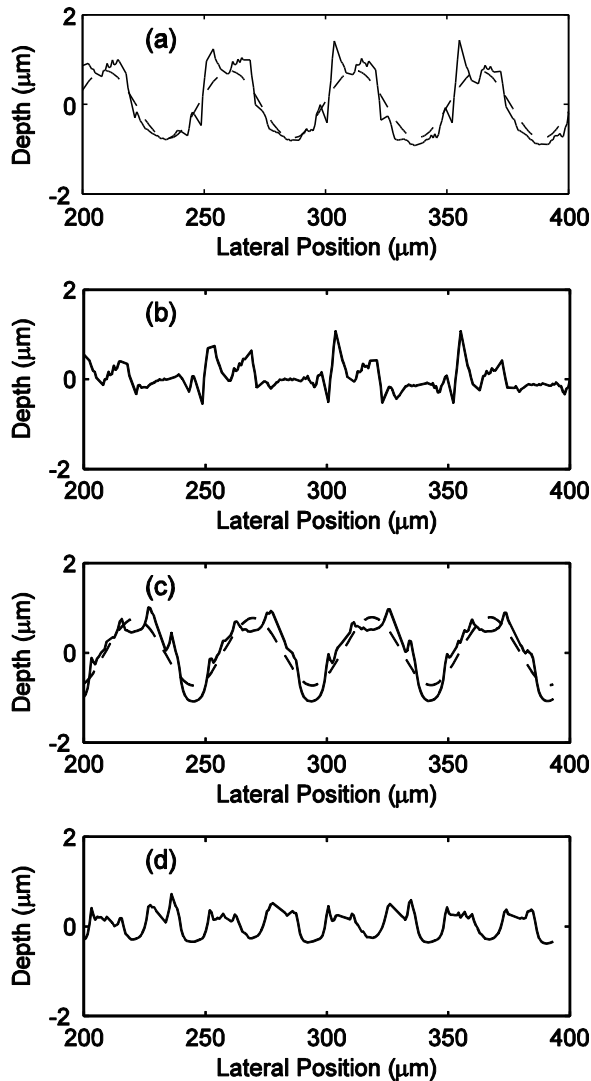


Figure 2.4.1.7.  
 (a) Surface profile measurement (solid line) with SROCT of a sinusoidal surface of  $1.5\ \mu\text{m}$  peak-to-peak amplitude and  $50\ \mu\text{m}$  period (Rubert and Co surface 528) and a sinusoidal fit to the measurement (dashed line).  
 (b) Residual between OCT measured profile and the sinusoidal fit shown in (a)  
 (c) Surface profile of the same Sine surface measured with a Veeco inc. Wyko NT1100 WLI (solid line) and a sinusoidal fit to measurement (dashed line).  
 (d) Residual between the WLI measured profile and sinusoidal fit shown in (c).

The dominating error in the measurement of profiles of sinusoidal surfaces, with broadband interferometry, is an intrinsic property of the finite lateral resolution of the systems. This is shown in the results of measurements of two sinusoidal surfaces. One where the performance of the OCT method is near identical to a commercial WLI profilometer and one where the lack of sensitivity of the commercial system meant that it was not able to resolve the complete surface while the OCT method could.

The final standard surface examined with the Thorlabs OCT and the Veeco WLI was the Rubert and Co surface 521. This is a sawtooth (Triangular) wave. The

period of the surface is 15  $\mu\text{m}$ , which is much smaller than the two sinusoidal surfaces measured though still larger than (approximately twice as large) the lateral resolution of the OCT system. The peak to peak amplitude is 1.6  $\mu\text{m}$ , which gives it similar ( $\sim 1:10$ ) aspect ratio to the larger sinusoid surface. The combination of these factors resulted in a surface that was difficult to measure.

Figure 2.4.1.8 shows the measured profiles with the techniques. Both techniques failed to resolve the surface correctly. After this failure, a second independent measurement was carried out with both techniques, which gave similar negative results. This surface is an example where the OCT method has the same limitation as the commercial WLI profilometer.

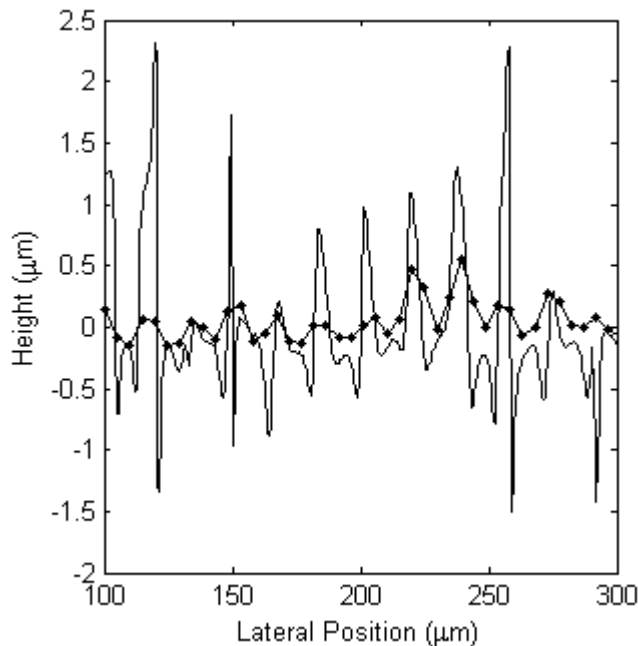


Figure 2.4.1.8.  
Part of surface profile  
measurements of a sawtooth  
surface (Rubert and Co  
surface 521) with the SROCT  
(line) and the Veeco WLI  
profilometer (line with points)

## 2.4.2 Random rough surfaces

This project used OCT multi-interface profilometry to measure the drying of varnish on ground glass substrates (chapter 6). These substrates are random rough surfaces that are optically matte. The use of OCT to measure such surfaces is starting to be explored<sup>53</sup>. For these random textured surfaces, speckle effects are expected to be the largest contributor of error. This section details the results from a method to estimate this error, for two different random rough surfaces.

To experimentally evaluate the error on random rough surfaces two different ground glass surfaces were used. The first being the fine rough surface previously used in another varnish study<sup>3</sup>, which was produced with grinding with 12 $\mu\text{m}$  aluminium oxide powder then donated to the research group. The measured surface roughness of this substrate, by this previous study of the surface with mechanical profiler with stylus tip radius of 2  $\mu\text{m}$ , was 0.67  $\mu\text{m}$ . The second rough surface used for the study was produced by the research group before the author's arrival. This consisted of a piece of glass that had been sandblasted with coarse sand, giving a much coarser rough surface. Figure 2.4.2.1 shows mechanically measured surface profiles of the two surfaces in order to highlight their relative scales. The measurement was carried out with the Veeco Dektak 6M profiler, with tip radius of 12.5 $\mu\text{m}$ .

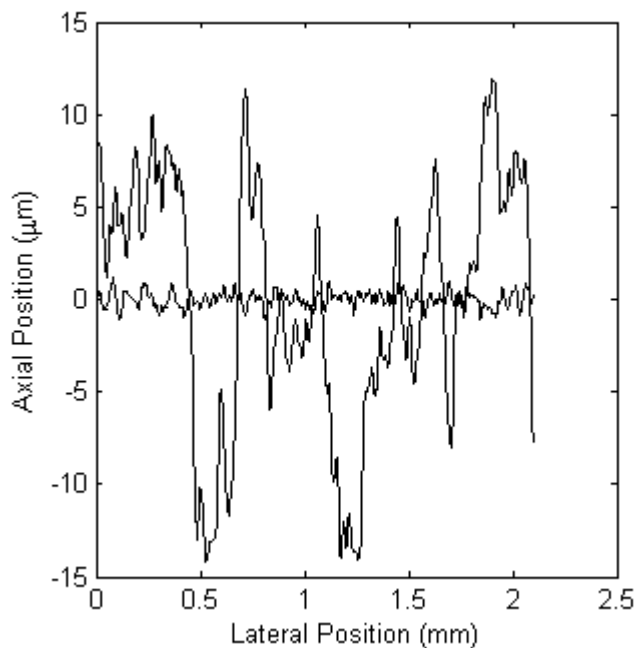


Figure 2.4.2.1. Mechanical profilometer measurements of the two surfaces used in this section for the evaluation of rough surface profile measurement with the OCT system.

When the two rough surfaces were examined with VSI and PSI they were found to be invisible to the method due to the low intensity of directly reflected light. The high sensitivity of OCT and the return to the user of all signal information allow these surfaces to be measured.

The OCT profile measurements of the rough interfaces were carried out by the same method as before. A free width Gaussian fit was carried out on the highest value pixel and 2 adjacent pixels either side. Figure 2.4.2.2 shows an example fit to the

coarse rough surface, the pixel intensity is significantly “noisier” than for smooth surfaces.

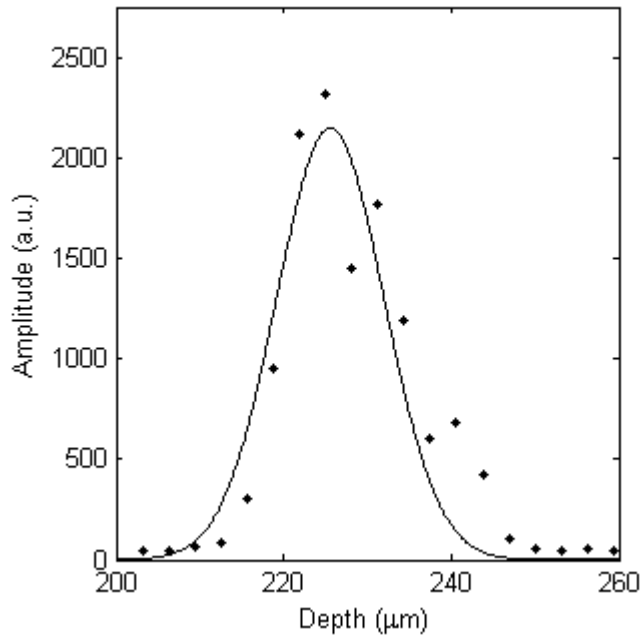


Figure 2.4.2.2.  
Axial pixel intensity  
across rough surface  
(points) and Gaussian fit  
(line) to find interface  
position.

In order to evaluate error in profile measurements, due to speckle, the properties of speckle need to be exploited. Speckle is dependent on the interactions of the optics of the measuring instrument and the surface being measured. In a FD OCT system, such as the Thorlabs instrument being used here, it is proposed that the relationship of the surface, that is being measured, with the optics of the instrument can be changed by moving the position of the surface axially in the image. This change in the optical paths may de-correlate the speckle pattern and its effect. It is presumed that an axial movement greater than the correlation length of the light ( $\sim$  Full Width Half Maximum (FWHM) of the PSF) should be sufficient to ensure complete de-correlation. The amount of axial shift for the measurement of speckle was always much greater than the PSF FWHM.

As has been shown, the position of the surface relative to the position of the focus of the instrument is an important consideration. The measurement of a surface away from the focus position can lead to large errors in the measurement. Hence consideration needs to be given to keep the positions of the surface measurements close to the focus. There should not be too large a separation between the profile measurements.

The Thorlabs OCT was used to image the surface at 4 different axial positions in the image. This was achieved by moving the 3 axis stage upon which the OCT probe is fixed, away from or towards the sample. The lateral shift for this movement is assumed to be negligible, due to geometric factors of the setup of the OCT probe on the stage some lateral shift may be introduced contributing an error between the profile measurements. A surface profile is then found from each measurement. Here the assumptions are needed that the statistics of the surface profiles and the errors behave as Gaussian (Normal) and the errors due to speckle of each measured profile are de-correlated. For each profile, the measured *rms* roughness, *M*, is given by

$$M^2 = R^2 + S^2 + E^2. \quad (2.4.2.1)$$

Where *R* is the real *rms* roughness, *S* is the standard deviation error due to speckle and *E* is the standard deviation due to other causes. With the averaging of image data before calculation of the profile, the other measurement errors, *E*, are the same as the standard flat surface, here approximated to 50nm.

If the residual, *K*, between two profiles is taken, the standard deviation of this is given by

$$K^2 = 2S^2 + 2E^2. \quad (2.4.2.2)$$

From the two above equations a calculation of the real *rms* roughness of a surface and the *rms* error due to speckle can be calculated for a pair of profiles. These were calculated for each possible pair of profiles to enable the calculation of a mean and standard deviation of the results.

Figure 2.4.2.3 shows (a) part of the OCT image and (b) corresponding profile measurements for the fine rough surface. It can be seen that the profile measurements are dissimilar. Table 2.4.2.1 (a), shows the standard deviation of the residuals and table 2.4.2.1 (b) shows the measured raw *rms* of the profiles. The profiles were measured at 100µm axial intervals and labelled by their height in the image. The focus was closest to the 300µm profile, this is apparent in the *rms* result of the measured profile as this has the lowest raw *rms* value.

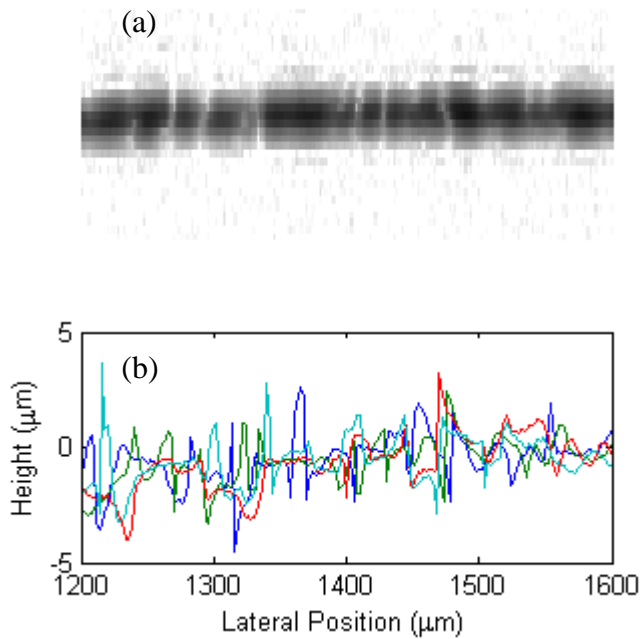


Figure 2.4.2.3.  
 (a) OCT image of part of the interface of the fine random rough surface.  
 (b) Profile measurements of the part of the interface for the separate measurements.

The Difference Between Measurements	Standard Deviation $\mu\text{m}$	The Difference Between Measurements	Standard Deviation
300 $\mu\text{m}$ – 200 $\mu\text{m}$	1.2324	400 $\mu\text{m}$ – 300 $\mu\text{m}$	1.0972
400 $\mu\text{m}$ – 200 $\mu\text{m}$	1.3743	500 $\mu\text{m}$ – 300 $\mu\text{m}$	1.3310
500 $\mu\text{m}$ – 200 $\mu\text{m}$	1.4929	500 $\mu\text{m}$ – 400 $\mu\text{m}$	1.1628

Measurement Height	<i>rms</i> (Std) Roughness Measured
200 $\mu\text{m}$	1.1709
300 $\mu\text{m}$	1.0625
400 $\mu\text{m}$	1.2222
500 $\mu\text{m}$	1.3086

For the fine rough surface Above – Table 2.4.2.1 (a) the standard deviation of residuals between pairs of measurements. Left – Table 2.4.2.1 (b) the measure standard deviation roughness of each raw profile.

The *rms* of the measured raw profiles was  $1.19 \pm 0.10\mu\text{m}$ , but the difference between the profiles at different measurement distance was higher at  $1.28 \pm 0.15\mu\text{m}$ . Table 2.4.2.2 shows, for each profile pair, the calculated surface roughness and speckle error. The mean  $\pm$  standard deviation of the calculated roughness was  $0.75 \pm 0.17\mu\text{m}$ , while for the calculated error due to speckle error it was  $0.91 \pm 0.10\mu\text{m}$ . The error (due to speckle) in the measurement of this surface is higher than the actual surface roughness. However, this statistical treatment does allow the acquisition of the real *rms* roughness value of the surface roughness, despite the error. The value of the *rms* measurement for the previous study<sup>3</sup>,  $0.67\mu\text{m}$ , is within

the error bounds of this measurement. This is an improvement over the known comparable study<sup>53</sup>, where they were limited (by speckle) in the measurement of standard random rough surfaces of low *rms* values.

Primary Profile	Secondary Profile	Speckle Error	Real Roughness
300um	200um	0.8700	0.6079
300um	400um	0.7742	0.7259
300um	500um	0.9398	0.4931
200um	300um	0.8700	0.7820
200um	400um	0.9705	0.6532
200um	500um	1.0545	0.5066
400um	200um	0.9705	0.7412
400um	300um	0.7742	0.9444
400um	500um	0.8207	0.9043
500um	200um	1.0545	0.7733
500um	300um	0.9398	0.9092
500um	400um	0.8207	1.0180

Table 2.4.2.2. Calculated speckle error and real *rms* roughness for each pairing of the measured profiles.

Figure 2.4.2.4 (a) shows part of an OCT image of the coarse rough surface. Compared to the fine rough surface, the structure is clear in the image as the scales are greater than the imaging resolution. The corresponding measured surface profiles are shown in Figure 2.4.2.4 (b). The profiles in this case are clearly more similar, with the structure in the images followed. The error in the profile measurement due to speckle will not exceed the imaging resolution of the system. Another source of error, due to the surface preparation, is also identified in this result. The production of the rough surfaces, by grinding or sandblasting, works by fracturing then removing the surface glass. However as the glass fractures by the application of stress, it will not always lead to a clean break of the glass. This will lead to the presence of subsurface cracks (fractures) in the final substrate. Above the lateral position 1300µm (figure 2.4.2.4) subsurface scattering is clearly evident in the image. This makes the automatic detection of which bright pixel corresponds to the interface more difficult than taking the brightest pixel within the region. This is shown in the profile measurements where two profiles follow the surface while two are diverted to the subsurface scattering.

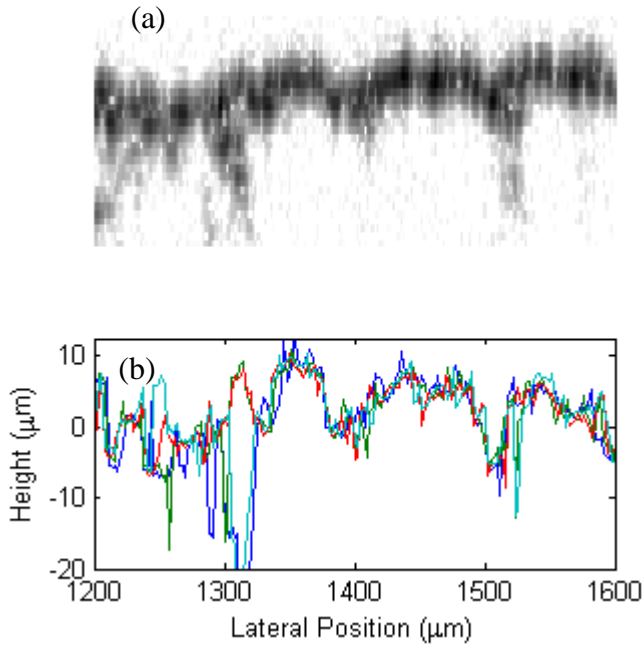


Figure 2.4.2.4.  
 (a) OCT image of part of the interface of the coarse random rough surface.  
 (b) Profile measurements of the part of the interface for the separate measurements.

Table 2.4.2.3 (a), shows the standard deviation of the residuals and table 2.4.2.3 (b) shows the measured raw *rms* of the profiles. The raw *rms* of the profiles was  $10.39 \pm 0.19\mu\text{m}$  and the *rms* residual between the profiles was  $4.38 \pm 0.65\mu\text{m}$ . In this case the difference between the profiles is smaller than the raw measured roughness of the profiles.

The Difference Between Measurements	Standard Deviation $\mu\text{m}$	The Difference Between Measurements	Standard Deviation
300 $\mu\text{m}$ – 200 $\mu\text{m}$	4.2284	400 $\mu\text{m}$ – 300 $\mu\text{m}$	3.4050
400 $\mu\text{m}$ – 200 $\mu\text{m}$	4.7603	500 $\mu\text{m}$ – 300 $\mu\text{m}$	4.6148
500 $\mu\text{m}$ – 200 $\mu\text{m}$	5.2716	500 $\mu\text{m}$ – 400 $\mu\text{m}$	4.0053

Measurement Height	<i>rms</i> (Std) Roughness Measured
200 $\mu\text{m}$	10.5773
300 $\mu\text{m}$	10.4665
400 $\mu\text{m}$	10.1353
500 $\mu\text{m}$	10.4003

For the coarse rough surface Above – Table 2.4.2.3 (a) the standard deviation of residuals between pairs of measurements. Left – Table 2.4.2.3 (b) the measure standard deviation roughness of each raw profile.

Table 2.4.2.2 shows, for each profile pair, the calculated surface roughness and speckle error. The measures *rms* surface roughness is  $9.91 \pm 0.18\mu\text{m}$  and error due to speckle of  $3.10 \pm 0.44\mu\text{m}$ . Though this speckle error is large, it is significantly

less than the *rms* roughness of the profile. For such a coarse rough glass substrate, OCT is adequate to measure its surface profile directly.

Primary Profile	Secondary Profile	Speckle Error	Real Roughness
300um	200um	2.9895	10.0304
300um	400um	2.4072	10.1858
300um	500um	3.2628	9.9448
200um	300um	2.9895	10.1459
200um	400um	3.3657	10.0274
200um	500um	3.7272	9.8987
400um	200um	3.3657	9.5600
400um	300um	2.4072	9.8452
400um	500um	2.8317	9.7316
500um	200um	3.7272	9.7093
500um	300um	3.2628	9.8751
500um	400um	2.8317	10.0072

Table 2.4.2.2.  
Calculated speckle error and real *rms* roughness for each pairing of the measured profiles.

For the measurement of the profile of any interface with OCT (or any other broadband interferometry technique), the error caused by speckle is dependent on its roughness. The measurements of the interface profile at different axial positions in the FD OCT image allows (assuming the errors become decorrelated) the calculation of error due to speckle in the profiles and the calculation of the real *rms* roughness. With this information, the use of rough surfaces in the project will be restricted to surfaces where the calculated real *rms* roughness is greater than the calculated speckle error. For rough surfaces speckle is the dominating error in the measurements.

### 2.4.3 Random rough second interface

The application of multi-interface OCT profilometry to a drying varnish coating on a rough glass substrate (13 $\mu$ m *rms* roughness), allows the simultaneous measurement of the smooth varnish surface profile and the substrate profile. To determine the accuracy of recovering the rough substrate profile, after correcting for both the optical thickness and refractive effects due to Snell's law, the coarse rough surface was initially measured with the SROCT over a lateral range of 10mm. Without moving the instrument or the substrate, a varnish solution of Regalrez 1094

dissolved in white spirit at a ratio of 1g of resin to 1ml of solvent was applied by a pipette from the side and left to spread. This was controlled so that approximately half the surface in the OCT image was covered with the solution.

Because of the massive difference in the intensity of the Fresnel reflections, from the air/varnish interface and varnish/glass interface, care needs to be taken in finding the second interface to distinguish it correctly from harmonic and ringing artifacts. In addition, a post processing algorithm for the removal of remaining ringing artifacts and anomalous points was devised and implemented in MATLAB. The 2D Snell's law refractive index correction was then carried out to find the correct second interface. A final result showing the rough substrate profile before and after the application of varnish and the difference between the two are shown in Figure 2.4.3.1. The outliers in the difference graph are incorrect identifications of the interface by the automatic routine due to the presence of image artefacts.

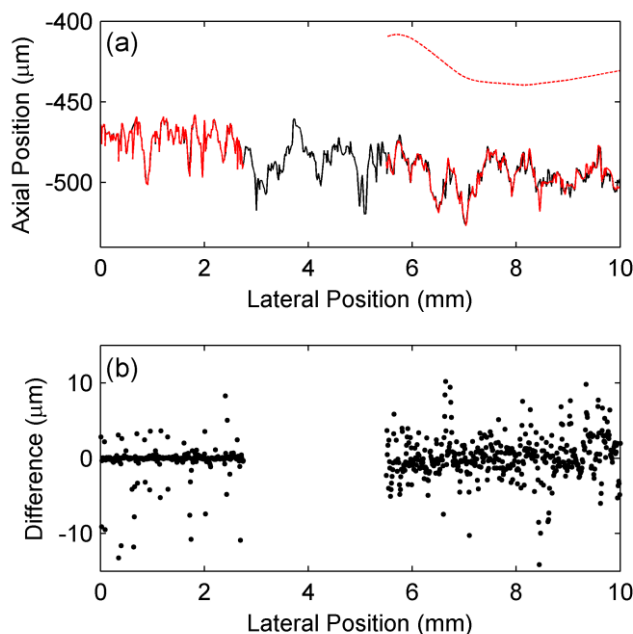


Figure 2.4.3.1.  
 (a) Profile of coarse glass substrate measured before (black line) and after (red line) deposition of a varnish solution of Regalrez dissolved in white spirit over half the measured profile. The varnish surface is shown by a dotted red line. The substrate profile below the varnish was recovered by assuming a refractive index of 1.49;  
 (b) Difference between the before and after profiles of the rough glass substrate.

To determine the effect of refractive index in the correction of second interface measurements, each measured varnish/substrate profile was corrected for a range of refractive indices. The *rms* of the difference between the measured glass substrate profile before application of the varnish and those of the same substrate profile recovered from below the varnish using various refractive index values are shown in

figure 2.4.3.2. A minimum occurs at the refractive index value corresponding to that measured in the next chapter. The minimum *rms* difference approaches the measured speckle error of the substrate surface. Figure 2.4.3.2 shows that for this coarse substrate, a refractive index accuracy of 0.05 is needed to ensure that the error due to refractive index correction is not significant compared to speckle error.

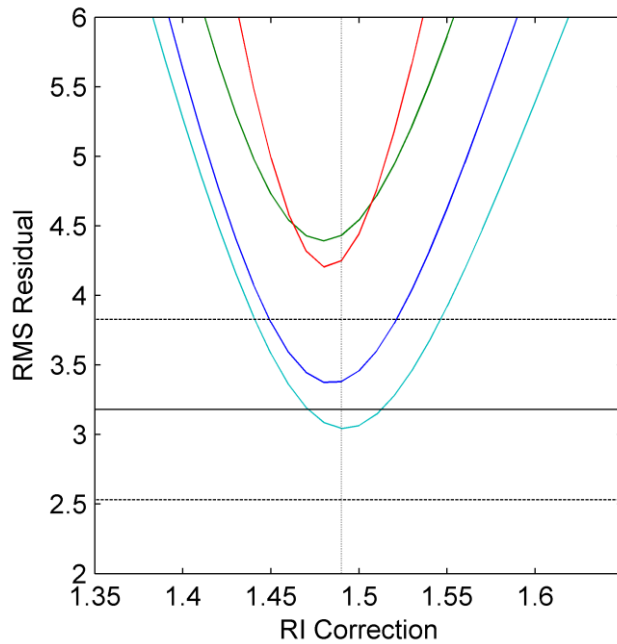


Figure 2.4.3.2. The rms difference between the corrected varnish/substrate interface measurements and the reference measurement before the deposition of the varnish is shown as a function of the assumed refractive index of the varnish. The colored lines show four repeats of this measurement. The dashed vertical line shows the measured refractive index of the varnish from section 3.2. The horizontal solid line shows the measured speckle error of the substrate surface using the method detailed in section 2.3. The dot dashed line is the  $\pm 1\sigma$  boundaries of this measurement.

## 2.5 Conclusion

Optical Coherence Tomography (OCT) shares the same physics as any other broadband interferometry profilometry technique. This means that it can achieve the same magnitude of precision. Here, for smooth surface a precision of  $\sim 55$  nm was achieved, the main limitation of reducing this value was lack of vibration suppression within the instrument. Errors due to speckle/diffraction when measuring random/regular rough surfaces with OCT are the same as any other broadband interferometry technique.

When measuring random rough interfaces speckle dominates the error. The maximum error is similar in magnitude to the FWHM resolution of the instrument. However this speckle error and the real *rms* roughness can be estimated with a

simple technique with FD OCT. This can be used as a validity checker for profile measurements of random rough surfaces.

Profilometry with OCT is a post processing technique, allowing any interface visible within an OCT image to be accurately profiled. The optimisation of OCT systems means that they have high sensitivity. This allows them to see faint (and speckely) interfaces, allowing their profile to be measured. This is ideal for multi-interface profilometry, where internal reflections are weak. The accuracy of this internal interface profilometry was shown for a coarse rough glass substrate covered by varnish. The error in the measurement was not much higher than the speckle error for measuring the interface without the varnish.

OCT systems have no additional limits to their performance, than other broadband interferometry profilometry techniques, but do offer greater sensitivity than some instruments. Rather than having two separate instruments, for profilometry and tomographic imaging, there is no reason that future instruments cannot be designed to do both. This would replace two specialised and expensive pieces of equipment with one instrument, with potentially better capabilities.

## 2.6 References

---

<sup>1</sup> Stout K. J. and Blunt L., Three Dimensional Surface Topography (Penton Press, 2000).

<sup>2</sup> Bennett J. M., and Mattson L., Introduction to surface roughness and scattering (Optical society of America, Washington, 1989).

<sup>3</sup> Elias Mady, de la Rie E. René, Delaney John K., Charron Eric and Morales Kathryn M., “Modification of the surface state of rough substrates by two different varnishes and influence on the reflected light”, Optics Communications, 266 (2), pp. 586-591 (2006).

<sup>4</sup> Poon Chin Y. and Bhusan Bharat, “Comparison of surface roughness measurements by stylus profiler, AFM and non-contact optical profiler”, Wear, 190, pp. 76-88 (1995).

<sup>5</sup> Tian Ailing, Lui X, Chetwynd D. G. and Cai Zhijian, “Stylus contact on short wavelength random surfaces: a simulation study”, Meas. Sci. Technol., 18, pp. 1694-1702 (2007).

- 
- <sup>6</sup> KLA\_Tencor Corporation, 2009, HRP-250, <http://www.kla-tencor.com/substrate/hrp-250.html>, Accessed 13/03/2009, Re-Accessed 19/04/2011.
- <sup>7</sup> Binnig G, Quate CF and Gerber C, “Atomic Force Microscope”, *Phys. Rev. Lett.* 56, pp. 930–933 (1986).
- <sup>8</sup> Rezende Camila A., Lee Lay-Theng and Galembeck Fernando, “Surface Mechanical Properties of Thin Polymer Films Investigated by AFM in Pulsed Force Mode”, *Langmuir*, 25 (17), pp. 9938-9946 (2009).
- <sup>9</sup> Gu Min, *Principles of three dimensional imaging in confocal microscopes*, World Scientific Publishing (1996).
- <sup>10</sup> Stifter D., “Beyond biomedicine: a review of alternative applications and developments for optical coherence tomography”, *Appl. Phys. B*, 88, 337-357 (2007).
- <sup>11</sup> Ling X., Pritzker M. D., Byerley J. J. and Burns C. M., “Confocal Scanning Laser Microscopy of Polymer Coatings”, *Journal of Applied Polymer Science*, 67, pp. 149-158 (1998).
- <sup>12</sup> Schreiber H and Bruning J H, Chapter 14 in *Optical Shop Testing*, Ed: Malacara D, John Wiley and Sons Inc (2007).
- <sup>13</sup> Veeco Inc., <http://www.veeco.com/pdfs/webinar-slides/A-First-Look-at-NT9080-webinar-slides-100408.pdf>, Accessed 13/07/2011.
- <sup>14</sup> Canielson Bruce L. and Boisrobert C. Y., “Absolute optical ranging using low coherence interferometry”, *Applied Optics*, 30 (21), pp. 2975-2979 (1991).
- <sup>15</sup> Lee Byron S. and Strand Timothy C., “Profilometry with a coherence scanning microscope”, *Applied Optics*, 29 (26), pp. 3784-3788.
- <sup>16</sup> Dresel Thomas, Hausler Gerd and Venzke Holger, “Three dimensional sensing of rough surfaces by coherence radar”, *Applied Optics*, 31 (7), pp. 919-925 (1992).
- <sup>17</sup> Endo Takashi, Yasuno Yoshiaki, Makita Shuichi, Itoh Masahide and Yatagai Toyohiko, “Profilometry with line-field Fourier-domain Interferometry”, *Optics Express*, 13 (3), pp. 695-701 (2005).
- <sup>18</sup> Reolon D., Jacquot M., Verrier I., Brun G. and Veillas C., “Broadband supercontinuum interferometer for high-resolution profilometry”, *Optics Express*, 14 (1), 128-137 (2005).
- <sup>19</sup> Tay C. J., Quan C. and Li M., “Investigation of a dual-layer structure using vertical scanning interferometry”, *Optics and Lasers in Engineering*, 45, pp. 907-913 (2007).

- 
- <sup>20</sup> Huang David, Swanson Eric A., Lin Charles P., Schuman Joel S., Stinson William G., Chang Warren, Hee Michael R., Flotte Thomas, Gregory Kenton, Puliafito Carmen A. and Fujimoto James G., “Optical Coherence Tomography”, 254 (5035), pp. 1178-1181 (1991).
- <sup>21</sup> Gao F., Leach R. K., Petzing J., and Coupland J. M., “Surface measurement errors using commercial scanning white light interferometers”, *Meas. Sci. Technol.*, 19, 015303 (2008).
- <sup>22</sup> Harasaki Akiko and Wynat James C., “Fringe modulation skewing effect in white light vertical scanning Interferometry”, *Appl. Opt.*, 39, pp. 2101-2106 (1997).
- <sup>23</sup> Goodman Joseph W., *Speckle phenomena in optics theory and applications*, Ben Roberts & Company (2007).
- <sup>24</sup> Harasaki Akiko, Schmit Joanna and Wynat James C., “Improved vertical-scanning interferometry”, *Applied Optics*, 39 (13), pp. 2107-2115 (2000).
- <sup>25</sup> Spagnolo G. Schirripa, Guattari G., Sapia C., Ambrosini D., Paoletti and Accardo G., “Three-dimensional optical profilometry for artwork inspection”, *J. Opt. A: Pure Appl. Opt.*, 2, pp. 353-361 (2000).
- <sup>26</sup> Spagnolo G. Schirripa, Guattari G, Sapia C, Ambrosini D, Paoletti and Accardo G, “Contouring of artwork surface by fringe projection and FFT analysis”, *Optics and Lasers in Engineering*, 33, pp. 141-156 (2000)
- <sup>27</sup> Bulut Karahan and Inci M. Naci, “Three-dimensional optical profilometry using a four-core optical fibre”, *Optics & Laser Technology*, 37, pp. 463-469 (2005).
- <sup>28</sup> Marie Iqbal and Qasrawi Hisham, “Virtual assembly of pottery fragments using moiré surface profile measurements”, *Journal of Archaeological Science*, 32, pp. 1527-1533 (2005).
- <sup>29</sup> Harizanova Jana and Sainov Ventseslay, “Three-dimensional profilometry by symmetrical fringes projection technique”, *Optics and Lasers in Engineering*, 44, pp. 1270-1282 (2006).
- <sup>30</sup> Brillaud Jean and Lagattu Fabienne, “ Digital correlation of grainy shadow images for surface profile measurement”, *Optik*, pp. 411-417 (2006).
- <sup>31</sup> Sansoni Giovanna, Trebeschi Marco and Docchio Franco, “Fast 3D profilometry based upon the projection of a single fringe pattern and absolute calibration”, *Meas. Sci. Technol.*, 17, pp. 1757-1766 (2006).
- <sup>32</sup> Mao Xianfu, Chen Wenjing and Su Xianyu, “Improved Fourier-transform profilometry”, *Applied Optics*, 46 (5), pp. 664-668 (2007).
- <sup>33</sup> Whitehouse David, *Surfaces and their Measurement*, Taylor Hobson Ltd (2002).

- 
- <sup>34</sup> Freund L. B. and Suresh S., *Thin Film Materials Stress, Defect Formation and Surface Evolution*, Cambridge University Press (2003).
- <sup>35</sup> Tompkins Harland G. and Irene Eugene A., *Handbook of Ellipsometry*, William Andrew Inc (2005).
- <sup>36</sup> Polikreti Kyriaki and Christofides Constanos, "Spectroscopic ellipsometry as a tool for the optical characterisation and ageing studies of varnishes used in Post-Byzantine icon reconstructions", *Journal of Cultural Heritage*, 7, pp. 30-36 (2006).
- <sup>37</sup> Fercher A. F., Drexler W., Hitzengerger C. K. and Lasser T., "Optical coherence tomography – principles and applications", *Rep. Prog. Phys.*, 66, 239-303 (2003).
- <sup>38</sup> Tomlins P. H. and Wang R. K., "Theory, developments and applications of optical coherence tomography", *J. Phys. D: Appl. Phys.*, 38, 2519-2535 (2005).
- <sup>39</sup> Drexler W. and Fujimoto J. G., *Optical Coherence Tomography Technology and Applications* (Springer, 2008).
- <sup>40</sup> Fercher A. F., Hizenberger C. K., Kamp G. and El-Zaiat S. Y., "Measurement of intraocular distances by backscattering spectral interferometry", *Optics Communications*, 117, 43-48 (1995).
- <sup>41</sup> Targowski P., Góra M. and Wojtkowski M, "Optical Coherence Tomography for Artwork Diagnostics", *Laser Chemistry*, doi:10.1155/2006/35373 (2006).
- <sup>42</sup> Liang H., Peric B., Hughes M., Podoleanu A. G., Spring M., and Roehrs S., "Optical Coherence Tomography in archaeological and conservation science - a new emerging field", *Proc. SPIE* 7139, 713915 (2008).
- <sup>43</sup> Liang H., Cid M. G., Cucu R., Dobre G., Kudimov B., Pedro J., Saunders D., Cupitt J., and Podoleanu A., "Optical coherence tomography: a non-invasive technique applied to conservation of paintings", *Proc. SPIE* 5857, 261-269 (2005).
- <sup>44</sup> Prykäri T., Czajkowski J., Alarousu E. and Myllyla R., "Optical Coherence Tomography as an Accurate Inspection and Quality Evaluation Technique in Paper Industry", *Optical Review*, 17 (3), 218-222 (2010).
- <sup>45</sup> Leitgeb R., Hitzengerger C. K., and Fercher A. F., "Performance of fourier domain vs. time domain optical coherence tomography", *Optics Express*, 11 (8), pp. 889-894 (2003).
- <sup>46</sup> Pedrotti Frank L., Pedrotti Leno M. and Pedrotti Leno S., Chapter 7 Interference of Light, in *Introduction to Optics*, Third Edition, (Pearson, 2007), pp 163 – 191.
- <sup>47</sup> Tang Kwong-Tin, *Mathematical Methods for Engineers and Scientists 3 Fourier Analysis Partial Differential Equations and Variational Methods*, Springer-Verlag (2007).

- 
- <sup>48</sup> Thorlabs Inc,  
<http://www.thorlabs.com/thorProduct.cfm?partNumber=OCT930SR&pn=OCT930SR#2005>, Accessed 14/07/2011.
- <sup>49</sup> Hu Zhilin and Rollins Andrew M., “Fourier domain optical coherence tomography with a linear-in-wavenumber spectrometer”, *Optics Letters*, 32 (24), pp. 3525-3527 (2007).
- <sup>50</sup> Chan Kenny K. H., and Tang Shou, “High-speed spectral domain optical coherence tomography using non-uniform fast Fourier transform”, *Biomed Opt Express*, 1 (5), pp. 1309-1319 (2010).
- <sup>51</sup> Izatt J. A. and Choma M. A., Ed. Drexler Wolfgang and Fujimoto James G., “Theory of Optical Coherence Tomography” in *Optical Coherence Tomography: Technology and Applications*, Springer (2008).
- <sup>52</sup> Ai Chiayu and Novak Erik L., “Centroid approach for estimating modulation peak in broad-bandwidth interferometry”, *United States Patent*, 5633715 (1997).
- <sup>53</sup> Amaral Marcello M., Ruele Marcus P., Caly Jose P., Samad Ricardo E., Vieira Nilson D. Jr., and Freitas Anderson Z., *Proc. SPIE 7390, 73900Z* (2009).
- <sup>54</sup> Ed. Gordon Colin G., *Vibration Control in Microelectronics, Optics, and Metrology (Proceedings Volume)*, *proc. SPIE 1619* (1992).
- <sup>55</sup> Ortiz Sergio, Siedlecki Remon Laura and Marcos Susana, “Optical coherence tomography for quantitative surface topography”, *Applied Optics*, 48 (35), pp. 6708-6715 (2009).
- <sup>56</sup> Feynman Richard P., Leighton Robert B. and Sands Mathew, Chapter 30 *Diffraction in Lectures on Physics: Volume 1*, Addison-Wesley (1963).
- <sup>57</sup> Akiko Harasaki and James C. Wyant, “Fringe modulation skewing effect in white-light vertical scanning Interferometry”, *Applied Optics*, 39 (13), 2101 – 2106 (2000).
- <sup>58</sup> Pircher M., Götzinger E. and Hitzenberger C. K., "Dynamic focus in optical coherence tomography for retinal imaging", *J. Biomed. Opt.*, 11 (5), 054013 (2006).
- <sup>59</sup> Andrei V. Zvyagin, K. K. M. B. Dilusha Silva, Sergey A. Alexandrov, Timothy R. Hillman, J. Armstrong, Takuya Tsuzuki and David D. Sampson, “Refractive index tomography of turbid media by bifocal optical coherence refractometry”, *Optics Express*, 11 (25), pp 3503 – 3517 (2003).
- <sup>60</sup> Gao F., Leach R. K., Petzing J., and Coupland J. M., “Surface measurement errors using commercial scanning white light interferometers”, *Meas. Sci. Technol.*, 19, 015303 (2008).

## 3 OCT multi-interface profilometry for dynamic refractive index measurements of drying droplets

### 3.1 Introduction

Surface profilometry is normally undertaken in standard atmospheric conditions, *i.e.* there is only the earth's atmosphere between the sample and instrument. The refractive index of the atmosphere approximates a vacuum closely ( $n \approx 1$ ) and is uniform from the interferometer to the sample, leading to no distortions of the light. However with the use of OCT (in this study) to measure internal interface profiles, the light must travel through the preceding material (Varnish layer) during the measurement. This refractive index is not approximate to one and is a finite layer between the interface and instrument. This changes the path the light takes (phase refractive index) and time the light takes to travel the path (group refractive index). For these interface measurements, these effects need to be corrected for and in order to correct for them the refractive index of the material needs to be known. This can be measured with the same instrument.

In biomedicine, the effect of refractive index on OCT images is something that is important. The light of the OCT instrument can pass through many layers of different refractive indexes. Correction of the refractive index distortions and the measurement of refractive indices of the biological materials are important topics within the OCT field.

Group refractive index has already been introduced at the end of chapter 2.1.3. The change in the speed of light, as it travels through materials, distorts the apparent axial distances in the OCT image. The apparent distance (optical distance) between two axial points is the product of the real distance and group refractive index of the material in-between. This will have a direct effect on the interface measurements, with the features axial scaling being distorted by the group refractive index of the material above the interface.

When light meets an interface that is non-normal to the direction of travel of the light, the direction of travel of light is changed by refraction. The change in direction of travel can be calculated from Snell's Law,

$$\frac{\sin(\theta_1)}{\sin(\theta_2)} = \frac{c_{P1}}{c_{P2}} = \frac{n_{P2}}{n_{P1}}, \quad (3.1.1)$$

where subscripts refer to the two materials either side of the interface,  $\theta$  is the angle of direction of travel from the normal of the interface,  $c_P$  is phase velocity and  $n_P$  is phase refractive index.

Phase and group refractive indices are related by dispersion,

$$n_G = \frac{n_P}{1 + \frac{\lambda}{n_P} \frac{dn_P}{d\lambda}} \approx n_P = n, \quad (3.1.2)$$

where  $\lambda$  is wavelength of the light. With OCT, the measurement of refractive index is of only group refractive index and the difference between phase and group refractive index is small compared to the refractive index values. So, for corrections, the phase refractive index is taken to be equal to the group refractive index. This general refractive index will now be represented without a subscript.

The reflection of light from the second interface can be considered by the path of the central axial (chief) ray of illumination and collection, which is shown in figure 3.1.1. With low NA optics (light approximates collimated), relatively long distance between the first and second interface and a matte second interface, this approximation can be justified. However, if these conditions are not met, it is shown later that it can be highly erroneous and misleading. The first interface's normal differs from the direction of travel of light by angle  $\theta$ , leading to refraction by angle  $\phi$ . As above the layer is atmosphere, its refractive index is taken as one. The refractive index of the layer is designated  $n$ . The light then travels a distance  $R$  where it encounters the second interface, where the reflection back upon the same path is considered.

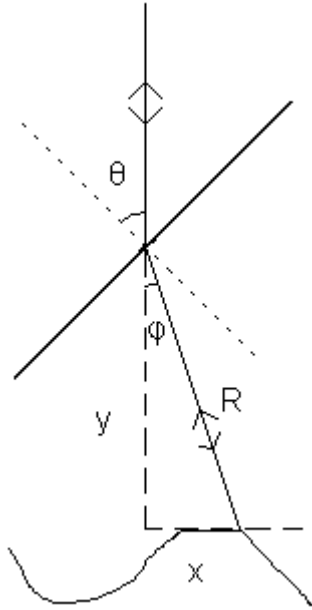


Figure 3.1.1  
Path of the optics chief ray  
of illumination and  
collection. This is used as an  
approximation to calculate  
distortion due to refractive  
index.

From Snell's law (equation 3.1.1) and trigonometry, the angle  $\varphi$ , the axial (initial direction of light) distance,  $y$ , and lateral distance,  $x$ , travelled through the layer can be calculated from  $R$ ,  $n$  and  $\theta$

$$\varphi = \theta - \sin^{-1}\left[\frac{\sin(\theta)}{n}\right], y = R.\cos(\varphi), x = R.\sin(\varphi). \quad (3.1.3)$$

$R$  can be calculated from the apparent optical distance,  $\Delta z'$ , between the two interfaces in the OCT axial data and  $n$ ,

$$R = \frac{\Delta z'}{n}. \quad (3.1.4)$$

This method is a 2d Snell's law calculation, similar to Podleanu et al<sup>1</sup>, and is equivalent to a Fermat principle approach<sup>2</sup>. As the OCT images used in these studies are two dimensional rather than 3 dimensional, the application of this method into the other lateral dimension<sup>3</sup> could not be undertaken.

In order to make these corrections, the materials refractive indices have to be known. To obtain these values they are measured by the OCT. The measurement of refractive index by OCT is a topic of current research interest for applications other than just internal interface profile measurement.

White Light (broad band) Interferometry is a well known technique for group refractive index measurement<sup>4</sup>. Figure 3.1.2 shows a diagram of the method. The relative optical path length in the sample arm of a Michelson interferometer is measured, with and without the sample in it. This is done by scanning the path length of the reference arm and measuring the distance with maximum fringe contrast for both measurements. The difference,  $D$ , between the two measurements is taken. The physical thickness,  $P$ , of the material is also measured, then group refractive index is given by

$$n_g = \frac{D}{P} + 1. \quad (3.1.5)$$

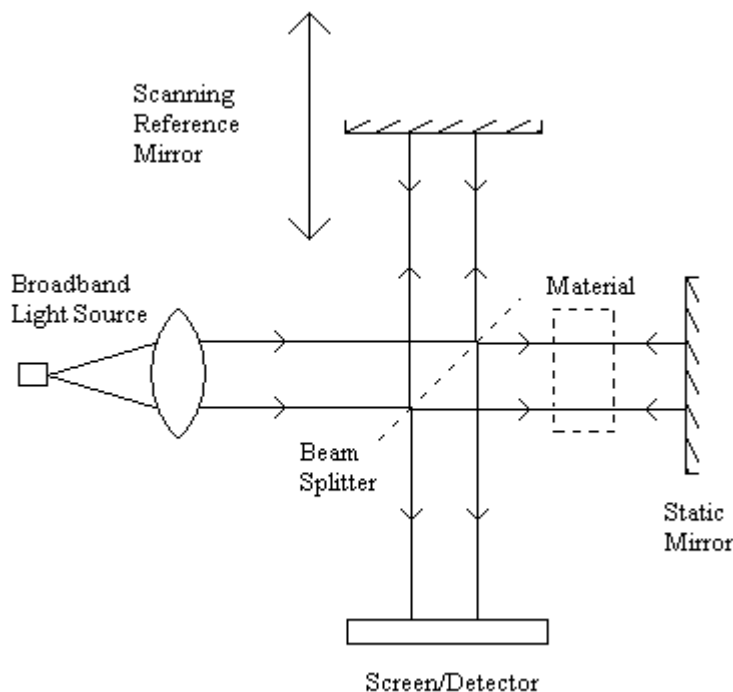


Figure 3.1.2  
Basic broadband  
Michelson  
interferometer setup  
for measuring group  
refractive index.

This can also be done in the Fourier domain with both mirrors fixed<sup>5</sup>. With OCT there are two main methods<sup>6</sup> used to measure refractive index. The first method is the optical length shifting method as described above. This can be implemented in two ways. Firstly exactly as described above with measurements with and without the sample, this is a 1D measurement only requiring measurement at one lateral position. The second implementation exploits OCT's 2D cross-sectional imaging to obtain the real and optical thicknesses simultaneously<sup>6</sup>. The material is deposited on a flat surface in the centre of the OCT image, the real position of the flat surface is interpolated from either side of the material allowing the measurement of the real

thickness as well as optical. This is the method that is exploited in this work. The use of the optical path method, without high precision interface measurement, by Wang et al<sup>7</sup>, measured the group refractive index of fused silica of ~1mm thickness to an accuracy of 0.005. With the high precision multi-interface profilometry method developed in this project it is expected to be able to measure group refractive index to the same or higher precision with much thinner samples.

The optical path length method is unable to measure refractive index *in vivo* for biomedical applications, due to the need for a reference surface. The second OCT method<sup>6</sup> to measure refractive index, focus tracking, is able to overcome this. Figure 3.1.3 is a diagram of the sample arm optics of an OCT in focus on the back surface of an object. The object interfaces are normal to the optical axis and smooth. The phase refractive index of an object changes the position of the focus from the apparent position. The light in such a system is usually modelled by a geometric optics ray tracing approximation. For the rays incident with an angle  $\theta$  from the optical axis the relationship between the distances P and F can be shown using Snell's law and trigonometry to be

$$P \tan \phi = F \tan \theta \quad (3.1.6)$$

where

$$\sin \phi = \frac{\sin \theta}{n_p}. \quad (3.1.7)$$

From this, the position of F is dependent on  $\theta$ . Any such optical system would have a ray distribution of  $\theta$  from 0 up to the numerical aperture of the system, leading to aberration of the focus. For a measurement of refractive index from the distances P and F, the result needs to be calculated with a single value of  $\theta$ .

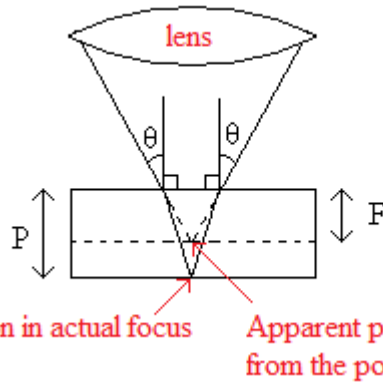


Figure 3.1.3  
Geometrical optics representation of the focus of an OCT sample arm through a material, for one ray angle  $\theta$ . It shows for a material of thickness  $P$ , the distance moved by the lens to change the position of focus from the top to the bottom,  $F$ .

Two approaches to the calculation of refractive index exist. If the numerical aperture of the system is significant the equations 3.1.6 and 3.1.7 can be solved for a median value of  $\theta$ , this is the approach that is usually made. However, if the numerical aperture of the system is low, the paraxial approximation ( $\sin t \approx t$  and  $\tan t \approx t$ ) can be applied to the equations. This simplifies the mathematics and removes the  $\theta$  dependence. For the illustrative purpose of this section, this is the regime that will be adopted. The relationship of  $F$  and  $P$  is now

$$F = \frac{P}{n_p} \quad (3.1.8)$$

The measurement of the apparent distance through the material, due to the time taken of the light to pass through it, is measured simultaneously by the broadband interferometer. This is known as the optical path length,  $O$ . This is independent of the focus effects, providing a second measured value. From equation 3.1.5 the optical path length is given by

$$O = D + P = n_g P. \quad (3.1.9)$$

If another approximation is made,  $n_g \approx n_p = n$ , then equations 3.1.8 (or non paraxial equivalent) and 3.1.9 can be solved simultaneously to retrieve the real thickness and refractive index from the two optical distances. The difference between  $n_g$  and  $n_p$  is usually of the order of 0.01, therefore this approximation is applicable for measurements of lower accuracy than this. For paraxial implementation here, the relationship between the two optical distances and the real thickness is

$$O.F = P^2 \quad (3.1.10)$$

and for refractive index is

$$\frac{O}{F} = n^2. \quad (3.1.11)$$

This method does provide a convenient way of measuring refractive index *in situ* or *in vivo*, but the accuracy of the method is reduced compared to the optical path analysis. For Wang et al<sup>7</sup> the accuracy was 0.01 compared with the 0.005 for the optical path length method. Further developments of this method include the use of bifocal optics to remove the need for scanning optics<sup>8</sup> and confocal optics<sup>9</sup>. The confocal optic system<sup>9</sup> also recovers separate group and phase refractive index by measuring dispersion from the broadening of the rear PSF from the front PSF. The inclusion of focus tracking into a broadband interferometer with reference interface within the sample arm also allows the measurement of thickness, group and phase refractive index simultaneously<sup>10, 11</sup>.

OCT methods, other than based on the optical path length and focus tracking methods, for measuring refractive index do exist. Refractive index can be calculated from the change in reflection and scattering intensities within a stacked layer of materials<sup>12</sup>. Also the phase refractive index can be fitted to the measured apparent optical thickness, of a parallel slice of material, as a function of inclination to optical path<sup>13</sup>.

### 3.2 Method

In this project the lack of control of focusing the instrument, the lack of need to measure the refractive indices of a varnish layers *in situ* and the desire for accuracy, led to the optical path method to be chosen. The novel aspect of the method was the implementation of high accuracy interface measurement into the 2 dimensional OCT cross-sectional method. This reduces the errors in the optical and physical thickness measurements. For the multi-interface profilometry measurements of drying varnish films, their refractive index needs to be known throughout the process. The method measures, dynamically, the refractive index of varnish droplets as they dry. This gives the required information on how the refractive index changes with concentration.

The varnish solution is initially a liquid. A droplet of liquid is applied to a known flat surface. The substrates (surfaces) used were microscope slides. These were presumed to be manufactured by a float process<sup>14</sup>, which ensures a flat smooth surface. When the surface profile of microscope slides were measured with the OCT system, no structure to the surface was apparent above instrument error. Figure 3.2.1 (a) shows an optical section, taken with the Thorlabs SR OCT, through the centre of a droplet of distilled water. The high precision profiles can then be found with the Gaussian fitting method for the sample-air interface, the apparent (optical) sample-substrate interface and the substrate-air interface. The profile positions are then corrected by the subtraction of the measured curvature of the image. The physical position of the substrate-sample interface is interpolated (by linear fit) through the droplet from the substrate-air profile on either side. Figure 3.2.1 (b) shows the measured interface positions after subtraction of the interpolated substrate position. The distances P and O, from which group refractive index is calculated (with equation 3.1.5), have been marked on this figure. The refractive index can be calculated at each measured point, with or without refraction correction. The shape of the droplet surface, and the angle between the normal of the interface and the optical axis, has significant influence on the accuracy of the measurement. These errors are measured and discussed in section 3.3.

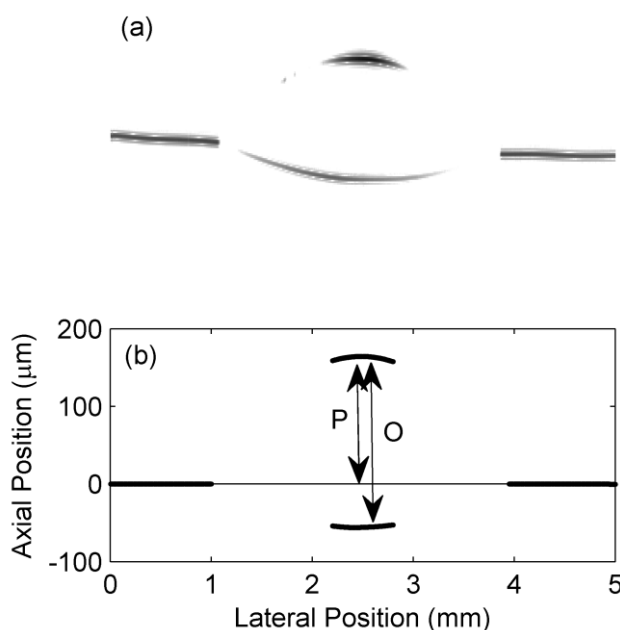


Figure 3.2.1  
 (a) FD-OCT cross-section image of a droplet of distilled water on a glass microscope slide.  
 (b) Fitted interface positions after correction for image curvature and subtraction of the linearly interpolated real position of the microscope slide interface. The distances P and O are marked.

An alternative implementation of this method is the measurement across the edge of a larger sample, with the extrapolation of the physical sample-substrate interface from one side only. This single sided extrapolation will have greater error, leading to additional error in the value P. This method is used once in section 3.3 to demonstrate independence of an error from image position.

The method as described is fine for liquid samples, which will have complete contact with the substrate they are placed upon. Solid samples will not make contact with the substrate, apart from at a few points, meaning that the method will not work without modification. Figure 3.2.2 show the method for a mica slide (34 $\mu$ m thick). When placed on the flat substrate, the thin plates do not sit flush to the surface. There is an air gap between the sample and the substrate giving an extra interface. This proves useful experimentally with four measurable positions, rather than three. The two distances measured, for refractive index calculation, are independent of each other. Figure 3.2.2 (a) shows an OCT cross section (500 $\mu$ m lateral range) across the edge of a mica slide placed upon a microscope slide. Figure 3.2.2 (b) shows the measured three apparent interfaces and the physical extrapolated position of the air-substrate interface. From these measurements the optical thickness of the material, O, and the apparent displacement of the substrate interface, D are calculated. From equation 3.1.5  $n_g$  is related to O and D by

$$\frac{n_G}{n_G - 1} = \frac{O}{D}. \quad (3.2.1)$$

The measured group refractive index was  $1.591 \pm 0.002$  for the birefringent mica. The real thickness of a sample can be calculated by O-D or O/ $n_g$ .

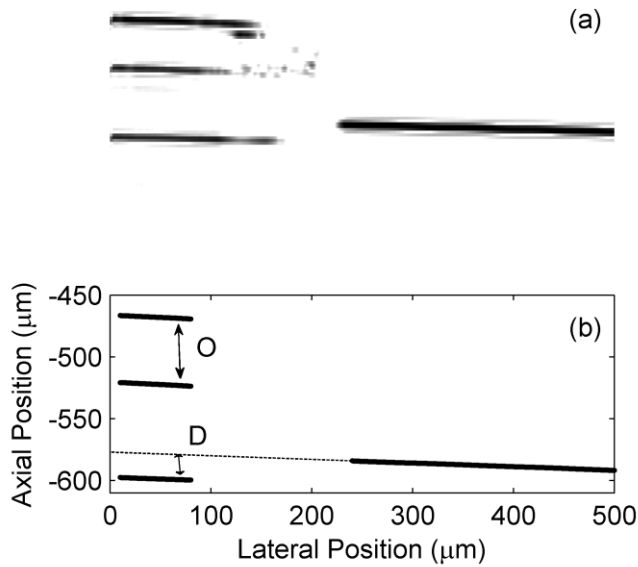


Figure 3.2.2  
 (a) OCT cross-sectional image across edge of mica slide placed on microscope slide.  
 (b) Fitted interface positions and extrapolation of real position of microscope slide surface. Distances O and D marked on.

### 3.3 Validation and distortion

To validate the method distilled water was used as a reference substance. The refractive index of distilled water has been previously studied in detail over the UV, visible and IR wavelengths. This allows an accurate reference group refractive index to be calculated at the wavelength of the OCT instrument (930nm) and temperature of the measurements (20°C). This was calculated using the phase refractive index and the rate of change of phase refractive index, with wavelength, values from Daimon and Masumura<sup>15</sup>. This paper gives refractive index at vacuum wavelengths 894.596 nm and 1014.26 nm of 1.327068 and 1.325273 respectively. So  $\Delta n/\Delta\lambda$  is  $0.015 \mu\text{m}^{-1}$  and  $n_p = 1.3265$  at 930nm. Using equation 3.1.2 the reference group refractive index is calculated to be 1.3406.

Previous figure 3.2.1 shows an example measurement of a distilled water droplet with the OCT system. Generally, the method proved satisfactory when measuring through at the centre of a droplet and having normal incidence of the light with the interfaces. However it was rapidly noticed that there was distortion of the measured refractive index values away from the centre of the droplet. It was noticed that as the slope of the droplets increased, away from the centre of the droplet, the refractive indices measured decreased.

To determine the dependence of the measured refractive index on the location on a droplet, a three dimensional measurement of a distilled water droplet was made. The droplet method was used. The three axial motorised stage was used to scan the OCT probe in dimension perpendicular to the OCT image, while streaming these images, to produce a three dimensional image data set. The refractive index was then measured as normal in each cross-sectional image. Figure 3.3.1 shows an image of the measured refractive index in each lateral position around the centre of the droplet. The centre of the droplet had the highest measured refractive index ( $1.341 \pm 0.002$ ) which corresponds to the reference value. Away from the centre of the droplet (where it is normal to the optical axis), the refractive index is seen to decrease with the increase in slope in both lateral dimensions.

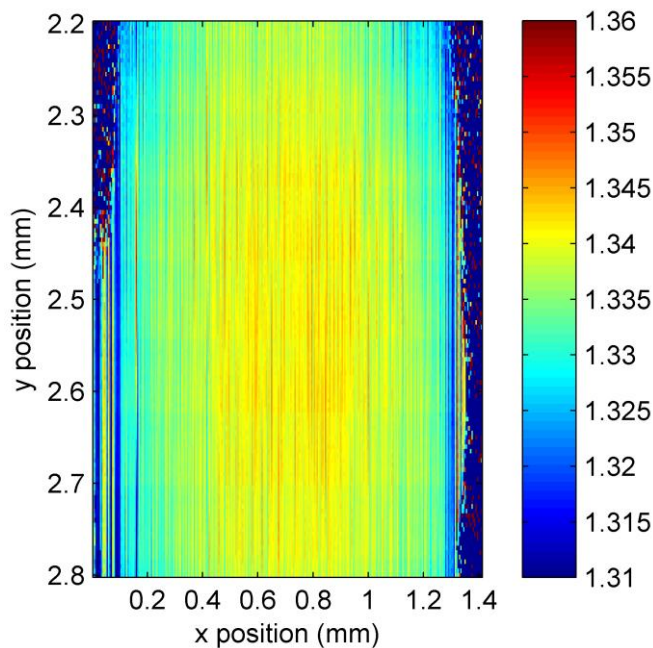


Figure 3.3.1. Image of the measured refractive index over the centre area of a distilled water droplet. The colour bar gives the correspondence with the measured refractive index

The measured refractive index was used to correct the real distance travelled from the air-liquid to the extrapolated liquid-substrate interfaces. Generally (assuming the angle between the normal of the substrate interface and the optical axis is small compared to the angle between the sample surface and the optical axis, the distortion of the substrate surface normal to optical axis was measured and used in the refraction correction) without refraction correction, the change of direction of the light at the surface interface would increase the physical path length. This would lead to an overestimate of refractive index, which is opposite to the distortion that is seen in the experimental results. Figure 3.3.2 shows an example of the refractive

indices measured from one cross section from figure 3.3.1 with and without refraction correction. As well as the correction being in the wrong direction, the magnitude of the difference between the corrected and uncorrected interface is small compared to the magnitude of the distortion.

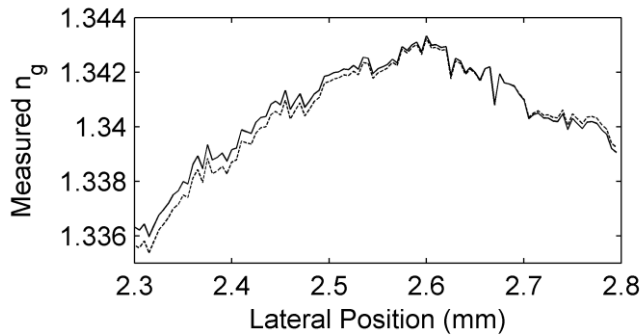


Figure 3.3.2. Measured group refractive index of one OCT cross-section from figure 3.3.1 with (dashed line) and without (solid line) refraction correction.

The method is going to be applied to measure drying varnish droplets. The method was applied to a drying distilled water droplet to measure the distortion of the measured values from the reference value. A droplet of distilled water was placed upon a microscope slide and then measured at a series of times as it dried by evaporation. Averages of 21 images were used for each measurement. Though the centre of the droplet can be selected in the optical section lateral dimension, the positioning of the optical section in the centre of the droplet in the other lateral dimension is less certain. Figure 3.3.3 (a) shows the measured values as a function of thickness, though the measured refractive index is dependent on position it is independent of absolute thickness. For the highest value (centre of droplet in cross-sectional dimension) of refractive index in each measurement, there is a trend of distortion for the earlier (thicker) measurements. This is likely to be due to the lack of central positioning in the other lateral dimension. The spread of data points decreases as the droplet dries, as the droplet dries with pinned edges it becomes flatter leading to lower distortion. For all the measurements figure 3.3.3 (b) shows the mean and standard deviation of the refractive index measurement at each lateral point. The dependence of distortion on position on the droplet is clear. This distortion is independent of the position of the measurements in the OCT image. Figure 3.3.4 shows an example measurement of refractive index from the edge of a droplet of Regalrez varnish solution. The results of these followed the same trend as the droplet placed in the centre of the OCT image, the distortion of refractive index is dependent on the slope of the droplet.

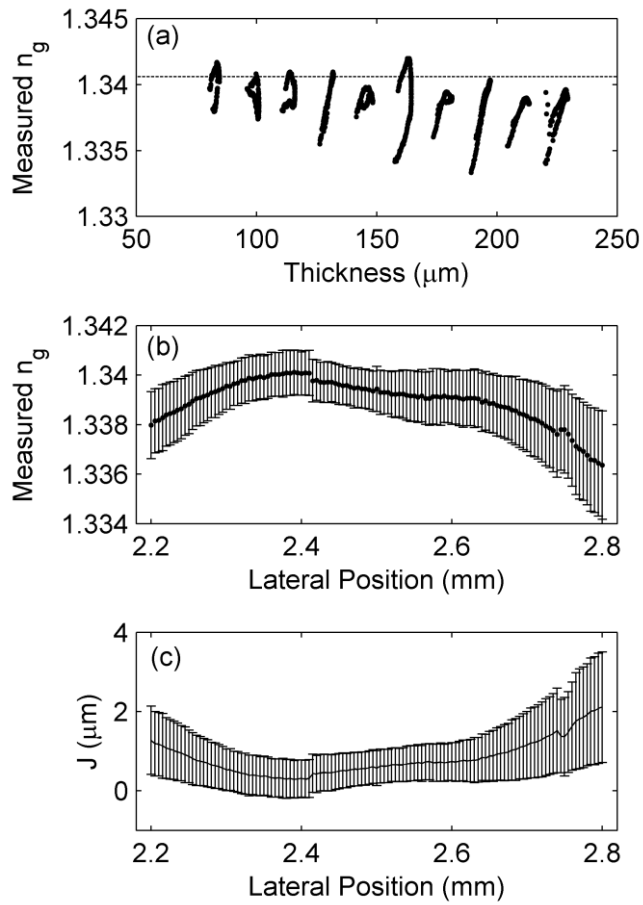


Figure 3.3.3  
 For the drying distilled water sample.  
 (a) Measured group refractive index vs. thickness.  
 (b) Mean and standard deviation of measured group refractive index vs. lateral position.  
 (c) Mean and standard deviation of the top surface distortion if the measured substrate positions and reference group refractive index are correct.

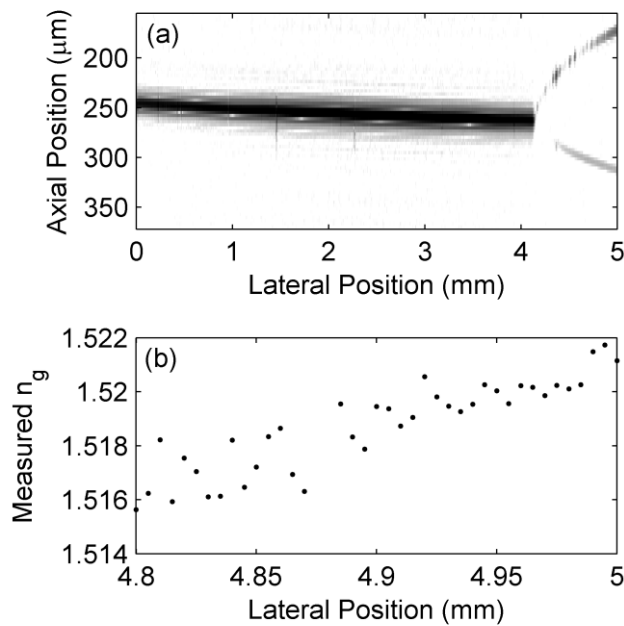


Figure 3.3.4.  
 (a) OCT image across edge of Regalrez varnish droplet.  
 (b) Measured group refractive index for last 200  $\mu\text{m}$  of image.

In the measurement of sinusoidal standard surfaces (chapter 2.4.1) it was shown that, with sloped and curved surfaces, significant systematic error in the measured position could occur. It is likely that such errors are also present in the measurement of the droplet surface (and even droplet-substrate interface due to the refraction of the surface). The distortion required in the top interface measurement,  $J$ , to distort the refractive index from the reference value to the measured value at each point was calculated assuming the error in the extrapolated (real) and measured droplet-substrate interface was negligible. Figure 3.3.3 (c) shows the mean and standard deviation of  $J$  for each position of the drying distilled water droplet. The positional distortion required is around two microns. This is a large value, the largest standard deviation of the residual for a sinusoidal surface (in focus) was  $0.9\mu\text{m}$  (Rubert surface 527, chapter 2.1.4). However, measurement out of focus (chapter 2.3.2) can produce large systematic errors of the magnitude of  $J$ .  $J$  is still lower than the maximum error on a random rough surface (chapter 2.4.2) and  $J$  is lower than the axial imaging resolution of the system. There is possibly associated error in the second interface measurement that may lower the  $J$  value required.

Considering again the refraction correction, it can be seen that no ray can travel the path shown in figure 3.1.1 if the bottom interface is smooth. If the only ray that does travel back down the same path, it came forward on, is considered, a much different prediction, that matches the experimental results, can be derived. Figure 3.3.5 shows the path of this ray, the substrate surface is assumed normal to the optical axis. The ray must have normal incidence with the substrate to travel back down the same path it travelled forward on. The angle between the normal of the surface and the optical axis is  $t$ , which can be calculated from Snell's law

$$\sin \theta = n \sin t . \quad (3.3.1)$$

The equivalent numerical aperture of this ray into the lens is  $\sin(\theta - t)$ . It can be seen that the distance the ray travels through the sample to the substrate,  $r'$ , is lower than the distance it would have travelled to the substrate without the sample,  $r$ . The ratio between these values is given by

$$\frac{r'}{r} = \cos[\sin^{-1}(n \sin t) - t]. \quad (3.3.2)$$

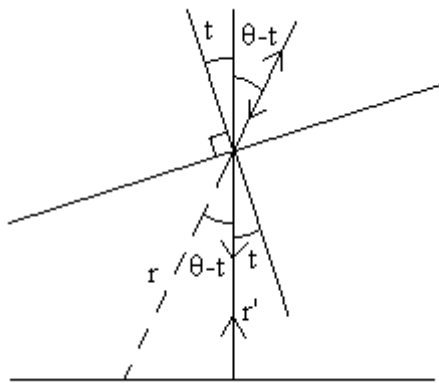


Figure 3.3.5.  
Geometry of a ray through  
a droplet sample, where  
the forwards and  
backwards paths are  
identical.

This new geometric optics derivation of the error is more promising for explaining the error in the refractive index measurements. The direction of the distortion predicted is the same, but now its potential magnitude needs to be compared with the experimental results. The dependent variable is the slope of the surface of the sample,  $t$ . Figure 3.3.6 (a) shows the measured slope of the surface of the drying distilled water droplet. The maximum slope measured is around 3 deg magnitude, though this is only a two dimensional measurement. Additional slope in the other lateral dimension will increase the total magnitude of the slope. The slope in the other lateral dimension will be approximately constant, and dependent on the displacement from the centre of the droplet in that dimension. At the edges of the lateral measurement (where the angle is greatest), the effect of the angle in the other dimension on total angle magnitude will be minimal. 3 deg will be taken as the maximum slope angle. Figure 3.3.6 (b) shows the calculated fractional error (by equation 3.3.2) due to the surface slope. At 3 deg the fractional error in the measurement would correspond to an error of 0.003 in the refractive index. This is of the magnitude of distortion that is seen in the experimental results, though the validity of the geometric optics model has not been proved.

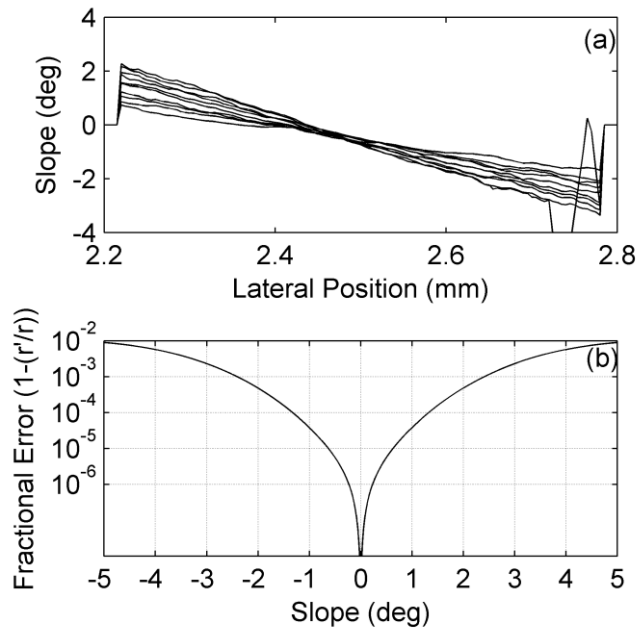


Figure 3.3.6.  
 (a) Measured slope of the surface of the drying distilled water droplet vs. position.  
 (b) Fractional error due to refraction, calculated from equation 3.3.2.

The droplet method of measuring group refractive index has been shown to be accurate to 0.002, if measured at the centre of the droplet with the substrate near normal to the optical axis. Away from the centre of the droplet, the measured value of refractive index is distorted below the true value. Two possible reasons have been identified for this. Firstly distortion of the measured interface positions due to diffraction effect on the PSF or secondly due to the refraction at the sample-air interface (surface). As a result of this distortion, the method will only be used to measure the refractive index at the centre of a droplet, with the substrate as close as possible to being normal to the optical axis. Under these conditions an accurate value for the refractive index will be measured.

### 3.4 Drying varnish results

Multi-interface profilometry with the Thorlabs OCT was to be used to measure varnish-substrate profiles while measuring the air-varnish profile simultaneously and dynamically. In order to determine the varnish-substrate interface correctly the refractive index of the varnish solution needs to be known. The varnish solution is made with two components, resin and solvent, which have different refractive indices. As the varnish solution dries by evaporation of solvent the ratio of solvent to resin changes, changing the net refractive index. The same method, as the drying distilled water droplet, was used to measure the refractive index of droplets of varnish solutions as they dry. Three varnish solutions were measured: Regalrez and white spirit, Regalrez and toluene, and AYAT and toluene.

Three droplets of Regalrez and white spirit varnish (1g of Resin to 1ml of solvent) were measured. The size of the droplet was only controlled approximately, to be of suitable diameter for the lateral measurement range. The time taken between the application of the droplet and first measurement was the time taken to position the OCT correctly for the measurement. This time varied between measurements. Measurements were taken at 5 minute intervals over 30 minutes. Figure 3.4.1 (a) shows the mean and standard deviation of the thickness of the varnish droplet over the measured points of each droplet. Figure 3.4.1 (b) shows the mean and standard deviation of the refractive index of the measured points of the droplets. The refractive index of the white spirit ( $n=1.41-1.44$ ) is lower than the refractive index of the Regalrez resin ( $n=1.52^{16}$ ). As the concentration increases, the refractive index of the droplet increases. The trend of this increase for the three droplets is clearly shown. A problem regarding the measurement of these samples is the shape of the droplets as they dry. In section 3.3 it was shown that the shape of the sample can lead to systematic errors in the measured value depending on the position of measurement. These errors were measured for droplet shaped samples but the effect of different shapes has not been tested experimentally. The deposit of solutions did not remain droplet shaped, instead forming a donut shape<sup>17</sup>. Figure 3.4.2 shows the OCT images at 0 and 15 minutes for one of the measurements, two of the three independent measurements followed this trend. The selection of points for the RI measurement was done automatically dependent on a threshold interface intensities

and a threshold thickness. The other repeat measurement (figure 3.4.1, (crosses)) had higher initial thickness but remained closer to droplet shape, apart from the measurement at 5 minutes where the droplet appeared to be inverting to a donut shape before rebounding back to a quasi droplet shape.

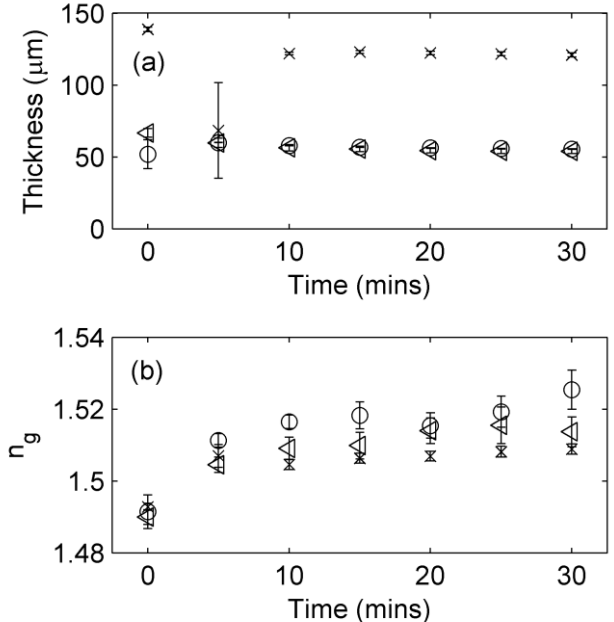


Figure 3.4.1. Three independent measurements (circles, triangles and crosses) of group refractive index of drying Regalrez and white spirit varnish. (a) Mean and standard deviation thickness of the point used for the measurement. (b) Mean and standard deviation measured group refractive index.

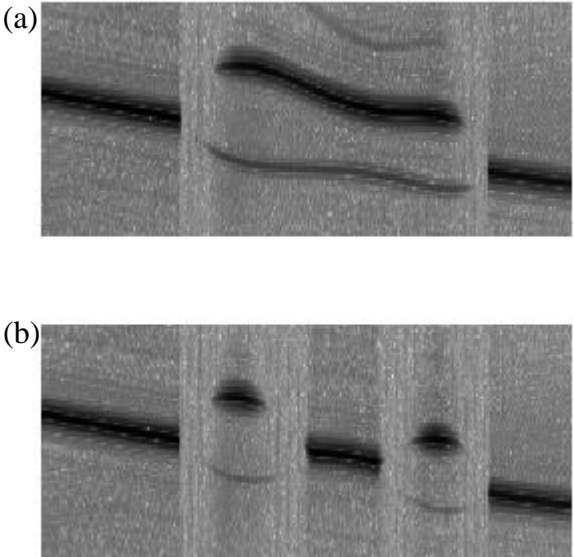


Figure 3.4.2. OCT images of Regalrez and white spirit deposit at (a) 0 and (b) 15 minutes from the start of the group refractive index measurement.

The other two solutions measured by this technique were Regalrez and Toluene (1g Resin to 1ml Solvent) and AYAT and Toluene (3g resin to 11ml solvent). The droplet shapes did not deform while drying for these two samples, this may have

been due to the higher volatility of toluene than white spirit. Figure 3.4.3 (a) shows the change in height of the two droplets over the measurement time. The lower initial concentration of the AYAT droplet has increased shrinkage with the evaporation of solvent, compared with the higher initial concentration of the Regalrez droplet. Figure 3.4.3 (b) shows the measured group refractive index of the two droplets as they dry. The refractive index of the Regalrez droplet is again found to increase with concentration. The refractive index of the AYAT droplet decreases as the concentration increases. AYAT is a PVAc resin, which has a refractive index of 1.47<sup>18</sup>, which is lower than the refractive index of the solvent toluene, ~1.50.

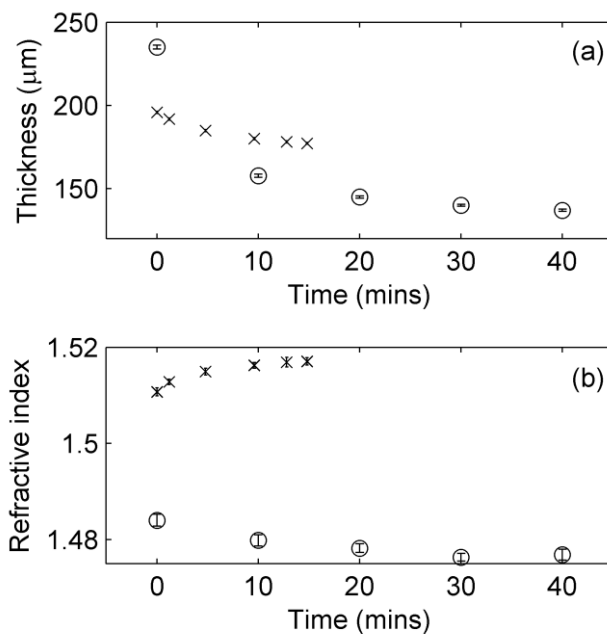


Figure 3.4.3.  
 (a) Mean and standard deviation (of lateral points in single measurement) height of the AYAT and toluene (o) and Regalrez and toluene (x) droplets.  
 (b) Group refractive index obtained from those measurements.

### 3.5 Conclusion

The two dimensional optical path length method, of measuring group refractive index with OCT, was used. The fitting of a Gaussian function to the PSF, allowed the positions of the interfaces to be found with high accuracy. For the 3D measurement of the distilled water droplet the standard deviation of the refractive index value was 0.002, over a range of lateral points at the centre of the droplet. There was no image averaging in this measurement, so this value corresponds to a positional accuracy of approximately 150nm. Away from the centre of a droplet, the group refractive index measured is distorted to a lower value than the reference. The cause of this distortion may be refraction or distortion of the PSFs due to diffraction

effects. The size of this distortion is dependent on the slope of the surface at the measurement point. Currently, when using this method (without correction for this distortion), the droplet should be placed on a substrate which is close to normal with the optical axis and the measurement carried out as close to the centre of the droplet as possible. Under these conditions the method is accurate to at least 0.002 (absolute error). The accuracy of refractive index value required (chapter 2.4.3) is 0.05, so the method is currently more than adequate for the purpose of this project.

Though this method has been developed for liquid samples, the same level of accuracy is possible with solid samples. The precision of a single measurement of a 34  $\mu\text{m}$  thick mica slide was also 0.002.

In previous studies thicker (typically 1mm) samples have been used, than was used here. The accuracy with which the distances O and P (or related) are measured determine the accuracy of the refractive index. The thicker samples mean that the errors in refractive index, due to the errors in the interface position measurements, are reduced. Though the error in thickness of previous work has typically been quoted to  $5\mu\text{m}^7$  (approximately FWHM imaging resolution) an accuracy ( $0.005^7$ ) approaching the value achieved here was obtained. If their measurement had been carried out on a  $150\mu\text{m}$  thick sample (typical height of droplets used in this study), the refractive index error would have been 0.03. The much improved position accuracy in this work gives potential improvement in the measurements of refractive index, with OCT, of over an order of magnitude.

### 3.6 References

---

<sup>1</sup> Podoleanu Adrian, Charalambous Ismini, Plesea Lucian, Dogariu Aristide and Rosen Richard, "Correction of distortions in optical coherencetomography imaging of the eye", *Phys. Med. Biol.*, 49, pp. 1277-1294 (2004).

<sup>2</sup> Westphal Volker, Rollins Andrew M., Radhakrishnan Sunita and Izatt Joseph A., "Correction of geometric and refractive image distortion in optical coherence tomography applying Fermat's principle", *Optics Express*, 10 (9), pp. 397-404 (2002).

<sup>3</sup> Ortiz Sergio, Siedlecki Damian, Grulkowski Ireneusz, Remon Laura, Pascual Daniel, Wojtkowski Maciej and Marcos Susana, "Optical distortion correction in

---

Optical Coherence Tomography for quantitative ocular anterior segment by three-dimensional imaging”, *Optics Express*, 18 (3), 2782-2796 (2010).

<sup>4</sup> Bor Z., Osvay K., Racz B. and Szabo G., “Group refractive index measurement by Michelson interferometer”, *Optics Communications*, 78 (2), pp. 109-112 (1990).

<sup>5</sup> Renlon D., Jacquot M., Verrier I., Brun G. and Veillas C., “High resolution group refractive index measurement by broadband supercontinuum Interferometry and wavelet-transform analysis”, *Optics Express*, 14 (26), pp 12744 – 12750 (2006).

<sup>6</sup> Tearney G. J., Brezinski M. E., Southern J. F., Bouma B. E., Hee M. R. and Fujimoto J. G, “Determination of the refractive index of highly scattering human tissue by optical coherence tomography”, *Optics Letters*, 20 (21), pp 2258 – 2260 (1995).

<sup>7</sup> Wang Xinyu, Zhang Chunping, Zhang Lianshun, Xue Lingling and Tian Jianguo, “Simultaneous refractive index and thickness measurements of bio tissue by optical coherence tomography”, *Journal of Biomedical Optics*, 7 (4), pp 628-632 (2002).

<sup>8</sup> Zvyagin Andrei V., Sliva K. K. M. B. Dilusha, Alexandrov Sergey A., Hillman Timothy R. and Armstrong Julian J., “Refractive index tomography of turbid media by bifocal optical coherence refractometry”, *Optics Express*, 11 (25), pp. 3503-3517 (2003).

<sup>9</sup> Kim Seokhan, Na Jihoon, Kim Myoung Jin and Lee Beyeong Ha, “Simultaneous measurement of refractive index and thickness by combining low-coherence Interferometry and confocal optics”, *Optics Express*, 16 (8), pp 5516 – 5526 (2008).

<sup>10</sup> Masamitsu Haruna, Masato Ohmi, Teruki Mitsuyama, Hideyuki Tajiri, Hideki Maruyama and Masahiro Hashimoto, “Simultaneous measurement of the phase and group refractive indices and the thickness of transparent plates by low-coherence interferometry”, *Optics Letters*, 23 (12), pp. 966 – 968 (1998).

<sup>11</sup> Hideki Maruyama, Shogo Inoue, Teruki Mitsuyama, Masato Ohmi and Masamitsu Haruna, “Low-coherence interferometer system for the simultaneous measurement of refractive index and thickness”, *Applied Optics*, 41 (7), pp 1315-1322 (2002).

<sup>12</sup> Tomlins Peter H. and Wang Ruikang K., “Matrix approach to quantitative refractive index analysis by Fourier domain optical coherence tomography”, *Opt. Soc. Am. A*, 23 (8), pp. 1897-1907 (2006).

<sup>13</sup> Tomlins Peter H., Woolliams Peter, Hart Christian, Beaumont Andrew and Tedaldi Matthew, “Optical Coherence Refractometry”, *Optics Letters*, 33 (19), pp 2272 – 2274 (2008).

<sup>14</sup> Pilkington L. A. B., “Review Lecture The float glass process”, *Proc. Roy. Soc. Lond. A.*, 314, pp 1 – 25 (1969).

---

<sup>15</sup> Masahiko Daimon and Akira Masumura, “Measurement of the refractive index of distilled water from the near-infrared region to the ultraviolet region”, *Applied Optics*, 46 (18), pp 3811 – 3820 (2007).

<sup>16</sup> Berns Roy S. and de la Rie E. Rene, “The Effect of the Refractive Index of a Varnish on the Appearance of Oil Paintings”, *Studies in Conservation*, 48 (4), pp. 251-262 (2003).

<sup>17</sup> Deegan Robert D., Bakajil Olgica, Dupont Todd F., Huber Greb, Nagel Sidney R. and Witten Thomas A., “Capillary flow as the cause of ring stains from dried liquid drops”, *Nature*, 389, pp. 827-829 (1997).

<sup>18</sup> Elias Mady, de la Rie E. René, Delaney John K., Charron Eric and Morales Kathryn M., “Modification of the surface state of rough substrates by two different varnishes and influence on the reflected light”, *Optics Communications*, 266 (2), pp. 586-591 (2006).

## 4 Nuclear Magnetic Resonance (NMR) for measurements of varnish

### 4.1 Introduction

Here the use of Nuclear Magnetic Resonance (NMR) relaxation and its imaging counterpart (Nuclear) Magnetic Resonance Imaging (MRI), to measure molecular and material properties of bulk varnish solutions and drying varnish films, is examined.

Nuclear Magnetic Resonance<sup>1</sup> (NMR) makes use of the precession of the magnetic moment of certain nuclei in externally applied magnetic fields. The instrument in this study is only sensitive to the magnetic moment of H<sup>1</sup> nuclei. Chemical bonds, within a material, shift the resonance frequency (rate of precession of magnetic moments) of adjacent nuclei. If NMR is carried out in a homogenous applied magnetic field, the spectra of the resonant frequencies within a material can be measured. This is known as NMR spectroscopy, which is used for chemical identification and characterisation. This project does not use NMR spectroscopy, but instead measures the decay properties of the total NMR signal, in an in-homogenous field, to recover physical information about varnish properties at the molecular level. NMR does not manipulate the nuclear spins of the material being measured, but it can still be regarded as a non-invasive technique at the molecular and macroscopic level.

The first purpose of the use of this technique in this project is to give a molecular perspective on the properties of different varnish solutions, and how these molecular measurements corroborate with macroscopic properties such as viscosity. The NMR T<sub>1</sub> and T<sub>2</sub> decay times of a molecule is highly dependent on the physical conditions surrounding it. The relationship between these NMR parameters and macroscopic properties (viscosity and self-diffusion) were modelled in the early days of NMR for simple liquids with the use of Bloembergen-Purcell-Pound (BPP) theory<sup>2</sup>. Here, the T<sub>1</sub> and T<sub>2</sub> decay times of the solvent and resin molecules were measured. As these are dependent on the molecular scale interactions of the magnetic spins, these provide information on the molecular behaviour of the varnishes. The knowledge of these decay times is also needed to interpret the MRI of drying varnish systems.

NMR in a unilateral field gradient is the ideal way to measure the self-diffusion coefficients of solvent and resin molecules in a varnish solution. The method provides an accurate direct measurement that does not make any changes to the system (such as the addition of slightly different tracer molecules). The decay of the Hahn echo in a magnetic field gradient is the most effective NMR method of measuring diffusion<sup>3</sup>. This is a useful method for polymer solutions<sup>4,5</sup> and here it is applied to two synthetic varnish solutions, one with low and one with high molecular weight, which highlights the difference between the resins molecular behaviour. Though the Hahn echo method is particularly accurate, it is a slow measurement. The diffusion information can also be extracted in the measurement of a series of  $T_2^{\text{eff}}$  times with Car-Purcell-Meiboom-Gill (CPMG) sequences. This can provide some increase in speed of diffusion measurement but the resulting values are distorted. By comparing measured values of self-diffusion from the Hahn echo and CPMG methods, this distortion can be measured. Corrected diffusion values can then be measured by the use of the CPMG sequence method.

The NMR/MRI instrument used in this work is a mobile unilateral single sided instrument<sup>6</sup> (NMR MOUSE), which is ideal for the measurement of the one dimensional system of drying coatings. The geometry of the system (see section 4.1.2) means that the technique can be applied to measure real drying coatings.

The use of NMR in the measurement of drying polymer films is not new<sup>7</sup>, the  $T_1$  and NMR spectra line width (proportional to  $T_2$ ) have previously been used to characterise the stages of a drying polymer. An NMR MOUSE instrument has also been used to measure dry oil paint coatings on paintings<sup>8,9</sup>. Here the NMR signal from the drying varnish coatings is measured. The development of the signal is then related to specific changes within the coating. The extent to which the technique can be used to non-invasively measure remaining solvent content, *i.e.* how wet the varnish still is, within real varnish coatings is evaluated.

### 4.1.1 Nuclear Magnetic Resonance and properties thereof

Nucleons (Protons and Neutrons) have a magnetic moment due to their quantum spins, which can take possible values defined as  $+1/2$  and  $-1/2$ <sup>1</sup>. In a nucleus the protons, and independently the neutrons, arrange themselves into quantised discrete energy states<sup>10</sup>. If possible the nucleons will organise themselves into pairs of an energy state with opposite spins, and if all the nucleons in a nucleus are paired up the nucleus has no magnetic moment. However for nuclei where the nucleons cannot form pairs in energy states (such as an uneven number of protons and/or neutrons) the imbalance of spins gives it a net nuclear magnetic moment. The simplest atom,  $H^1$ , consists of a single proton nucleus. Its nuclear magnetic moment is therefore that of the proton.  $H^1$  is highly abundant in a wide variety of materials, including varnish resins and solvents, making its NMR ideal for use in this project.

If a hydrogen nucleus is placed in an externally applied magnetic field,  $B_0$ , the orientation of the magnetic moment is dependent on that field. However the energy states of this magnetic moment are quantised. Figure 4.1.1.1 shows the two possible energy states of the nuclear magnetic spin with  $\phi$  the angle between the nuclear magnetic moment and the magnetic field. The magnetic moment of the nucleus is not stationary but precesses around the polarising magnetic field (analogous to a spinning top) with a determined angular frequency (the Larmor frequency  $\omega_0$ ) given by<sup>11</sup>

$$\omega_0 = \gamma B_0, \quad (4.1.1.1)$$

where  $\gamma$  is the gyromagnetic ratio of the nucleus. Note that the polarising magnetic field strength determines the Larmor frequency.

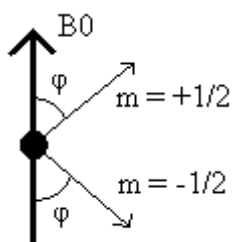


Figure 4.1.1.1  
The two magnetic moment energy states for a hydrogen nucleus.

For NMR measurement techniques, it is the properties of a large collection of these nuclei that is important. In the presence of an external (applied) magnetic field (in

steady state) there exists an energy difference between the two states, due to the magnetic field. However this energy difference is usually very small compared to  $kT$ , where  $k$  is the Boltzmann constant and  $T$  is absolute temperature. This small energy difference causes a small fractional in-balance in the distribution of the magnetic spins of the different nuclei between the two states. This results in a non-zero net magnetisation of the ensemble in the direction of the magnetic field. The phases of the Larmor precessions, of each nuclei, in the ensemble are incoherent with each other (random distribution of phases), so there is no net magnetisation in the (Cartesian) dimensions perpendicular to the applied polarising field.

The application of an electromagnetic wave, of a frequency equal to the Larmor frequency, to this ensemble can allow the user to manipulate the precessions of the magnetic moments<sup>11</sup>, *i.e.* flipping the net magnetisation to a defined direction away from the polarising field ( $z$  axis) direction. The resulting flip of the magnetisation is determined by the strength, duration and polarisation of the electromagnetic pulse. Here different applied electromagnetic waves (pulses) will be defined by their resulting changes to the magnitude and direction in net magnetisation of the ensemble of nuclei (*e.g.* any pulse that results in the  $90^\circ$  rotation in the  $x$  plane will be referred to as a  $90^\circ$  pulse in the  $x$  plane), the nature (strength, duration, polarisation etc.) of these pulses are not important here.

Take a  $90^\circ$  pulse in the  $x$  plane, initially applied to a sample (assumed in thermodynamic equilibrium) in the external magnetic field. The produced net magnetisations, across the sample, can be treated classically (non-quantised). These net magnetisations precesses in the same manner as the individual nuclear magnetic moments. This is shown in figure 4.1.1.2, where a group of nuclei have a net magnetic moment,  $M$ , that precesses around the applied magnetic field.

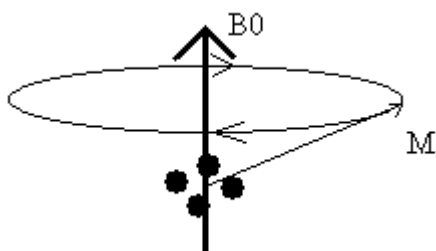


Figure 4.1.1.2  
The net magnetic field of an ensemble of hydrogen nuclei after the application of a EM pulse at the Larmor frequency.

Now consider ensembles (or individual nuclei) at different positions within the sample. If the polarising magnetic field is different in different positions (it is, mainly due to the field gradient, with measurements with the NMR MOUSE), these different ensembles (individual nuclei) precess at different frequencies. This leads to them rapidly becoming out of phase, with each other, and the net precessing magnetic field is lost.

An echo is, if the precessions of the magnetic moments of the ensembles (individual nuclei) are brought back into phase, a reoccurrence of the net magnetic moment producing a detectable EM wave (signal) at some time after the initialisation pulse. To recover an echo the net magnetisation of the different identical ensembles can be flipped by a  $180^\circ$  pulse, in either plane perpendicular to the polarising magnetic field (x plane for Carr-Purcell (CP)<sup>12</sup> and y plane for Carr-Purcell-Meiboom-Gill (CPMG)<sup>13</sup>), after a time delay  $\tau$ . This puts the net magnetic moments at how they would have been at a hypothetical time  $-\tau$ . After another time delay of  $\tau$ , the magnetic field inhomogeneities that had caused the net magnetisations to diverge from coherence now work in the opposite direction bringing them back into phase. Now being “in phase” the precession of the total magnetisation then produces an EM wave at the Larmor frequency, which is then detected. Figure 4.1.1.3 shows a diagram of a pulse sequence and detected signal. The re-phasing (or “refocusing”)  $180^\circ$  pulse is repeated at  $2\tau$  (or  $1T_E$ ) intervals to produce a train of echoes.

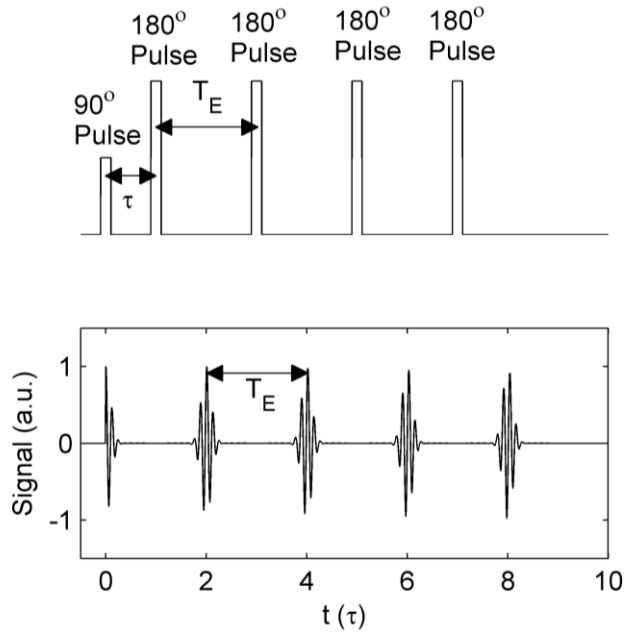


Figure 4.1.1.3  
 Sketch of the production of a  
 NMR echo train.  
 (Top) A time course or  
 “sequence” of EM pulses  
 that produces a suitable  
 change in the orientation of  
 magnetic precessions.  
 (Bottom) The resulting  
 induced EM emission from  
 sample

The NMR signal (echo amplitude) detected after the initial  $90^\circ$  initialisation pulse decays with time. There are two processes within the net magnetisations that are important to understanding this effect. In this work they will usually be identified by their resulting exponential decay times  $T_1$ ,  $T_2$  and  $T_2^{\text{eff}}$ .

The  $T_1$  time constant refers to the longitudinal relaxation<sup>11</sup>. The displacement of the net magnetisation away from the  $B_0$  direction moves the system away from thermodynamic equilibrium. If left alone the net magnetisation will revert back to the longitudinal ( $B_0$ ) direction. Fig 4.1.1.4 (a) and (b) show this relaxation of the magnetic moment. However, in pulse sequences with  $180^\circ$  pulses used to form the echo signals, these also flip the longitudinal component of magnetisation (Figure 4.1.1.4 (c)) resulting in the initial magnitude of the longitudinal magnetisation being recovered when the spin echoes are measured (Figure 4.1.1.4 (d)). If the system is left without any NMR pulses applied, then the net magnetisation in the direction of  $B_0$  will increase in the manner given by<sup>11</sup>

$$M_z(t) = M_z^0 - M_z^0 \exp\left(\frac{-t}{T_1}\right) + M_z(0) \exp\left(\frac{-t}{T_1}\right), \quad (4.1.1.2)$$

where  $M_z$  is the magnetisation in the direction of  $B_0$  and  $M_z^0$  is the equilibrium magnetisation.

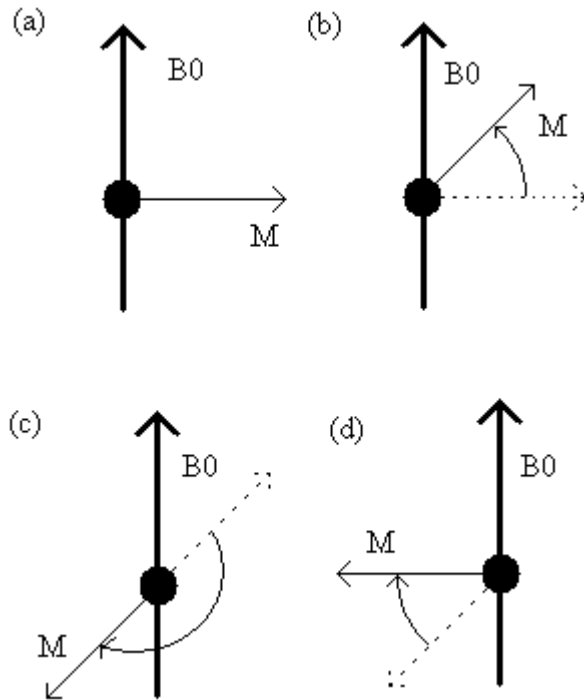


Figure 4.1.1.4  
 The change in the longitudinal magnetisation during the pulse sequence. Note the precession of the magnetic moment has been ignored for illustrative purposes.  
 (a) Immediately after the 90deg initialisation pulse or during echo.  
 (b) Longitudinal magnetisation decay.  
 (c) Flip of the magnetisation due to 180deg pulse.  
 (d) Decay of magnetisation to the initial longitudinal magnitude for the next echo.

In the echo sequence described (Figure 4.1.1.3), the net magnetisation precessions are re-phased with a 180° pulse. In order for this to produce an echo, the processes that cause the de-phasing must be reversible. So far as constant field inhomogeneities are concerned, this is the case. However, in this project, there are two other irreversible processes that lead to the decay of the magnetic moment coherence (transverse magnetisation) over time. The first, that is the process which leads to the true  $T_2$  time of the material under investigation, are the interactions between adjacent nuclei precessions that result in random phase changes. This is known as spin-spin<sup>14</sup> interaction (relaxation). The result of this is an exponential decay of the transverse magnetisation (which induces the NMR signal),  $M_{xy}$ . This is given by

$$M_{xy}(t) = M_{xy}(0) \exp\left(\frac{-t}{T_2}\right). \quad (4.1.1.3)$$

If the strength of  $B_0$  is in-homogenous, over the sample being measured, a nuclei will experience different field strengths dependent on its position within the sample. If the position of the nuclei do not change with time, within the applied field, these differences are static and corrected for by the re-phasing pulses. However, if the nuclei (part of a molecule) moves around within the sample (diffusion), the

polarising magnetic field it experiences is not static and the re-phasing will be incorrect. This leads to additional reduction of the signal. The rate of reduction of signal is dependent on  $T_E$ , because the greater the time between re-phasing pulses, the larger the displacement within the in-homogeneities. The decrease in signal of the echoes due to the combined effect of  $T_2$  and diffusion will be referred to as  $T_2^{\text{eff}}$  in this work.

For a nuclei, an applied EM re-phasing pulse is not necessarily of identical frequency to the Larmor frequency and neither is it necessarily perfect in strength to provide precisely a  $180^\circ$  flip of the magnetisation. For a re-phasing pulse's impact on the magnetic moment of an ensemble of nuclei, the behaviour of the resulting magnetisation can be split into 3 states<sup>15,16</sup>. They are  $M_+$  with the phase dispersing in the same direction as after the initial  $90^\circ$  pulse,  $M_-$  with the phase dispersing in the direction intended after the first  $180^\circ$  to form the echo and  $M_0$  with the magnetisation in the direction of  $B_0$  resulting in the “storage” of the phase information. At each application of  $180^\circ$  pulses the magnetisation states can change or remain the same. An echo is formed when equal amount of time has been spent in the + and - states during the “coherence path”. The ideal (direct echo) coherence path described here is

*90deg pulse, +, 180deg pulse, -, echo, -, 180deg pulse, +, echo, +...*

For the first echo (this will now be referred to as the Hahn<sup>17</sup> echo), this is the only coherence path that is available. For 2<sup>nd</sup> and subsequent echoes, more coherence paths become available thereby increasing the signal. However the decay properties of these additional coherence paths can be different from that of the direct echo. This means that real measured data is distorted from relationships derived for the direct echo coherence path only.

#### 4.1.2 NMR MOUSE

Figure 4.1.2.1 shows a diagram of the instrument that was used in this project, a NMR MOBILE Universal Surface Explorer (MOUSE)<sup>18</sup>. This instrument uses an arrangement of permanent magnets to create a uniform slice of magnetic field outside the instrument that is used as the sensitive volume for NMR. Within this

volume there is a strong unilateral gradient in the magnetic field,  $B_0$ , perpendicular to the slice. The magnetic field vector is in the plane of the slice. The dimensions of the slice are approximately 1cm radius and 500 $\mu$ m (maximum) thickness, though the sensitivity of the instrument through the slice is Gaussian rather than top hat. The field strength ranges from 0.2527T at the bottom of the selected slice to 0.2471T at the top. The transmission and detection loop is fixed at various distances from the sensitive profile volume by a choice of plastic spacer. The closer the loop is to the sensitive volume the higher the sensitivity is. However the positioning of the loop also determines the depth the selected slice can physical be placed within the sample, the smaller the gap the less the possible physical penetration depth.

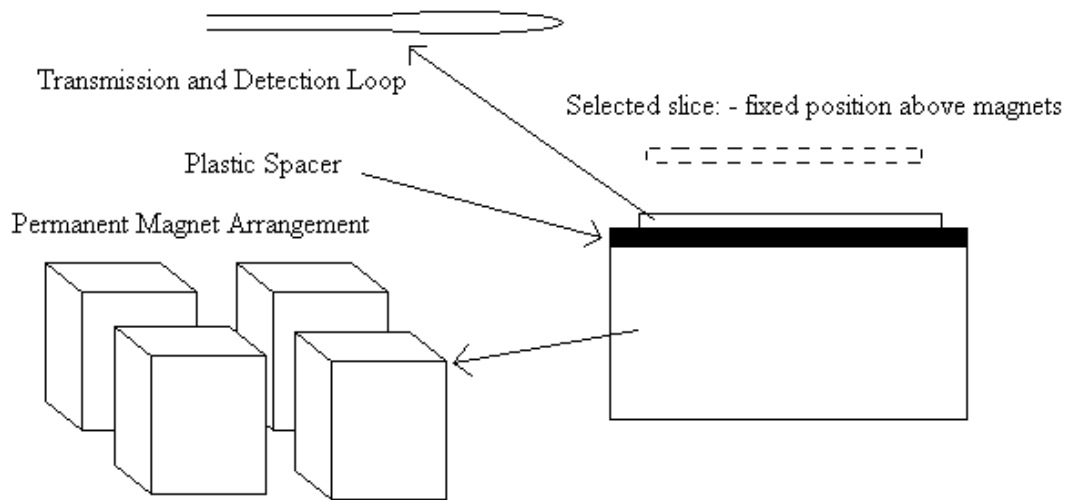


Figure 4.1.2.1  
Diagram of NMR MOUSE used in this project.

The main use of the magnetic field gradient, in the selected slice, is to provide a 1 dimensional imaging capability. From previous equation 4.1.1.1 it can be seen that the precessional frequency of a nucleus at a given position is determined by the magnetic field strength at that point. The detection of the NMR signal ( $M_{xy}$ ) for each echo (i) is the summation of all (N) the precessional fields (including their frequency), given by

$$M_{xy,TOI}(t) = \sum_{i=1}^{i=N} M_{xy,i} \cos(t\gamma B_i + \delta_i). \quad (4.1.2.1)$$

By use of a Fourier transform on the temporally captured spin echoes, the axial (vertical) distribution of the signal is recovered as

$$M_{xy,TOT}(B) = |FT[M_{xy,TOT}(t)]| = |FT[\sum M_{xy,i} \cos(t\gamma B_i + \delta_i)]| = \sum M_{xy,i} \gamma B_i(B). \quad (4.1.2.2)$$

The magnetic field strength as a function of position of this particular instrument has previously been measured to be linear with a gradient of 11.38T/m<sup>19</sup>. This means that the position is mapped linearly to field strength, hence the resolved NMR signal frequency. For all experiments in this project, the echoes were Fourier transformed and the amplitude taken from this spatial resolved data.

With the MOUSE instrument a CPMG train was used to produce the NMR signal in the in-homogenous field<sup>20</sup>. With the field gradient the EM pulse cannot be perfectly tuned to the range of Larmor frequencies, and this means that a number of coherence paths exist for the train<sup>15, 16</sup>. As the Hahn echo is free of these distortions, its use is the most accurate method of measuring physical parameters. However, as there is only one of these echoes per train, it is slow in producing high signal to noise data. Due to the increase in the coherence paths, if  $\frac{T_E}{T_2^{eff}}$  is small the amplitude of the second and third echo increase respectively. Further increase in the signal beyond the third echo has not been seen, so from the third echo onwards the signal was treated like an undistorted CPMG train of direct echoes. However the presence of other coherence pathways leads to systematic error of extracted parameters.

Due to the relatively low (0.25T) polarising field strength, the signal to noise of the signal produced by one experiment (pulse train) is low. For most measurements with the instrument the pulse sequence has to be repeated a number of times,  $N_R$ , with the last echo of the previous train separated from the 90° pulse by a time,  $T_R$  (repetition time). The echo train measurements are then summed together to give a final high signal to noise result. The purpose of the  $T_R$  time is to let the longitudinal magnetisation relax to the thermodynamic equilibrium. If the magnetisation has not completely relaxed, its lower magnitude of magnetisation reduces the amplitude of the resulting signal. It also changes the coherence pathways component of signals in

the later echoes<sup>21</sup>. The  $T_R$  time is usually much longer than  $T_E N_E$ , where  $N_E$  is the number of echoes, so determines the time taken to do experiments along with  $N_R$ .

## 4.2 NMR MOUSE Self-diffusion measurements of solvent varnishes

The strong magnetic field gradient of the NMR MOUSE enables highly accurate measurement of self-diffusion coefficients. The first use of the method was the measurement of the self-diffusion coefficients within bulk varnish solutions. In this section the methods and results are detailed.

### 4.2.1 Methods

The purity of the Hahn spin echo means that amplitude of this echo can be directly related to the value of the self-diffusion coefficient,  $D$ , the magnetic field gradient strength,  $G$ , and the echo time,  $T_E$ , without any need for empirical calibration. There will also be the decay of the signal due to the true  $T_2$  of the material (previous equation 4.1.1.3). The result is that the amplitude of a Hahn echo,  $A$ , is given by

$$A = A_0 \exp\left(-\frac{D\gamma^2 G^2 T_E^3}{12}\right) \exp\left(\frac{-T_E}{T_2}\right) + C_0, \quad (4.2.1.1)$$

where  $\gamma$  is the gyro-magnetic constant of hydrogen nuclei,  $A_0$  is amplitude at  $T_E=0$  and  $C_0$  is a noise floor due to thermal sources of signal.

In most current NMR measurements of self-diffusion<sup>22</sup> the magnetic field gradient is varied allowing the fitting of  $D$  while  $T_2$  decay becomes part of the amplitude constant. This method is called Pulsed Field Gradient (PFG). The NMR mouse has a fixed magnetic field gradient so this approach is not possible, instead the  $T_E$  time is varied. The immediate disadvantage of this is that the effect of  $T_2$  is no longer constant, adding an extra parameter to be fitted to the data. However, due to the strong field gradient of the instrument, the effect of  $T_2$  in the decay of the signal with  $T_E$  was usually negligible (for low viscosity liquid samples). As a result of this, the fitted relationship was approximated to

$$A \approx A_0 \exp\left(-\frac{D\gamma^2 G^2 T_E^3}{12}\right) + C_0. \quad (4.2.1.2)$$

The Hahn echo method provides an accurate method of measuring the self-diffusion coefficients, though as only one echo is used per measurement it is slow in producing high signal to noise data. The CPMG train (third echo onwards) with a large amount of echoes recovered in a single measurement has the potential of providing a faster method of measuring the diffusion, with the same error due to signal to noise. It also provides a quasi-independent method of measuring diffusion and allows the calculation of the real  $T_2$  time (see also section 4.3.1) in order to confirm that the  $T_2$  can be ignored in the decay of the Hahn echo method.

The decay of the CPMG train is an exponential, with decay constant  $T_2^{\text{eff}}$ , given by

$$A(t) = A_0 \exp\left(\frac{-t}{T_2^{\text{eff}}}\right). \quad (4.2.1.3)$$

A series of measurements are taken with different  $T_E$  times and their  $T_2^{\text{eff}}$  were measured by fitting. The relationship between  $T_E$  and  $T_2^{\text{eff}}$  is

$$\frac{1}{T_2^{\text{eff}}} = \frac{DG^2\gamma^2}{12} T_E^2 + \frac{1}{T_2}. \quad (4.2.1.4)$$

$1/T_2^{\text{eff}}$  is then plotted against  $T_E^2$  and a linear fit made. The diffusion is calculated from the slope of the fit, while the y axis intercept gives the true  $1/T_2$  time of the material. If equations 4.2.1.3 and 4.2.1.4 are combined and  $t$  set to  $T_E$  equation 4.2.1.1 is recovered.

## 4.2.2 Calibrations

To measure the accuracy of both methods, they were applied to 5 pure substances previously measured with high precision, as a function of temperature, by a PFG method<sup>23</sup>. The reference values were calculated for 20°C, the measurements were carried out in an air conditioned lab with temperatures kept within 2°C of this value. The local temperature of the samples were not measured. Table 4.2.2.1 shows the experimental parameters used for the Hahn echo measurements. The  $T_E$  times were

chosen to provide high sampling of the curve from 200 $\mu$ s (shorter  $T_E$  times than this were demanding on electronics) until the signal was negligible above noise and a reasonable amount of the noise floor had been measured. The  $T_R$  time was selected to maximise the signal to noise measurement for a set time measurement. The averaged repeats per measurement ( $N_R$ ) were set automatically to give two minute experiments.

	$T_E$ ( $\mu$ s)	$T_R$ (ms)	$N_R$
Cyclohexane	200:20:2000	2000	60
Distilled Water	200:40:2000	3000	40
Dodecane	200:40:3000	2000	60
DMSO	200:20:4000	3000	40
Pentanol	200:20:4000	4000	30

Table 4.2.2.1  
NMR settings used to measure the self-diffusion in 5 pure liquids by the Hahn echo method.

Figure 4.2.2.1 shows the Hahn echo fit and residual for pentanol. Appendix 2.1 gives the same results for the other four molecular liquids. The quality of the fits to the data are visually very good, though the residual of the fits do show noticeable structure. The inclusion of  $T_2$  within the fitting did not provide reasonable values (the  $T_2$  values were exceedingly long or negative depending on whether the fitted parameter was  $T_2$  or  $1/T_2$ ) due to the negligible effect of the term on the results. The distortion of the fit appears to be due to a different effect.

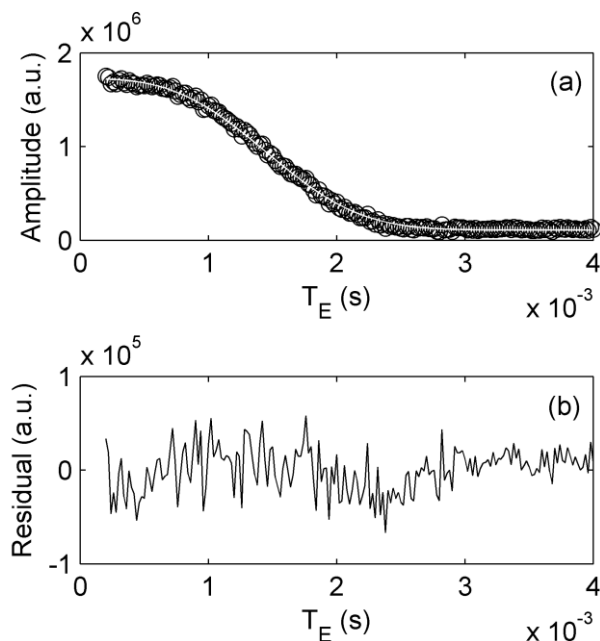


Figure 4.2.2.1  
 (a) The Hahn echo amplitude (black circles) measured as a function of  $T_E$  value for pentanol and diffusion fit (white line).  
 (b) Residual of the data from the fit.

Table 4.2.2.2 shows the parameters used for the CPMG method of measuring diffusion. The  $T_E$  values used were the ones where the  $T_2^{\text{eff}}$  could be fitted. For  $T_E$  values greater than this there is too little signal left within the CPMG train due to the temporal sampling being too great compared to the  $T_2^{\text{eff}}$ . Figure 4.2.2.2 shows an example  $T_2^{\text{eff}}$  fit for pentanol and the measured  $T_2^{\text{eff}}$  time against  $T_E^2$ . The same figures for the other molecular liquids are given in appendix 2.2. The extrapolation of all the trends pass close to or beneath the origin of the graphs, hence the accuracy of this data is insufficient to calculate  $T_2$  by this method for these molecular liquids. For all the measurements  $T_2^{\text{eff}}$  is dominated by diffusion.

	$T_E$ ( $\mu\text{s}$ )	$N_E$	$T_R$ (ms)	$N_R$
Cyclohexane	200:20:400	256	2000	60
Distilled Water	200:40:640	256	3000	40
Dodecane	200:40:700	256	1000	120
DMSO	200:20:500	256	3000	40
Pentanol	200:20:900	256	4000	30

Table 4.2.2.2  
 NMR settings used to measure the self-diffusion in 5 pure liquids by the CPMG echo method.

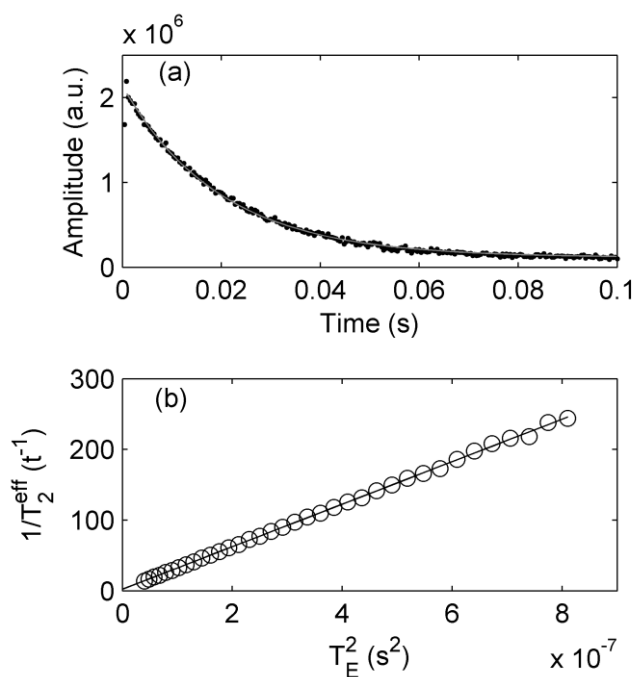


Figure 4.2.2.2  
 (a) Example of a CPMG train (black dots) and fitted  $T_2^{\text{eff}}$  decay (grey line) for pentanol.  
 (b) The measured  $T_2^{\text{eff}}$  times (circles) and fitted diffusion relationship (line).

Table 4.2.2.3 gives the referenced and measured values of diffusion for the pure liquids. To evaluate the accuracy of both methods the fractional difference (factor a and b) with the reference values were taken. The Hahn echo method produced  $15 \pm 6\%$  higher values than the reference. There are several potential reasons for the discrepancy of Hahn values. Firstly  $D$  has a strong dependence on temperature, it is possible that the local temperature of the sample was elevated a few degrees above  $20^\circ \text{C}$ . However, to explain all the discrepancy would require elevation of up to  $10^\circ \text{C}$  for cyclohexane and  $\text{DMSO}^{23}$ . Contamination of the samples measured is also a possibility. The majority of the samples came from opened reagent grade Winchesters, where absolute purity from substances such as water is not assured. The gradient of the magnetic field was taken from a previous measurement<sup>19</sup>, it is possible that there were errors in this measurement or that the magnets have degraded since the measurement. Due to the uncertainty in the source (instrument or samples) of the error in this calibration measurement, no corrections were subsequently made for it. The resulting error of this method is 21% (random + systematic), which proved sufficient for the comparison of the molecular behaviour of AYAT and Regalrez varnish solutions.

Sample	Reference $\times 10^{-9} \text{ m}^2 \text{ s}^{-1}$	Hahn Echo $\times 10^{-9} \text{ m}^2 \text{ s}^{-1}$	Factor a	CPMG $\times 10^{-9} \text{ m}^2 \text{ s}^{-1}$	Factor b	Factor c
Cyclohexane	1.29	1.54	1.19	2.41	1.87	1.56
Distilled Water	2.02	2.23	1.10	3.19	1.58	1.43
Dodecane	0.74	0.80	1.08	1.16	1.57	1.45
DMSO	0.66	0.81	1.23	1.26	1.91	1.55
Pentanol	0.24	0.28	1.16	0.39	1.62	1.39

Table 4.2.2.3

Referenced and measured diffusion values of the 5 pure liquids. Also the ratios between the measured values, a = Hahn/Reference, b = CPMG/Reference and c = CPMG/Hahn.

It is expected that the error in the CPMG method is higher than the Hahn echo method, due to the distortion of later echoes by multiple coherence pathways. These results match this expectation, with the CPMG diffusion value being  $71 \pm 17\%$  higher than the reference values. As the CPMG method results are distorted from the Hahn echo results by a known process, and the other variables should be near identical, it is useful to compare the fraction difference (Factor C) between these measurements. There is a  $48 \pm 8\%$  increase in the diffusion value, alternatively this can be represented by a linear correction factor between the two methods of  $1.48 \pm 0.08$  that was used in subsequent measurements.

### 4.2.3 Diffusion results of a polymer varnish

A varnish solution consists of a variety of different molecular species, these species will have their own self-diffusion constant dependent on the molecules' properties and interactions with other components of the solution. With the use of toluene (a singular molecular species) as a solvent, only one diffusion value for it should be present. AYAT may be considered a singular molecular species but it is polydisperse, the self-diffusion of large and small resin molecules will be different. However, in this case the difference in diffusion between the resin molecules is negligible compared to the difference between the resin and the solvent. All (N) molecules within the varnish solution contain hydrogen atoms, so for the Hahn method of measuring self-diffusion the total amplitude of the signal is given by

$$A = \sum_{i=1}^N \left[ A_i \exp\left(-\frac{D_i \gamma^2 G^2 T_E^3}{12}\right) \right] + C_0, \quad (4.2.3.1)$$

where  $D_i$  and  $A_i$  is the self-diffusion coefficient and amplitude of individual components of the solution respectively. With the approximation of treating the solution as two monodisperse molecules, solvent, S, and resin, R, equation 4.2.3.1 becomes

$$A = A_S \exp\left(-\frac{D_S \gamma^2 G^2 T_E^3}{12}\right) + A_R \exp\left(-\frac{D_R \gamma^2 G^2 T_E^3}{12}\right) + C_0. \quad (4.2.3.2)$$

The AYAT varnish solutions were measured with the  $T_E$  times given in table 4.2.3.1. Figure 4.2.3.1 shows the Hahn echo data for the solution of 3g AYAT and 11ml toluene. The NMR signal can be seen to be the addition of the separate signals, from the resin and solvent, diffusing at very different rates. Equation 4.2.3.2 is seen to fit the data well. To measure the fits accuracy, the ratio of the fitted amplitudes and mass ratio can be compared. The amplitude constant of the NMR signal is proportional to the amount of  $H^1$  nuclei, the percentage of mass composed of  $H^1$  for the toluene is 8.7% and for AYAT is 7.0%. The ratio,  $k$ , between these values is 0.8. Table 2.3.3.1 gives the NMR amplitude ratio and mass ratios for the AYAT sample, which are related by  $A_R/A_S=k(M_R/M_S)$ . Least square regression gives  $k$  as  $0.88 \pm 0.12$  which matches the expected value.

Resin mass (g)	Solvent volume (ml)	$T_E$ ( $\mu$ s)	$A_R/A_S$	$m_R/m_S$
0.5	13.5	200:80:5500	0.03	0.04
1	13	200:80:5000	0.04	0.09
2	12	200:160:10000	0.15	0.19
3	11	200:160:10120	0.32	0.31
4	10	200:80:25000	0.34	0.46
4.5	9.5	200:160:10120	0.52	0.55
5	9	200:80:10040	0.53	0.64

Table 4.2.3.1  
Varnish solution composition,  $T_E$  times used for measurement, measured amplitude ratio and mass ratio for the solvent and resin, for the AYAT and toluene solutions.

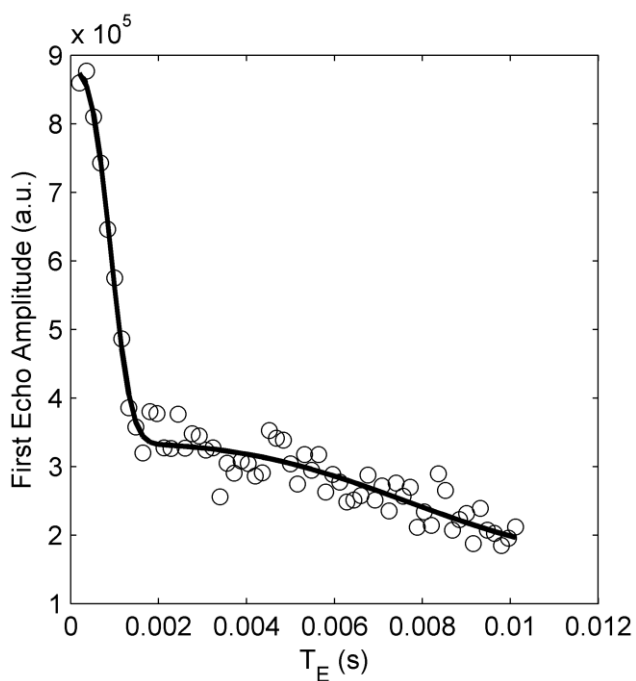


Figure 4.2.3.1  
Hahn echo amplitude and  
two component diffusion  
fit for 3g of AYAT  
dissolved in 11ml of  
toluene.

At the low concentration and high concentration extremes there are separate issues in the measurement of the diffusion of the polymer by this method. Figure 4.2.3.2 shows the Hahn data and fit for the lowest concentration sample (0.5g of resin to 13.5ml of solvent), where due to the low concentration of the resin the signal to noise ratio (for the resin) is extremely small. This affects the accuracy of the amplitude and diffusion coefficient measured for the resin, but has minimal effect on the accuracy of the solvent parameters. Figure 4.2.3.3 shows the highest concentration sample measured (5g of resin to 9ml of solvent), the slow diffusion of the polymer and the higher viscous nature of the sample means that the  $T_2$  time of the polymer is no longer negligible (see section 4.3.1). It can be seen that for the resin section, the fit does not pass through the centre of the data and the data appears more linear due to the exponential  $T_2$  decay. As a result of the distortion of the data by  $T_2$ , the measured value of resin  $D$  for this sample was higher than the next more dilute sample.

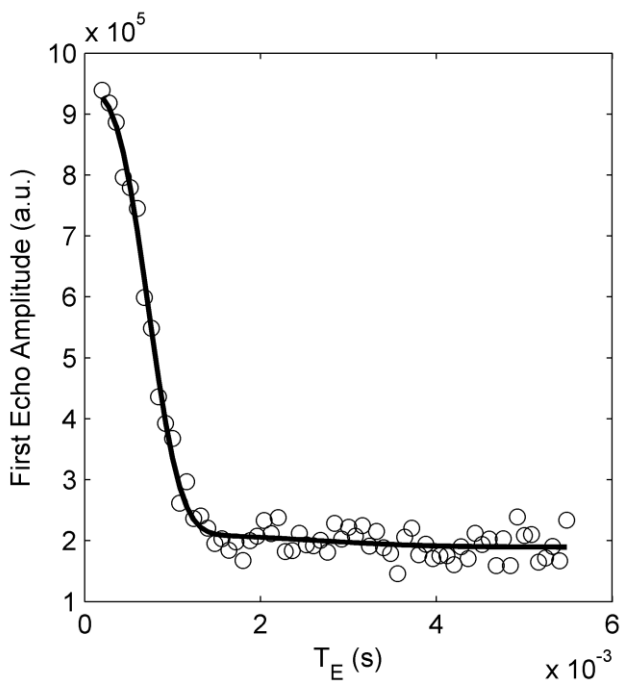


Figure 4.2.3.2  
Hahn echo amplitude and  
two component diffusion  
fit for 0.5g of AYAT  
dissolved in 13.5ml of  
toluene.

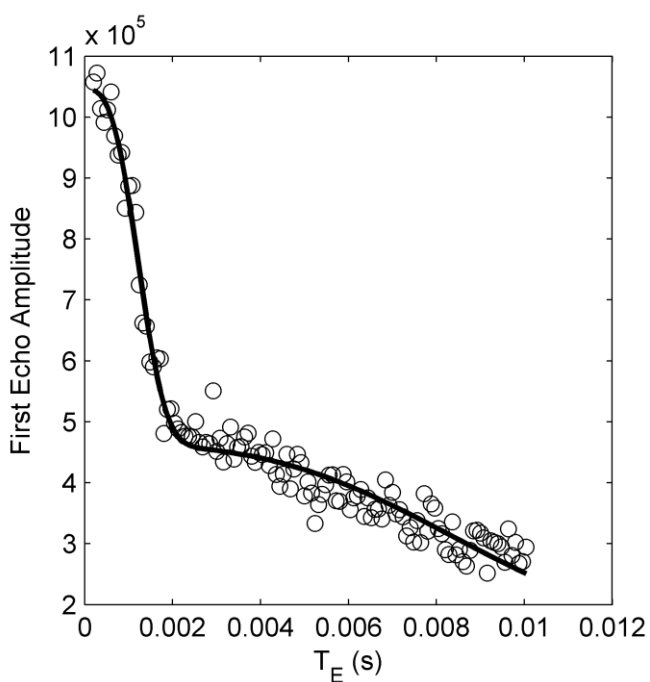


Figure 4.2.3.3  
Hahn echo amplitude and  
two component diffusion  
fit for 5g of AYAT  
dissolved in 9ml of  
toluene.

Figure 4.2.3.4 shows the measured diffusion results for the resin and solvent for the AYAT varnish. The diffusion coefficients of the resin and solvent are orders of magnitude different for any concentration. This result gives an important picture of the behaviour of this polymer varnish at the molecular level. The large resin molecules are immobile compared with the solvent molecules. The rapid decrease in diffusion, with increased concentration, at low concentrations is likely to be due to polymer molecules inability to move past each other easily. At extremely low

concentration a polymer molecules are able to diffuse through the solvent. As the concentration increases the polymer molecules will increasingly collide and then (at higher concentrations still) entangle with each other, leading to the much reduced self-diffusion coefficient. This is consistent with the expected behaviour<sup>24</sup> of a polymer. The low diffusion of AYAT is in strong contrast to the high mobility of Regalrez 1094 (next section). The CPMG measurement of diffusion proved much less reliable than the Hahn method, the CPMG diffusion results for AYAT are given within section 4.3.1.2.

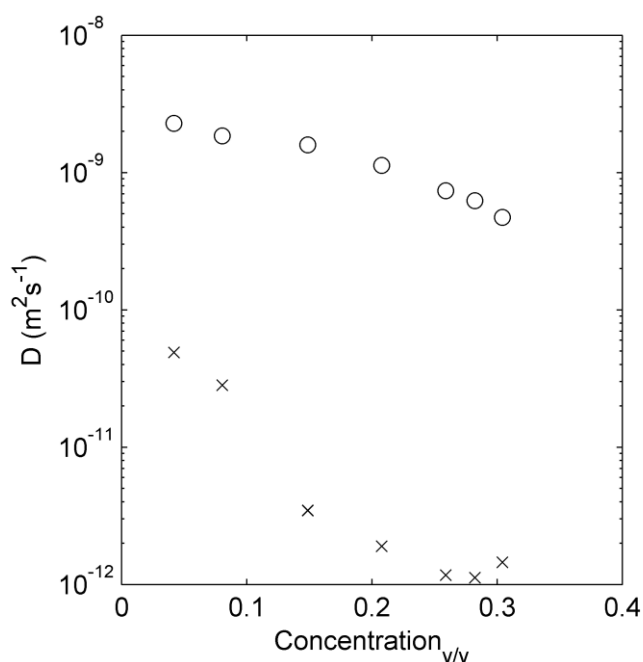


Figure 4.2.3.4  
Measured self-diffusion values of the solvent and resin by the Hahn echo method for AYAT and toluene solutions.

#### 4.2.4 Diffusion results of a low molecular weight varnish

Figure 4.2.4.1 shows the Hahn echo data for a Regalrez and Toluene solution (4g of resin to 20ml of solvent), where unlike the AYAT solutions there is only one diffusion decay immediately resolvable. The resin molecules are diffusing at a similar rate to the solvent molecules, which is why they are not resolvable. As a result only a single net diffusion was fitted to the data. This fitted relationship is visually good, the difference in diffusion of the solvent and resin molecules is small enough for a single diffusion value to be a good approximation. However the resolution limit, of this method, for differentiating two substances by their diffusion has not been measured.

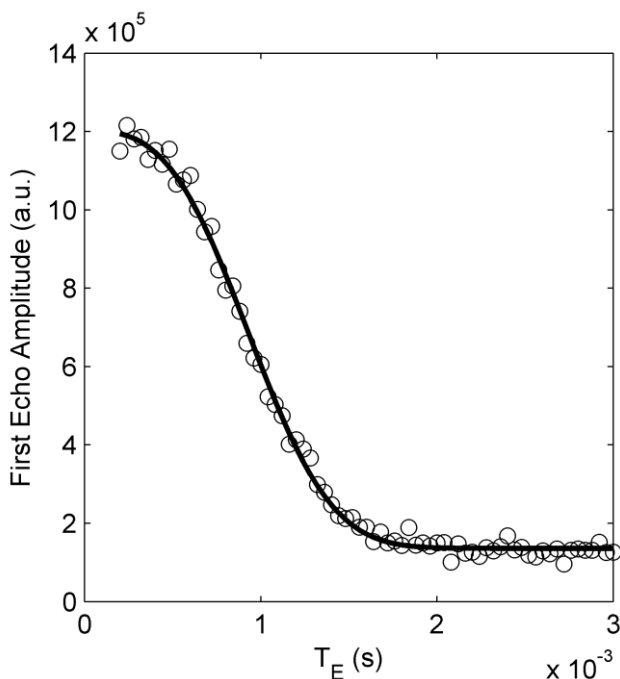


Figure 4.2.4.1  
Hahn echo amplitude and  
single component diffusion  
fit for 4g of Regalrez  
dissolved in 20ml of  
toluene.

As the concentration of Regalrez increases, the resulting change in the NMR properties (section 4.3) of the resin and solvent leads to a single diffusion decay no longer approximating the Hahn data. Figure 4.2.4.2 show the Hahn data for the highest concentration Regalrez sample measured, here the decay is clearly not approximate to a single (or sum of two) diffusion decay. From section 4.3.1.3 it is expected that the NMR decay from the resin is dominated by  $T_2$ , while diffusion is still the dominating aspect for the solvent. To minimise the fitted parameters, just the dominating decay components of each source of signal (resin and solvent) were fitted. The resulting fitting equation is given by

$$A = A_R \exp\left(-\frac{T_E}{T_{2R}}\right) + A_S \exp\left(-\frac{D_S \gamma^2 G^2 T_E^3}{12}\right) + C_0. \quad (4.2.4.1)$$

This approximated fit (shown in figure 4.2.4.2) appears to match the data well. Attempts at complete fitting of both diffusion and  $T_2$  for both components were unsuccessful and the use of a constant solvent  $T_2$  (42ms) measured in section 4.3.1.3 in the fit made a negligible difference. As with the measurement of the AYAT samples, the ratio of the fitted amplitudes can be compared with the expected value to give an indication of accuracy. The percentage of the Hydrogen component of mass in Regalrez  $((C_8H_{14}.C_9H_{16})_x)$  from chapter 1.1.4) is 12.8% giving  $k = 1.47$ , giving a theoretical amplitude ratio is 4.2. The measured amplitude ratio was 2.1,

which indicates a significant error. The measured resin  $T_2$  time was 0.4ms compared with 1.1 ms measured in section 2.4. The measured solvent diffusion was  $3.8 \times 10^{-11} \text{ m}^2 \text{ s}^{-1}$  compared with  $5.76 \times 10^{-11} \text{ m}^2 \text{ s}^{-1}$  in section 4.3.1.3.

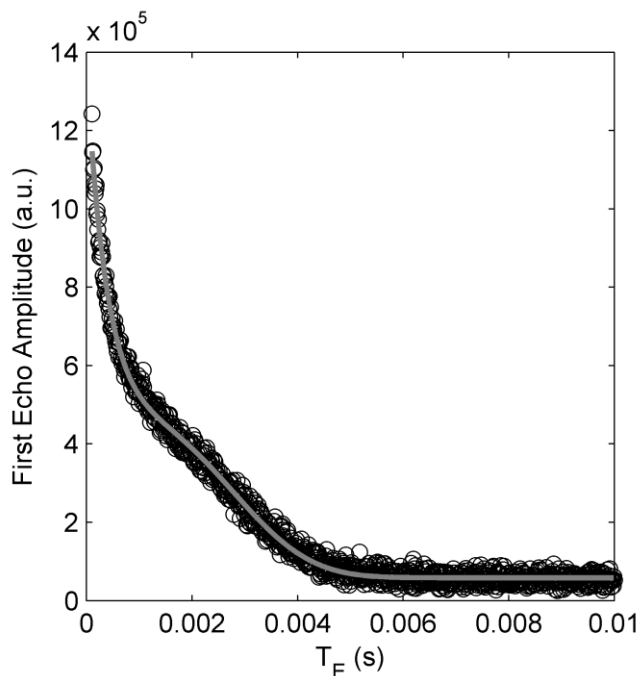


Figure 4.2.4.2  
Hahn echo amplitude  
and fit of equation  
2.3.4.1 (grey) for 10g of  
Regalrez 1094 dissolved  
in 4ml of toluene.

Figures 4.2.4.3 and 4.2.4.4 show the results for a 12g resin to 20ml solvent sample and a 20g resin to 20ml solvent sample respectively. For these concentrations, the NMR signal data is not as accurately represented by the two approximations used for the low and high concentration samples. For the 12g20ml sample (Figure 4.2.4.3) the single diffusion fit is still close in shape but there is significant systematic differences. For the 20g20ml sample (Figure 4.2.4.4) the data is substantially different from the single net diffusion fit and was the highest concentration sample that this single net diffusion value was measured. However the high concentration approximation (equation 4.2.4.1) can be seen to be incorrect in shape at low  $T_E$  times.

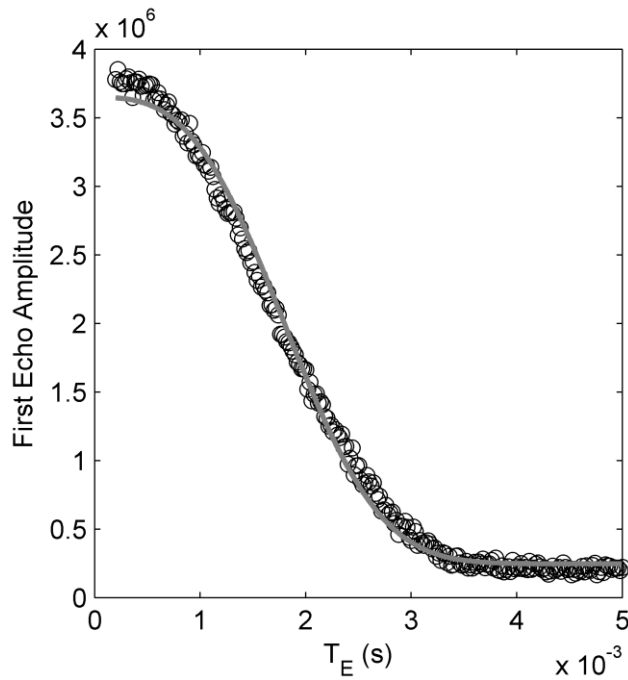


Figure 4.2.4.3  
Hahn echo amplitude and  
single component diffusion  
fit for 12g of Regalrez  
dissolved in 20ml of  
toluene.

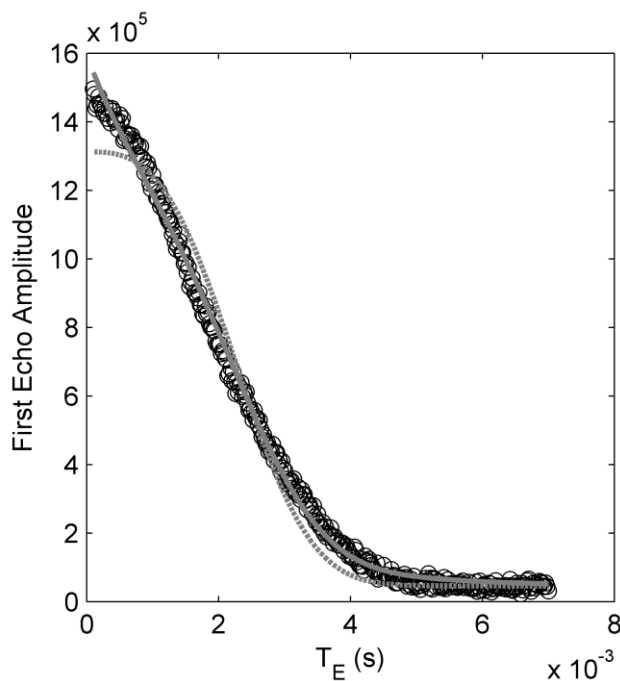


Figure 4.2.4.4  
Hahn echo amplitude,  
single component  
diffusion fit (grey dotted)  
and fit of equation 2.3.4.1  
(grey solid) for 20g of  
Regalrez dissolved in  
20ml of toluene.

The single net diffusion value for a larger set of samples was carried out with the CPMG method and fitting of a single  $T_2^{\text{eff}}$  for each CPMG train. Figure 4.2.4.5 shows the results for the low concentration samples. The method can be seen to produce results consistent with the single diffusion approximation. Figure 4.2.4.6 shows the results for three more concentrated samples. The data for the 16g of resin to 20ml solvent and the 20g resin to 20ml solvent samples still follow the desired behaviour for the majority of points. However the distortion of the results can be

seen at low  $T_E$  times. For the 9g resin to 5ml solvent sample, where the Hahn data shows that the single net diffusion approximation is no longer appropriate, the resulting CPMG results are far more distorted and a net diffusion fitting cannot be justified.

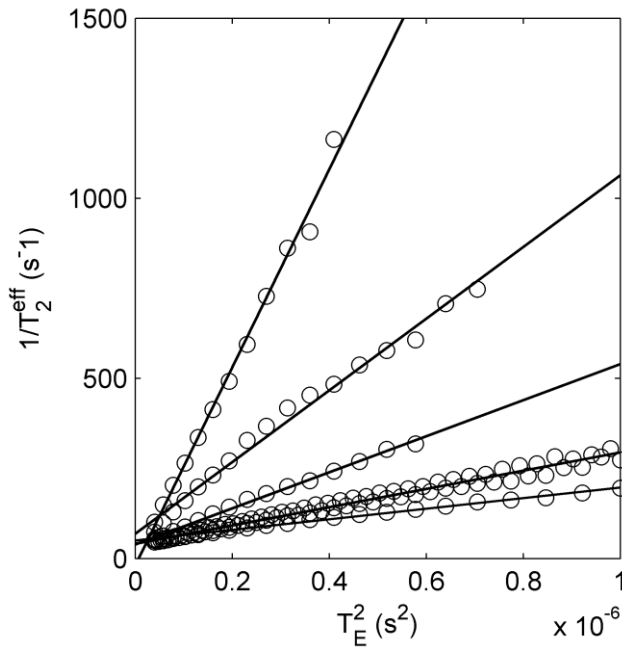


Figure 4.2.4.5  
From highest slope to least slope the CPMG measured  $T_2^{\text{eff}}$  and diffusion fits for pure toluene, 2g resin to 20ml solvent, 4g resin to 20ml solvent, 8g resin to 20ml solvent and 12g resin to 20ml solvent.

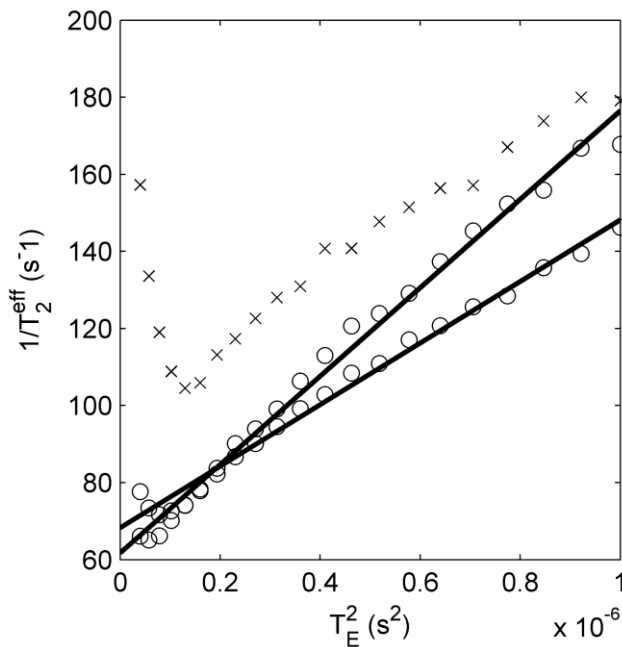


Figure 4.2.4.6  
From highest slope to least slope the CPMG measured  $T_2^{\text{eff}}$  and diffusion fits for 16g resin to 20ml solvent and 20g resin to 20ml solvent (circles). The measured single  $T_2^{\text{eff}}$  for 9g resin to 5ml of solvent is also shown (x).

Table 4.2.4.1 allows the comparison of the net diffusion results for the two methods. Three of the four Hahn measurements show good correspondence to the CPMG data, the reason for the discrepancy of the measurement of 4g resin to 20ml solvent

sample is unknown. The viscosities of these samples were measured by the flow method with TA rheometer. Self-diffusion is usually proportional to the reciprocal of viscosity, such as the Stokes-Einstein equation for spherical particles. Figure 4.2.4.7 shows this relationship for the Regalrez solutions.

Resin mass (g)	Solvent vol (ml)	Hahn D $10^{-9} \text{ m}^2 \text{ s}^{-1}$	CPMG D $10^{-9} \text{ m}^2 \text{ s}^{-1}$
0	1	2.21 (incomplete curve*)	2.39
2	20		0.865
4	20	1.06	0.434
8	20		0.220
12	20	0.147	0.128
16	20		0.0997
20	20	0.0740	0.0694

Table 4.2.4.1  
Net diffusion measurements for both the Hahn and CPMG methods for Regalrez and Toluene solutions.  
\*See appendix 2.1, figure A2.1.5 to see the data and fit.

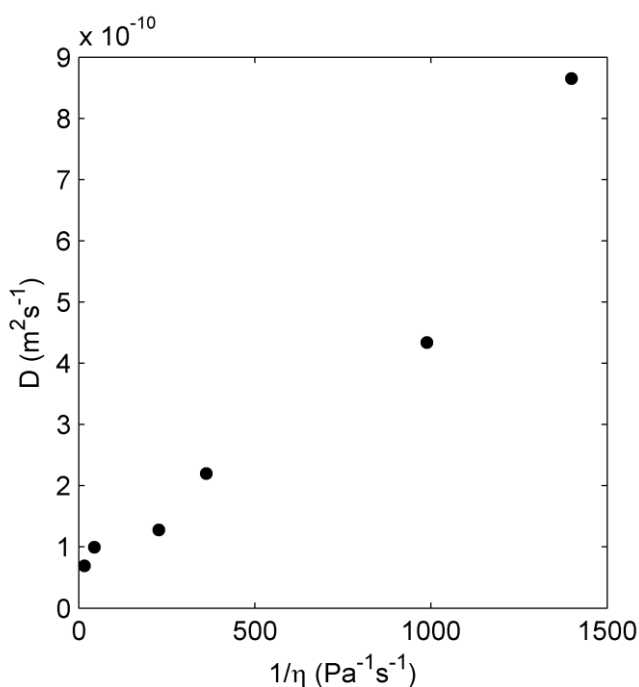


Figure 4.2.4.7  
CPMG measured net diffusion against  $1/\text{viscosity}$  for the Regalrez and toluene solutions.

### 4.3 NMR $T_1$ and $T_2$ times of varnish solutions

The  $T_2$  and  $T_1$  times of the resin and solvent in the Regalrez and AYAT solutions were measured. These measurements served two purposes for the project, firstly provide information on the behaviour of the resin and solvent molecules of varnish solutions as they dry, see section 4.4 for the resulting description. Secondly, NMR is

also used to monitor drying varnish systems (sections 4.5 and 4.6). For the interpretation of the resulting data, the change of the varnishes NMR signal properties, as a function of concentration, needs to be known.

As described for diffusion measurements (section 2.3) the NMR signal is the sum of the solvent and resin contributions, each of these with their own  $T_1$ ,  $T_2$  and diffusion times. The resolving of these is carried out by two component fitting to the experimental data.

### 4.3.1 $T_2$

#### 4.3.1.1 Method

The CPMG trains of the solutions were measured over a range of  $T_E$  values, for each of which the amplitude ( $A$ ) of the signal is given by

$$A = A_R \exp\left(\frac{-t}{T_{2R}^{eff}}\right) + A_S \exp\left(\frac{-t}{T_{2S}^{eff}}\right) + C_0, \quad (4.3.1.1)$$

where  $A_R$  and  $A_S$  is the amplitudes (at  $t=0$ ) of the resin and solvents respectively and  $T_{2R}^{eff}$  and  $T_{2S}^{eff}$  are their effective  $T_2$  decay times. However to reduce the degrees of freedom in the fitting, the ratio of amplitudes can be kept constant to the theoretical value determined from concentration. For these measurements it is important that  $T_R \gg T_{1max}$  ( $T_1$  of component, within the solution, with highest value), so that  $T_1$  does not have any impact on the amplitudes of the signals. After the fitting of the solvent and resin  $T_2^{eff}$  times for each  $T_E$  time, the real  $T_2$  and diffusion coefficients (with 1.48 correction factor) can be measured from equation 4.2.1.4.

#### 4.3.1.2 AYAT Results

Figure 4.3.1.2.1 shows the measured resin and solvent  $T_2^{eff}$  times for an AYAT and toluene solution, of a sample of 2g of resin to 12ml of solvent. The extraction of the diffusion (corrected) and true  $T_2$  times of both components is straightforward in the range of  $T_E$  values where their  $T_2^{eff}$  are sufficiently different. However for  $T_E$  times where their  $T_2^{eff}$  are similar, the double exponential fit fails to resolve them. In this

case results in both fitted components tend to be dominated by the solvent contribution. Figure 4.3.1.2.2 shows the measured  $T_2^{\text{eff}}$  for the higher concentration of 5g of resin to 9ml of solvent. For low concentrations the diffusion trends are clear, but as the concentration increases the diffusion of the resin becomes relatively less significant, than the true  $T_2$ , to the  $T_2^{\text{eff}}$  times. As concentration increases, the diffusion of the molecules is reduced, lowering its contribution to  $T_2^{\text{eff}}$ , while its true  $T_2$  times decreases which increase its contribution to  $T_2^{\text{eff}}$ . 5g of resin to 9ml of solvent was the highest concentration where the polymer diffusion was measured and the error in this measurement was high. At this concentration the solvent  $T_2^{\text{eff}}$  is still dominated by diffusion.

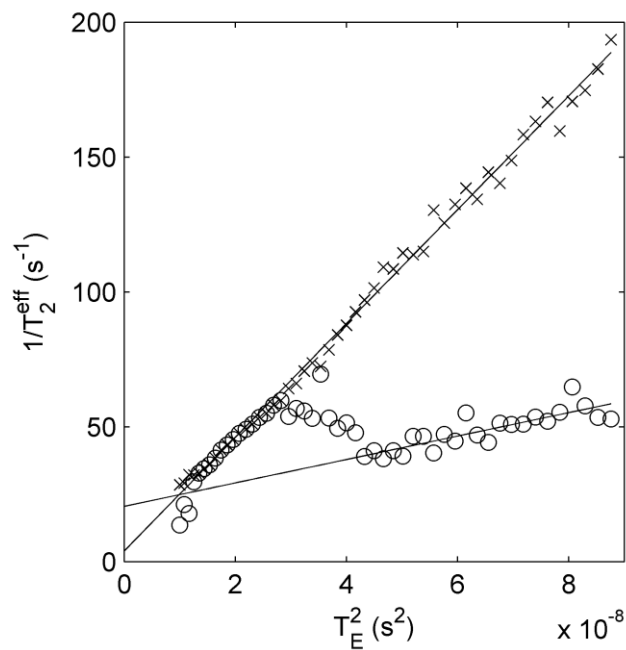


Figure 4.3.1.2.1  
 $T_2^{\text{eff}}$  measurements and diffusion fits for the resins and solvent, in a 2g of resin to 12ml of solvent solution of AYAT and toluene. Circles correspond to resin and crosses correspond to solvent.

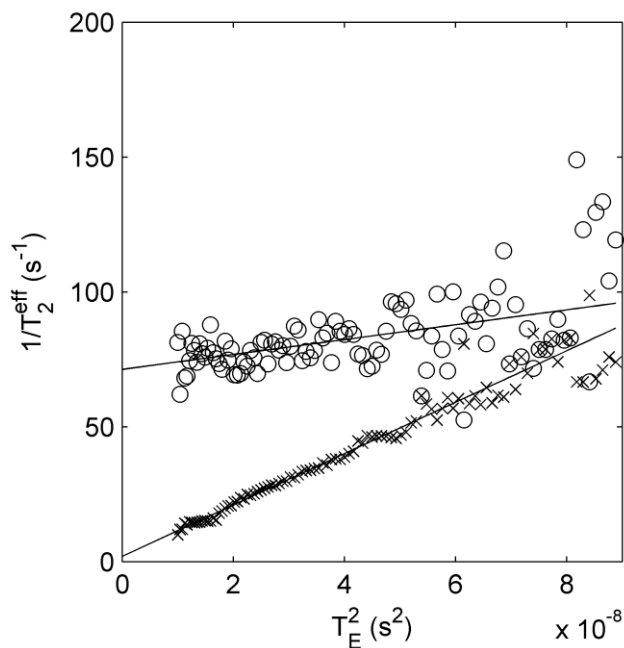


Figure 4.3.1.2  
 $T_2^{\text{eff}}$  measurements and  
diffusion fits for the resins  
and solvent in a 5g of  
resin to 9ml of solvent  
solution of AYAT and  
toluene.

The NMR behaviour needs to be known past concentrations that could be practically (complete homogeneity in sensible timescale) achieved by mixing resin into solvent. To produce higher concentration solutions a small amount of, 4g of resin to 10ml solvent, solution was placed in a specifically constructed vial. The higher concentration solution was produced by subsequently uncapping the vial and allowing the solvent to evaporate. The vial was then recapped and allowed to homogenise before the NMR measurement. The concentration was then calculated from the mass. Figure 4.3.1.2.3 shows the  $T_2^{\text{eff}}$  results for the highest concentration measured (resin mass fraction of 0.7173). The dependence, due to diffusion, of  $T_2^{\text{eff}}$  on  $T_E$  is negligible for both solvent and resin. The measured values of  $T_2^{\text{eff}}$  are, within experimental error, equal to the true  $T_2$  times.

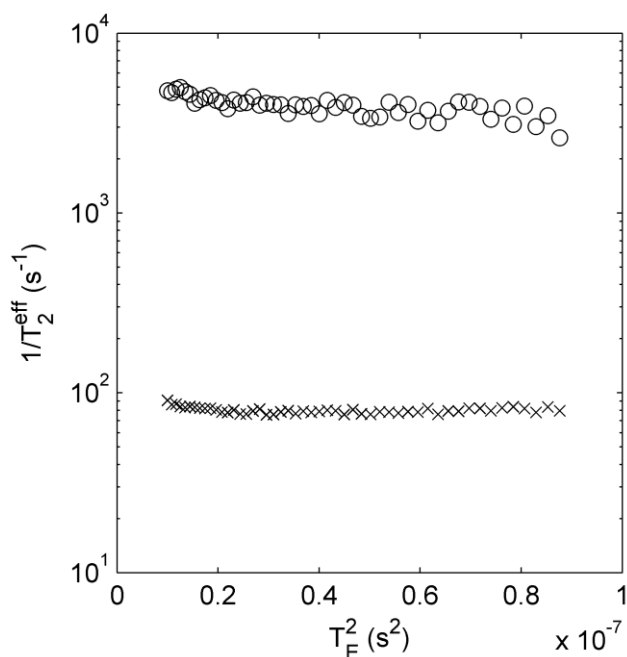


Figure 4.3.1.2.3  
 $T_2^{\text{eff}}$  measurements for the resins and solvent for a solution of AYAT and toluene, of 0.7173 mass fraction of resin.

Appendix 2.3 provides the remaining figures of the AYAT and toluene  $T_2$  results. The measured  $T_2$  and diffusion times for all the samples are given in table 4.3.1.2.1. As with the Hahn method of diffusion measurement (previous figure 2.3.3.4), the resin diffusion is orders of magnitude lower than the solvent diffusion. However, this method produced a higher diffusion rate than the Hahn method. Due to the distortions of the CPMG train and increased steps in the processing, the CPMG measurement of  $D$  is the least reliable. The resin  $T_2$  times decrease with concentration, the relatively short times means that the error is relatively low and this trend is not erroneous. For the solvent, apart from the two most concentrated samples, the long  $T_2$  times means that the error in its extrapolation from the measured  $T_2^{\text{eff}}$  is substantial, and this is seen in the results showing no trend. For the two highest concentration samples the solvent  $T_2$  times are short enough to be measurable by the method and can be seen to be decreasing further with concentration like the resin.

Concentration	T <sub>2R</sub> (ms)	D <sub>R</sub> 10 <sup>-9</sup> m <sup>2</sup> s <sup>-1</sup>	T <sub>2S</sub> (ms)	D <sub>S</sub> 10 <sup>-9</sup> m <sup>2</sup> s <sup>-1</sup>
1g resin 13ml solvent	53.8	0.754	173	2.27
2g resin 12ml solvent	48.7	0.377	252	1.83
3g resin 11ml solvent	28.6	0.127	157	1.24
4.5g resin 9.5ml solvent	13.8	-	-	1.18
5g resin 9ml solvent	14	0.240	502	0.828
0.4896g resin per total 1g	2.12	-	51.5	0.00544
0.7173g resin per total 1g	0.253	-	12.5	-

Table 4.3.1.2.1  
Measured T<sub>2</sub> and D values, for solvent, <sub>s</sub>, and resin, <sub>R</sub>, molecules,  
from the CPMG method in AYAT and toluene solutions.

### 4.3.1.3 Regalrez Results

Figure 4.3.1.3.1 shows the measured T<sub>2</sub><sup>eff</sup> for the resin and solvent in the low concentration (4g resin to 20ml of solvent) Regalrez and toluene solution. Unlike for the Hahn echo diffusion measurements (section 4.2.4), the method was successful in resolving the separate signals from the solvent and resins. The results are similar to the low concentration polymer varnish (section 4.3.1.2), though the magnitude of the diffusion (the gradients in the graph) of the solvent and resin for the low molecular weight Regalrez are closer than the high molecular weight AYAT resin. This measurement suggests that the solvent diffuses approximately three times faster than the resin. Like the AYAT results, the extrapolated T<sub>2</sub> time of the resin is significantly shorter than the T<sub>2</sub> time of the solvent. At low T<sub>E</sub> values, the T<sub>2</sub><sup>eff</sup> of the resin and solvent are too similar to be resolved correctly.

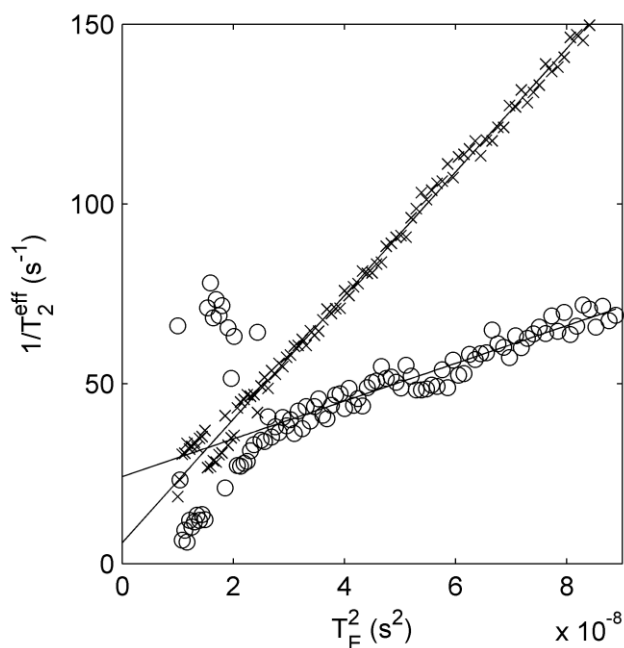


Figure 4.3.1.3.1  
 $T_2^{\text{eff}}$  measurements for the resins (circles) and solvent (crosses) in a 4g of resin to 20ml of solvent solution of Regalrez and toluene.

In figure 4.3.1.3.2 the measured  $T_2^{\text{eff}}$  values, for the concentration of 12g of resin to 20ml of solvent, are shown. This concentration provided a distortion of the results, giving the resin diffusion (gradients in graph) to be higher than that of the solvent. This would be unlikely to be true and has not been shown for any other samples. The measurement of the distortion of CPMG diffusion measurement was only carried out, with molecular liquids (section 4.2.2), where the  $T_2$  time was sufficiently long that it could be neglected. It is possible that the distortion of the CPMG results is also dependent on  $T_2$ , hence in this case the resin diffusion value would be distorted a different amount than that of the solvent. The measured  $T_2^{\text{eff}}$  points themselves also show systematic deviations from the linear relationship, this may be related to the previous point or maybe inherent from a problem in the fitting of the bi-exponential decay for this sample. Figure 4.3.1.3.3 shows the result for the next higher concentration (20g of resin to 20ml of solvent) measured, which matches the results of the other high concentration Regalrez solutions (see appendix 2.6) and high concentration AYAT solutions (section 4.3.1.2). The measured  $T_2^{\text{eff}}$  of the resin is independent of the  $T_E$  time (hence the effect of diffusion is negligible to this result) and its  $T_2$  is rapidly shortening with increased concentration. The solvent is still diffusing freely, albeit at a slower rate than if it was at a lower concentration, and its true  $T_2$  time is still relatively long.

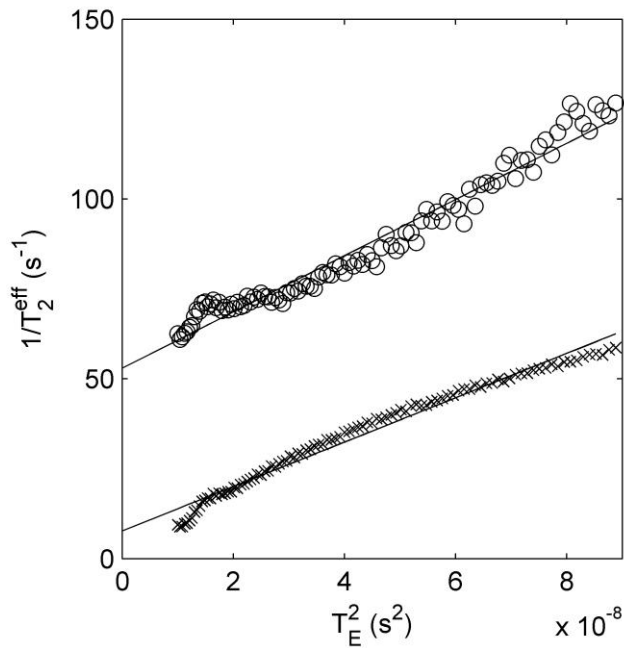


Figure 4.3.1.3.2  
 $T_2^{\text{eff}}$  measurements for the resins (circles) and solvent (crosses) in a 12g resin to 20ml solvent solution of Regalrez and toluene.

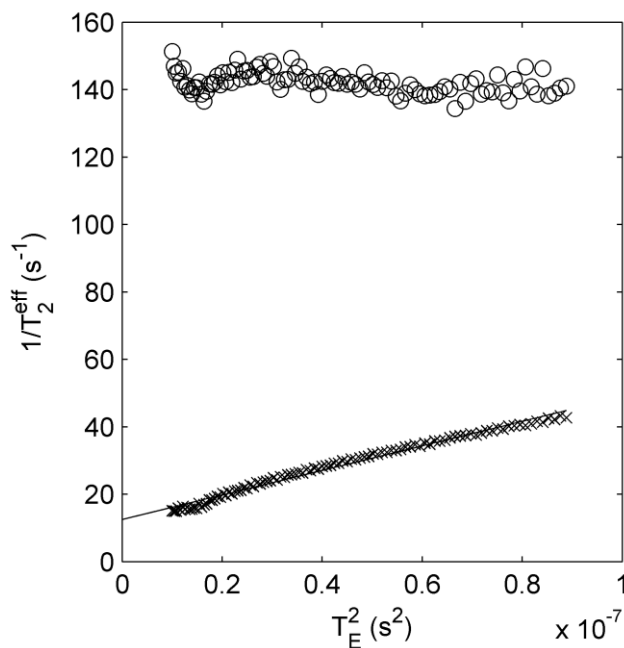


Figure 4.3.1.3.3  
 $T_2^{\text{eff}}$  measurements for the resins (circles) and solvent (crosses) in a 20g resin to 20ml solvent solution of Regalrez and toluene.

Like for AYAT (section above), higher concentration than could be reasonably made by mixing alone were produced by evaporation from a small custom made vial. Figure 4.3.1.3.4 shows the resulting data for sample with 0.8 mass fraction of resin. At this concentration the remaining NMR signal from the sample is highly reduced. The extrapolations of the trend in the resin  $T_2$  times, from lower concentrations, indicate that this is likely to be shorter than can be measured by this NMR MOUSE, at this concentration. As the varnish is tending towards a solid state its NMR

properties are becoming more reminiscent of that, characterised by extremely rapid  $T_2$  decays<sup>25</sup>. The measured  $T_2$ , of the other highly concentrated solutions, indicate that the  $T_2$  time of the solvent also drops as the concentration increases. The resulting data for this sample has negligible amplitude in comparison to the other concentrations measured, but still shows a decay. This signal is assumed to come from the small amount of solvent remaining (the  $T_2$  of the resin now being too short for the signal to be detected) and a single  $T_2^{\text{eff}}$  decay is fitted. The resulting  $T_2^{\text{eff}}$  values do not show significant dependence on  $T_E$ , suggesting that the diffusion coefficient is negligibly small. The  $T_2$  time of the solvent is now much shorter than at low concentrations (2ms compared with greater than 100ms), presumably as its molecules are constrained between the resin molecules.

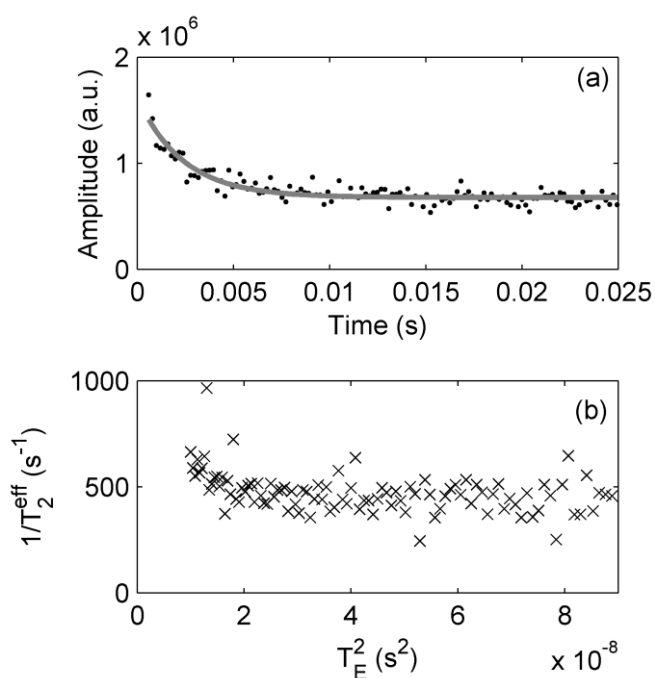


Figure 4.3.1.3.4  
 (a) Example data and single exponential fit for a, mass concentration of 0.8, solution of Regalrez and toluene  
 (b) Single  $T_2^{\text{eff}}$  measurements versus  $T_E$ .

Table 4.3.1.3.1 gives the final diffusion and  $T_2$  values for the solvent and resin of the Regalrez solution measured by the CPMG method. The measured  $T_2$  values for the resin and solvent and the solvent diffusion both show a consistent decreasing trend with concentration. The diffusion result for the 12g resin to 20ml of solvent has already been highlighted as potentially erroneous and no diffusion measurement were possible for the resin at concentrations higher than this.

Concentration	T <sub>2R</sub> (ms)	D <sub>R</sub> 10 <sup>-9</sup> m <sup>2</sup> s <sup>-1</sup>	T <sub>2S</sub> (ms)	D <sub>S</sub> 10 <sup>-9</sup> m <sup>2</sup> s <sup>-1</sup>
4g resin to 20ml solvent	41.4	0.422	171	1.38
12g resin to 20ml solvent	18.9	0.628	130	0.496
20g resin to 20ml solvent	7.04	-	80.1	0.293
9g resin to 5ml solvent	3.31	-	69.3	0.209
10g resin to 4ml solvent	1.10	-	43.2	0.0576
0.8g resin per total 1g	-	-	2.11	-

Table 4.3.1.3.1  
Measured T<sub>2</sub> and D values from the CPMG method in Regalrez and toluene solutions.

### 4.3.2 T<sub>1</sub>

To measure the T<sub>1</sub> times of the components of the varnish solutions, a version of the saturation recovery method was used. As described by section 4.1.2, the MOUSE takes the sum of the multiple produced echo trains separated by a time T<sub>R</sub>. If the T<sub>R</sub> is relatively short, then the excited net magnetic spins have not relaxed before the 90° initialisation pulse. The 90° pulse does not bring the magnetisation into the transverse plane and the resultant signal is reduced. When the steady state is reached within a train of repeats the magnitude of the signal is given by

$$A = A_0 \left[ 1 - \exp\left(\frac{-T_R}{T_1}\right) \right]. \quad (4.3.2.1)$$

With the use of series of measurements with different T<sub>R</sub> times, and with dummy measurements without recording at the start of each measurement to ensure steady state is reached, the T<sub>1</sub> can be calculated from the magnitude of the signal.

From section 4.3.1, the T<sub>2</sub><sup>eff</sup> of each component is known at any selected T<sub>E</sub> value. The T<sub>E</sub> value can be chosen to ensure that the resin and solvent T<sub>2</sub><sup>eff</sup> are sufficiently different so that they can be easily resolved. The fitting of equation 4.3.1.1 to the different T<sub>R</sub> data sets with these T<sub>2</sub><sup>eff</sup> fixed and the amplitudes fitted is then carried out. Equation 4.3.2.1 can be fitted to the amplitudes of each component as a function of T<sub>R</sub> to recover their separate T<sub>1</sub> values.

Figure 4.3.2.1 shows the fitted amplitudes of the resin and solvent in a AYAT solution of 4.5g of resin to 9.5ml of solvent. The  $T_1$  fits (equation 4.3.2.1) to these measured amplitudes are seen, in the figure, to be an approximate match to the shape of the data. However there were some distortions of the fitted amplitudes from the expected function. Table 4.3.2.1 shows the results for the AYAT and toluene solutions, where the accuracy of the technique was evaluated by comparing the measured amplitude ratio between the resin and solvent with the mass ratio (they should be proportional). This is in an identical manner as was done for the Hahn echo method, see section 4.2. It can be seen that the amplitude ratio shows very poor correlation with the mass ratio, suggesting that the error in the result must be extremely large. The multiple steps, and fits, used for this measurement has increases the amount of opportunities for errors to be introduced.

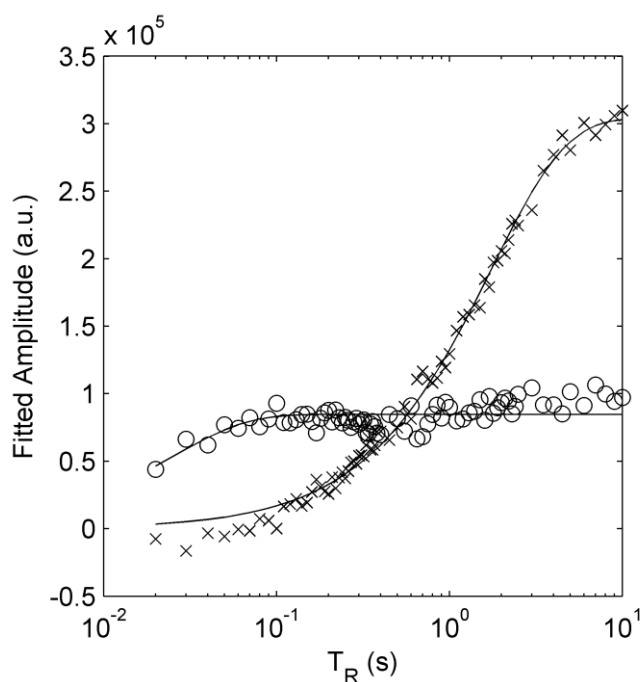


Figure 4.3.2.1  
Fitted NMR amplitudes of solvent (crosses) and resin (circles) against  $T_R$  times for an AYAT and toluene solution, of a 4.5g resin to 9.5ml solvent.

Concentration	$A_R/A_S$	$m_R/m_S$	$T_{1S}$	$T_{1R}$
1g resin to 13ml solvent	0.36	0.09	3.1	2.1
2g resin to 12ml solvent	0.26	0.19	3.0	0.14
4.5g resin to 9.5ml solvent	0.28	0.55	1.7	0.025
5g resin to 9ml solvent	0.46	0.64	1.9	0.084
0.4896 resin per total 1g	2.7	0.96	0.098	0.026
0.7173 resin per total 1g	-	2.5	0.085	-

Table 4.3.2.1  
NMR amplitude ratios, mass ratios and measured solvent and resin  $T_1$  times for AYAT and toluene solutions.

Due to the large errors, quantitative information cannot be retrieved from the  $T_1$  data of AYAT and toluene solutions (Table 4.3.2.1), though some qualitative trends in the data are apparent. As observed previously for the measured  $T_2$  times (section 4.3.1),  $T_{1R}$  is lower than  $T_{1S}$ , for all samples, and as concentration is increased the  $T_1$  times are reduced.

Table 4.3.2.2 shows the  $T_1$  results for Regalrez and toluene solutions, the correlation of the amplitude ratio with the mass ratio is seen to be better than the AYAT solutions. A least square regression analysis of the data gave  $k$  (amplitude ratio/mass ratio) to be equal to  $1.53 \pm 0.13$ , which matches the theoretical value (section 4.2.4)  $k = 1.47$ . Again the  $T_1$  time of the solvent is higher than that of the resin and decreases with concentration. However the resin  $T_1$  results for these solutions do not clearly show a decreasing trend. A potential reason for this lack of decrease is discussed in section 4.5.4.3.

Concentration	$A_R/A_S$	$m_R/m_S$	$T_{1S}$	$T_{1R}$
12g resin to 20ml solvent	1.1	0.69	0.74	0.19
20g resin to 20ml solvent	2.3	1.2	0.18	0.0087
9g resin to 5ml solvent	3.0	2.0	0.27	0.014
10g resin to 4ml solvent	4.3	2.9	0.12	0.022
0.8g resin per total 1g	-	4	0.051	-

Table 4.3.2.2  
NMR amplitude ratios, mass ratios and measured solvent and resin  $T_1$  times for Regalrez and toluene solutions.

#### 4.4 Molecular descriptions, of high and low molecular weight varnish solutions, from the NMR evidence

One of the purposes of using NMR on bulk samples of varnish solutions was to provide evidence about the processes that are happening at the molecular level. The NMR measurements were carried out on a low molecular weight resin (Regalrez) and a high molecular weight resin (AYAT), showing important differences and similarities in their behaviour. Figure 4.4.1 shows the molecular interpretation that can be made for the two solutions at three concentrations. For dilute solutions (Figure 4.4.1 (a)) the most important difference between the high and low molecular

weight resins is the diffusion values. The large molecular weight resin diffuses much slower, due to its molecular size restricting their ability to move past each other. This leads to the diffusion of the resin molecules being orders of magnitude lower than that of the solvent. The small low molecular weight resin molecules are much more able to diffuse past one another and its diffusion coefficient is of the same order of magnitude to that of the solvent. The  $T_2$  (and  $T_1$ ) values of the resin and solvent are both greater than 100ms at low concentrations, as is typical of a low viscosity liquid. As the concentration reaches 30 to 40% resin (Figure 4.4.1 (b)) the polymer molecules are unable to diffuse past each other at a measurable rate. The measurement of the diffusion of the resin within the Regalrez solution (figure 4.3.1.3.2) at this concentration seemed to be highly erroneous but the resin is still likely to be diffusing, given the contrast with the results of higher concentrations. The ability of the Regalrez molecules to diffuse at this concentration, in contrast to AYAT, is due to its smaller molecules reduced tendency to block each other. As the concentration increases the amount of resin-resin molecular interactions increases, which is shown by the decreasing  $T_2$  (and  $T_1$ ) values. The description of the mechanisms which cause these decreases are beyond the scope of this thesis. As the concentration increases further (figure 4.4.1 (c)) the diffusion of the low molecular weight resin also becomes negligible, though it will still be less entangled than the polymer resin. Resin-resin interactions start to dominate over resin-solvent interactions, as is shown by the decrease of  $T_2$  values of the resin. As the concentration increases further beyond practically mixable concentrations the diffusion of the solvent becomes negligible as it is constrained between the molecules of the resin. This interpretation is supported by the decrease in  $T_2$  (and  $T_1$ ) values of the solvent at these concentrations.

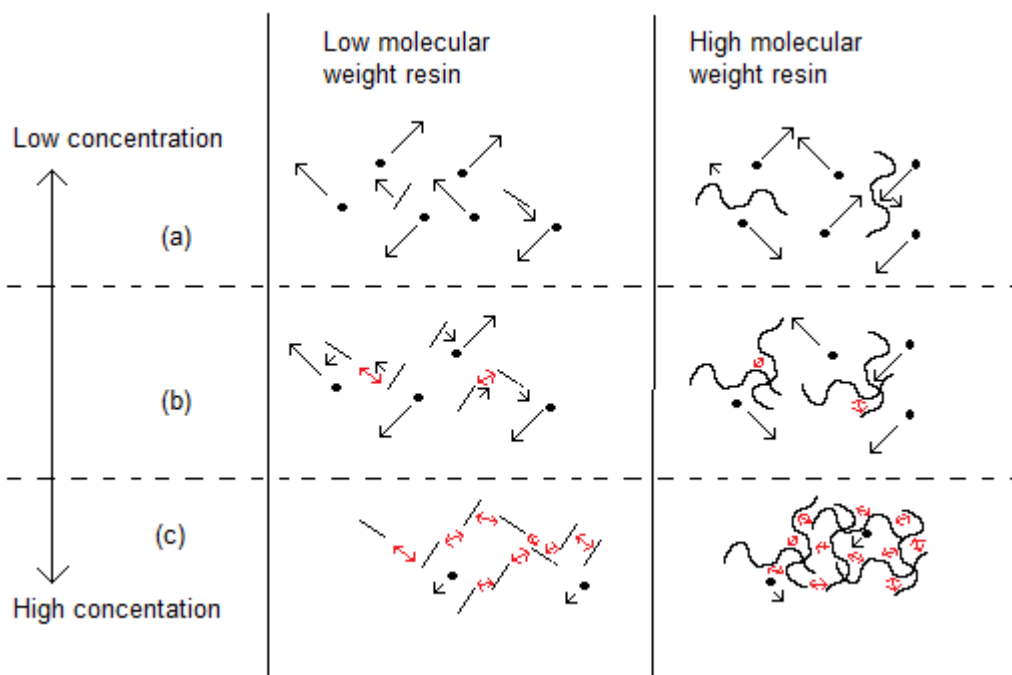


Figure 4.4.1  
 Diagram of the molecular behaviour of low and high molecular weight resin varnish solutions at three increasing concentrations (a)-(c). Rods and chains respectively represent short and long resin molecules, black dots represent solvent molecules. Black arrows represent the rate of travel (diffusion) and red double arrows represent resin-resin molecular interactions.

## 4.5 Welled drying

So far, within this chapter, the NMR properties of static (bulk) varnish solutions have been measured. It was desired to apply NMR Imaging (MRI) to dynamic (drying) varnish systems. The NMR MOUSE provides the unilateral imaging capabilities required. However, to enable physical interpretation of drying systems from MRI imaging only, first the results need to be analysed for a system that has been measured with other techniques. Here, measurements of the system is made with mass balance and OCT. Mass balance measurement provides the concentration and rate of evaporation of the system. OCT measurement provides the thickness and interface texture of the system.

With the NMR/MRI measurement, the more material (higher signal to noise) and slower the dynamics (greater the amount time to do measurements) of the measurement, the greater the amount of information that can be extracted. The

purpose of this section was to provide understanding of the NMR behaviour of varnish as it dried, and how this relates to physical processes within the varnish. The experiment was designed to achieve this. These drying experiments were carried out with much thicker amounts of varnish than is used in practice for coating paintings.

These thick film measurements provided an intermediate step between the bulk measurements, described so far in this chapter, and thin film measurements, described in section 4.6.

### 4.5.1 Method

Shallow wells were constructed from pieces of 1mm thick microscope slides. Figure 4.5.1.1 shows cross-sectional drawing of these wells and figure 4.5.1.2 is a photograph of one. The glass pieces were bonded and sealed with an epoxy glue (Araldite Rapid), which was checked to be resistant to the solvent effects of toluene. The size of all the wells was 2.5x2.5 cm. For the measurements 800 $\mu$ l of, 2g of resin to 12ml solvent, solution was pipetted into the well. This amount ensured that, after deposition, the varnish sample was distributed in the well in a repeatable manner. The resulting initial thickness of varnish solution in the well was approximately 1mm. The sample was then kept in unenclosed conditions during measurement, so that the solvent can evaporate and the sample dries. Three varnish solutions were used in this work: AYAT and Regalrez 1094 dissolved in toluene, and Regalrez 1094 dissolved in white spirit (Bartoline Premium Low Odour White Spirit, BS245).

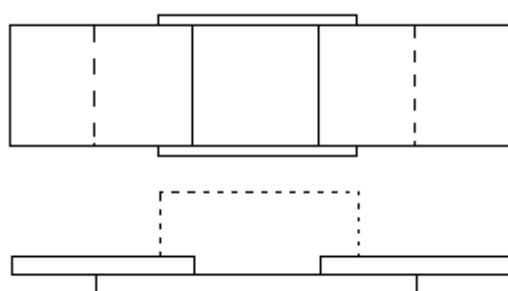


Figure 4.5.1.1  
Cross-sectional diagrams of  
constructed wells. (Top) From  
above.  
(Bottom) From side.



Figure 4.5.1.2  
Photograph of a constructed well.

After the deposition of the varnish solution into the well, the three different instruments were used to measure the samples. First the results from the reference measurements of the system, mass balance (section 4.5.2) and OCT (section 4.5.3) are given. The NMR MOUSE was used to image and measure the NMR signal,  $T_2$  and  $T_1$  times of the sample during the drying process (specific method details and results given in section 4.5.4).

#### 4.5.2 Mass balance results

The mass of the constructed well was measured before the deposition of the varnish solution. After the deposition, the total mass of the system was measured while the solvent evaporated. The empty mass was simply subtracted to give the total varnish mass. From the initial measured varnish mass and the initial concentration, the concentration of the solution throughout the measurement can be calculated. Figure 4.5.2.1 shows the mass results of the three solutions, two repeats for Regalrez and white spirit and Regalrez and toluene, and four repeats for AYAT and toluene. The difference in the drying of the three solutions is clearly visible. The greatest difference, between the solutions, is due to the volatility of white spirit ( $<1\text{kPa}^{26}$ ) and toluene ( $\sim 5\text{kPa}^{27}$ ), which results in the evaporation of the white spirit samples to be approximately ten times slower than for the toluene samples. The effect of the resin does have a small effect on the evaporation rate of the solvent, particularly at the knuckle between the fast and slow stages of drying. The AYAT samples have a much more rounded knuckle, which may be due to the high viscosity properties of this polymer solution restricting diffusion more than the Regalrez sample. This would lead to the AYAT samples being less axially homogenous than the Regalrez samples.

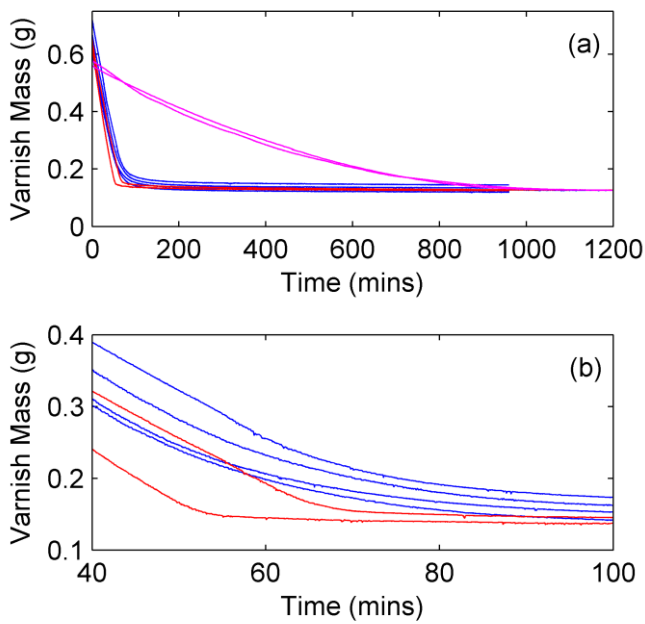


Figure 4.5.2.1

(a) Varnish masses as a function of drying time for independent measurements of AYAT and toluene (blue), Regalrez and Toluene (Red) and Regalrez and white spirit (Magenta) solutions.

(b) Expansion of the knuckles for the toluene solutions above.

Figure 4.5.2.2 (a) shows the mass concentration versus time calculated for the two toluene solutions. The difference in the knuckle behaviour is even more apparent for this plot. The fast (initial) and slow (later) stages of drying of varnish coatings is well known<sup>28</sup>. For these samples, the concentration boundary between the fast and slow drying stages is around 0.75 concentration for both resins. This is no more concentrated than the highest concentrated sample of Regalrez 1094 (0.81) where the Newtonian viscosity (section 2.1.2) was measured. Regalrez 1094 has a reputation of being slow drying (see chapter 1.4.2), which is not necessarily true. The reason, that Regalrez 1094 coatings remains tacky, is that it still is a fluid at the concentration it enters the slow drying stage. This explanation is physical rather than due to any chemical affinity.

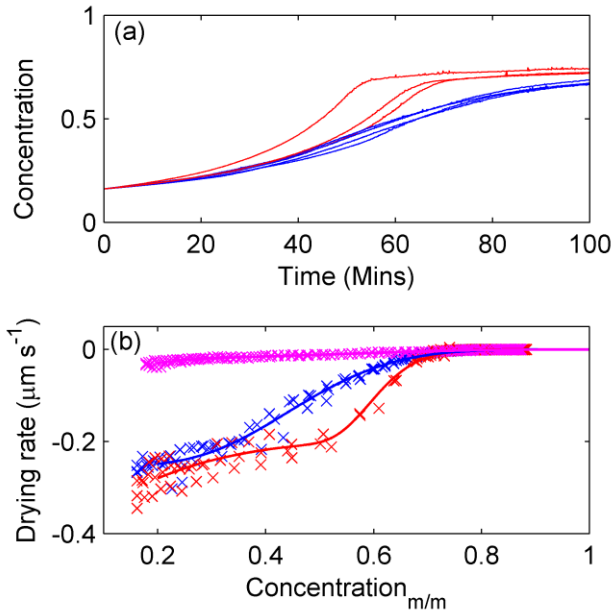


Figure 4.5.2.2

(a) Time course of the measured concentration (fraction of varnish mass that is resin) for Regalrez (Red) and AYAT (Blue) dissolved in toluene for the welled drying samples.

(b) Measured drying rate (calculated as an absolute rate of change in thickness assuming an ideal solution) as a function of concentration for the two solutions above plus Regalrez and white spirit (magenta).

The rate of evaporation, as a function of concentration, is needed for the modelling of drying films (chapter 6). This can be measured from the differential of mass data and converted to a rate of change of thickness from the well area and the density of the solvent. Figure 2.6.2.2 (b) shows the results for the three solutions. In order to obtain a noise free function that can be used for modelling, an empirical relationship was fitted. This was given by

$$R = K_1 + K_4 - K_1 \exp\left[-\left|K_2(1-C)^{K_3}\right|\right] - K_4 \exp\left[-\left|K_5(1-C)^{K_6}\right|\right], \quad (4.5.2.1)$$

where  $R$  is the evaporation rate,  $K_i$  are the fitted parameters and  $C$  is concentration. These functions are seen to provide a visually satisfactory fit in figure 2.6.2.2 (b).

### 4.5.3 OCT

Optical Coherence Tomography measurements were taken during the drying. This allowed the multi-interface profilometry technique to be applied, allowing the measurement of the thickness and surface roughness of the varnish samples as they dried. The OCT measurement consisted of 1000 lateral points over a 10mm range. Early in the drying, the optical thickness of the samples was greater than the axial range of the FD OCT used. This meant that the thickness could not be measured, by the method, for early times. All the samples surfaces developed low frequency roughness during the drying, the Regalrez roughness lateral dimensions were lower

than AYAT and confined by the container. The dominating factor for these samples was likely to be surface tension interactions with the container, evidence of this is presented below. The slightly higher frequency developed by the AYAT sample was reminiscent of the low frequency roughness developed by the Regalrez samples in chapter 6. The increased thickness of the sample is likely to be the reason that flow cells can develop to a magnitude, in the welled AYAT drying, that they did not in the thin applicator spread AYAT samples in chapter 6.

Figure 4.5.3.1 shows the measured thickness and roughness results for a AYAT and toluene sample. The rapid reduction of thickness in the fast drying stage is clearly shown, while the surface roughness during this period remains relatively low. At the transition from the fast to slow drying stages, the roughness rapidly increases to its maximum value. The reason for the development of this roughness to happen at this point is unknown, and it does not match the development of the (suspected) flow cell roughness within applicator spread film in chapter 6. One possible reason for the development of the roughness, at this point, is that the distribution of the resin is already inhomogeneous in the fast drying stage, where flow cells may occur, but as the solvent is still free at this point it is redistributed (with only small concentration gradients at these low concentrations) to minimise total surface energy. At the transition the solvent is no longer able to be redistributed as it evaporates, forming the texture determined by the distribution of resin. To confirm this hypothesis requires further experimental work. However this behaviour does not appear to be of direct relevance to the scope of this thesis, so this has not been pursued. After the transition the surface roughness relaxes for a period until a quasi-steady state is reached. This result is indicative that the AYAT solution, though of high viscosity, at this point is undergoing levelling. However note if the concentration is laterally homogenous, at this point, shrinkage by the solvent evaporation will also act to reduce the roughness.

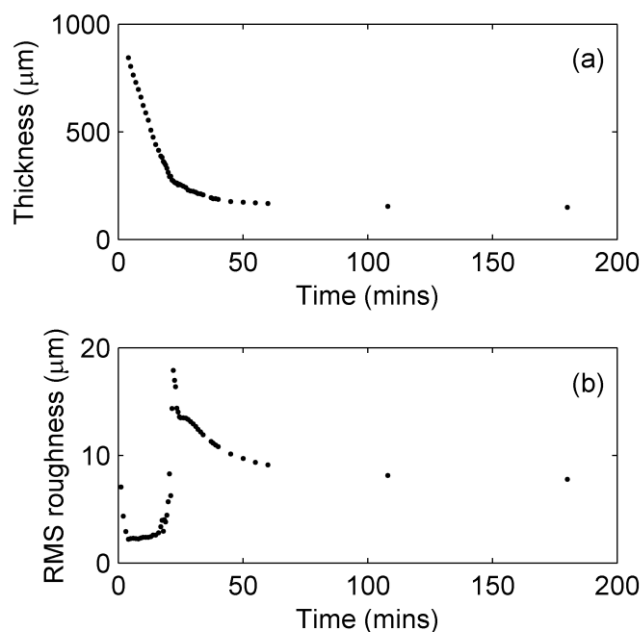


Figure 4.5.3.1  
 (a) OCT measured thickness in centre of welled drying AYAT and toluene sample.  
 (b) OCT measured *rms* roughness from the 10mm surface profile.

Figure 4.5.3.2 shows the OCT thickness and roughness results, along with simultaneous measured mass, for a Regalrez and toluene sample. The simultaneous mass measurements were achieved by setting up the OCT probe above a mass balance on which the sample was placed. There are important differences in the behaviour of this Regalrez measurement compared to the AYAT measurement. Some repeats of the Regalrez samples showed similar roughness development as the AYAT samples, for the repeat shown however the measured roughness can be seen to be developing steadily throughout the fast drying period. The repeats were done at different times and there may have been slight differences in their conditions. The most important difference between all the Regalrez samples, compared to the AYAT samples, was that after the transition the measured thickness in the middle of the well increased. This is also clear in the NMR results in the section below. The apparent mechanism that is causing this is sketched in Figure 4.5.3.3. As the solution becomes thinner in dimensions as it dries the interface energy wants to be minimised, at a certain point this pulls the varnish solution away from the walls of the well and into the centre. This point is after the transition and means at this stage the viscosity of the Regalrez solution is low enough for this to occur. For the AYAT solution, the higher viscosity makes this mechanism impossible to occur.

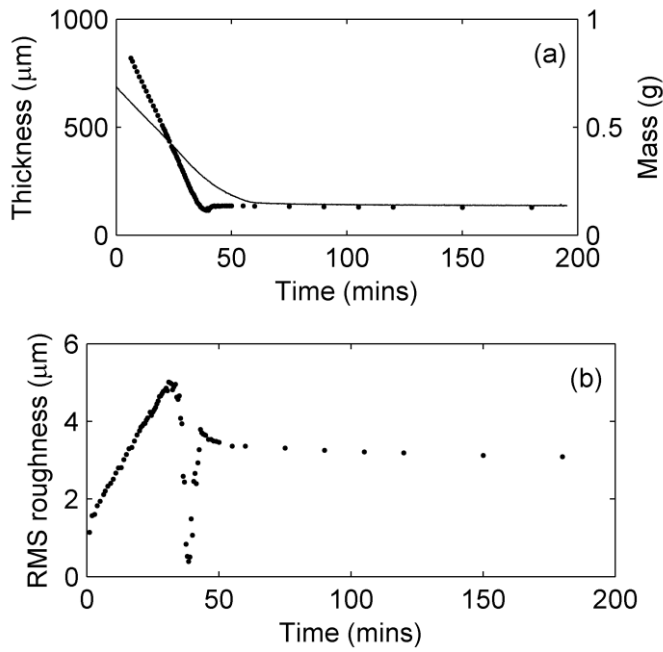


Figure 4.5.3.2  
 (a) OCT measured thickness in centre of welled drying Regalrez and toluene sample (points) with the simultaneously measured sample mass (line).  
 (b) OCT measured *rms* roughness from the 10mm surface profile.

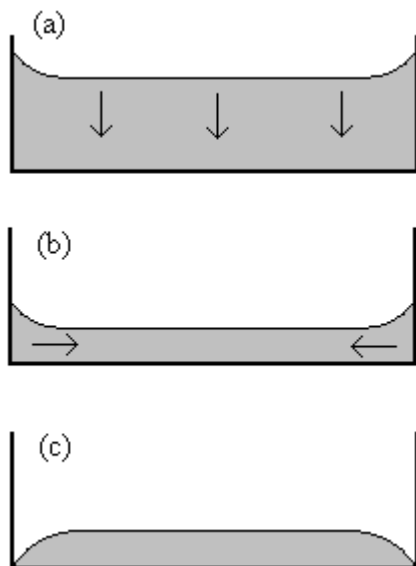


Figure 4.5.3.3  
 Sketch of interpreted behaviour of the Regalrez welled drying samples.  
 (a) Initial evaporation thins sample.  
 (b) At a certain point surface tension draws material away from the walls of the container.  
 (c) Final distribution of dry varnish observed.

Figure 4.5.3.4 shows the combined OCT and mass balance results for Regalrez and white spirit solution. The result features are identical to the toluene solution but the time axis is expanded due to the low evaporation rate of white spirit.

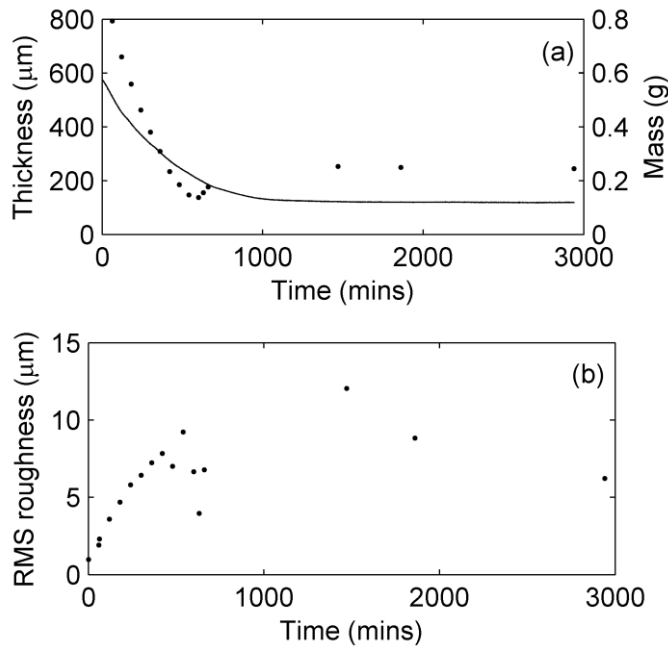


Figure 4.5.3.4  
 (a) OCT measured thickness in centre of welled drying Regalrez and white spirit sample (points) with the simultaneously measured sample mass (line).  
 (b) OCT measured *rms* roughness from the 10mm surface profile.

#### 4.5.4 NMR Imaging (MRI)

##### 4.5.4.1 Mean amplitude (intensity) images

To provide normalised (axial sensitivity) 1D images through the centre of the drying well, three separate measurements were taken with identical setups. Firstly with no sample placed upon the NMR MOUSE the thermal noise floor was measured and secondly the sample bottle, of the used solution, was used to measure the sensitivity profile of the instrument. For both these samples, averaging of multiple measurements was used to increase the signal to noise. Thirdly the welled samples were measured as they dried. The NMR parameters used for the measurements were 32 spin echoes in the echo train (to increase signal to noise by enabling averaging of echoes where there is significant signal left throughout the drying process), with a  $T_E$  time of  $140\mu\text{s}$  (short  $T_E$  to increase spin echoes captured within signal decay without pushing instrumental limits), a  $T_R$  time of 200ms (sufficient relaxation time to recover signal at all stages of drying) and 1200 repeats per measurement to give a four minute sampling time. Each echo was Fourier transformed to resolve the signal spatially and for each position the intensity was averaged over all the echoes to increase signal to noise. The thermal noise floor measurement was then subtracted from both the bottle and sample measurements. As previously stated the sensitivity of the instrument is not of top hat shape across the sensitive volume. In order to

produce a normalised profile the sample results is then divided by the homogenous bottle result (which is a measure of the sensitivity profile). As the drying of the sample became slower, box car averaging was used to improve signal to noise further for the later measurements.

Figure 4.5.4.1.1 shows the result for a drying AYAT and toluene sample, where several features of the drying process are identified by this method. The thinning of the sample is seen during the first 60 minutes, which is the fast stage of solvent evaporation. Initially the intensity of the NMR signal increases, which is due to the decrease in  $T_1$  times of the solution and these  $T_1$  times not being negligibly small compared with the  $T_R$  time of the measurement. From section 4.3.2 it is known that as the concentration of the varnish samples increases, the  $T_1$  times of the solvent and resin decrease. The initial values of  $T_1$  are of the order of 1s. The  $T_R$  time of the measurement was 0.2s, which means that, in the early stages of the measurement, the magnetisation of the nuclear spins cannot fully relax, before the  $90^\circ$  initialisation pulses, leading to loss of signal. As the  $T_1$  times of the solution decrease with increasing concentration, there is less loss of signal due to insufficient relaxation and there is a relative increase in signal. Further evidence of this effect is shown later in this section. At around 40 minutes a maximum in signal intensity is seen before it starts reducing. There are two possible independent causes of a loss of signal: loss of  $H^1$  nuclei (amplitude) or decrease of  $T_2^{\text{eff}}$ . The volume density of hydrogen nuclei within the dry resin is similar to the volume density of hydrogen nuclei in the solution, as the mass fraction of hydrogen in the solvent and resin is similar and there will only be small differences in density of the materials. Decrease in volume density of hydrogen nuclei cannot be the reason for this magnitude of loss in intensity. The length of the echo train from which the signal is averaged is 4.5ms, and if the  $T_2^{\text{eff}}$  value is much greater than this there is little impact on the integrated signal. However as the  $T_2^{\text{eff}}$  values are reduced, as the concentration increases, the echo train will be tapered, thereby reducing the signal. From section 4.3.1, it is known that the  $T_2$  times of the solvent and resin becomes significantly short as the concentration of the varnish solution becomes high. The tapering of the signal, by this decrease in the  $T_2$  times, was the likely reason for the decay in the signal. The measured  $T_2$  times from this measurement are presented further below. At high concentrations the intensity of the signal continues to reduce, as the solvent

evaporates during the slow drying stage. The final feature of the graph is a distortion of the relative position of the selected slice to the sample around 2500mins, but this is most likely an instrumental effect due to temperature variations<sup>19</sup>.

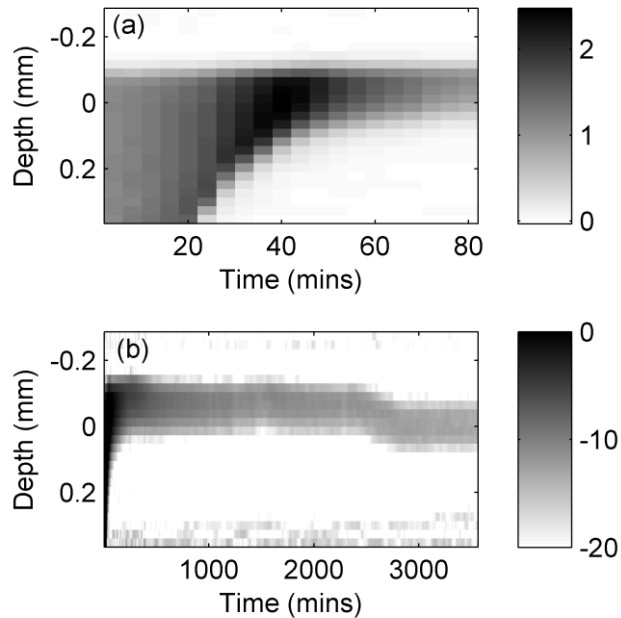


Figure 4.5.4.1.1  
 (a) NMR linear intensity image of welled drying AYAT and toluene solution over first 80 minutes.  $T_R = 200\text{ms}$ .  
 (b) dB image over longer drying period.

Figure 4.5.4.1.2 shows the same results for a Regalrez and toluene solution. The majority of the features, of this result, match those for AYAT. However there is one additional point to the Regalrez results, the bulging of the solution identified in the OCT results (section 4.5.3) at around 50 minutes measurement time. Figure 4.5.4.1.3 shows the results for the Regalrez and white spirit solution where, in spite of slower drying, it still goes through the same stages as the toluene solutions.

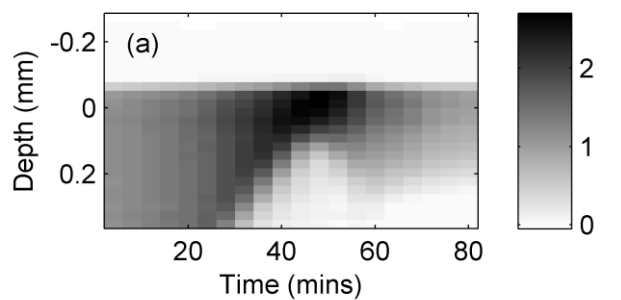


Figure 4.5.4.1.2  
 (a) NMR linear intensity image of welled drying Regalrez and toluene solution over first 80 minutes.  $T_R = 200\text{ms}$ .  
 (b) dB image over longed drying period.

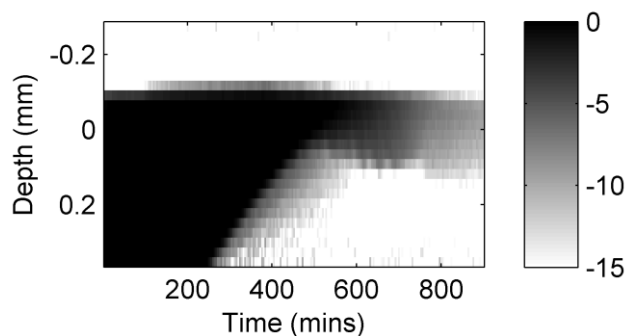
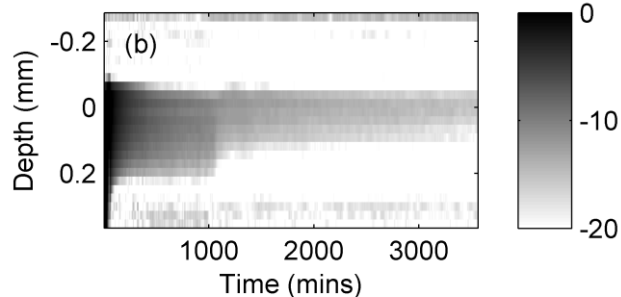


Figure 4.5.4.1.3  
 NMR dB intensity image of welled drying Regalrez and white spirit solution.  $T_R = 2000\text{ms}$ .

To confirm the dependence of the NMR signal intensity, in the early stages of drying, on the  $T_R$   $T_1$  relationships of the solution, the method was repeated with a  $T_R$  time of 2s (10 times greater than the original value). This will reduce the initial reduction of signal due to incomplete relaxation of the magnetisations (by long  $T_1$  times). Figure 4.5.4.1.4 shows the results for AYAT and Regalrez in toluene. As expected the relative reduction in the signal intensity for the early stages is reduced, while the rest of the features of the measurements remains the same.

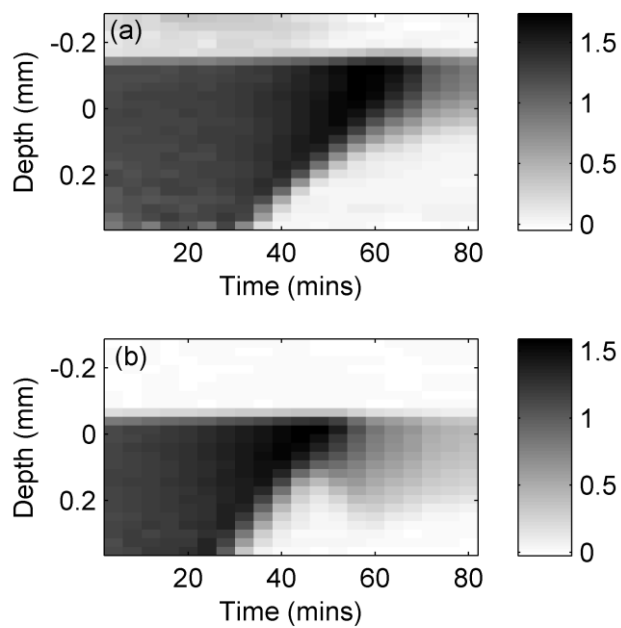


Figure 4.5.4.1.4  
 (a) NMR linear intensity image of welled drying AYAT and toluene solution over first 80 minutes.  $T_R = 2000\text{ms}$ .  
 (b) NMR linear intensity image of welled drying Regalrez and toluene solution over first 80 minutes.  $T_R = 2000\text{ms}$ .

#### 4.5.4.2 Net $T_2$ images

It is proposed that the main mechanism, for the decrease in signal from a drying layer, is the decrease in the  $T_2$  values with increased concentration that was shown in section 4.3.1. To confirm the decrease in  $T_2$  times in the samples, their values were measured from the NMR mean amplitude (intensity) image data with  $T_R$  of 2s. For the intensity imaging, the amplitudes (from each axial position) of all the echoes had been averaged. However to produce a  $T_2$  image, a net  $T_2^{\text{eff}}$  decay was fitted to the echoes (third echo onwards) for each position instead. The signal to noise of this data was not sufficient for the fitting of the two  $T_2^{\text{eff}}$  decays to produce meaningful results. Figure 4.5.4.2.1 shows the results for the AYAT and Regalrez samples dissolved in toluene. The continued decrease in the  $T_2$  value throughout the measurements is clearly shown. The length of the echo train is static (4.5ms) throughout the measurement, meaning that it is only optimised for  $T_2^{\text{eff}}$  times of slightly lower value than this. The early  $T_2^{\text{eff}}$  measurements are of the order of 50ms, which is in reasonable agreement of the expected low concentration  $T_2^{\text{eff}}$  values from sections 4.3.1.2 and 4.3.1.3. After 15 hours of drying the measured net  $T_2^{\text{eff}}$  are of the order of 0.5ms, which is ten times shorter than the echo train. This decrease in the net  $T_2^{\text{eff}}$  values corresponds well with the decrease in the intensity image signal.

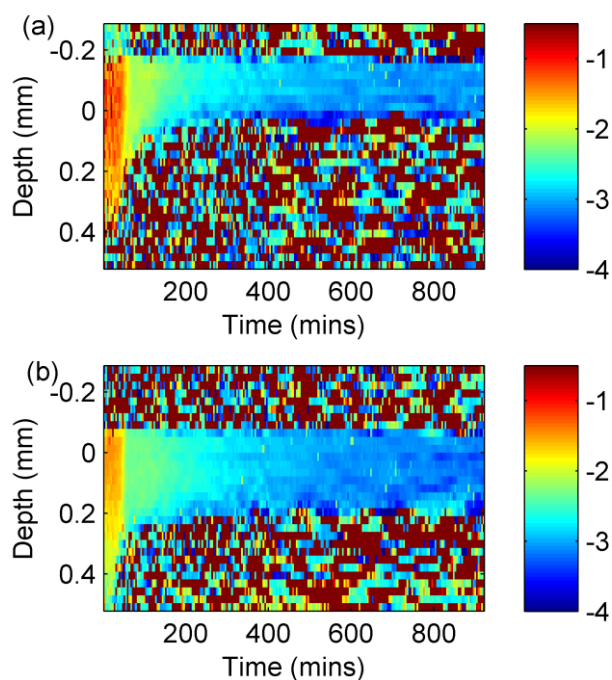


Figure 4.5.4.2.1  
 (a) Image scale of  $\log_{10}(T_2^{\text{eff}})$  for welled drying AYAT and toluene sample,  $T_R=2\text{s}$ . Initial red area  $T_2^{\text{eff}}$  approximately 50ms, final dark blue corresponds to approximately 0.5ms.  
 (b) As (a) for Regalrez and toluene sample.

#### 4.5.4.3 Net $T_1$ imaging and measurement

To produce  $T_1$  equivalent images, to the  $T_2^{\text{eff}}$  images in the section above, additional measurements of the welled drying samples were undertaken with a different NMR method. Like for the bulk solutions, a saturation recovery sequence was used to measure  $T_1$  times. During the measurement the “total” net  $T_1$  time was calculated automatically after each measurement and the  $T_R$  times set appropriately for the next measurement. As the net  $T_1$  time of the sample changes, hence the time taken to do a single measurement also changes. Like the mean intensity and  $T_2$  images, the  $T_1$  values were measured at each axial position to produce the axial and temporal resolved images. Figure 4.5.4.3.1 shows a result for an AYAT and toluene solution. The long  $T_1$  time of the dilute solution lasts until 50 minutes into the measurement, which is when the transition from fast to slow drying stages occurs. After passing this transition, which sees a rapid change in the measured net  $T_1$  value, the measured net  $T_1$  plateaus at a relatively short  $T_1$  time of 100ms.

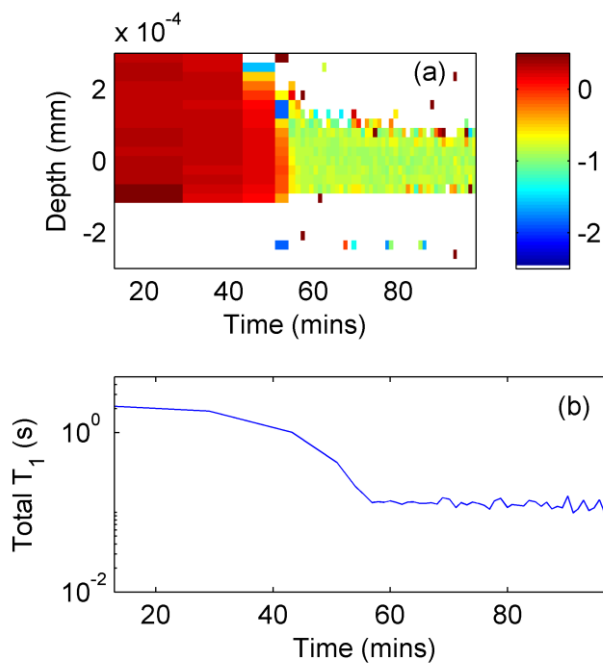


Figure 4.5.4.3.1  
 (a) Net  $\log_{10}(T_1)$  image for welled drying AYAT and toluene sample.  
 (b) Measured “total”  $T_1$  from all signal.

Figure 4.5.4.3.2 shows the result for a Regalrez and toluene solution. The behaviour of the  $T_1$  values is much the same as the AYAT solution. The transition, from fast (long  $T_1$ ) to slower (short  $T_1$ ) drying rates, again evident at 50 minutes drying. However at this point the measured net  $T_1$  times reduce to lower values ( $\sim 20$ ms) than for the AYAT sample. After this minimum, the measured net  $T_1$  times increase moderately. There are two possible reasons for this increase, firstly the single net  $T_1$  fitting to the data containing multiple  $T_1$  times may introduce artefacts in the fit as the relative properties of each source (resin and solvent) change. As the concentration increases, the  $T_2$  time of the resin is known to decrease (section 4.3.1) until the signal from the resin becomes undetectable by the instrument. Although the  $T_2$  time of the solvent also decreases, it remains long enough still to be detected after the resin cannot. As the signal from the resin becomes insignificant the fit of the net  $T_1$  should tend to the  $T_1$  time of the solvent which is likely to be higher than its net place between the solvent and resin. The second possibility is that the increase in  $T_1$  is a general increase in the  $T_1$  time of one of the components. BPP<sup>29</sup> theory predicts that as viscosity of a material increases the  $T_1$  and  $T_2$  times of the solution decrease until a certain value. This decrease in these values is apparent throughout this chapter. After a certain value of viscosity is reached,  $T_1$  values are predicted to start increasing again while  $T_2$  remains decreasing. Although in section 4.3.2 it was concluded that the general trend of the  $T_1$  values was that they decreased with concentration, re-examination of the measured resin  $T_1$  values for

the Regalrez resin in table 4.3.2.2 indicates that there may be an increase with concentration for the more concentrated samples. However the errors found in section 2.4.2 for that method with the AYAT samples mean that the Regalrez results are not reliable without independent verification. As a result, the cause of the increase in the measured  $T_1$  values cannot be determined. Also to be noted is that BPP theory is only strictly applicable to the most simple fluids. The drying varnish solution maybe too complex for the theory to hold.

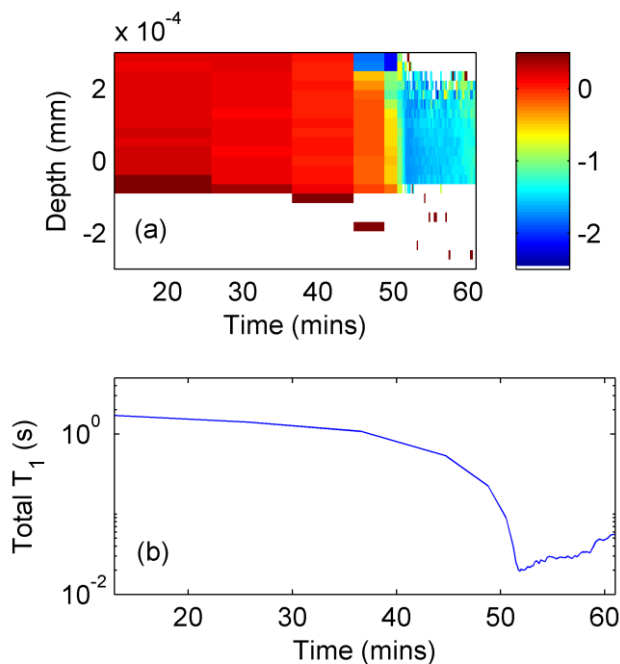


Figure 4.5.4.3.2  
 (a) Net  $\log_{10}(T_1)$  image for welled drying Regalrez and toluene sample.  
 (b) Measured “total”  $T_1$  from all signal.

In addition, to prove that the increase in the measured net  $T_1$  time was not dependent on the welled drying setup, the method was repeated on the Regalrez and toluene sample bottles. Figure 4.5.4.3.3 shows the results of these measurements. The initial decrease in the net  $T_1$  time, with concentration increase, is apparent. For the highest two concentrated sample the net  $T_1$  time did increase with concentration. These two measurement were repeated, the difference between the repeats were negligible compared to the difference between the two concentrations. This result confirms that indeed this method is measuring an increase in the “net”  $T_1$  time with concentration for high concentration Regalrez and toluene solutions, but did not provide any additional information to distinguish the cause.

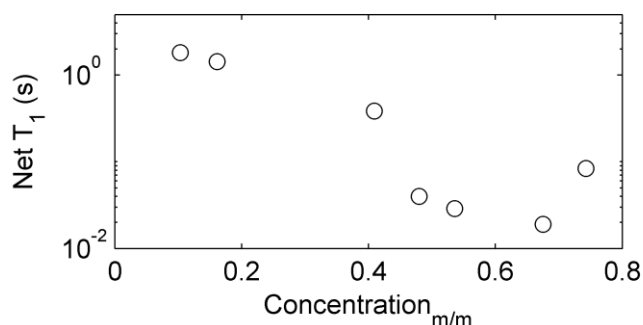


Figure 4.5.4.3.3  
Measure net T<sub>1</sub> times of Regalrez and toluene solutions as a function of concentration.

### 4.5.5 Welled drying discussion

One of the purposes of this section was to provide an intermediate step between bulk property measurement and drying film of varnish. The results confirmed the NMR properties, measured for bulk varnish solutions, are identical within a drying environment. The work also provided information regarding what the behaviour of the varnish coatings (of realistic thicknesses) was likely to be, this enabled better designed experiments. The mass balance results confirmed that the varnish systems do indeed have two distinct stages of drying, that has previously been reported<sup>28</sup>. The transition between these stages is fairly abrupt and occurs around 75% concentration. The low viscosity, of the low molecular weight resin Regalrez, allows solutions of it to behave as a fluid at this point. This was seen with the redistribution of the Regalrez samples after this point. This effect does not occur for AYAT varnishes, indicating that the high molecular weight AYAT varnish is far too viscous to behave as a fluid at this point. For MRI imaging (with relatively low T<sub>R</sub> times) of drying solvent varnishes, the available signal is initially increased by the fall in the T<sub>1</sub> values within the sample with increased concentration. The available NMR signal then falls to a tiny fraction, of the initial amount, as decreasing T<sub>2</sub> times reduces the amplitude of the echo train. An increase in net T<sub>1</sub> time for high concentration Regalrez samples is identified. The mechanism for this has not been determined but maybe due in part to the increase predicted by BPP theory, for the resin.

### 4.6 Measurement of drying varnish coatings with NMR/MRI

The reduced amount of material and rapid drying of a realistic film of varnish, compared to the welled samples of section 4.5, makes their measurement much

more challenging. The shorter time scale sampling, needed to record the faster dynamics, and the reduction of the amount of material means that less information can be extracted than for the welled samples. The information from the welled samples and bulk measurements, however, can be used to complete the interpretation of simple intensity imaging.

A film of varnish was applied onto a smooth 2mm A4 glass plate with the use of a bird-type applicator (see chapter 6.3.2). The drying film was then imaged using the NMR MOUSE, with a  $T_E$  time of 100 $\mu$ s (the lower limit for this instrument), 128 echoes (capture significant length of echo train at start of measurement, not all echoes maybe needed for maximum signal to noise at a measurement time),  $T_R$  of 300ms (sufficient relaxation time to recover signal at all stages of drying) and 1000 repeats per measurement giving an experiment time of 5 minutes. The three solutions used were: (i) Regalrez and toluene, (ii) Reglarez and white spirit, both with a concentration of 7g resin to 7ml of solvent and 100 $\mu$ m applicator gap, and (iii) AYAT and toluene, with a concentration 3g resin to 11ml solvent and 225 $\mu$ m applicator gap.

For the total signal, the net  $T_2$  time was fitted (3<sup>rd</sup> echo onwards) for each measurement. Figure 4.6.1 shows the results over the first 250 minutes for the three solutions. The net  $T_2$  time decreases throughout the measurement, dropping below 1ms for within 20 minutes for the toluene samples and 50 minutes for the white spirit sample. Following this decreases of the  $T_2$  times, the  $T_2$  values are too short to be reliably measured (the spread of the measured  $T_2$  values is greater than their mean amplitude). Again the white spirit varnish results can be seen to be undergoing the same behaviour but at a slower rate.

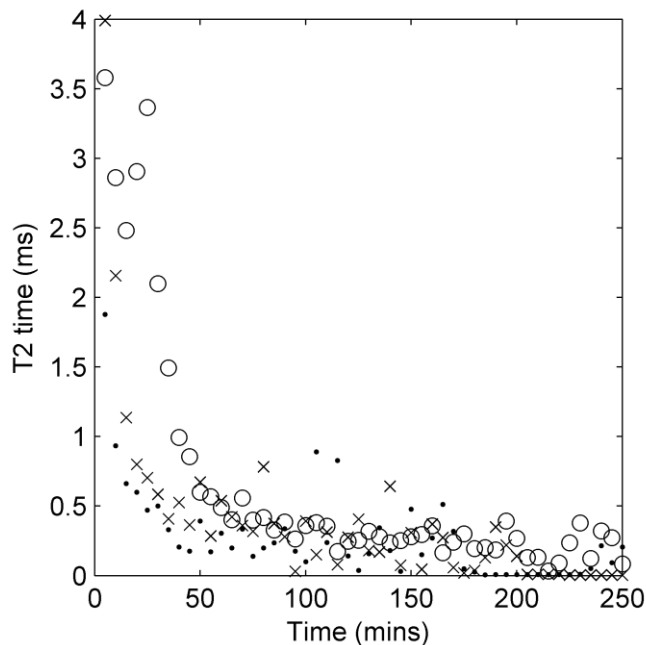


Figure 4.6.1  
 $T_2$  measured from total signal of applicator applied films of AYAT and toluene (crosses), Regalrez and toluene (dots) and Regalrez and white spirit (circles).

The production of the unilateral NMR images was carried out taking the mean amplitude of the first 3 echoes in the train (to maximise signal to noise) at the resolved position. Figure 4.6.2 shows the three images for the solutions. The signal to noise of the toluene varnishes rapidly becomes too small to be confident in the identification of signal from the coating in the image. The signal from the Regalrez and white spirit solution remains above the background noise until after 600minutes of drying. Though the NMR imaging and relaxation of the two toluene samples indicate that their behaviour at the molecular level is similar, the mechanical properties of the film were check by touching periodical. The AYAT films were dry within 20 minutes of the start of the experiments, while after 120 minutes the Regalrez and toluene samples still exhibited slight tack. This reinforces that it is a physical process that leaves Regalrez coatings tacky for longer, compared to other coatings, with the solvent being no slower to evaporate from the sample. Complete physical dryness of the Regalrez and toluene films appeared to occur after two days of drying.

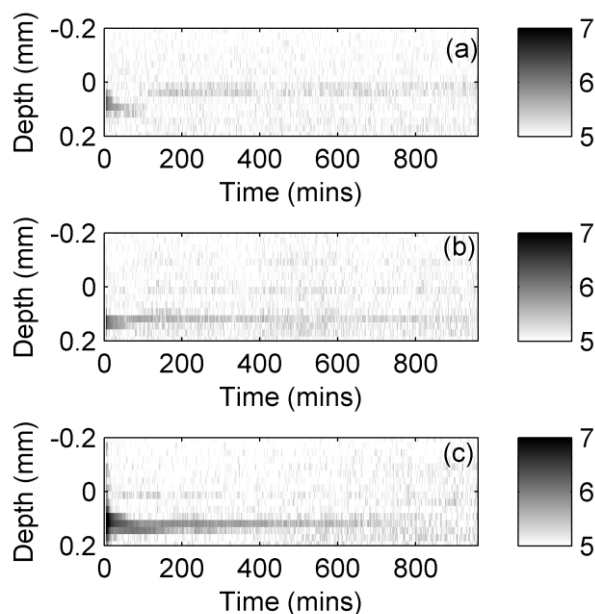


Figure 4.6.2  
Unilateral  $\log_{10}$ ( NMR  
intensity (non-  
normalised)) image of  
applicator applied drying  
films of  
(a) Regalrez and toluene  
(b) AYAT and toluene  
(c) Regalrez and white  
spirit.

One of the objectives of this work was to evaluate whether unilateral MRI could be used for the non-invasive measurement of the wetness of drying varnish coatings on real paintings. The rapid decrease of the material  $T_2$  times, as the material tends towards a solid state, means that the instrument used had insufficient signal to noise if the coatings are not obviously wet. However with the use of an NMR system where the  $T_E$  time can be lowered substantially further, such as in a previous study (with  $T_E=34\mu\text{s}$ ) measuring dry oil paints<sup>30</sup>, increasing the solid state ability, it may be possible to quantify the amount of solvent left within an apparently dry coating.

## 4.7 Conclusion

Nuclear Magnetic Resonance (NMR) relaxometry provided information on the processes happening at the molecular levels of the varnish solution. This included the measurement of the resin and solvent self-diffusion coefficients. This showed the difference between the behaviour of a low molecular weight resin and a polymer resin molecules within solutions. This highlighted the extent to which the physical parameters (*i.e.* size) of the resin molecule influence their behaviour within a solution. The diffusion coefficient of the polymer resin was orders of magnitude slower than that of the low molecular weight resin. The diffusion coefficient values of the low molecular weight resin were similar to that of the solvent. The increased molecular size of polymer resins highly inhibits their molecules mobility. This

results in highly viscous solutions (see chapter 5) with poor levelling capabilities (see chapter 6). For both solutions, the  $T_2$  relaxation times of the solvent and resins were measured to decrease as concentration increases. This correspond to the molecular interactions of the solution tending towards solid state behaviour. In the majority of cases, this decreasing trend with concentration was also observed for  $T_1$  measurements. Despite the physical (molecular size and dry to the touch properties) and diffusion differences between the AYAT and Regalrez solutions, there were only small differences in their  $T_1$  and  $T_2$  behaviour. At any concentration, the local conditions experienced by the nuclear spins is largely independent of the macroscopic properties of the solution. This highlights that there are no significant differences in molecular interactions between the solutions, but differences in macroscopic properties are due to the physical (geometric) effects of larger resin molecules.

The small amount of solution per unit area and rapid dynamics, of film drying experiments, limited the amount and quality of direct data that could be taken. To provide an interim drying system, that allowed a large amount of informative data to be captured from a dynamic drying system, a welled setup was used. Mass measurement provided accurate values of the evaporation of solvent with time, and the OCT measurements showed the corresponding change in thickness and development of roughness at the centre. These two methods showed the dynamics of the systems. Particularly significant was the fact that the transition between fast and slow drying rates was independent of viscosity, as demonstrated by the Regalrez samples exhibiting fluid behaviour after the transition. The NMR results from the system showed good agreement with the measurements of the static (bulk) solutions. The effects of  $T_1$  and  $T_2$  times, on the signal of the MRI images, were clearly shown.

The NMR MOUSE instrument was shown to be able to image applied varnish films, of realistic thicknesses, through the early stages of drying. As the amount of solvent is reduced, during the slow drying stage, the  $T_2$  times within the varnish material decrease towards typical solid state values. The reduction of the  $T_2$  values, to much lower than the shortest  $T_E$  possible with the instrument used, lead to the resulting signal to noise to rapidly become negligible for significantly dry coatings. However, the use of a NMR/MRI instrument tailored for solid state systems may provide a

method of accurately measuring the solvent content, non-invasively, of higher concentration coatings.

## 4.8 References

---

- <sup>1</sup> Abragam A., Principles of Nuclear Magnetism, Oxford University Press (1961).
- <sup>2</sup> Bloembergen N., Purcell E. M. and Pound R. V., “Relaxation Effects in Nuclear Magnetic Resonance Absorption”, Physical Review, 73 (7), pp. 679-712 (1948).
- <sup>3</sup> Carr H. Y. and Purcell E. M., “Effects of Diffusion on Free Precession in Nuclear Magnetic Resonance Experiments”, Physical Review, 94 (3), pp. 630-638 (1954).
- <sup>4</sup> Von Meerwall Ernst D., “Self-Diffusion in Polymer Systems, Measured with Field-Gradient Spin Echo NMR Methods”, Advances in Polymer Science, 54, pp. 3-29 (1983).
- <sup>5</sup> Grythe Kai F., Hansen Finn K. and Walderhaug Harald, “NMR Self-Diffusion and Viscosity of Polyurethane Formulations for Rocket Propellants”, J. Phys. Chem. B, 108, pp. 12404-12412 (2004).
- <sup>6</sup> Blumich b., Perlo J. and Casanova F., “Mobile single-sided NMR”, Progress in Nuclear Magnetic Resonance Spectroscopy, 52, pp. 197-269 (2008).
- <sup>7</sup> Errede L. A. and Newmark Richard A., “Polymer Drying. VII. <sup>1</sup>H-NMR Studies of Evaporation from Liquid Saturated Poly(Styrene-co-Divinylbenzene)”, Journal of Polymer Science: Part A, 30, pp. 1155-1161 (1992).
- <sup>8</sup> McDonald Peter J. and Keddie Joseph L., “Watching paint dry: Magnetic resonance imaging of soft condensed matter”, Europhysics News, 33, pp. 48-51 (2008).
- <sup>9</sup> Presciutti Fedrica, Perlo Juan, Casanova Federico, Glogglar Stefan, Miliani Costanza, Blumich Bernhard, Brunetti Brunetto Giovanni and Sgamellotti Antonio, “Noninvasive nuclear magnetic resonance profiling of paint layers”, Applied Physics Letters, 93, 033505 (2008).
- <sup>10</sup> Cook Norman, Models of the Atomic Nucleus, Springer Verlag (2006).
- <sup>11</sup> Liang Zhi-Pei and Lauterbur Paul C., Principles of Magnetic Resonance Imaging A signal Processing Perspective, IEEE (2000).
- <sup>12</sup> Carr H. Y. and Purcell E. M., “Effects of Diffusion on Free Precession in Nuclear Magnetic Resonance Experiments”, Phys. Rev., 94 (3), pp. 630-638 (1954).
- <sup>13</sup> Meiboom S. and Gill D., “Modified Spin - Echo Method for Measuring Nuclear Relaxation Times”, Review of Scientific Instruments, 29 (8), pp. 688-691 (1958).

- 
- <sup>14</sup> McRobbie Donald W., Moore Elibeth A., Graves Martin J. and Prince Martin R., *MRI From Picture to Proton*, Cambridge University Press (2003).
- <sup>15</sup> Hürlimann M. D., “Diffusion and Relaxation Effects in General Stray Field NMR Experiments”, *Journal of Magnetic Resonance*, 148, pp. 367-378 (2001).
- <sup>16</sup> Song Y. -Q., “Categories of Coherence Pathways for the CPMG Sequence”, *Journal of Magnetic Resonance*, 157, pp. 82-91 (2002).
- <sup>17</sup> Hahn E. L., “Spin Echoes”, *Phys. Rev.* 80 (4), pp. 580-594 (1950).
- <sup>18</sup> Blümich B., Blümmler P., Eidmann G., Guthausen A., Haken R., Schmitz U., Saito K. and Zimmer G., “The NMR-mouse: construction, excitation, and applications”, *Magnetic Resonance Imaging*, 16 (5-6), pp. 479-484 (1998).
- <sup>19</sup> Adriaensen Hans, *Dynamic spatially resolved unilateral NMR measurements of liquid ingress and vapour adsorption and desorption in heterogeneous layered fabrics*, PhD Thesis, Nottingham Trent University (2010).
- <sup>20</sup> Goelmann Gadi and Prammer Manfred G., “The CPMG Pulse Sequence in Strong Magnetic Field Gradients with Applications to Oil-Well Logging”, *Journal of Magnetic Resonance Series A*, 113, pp. 11-18 (1995).
- <sup>21</sup> Hurlimann Martin D., “Encoding of diffusion and  $T_1$  in the CPMG echo shape: Single-shot  $D$  and  $T_1$  measurements in grossly inhomogeneous fields”, *Journal of Magnetic Resonance*, 184, pp. 114-129 (2007).
- <sup>22</sup> Von Meerwall Ernst D., “Self-Diffusion in Polymer Systems, Measured with Field-Gradient Spin Echo Methods”, *Advances in Polymer Science*, 54, pp. 3-29 (1983).
- <sup>23</sup> Holz Manfred, Heil Stefan R. and Sacco Antonio, “Temperature dependent self-diffusion coefficients of water and six selected molecular liquids for calibration in accurate  $^1\text{H}$  NMR PFG measurements”, *Phys. Chem. Chem. Phys.*, 2, pp. 4740-4742 (2000).
- <sup>24</sup> Tabor D., *Gases, liquids and solids and other states of matter*, Third Edition, Cambridge University Press (1991).
- <sup>25</sup> Duer Melinda J., *The basics of Solid-State NMR in Solid-State NMR Spectroscopy Principles and Applications*, Blackwell Science (2002).
- <sup>26</sup> Bartoline Ltd, *White Spirit (BS 245) Product Information Sheet* (2008).
- <sup>27</sup> Lide David R., “*CRC Handbook of chemistry and Physics*”, 90<sup>th</sup> Edition, CRC (2009).
- <sup>28</sup> Feller Robert L., Stolow Nathan and Jone Elizabeth H., *On Picture Varnishes and their Solvents*, National Gallery of Art Washington (1985).

---

<sup>29</sup> Bloembergen N., Purcell E. M. and Pound R. V., “Relaxation Effects in Nuclear Magnetic Resonance Absorption”, *Physical Review*, 73 (7), pp. 679-712 (1948).

<sup>30</sup> Presciutti Fedrica, Perlo Juan, Casanova Federico, Glogglar Stefan, Miliani Costanza, Blumich Bernhard, Brunetti Brunetto Giovanni and Sgamellotti Antonio, “Noninvasive nuclear magnetic resonance profiling of paint layers”, *Applied Physics Letters*, 93, 033505 (2008).

## 5. Rheology of varnish solutions

### 5.1 Introduction

Previously the rheology of varnish solutions has been discussed as important to the levelling of varnish coatings (see chapter 1.3.5 for summary). The most important relationship is how the viscosity changes with concentration for the different varnish solutions. However experimental measurements of these relationships have been limited to a couple of points at low concentrations per varnish solution, presented by Feller et al<sup>1</sup>. Since then there has been no attempt to experimentally detail these crucial relationships. The focus of recent research has been measuring the molecular mass distribution of the resins<sup>2</sup> and relating these directly to the levelling performance of different coatings<sup>2, 3</sup>. This approach misses out the crucial link between these variables. Here the rheology of solutions with different resins has been measured in detail. This provides the experimental data that is needed to understand the levelling of drying varnishes. In chapter 6 the levelling of varnish coatings will be modelled to test how well the levelling theory matches reality. To do this, the fitted relationships between viscosity and concentration, measured in this chapter, are essential. The modelling cannot be carried out without this knowledge of rheology.

As the viscosity-concentration function of varnish solutions are important, the relative importance of the factors that determine this relationship need to be measured. The molecular mass, of the resin, will have a strong influence on this viscosity function. Resin molecular mass, however, is not mono-disperse (all molecules the same size) but poly-dispersed. The shape of the molecular mass distributions varies for each resin. To statistically describe the molecular mass distribution, different weighted averages of mass are used. They are (previous equation 1.3.5.6)

$$\bar{M}_n = \frac{\sum M_i N_i}{\sum N_i}, \bar{M}_w = \frac{\sum M_i^2 N_i}{\sum N_i M_i}, \bar{M}_z = \frac{\sum M_i^3 N_i}{\sum N_i M_i^2}, \bar{M}_v = \left[ \frac{\sum M_i^{1+a} N_i}{\sum N_i M_i} \right]^{\frac{1}{a}}. \quad (5.1.1)$$

At infinitely dilute concentrations the intrinsic viscosity (previous equation 1.3.5.5)

$$[\eta] = \lim_{C_m \rightarrow 0} \frac{\eta(C_m) - \eta_0}{\eta_0 C_m} \quad (5.1.2)$$

is related to molecular mass, for a pair of solvent and resin chemical species, by the Mark-Houwink equation, (previous equation 1.3.5.4)

$$[\eta] = K \bar{M}_v^a. \quad (5.1.3)$$

The molecular weight average in the Mark-Houwink relationship is the viscosity average molecular weight. The calculation of this is dependent on the value of a, but is usually close to (“within 20%”<sup>4</sup> of) weight averaged molecular weight. Viscosity averaged molecular mass for the resins are unknown. It will be assumed here that  $\bar{M}_v \approx \bar{M}_w$ . The results for comparison of the correlation of  $[\eta]$  with  $\bar{M}_w$ , compared with  $\bar{M}_n$  and  $\bar{M}_z$ , will be partly dependent on how accurate this assumption is. Increased correlation, of  $[\eta]$  with  $\bar{M}_w$  compared to  $\bar{M}_n$  and  $\bar{M}_z$ , would indicate that the assumption is reasonable.

Using the experimentally measured functions, for varnish resins, correlation between the molecular mass averages with low and high concentration viscosity behaviour will be examined. For different solvent-resin combinations, the values a and K in the Mark-Houwink equation (equation 5.1.3) vary. However, as varnish coatings have similar properties, the variation in a and K values may be less significant than the variation in the molecular mass averages. Alternatively, the glass transition temperatures of the resins are similar but dependent on molecular weight (for a single molecular species). Thermodynamic relationships, that leads to the glass transition being similar for different resins with different molecular weight, may influence the K and a values. This may result in a dependence of the K and a values on molecular weight. The potential for such a relationship means that a general K and a value, fitted to the results from all the resins, may not be representative of the K and a values of each resin. However, showing that a general relationship does exist (using weight averaged molecular weight) would prove that weight average molecular weight is the most important criteria (of the mass averages) for low concentration varnish viscosity. This has been suggested to be the case in previous work<sup>3</sup> (work erroneously directly refers to weight averaged

molecular mass rather than stating it is an approximation of viscosity averaged) but has not been shown experimentally for varnishes. With a general Mark-Houwink relationship for varnish resins the intrinsic viscosity for a resin, that has not been measured, can be estimated from molecular mass only.

It is unknown which molecular mass average is the most important for the viscosity of high concentration solutions. If it was shown that the number average molecular weight determines viscosity at high concentrations (while weight average determines low concentration viscosity), a reason for the preference of natural resins for handling and visual properties would be identified. The high polydispersity ( $\bar{M}_w$  higher relative to  $\bar{M}_n$ ) of natural resins would give high viscosity at low concentration, so feels thicker when being applied, while remaining at low viscosity at high concentrations, giving good levelling properties. Here the correlation of the different molecular weight averages with high viscosity behaviour will be examined to determine which has the most significance. A positive result, matching the suggested hypothesis, would be the best correlation with  $\bar{M}_n$ . To do this the high viscosity behaviour needed to be quantified, which was done using the concentration at which a threshold viscosity is met.

The rheology of varnish solutions may also be important in the wetting of complicated rough surfaces (chapter 7).

## 5.2 Methods

As a solvent varnish dries its concentration increases. To measure the rheology of the varnishes across as wide a range of concentrations as possible, varnish solutions were prepared in sealed vials with a measured mass of resin and a measured volume of solvent. The solutions of varnish were left until completely dissolved. Shaking the samples by hand, use of a vortex mixer and use of an ultrasonic bath were used to increase the rate of dissolution where appropriate. For the dammar samples, small amounts of undissolved tree bark were present in the resin. For the lower concentration these could be removed by the use of a PTFE syringe filter (20 $\mu$ m) but it was impractical to filter the higher viscosity solutions. However no significant

differences were found in the measured viscosity, between filtered and unfiltered samples. This un-dissolved volume may have caused a small error in the calculated concentration.

Two rheometers were used in this project, the first was a TA instruments CSL<sup>2</sup> 100 Carri-Med Rheometer and the second a Brookfield LVDV-II + Pro Viscometer (PC controlled to give rheometer capabilities). Figure 5.2.1 gives a diagram of the setup of the two instruments. The Brookfield instrument was used with two cone and plate geometries, of different radii. The spinning cone of the cone and plate setup creates uniform shear rate within the sample. The shear rate of a fluid between two plates is defined as  $\dot{\gamma} = \frac{v}{h}$ , where v is velocity difference between the plates at that position and h is the spacing between the plates at that position. Figure 5.2.2 (a) gives the geometric cross section of the cone and plate system. The velocity difference, between the spinning cone and the plate, is a function of the radial distance, r, and is given by  $v = 2\pi r f$ , where f is the rotation frequency. The spacing is also a linear function of r and is given by  $h = r \tan \theta$ , where  $\theta$  is the cone angle. The shear rate is then given by

$$\dot{\gamma} = \frac{2\pi f}{\tan \theta}. \quad (5.2.1)$$

Note that this is independent of r, so the shear rate is the same over the entire sample. The instrument spins over a series of angular frequencies (corresponds to shear rate) and measures the torque (corresponds to shear stress) required to achieve those rates. Measurements of shear stress can be taken over a range of quasi-constant shear rates. This is known as the flow method.

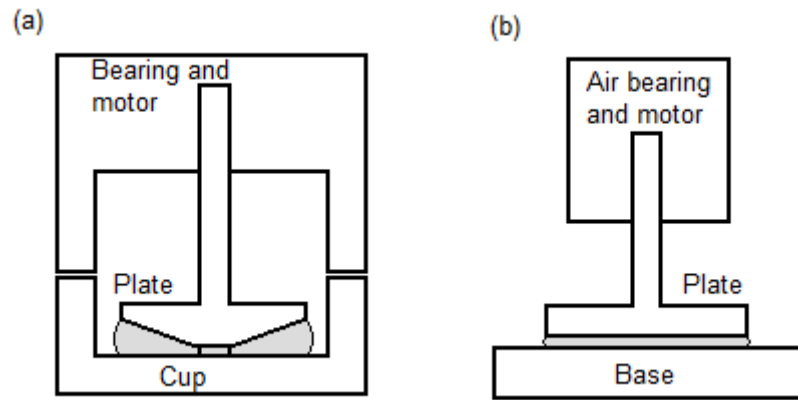


Figure 5.2.1  
 Diagram of the two Rheometers used in this project. (a) Brookfield LVDV-II + Pro Viscometer. (b) TA instruments CSL<sup>2</sup> 100 Carri-Med Rheometer.

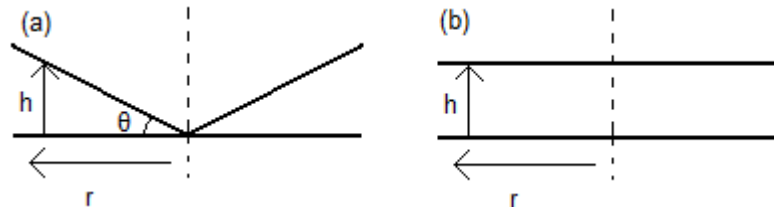


Figure 5.2.2  
 Diagram of the geometry of (a) cone and plate and (b) parallel plate rheometer.

The wide range of viscosities of a varnish, across the measured concentration range, means that the set of shear rates measured varies from sample to sample. For the most viscous samples, the small radius (large angle) geometry was used to enable lower shear rates and increased shear stress (with same torque) to be achieved. Even with this setup the measurement of the highest viscous samples was technically challenging. So instead, the oscillation mode with TA rheometer was used to measure dynamic viscosity. The main advantage of the Brookfield instrument, over the TA rheometer, was that the base plate was in the form of a cup which formed a sealed chamber with the viscometer. This reduced the drying of the samples during measurements. The correct relative positioning of the cone and base, in order to be able to carry out the measurements accurately, was achieved with use of an electrical circuit. When a moulded ring on the cone touched the base, the electrical

circuit was completed. The position of the cone was adjusted until the circuit was just broken, then moved a fixed distance further apart.

The TA Rheometer is a more technically able instrument than the Brookfield instrument, with the ability to measure viscoelastic properties by oscillation. However, the physical setup of the system gave disadvantages to its use. Firstly the sample was not in a sealed container, allowing drying of the sample at the geometry edges, causing inhomogeneous and incorrect concentration. Secondly the geometry available was a parallel plate (2cm radius) rather than a cone and plate. Here the spacing between plates is independent of position, which results in the shear rate being dependent on r and is given by

$$\dot{\gamma} = \frac{2\pi r f}{h}. \quad (5.2.2)$$

For a single measurement a range of shear stresses and shear rates are being measured simultaneously and an average results is produced. A benefit of the parallel plate is that the range of shear stresses and rates can be selected without replacing the plates, by changing the gap. In this project the gap settings for the instrument used were 100 and 200 $\mu\text{m}$ . The gap setting was set manually, with an inbuilt micrometer, from the position where the plates touched. The positioning error was 10 $\mu\text{m}$ .

Oscillation<sup>5</sup> mode used with TA rheometer applies sinusoidal strain,  $S = S_0 \cos(\omega t)$  to the sample (giving strain rate of  $\dot{\gamma} = -S_0 \omega \sin(\omega t)$ ). The resultant stress is measured by the instrument at all points during the oscillation. The dynamic shear modulus (stress/strain) can be represented by the sum (  $G^* = G' + iG''$  or  $G^* \cos(\omega t) = G' \cos(\omega t) + G'' \sin(\omega t)$  ) of the elastic (storage modulus  $G'$ , proportional to strain) and viscous (loss modulus  $G''$ , proportional to strain rate) components. For each measurement the instrument resolved both modulus components from the stress and strain wave forms, which requires the inertia of the instrument to be measured and included in calculations. For each sample, measurements were taken over a range of angular frequencies ( $\omega$ ). The simplest

reasonable viscoelastic model of varnish solutions is the Maxwell model (Appendix 5). Assuming this model it can be shown<sup>5</sup> that  $G''$  is related to viscosity by

$$G'' = \frac{\eta\omega}{1 + \omega^2\tau^2} \quad (5.2.3)$$

where  $\tau$  is the Maxwell relaxation time (exponential decay constant of shear stress with applied shear strain). If  $\omega\tau \ll 1$  then viscosity is approximated to the dynamic viscosity,  $\eta'$ , given by

$$\eta \approx \frac{G''}{\omega} = \eta' \quad (5.2.4)$$

The elastic part of the modulus is given by

$$G' = \frac{\eta\tau\omega^2}{1 + \omega^2\tau^2} = \tau\omega G'' \quad (5.2.5)$$

If  $G'/G'' \gg 1$  the dynamic viscosity is an accurate measurement of Newtonian viscosity.

Both instruments had temperature control via the base plate. The Brookfield instrument controlled temperature by use of a closed water circuit, with heater and cold sink. The TA rheometer temperature control was via an external water supply and Peltier plate, though the Peltier plate was not used. The temperature used for all measurements was  $20 \pm 2$  °C.

At the start of the project the TA rheometer was used exclusively for the preliminary measurements, carrying out all the flow and oscillation measurements. When the Brookfield instrument became available this was used to carry out all the flow measurements, due to its advantages in limiting the sample drying during the measurements. The TA rheometer carried out all the oscillation measurements of dynamic viscosity (via  $G''$ ) and  $G'$  for the most viscous samples in the project.

The main solvent used for the varnish solutions was Toluene, which has a viscosity of 0.56 mPa s at 25°C and 0.778 at 0°C<sup>6</sup>. Linear interpolation gives a viscosity of 0.6 mPa s at 20°C. To confirm the calibration of both instruments at the start of

measurements of varnish concentration sets, samples of pure toluene were measured first. Figure 5.2.3 gives the result for a selection of these measurements from the Brookfield instrument along with the reference Newtonian viscosity. There are noticeable errors in the measurements but these are small (<10%) compared to the viscosity differences of the measured varnish solutions (orders of magnitude).

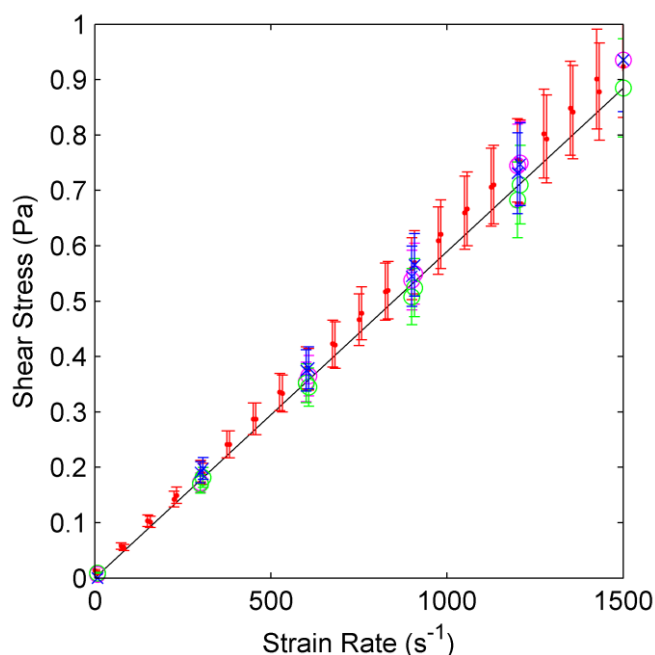


Figure 5.2.3  
Flow rheology results of a selection of pure toluene measurements from different measurement sets (colours). The black line shows the reference viscosity of toluene.

## 5.3 Results

### 5.3.1 Rheological characterisation of varnish solutions

Figure 5.3.1.1 shows flow method measurements for two concentrations of the polymer resin Paraloid B72 (in toluene). This is an example of a large polymer resin that would be more likely, than lower molecular weight resins, to show non-Newtonian behaviour. Appendix 3 provides similar graphs for all the other resins measured. In all cases a concentration of 2g of resin dissolved in 12ml of toluene and the highest concentration, for the specific solvent resin combination, measured by the flow method is shown. All these results show no significant deviation from Newtonian behaviour (linear passing through origin).

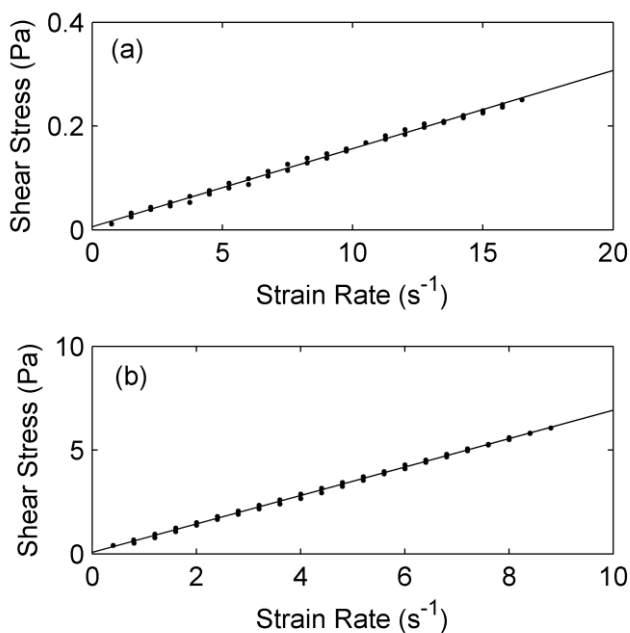


Figure 5.3.1.1  
Flow rheology of Paraloid B72  
measured at concentrations of  
(a) 2g resin to 12ml solvent and  
(b) 5g resin to 9ml solvent.

As well as providing the dynamic viscosity in place of viscosity for the most viscous samples, the oscillation method provides additional sensitivity to non-Newtonian behaviour. Figure 5.3.1.2 gives the oscillation results for the most viscous (concentrated) samples of the measured resins. For the two polymer resins an elastic component of the modulus is being measured at the higher measured frequencies, however it is still small compared to the viscous component under the measured conditions. For the non-polymer resins no elastic component of the modulus is detected, despite the higher concentrations to get the high viscosity. These oscillation and flow results support the opinion that typical solvent varnish behaviour is strongly Newtonian. The need to consider more complex rheological behaviour in levelling (and other processes) is unlikely.

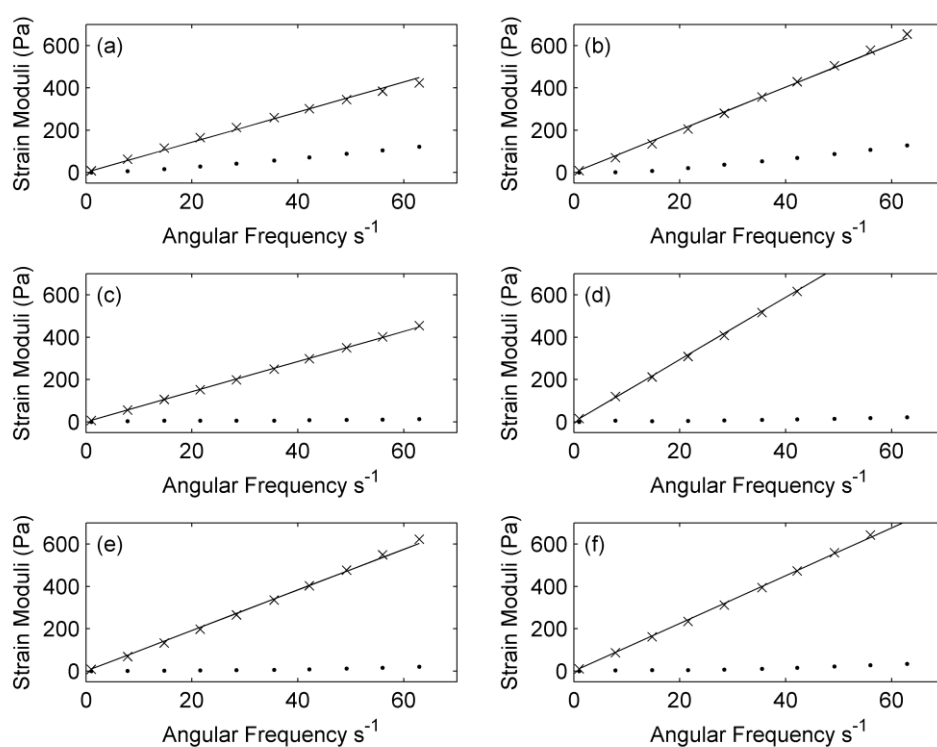


Figure 5.3.1.2.

Viscous moduli ( $G''$ ) (x), with dynamic viscosity fit (line), and elastic moduli ( $G'$ ) (dot) measured by the TA rheometer in Oscillation mode for highest viscosity ( $\sim 10$  Pa S) mixed for a selection of varnish resins in toluene.

(a) AYAT (5g9), (b) Paraloid (7g7), (c) Dammar Unfiltered (10g4), (d) MS2A (10g4), (e) Laropal (10g4) and (f) Regalrez 1094 (11g3).

### 5.3.2 Viscosity-concentration functions: dependence on resin

Figure 5.3.2.1 shows all the measured viscosities for the resins, dissolved in toluene, over the measurable range of concentrations. The high viscosity of the two polymer resins compared to low molecular weight resins is immediately apparent. For all but the most dilute concentrations, the polymer resin solutions are orders of magnitude more viscous than the low molecular weight resin solutions. The differences in viscosity, between the low molecular weight resins, are not as large. The measured relationships between viscosity and concentration, for the low molecular weight resins, are similar. Most pass the limit of measurable viscosity around a concentration of 0.7, though Regalrez 1094 is substantially less viscous being measurable to nearly 0.8.

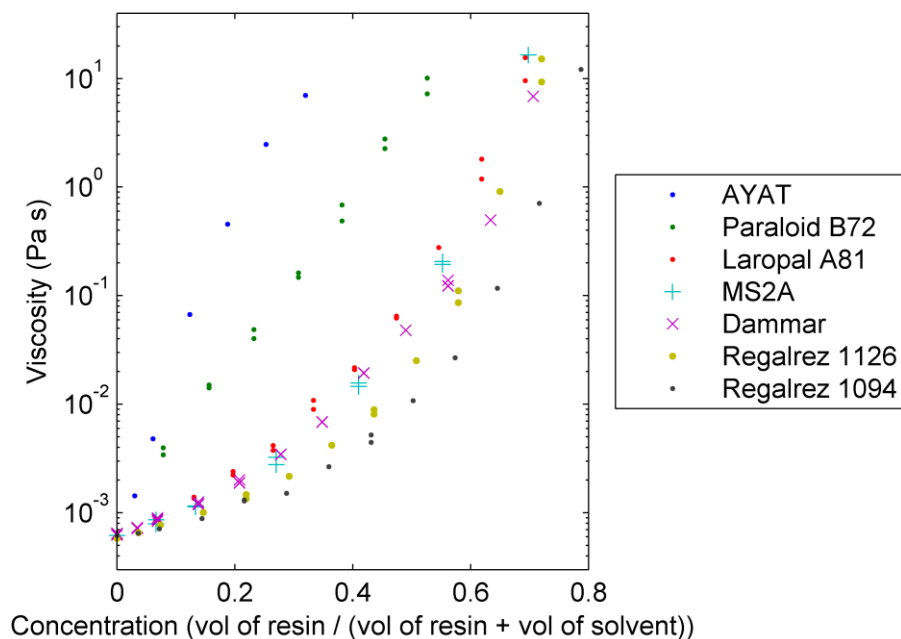


Figure 5.3.2.1. Viscosity of various varnish resins dissolved in toluene measured as a function of concentration.

With the complete viscosity-concentration relationships for these seven varnish resins (dissolved in toluene), there is an opportunity to compare trends in viscosity with recently measured molecular weight statistics for the resins<sup>2</sup>. First whether there was an experimental (Mark-Houwink) relationship between the intrinsic viscosity and weight averaged molecular mass, of the varnish resins, was examined. To do this, the intrinsic viscosity had to be extracted from the viscosity results. Figure 5.3.2.2 shows the extrapolation of intrinsic viscosities (at 0 concentration) from the lowest concentration values for the different varnish solutions.

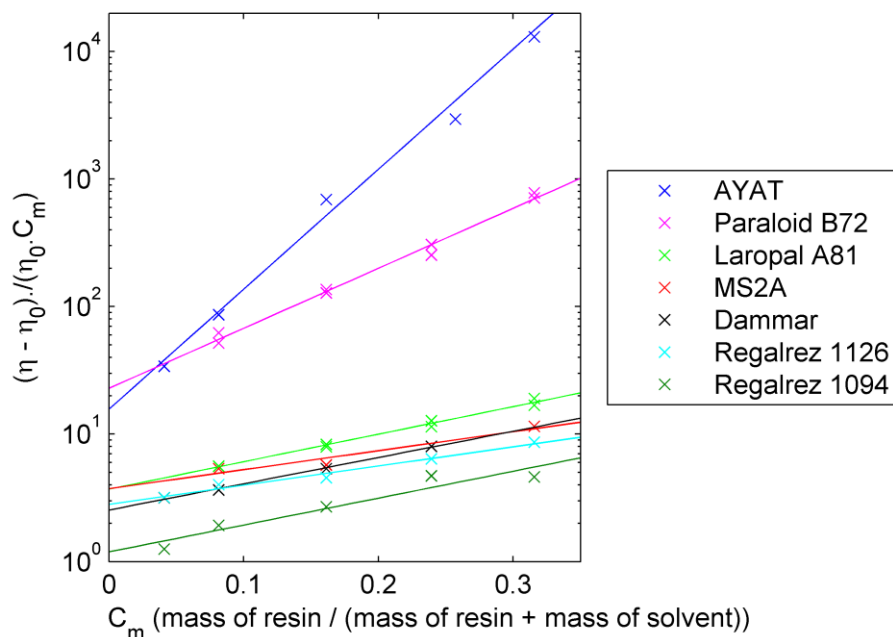


Figure 5.3.2.2. Intrinsic viscosity extrapolation (at 0 concentration) for the measured resins dissolved in toluene.

Figure 5.3.2.3 compares the measured intrinsic viscosities with the  $\bar{M}_n$ ,  $\bar{M}_w$  and  $\bar{M}_z$  values reported by de la Rie et al<sup>2</sup>. The correlation coefficients for the three graphs are  $0.94 \pm 0.06$  for  $\bar{M}_w$ ,  $0.93 \pm 0.08$  for  $\bar{M}_n$  and  $= 0.93 \pm 0.08$  for  $\bar{M}_z$ . None of the molecular weight averages are significantly more correlated with intrinsic viscosity. However, for the low molecular weight resins,  $M_w$  visually appears better correlated. If the polymer resins are not included in the calculation of the correlation coefficient the values are  $0.82 \pm 0.27$  for  $\bar{M}_w$ ,  $0.50 \pm 0.50$  for  $\bar{M}_n$  and  $= 0.66 \pm 0.41$  for  $\bar{M}_z$ . The weight averaged molecular weight appears the closest correlated with intrinsic viscosity, though the results are not conclusive. The error bounds on these measurements are for 68.2% confidence level. The large errors in the correlation values, when the polymer resins are ignored, of  $\bar{M}_n$  and  $\bar{M}_z$  mean that no meaningful correlation was found. However for  $\bar{M}_w$  the error in the correlation value was significantly lower than the value, showing that there is correlation between  $\bar{M}_w$  and intrinsic viscosities for the low molecular weight resins. For  $\bar{M}_w$  (figure 5.3.2.3 (a)), linear regression gives the general Mark-Houwink constants as  $a = 0.45 \pm 0.08$  and  $\log_{10}(K) = -1.0 \pm 0.3$ .

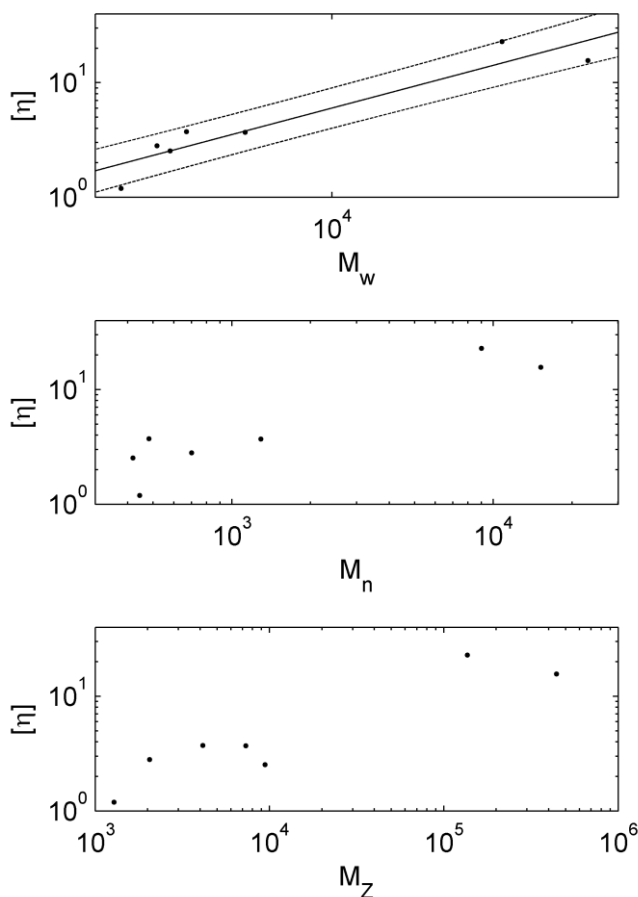


Figure 5.3.2.3. Comparison of the measured intrinsic viscosity of the measured resins in toluene with their molecular weight averages<sup>2</sup>. The black line shows the Mark-Houwink relationship fitted, the dashed line gives the 68.2% certainty bounds of points falling within these values.

The molecular weight dependence for the viscosity of high concentration varnish solutions was expected to be more complex than for intrinsic viscosity. It was hypothesised that it was the polydispersity of the natural resins that gave them better handling properties (higher viscosity) at low concentration. This is due to higher  $\overline{M}_w$  increasing the intrinsic viscosity, while the low  $\overline{M}_n$  reduced the viscosity at higher concentrations. To quantify the high concentration viscosity behaviour of the varnish solutions, the value of the concentration of solvent where viscosity equalled 10 Pa s was taken from the extrapolated trends (see below). This was around the highest viscosity where experimental data could be taken. Figure 5.3.2.4 shows the value of this concentration compared with the molecular weight averages. It can be seen that, from these results,  $\overline{M}_w$  still has the strongest correlation, though it should be noted that the correlation appears less than for intrinsic viscosity. This does not support the hypothesis, that  $\overline{M}_n$  determines high concentration viscosity, though the

results are not conclusive. Particularly for the low molecular weight resins, the different solution interaction properties between the solvent and resin molecules may mask trends due to molecular mass. Other factors, such as the glass transition temperature, may also influence the high concentration viscosity.

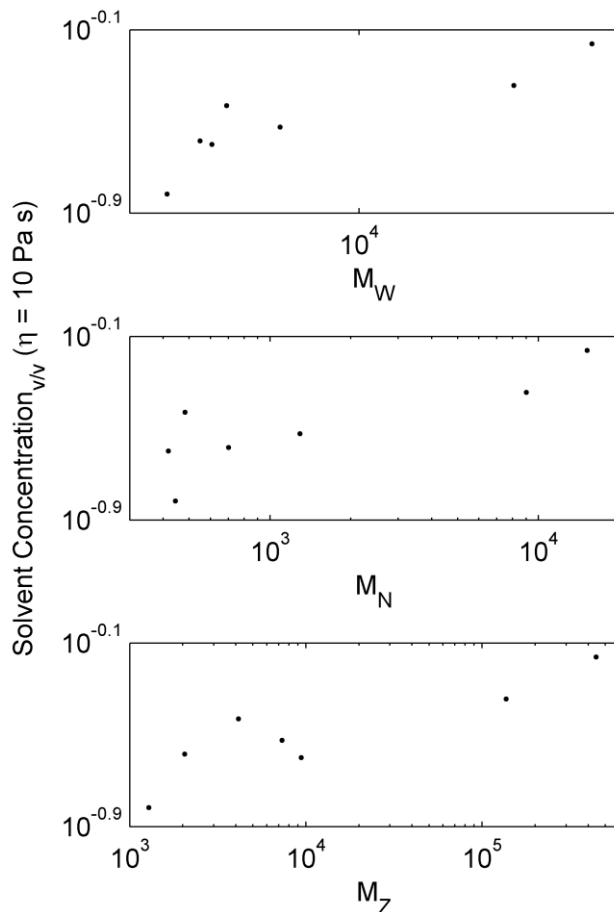


Figure 5.3.2.4. Comparison of the measured concentration where the viscosity equals 10 Pa s, for the measured resins in toluene, against their molecular weight averages<sup>2</sup>.

The important application of this data was the fitting of the empirical viscosity functions, to it, required for modelling the drying and levelling of varnish coatings in chapter 6. For the low molecular weight varnishes a cubic fit to the log of viscosity against concentration were used. Figure 5.3.2.5 shows these fits to the measured viscosity. The visual quality of the fits to the measured viscosities appears good. The accuracy of the extrapolation of this trend, to higher concentrations than could be measured, is unknown for these resins. In this graph it is also worth noting the differences in the shape of the curves for each resin, despite the failure of figure 5.3.2.4 to demonstrate a trend of viscosity with an average molecular weight other than  $\bar{M}_w$ . Note the curve of dammar resin, at low concentrations the viscosity is similar to MS2A, however the increase in the gradient is lower and at higher

concentrations the viscosity of dammar is similar to Regalrez 1126. This flatter curve is also evident in Laropal A81, which, as the highest molecular weight resin of this set, has clearly the highest viscosity at concentration of 0.3 but at the higher concentrations the viscosity is similar to MS2A. It can be concluded that though the shape of the viscosity functions, of the low molecular weight resins, are similar they are not just differently scaled versions of the same function.

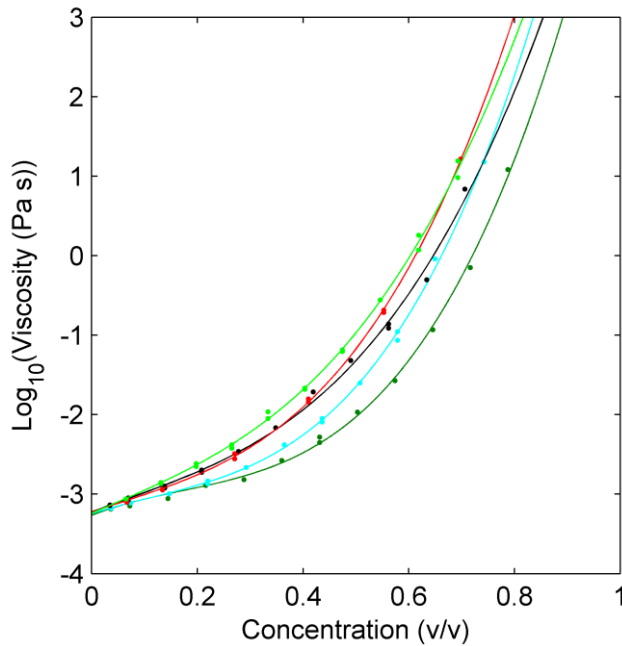


Figure 5.3.2.5.  
Fitted empirical cubic relationship of the log of viscosity vs the concentration for the low molecular weight resins measured.  
Dark green – Regalrez 1094, Cyan – Regalrez 1126, Black – Dammar, Red – MS2A and Light Green - Laropal A81.

Figure 5.3.2.6 shows the empirical fits of viscosity for the two polymer vanishes measured and one of the low molecular weight resins (Laropal A81) for comparison. Visual inspection of the two polymer resins gave little indication of a need to fit anything other than first order polynomial. However the extrapolation of this trend for Paraloid B72 would predict that it would have equal viscosity to Laropal A81 at a concentration of 0.8. The molecular weight difference between the two resins would make this an unlikely result. The much larger molecules of Paraloid B72 should be much less able to move past each other at any concentration. An identical fit, to the low molecular resins, was carried out for the Paraloid B72 viscosities. This produced an extrapolation that seemed more reasonable compared with the low molecular weight resins. Strong evidence that the cubic extrapolation, for Paraloid B72, was more accurate than the linear extrapolation is given in chapter 6.5.3. Both extrapolations were used in the modelling of levelling a Paraloid B72 coating and

the two results were compared to the experimental result. The cubic extrapolation gave a result much closer to the experimental data.

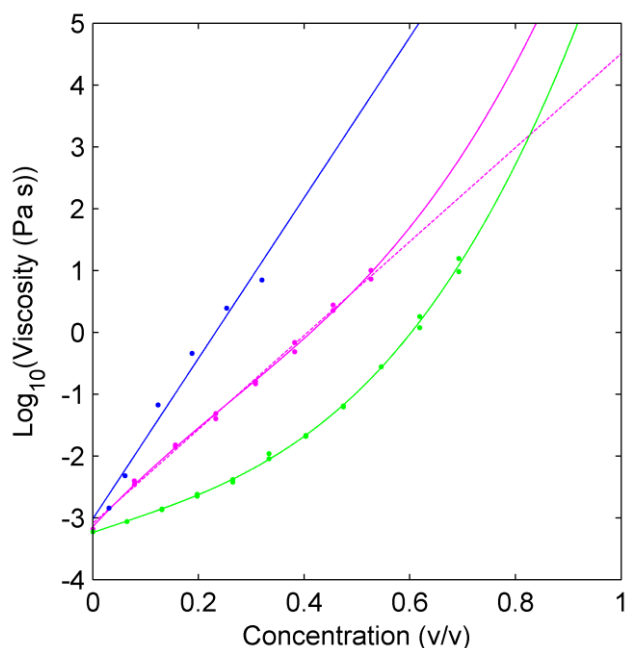


Figure 5.3.2.6.  
Fitted empirical relationships of the log of viscosity vs. the concentration for the low molecular weight resins measured.  
Blue – AYAT (linear fit),  
Magenta – Paraloid B72 (solid line cubic fit, dotted line linear fit),  
and Light Green - Laropal A81 (cubic fit).

### 5.3.3 Viscosity-concentration functions: dependence on solvent

To address the effect of the solvent on the viscosity of solutions two scenarios were chosen. Firstly it was desired to use white spirit as a solvent for Regalrez 1094 in film drying measurements (Chapter 6.4.3) due to its use in real applications and health and safety benefits. In figure 5.3.3.1 the change in viscosity by the use of this solvent is evident. While Regalrez 1094 dissolved in toluene was the least viscous solution measured in this study, the change of solvent to white spirit increased the viscosity to be similar to the other low molecular resins (such as Regalrez 1126) in toluene. In terms of performance of the levelling of low molecular weight resins, the choice of solvent is a significant factor in the viscosity of a drying film. However, for the case of this change of solvent for Regalrez 1094, in chapter 6.5.4 it is shown by modelling that the difference in viscosity is negated by (and insignificant to) the difference in volatility. White spirit is approximately ten times less volatile than toluene.

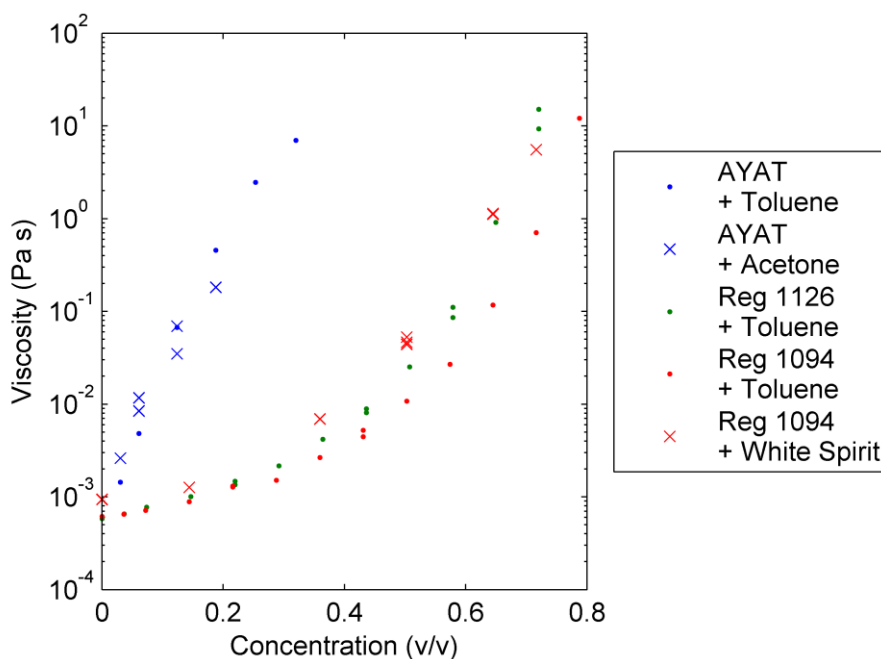


Figure 5.3.3.1. The change in viscosity-concentration relationships due to the solvent used for AYAT and Regalrez 1094.

The second scenario investigated was for AYAT dissolved in acetone. Previous studies<sup>7, 8</sup> have investigated the mechanical property differences of dried AYAT films produced from toluene and acetone solution. The difference in mechanical properties was explained by the behaviour of the radius of gyration of the AYAT in solution. Acetone, as a poor solvent for AYAT, reduced the radius of gyration. The difference in the spread of the molecule would be expected to change the viscosity. The measured viscosities of AYAT in solutions of acetone and toluene are shown in figure 5.3.3.1. The extremely high volatility of acetone proved problematic in the measurement of viscosity due to drying of the sample during measurement. The measured viscosities for AYAT and acetone solutions did not show a significant variance of viscosity, from toluene solutions of the same concentration, especially when compared to the viscosity differences between different resins.

## 5.4 Conclusion

The measurement of the rheology of varnish solutions showed that their behaviour is highly Newtonian. The two polymer resins showed some viscoelastic properties at concentration where viscosity was approximately 10 Pa s. The low molecular weight resins at much increased concentration, to produce a viscosity of ~10 Pa s,

did not show any non-Newtonian properties. The rheology of low molecular weight varnish solutions can be regarded much simpler than much of the rheological behaviour found in the general polymer field. The solutions of low molecular weight resins remain Newtonian for measurable concentrations.

To qualitatively compare the expected levelling properties of two solutions or quantitatively model them, the viscosity of the solutions as a function of concentration is a necessity. Here these functions, for art conservation varnishes, have been experimentally measured for the first time. The high molecular weight polymer resins have much different viscosity functions, compared to low molecular weight resins. The differences between the low molecular weight resins were much smaller. The use of different solvent can manipulate the viscosity to the extent equivalent to the differences between the low molecular weight resins.

The empirical viscosity functions measured in this chapter were essential for the modelling of levelling carried out in chapter 6. The experimental work within this chapter provides an essential knowledge base to understand the behaviour of solvent varnish solutions.

As they are so important to the levelling, hence appearance, of coatings, knowledge of the viscosity function's dependence on the components of the solution would be an important tool for developing and choosing varnishes. Though it has been shown here that viscosity is correlated with molecular weight, especially for polymer resins, describing the viscosity at different concentrations by the molecular weight averages alone is not reasonable. Other factors, such as the solvent-resin combination, are very significant in determining these functions. This again shows the need for the experimental measurement of these viscosity-concentration functions.

## 5.5 References

---

<sup>1</sup> Feller Robert L., Stolow Nathan and Jone Elizabeth H., *On Picture Varnishes and their Solvents*, National Gallery of Art Washington (1985).

<sup>2</sup> De la Rie E. Rene, Delaney John K., Morales Kathryn M., Maines Christopher A., and Sung Li-Piin, "Modification of Surface Roughness by Various Varnishes and Effect on Light Reflection", *Studies in Conservation*, 55, pp. 134-143 (2010).

---

<sup>3</sup> Delaney John K., de la Rie E. René, Elias Mady, Sung Li-Piin and Morales Kathryn M., “The Role of Varnishes in Modifying Light Reflection from Rough Surfaces”, *Studies in Conservation*, 53 (3), pp. 170-186 (2008).

<sup>4</sup> Odian George, *Principles of Polymerization*, Fourth Edition, John Wiley & Sons (2004).

<sup>5</sup> Barnes H. A., Hutton J. F. and Walters K., *An introduction to Rheology*, Elsevier (1989).

<sup>6</sup> Lide David R., “*CRC Handbook of chemistry and Physics*”, 90<sup>th</sup> Edition, CRC (2009).

<sup>7</sup> Hansen Eric F., Derrick Michele R., Schilling Micheal R. and Garcia Raphael, “The effects of solution application on some mechanical and physical properties of thermoplastic amorphous polymers used in conservation: Poly(vinyl acetate)s”, *JAIC*, 30 (2), pp. 203-213 (1991).

<sup>8</sup> Opena Mareike and Jagers Elisabeth, “Effects of Solvents on the physical properties of Polymeric Films”, *Proceedings of Cleaning 2010 New insights into the cleaning of paintings*, pp. 69-71 (2010).

## 6. Development of surface roughness of drying varnish

### 6.1 Introduction

The surface roughnesses of various varnish coatings, after they have been applied to rough substrates (ground glass) and dried, have previously been measured. This has been done by examining the distinction of image gloss (in transmission)<sup>1</sup> and measuring the surface roughness by mechanical<sup>2</sup> and confocal<sup>3</sup> means. Low molecular weight natural and synthetic resins have been shown to be significantly better at producing a smooth surface than high molecular weight polymers. For all varnishes, the higher spatial frequencies, of the substrate roughness, are filtered (reduced) to a greater extent than lower spatial frequencies. By modelling the optical reflection (see chapter 1.2) it has been shown that this difference in surface roughness of varnish coatings is a more important factor than the difference in refractive index.

Though the previous work on varnishes for art conservation has related the final surface roughness to the molecular weight, the processes that happen to link this starting variable and end result have not been adequately studied for this specific topic (see chapter 1.3.5). This process, levelling, has been better researched in other coating fields. This project applies the knowledge, from these other fields, to model the formation of roughness on a varnish coating. The accuracy of the derived model is then measured with the OCT multi-interface profilometry technique developed in chapter 2.

The physics of film levelling is reasonably well understood<sup>4, 5, 6, 7</sup>, though most mathematical models have limits on their applicability. The earliest model, the “no-flow point” model<sup>8, 9</sup>, of the levelling of varnishes introduced that as the solvent evaporates, from the surface of the film, the volume of the varnish layer is reduced. Each lateral point on the varnish film can be considered a vertical column of varnish, the evaporation and shrinkage at each point is independent of other lateral points. The varnish column remains in contact with the substrate and loses volume by changing its height. The columns are assumed to always be homogenous through their height (concentration uniform). The rate of evaporation is dependent on concentration. As the varnish columns become different in their concentration, the

rates of evaporation differ as well and the surface profile takes on the profile of the substrate. As the surface roughness develops, flow of material happens within the film, the effect of which is to level the formed roughness. The pressure driving this levelling flow is from the action of surface tension and the geometry of the surface. The greater the curvature of the surface the greater the pressure driving the levelling flow. The resistance to the levelling flow is the shear stress due to the rheology of the material. Chapter 1.3.5 provides more detailed explanation of these points.

To provide an analytical mathematical solution to the levelling of a liquid film, Orchard<sup>4</sup> considers the surface profile as a sum of independent Fourier components. An exponential decay of the amplitude can be found for each Fourier component. In the limits of  $a_0 \ll h \ll \frac{\lambda}{2\pi}$ , where  $a_0$  is initial amplitude of the Fourier component of the roughness,  $h$  is the thickness of the film and  $\lambda$  is the spatial wavelength of the Fourier component, the mathematical solution is given by

$$a(\lambda) = a_0 \exp \left[ -\frac{16\pi^4 \gamma h^3}{3\lambda^4} \int \frac{1}{\eta(t)} dt \right] \quad (6.1.1)$$

where  $\gamma$  is surface tension and  $\eta$  is viscosity. Orchard<sup>4</sup> details work carried out by Roesler that compares results obtained from Orchard's approach and results obtained with the method used in this work (see section 6.2). The result of this showed reasonable agreement of the two methods up to  $a_0/h = 0.8$ . Orchard also provides the mathematical solutions for when film thickness is not thin in comparison to the spatial wavelength, *i.e.*  $h \ll \frac{\lambda}{2\pi}$  is not true. In this case the dependence on  $\lambda$  is different.

Delaney et al<sup>10</sup> refer to equation 6.1.1 to provide an explanation of the spatial filtering of surface roughness by varnish. Their work did not investigate the accuracy of this relationship or use it to predict surface roughness for different coatings. In this chapter a different mathematical approach is used to numerically model the surface profile on a random rough surface. Rather than immediately splitting the profile into Fourier components, a differential approach to the geometry

is used to calculate the levelling pressure and flow from the Navier-Stokes equation (equation 1.3.5.3) at discrete points<sup>11</sup>. For the modelling of varnish systems, a term<sup>12</sup> for the development of the roughness, due to evaporation, also has to be included.

The derivation of this lubrication approximation model is based on Stillwagon and Larson's paper<sup>11</sup>. The model is two dimensional, using normal to the film ( $z$ ) and one lateral dimension ( $x$ ). The other lateral dimension ( $y$ ) is not used here. Figure 6.1.1 is a diagram of the two interface positions and the thickness of the film as a function of lateral ( $x$ ) position. This gives the definitions of surface profile ( $\Phi(x)$ ), substrate profile ( $s(x)$ ) and thickness ( $h(x)$ ) used below.

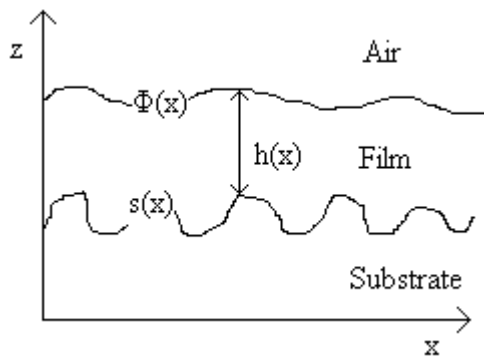


Figure 6.1.1  
Diagram of film on substrate for numerical differential lubrication approximation in two dimension.

The model considers a film of liquid on a solid, with solid-liquid interface at  $z(x) = s(x)$  and liquid-air interface at  $z(x) = h(x) + s(x) = \Phi(x)$ . The change of thickness with lateral position of  $\frac{dh}{dx} \ll 1$  ensures a linear dependence of flow rate with height in film. The liquid is Newtonian in flow behaviour, with no slip at solid-liquid interface ( $v = 0$  at  $z(x) = s(x)$ ) and no shear stress at the liquid-air interface ( $\frac{dv}{dz} = 0$  at  $z = h(x) + s(x)$ ). The incompressible Navier - Stokes equation (equation 1.3.5.3), if inertia within the liquid is negligible, can be given by

$$\frac{\partial p}{\partial x} + \eta \frac{d^2 v}{dz^2} = 0 \quad (6.1.2)$$

where  $p$  is pressure and  $v$  is velocity. This is integrated twice with respect to  $z$ , within the stated limits, giving

$$v = \frac{1}{\eta} \frac{\partial p}{\partial x} \left( \frac{1}{2} z^2 - hz \right). \quad (6.1.3)$$

Remaining in two dimensions (same as the system being identical out to  $\pm \infty$  in the y dimension) the rate of change of one dimensional volume,  $dh/dt$ , of every lateral

element, must be conserved with the lateral differential of total flow ( $Q = \int_{s(x)}^{h(x)+s(x)} v dz$ )

giving

$$\frac{\partial h}{\partial t} + \frac{\partial Q}{\partial x} = 0. \quad (6.1.4)$$

Substituting equation 6.1.3 into 6.1.4, and solving the definite integral gives

$$\frac{\partial h}{\partial t} = \frac{1}{3\eta} \frac{\partial}{\partial x} \left( \frac{\partial p}{\partial x} h^3 \right), \quad (6.1.5)$$

which defines the resistance to flow in the film caused by the pressure gradient.

The pressure gradient, that drives flow in the system, comes from surface tension. It is thermodynamically favourable for the surface energy to be minimised in steady state. This means the reduction of the surface area (profile  $\Phi(x)$ ) to a minimum, a flat surface. The curvature,  $R$ , of the surface cause capillary pressure given by

$$p = \frac{\gamma}{R} \quad (6.1.6)$$

where  $\gamma$  is the surface tension. Note that this is half the Laplace pressure of a spherical interface (equation 1.3.5.1) as the radius of curvature in the y dimension is infinite.  $1/R$  is approximated to the second differential of the surface profile allowing the lubrication approximation for the levelling flow across the whole profile length to be defined as

$$\frac{\partial \Phi(x)}{\partial t} = \frac{1}{3} \frac{\gamma}{\eta} \frac{\partial}{\partial x} \left[ \left( \frac{\partial^3 \Phi(x)}{\partial x^3} \right) h(x)^3 \right]. \quad (6.1.7)$$

This approximation is correct in the limits  $\frac{d\Phi}{dx} \rightarrow 0$  and  $\frac{dh}{dx} \rightarrow 0$ . This version of the model does not take into account the roughness in the y dimension, as the experimental data used for the substrate profile and surface profile comparison is

only two dimensional. The concentration (hence viscosity) is assumed to be homogenous in the film at each lateral point, which is not the case as there is expected to be an axial concentration gradient. The impact of this gradient is unknown. The model also assumes that the material rheology is Newtonian, in chapter 5 it was shown that this is generally the case for varnish solutions. In a situation where the rheology of a film is non-Newtonian, it is possible to incorporate such behaviour into lubrication approximation models<sup>13</sup>. The model did not take into account the effect the modelled levelling flow and concentration gradient driven diffusion, have on the concentration at each lateral point.

OCT multi-interface profilometry can be used to measure a film-air interface while simultaneously measuring the corresponding substrate-film interface beneath. This measurement can be done dynamically for a drying varnish film. With the substrate profile, the development of the surface profile can be modelled with the lubrication approximation. Direct evaluation of the performance of the model, with the experimental results, can be done by comparison of surface profiles.

From the models, several factors are apparent that may affect the surface roughness of dry varnish films, which have been applied onto rough substrates. They are evaporation rate, viscosity, dry coating thickness and starting condition (i.e. initial thickness and concentration of applied film). The evaporation rate and viscosity will be dependent on the resin and solvent of the solution. The relative importance of these variables, on the development of surface roughness, will be evaluated by experimental measurements and modelling.

Section 6.2 will evaluate the substrate and surface roughness, and the varnish thickness, of real varnish coatings. This is to illustrate the scales at which the experimental and modelling work should be carried out. Section 6.3 details the experimental method for the work carried out in this chapter. Section 6.4 gives the experimental results obtained. Section 6.5 describes how these measurements were modelled and gives the comparison of the model results to the experimental results.

## 6.2 Dimensions of real painting systems

For the experimental work and modelling, of this project, to be of the most use, to understanding how real conservator applied varnish coatings behave, the scales involved have to be as close to the real situation as possible. Here a brief overview of the scaling of the dimensions in real painting systems is given.

### 6.2.1 Paint and varnish roughness

The real surface roughness of unvarnished paintings (the substrate) is an important parameter in the final surface profile of a varnish coating. The specific roughness of any painting will be dependent on the materials used and the artist's technique. Figure 6.2.1.1 shows part of an OCT image of a test painting where a varnish coating has just been removed. As well as providing an idea of the scales of the surface greater than the imaging resolution, the OCT image also provides information on the surface reflection properties. Notice in this image the reflection from the surface does not stand out (at any point) from the reflection from the volume of the paint (compare to Figure 6.2.1.2). This is due to no specular reflection being measured from the paint surface, indicating a rough surface over optical distances.

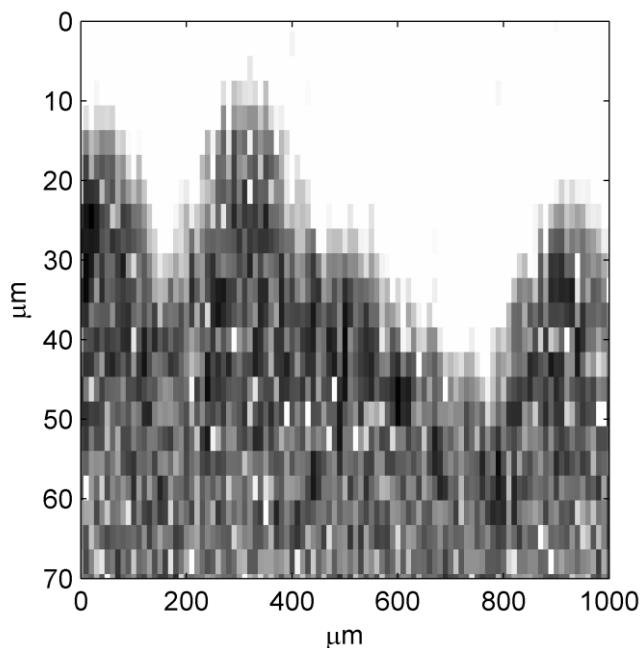


Figure 6.2.1.1  
Section of an OCT image of a  
rough unvarnished test painting.

The nature of unvarnished painting surfaces and substrates used to mimic these need to be considered. The magnitude (and source) of the roughness varies with lateral scales. An approximate mathematical and conceptual model of the profile of the surfaces may be a random fractal line<sup>14</sup>. The surface profile can be thought of as appearing similar over a variety of scales. As a result the magnitude of roughness at any lateral scale must be dependent on that lateral scale. Also considering the aspect ratio (axial dimension/lateral dimension) of features. The durability of features with an aspect ratio of greater than one is low, that is they are likely to have been broken off or not have formed in the first place. The resultant magnitude of roughness for any lateral scale is expected to be less than that lateral scale.

The ground glass substrates used to simulate painting surfaces in this and the following chapter, as well as in previous studies<sup>2, 3</sup>, are produced by fracturing the surface of the glass. The result of this method is that the roughness at all scales comes from the same process and its properties are expected to be intrinsically fractal<sup>14</sup>. The causes of roughness at different scales (including form and texture) of a paint surface are different. At larger scales the artist may have used the paints to provide an intentional three dimensional form to the surface or the paint may have taken the form of the substrate it has been applied to (seen for canvas cut off sample, see figure 6.2.1.3 for resulting surface profile). The lateral scales of these features are mm upwards. At a slightly higher spatial frequency there is texture induced by brush marks that do not flow out after application of the paint, the scale of these are around  $1\text{mm}^{-1}$ <sup>6</sup>. At lower spatial dimensions, the roughness of the paint will be determined by its material properties as it dries. A major difference between the drying of the paint and drying of varnishes is the content of solid particles (colloids) of the pigment. Unlike varnishes, paint coatings do not necessarily produce a smooth surface when applied to a smooth substrate. The magnitude of roughness at this microscopic scale is dependent on the paint. Hedley<sup>15</sup> provides some SEM images of the surface of linseed oil paint films in his study of degradation by cleaning. These images showed a variety of roughness. These were of micron height magnitudes, within lateral ranges of  $100\mu\text{m}$ . Analysis of a smoother unvarnished paint with confocal and SEM<sup>16</sup>, again for assessment of damage by cleaning, shows that the amplitude of roughness is dependent on lateral dimensions.

The final surface roughness, of real varnish finishes, is of importance to relate the experimental results with real conservation scenarios. Figure 6.2.1.2 shows part of an OCT image and measured profile of a varnished painting within the national gallery collection (Catalogue Number NG3085, Vittore Carpaccio, The Departure of Ceyx, oil on spruce panel, ~1505). The glossy surface is apparent in the OCT image, and the surface profile shows less than 5 $\mu\text{m}$  deviation over a profile length greater than 1.5mm. Note that the surface roughness in this profile will be an overestimate due to speckle.

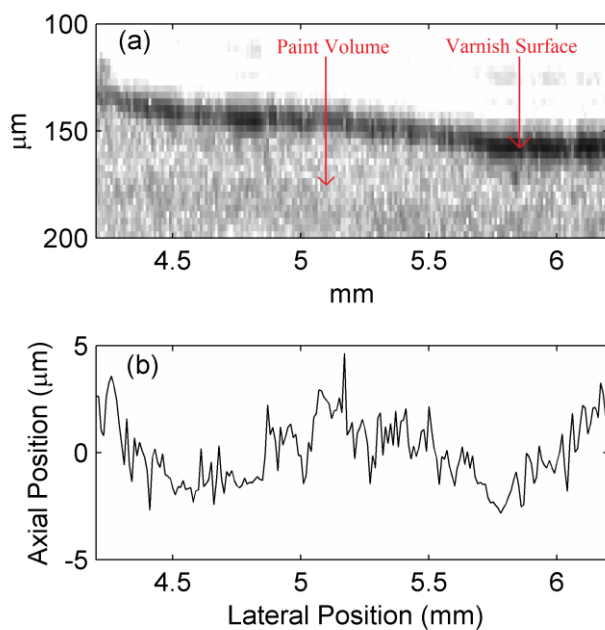


Figure 6.2.1.2  
 (a) OCT cross-section image of a varnished 16<sup>th</sup> C. oil painting in the National Gallery collection (NG3085). Note that the volume of the varnish is not resolvable due to low thickness.  
 (b) Surface profile measured

Figure 6.2.1.3 shows the surface profile of a varnished brown painted canvas off cut measured with a mechanical profilometer. The low frequency features are large (inherited from the canvas substrate), but there is little high frequency roughness resulting in a smooth profile.

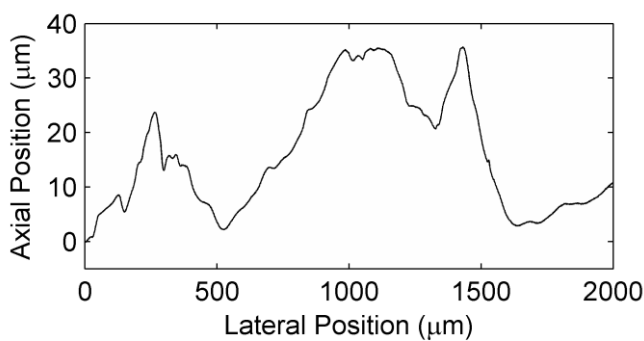


Figure 6.2.1.3  
 Stylus measured surface profile of a varnished, painted canvas cut off.

In conclusion the magnitudes of roughness, of the substrate, required for this work to be of most relevance is of the order of microns, with spatial period from hundreds of microns to 0.5 microns (approximately wavelength of light hence diffraction limit). After the application of varnish the final surface roughness will be smoother, especially at higher frequencies, so the amplitudes of roughness will decrease to nm level.

### 6.2.2 Varnish thickness

The development of roughness of a varnish, and the ability to resolve its top and bottom interfaces by imaging, is dependent on the thickness of the varnish coating. The measurement of real paintings with OCT allows some identification of real varnish coating thickness. Figure 6.2.1.2 is typical for a lot of varnish coatings, in that the varnish layer is thinner than can be resolved in the OCT image, which means that the final thickness is  $\sim 10\mu\text{m}$  or less. This is typical of modern conservator applied coatings, such as for the glass plates in chapter 7.2. Elias et al<sup>17</sup> produced varnished painted samples and measured the thickness with OCT and confocal microscopy. The thickness of the varnish sample presented varied from several microns to  $30\mu\text{m}$ .

However, varnish coatings thicknesses are not particularly uniform. Figure 6.2.2.1 shows part of an OCT image of a 15<sup>th</sup> C painting (National Gallery Collection number NG750). The transparent layer, that can be seen between the high specular reflectance of the (varnish) surface and the scattering of the paint layer(s), is the varnish coating. The thickness of this layer is approximately 35 microns. In conclusion, real dry varnish thicknesses values are taken to lie between  $5\mu\text{m}$  and  $50\mu\text{m}$

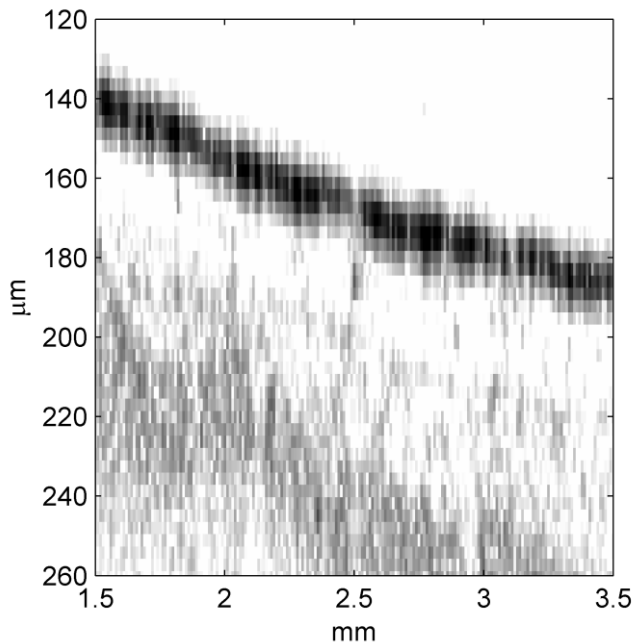


Figure 6.2.2.1  
OCT cross-section image of a  
varnish coating on 15<sup>th</sup> C. oil  
painting in the National Gallery  
collection (NG750).

## 6.3 Experimental method

### 6.3.1 Substrate preparation

For the measurements of the development of surface roughness of varnish coatings, drying on rough substrates, suitable rough substrates needed to be created. The material used for the substrate was glass due to its lack of volume scattering for OCT measurements and chemical and solute resistance to the solvents used. For the production of suitable substrate profiles, two processes were developed and used. Also considered early in the project were SU8 pillared surfaces but these were not possible to produce on a substrate big enough for applicator use as well as concerns about the solvent resistance and durability of the pillars.

Ground glass plates were produced to provide a random rough surface of *rms* roughness around 10μm. Appendix 4.2 provides the details on the production of this surface.

How glass fractures after exposure to laser cutters has previously been examined by OCT<sup>18</sup>. This fracturing of glass was developed to produce trenches of controllable depth. This development is detailed in appendix 4. OCT profilometry has been used to characterise the produced trenches. The laser cut trenches are used as a regular

(defined profile shape) rough substrate. Such surfaces have been used in previous modelling of levelling<sup>11, 12</sup>. In this work they are used for one demonstration of the difference between a high viscosity and low viscosity coating.

### 6.3.2 Application

For the experiments, the films of varnish applied onto the substrates have to be consistent. The initial thickness also has to be controllable to allow study of all desired parameters. This was done by the use of an applicator. An amount of varnish solution dependent on the film thickness to be applied (usually in the region of 1ml) was pipetted onto the surface of the ground glass substrate. A bird type applicator was then used to apply this material, as a film, over an area of the substrate. Figure 6.3.2.1 shows a bird type applicator, it consists of a narrow rectangular stainless steel surface with bevelled sides, which is suspended above and parallel to the substrate by the use of legs that sit on the substrate. The gap between the surface of the applicator and the surface of the legs is precisely adjustable. The bird type applicator is used to push the reservoir deposited varnish across the surface, while through the gap an even film is deposited behind.

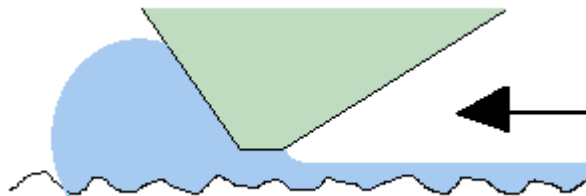


Figure 6.3.2.1  
Diagram of how bird type applicator applies coating.

The thickness of the film deposited is dependent on the applicator gap setting but not equal to it. To calibrate the real deposited thickness with the applicator gap, a solution of Regalrez and white spirit (1g of resin to 1ml of solvent) was applied to ground and smooth glass substrates with different applicator gaps. The mean initial thickness was then measured by OCT multi-interface profilometry. White spirit was chosen as the solvent for these measurements due to its relatively low volatility. The amount of evaporation between application and first measurement of the film thickness was minimal. The results of the measured initial mean thickness versus applicator gap are shown for a ground rough surface and a blank flat surface in Figure 6.3.2.2. The relationship between gap setting and applied thickness is linear.

The relationship for the rough surface does not pass through the origin. This is due to the legs of the applicator sitting on top the roughness of the substrate rather than at the mean height of the profile, increasing the mean gap. This relationship is used to calibrate all the modelling starting thickness to the corresponding experimental results. The relationship of applied thickness to applicator gap may have some dependence on factors such as the viscosity of solutions. However these were ignored due to the high volatility of toluene making measurement of initial thickness of the other solutions used impractical. The Regalrez and white spirit relationship was used for all solutions. The applied thickness of a coating (with a single applicator shape) is expected to approximate the same fraction of the applicator gap for any solution<sup>6</sup>, so the error in the estimated initial thickness will not be great.

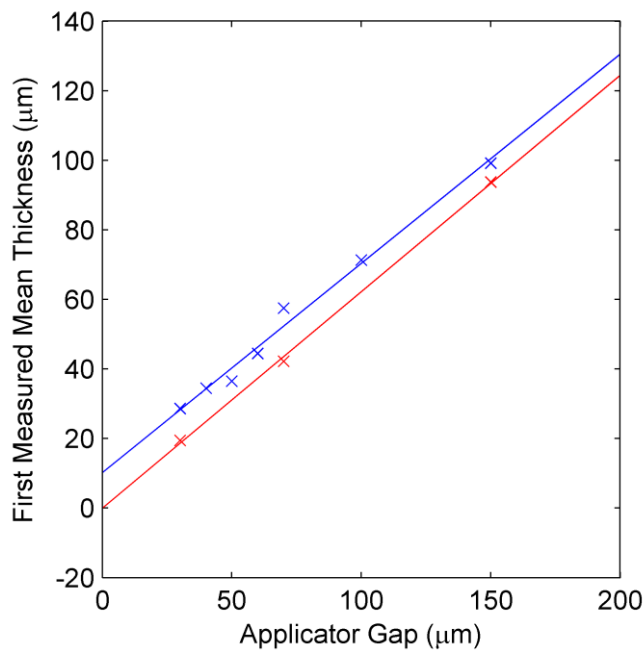


Figure 6.3.2.2  
First measured (OCT multi-interface profilometry) mean thickness vs. applicator gap. Blue – for ground substrate. Red – For smooth substrate.

### 6.3.3 OCT measurement

After the application of a varnish solution to a substrate, it was then placed under the OCT system and measured continually as the varnish dried. The OCT measurements were usually taken over a profile length of 10mm with lateral sampling spacing of 10μm. A boxcar averaging tool on the instrument was used to increase the signal to noise of the images. This worked by increasing the lateral sampling density by 5, but only returning the average of each 5 adjacent axial data

sets to the user. Only every 10<sup>th</sup> OCT image was used in the processing of the data, in order to reduce the processing time and total data volume retained. The resultant temporal sampling resolution was 10.44s, which was more than sufficient to capture the drying behaviour.

The low refractive index difference of the varnish-substrate interface ( $\Delta n \sim 0.01$ ) compared with the varnish-air interface ( $\Delta n \sim 0.5$ ) are much different. The reflection types of the two interfaces are also different, specular for the air-varnish interface and diffuse for the varnish-substrate interface. As a result the signal from the varnish-air interface is generally many orders of magnitude bigger than the varnish-substrate interface. The substrate profile can then be smaller than image artefacts from the surface. A high degree of processing was subsequently needed to ensure the substrate profile recovered was free from erroneous points.

The first stage of recovering both profiles was the designation by the user of the axial range in the OCT image within which the two interfaces were always located. The purpose of this was to exclude harmonic artefacts of the air-varnish interface and reduce the time taken by the following search routine. For each axial column, the automatic search routine then located the highest value pixel in the axial range. This in the majority of cases would correspond to the air-varnish interface. The search routine would then find the highest value pixel in the range of a set number of pixels beneath the first result and the end of the search range. This would correspond to the varnish-substrate interface. The fitting of the interface positions using Gaussian fits was then carried out and the curvature of the image corrected for.

The varnish-air interface profiles recovered at each measured time are generally free from errors, due to the large amount of signal from the surface. However, due to their low signal, the second interface measurements contain a large amount of erroneous points. At certain times during a measurement, the presence of image artefacts from the air-varnish interface obscured the correct determination of the varnish-glass interface. The raw profiles were examined to find a temporal series of data free of major artefacts. The median of each position in these temporal series were taken, which removed the majority of erroneous points.

By this stage both profiles were free of the majority of erroneous points, though some obviously erroneous points sometimes remained. To remove these, an automatic process was used to identify them in the profiles. Points lying a distance, further than is reasonably likely to be a surface feature, from the profile are easily identified. The differential of the profiles would normally fit in a certain magnitude limit. Singular points lying a distance from the profile results in higher magnitude of the differential, which was used to identify and remove the erroneous points. After the removal the points are replaced by a linear interpolation of the adjacent “good” points either side.

The last stage was to correct the clean substrate profile for refractive index effects. The varnish surface profile (absolute positions) used for this correction was the median profile, of the temporal range used for cleaning the substrate profile. The real positions of the substrate profile were calculated with the method described in chapter 3.1. The small lateral displacements due to refractive index were ignored when calculating the correlation coefficients.

## 6.4 Experimental Results

### 6.4.1 Laser cut trench substrate

Single trenches were produced along A4 plates of 2mm glass using the N5 specifications from appendix table A4.2.1. These were then used to apply films of Reglarez and toluene (3g of resin to 11ml solvent) and AYAT and toluene (1g resin to 1ml solvent) varnish coatings by applicator. The applicator gap was 100 $\mu$ m for the Reglarez solution and 225 $\mu$ m for the AYAT solution. This was to give approximately the same dry thickness for both coatings. The applicator was moved parallel to the trench. Two independent measurements were done for each varnish. Figure 6.4.1.2 shows the measured surface profiles recorded at 1min 45s intervals. The AYAT profiles (Figure 6.4.1.2 (a) and (b)) were found to start off flat before shrinking to a close resemblance of the trench profile, with only the highest spatial frequencies features removed. The low frequency aspects of the shape developed before the high frequency components. The Reglarez profiles (Figure 6.4.1.2 (c) and (d)) had a low frequency wavy profile from the initial measurement which changed little with the measurement time.

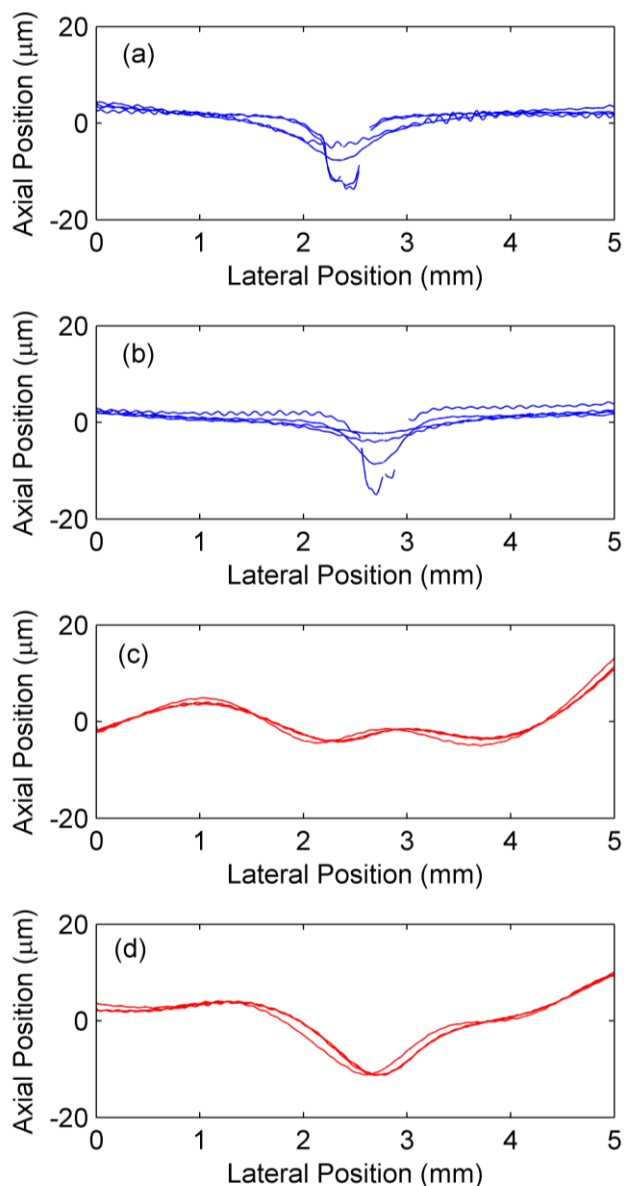


Figure 6.4.1.2  
 Measured surface profiles of drying varnish coatings applied upon laser cut trench substrates at 1min 45s intervals during drying.  
 (a) AYAT repeat 1  
 (b) AYAT repeat 2  
 (c) Regalrez repeat 1  
 (d) Regalrez repeat 2

The measurement of the two varnish films, on the trench profiled substrates, showed clearly their much different behaviour. The profile of the high viscosity AYAT coating behaves as a poor levelling coating. The starting conditions are as a flat film but as it shrinks by the evaporation of solvent, it conforms to the shape of the substrate. The limited flow within the film allows the levelling of the highest spatial frequency aspects of the substrate profile. The Regalrez coatings obtain a low frequency roughness from before the first measurements. During the measurement period the surface profile does not change significantly. The cause of this roughness is not directly related to the substrate. Levelling (shrinkage) induced roughness, which is seen in the AYAT coating, is not apparent.

## 6.4.2 Ground substrates: different resins

Here the results for varnish coatings, with different resins, drying on ground glass substrates are presented. AYAT and Reglarez 1094 solutions have been used in previous studies<sup>2</sup>, and in the previous section, to compare the effect of resin molecular weight (influence on viscosity). These two resins are at the opposite ends of the molecular weight scales for synthetic varnishes. The surface roughnesses produced by these two resins are very different. For this section the two will be again used to gain an understanding of the processes that determine roughness at the two extremes of molecular weight. Then solutions of resins with intermediate molecular weights will also be evaluated.

An AYAT toluene varnish was applied at a concentration of 3g of resin dissolved in 11ml of solvent and an applicator gap of 225 $\mu$ m. Figure 6.4.2.1 shows the results of the substrate profile and surface profiles at 10s, 3min 40s, 5min 30s and 14min measurement time for two different repeats. The development of surface profile can be viewed as a video giving a direct visualisation of how this polymer varnish shrinks to the substrate profile.

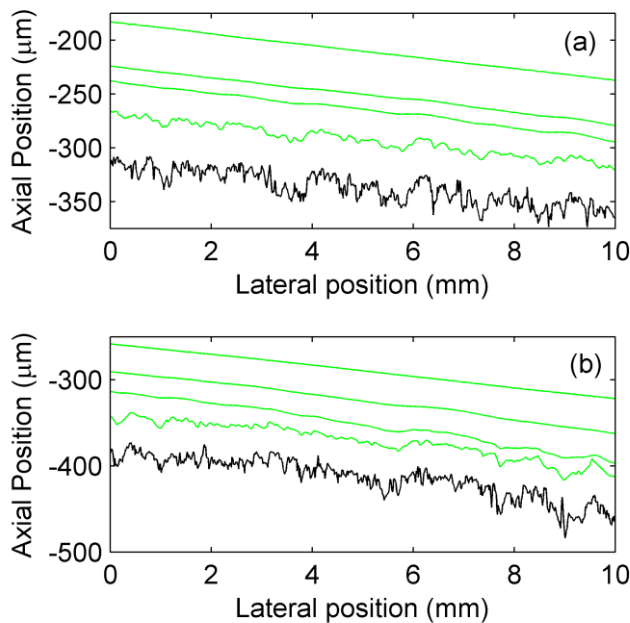


Figure 6.4.2.1  
Two independent measurements ((a) and (b)) for the OCT multi-layer profilometry results of AYAT and toluene coating on ground glass substrate. Black lines show varnish-glass interface and green lines show varnish-air interface at 10s, 3min 40s, 5min 30s and 14min into measurement.

With both interface profiles measured important statistics of the surface development can be extracted. For the two independent measurements, figure

6.4.2.2 (a) gives the *rms* roughness development. Fast Fourier transforms can be used to implement low pass and high pass filters of the surface profile. This was done to select spatial frequencies below (dotted line) and above (dashed line)  $1\text{mm}^{-1}$  and the *rms* of the resultant profile measured. It can be seen that before 5 minutes drying the low spatial frequency components cause the majority of the *rms* roughness, while the high frequency part of the surface only has an impact on the total *rms* roughness after 5 minutes. There is a large difference in the magnitude of roughness between the two measurements. This maybe related to the difference in low frequency substrate roughness of the two measurements. The difference in the high pass filtered roughness is much smaller than the difference in the low pass filtered roughness.

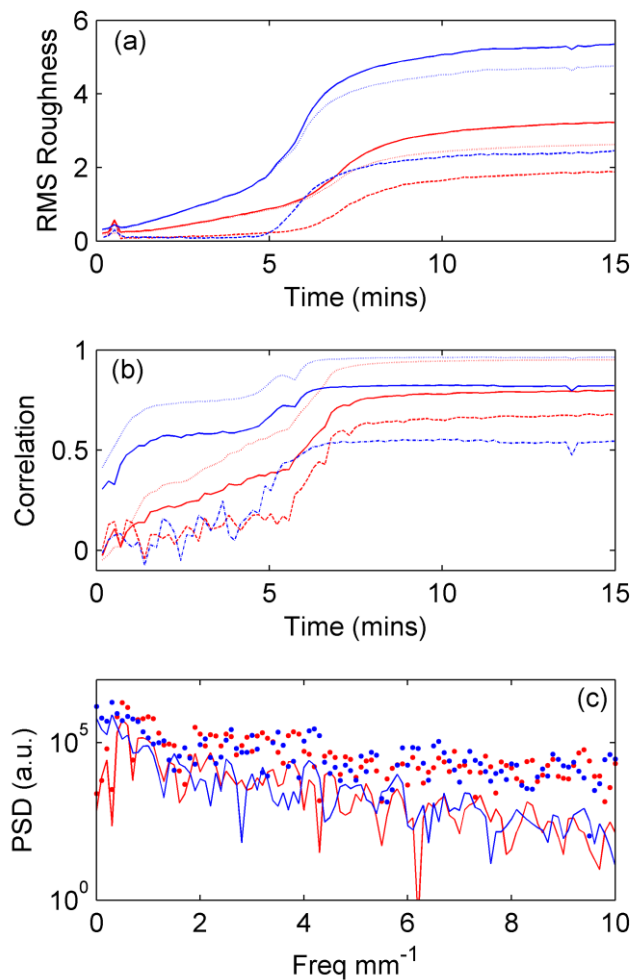


Figure 6.4.2.2  
 From the two repeats (blue and red) shown in figure 6.4.2.1. (a) RMS roughness and (b) correlation, solid line – total, dotted line low pass filtered ( $<1\text{mm}^{-1}$ ) and dashed line high pass filtered ( $>1\text{mm}^{-1}$ ). (c) Substrate (points) and coatings final (lines) PSDs.

With the ability to extract the profile of both interfaces from the OCT data, the correlation between them can be calculated. The cross correlation coefficient,  $r$  (equation 6.4.2.1) gives the normalised measure of how well two profiles (or signals),  $P$  and  $Q$ , match. The assumption has been made that the mean (and slope) have already been subtracted from the profiles. This is an important statistic as it shows and quantifies the varnish shrinking to the substrate. The cross correlation for AYAT (Figure 6.4.2.2 (b)) can be seen to follow the same trends as the *rms* roughness. The measured correlation is dependent on the measured roughness during a measurement.

$$r = \frac{\sum(P_i Q_i)}{\sqrt{\sum(P_i^2)} \sqrt{\sum(Q_i^2)}} \quad (6.4.2.1)$$

Figure 6.4.2.2 (c) shows the PSDs of the final measured surface profile and the substrate profile for the two independent measurements. The increased reduction in the amplitude of high spatial frequencies substrate roughness, compared with low spatial frequencies, by the AYAT varnish is clearly shown.

For the Regalrez and toluene varnish coating (1g Resin dissolved to 1 ml solvent, applicator gap 100µm), which was designed for the coating to be of similar dry thickness to the AYAT coating, four repeats were carried out (3 repeats after each other, the fourth repeat was carried out at a later date and with a fresh sample solution). Figure 6.4.2.3 shows the surface and substrate profiles at the same time intervals from the start of the OCT measurement as shown for AYAT (10s, 3min 40s, 5min 30s, 14min.) for four independent measurements. There is a stark difference with the results for AYAT. Due to the higher starting concentration the observed changing in thickness is expected to be smaller, though the final thickness change is still much lower than if the measurement was of an ideal solution measured from the start of drying. With a one to one ratio of resin and solvent, an ideal solution would lose half its volume with the evaporation of all the solvent. It is clearly shown that the overall surface roughness does not develop like AYAT, the majority is of extremely low spatial frequency (compared with scales that will cause diffuse reflection) and develops at application or soon after.

Figure 6.4.2.4 (a) shows the development of *rms* roughnesses for the four independent measurements. The low spatial frequency roughness has developed from the start of the measurement but the surface is still in flux up to 2.5 minutes in the measurement. The component of roughness above  $1\text{mm}^{-1}$  spatial frequency is of negligible contribution to the total *rms* roughness. The correlation results (Figure 6.4.2.4 (b)) closely match the *rms* roughness results, the high spatial frequency correlation measured is not above noise, while low spatial frequency measurements are consistent in each measurement. The value of the low frequency experimental correlation coefficients between the measurements is not consistent between measurements and the values are much lower than for AYAT. The low frequency surface profiles of Regalrez are highly independent of substrate but the profile remains the same within one measurement, hence the correlation is a random value for a measurement but remains the same for that measurement.

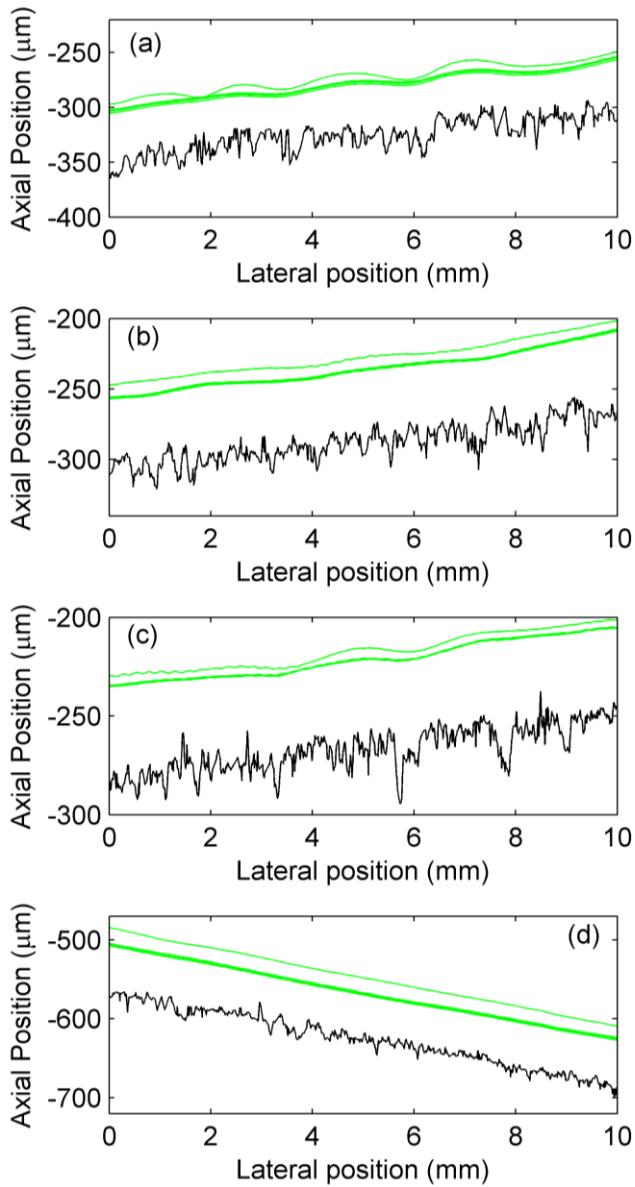


Figure 6.4.2.3  
 Four repeats (a)-(d) for the OCT multi-layer profilometry results of Regalrez and toluene coating on ground glass substrate. Black lines show varnish-glass interface and green lines show varnish-air interface at 10s, 3min 40s, 5min 30s and 14min into the measurement.

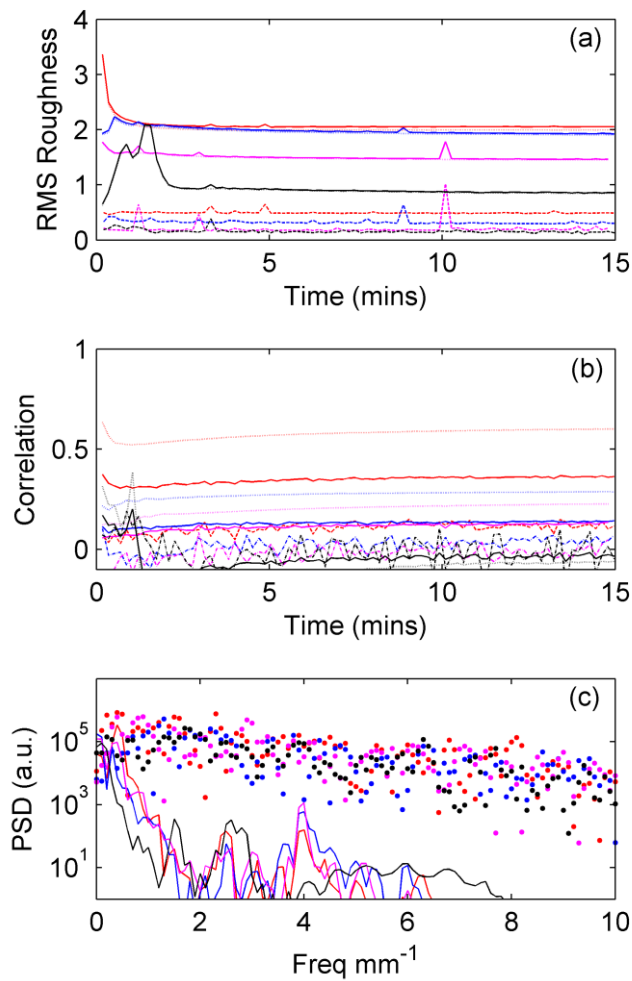


Figure 6.4.2.4  
 For the four independent measurements (blue, red, magenta and black(new sample)) shown in figure 6.4.2.3.  
 (a) RMS roughness and (b) correlation, solid line – total, dotted line low pass filtered ( $<1\text{mm}^{-1}$ ) and dashed line high pass filtered ( $>1\text{mm}^{-1}$ ).  
 (c) Substrate (points) and coatings final (lines) PSDs.

Figure 6.4.2.4 (c) shows the PSDs for the substrate and final surface profile, of the four independent measurements. The results were consistent for all the measurements. There was only significant amplitude for the extremely low spatial frequencies for the varnish roughness. The measured amplitude beyond  $2\text{mm}^{-1}$ , in the surface PSDs, is the vibrational noise in the measured profiles.

To determine whether the roughness developed by Regalrez is an independent effect from the substrate, “blank” measurements were carried out on un-ground (smooth/flat) glass substrates. These were carried out with the initial three repeats. These were also carried out with an AYAT varnish (1.8491g of resin to 10ml of solvent, applicator gap of  $100\mu\text{m}$ ) to give the same applied thickness and viscosity, for comparison. Figure 6.4.2.5 (a) shows the PSD of the final surface profile of these “blanks”. The PSD of Regalrez is similar in shape to the rough substrate

method. The shape of the development of Regalrez's surface *rms* roughness (Figure 6.4.2.5 (b)) is also similar. The magnitude of roughness developed is the lower than for the rough substrate. The PSD of the “blank” AYAT coatings is of similar shape to Regalrez, but has significantly lower low frequency amplitude. The *rms* roughness is much lower than Regalrez, but does show significant fluctuation and increased values within the first three minutes.

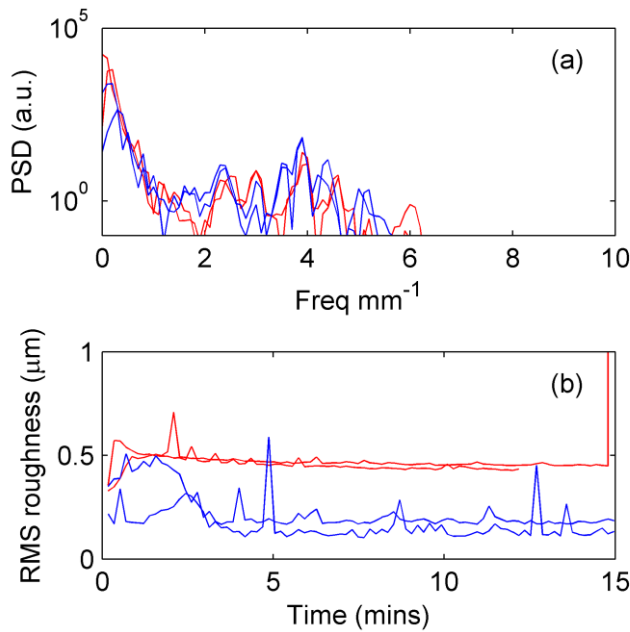


Figure 6.4.2.5  
 (a) PSDs of AYAT (blue) and Regalrez (red) coatings applied to a smooth glass substrate.  
 (b) The development of *rms* roughness for the coatings.

With the formation of low frequency roughness, for the Regalrez layers, having been shown to be caused by a mechanism independent of substrate roughness, though it is exacerbated by it, a probable causes can be identified. The low spatial frequency of the roughness is typical of the benard-marangoni effect<sup>19</sup>. An alternative cause maybe uneven initial distribution by the applicator.

Previous work<sup>2</sup>, which measured the roughness of Regalrez coatings applied to ground glass substrates, did not report this low frequency roughness. The reason for this was that the profile length used for the measurements was only 2mm, so is not sensitive to roughness of spatial periods longer than this. Figure 6.4.2.6 shows a 10mm surface profile, measured with OCT, of a donated Regalrez sample from their study. This profile shows the same low frequency waviness as has dominated the Regalrez results in this study, the high frequency noise of the profile was due to the dirt and damage to the old sample.

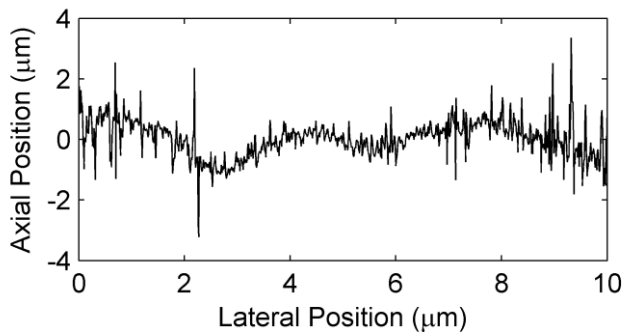


Figure 6.4.2.6  
Measured 10mm surface  
profile for Regalrez film  
sample used in a previous<sup>2</sup>  
study.

AYAT and Regalrez form the high and low ends of the molecular weight spectrum of varnishes. To fill in the molecular weights between these two resins, three more different varnish resins were chosen. Paraloid B72 (polymer with lower molecular weight and viscosity than AYAT), Laropal A81 (Highest viscosity of the low molecular weight resins measured in chapter 5.2.2) and Dammar (a natural resin). The experiments used the same parameters as the Regalrez measurements, the resins were all dissolved in toluene at a ratio of 1 gram to 1 ml of solvent. The solutions were then applied to the ground glass substrate with the applicator with a gap of 100 $\mu$ m, and then measured with OCT. A single measurement was done for each of the three new resins.

Figure 6.4.2.7 shows the final surface profile of the three resins, plus Regalrez 1094. The surface of the polymer, Paraloid B72, is seen to be much rougher than the low molecular weight resins. Its surface profile is similar to AYAT (the other polymer resin previously measured). The surface profiles of Laropal A81 and Dammar look very similar, with lower high frequency roughness than Paraloid B72. The surface profile of Regalrez 1094 coating is the smoothest. These results can be related to the viscosity of the resins measured in chapter 5.2.2. Regalrez 1094 was significantly less viscous than the other low molecular weight resins, this has led to it giving the smoothest profile. Paraloid B72 is much more viscous than the low molecular weight resins, hence surface levelling is much less giving the rougher profile. Figure 6.4.2.8 shows the PSDs of these results. This again shows the points picked from the surface profiles, the highest viscosity Paraloid B72 is the worst leveller, Laropal A81 and dammar, with similar viscosities show similar results and the lowest viscosity resin, Regalrez 1094, has the best surface levelling.

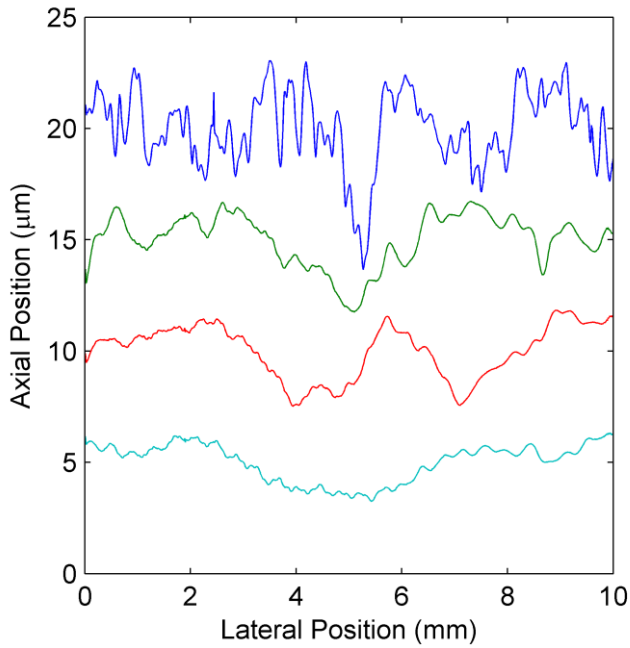


Figure 6.4.2.7  
Final surface profiles, measured with OCT, for Paraloid B72 (blue), Laropal A81 (Green), Dammar (Red) and Regalrez 1094 (Cyan) coatings applied to ground glass substrate. Displayed level and displaced from each other for comparison.

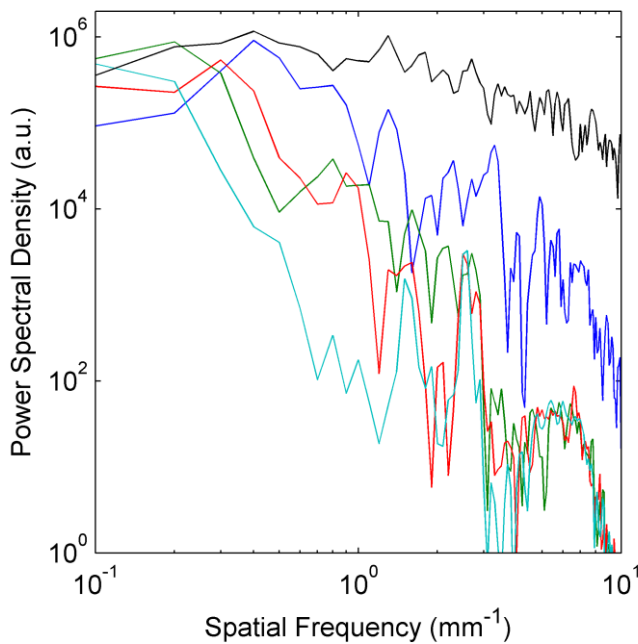


Figure 6.4.2.8  
Final PSDs, of the surface profiles (figure 6.4.2.7), of Paraloid B72 (blue), Laropal A81 (Green), Dammar (Red) and Regalrez 1094 (Cyan) coatings applied to ground glass substrate. The black line shows the mean PSD of the substrate profiles for all the measurements.

Figure 6.4.2.9 (a) shows the development of surface roughness for the four measurements. The development of the surface roughness of the polymer Paraloid B72 matches the results obtained with the other polymer AYAT. The roughness starts at a low value and develops through the drying process as it shrinks to the substrate. The low molecular weight resins behave in the same manner as Regalrez 1094, the roughness develops during application or between application and first measurement. Figure 6.4.2.9 (b) shows the development of correlation of the surface

profile with the substrate profile. The correlation of Paraloid B27 follows the development of *rms* roughness and the final surface roughness is highly correlated with the substrate. The magnitude of the correlation of the low molecular weight resins will not be accurate due to the random (but consistent for on profile) nature of the low frequency roughness. The shape of the low molecular weight correlation function is consistent though (apart from the dynamic period of the Regalrez 1094 sample), the correlation shows an increase during drying. This shows that the coatings are shrinking to the substrate.

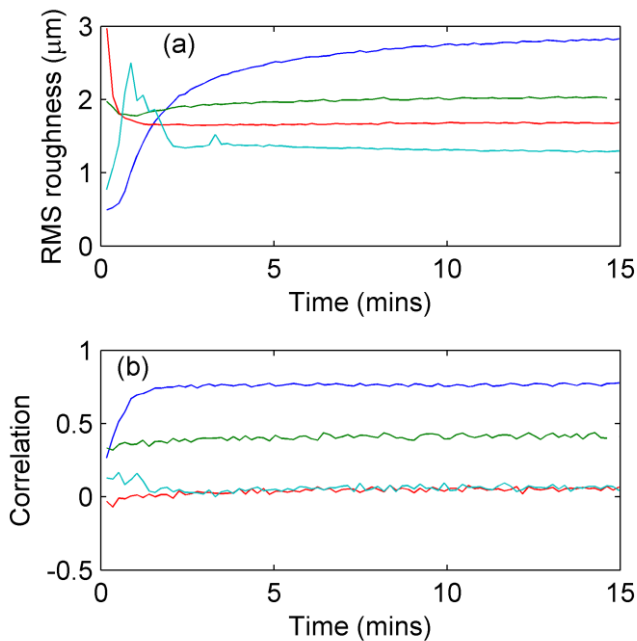


Figure 6.4.2.9  
 (a) Measured development, during drying, of total rms roughness of Paraloid B72 (blue), Laropal A81 (Green), Dammar (Red) and Regalrez 1094 (Cyan) coatings applied to ground glass substrate.  
 (b) The measured correlation with the substrate profile for the above measurements.

Figure 6.4.2.10 shows the development of *rms* roughness and correlation for spatial frequencies less than  $1\text{mm}^{-1}$ . These behave similar for the total values, though there are some differences. The low frequency roughness of Paraloid is highly correlated to the substrate. This shows that the sample roughness is inherited from the substrate, rather than from the unrelated (to the substrate) process that dominates the low frequency roughness of low molecular weight resins. The result for Laropal A81 shows high correlation, though this does not develop during drying to the same extent as Paraloid. The accuracy of this high value is unknown without repeat measurements and likely to be a fluke.

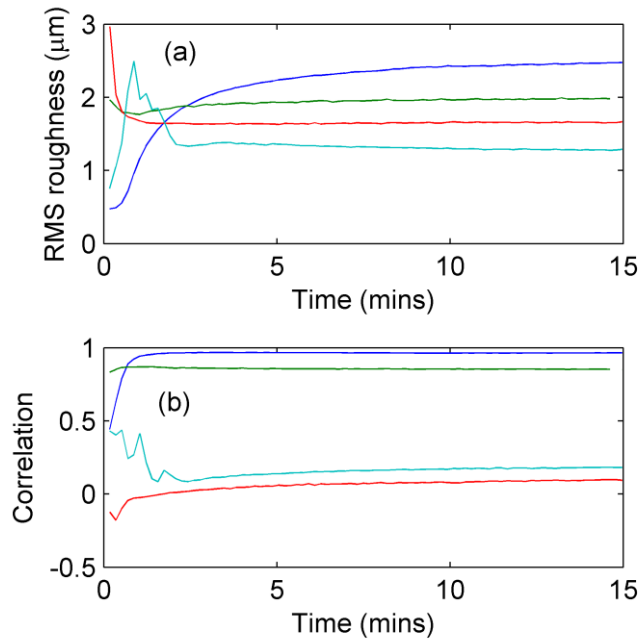


Figure 6.4.2.10  
 (a) Measured development, during drying, of low pass spatial frequency filtered ( $<1\text{mm}^{-1}$ ) rms roughness of Paraloid B72 (blue), Laropal A81 (Green), Dammar (Red) and Regalrez 1094 (Cyan) coatings applied to ground glass substrate.  
 (b) The measured correlation with the substrate profile for the above measurements.

Figure 6.4.2.11 shows the development of *rms* roughness and correlation for spatial frequencies greater than  $1\text{mm}^{-1}$ . These results are expected to be dominated by surface levelling roughness. All the samples start with (vibrational) noise floor roughness and near zero correlation. The roughness and correlation then develop as the samples dry. There is a clear order of magnitude to this surface roughness and correlation, developed by levelling, for the four samples. Paraloid is clearly the worst levelling, but for the low molecular weight resins there is an order of Laropal, Dammar and Regalrez 1094. This matches the rheology (and molecular weight) trends of the resin, the more viscous the samples (higher molecular weight) the poorer the levelling.

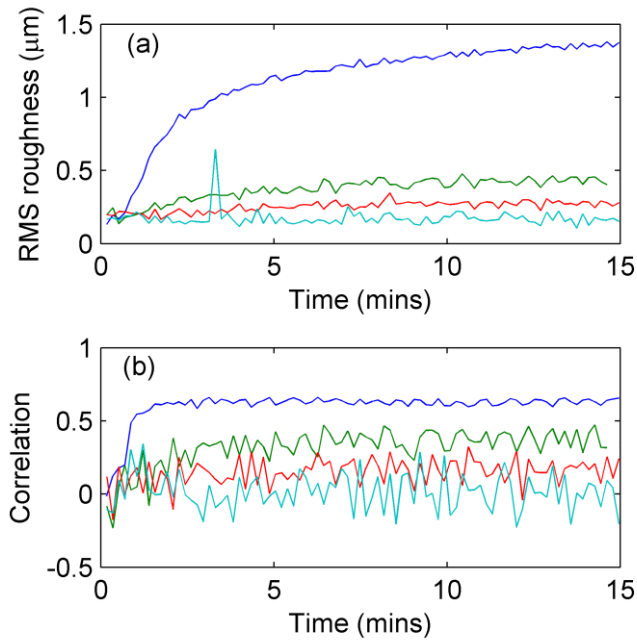


Figure 6.4.2.11  
 (a) Measured development, during drying, of high pass spatial frequency filtered ( $>1\text{mm}^{-1}$ ) rms roughness of Paraloid B72 (blue), Laropal A81 (Green), Dammar (Red) and Regalrez 1094 (Cyan) coatings applied to ground glass substrate.  
 (b) The measured correlation with the substrate profile for the above measurements.

### 6.4.3 Ground substrates: different thicknesses (dry and initial)

The next part of the work was to look at the dependence of surface roughness on the thickness of the applied film of varnish. To carry out this work, solutions of Regalrez 1094 and white spirit were used. White spirit was chosen as the solvent for two main reasons. The first reason was, on health and safety grounds, with the application of multiple films in an open laboratory environment, white spirit is less toxic than toluene. The second being that white spirit is a solvent that is more likely to be used by conservators. White spirit and Regalrez has some difference in the viscosity - concentration function compared to toluene and Regalrez solutions, though this is not the largest difference (by magnitude) between the two. The volatility between the two solvents is a much greater difference. White spirit evaporates approximately one order of magnitude slower than toluene (chapter 4.5.2 and section 6.5.2). As has been shown in the previous section the surface roughness due to substrate roughness is likely to be negligible compared to other effects for Regalrez. The increased drying time of white spirit is likely to further reduce the amplitude of the levelling roughness, which will make its detection and measurement more difficult. It was hoped that by examining thinner coating thicknesses this problem could be negated. Also it was hoped that the critical thickness may be identified, below which levelling dominates the total *rms* roughness.

The first section of this work was to examine the effect of the final thickness of a varnish coating. This thickness was controlled by applying the same concentration (1g of resin 1 ml of solvent) with different applicator gaps (30, 40, 50, 60, 70, 80, 100 and 150 $\mu\text{m}$ ). The roughnesses of the varnish coatings were measured 1 month and 5 months after application. OCT was used to measure 6 independent surface profiles on each sample (10mm and 1000 lateral points). The mean and standard deviation of the total *rms* roughness and the *rms* roughness after applying a high pass filter ( $>1\text{ mm}^{-1}$ ) are shown in figure 6.4.3.1. The total *rms* roughness is almost independent of film thickness. The effect that causes the very low frequency roughness dominates, which ensures the total *rms* roughness stays high independent of thickness. However, below 50 $\mu\text{m}$  the high frequency *rms* roughness increased. At these lower thicknesses it is expected that levelling will be more important to the surface roughness.

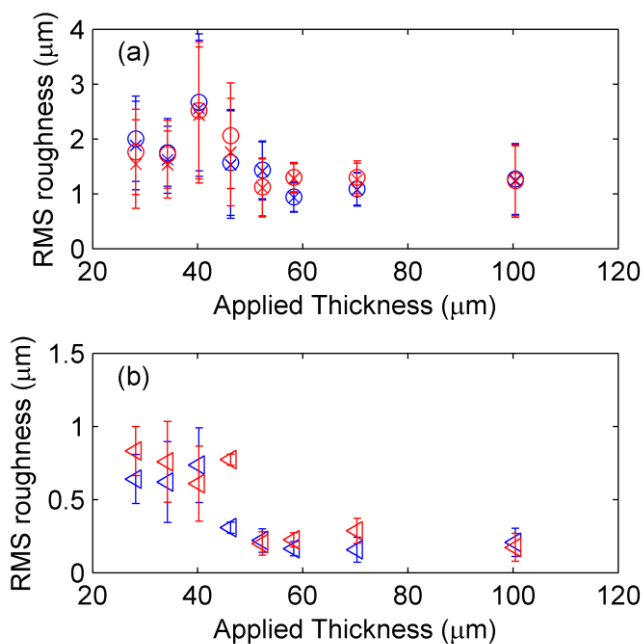


Figure 6.4.3.1  
 (a) Total and low frequency ( $<1\text{mm}^{-1}$ ) *rms* roughness for ground glass plates of different applied thicknesses of Regalrez and white spirit varnish. Measure 1 (blue) and 5 (red) months after application.  
 (b) The corresponding high frequency roughness measurements.

After the application of each coating, multi-interface OCT profilometry was used to measure them as they dried. The *rms* roughness (Figure 6.4.3.2(a)) is seen to fluctuate during the drying process. This is seen to the greatest effect in the thicker samples. The same effect is also seen in the film thickness measurements (Figure 6.4.3.2(b)) for the two thickest samples (100 and 150 $\mu\text{m}$ ). These samples increase in thickness at times during the drying process. This can be explained by the

movement of varnish around the film as it dries, as the effects of this were noted visually in the unevenness (of the gloss) of the thicker samples. The cause of the varnish movement was not identified, though maybe a result of Benard-Marangoni effects.

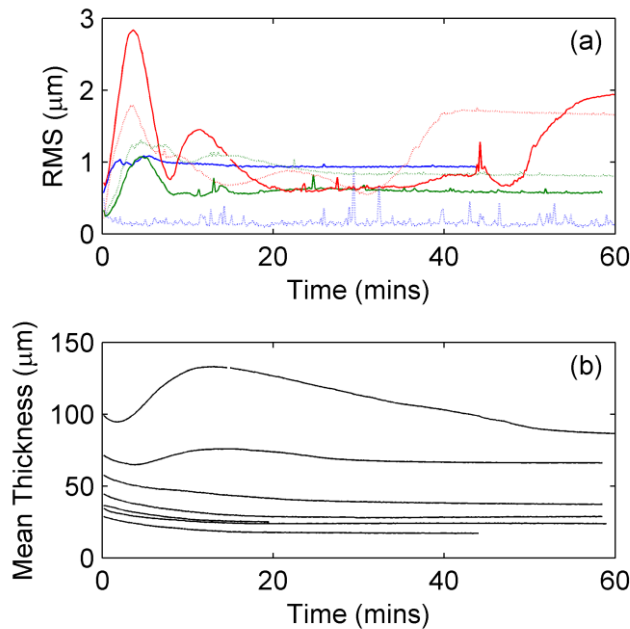


Figure 6.4.3.2

(a) Experimentally measured development of rms roughness for regalrez and white spirit coatings applied with 30 (blue), 70 (green) and 150 (red)  $\mu\text{m}$  applicator gaps. Solid lines for ground and dotted lines for smooth substrates.

(b) Measured mean thickness development for all Regalrez and white spirit samples.

To confirm the independence of the assumed Benard-Marangoni effects from the substrate, repeats of these measurements were carried out on smooth glass substrates with applicator gaps of 30, 70 and 150 $\mu\text{m}$ . The behaviour of the *rms* roughness (dotted line in Figure 6.4.3.2 (a)) for 70 and 150 $\mu\text{m}$  gaps was similar to the rough substrate with little difference. For the smallest gap however, the resultant surface profile was smooth when there is no roughness, in contrast to the rough substrate. For the thinner coatings the roughness was dependent on substrate roughness.

Figure 6.4.3.3 shows the measured correlation coefficients, for the thinner samples, of the surface and substrate profiles with the measurement time. The value of the correlation varied but a consistent shape is seen. This matches the previous results for the Regalrez and toluene coating (previous figure 6.4.2.4), the quasi-random surface profiles give consistent but random values for a single measurement. Small changes in the surface profile, during drying, lead to the shape of the correlation in each sample. These changes must come from the same cause in all measurements, and the change must be related to the substrate profile. Hence the shape in the

correlation is, most likely, from the levelling component of roughness. There is an initial peak followed by a minima then increased again, giving a distinctive tick shape. This is could be due to the relative ratio between evaporation (formation of correlated roughness) and viscosity (levelling of the roughness) at each time during the process. Initially the evaporation is stronger leading to the correlation peak. The levelling then relatively increases as evaporation falls leading to the minima. Finally, the increase in viscosity catches up with the decrease in evaporation again, leading to the fresh increase in correlation. The initial peak appears displaced to later times as thickness increases, this is expected as the thicker samples take longer to dry. Displacement of the minima, with thickness, does not seem as well correlated however.

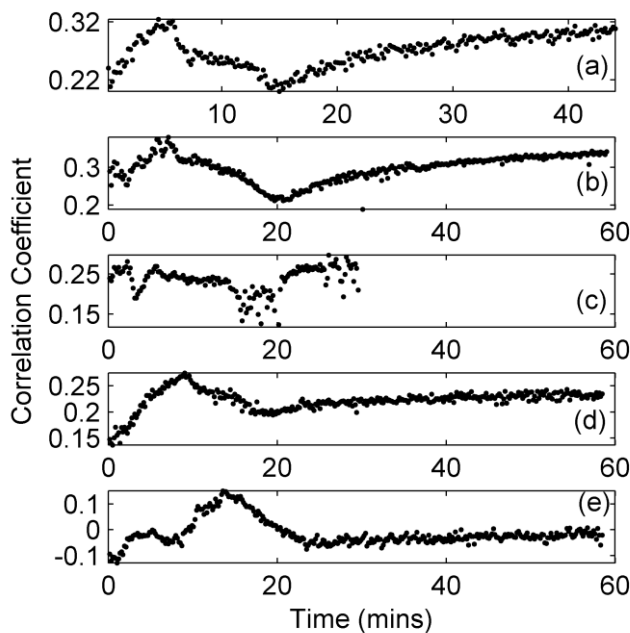


Figure 6.4.3.3  
Measured development of correlation coefficient for regalrez and white spirit coatings applied with (a) 30, (b) 40, (c) 50, (d) 60 and (e) 70  $\mu\text{m}$  applicator gaps.

In addition to dependence on final thickness of roughness, by adjusting the concentration along with the applicator gap the final thickness can be kept the same while changing the initial thickness. For the 50 $\mu\text{m}$  gap measurement from the previous thickness experiments, two additional experiments were carried out with 90 $\mu\text{m}$  and 120 $\mu\text{m}$  applicator gaps. The *rms* roughnesses for the three measurements were measured after 1 month of drying (Figure 6.4.3.4). For the total *rms* roughness there was no evidence for any trend beyond the standard deviation of the measurements. However, after the removal of the low frequency roughness by a high pass filter ( $>1\text{mm}^{-1}$ ), the *rms* roughness shows a significant increase for the

highest starting thickness. In addition, by examining the high pass filtered correlation measurements during drying (Figure 6.4.3.5) the same shape seen in the previous thickness measurements before is identified. With the displacement of the initial concentration at the start of the measurements, a displacement of the positions of the features, to later times with increased thickness, are expected for the measurements. This trend is not clearly identified by these measurements.

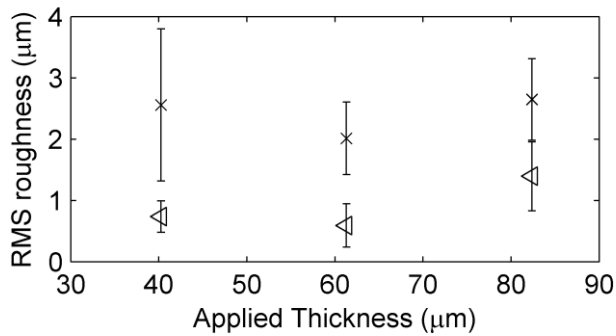


Figure 6.4.3.4  
Measured dry *rms* roughness (x – total, triangle – highpass filtered) of different applied thickness but similar dry thickness.

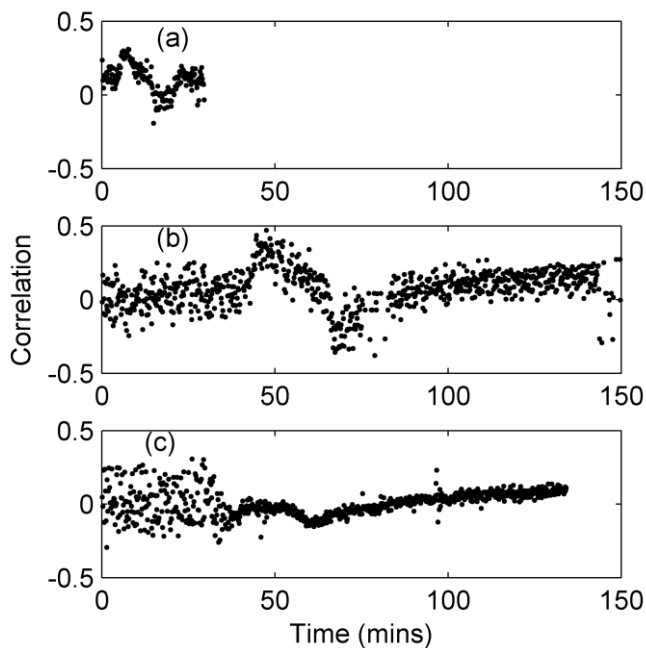


Figure 6.4.3.5  
Measured correlation (after high pass  $>1\text{mm}^{-1}$  filtering) development for the three applied thicknesses of (a)  $\sim 40\mu\text{m}$ , (b)  $\sim 60\mu\text{m}$  and (c)  $\sim 80\mu\text{m}$ . The dry thicknesses are approximately the same.

#### 6.4.4 Discussion

So far in this chapter the surface roughness development has been experimentally measured for different resins and starting and finishing thicknesses. These results can be linked with the intuitive relationships expected from levelling. Two separate causes of surface roughness were identified in these experimental results. The first of them is the levelling of substrate roughness by a shrinking (drying) varnish film.

This is a source of light scattering roughness, and is a key part of this project. The second source produces low frequency roughness of spatial period that is greater than would induce significant non-specular reflection. This is not of significant interest to this project, though is of interest in other coating areas where “orange peel” surface defects are a problem<sup>20</sup>. The cause of this low frequency roughness in these measurements is likely to be due to the Benard-Marangoni effect, though uneven application has not been ruled out. Strong identification of the cause, of this low frequency roughness, is not important to this project as the effects on the measurements have been determined experimentally.

## 6.5 Modelling the formation of roughness

Though the experimental results have been linked intuitively with the shrinking and levelling of the varnish coating, as it dries, how close the surface profiles match the theory has not been tested. To evaluate this, the experimental profiles need to be compared to profiles modelled from the theory.

### 6.5.1 Numerical differential lubrication approximation

Equation 6.1.7 predicts the levelling flow of a liquid film with a textured surface. This will be used for numerical modelling of a varnish film surface profile, as it dries. The formation of this roughness, as the varnish coating dries, needs to be included in the model. It is adapted by the addition of a drying term into the equation<sup>12</sup>, which changes the height of the varnish columns (as well as the columns concentration). The volume drying rate in units of  $\mu\text{m s}^{-1}$  is calculated as an empirical function of concentration,  $E(C)$  (where  $C$  is concentration (mass or volume)), the measurements of which are described in section 6.5.2 and chapter 4.5.2. The viscosity can also be inputted as an empirical function of concentration, these empirical relationships have been measured in chapter 4.

The equation is modelled numerically in discrete time steps,

$$\Delta h = \left\{ \frac{1}{3} \frac{\gamma}{\eta(C(x))} \frac{\Delta}{\Delta x} \left[ \left( \frac{\Delta^3 \Phi(x)}{\Delta x^3} \right) h(x)^3 \right] + E(C(x)) \right\} \Delta t . \quad (6.5.1)$$

After each time step the concentration for each lateral point is recalculated. The modelling was carried out using the measured substrate profile from the corresponding multi-interface OCT profiles. The modelled initial surface profile was flat. The initial mean thickness of the film mean was taken from the calibrated application thickness (section 6.3.2). The concentration for all points was uniform and set to the applied concentration.

This model was run in Matlab (on a desktop PC with Intel Xeon quad core 2.5Ghz (E5420) processor and 3GB RAM). The main computational problem was keeping  $\Delta t$  small enough to keep the routine stable while also reducing the run times of the models. The run time for one model typically took one night.

To reduce the run time of the model a couple of steps were carried out. The threshold of stability as a function of time and lateral spacing is expected to scale as  $\Delta t \sim (\Delta x)^4$ <sup>11</sup>. So the lateral spacing of the substrate profile was reduced by a factor 5 (averaged consecutive 5 points). Hence, the high frequency cut off of the models is  $10\text{mm}^{-1}$  (Nyquist). The second method was to compute equation 6.2.7 in two parts. The fine time spacing was not required for the evaporation, concentration and viscosity calculations, so this was done separately with  $N=10^5$  times coarser sampling. The resultant flow diagram of the model is shown in figure 6.5.1. To constrain the behaviour of the model at each end of the profile, two points were added to the substrate profile at either end with the same value as the first or last point. The levelling of these points can not be calculated but, with the addition of these two points, the slope of the surface profile is forced to be flat at its ends, rather than an arbitrary slope.

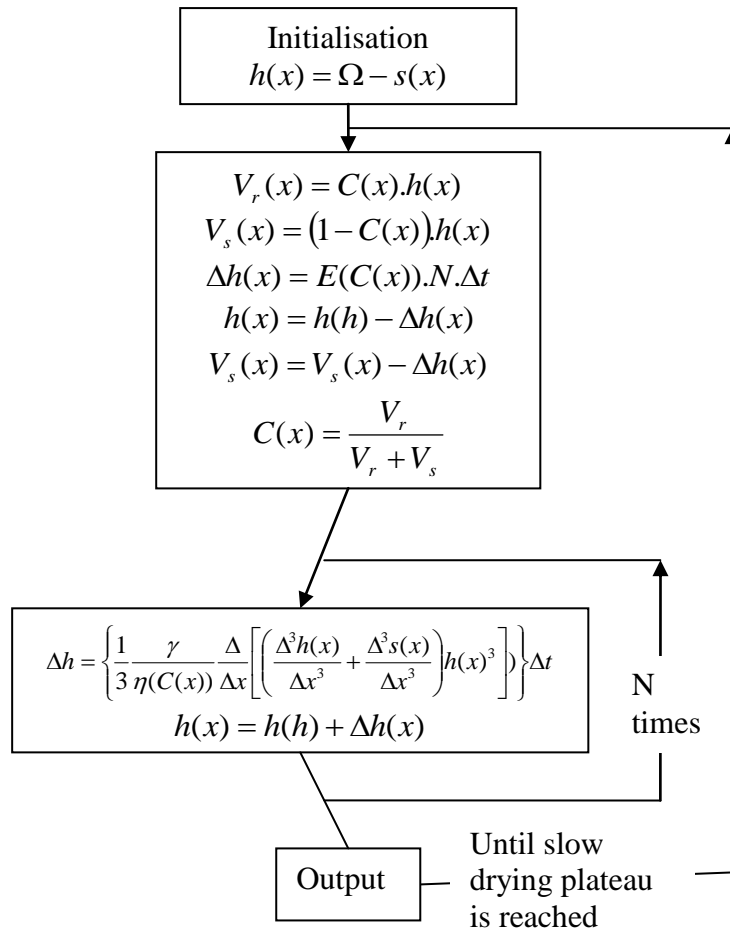


Figure 6.5.1  
Flow chart of program to model the development of the surface profile of a solvent varnish coating drying upon a known substrate profile.  $\Omega$  is the calibrated mean thickness.  $s(x)$  is the substrate profile. Note that surface profile  $\Phi(x) = h(x) + s(x)$ .  $V_r(x)$  is height (volume) fraction of resin for each varnish column.  $V_s(x)$  is height (volume) fraction of resin for each varnish column.  $C(x)$  is volume concentration (ideal solution assumed).

## 6.5.2 Evaporation function measurement

The drying rate of a varnish film is determined by three processes (see chapter 1.3.4 for more detailed explanation). These processes are the transport of the solvent through the varnish to the surface, the evaporation of the solvent from the surface to the atmosphere and finally the removal of the solvent from the vicinity by transport in the immediate atmosphere. Rather than modelling this process, the drying rate was experimentally measured for input into the drying model. These drying rates were measured for films of the same dimensions and in similar conditions. This was due to the drying rate dependence on these variables.

The welled drying data (chapter 4.5.2) was used for comparison in some modelling. However, the welled drying setup with its large thickness was not representative of the applicator drying system.

The large (6mm A4 sized) glass plates used for the multi-layer OCT measurements were too heavy for the sensitive mass balance. Small pieces of 2mm plate glass were used instead, which were prepared in the same way as the larger plates by grinding with sand. Small amounts (200 $\mu$ l for Regalrez and 400 $\mu$ l for AYAT) of the varnish solutions were applied by applicator with the appropriate gap setting and then the plate piece placed upon the mass balance. The data from the mass balance was logged automatically via desktop PC with a simple application written in Labview. The measurements were taken at 1 second intervals.

The empirical function required from the measurement was the rate of change of thickness (profile height/position) as a function of concentration. To achieve an empirical relationship, analytical functions were fitted to the raw mass data. Different functions were fitted for AYAT and regalrez, they were chosen by their ability to be visibly similar to the raw data and match the desired constraints. The constraints were that the function can be piecewise but should be monotonic and continuous. Also its first differential should be continuous and monotonic.

First the measurement of the glass plate before the application of the varnish solution is carried out. Figure 6.5.2.1 (a) shows the mass measurement of a glass piece being placed and removed from the mass balance four times. If care is not taken in placing the glass piece on the mass balance delicately, the response of the mass balance is recorded as it recoils. This is shown in the first two measurements in figure 6.5.2.1 (a). The erroneous increase in mass in early measurements is undesirable. The last two measurements, where more care seemed to be taken on placing the sample on the mass balance, do not show this effect. Measurements of the mass of the glass pieces were taken in this way before each measurement. This mass was subtracted from the raw drying mass to give the varnish mass.

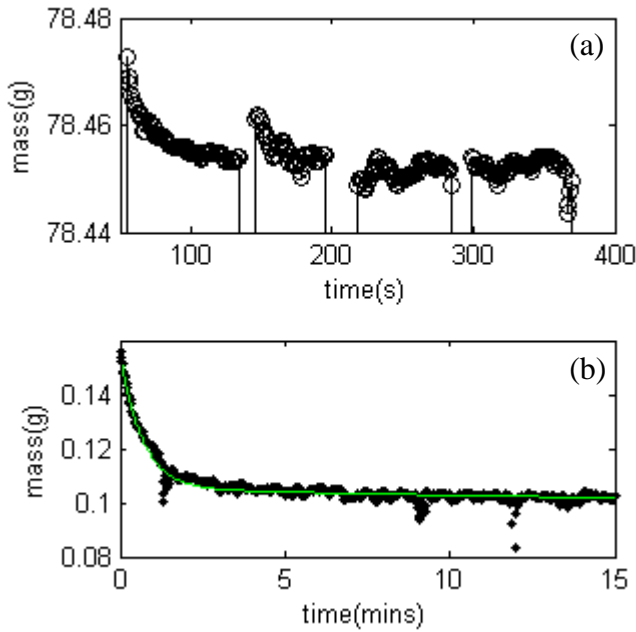


Figure 6.5.2.1  
 (a) Mass measured when repeatedly placing and removing glass plate on mass balance.  
 (b) Measured mass and fitted function (equation 6.5.2.1) of Regalrez toluene varnish coating upon ground glass plate.

The varnish was applied to the glass piece with the applicator. Figure 6.5.2.1 (b) shows the varnish mass results for a Regalrez toluene varnish (1g of resin dissolved in 1 ml of solvent) measured. The analytical function fitted to this data is given by

$$M(t) = K_1 \exp[K_2 t] + (A - K_1 - K_4) \exp[K_3 t] + K_4 \quad (6.5.2.1)$$

where  $A$  is the first experimental mass value,  $K_i$  are the fitted values and  $t$  is time. This is entirely an empirical function, to provide data smoothing and interpolation, with no physical basis. The quality of the fit is reasonable, but distortions of the data from the fit are apparent. Given the error from other sources, the quality of the fit was deemed sufficiently accurate.

With mass as a function of time, the mass concentration, and drying rate can be derived from this, also as functions of time. The mass concentration as a function of time is given by

$$C_m(t) = \frac{M_0 C_0}{M(t)} \quad (6.5.2.2)$$

where  $M_0$  is the applied mass of varnish and  $C_0$  is the application concentration. The application concentration is known, however the applied mass is uncertain as significant evaporation happens between application and the first mass measurement.

To compensate for this, the time between application and first measurement was measured with a stop watch. From the first few mass points the application mass was calculated by linear extrapolation (Figure 6.5.2.2 (a)). Figure 6.5.2.2 (b) shows the concentration calculated independently from the raw and fitted mass.

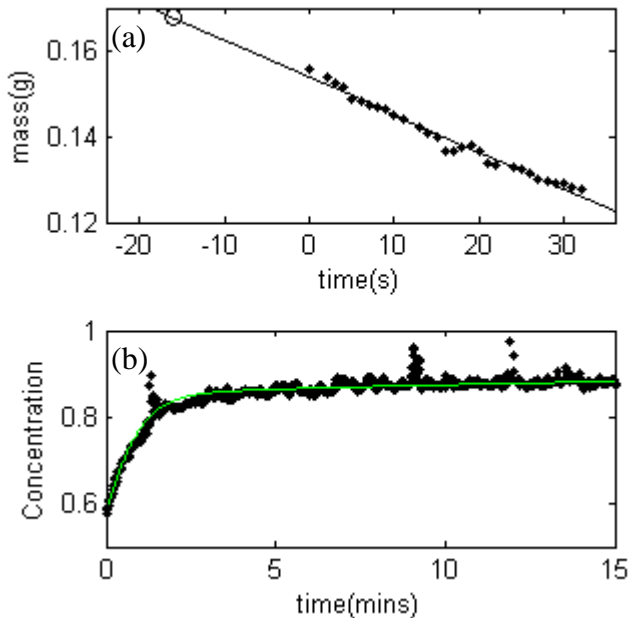


Figure 6.5.2.2  
 (a) Early measured mass from Fig 6.5.2.1(b) and linear extrapolation to recover applied mass.  
 (b) Concentration vs. time calculated from mass data points (points) and mass fit (line).

The rate of evaporation can be calculated as the differential of the fitted mass function, this is then converted into rate of change of thickness using the density of the solvent. The two functions are plotted against each other and interpolation between the points is used to create the final function. The resulting functions from the four measurements of Regalrez and toluene varnish are shown in figure 6.5.2.3 (a). The spread of the lines show the high error of the measurement. Figure 6.5.2.3 (a) also includes the evaporation function obtained from the welled sample data (chapter 4.5.2). This much thicker and more enclosed sample is seen to have a lower rate of evaporation. An alternative method of producing a suitable evaporation function is by averaging of the data points and calculating it directly. Here this method will be used to show the accuracy of the fitted functions. The fitted function can be seen to show some distortion from the values obtained (circles in figure 6.5.2.3 (a)) but these differences are small compared to between the independent measurements. The largest source of error is the estimation of the starting mass at application. This error is common to both methods. To evaluate whether the fitted method is distorted at low evaporation rates the two methods can be compared on a

logarithmic scaled graph (figure 6.5.2.3 (b)). Both methods show excellent agreement at low evaporation rates, there is no distortion of the fitted function here. Again the importance of the common error (initial starting mass) in the measurements is highlighted.

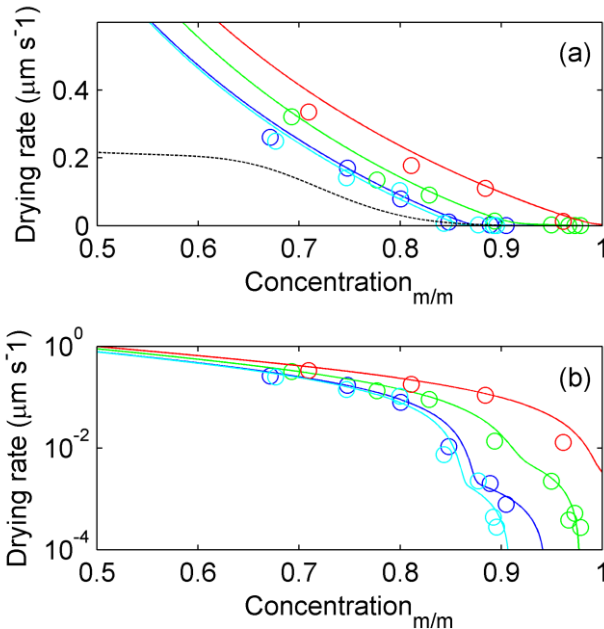


Figure 6.5.2.3  
 (a) Measured evaporation function for 4 repeats of the method (coloured lines) for Regalrez and toluene. Also shown is the function obtained from a well-drying method (black dashed line). The results obtained from averaging the data point and using them directly is shown by the circles.  
 (b) The function and averaging methods shown on a logarithmic scale.

Figure 6.5.2.4 shows the results from the same methods for Regalrez and white spirit solutions. The low volatility of white spirit reduced the error in the initial mass extrapolation, the resulting evaporating functions are less scattered. The disagreement between the fitting and averaging is significant at high evaporation rates in this case. Though, again both methods show excellent agreement at low evaporation rates.

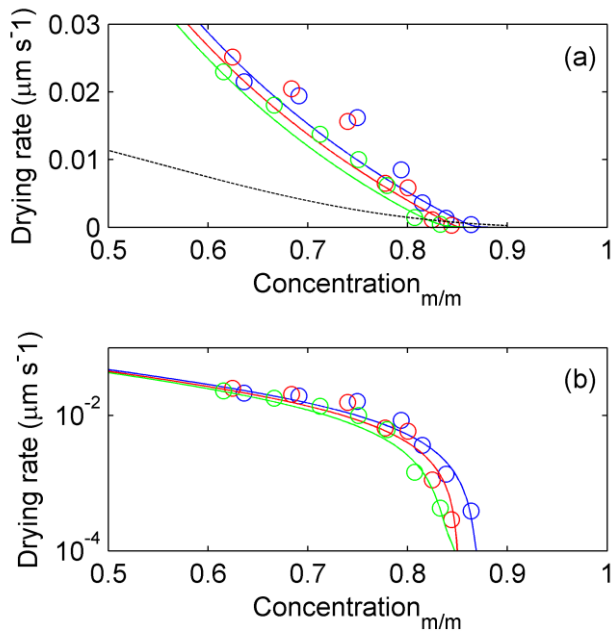


Figure 6.5.2.4  
As figure 6.5.2.3 for  
Regalrez and White  
spirit varnish.

For AYAT and toluene varnish (3g resin to 11ml solvent), the varnish film was applied with the 225 $\mu$ m gap. The different starting concentration meant that a different empirical function was needed to fit the mass data. Figure 6.5.2.5 (a) shows the measured mass for one measurement. The shape of the experimental data led to a need to use a two piece mathematical function. To fit the knee of the curve a two part powered exponential was used, this was

$$M = K_1 \exp[K_2(t + K_8)^{K_3}] + K_4 \exp[K_5(t + K_9)^{K_6}] + K_7. \quad (5.3.3)$$

The differential of the resulting equation had a minimum after zero time, this contravened the criteria that the differential was monotonic (ensures evaporation rate was not increasing with concentration). So at this minimum, the function was taken as linear, with the gradient of the minimum differential. The two resulting functions were then combined by interpolation. The function was then handled numerically. In figure 6.5.2.5, the function can be seen to be a reasonable fit to the raw mass and concentration data. The main discrepancy is at the knee of the curve, where it is too blunt.

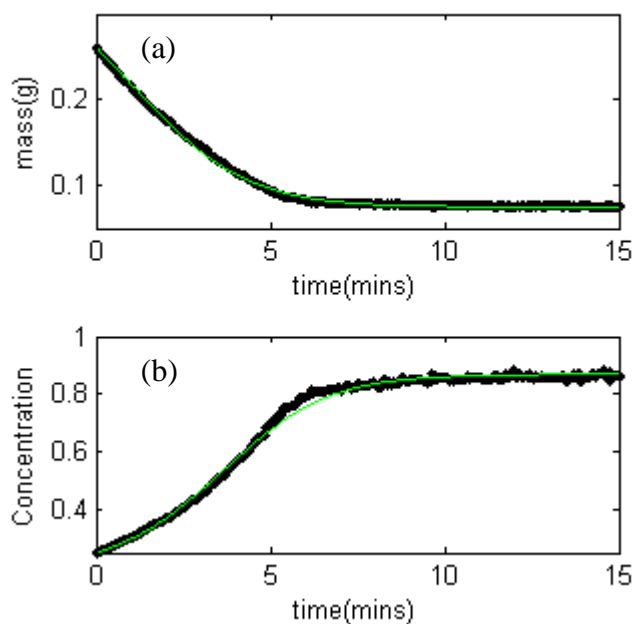


Figure 6.5.2.5  
 (a) Measured mass and fitted function (eq. 5.3.3) of AYAT toluene varnish coating upon ground glass plate.  
 (b) Concentration vs. time calculated from mass data points (points) and mass fit (line).

The lower initial concentration means that error due to initial evaporation is reduced over the Regalrez toluene varnish. Three independent measurements of the empirical function (Figure 6.5.2.6 (a)) show small amounts of spread. Again the applicator drying samples are seen to be faster than the welled sample. Comparison with the averaging method (circles figure 6.5.2.6) show reasonable agreement between the two methods. There is some discrepancy at higher evaporation rates, but the low evaporation rates show excellent agreement in the logarithmic graph (figure 6.5.2.6 (b)).

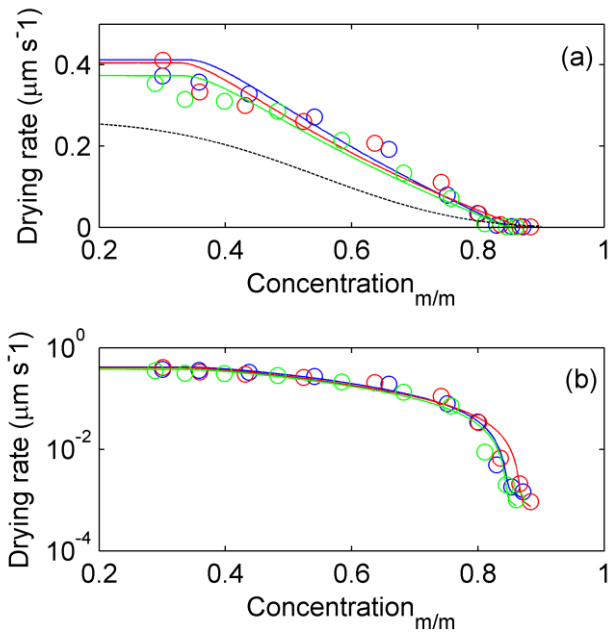


Figure 6.5.2.6  
 (a) Measured evaporation function for 4 repeats of the method (coloured lines) for AYAT and toluene. Also shown is the function obtained from a well-dried method (black dashed line). The results obtained from averaging the data point and using them directly is shown by the circles.  
 (b) The function and averaging methods shown on a logarithmic scale.

### 6.5.3 Modelling results: different resins

For an OCT measurement of an AYAT and toluene applied film, modelling was carried out using two different evaporation functions, an applicator and a well-dried function. This was done to determine the importance of the difference of the evaporation functions to the model results. Both these modelling results were compared to the experimental results. This was to identify inaccuracies in the model. Figure 6.5.3.1 shows the measured and the two modelled profiles for the AYAT sample at different time intervals. Figure 6.5.3.2 shows the mean thickness, the *rms* roughness and correlation against time, and PSDs of the final profiles.

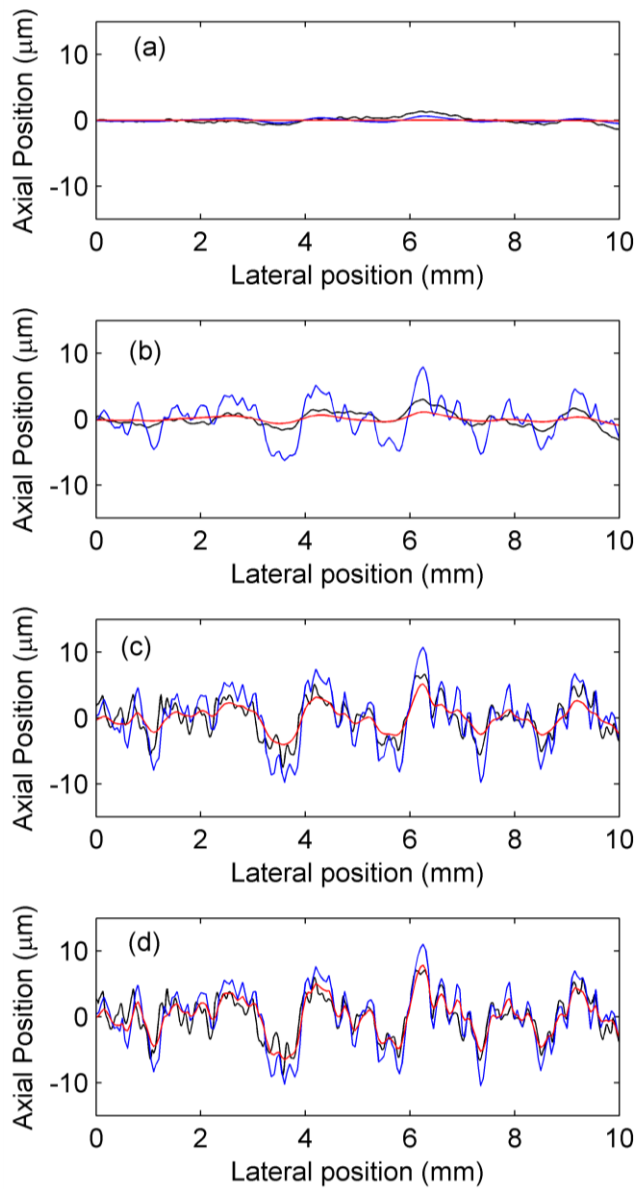


Figure 6.5.3.1  
 For a AYAT and toluene coating, at measurement times of (a) 3mins, (b) 6mins, (c) 9mins and (d) 12mins. The measured (black) and modelled, using the welled (red) and the applicator (blue) measured evaporation functions, surface profiles.

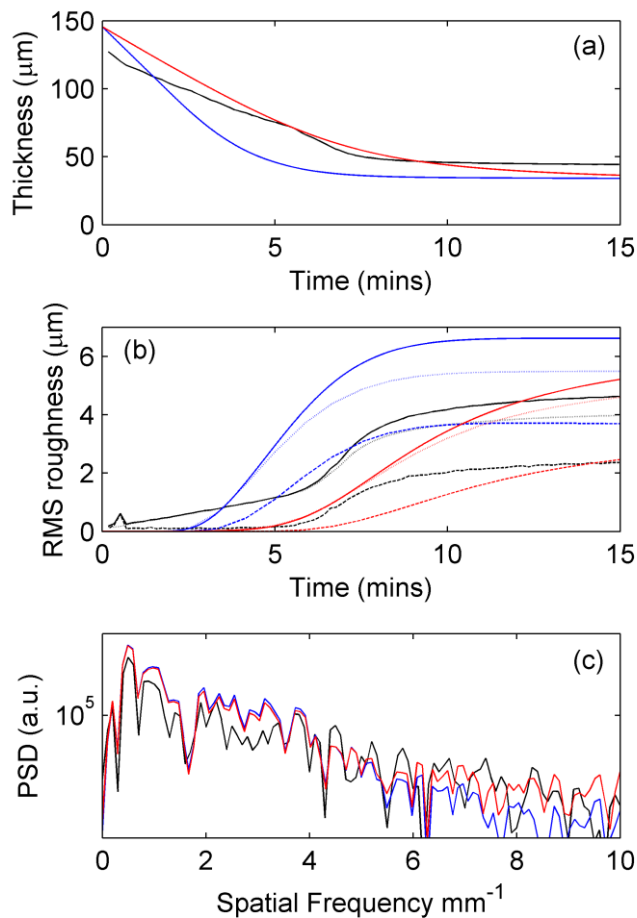


Figure 6.5.3.2

From the results shown in figure 6.5.3.1 (same colour codes), the development with time of

(a) Thickness

(b) *rms* roughness, solid line total, dotted line low pass filtered ( $<1\text{mm}^{-1}$ ) and dashed line high pass filtered ( $>1\text{mm}^{-1}$ ).

Also shown is

(c) The PSDs of the final surface profiles.

It is seen in the results that the evaporation function measured for the applicator film lead to a faster development of roughness than is seen in the experimental applicator results. The modelled thickness decreases too quickly and as a result the roughness develops earlier in the drying process. An important difference between the model and experimental results is the difference in final thickness. This is likely (in part at least) to be due to the change of volume with the removal of solvent mass. In the modelling the varnish solution is assumed to be ideal, however this will not be the case and the volume lost due to solvent evaporation is being over estimated (assuming toluene is a “good” solvent for AYAT). This has already been seen in the experimental results for Regalrez and toluene solutions, where the effect is immediately obvious without comparison to modelling results. The welled drying evaporation function provides modelling results that underestimate the speed of the development of roughness, though its total shrinkage over the 15 minutes is still higher. Both models (independent of the two evaporation functions) correctly show the delay in the development of high spatial frequency roughness compared with the

low frequency component. The difference between the final PSDs of the two evaporation functions is minimal, compared to the structure within a single measurement of a profile. The models predict the final surface PSD function well, though there are some systematic discrepancies.

The magnitude of correlation between two profiles is highly dependent on their signal(amplitude)-noise(error) ratio. To account for this in the calculation of the predicted correlation from the models, the effect of vibration on the varnish-air (lowest amplitude) interface was included. To do this six vibration profiles (standard flat surface) were measured. Each vibrational profile was added to the modelled surface profiles and the correlation coefficient calculated. The one standard deviation bounds were taken from the resulting 6 separate correlation trends. This was done for the unfiltered, low pass filtered and high pass filtered profiles, for both models. Figure 6.5.3.3 shows these modelled bounds along with the experimentally measured result. The welled evaporation function model provided a much closer match to the experimental results, than the applicator drying function model which was too rapid. Unlike for *rms* roughness, the welled drying model correlation is not slower than the measured value.

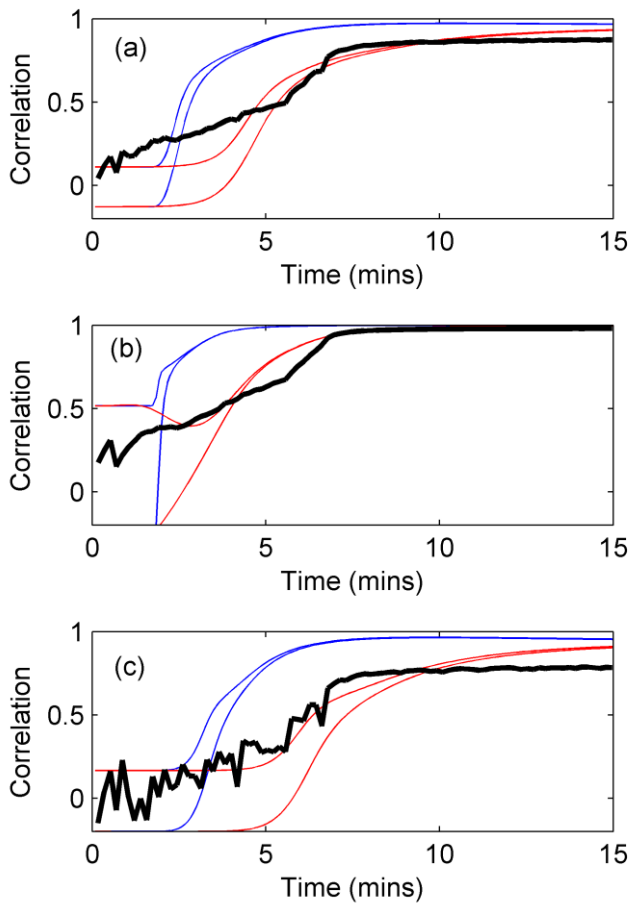


Figure 6.5.3.3  
 For an AYAT and toluene coating, the modelled one standard deviation bounds of cross-correlation using welled (red) and applicator (blue) measured evaporation function, along with the experimentally measured correlation (thick black). For (a) Unfiltered Profiles (b) low pass filtered ( $<1\text{mm}^{-1}$ ) and dashed line. (c) high pass filtered ( $>1\text{mm}^{-1}$ )

The modelling for a Regalrez and toluene measurement was again carried out using applicator and welled drying evaporation functions. Figure 6.5.3.4 shows the modelled surface profiles were again compared to the experimental results at different times during the drying process. It is seen that the measured low frequency roughness does not follow the modelled results. The change of the measured and modelled profiles with time is negligible. Figure 6.5.3.5 shows the mean thickness, the *rms* roughness and correlation against time, and PSDs of the final profiles. As was clear from the experimental results, the measured change in thickness is not of the same magnitude of the model. The difference between the initial measured and modelled mass is likely to be due to the evaporation of toluene between application and first measurement. However, for this to be of the explanation of the difference in the final thickness, the calibration of actual applied thickness would also have to be significantly wrong. To establish, with certainty, whether this potential experimental error or the volume behaviour of the varnish solutions is the cause of

the discrepancy between modelled and measured final thickness, the density of different concentrations of solution can be measured. This will determine how far the behaviour is from ideal and this can be included in the models. The comparison of this modelling result with the experimental results would determine whether non-ideal behaviour was the cause.

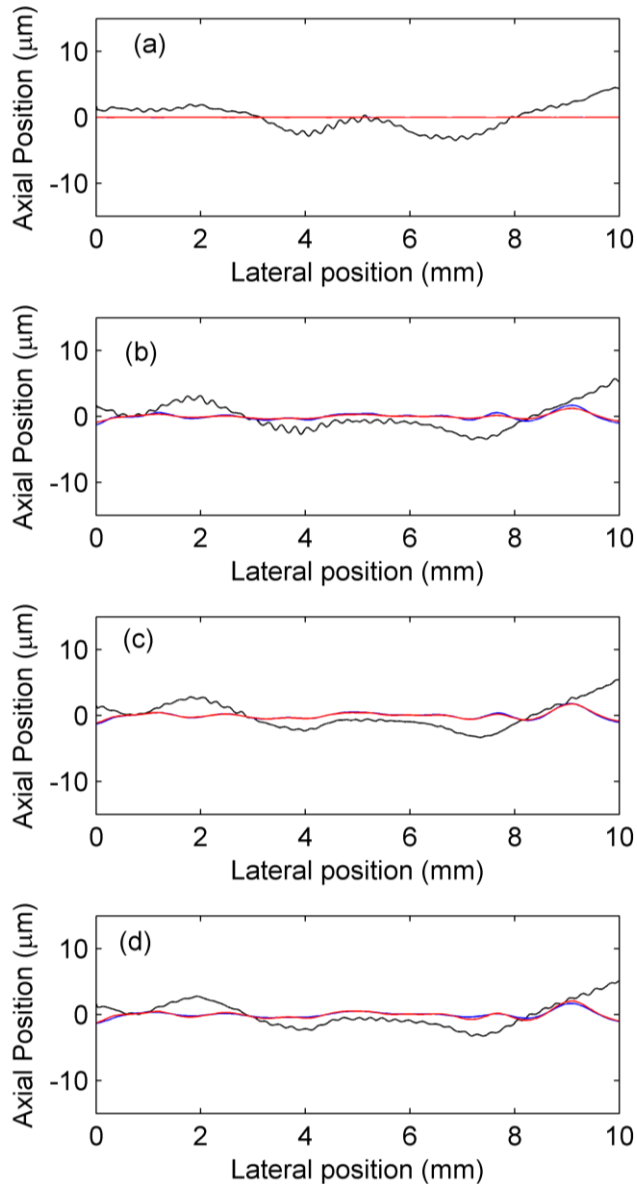


Figure 6.5.3.4  
For a Regalrez and toluene coating, at measurement times of (a) 0, (b) 3mins, (b) 6mins and (d) 15mins. The measured (black) and modelled, using wetted (red) and applicator (blue) measured evaporation function, surface profiles.

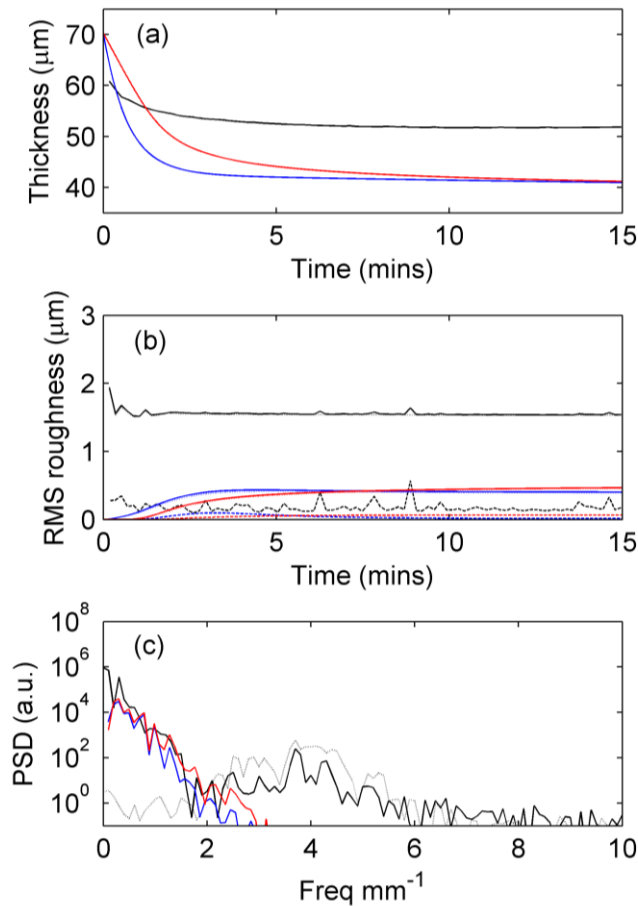


Figure 6.5.3.5  
 From the results shown in figure 6.5.3.4 (same colour codes), the development with time of  
 (a) Thickness  
 (b) RMS roughness, solid line total, dotted line low pass filtered ( $<1\text{mm}^{-1}$ ) and dashed line high pass filtered ( $>1\text{mm}^{-1}$ ).  
 Also shown is  
 (d) The PSDs of the final surface profiles, the grey dotted line shows the measured PSD for a standard flat surface (OCT vibrational noise).

The two models predict the development of low frequency ( $<1\text{mm}^{-1}$ ) *rms* roughness within the first five minutes of drying but do not reach the magnitude of the experimental roughness. Apart from the lowest spatial frequencies, the modelled final PSDs match the experimental results. The experimentally measured low frequency roughness has already been shown to be from a source other than levelling. Comparison with the PSD measured from a standard flat surface, shows that the high frequency PSD component, in the experimental results, is due to the vibrational noise. Figure 6.5.3.6 shows the modelled and experimental correlation results. The measured low frequency roughness of the Regalrez coating is much lower than the model predictions. This is due to the measured low frequency roughness being independent of the substrate and levelling process. The modelled high frequency roughness correlation shows better agreement with the experimental results. At the high spatial scale the low frequency mechanism is of less importance to the experimental results.

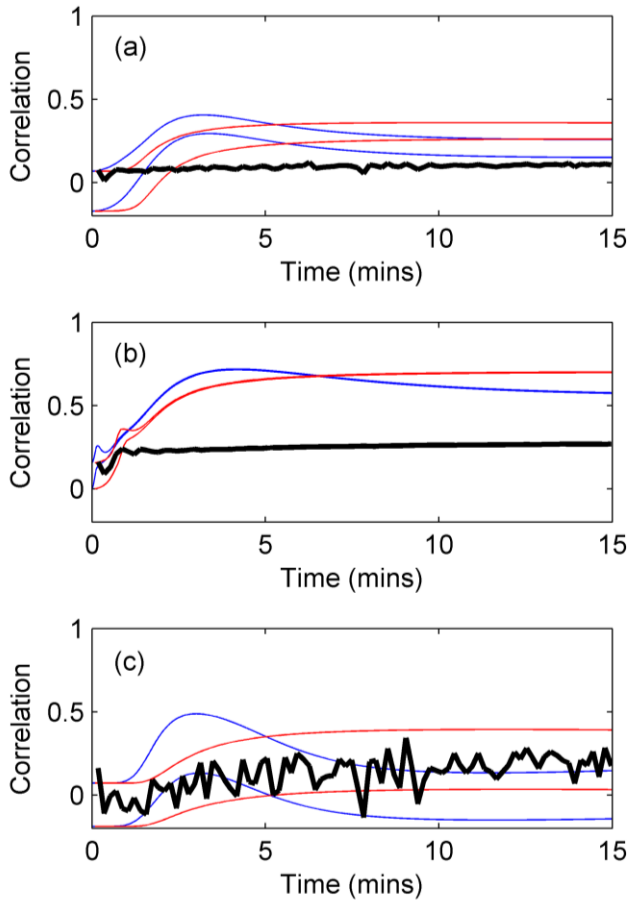


Figure 6.5.3.6  
 For a Regalrez and toluene coating, the modelled one standard deviation bounds of cross-correlation using welled (red) and applicator (blue) measured evaporation function, along with the experimentally measured correlation (thick black). For (a) Unfiltered Profiles (b) low pass filtered ( $<1\text{mm}^{-1}$ ) and dashed line. (c) high pass filtered ( $>1\text{mm}^{-1}$ )

For the other resin measurements (applied at a concentration of 1g resin to 1ml solvent and applied with an applicator gap of  $100\mu\text{m}$ ) the system was modelled with the Regalrez applicator evaporation function and the measured viscosity function of the resins (chapter 5.2.2).

The next resin to be examined is Paraloid B72. The application concentration was the maximum concentration at which the viscosity was measured for this resin. Hence as a result of this the accuracy of the extrapolated viscosity function will determine the accuracy of the modelled results. This can be used in reverse, by comparing the results from models (using different viscosity extrapolation) with the experimental result, to determine which extrapolation is the most accurate. In chapter 5.2.2 it was shown that the viscosity function, of Paraloid and toluene solution, beyond the highest measurable viscosity was dependent on how the trend was extrapolated. Figure 6.5.3.7 is a copy of figure 5.2.2.6. It shows the two extrapolated functions for the viscosity of Paraloid. These functions were a linear and cubic fit to the logarithmic data. To confirm which viscosity trend gave the

most reasonable prediction of surface roughness, the modelling was carried out with both viscosity extrapolations and compared with the experimental result. Figure 6.5.3.8 shows the final surface profiles and PSDs, and also shows the development of the *rms* roughness. The cubic viscosity function gave by far the closest match to the experimental result. The lower viscosity of the linear extrapolation allowed too much smoothing. Like AYAT the performance of the model for the polymer resin Paraloid B72 was excellent. Levelling was the most significant factor in the measured surface profiles.

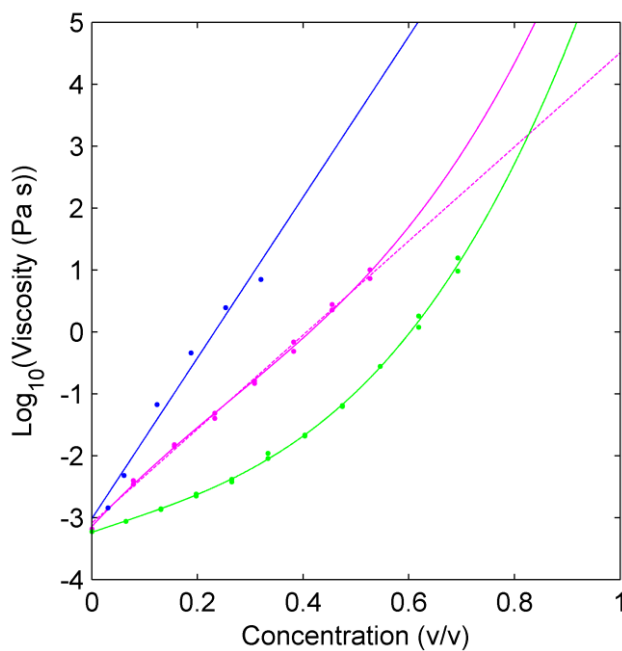


Figure 6.5.3.7  
Fitted empirical relationships of the log of viscosity vs. the concentration for the low molecular weight resins measured.  
Blue – AYAT (linear fit),  
Magenta – Paraloid B72 (solid line cubic fit, dotted line linear fit),  
and Light Green - Laropal A81 (cubic fit).

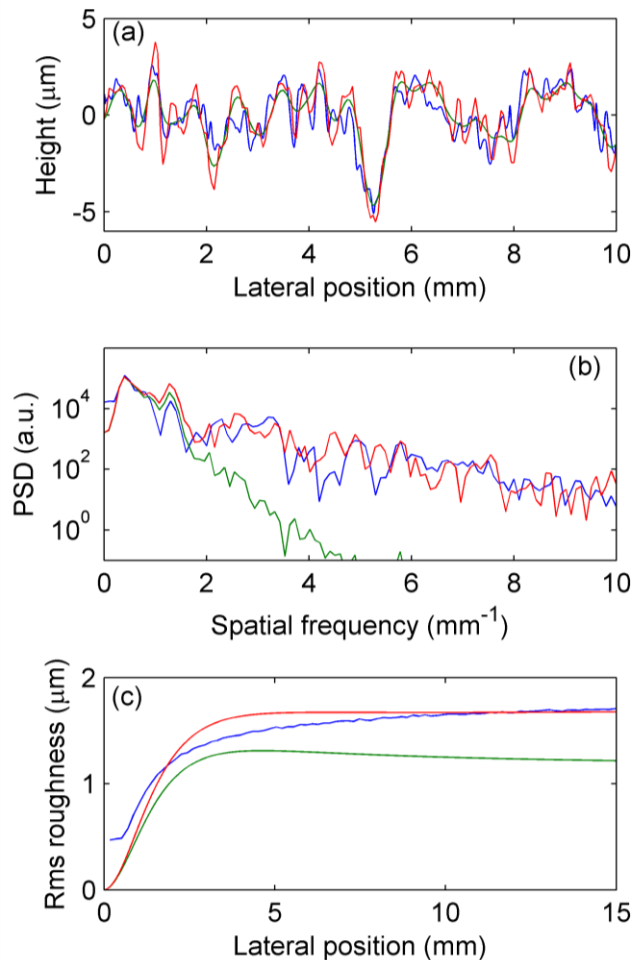


Figure 6.5.3.8  
 For the one repeat of a Paraloid B72 varnish the  
 (a) Final Profiles  
 (b) Final PSDs  
 (c) Development of RMS roughness  
 For the measured (blue), and modelled (cubic extrapolation (red) and linear extrapolation (green) of viscosity) surface profiles.

The next resin down the molecular mass/viscosity scale is Laropal A81, the most viscous of the low molecular weight varnishes. Figure 6.5.3.9 (a) shows a small amount of visible correlation of the modelled and measured surface profile, however the low frequency features of the measured profile are more significant. The PSDs are a reasonable match within noise (Figure 6.5.3.9 (b)), while the experimental results show a small (insignificant to the initial roughness) increase in the *rms* roughness during drying (Figure 6.5.3.9 (c)) similar to the shape modelled. As a more viscous varnish than Regalrez 1094 more development of surface roughness from the substrate profile is evident for Laropal A81, but is still dominated by other factors for this scale.

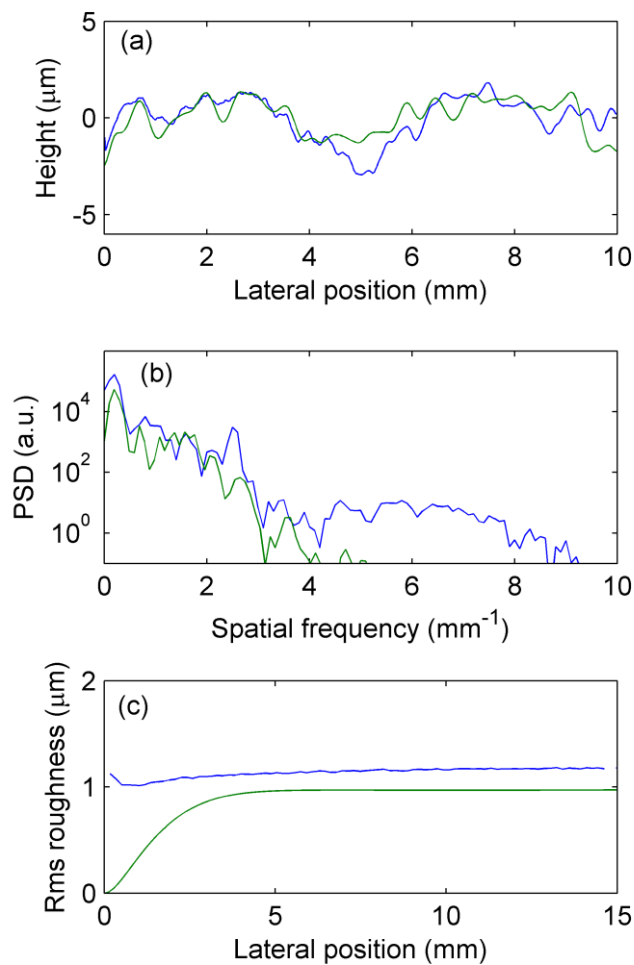


Figure 6.5.3.9  
 For the one repeat of a  
 Laropal A81 varnish the  
 (a) Final Profiles  
 (b) Final PSDs  
 (c) Development of RMS  
 roughness  
 For the measured (blue),  
 and modelled (green)  
 surface profiles.

The experimental and modelling result for the natural resin Dammar (Figure 6.5.3.10) can be seen to be slightly smoother than for Laropal. The higher spatial frequency components can be seen to be removed. The distortion between the experimental and model results has increased, as a result of the lower importance of levelling to the total surface roughness. The measured *rms* roughness does not show any increase during drying, just some relaxation of the initial roughness. For dammar the accuracy of the modelling is the same as Regalrez, the low frequency component of roughness is dominated by a process which is not levelling.

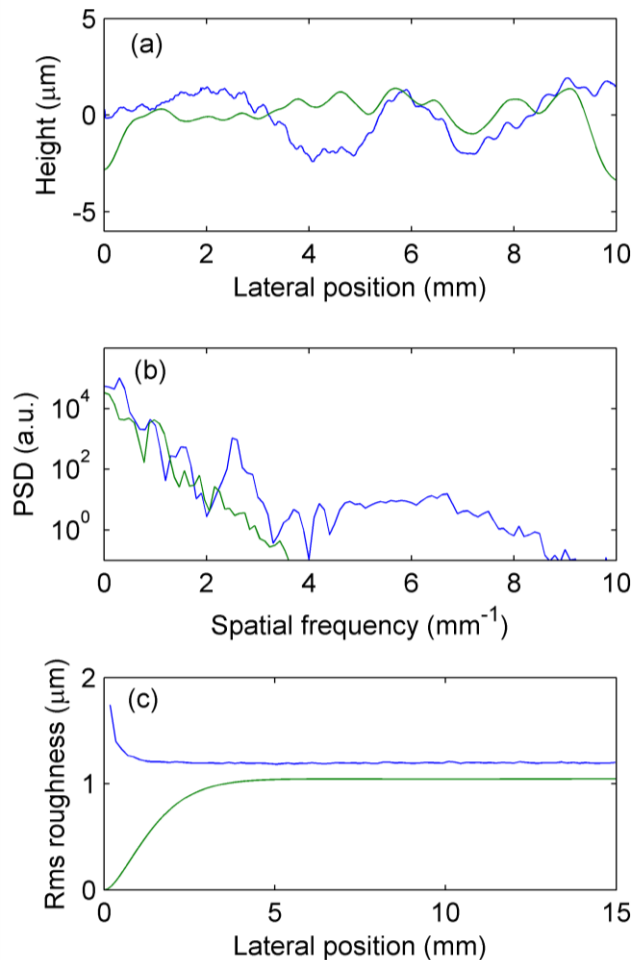


Figure 6.5.3.10  
 For the one repeat of a dammar varnish the  
 (a) Final Profiles  
 (b) Final PSDs  
 (c) Development of RMS roughness  
 For the measured (blue), and modelled (green) surface profiles.

Delaney et al<sup>3</sup> had previously discussed modelling varnish surface roughness using a spatial frequency filter. The modelling results presented here can be used to calculate the shape of this filter. This is done by dividing the PSD of the modelled final surface profile by the PSD of the substrate profile used in the model. This modelled PSD provides a smooth window result. These predicted windows, for various coating parameters, have the potential to be used to provide conservators with a reference to predict the appearance (due to surface roughness) of a coating they wish to apply.

Figure 6.5.3.11 shows the modelled spatial frequency window for the coatings of the five resins (dissolved in toluene). It should be noted that the starting point for the AYAT coating differs from the rest, with lower starting concentration (higher starting thickness) but approximately the same final thickness. This will increase the 0 frequency scaling, which is determined by the initial volume concentration (levelling flow cannot happen over an infinite distance). It can be seen that the two

polymer varnishes are in a different behaviour regime than the low molecular weight varnishes. The levelling of the polymer varnishes is far worse than the low molecular weight resins. This is due to the much higher viscosity of the solutions of these resins. The differences between the low molecular weight resins are much smaller but are still apparent. Laropal is predicted to be the the worst levelling of the three, then followed by Dammar and then Regalrez 1094 being the best. This matches the experimental high spatial frequency *rms* roughness and correlation shown in previous figure 6.4.2.11.

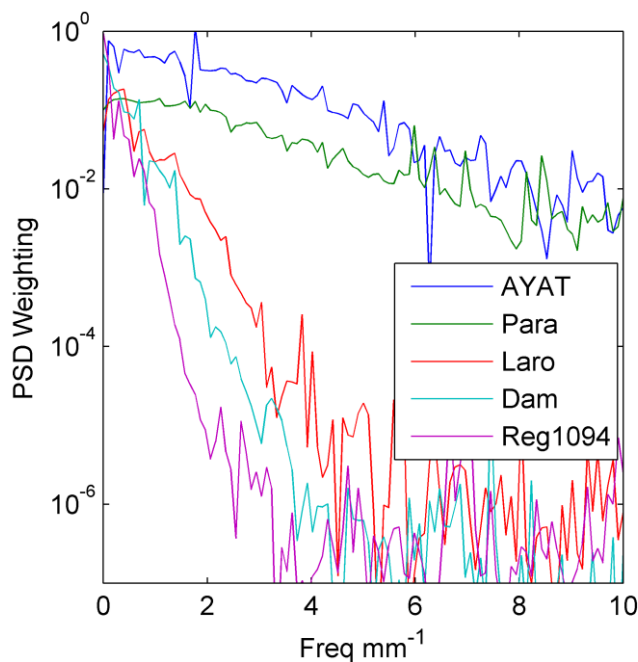


Figure 6.5.3.11  
The PSD weighting functions of substrate roughness calculated from the modelling results for the coatings of the 5 varnish resins dissolved in toluene.

For polymer resins, the use of the lubrication approximation model, the final surface profiles closely match the experimental results. For the low molecular weight resins and the 10mm profile a different process, other than levelling, dominates the surface profile. Direct comparisons of profiles do not show much agreement. However, by only looking at spatial features greater than  $1\text{mm}^{-1}$ , the experimental and modelling results show the same trends. Comparison of experimental and modelling PSDs show good agreement for the low molecular resin, apart from the lowest spatial frequencies.

The accuracy of the modelling could not have been measured without the multi-interface OCT profilometry technique. This allowed direct comparison between the modelled and measured surface profiles at all stages of drying. With the comparison

of experimental and modelling results, a future refinement of the modelling can be identified. This is the measurement of non-ideal behaviour of density of the solutions and inclusion into the modelling. This will either improve the accuracy of the model further or identify the extent of experimental error in the initial thickness.

#### 6.5.4 Modelling results: different thicknesses

The dependence of the *rms* roughness, of a Regalrez and white spirit coating, on the thickness of an applied coating has been experimentally measured in section 6.4.3. To get the expected relationship between surface roughness and thickness, a single substrate profile was used to model the development of the surface profile for three different applied thicknesses. This modelling was carried out using the applicator measured evaporation function and viscosity function for the white spirit coating measured. Figure 6.5.4.1 shows the modelled and measured total and high pass ( $>1\text{mm}^{-1}$ ) filtered *rms* roughnesses. There is a large difference between the magnitude of roughness predicted and the measured values. For the total roughness, this can be explained by the low frequency process, other than levelling, identified previously. However, the high frequency roughness is expected to be free of this substrate independent process but the large difference is still apparent. For the Regalrez and white spirit coating the model failed to match the magnitude of roughness of the experimental values. The reason for this was not identified. Despite the fact that the magnitude of the modelled values were incorrect, the shape of the relationship between roughness and thickness is similar. This is suggestive that the measured increase in roughness, with decreased thickness, is due to levelling.

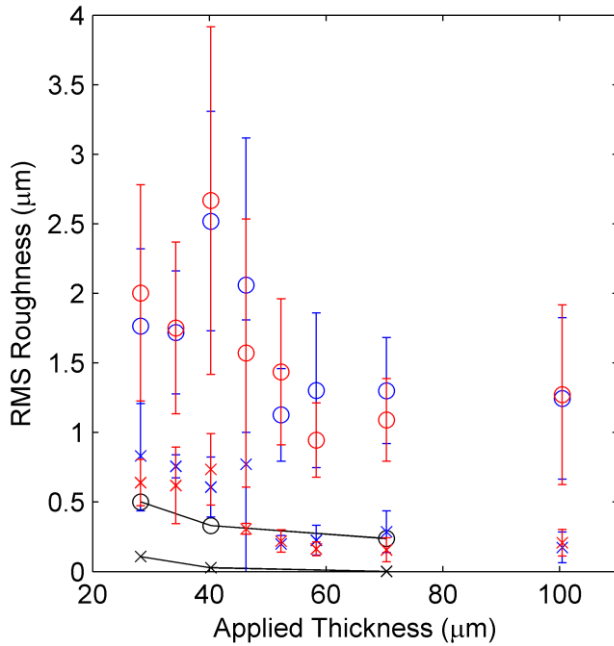


Figure 6.5.4.1  
 Experimental (blue 1 month and red 4 months after application) rms roughness for regalrez and white spirit coating. Black shows the values obtained from modelling. Circles show total *rms* roughness and crosses show highpass ( $>1\text{mm}^{-1}$ ) spatial filtered *rms* roughness.

To evaluate the effect that the viscosity and evaporation functions, used for the Regalrez and white spirit coatings, had on the modelling results, the modelling was also carried out with the evaporation and viscosity parameters for toluene. These are compared to the white spirit results in figure 6.5.4.2. In the model, the faster evaporation rate, for toluene, dominates the small difference in viscosity. This leads to an increase in the modelled roughness. That the roughness is the same magnitude of the measured roughness, of Regalrez and white spirit system, is coincidental. However the similarity in the relationship, of *rms* roughness with applied thickness, shape is significant. Again the experimental increase in roughness, with decreased thickness, is of a similar mathematical relationship predicted by levelling.

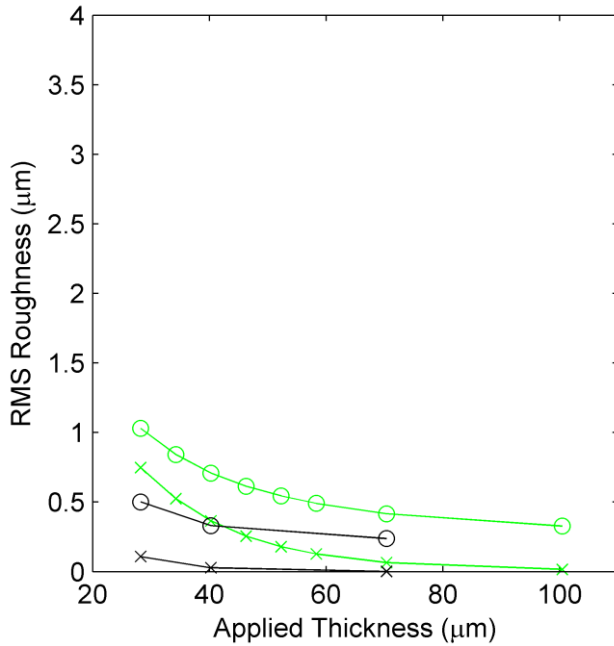


Figure 6.5.4.2  
 Modelled values of *rms* roughness as a function of applied thickness. Black shows the values obtained for a Regalrez and white spirit solution. Green shows the values modelled for a Regalrez and toluene solution. Circles show total *rms* roughness and crosses show highpass ( $>1\text{mm}^{-1}$ ) spatial filtered *rms* roughness.

## 6.6 Conclusion

Multi-interface profilometry with OCT has measured the development of roughness, and its relationship with the substrate profile, for coatings of different resins and thickness. These results have allowed a very direct evaluation of the performance of a lubrication approximation model of surface levelling. For high molecular weight polymer varnishes, the high viscosities of these solutions mean that the surface profile is dominated by levelling roughness. The modelling of levelling provided surface profiles of high accuracy to the experimentally measured profiles. In the low molecular weight resins, the 10mm profile lengths used in this study identified another effect that dominates very low spatial frequency roughness. The cause of this effect has not been conclusively identified, as this was not of interest in the project. The likely causes are the Benard-Marangoni effect or inhomogeneous application. For higher spatial frequencies the levelling induced roughness can still be identified in the experimental results. The experimentally measured behaviour of the levelling roughness is a close match to the model predictions.

The measurement of the roughness dependence on film thickness, with a Regalrez and white spirit varnish, this showed the high frequency (levelling) roughness decreased with increased thickness of the dry film. For experimental results of a different starting concentration, but same dry thickness, the difference in surface

roughness was negligible. Modelling of this system predicted a similar shaped relationship between thickness and roughness, though the magnitude of the roughness predicted by the modelling of the Regalrez and white spirit system was much lower than the real roughness.

The varnish thickness this study has worked on is of around 40 $\mu$ m dry thickness. This is of the high end of real varnish thickness. Though previous studies<sup>3</sup> have used 76 $\mu$ m (applied) thicknesses (and with lower roughness substrates as well). Conservator applied thicknesses are typically lower than these used. At lower thicknesses the varnish surface roughness will be increasingly dominated by levelling roughness. The prediction of surface levelling differences will be of increased importance. The aim of the next chapter is to measure conservator applied coatings to see if the behaviour measured in controlled experiments matches' reality. The next chapter will also identify whether other factors in film appearance have been wrongly overlooked.

## 6.7 References

<sup>1</sup> Berns Roy S. and de la Rie E. René, "The relative importance of surface roughness and refractive index in the effects of varnishes on the appearance of paintings", 13<sup>th</sup> Triennial Meeting Rio de Janeiro Preprints, vol I, pp. 211-216 (2002).

<sup>2</sup> Elias Mady, de la Rie E. René, Delaney John K., Charron Eric and Morales Kathryn M., "Modification of the surface state of rough substrates by two different varnishes and influence on the reflected light", Optics Communications, 266 (2), pp. 586-591 (2006).

<sup>3</sup> Delaney John K., de la Rie E. René, Elias Mady, Sung Li-Piin and Morales Kathryn M., "The Role of Varnishes in Modifying Light Reflection from Rough Surfaces", Studies in Conservation, 53 (3), pp. 170-186 (2008).

<sup>4</sup> Orchard S. E., "On surface levelling in viscous liquids and gels", Appl. Sci. Res., 11 (A), pp. 451-464 (1962).

<sup>5</sup> Kornum L. O. and Nilsen H. K. Raaschou, "Surface defects in drying paint films", Progress in Organic Coatings, 8, 275-325 (1980).

<sup>6</sup> Patton Temple C., Paint Flow & Pigment Dispersion, 2<sup>nd</sup> Ed., John Wiley & Sons, inc. (1979).

<sup>7</sup> Weinstin Steven J. and Ruschak Kenneth J., "Coating Flows", Annu. Rev. Fluid. Mech. 36, 29-53 (2004).

- 
- <sup>8</sup> Bruxelles G. N. and Mahlman B. H., “Glossiness of Nitrocellulose Lacquer Coatings”, Official digest – Federation of Paint and Varnish Production Clubs”, 351, pp. 299-314 (1954).
- <sup>9</sup> Feller Robert L., Stowlow Nathan and Jones Elizabeth H., On Picture Varnishes and their Solvents, National Gallery of Art, Washington (1985).
- <sup>10</sup> Delaney John K., de la Rie E. René, Elias Mady, Sung Li-Piin and Morales Kathryn M., “The Role of Varnishes in Modifying Light Reflection from Rough Surfaces”, Studies in Conservation, 53 (3), pp. 170-186 (2008).
- <sup>11</sup> Stillwagon L. E. and Larson R. G., “Fundamentals of topographic substrate leveling”, J. Appl. Phys. 63 (11), pp. 5251-5258 (1988).
- <sup>12</sup> Bullwinkel Mathew D., Gu Jiren and Campbell Gregory A., “The Effect of Drying Rate on Film Levelling Over an Uneven Substrate Surface”, ANTEC '97, pp. 2227-2230 (1997).
- <sup>13</sup> Iyer Rajan R. and Bousfield Douglas W., “The leveling of coating defects with shear thinning rheology”, Chemical Engineering Science, 51 (20), 4611-4617 (1996).
- <sup>14</sup> Russ John C., Fractal surfaces, Volume 1, Plenum Press (1994).
- <sup>15</sup> Hedley G., Odlyha M., Burnstock A., Tillinghast J. and Husband C., “A study of the mechanical and surface properties of oil paint films treated with organic solvents and water”, Journal of Thermal Analysis and Calorimetry, 37 (9), pp. 2067-2088 (1991).
- <sup>16</sup> Van de Berg Klass Jan, Daudin Maude, Joosten Ineke, Wei Bill, Morrison Rachel and Burnstock Aviva, “A Comparison of Light Microscopy Techniques with Scanning Electron Microscopy for Imaging the Surface Cleaning of Paintings”, 9th International Conference on NDT of Art, (2008).
- <sup>17</sup> Elias Mady, Magnain Caroline and Frigerio Jean Marc, “Contribution of surface state characterisation to studies of works of art”, Applied Optics, 49 (11), pp. 2151-2160 (2010).
- <sup>18</sup> Demos Stavros, Staggs Mike, Kaoru Minoshima and Fujimoto James, “Characterization of laser induced damage sites in optical components”, Optics Express, 10 (25), pp. 1444-1450 (2002).
- <sup>19</sup> Abbasian A., Ghaffarian S. R., Mohammadi N., Khosroshani M. R. and Fathollahi, “Study on different planforms of paint’s solvents and the effect of surfactants (on them)”, Progress in Organic Coatings, 49, pp. 229-235 (2004).
- <sup>20</sup> Orr Edward W., Performance enhancement in coatings, Carl Hanser Verlag (1998).

## 7 Optical properties of conservator applied and aged coatings

### 7.1 Introduction

In the previous chapter, the surface levelling of different varnish coatings has been measured and modelled. This provides understanding on how the properties of a varnish solution determine the properties of surface roughness and hence the coatings appearance. However, this work has been carried out under controlled experimental conditions, using an applicator to control the deposited thickness. The thicknesses of the coatings, applied by the applicator, were similar to those of thickest coatings that maybe found on real paintings. Conservator applied coatings will generally be thinner than those used in the previous chapter. The control of the amount of varnish deposited with the use of different solutions and application techniques is unknown. Differences in the real application of varnish coatings may render some of the levelling differences between different solutions negligible. To test how well the measured and predicted trends in resin levelling performance match the results achieved by conservators, in this chapter conservator applied coatings were measured.

The gloss of the surface is not the only physical mechanism that would change the impact a varnish has on the appearance of a surface. Scattering of white light from other parts of the optical system may also occur. When measuring the conservator applied coatings, scattering of light from beneath the surface was serendipitously found (See figure 7.2.5.1 (a) for an OCT image of a varnish coated glass plate clearly showing scattering from underneath the surface). The cause of this scattering was identified as voids. Processes that could lead to the formation of voids are incomplete wetting, penetration and continued adhesion. This is introduced in section 7.1.1. Scattering from within the volume of an aged varnish is another possible source of diffuse white light on a real painting. This is introduced in section 7.1.2. For the measurement of these different properties, OCT will again be used. Profilometry with OCT has already been extensively used in the thesis. The use of OCT for gloss measurement, subsurface scattering and volume scattering is introduced in section 7.1.3.

### 7.1.1 Wetting, penetration and adhesion

The potential for the lack of complete contact of a varnish coating to the paint surface (the bottom varnish interface being the paint surface at all lateral points) has long been identified as a potential mechanism which would affect appearance<sup>1</sup>. Voids between the varnish and paint layers would have much higher light scattering than the varnish-paint interface due to the greater difference in refractive index. The amount of light scattered would also be dependent on the scale of the voids, which determine the regime of scattering. Figure 7.1.1.1 shows the optical system of different scales of such voids. The simplest case is a large void with dimensions much higher than the wavelength of light. With the void there is an addition of two more highly reflecting interfaces ( $\Delta n \sim 0.5$ ) with the removal of only the low reflecting interface (max  $\Delta n \sim 0.05$ ). The paint - void interface is exactly identical to the unvarnished paint surface, diffusely scattering white light. The two varnish interfaces do nothing to increase the chroma and only add more reflected white light. The specular to diffuse ratio of this additional light will be dependent on the roughness properties. The diffusely reflected light, from these interfaces, is extra to the diffusely reflected light from the unvarnished surface. If the void dimensions become of similar dimensions to the wavelength of light, the consideration of these voids as effective white pigment particles on the paint surface will be more appropriate. At these scales the light scattering will be best described by Mie theory<sup>2</sup>. For voids much smaller than the wavelength of light, the scattering regime will be Rayleigh<sup>2</sup>. The total amount of scattered light will become negligible to the visual appearance of the system, if the void dimensions are lower than a certain size.

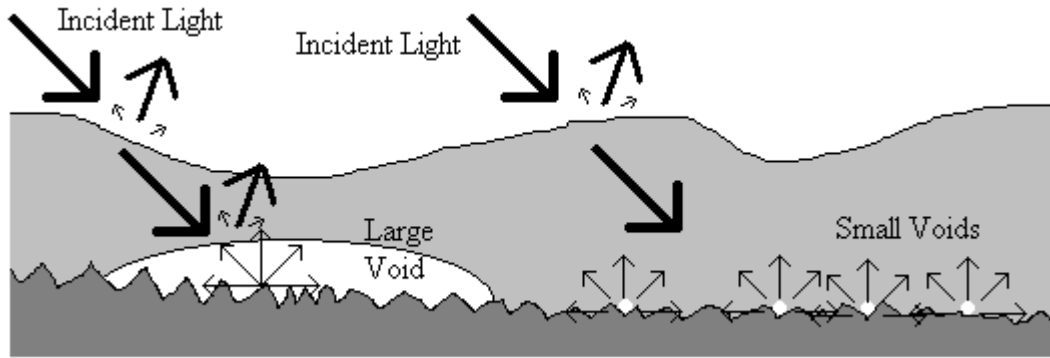


Figure 7.1.1.1

Diagram of light (arrows) incident upon a varnished paint surface, with voids present. On the left a large void is present, the interfaces of this void is treated in the same manner as varnish-paint and varnish surface interfaces. To the right, smaller voids are better described as scattering particles (same as white pigment particles).

Direct evidence for such scattering has previously<sup>3,4</sup> not been found and the effect has been generally ignored in recent modelling and experimental studies (see chapter 1.2 for references and discussion) on the appearance of varnish coatings. Here the use of OCT, to measure conservator applied varnish coatings on ground glass substrates, does find evidence of voids.

Before the mechanisms that might form such voids are considered, the previous assumptions about the surface need to be re-evaluated. Figure 7.1.1.2 shows a hypothetical cross section a substrate, which shows the different features that are possible. Describing a surface by a surface profile assumes that there is only one height position of the surface at each lateral location. Overhangs, cracks and pores extending underneath the surface do not meet this assumption. For the ground glass substrates, used here, subsurface fracturing was identified and real paint surfaces maybe porous<sup>1,4</sup>. Neither fractured glass nor porous paint is well represented by a surface profile of an impervious material.

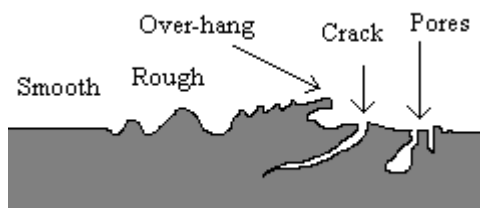


Figure 7.1.1.2

Cross-section through hypothetical surface, showing features that can (smooth and rough surfaces) and cannot (over-hangs, cracks and pores) be represented by a surface profile.

For there to be no voids at the surface, the varnish needs to be in contact with the entire surface. The mechanism where a solid surface is covered by a liquid is wetting. De Genes et al<sup>5</sup> provides an overview of the physics associated with wetting. Here the physics of relevance to the varnish wetting of the ground glass substrates and real paint substrates will be reviewed.

The energy associated with an air – liquid interface (surface tension) has previously been considered in relation to varnish levelling, in this thesis. Any interface between two different materials has with it an associated energy or interfacial tension. Usually these interfacial tensions are considered and measured by the contact angles at the triple line of three substances.

Figure 7.1.1.3 (a) shows a small (effects due to gravity are negligible) droplet of the liquid placed on a perfectly smooth sample of the solid substrate. To minimise the total surface energy the droplet is a spherical cap with contact angle,  $\theta$ , defined by the Young relation

$$\cos(\theta) = \frac{\gamma_{SG} - \gamma_{SL}}{\gamma_{GL}} \quad (7.1.1.1)$$

where  $\gamma_{SG}$ ,  $\gamma_{SL}$  and  $\gamma_{GL}$  are the surface tension/energy of the solid-gas, solid-liquid and gas-liquid interfaces respectively. The presence of air-bubbles (scattering voids) on a varnish-substrate interface is the inverse of this representation and is shown by figure 7.1.1.3 (b). The contact angle at the triple line of the three materials remains the same, so the internal void contact angle becomes  $180 - \theta$ .

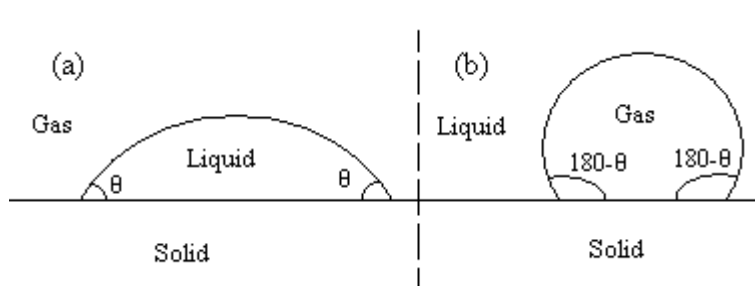


Figure 7.1.1.3  
Diagram of the contact angle of (a) a liquid droplet and (b) a gas bubble on a flat solid substrate.

The contact angle ( $\theta$ ) is real only if the right hand side of equation 7.1.1.1 is in the limits -1 to 1. If the right hand side of equation 7.1.1.1 is greater than one, it is more energetically favourable for the liquid to spread as a thin film across the surface than

stay as a droplet. This is known as total wetting. If the varnish coating falls into this regime, then complete surface wetting would be expected. Any void would be detached from the surface at the thermodynamic equilibrium of a total wetting system. If  $\theta$  is real then partial wetting occurs. Partial wetting is characterised into two different regimes. The first, when  $\gamma_{SL} > \gamma_{SG}$ , the contact angle is greater than  $90^\circ$  and the system is described as “mostly non-wetting”. The second, when  $\gamma_{SL} < \gamma_{SG}$  the contact angle is less than  $90^\circ$  and the system is described as “mostly wetting”.

The real substrates (paint surfaces) that varnish coatings are applied to are not smooth. The paint surface or ground glass substrates (for experiments) have significant roughness. This roughness has two effects on partial wetting systems. Firstly, the positions of the triple lines of the three materials are pinned by the roughness. This means that for the edge of droplets and spread of films, there is hysteresis between advancing and receding contact angles. This is due to the energy needed to overcome the pinning. Secondly, the surface area of the interface, per area of plane, increases with the surface roughness. There exist two approaches to model this. The Wenzel approach reformulates equation 7.1.1.1 to take into account the increased surface area. The resulting contact angle,  $\theta^*$ , for the rough surface is related to the Young contact angle,  $\theta$ , by

$$\cos \theta^* = r \cos \theta, \quad (7.1.1.2)$$

where  $r$  is the roughness value defined by total surface area per plane area, so that a perfectly smooth surface has a value of 1.

From equation 7.1.1.2 it can be seen that surface roughness will emphasise “mostly wetting” or “mostly non-wetting” surfaces, as if the contact angle is above  $90^\circ$  it will be increased and if it is below  $90^\circ$  it will be decreased. In terms of varnish coatings if the Young contact angle is above  $90^\circ$  then it would be expected to be difficult to force the varnish to wet the surface as the roughness is discouraging wetting. Dependent on the aspect ratio of the rough surface features, trapping of air bubbles at the surface may become thermodynamically favoured. Previous<sup>4</sup> approximate measurements of the contact angle of a range of varnishes on an oil paint substrate gave contact angles of 20 to  $30^\circ$ .

The more probable case for a varnish coating is a “mostly wetting” system. The roughness of the substrate then promotes wetting. However, the increase in roughness cannot decrease the wetting angle to below  $0^\circ$  to a total wetting system. This is due to a consideration of the Cassie-Baxter model, which considers a plane across the highest points of the rough surface. If the volume between this plane and the substrate is filled with the liquid, this plane acts as a heterogeneous surface of solid and liquid to the liquid above the plane. The resulting contact angle of the liquid above the plane is then given by

$$\cos \theta^* = 1 - \Phi_s + \Phi_s \cos \theta \quad (7.1.1.3)$$

where  $\Phi_s$  is the fraction of the plane that is the solid surface. However, this is the contact angle of the (bulk) varnish above the roughness of the surface. This bulk varnish is partially sat upon an “absorbed” film, which can wet beyond the edge of the bulk varnish. The criterion for the impregnation of this “absorbed” film beyond the bulk varnish is<sup>5</sup>  $\theta < \theta_c$ , where

$$\cos \theta_c = \frac{1 - \Phi_s}{r - \Phi_s}. \quad (7.1.1.4)$$

This is also the boundary condition for the transition between equation 7.1.1.2 and 7.1.1.3. Note that there must be islands of un-wetted substrate within an absorbed film.

The spreading of varnish onto a substrate is a dynamic process which does not necessarily reach thermo-dynamical equilibrium<sup>6</sup>. The varnish is forced to cover a large area by brushing or spraying. The flow of varnish during/after application will be limited by its viscosity and pinning of triple lines. It seems unlikely (assuming a strongly wetting system) that a conservator will not be able to wet the surface profile of the substrate during application of a varnish. An even spraying technique or the shearing of the varnish across the whole surface during brushing would lead to the varnish touching all points on the surface profile. After contact with the surface profile by the varnish has been made, the energy required to overcome the pinning of triple lines will prevent de-wetting. However the presence of features such as overhangs, fracturing or pores in the substrate may lead to trapping of air.

As the varnish is spread over the entrance to these features, in order to fill them it will need to be pulled inside by capillary action and the air, initially within the feature, removed to the outside. If the strength of the capillary action is weak compared to the viscosity of the coating, then the varnish will not be able to penetrate these features before it has dried.

During (or immediately after) the application process (by inadequate wetting or penetration) is not the only time that voids may be formed. Figure 7.1.1.4 is a diagram of a pore that is filled with varnish solution during application. The volume of this pore is fixed. The initial volume of the varnish,  $V_1$ , is the same as the pore but as (if) the solvent is removed from the solution within the crack/pore, the volume of this solution will want to be decreased, to  $V_2$ . To replace this volume, varnish solution will have to flow into the feature through its entrance. As the coating dries the flow of this material may become too restricted to replace the lost volume. At this point loss of adhesion and creation of air voids maybe the only way of filling the volume and maintaining pressure.

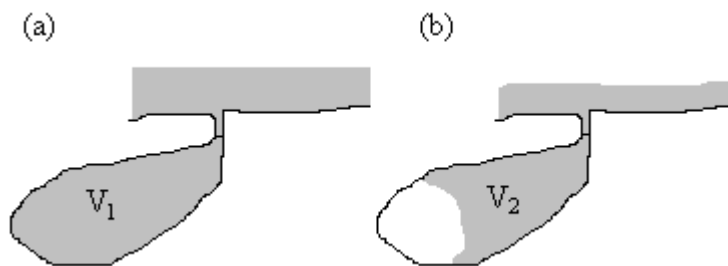


Figure 7.1.1.4  
(a) Pore filled with varnish during application  
(b) As the varnish within the pore dries, it no longer has the volume to fill the pore.

## 7.1.2 Volume Scattering

Another source of scattered white light from a varnish paint layer system is volume scattering within the varnish itself. Varnish is ideally perfectly transparent at optical wavelengths, with no scattering or absorption. Most freshly applied varnish coatings closely approximate this and with application thickness of only a few microns in a conservator applied varnish there is little concern. However, inappropriate or intentional selection of components of a varnish solution may produce a scattering coating. With aging, varnishes degrade due to chemical reactions and, as they are glasses, they may also change due to physical aging. If these processes cause

physical changes to the structure of the varnish material, such as fracturing, they may induce scattering by the coating. To evaluate the potential magnitude, to confirm whether or not this is a significant factor in appearance, the scattering within several aged varnish samples was measured. This work is detailed in section 7.4.

### 7.1.3 OCT for other optical measurements

The experimental measurements in this chapter are all done with OCT. As well as multi-interface profilometry, OCT images can give further information about the optical properties of a varnish coating system.

The intensity of the OCT signal, from the surface reflection, is dependent on the gloss of the surface and the difference between the axial direction and the normal direction of the local plane of the surface. As a result the measurement of the signal intensity distribution, of the pixels corresponding with the surface, provides information on the gloss of the surface. This has previously been used in the measurement of paper<sup>7</sup>. This gloss measurement provides an alternative (if surface profile cannot be distinguished correctly from other signals) or complementary method to the surface profile measurement. For the measurement of conservator applied coatings, in this chapter, gloss measurement provides a method of characterising surface roughness when surface profile measurements are impaired by scattering from beneath the surface (such as subsurface scattering or signal from a paint layer). This allows the optical quality of different varnish coatings to be straight forwardly assessed when the measurement of the surface profile is too challenging.

OCT is used to detect the diffuse scattering of white light at places other than the interfaces in varnish systems. The detection of voids within a varnished substrate has not previously been made and the possibility ignored. Serendipitously, when measuring conservator applied varnish coatings, on ground glass substrates, scattering from such voids were detected with OCT. By measuring the highest OCT signal amplitudes from beneath the top signal (usually surface) for each lateral

position, then comparing the amplitudes by use a histogram, the subsurface scattering can be quantified for different coatings.

For the scattering of light from within the volume of materials, the magnitudes of OCT signal from within a volume of material can be taken. These measurements of different coatings were compared by the use of histograms, like was done for the subsurface scattering and gloss measurements. Different intensities and densities of scattering points would give different shaped histograms.

## 7.2 Conservator applied coatings: ground glass plates

### 7.2.1 Methods: applied coatings

To develop the experimental setup used in chapter 6 to a more realistic application, three ground glass plates were again used but the method of application was changed to practices used by conservators. The three glass plates were sent to the National Gallery in London where the conservators applied different varnish combinations. The three plates were separated into different areas with the different coatings. Figure 7.2.1.1 is a diagram of the sectioning of each plate and gives the coating applied for each section. The first plate was used to test differently applied dammar coatings ( $0.25 C_m$  in “terpenalin”). For the first third of the plate, the dammar solution was applied with a brush, while the last third it was applied by spraying. The middle third, of this plate, overlapped both techniques, with the brushing being carried out first. Brushed then sprayed combinations of varnish coatings are common practice by conservators. There are two reasons for this practice. The first is due to the ability to apply the second coating without unintentionally removing the first, as would occur with brushed application, of the second coating, with a solvent compatible with the first coating. The second reason is that, by controlling the concentration at which the sprayed varnish droplets impact on the painting, some control of the final surface roughness is given, allowing the surface gloss to be controlled.

Dammar Brushed	Paraloid Brushed	1)	2)
Dammar Brushed then Sprayed	Paraloid Brushed then MS2A Sprayed	4)	5)
Dammar Sprayed	MS2A Sprayed	3)	

Figure 7.2.1.1

Conservator applied coating sections of three glass plates, showing what coatings were applied in each section. The numbered sections of the third plate are 1) Brushed Regalrez, 2) Brushed MS2A, 3) Sprayed MS2A, 4) Brushed Regalrez + MS2A Sprayed and 5) Brushed MS2A + MS2A sprayed.

The second glass plate was again split into thirds with the same approach to brush and spray application. For this plate two different synthetic varnishes were used, Paraloid B72 for the brushed varnish (in xylene 0.1  $C_m$ ), and MS2A sprayed varnish (in White Spirit 0.08  $C_m$ ). This plate allows the comparison between the performance of a poor levelling resin (Paraloid B72) applied by brush with a good levelling resin applied by spraying.

The third plate was split into 5 areas with different combinations of two low weight synthetic varnishes, Regalrez 1094 (in “Alcasol D40” 0.2  $C_m$ ) and MS2A (in White Spirit 0.08  $C_m$  for spraying and 0.3  $C_m$  for brushing). The combinations used were:- 1) Brushed Regalrez, 2) Brushed MS2A, 3) Sprayed MS2A, 4) Brushed Regalrez + MS2A Sprayed and 5) Brushed MS2A and MS2A sprayed. This plate allows the comparison between these two low molecular weight synthetic resins. There are some differences between the resins. In terms of levelling performance, the viscosity-concentration function (measured in toluene, chapter 4) of MS2A has higher viscosities than Regalrez 1094. In the measurements and modelling of levelling, Regalrez performed better than MS2A. As a result Regalrez 1094 is expected to produce the smoother surface. There are some differences in the properties of the dry film. Regalrez 1094 is known to be tacky when handled<sup>8</sup>

(without any trace of solvent). MS2A is regarded to be a brittle as a film<sup>9</sup>. These properties may be due to glass transition temperature, chapter 1.3.7 gives a discussion on this.

To provide a reference for performance of the different coatings, an unvarnished ground glass plate was also measured by the same methods. This allowed quantification of the total effect that each varnish has on the rough glass substrates.

### 7.2.2 Methods: measurement of plates

To confirm that the OCT gloss measurements matched the visual perception of each coating, for each plate the different varnished sections were judged visually into an order of gloss. This was done before any other measurement. This provided a quasi-independent subjective opinion, as the measurement results could not influence opinion. Disagreement between the opinion and OCT gloss results would highlight problems in the methods.

OCT was used to measure the surface roughness and optical gloss. The thickness of the dried varnish coatings were less than the resolution of the OCT system, so multi-interface profilometry with the substrate interface could not be carried out. The OCT data was taken with 1000 lateral points over a range of 10mm. Instrument averaging of 5 was used. To accurately quantify the roughness of the surface and the errors of the measurement, the speckle measurement approach from chapter 2.4.2 was used. OCT was used to take three measurements of a profile (each measurement was taken from an average of 21 image data sets) at different axial positions in the OCT image. The three measurements allowed the real roughness and measurement error to be calculated. For each sample this was repeated 6 times.

Before the fitting of Gaussian functions to its axial image data to obtain its profile, the varnish-air interface (the surface) was found automatically. However, it was found that for some samples that scattering from beneath the surface was often of higher intensity than the signal from the surface. This was unexpected and led to difficulties recovering the surface. To increase the stability of finding the surface, and recover the magnitude of the subsurface scattering, the following algorithm was

used. Within the user defined axial range the highest intensity signal was found. The highest pixel and the 6 pixels above and below were then disregarded for a second search of the axial range. The highest value pixel was again taken if it was above a threshold intensity. If this second search returned a pixel, the surface profile was fitted at the top pixel of the returned two and the intensity of the bottom pixel was recorded. The intensities of the recorded bottom pixels were then plotted on histograms to compare the samples.

To calculate the power spectrum density for the roughness of each segment, after the measurement and correction for distortion of each profile, the average profiles of each set of speckle measurements were taken. The PSD of these averaged profiles were calculated, and for the 6 measurements of each segment the PSD was averaged.

An alternative to measuring the surface profile is the measurement of surface gloss by OCT<sup>7</sup>. A glossy surface (low high frequency roughness) will produce a high signal when the surface is near normal to the measurement direction as the light is specularly reflected back into the instrument. If the surface is away from the normal direction the light is specularly reflected away from the instrument leading to low or no detectable signal. These glossy varnish surfaces still have significant low frequency roughness, which produces a range of surface normal directions. This gives the glossy surfaces a wide dispersion of intensity signals. In contrast, a matte surface (large amount of high frequency roughness) will scatter light in all direction from the surface, independent of the direction local plane of the surface. Aside from speckle effects, the intensity of the surface detected by the instrument, at different positions, will be more uniform. To measure this with OCT the intensity of the surface pixels were taken and recorded for each sample. Histograms of the pixel intensities give characterisation of the surfaces gloss.

### 7.2.3 Results: uncoated ground glass reference

Figure 7.2.3.1 shows an OCT image of an uncoated surface. The rms surface roughness and speckle error was measured by the axial shifting method. Table 7.2.3.1 gives the measured values for the uncoated surface.

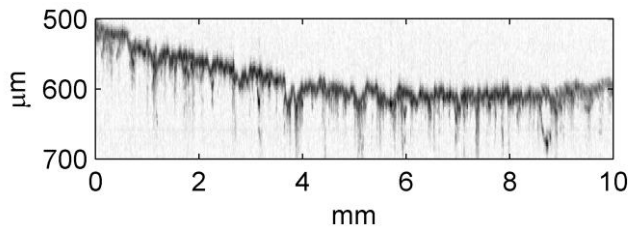


Figure 7.2.3.1  
OCT image of  
uncoated ground  
glass substrate.

	<i>rms</i> Roughness ( $\mu\text{m}$ )	Measured Error ( $\mu\text{m}$ )
Uncoated	$6 \pm 1$	$2.0 \pm 0.4$

Table 7.2.3.1  
Measured *rms* roughness and error using axial  
shifted profile method.

In chapter 2.4.2 subsurface fracturing had been identified in a sandblasted glass substrate. This fracturing, for the ground glass substrates used here, is also clearly apparent in figure 7.2.3.1. This is visible to the OCT system due to the fractures scattering light. Figure 7.2.3.2 (a) is the histogram of the identified subsurface scattering for the uncoated ground substrate. The subsurface scattering identified is significant and as there is no coating it is all from below the defined glass interface (surface profile). This subsurface scattering cannot be due to lack of wetting or adhesion at the surface profile but comes from voids due to fractures. If a dry varnish coating fills these fractures, then this subsurface scattering will be substantially reduced.

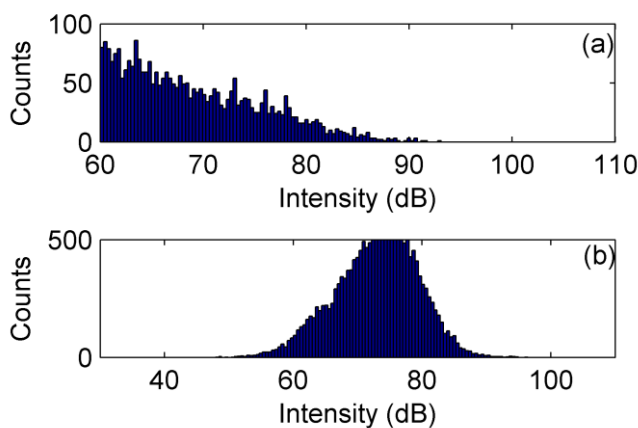


Figure 7.2.3.2  
(a) Histogram of measured  
subsurface scattering of  
uncoated substrate.  
(b) Histogram of surface  
pixel intensity (gloss).

Figure 7.2.3.2 (b) shows the intensity of the identified surface pixels. This uncoated surface is the reference of the matte starting surface to evaluate the performance of

the varnish coatings. The distribution of the histogram is narrow with the peak counts above 500.

### 7.2.4 Results: dammar coated plate

For the dammar coated plate there was a clear order in the visual assessment of glossiness. The brushed dammar appeared least glossy, followed by sprayed, then brushed then sprayed was the glossiest. Figure 7.2.4.1 shows the OCT image and surface profile results for the dammar plate. The appearance of the OCT images match the visual observations, this is confirmed by the examination of a histogram of the surface pixel intensities in decibels (figure 7.2.4.2). An increase in higher intensity pixels is seen with the increase in apparent gloss.

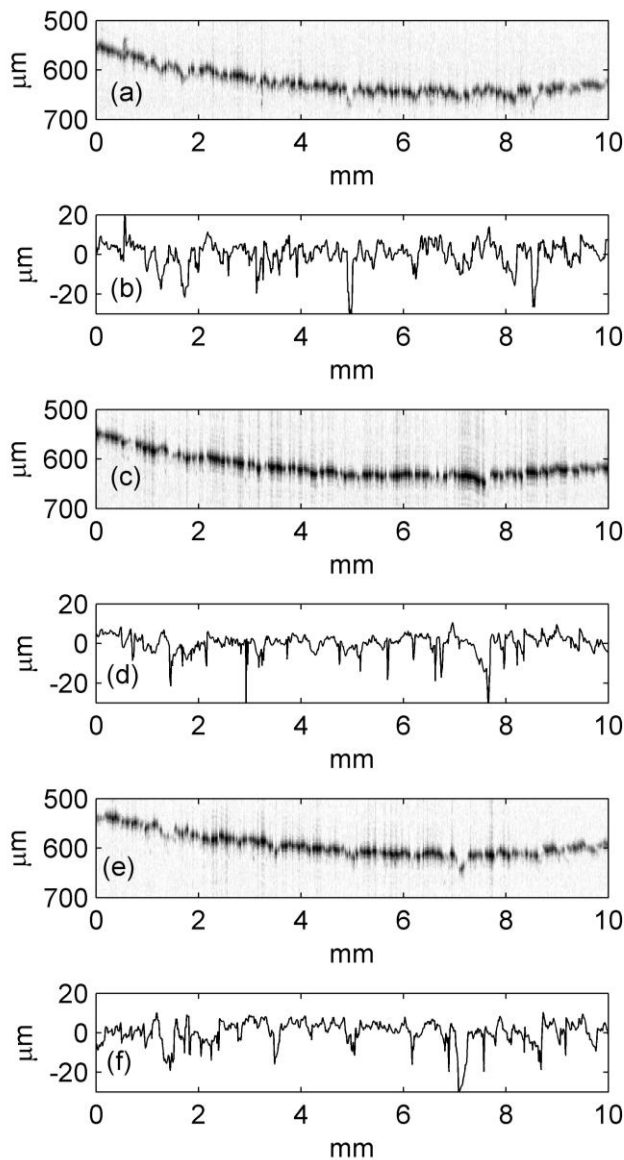


Figure 7.2.4.1  
(a,c,e) OCT images  
and (b,d,f) their  
measured surface  
profiles of dammar  
coated ground glass  
substrate by methods:-  
(a,b) brushed,  
(c,d) brushed then  
sprayed and  
(e,f) sprayed.

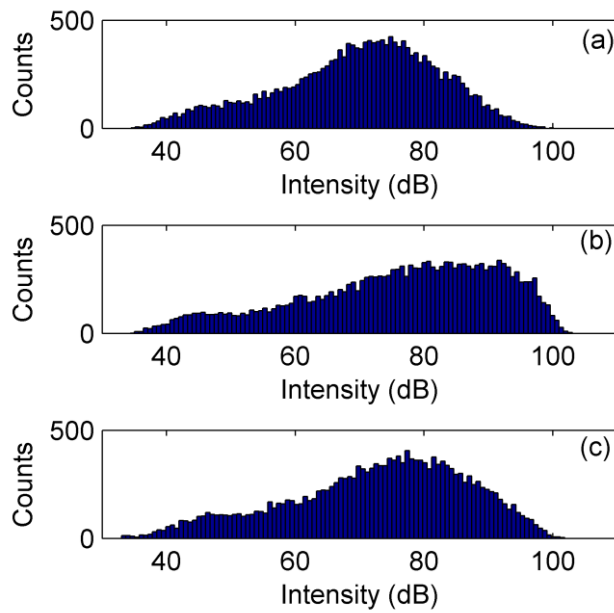


Figure 7.2.4.2  
Histogram of surface pixel intensity (gloss) of dammar coated ground glass substrate by methods:-  
(a) brushed,  
(b) brushed then sprayed and  
(c) sprayed.

Table 7.2.4.1 gives the measured RMS roughness and error values of the three dammar sections. These values matched the findings from the gloss measurement. There are significant differences in the rms roughness values, with the brushed varnish being the roughest and brushed and sprayed the smoothest. The difference in the measured speckle error between the brushed and sprayed coating is negligible compared to the standard deviation. There is an increase in the measured speckle error of the brushed and sprayed coating, which is explained below. Figure 7.2.4.3 shows the PSD of the coatings roughness. These follow the same trends as the rms roughness but do contain significant noise.

	<i>rms</i> Roughness ( $\mu\text{m}$ )	Measured Error ( $\mu\text{m}$ )
Dammar Bushed	$6.3 \pm 0.3$	$1.5 \pm 0.3$
Dammar Brushed then Sprayed	$4.0 \pm 0.4$	$1.7 \pm 0.3$
Dammar Sprayed	$5.1 \pm 0.6$	$1.4 \pm 0.3$

Table 7.2.4.1  
Measured rms roughness and error using the axial shifted profile method.

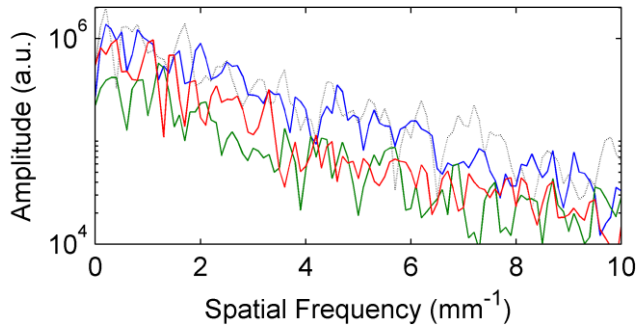


Figure 7.2.4.3  
PSD of dammar coated ground glass substrate by methods:- brushed (blue), brushed then sprayed (green) and sprayed (red). The measured PSD of the uncoated plate (dotted black).

Figure 7.2.4.4 shows the measured subsurface scattering for the dammar plate. Compared to the uncoated plate the subsurface scattering is negligible. However in the brushed and sprayed section there is a significant peak at extremely high intensities (100dB). This is due to the surface search algorithm and the high glossiness of this section. Due to the high signal from surface, there is an increased amount of ringing artefact signal. These artefacts are clearly evident in figure 7.2.4.1 (c). For the highest signal points of the surface the ringing artefacts in front of the surface become higher than the threshold of the second peak search and are identified as the surface. The high signal from the actual surface is then identified as substrate scattering. This misidentification of the surface results in the higher measured error for the brushed then sprayed coating.

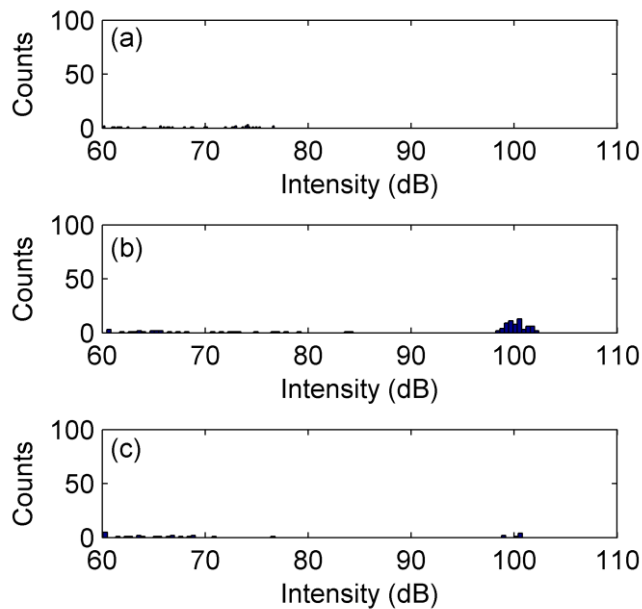


Figure 7.2.4.4  
Histograms of measured subsurface scattering of dammar coated ground glass substrate by methods:- (a) brushed, (b) brushed then sprayed and (c) sprayed.

Overall the results from the dammar coated plate were unsurprising. The trend of the surface roughness and gloss measurements matched and the effect of non-

surface signals on the OCT measurement was negligible. The trend in performance of surface levelling of the three components is likely to be due to the amount of dammar varnish applied by the methods. The brushed and sprayed coating which certainly has the most varnish applied (the sum of the other two thirds) is the most glossy. It is possible that the sprayed coating was thicker than the brushed coating, giving the glossier coat. It was not possible to measure the final thickness of the coating in this measurement and the amount of varnish applied was not measured.

### 7.2.5 Results: Paraloid B72 and MS2A coated plate

Figure 7.2.5.1 shows example OCT images and profiles for the plate. Where the paraloid varnish has been brushed on first, large amounts of signal is seen to be coming from underneath the surface (Figure 7.2.5.1 (a) and (c)). The effect does not appear as bad for where the MS2A varnish had been sprayed only (Figure 7.2.5.1 (e)) but is still significant. The results of this in the profile measurements are evident despite the double search algorithm. In figures 7.2.5.1 (b) and (d) (and (f) to a lesser extent), the measured profiles clearly jump from the surface, to signal beneath it, at a significant amount of points. This is exaggerated by areas of minimum signal from glossy surfaces.

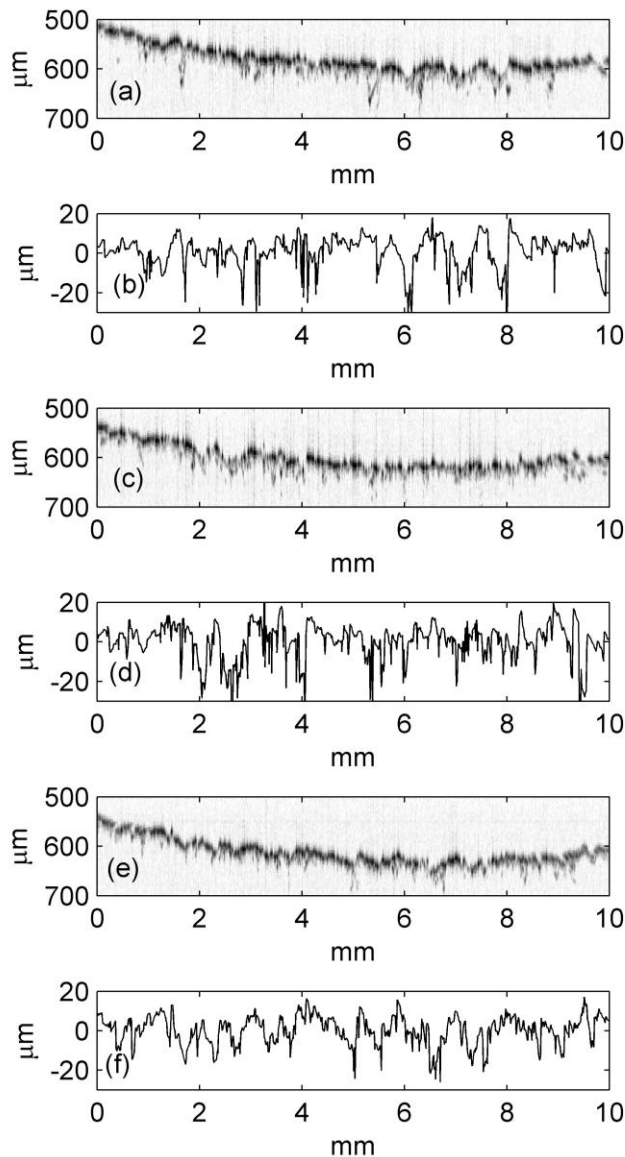


Figure 7.2.5.1  
(a,c,e) OCT images  
and (b,d,f) measured  
surface profiles of:-  
(a,b) brushed Paraloid  
B72,  
(c,d) brushed Paraloid  
B72 then sprayed  
MS2A and  
(e,f) sprayed MS2A.

Figure 7.2.5.2 shows the surface pixel intensity results for this plate. Like the dammar plate the brushed and sprayed section was the glossiest, with the highest spread of intensities. However the brushed Paraloid proved to be glossier than the sprayed MS2A. The high molecular weight resin, Paraloid, was expected to produce a rougher surface as its levelling is poorer than the low weight, low viscosity, resin MS2A (chapter 6). The visual evaluation of gloss matched the OCT gloss results.

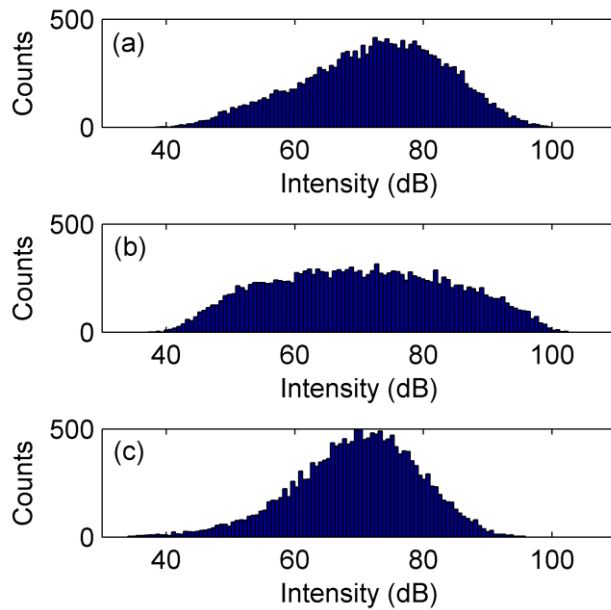


Figure 7.2.5.2  
Histogram of surface pixel intensity (gloss) of:-  
(a) brushed Paraloid B72,  
(b) brushed Paraloid B72 then sprayed MS2A and  
(c) sprayed MS2A.

As seen in figure 7.2.5.1, the high amount of error due to subsurface scattering led to the profile measurements of the surface by OCT to be unreliable. The *rms* roughness values measured from these are unlikely to be reliable. Table 7.2.5.1 shows the measured *rms* roughness and error of the three sections. Due to the increase of the subsurface scattering induced error, with increased surface gloss, the brushed and sprayed section gave the highest measured roughness and error. The MS2A sprayed coating gave the lowest error in the measurement but still gave a higher *rms* roughness than the paraloid brushed coating. The roughness results confirm that the sprayed MS2A coating is more matte than the brushed paraloid. Figure 7.2.5.3 shows the measured PSD for the plate. Due to the error in the profile measurements, the measured PSDs were indistinguishable above the noise.

	<i>rms</i> Roughness ( $\mu\text{m}$ )	Measured Error ( $\mu\text{m}$ )
Paraloid B72 Brushed	$7.7 \pm 0.6$	$2.1 \pm 0.5$
Paraloid B72 Brushed then MS2A Sprayed	$8.9 \pm 0.9$	$2.9 \pm 0.5$
MS2A Sprayed	$8.5 \pm 0.7$	$1.8 \pm 0.4$

Table 7.2.5.1  
Measured *rms* roughness and error using axial shifted profile method.

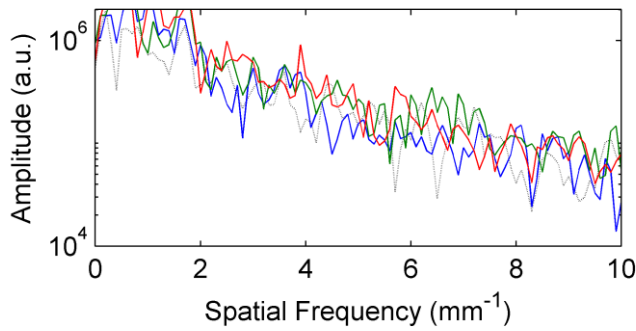


Figure 7.2.5.3  
PSD of coated ground glass substrate by:- B72 brushed (blue), B72 brushed then MS2A sprayed (green) and MS2A sprayed (red). The measured PSD of the uncoated plate (dotted black).

The most important result from this plate was the subsurface scattering results. Figure 7.2.5.4 shows the histogram of found subsurface pixel intensity. Unlike the dammar plate, all the sections gave significant scattering from beneath the surface. The MS2A sprayed coating has the least subsurface scattering of the three sections, while the scattering is higher in the two sections where Paraloid has been brushed on first.

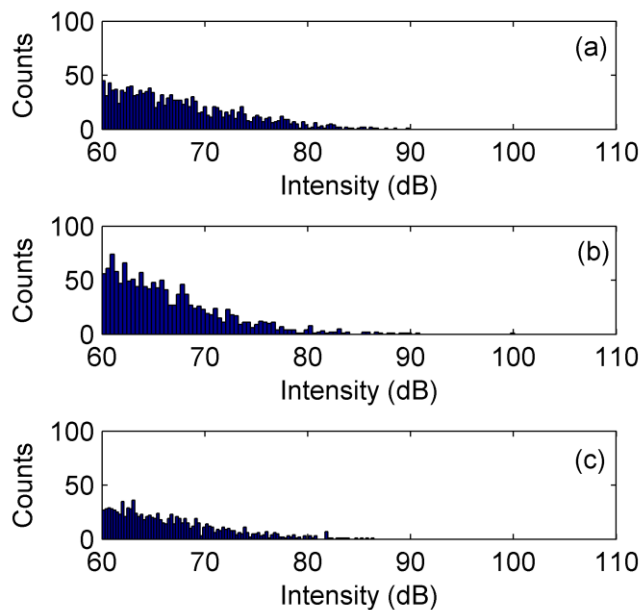


Figure 7.2.5.4  
Histograms of measured subsurface scattering of:-  
(a) brushed Paraloid B72,  
(b) brushed Paraloid B72 then sprayed MS2A and  
(c) sprayed MS2A.

The experimental results for this plate showed that the brushed Paraloid coating gave a smoother and glossier coating than the sprayed MS2A coating, which was unexpected. This may be due to different amounts of amounts of varnish being applied. These varnish coatings did not fill subsurface fractures well, even though the dammar coatings of the previous section and some of the coating of the next section did. These differences in the subsurface wetting behaviour, of different varnish coatings, had not been expected.

## 7.2.6 Results: Regalrez and MS2A coated plate

Figure 7.2.6.1 shows the histogram of the found subsurface scattering pixels intensities for the 5 sections of the MS2A and Regalrez plate. This plate produced the greatest contrast of results regarding subsurface scattering. The highest subsurface scattering is in the MS2A sprayed coating, this result is a match to the MS2A sprayed coating on the Paraloid and MS2A plate (Figure 7.2.5.4). Where MS2A had been brushed on first there was a low amount of subsurface scattering. Where Regalrez had been brushed applied initially the subsurface scattering was negligible. The difference between the MS2A and Regalrez subsurface scattering results is very important, as it shows a difference between the wetting, penetration or adhesion of the two coatings.

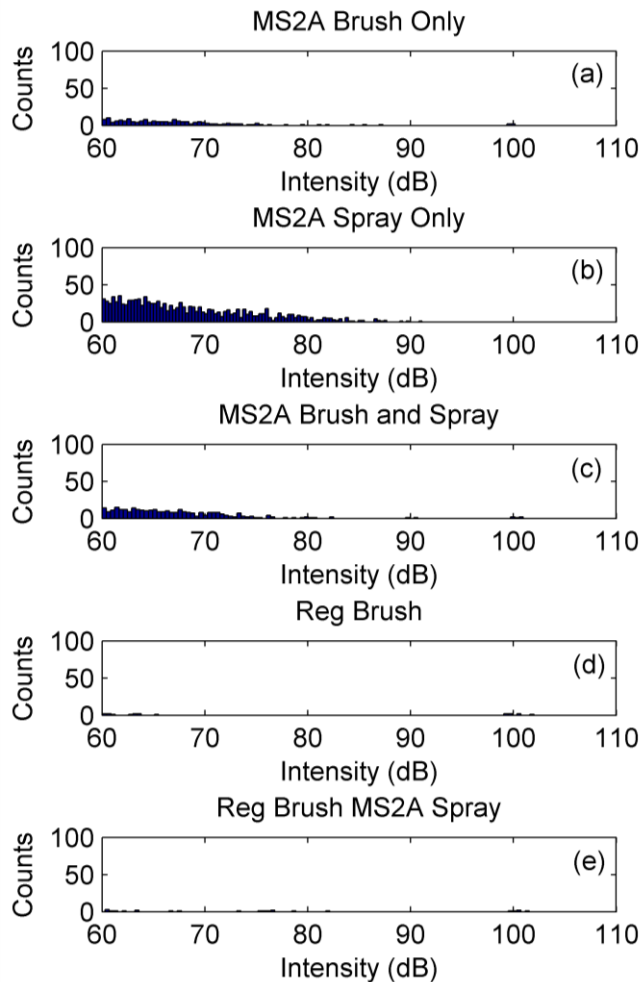


Figure 7.2.6.1  
Histograms of measured subsurface scattering of:-  
(a) brushed MS2A,  
(b) sprayed MS2A,  
(c) brushed then sprayed MS2A,  
(d) Regalrez Brushed and  
(e) Regalrez Brushed and MS2A sprayed.

The segments of the MS2A and Regalrez plate were visually judged in order of most to least glossy as:- 1) MS2A Brush + Spray, 2) Reg Brush + MS2A sprayed, 3) Reg Brushed, 4) MS2A Brushed, 5) MS2A sprayed. Figure 7.2.6.2 shows the

histograms of surface pixel intensity for each section, these OCT results matched the visual judgment.

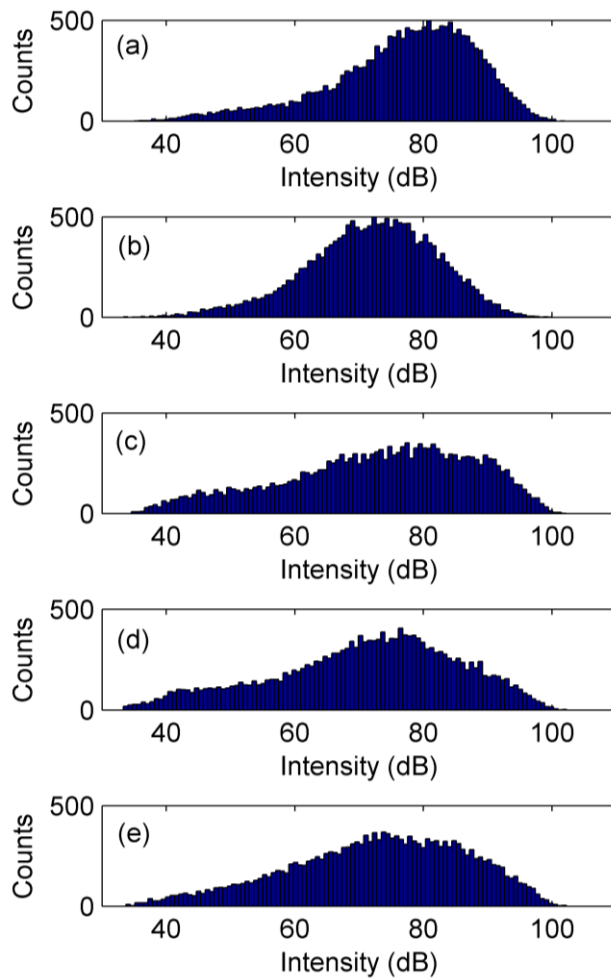


Figure 7.2.6.2  
Histogram of surface pixel intensity (gloss) of:-  
(a) brushed MS2A,  
(b) sprayed MS2A,  
(c) brushed then sprayed MS2A,  
(d) Regalrez Brushed and  
(e) Regalrez Brushed and MS2A sprayed.

Table 7.2.6.1 shows the measured *rms* roughness and error from the sets of speckle measurement profiles. For the MS2A coatings the sprayed coating is the roughest matching the gloss results. The brushed and sprayed coating was expected to be smoother than the brushed only coating, due to the application of a larger amount of varnish. However this was not the case for the measured roughness, though it was for the measured error. The measured *rms* roughness of the MS2A brushed coating increased after applying a second coat by spraying. Figure 7.2.6.3 shows example OCT images and surface profiles for the MS2A coated sections. Examination of these results for the MS2A brushed only and MS2A sprayed only coating shows that the error due to misdetection of the surface is low. There was an increase in the surface misdetection error for the brushed and sprayed sample. The sprayed coating of MS2A, on top of the brushed coating, had changed the surface state. This resulted

in the apparent roughness, over the scales of the measurement, increasing. It is possible that the spray application is lowering the high frequency roughness (increasing gloss and decreasing speckle error) but increasing the low frequency roughness (increased *rms* roughness).

	<i>rms</i> Roughness ( $\mu\text{m}$ )	Measured Error ( $\mu\text{m}$ )
MS2A Brushed	$3.6 \pm 0.8$	$2.2 \pm 0.4$
MS2A Brushed then Sprayed	$5.2 \pm 0.4$	$1.9 \pm 0.5$
MS2A Sprayed	$6.6 \pm 0.6$	$1.9 \pm 0.4$
Regalrez 1094 Brushed	$5.2 \pm 0.8$	$1.7 \pm 0.4$
Regalrez 1094 Brushed then MS2A Sprayed	$5.2 \pm 1.1$	$1.5 \pm 0.3$

Table 7.2.6.1  
Measured *rms* roughness and error using the axial shifted profile method.

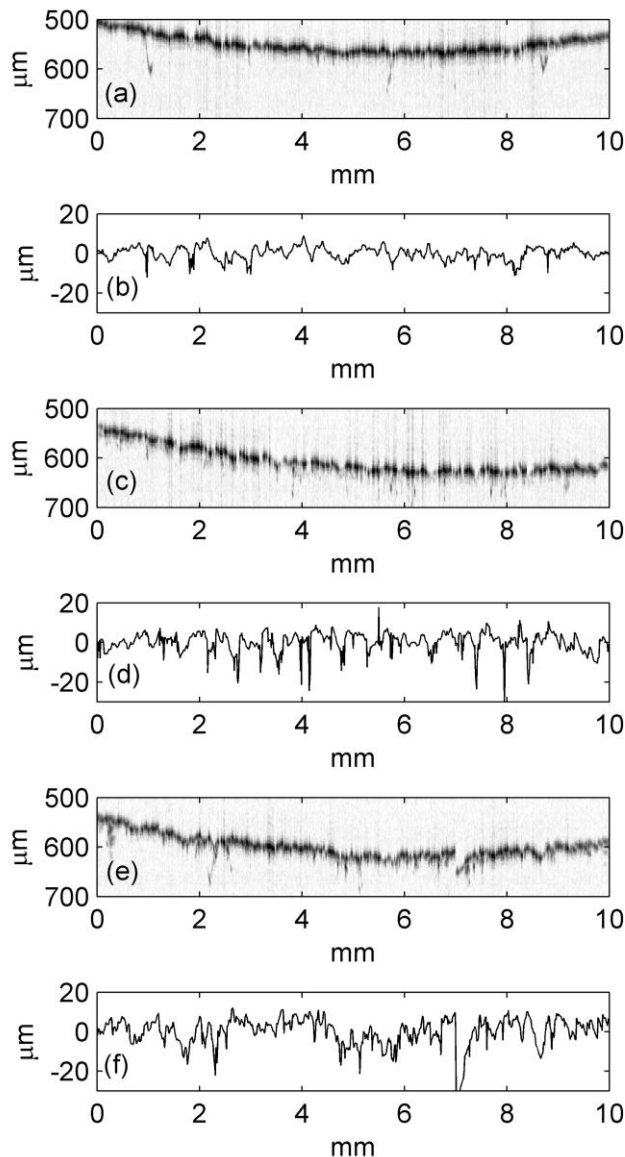


Figure 7.2.6.3  
 (a,c,e) OCT images  
 and (b,d,f) measured  
 surface profiles of the  
 MS2A coated ground  
 glass substrate by  
 methods:-  
 (a,b) brushed,  
 (c,d) brushed then  
 sprayed and  
 (e,f) sprayed.

The *rms* roughness results for the two sections where Regalrez had been brushed on initially were indistinguishable. The speckle error measurement did show some decrease with the sprayed application of MS2A, though, like for the MS2A brushed coatings, less than the one standard deviation bounds. The sprayed coating does appear to lower the high frequency roughness again. The sprayed coatings of MS2A, on top of brushed coatings, show evidence for reducing high frequency surface roughness. However, the application of the coating may increase low frequency surface roughness.

The most important (and conclusive) result from the MS2A and Regalrez plate is the difference in subsurface scattering between the coatings. Where Regalrez has been brushed on first, there was no significant scattering identified, where MS2A has

been brushed on first there was moderate subsurface scattering and where MS2A has been sprayed directly on to the substrate the scattering was the most significant. The visual gloss observation matched the measurement of gloss with OCT. The gloss increased with the amount of varnish applied. The measured net roughness over the scales of this experimental work for this did not correspond directly to the measured surface gloss. There is not necessarily a correlation of the high frequency roughness that determines gloss with the low frequency roughness included in these measurements.

### 7.2.7 Discussion: all conservator coated glass plates

The results of this experimental work are of fundamental importance to understanding the optical effects that influence the appearance of real varnish coatings on paintings. Recent experimental work has focused on the development of surface roughness with the assumption that wetting and adhesion of the varnish to the substrate always remains complete. By using OCT to examine varnish coatings applied by conservators to ground glass substrates, scattering of light from beneath the coating surface was observed. This showed that the wetting and adhesion to the entire complex (including features not defined by a surface profile) surface was not complete for some coatings. This is the first known experimental data that shows conclusively that this effect can occur for painting varnishes. Though it is unknown how well the fractured glass surfaces, used in this study, represent porous paint surfaces.

For these ground glass plate measurements, the presence of subsurface scattering was dependent on the initial varnish coating used. For the samples where dammar or Regalrez had been used as the initial coat, no significant subsurface scattering was present. For samples where Paraloid B72 or MS2A were the initial coat, the presence of subsurface scattering was very significant.

Three possible processes have been identified as the cause of this subsurface scattering. The first of these is the lack of capillary penetration by the varnish solutions into subsurface cracks and voids. The second potential reason is incomplete wetting of the rough surface profile during application causing air

bubbles attached to the surface profile. The third potential reason is the breaking of the adhesion of the varnish coating to the surface (that has been successfully wetted and voids filled) during drying due to internal stresses. As the measured subsurface scattering for coated plates never exceeded the scattering of the uncoated plate, this is suggestive that it is the varnishes penetration ability that results in the differences. If the varnish was not wetting or adhering to the surface then the amount of scattering would be increased compared to the blank substrate. Voids created at the surface profile would be in addition to the subsurface voids in the uncoated sample.

The gloss and surface roughness results did not provide conclusive confirmation of dominance of the resin in the levelling performance of coatings. It had been expected that Paraloid coatings would give a much rougher surface, than the other coatings used, due to the poor levelling properties of the polymer resin. In the comparison of brushed Paraloid coatings to brushed coatings of MS2A and Regalrez, Paraloid did give the rougher surface. However, when brushed Paraloid was compared to a spray coating of MS2A, this was not the case. It is possible that the amount of varnish applied in the spray coatings of MS2A was substantially lower than the other coatings.

Though this section of work has measured conservator applied coatings, these have been applied to ground glass substrates. The reason for this was to remove signal that is not from interfaces (*i.e.* remove the scattering signal from the volume of a paint) from the OCT measurements. The interaction of a varnish coating with a glass substrate may have differences to its interaction with a real paint surface.

## 7.3 Conservator coated painted canvas samples

### 7.3.1 Method

As well the conservators at the National Gallery applying varnish coatings to ground glass substrates they were also provided with 3 painted canvas off cuts. Two of them were painted brown and one dark brown/black. The composition of the paint was unknown, presumed oil paint. Figure 7.3.1.1 is a photograph of the three coated samples. A dammar coating (0.25 C<sub>m</sub> in “terpenalin”) was applied to the black

canvas piece and on one of the pieces of brown canvas a paraloid B72 varnish (0.1  $C_m$  in xylene) coating was applied. For the second brown canvas piece a glossier (than Paraloid B72) coating was applied, unfortunately the record of what was applied has been lost. It can be seen in figure 7.3.1.1 that the Paraloid coating appears to have less gloss than the other two coatings. The colour of the Paraloid coated sample is seen to be lighter than the glossy brown sample.

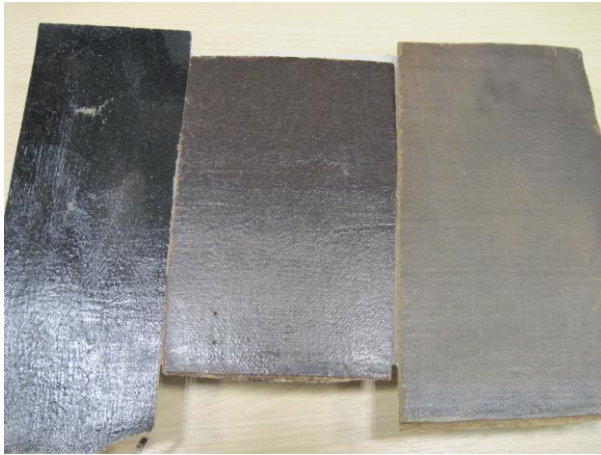


Figure 7.3.1.1  
Photograph of three painted canvas samples with conservator applied varnish coatings. Left is the black canvas piece coated with dammar, middle is brown canvas piece with unknown coating and right is a brown canvas piece coated with Paraloid B72.

The OCT data, for these samples, was taken by the same method as the ground glass plates (section 7.2.2). Surface profile and gloss measurements were attempted for these samples. The measurement of subsurface scattering was not attempted from the results, as the signal from the volume of the paint, rather than from voids, would dominate the returned intensities.

### 7.3.2 Results

Figure 7.3.2.1 shows example OCT images and profiles for the three samples. The paint samples all scatter light from their volume, this signal leads to the automatic algorithm for the initial finding of the surface (so that fitting can be carried out) to fail. This is especially the case when the signal from the varnish surface is weak, due to high gloss and a significant angle between the optical axis and the normal of surface. This is most evident in the results for the dammar coating on black (Figure 7.3.2.1 (a,b)) which was the glossiest sample. Where the varnish surface is close to normal to the OCT optical axis (between lateral positions 7 and 8mm) it is clearly visible in the image and the profile measured is smooth. Elsewhere on the profile, where the surface signal is not high, the measured profile positions are within the

volume of the paint. Due to the majority of the length of measured profiles being erroneous, their statistics cannot be considered.

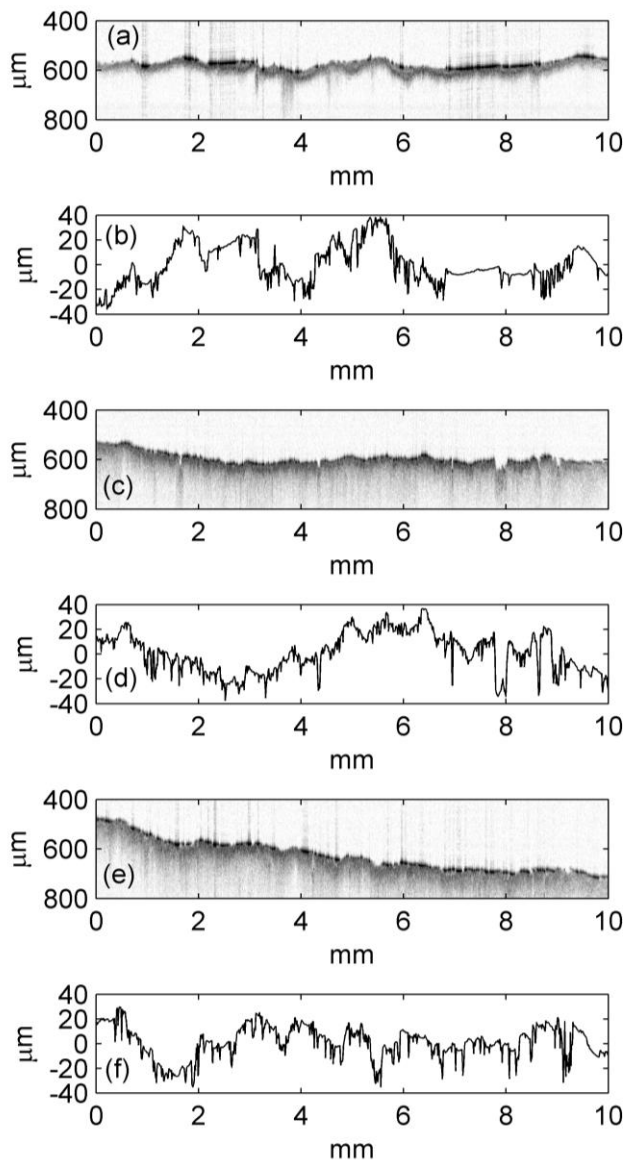


Figure 7.3.2.1  
OCT images (a,c,e)  
and measured surface  
profiles (b,d,f) of  
coated painted canvas  
substrate by:-  
(a,b) dammar on  
black,  
(c,d) paraloid on  
brown and  
(e,f) unknown coating  
on brown.

The intensity of the recovered pixel, in the automatic surface search, can still provide the gloss information of the surface. It also has the potential to quantify the proportion of the points on the erroneous profiles that are actually of the surface. Figure 7.3.2.2 shows the histograms of the returned pixel intensities for the samples. The result for the black dammar sample gives two peaks in intensity count. The peak around 65dB comes from where the surface algorithm returns points from within the volume of the paint. The high intensity peak, maximum around 90 dB, comes from the glossy specula refraction from the varnish surface. In comparison the matte coating of Paraloid produces a single peak in counts around 75dB.

Comparison of the OCT images and profiles (Figure 7.3.2.1 (c,d)) indicate that, due to the more consistent signal from the matte surface, the detection of the paint volume rather than the surface is reduced. The intensity of the signal from the surface is also closer to the intensity of the paint volume scattering signal. These contribute to the presence of a single peak rather than a split double peak. The glossy reflections at 90dB are minimal for the Paraloid coating.

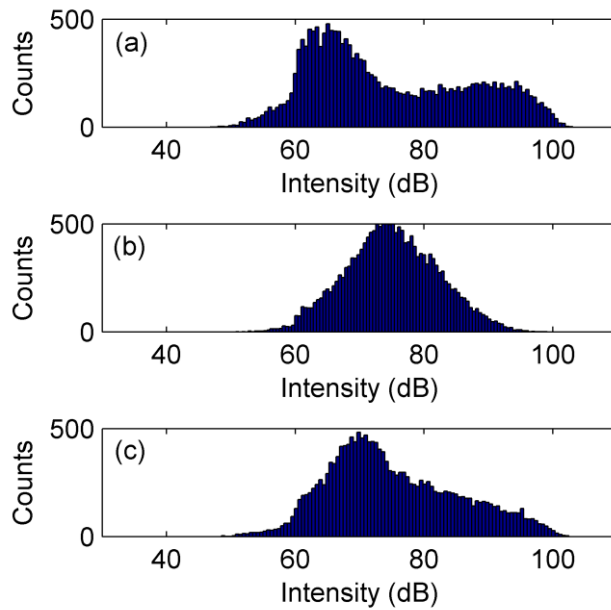


Figure 7.3.2.2  
Histogram of surface pixel intensity (gloss) of coated painted canvas substrate by:- (a) dammar on black, (b) paraloid on brown and (c) unknown coating on brown.

The unknown sample falls between the regimes of Paraloid and dammar on black. There is significant gloss signal around 90dB but it is not sufficient to form a separate peak. The subsurface signal results in the peak intensity occurring at approximately 70dB.

The results of comparing a conservator applied Paraloid coating on a real painting surface to the dammar coating and the unknown coating showed that the Paraloid coating gave a more matte appearance. Though in this case the surface roughness was not measured, by OCT, it is almost certain that this is due to the Paraloid coating having a rougher surface. In chapter 6 significantly poorer levelling ability of polymers, compared to low molecular weight resins, has been shown by modelling and experimental studies. The results in this section show no deviation of this trend for when real paint substrates are used (rather than glass).

## 7.4 Volume scattering measurements

### 7.4.1 Method

To determine whether volume scattering in aged varnish coatings is a significant factor in their appearance, OCT was used to measure the volume scattering in a set of aged varnish samples. These varnish coatings had been spread onto flat impervious substrates at various dates. The conditions in which the samples had been kept varied. Table 7.4.1.1 details the composition, the age and known conditions the sample has been exposed to for the seven varnish samples.

	Varnish Composition	Date of sample	Conditions/Notes
1	Boiled linseed and Mastic	1991	
2	Dammar and Pure Turps	~1990	
3	Wood Pitch (Picea Abies)	27 <sup>th</sup> Feb 1975	Kept in a light box for some of the period.
4	AW2 in white spirit	5 <sup>th</sup> Sep 1952	
5	H+W Terpene	sample dated 1882, spread 14 <sup>th</sup> July 1978	May have been kept in a light box for some of the period.
6	Mastic Turpentine	1952	Yellowed and cracked after 14 years exposure to daylight on NG roof
7	Mastic and Turpentine	1998	

Table 7.4.1.1  
The composition and notes of the aged varnish samples measured.

OCT measurements of static cross-sections through the varnish samples were taken for initial qualitative assessment of the coatings and data quality. Averages of 60 data sets were used to produce high signal to noise images. Volume data sets of the varnish samples were also taken. Where the varnishes were of sufficient thickness and the surface signal was consistently strong an automatic routine was implemented to recover pixel intensities in the volume of the varnish. If scattering occurs in the volume of the varnish the net pixel intensities will be increased. The high sensitivity of OCT enables any significant scattering to be detected, though it is also susceptible to detecting low intensity artefacts in the area caused by strong reflections outside the volume.

To recover a selection of pixels from within the volume of the varnish automatically, the surface pixel was found as the highest pixel value for each axial data set. After the surface pixel position had been recovered for one 2D data set, erroneous finds were discounted by not using axial data sets where the found pixel position was outside set limits of the surface plane. For the remaining surface pixels, the values of the pixels 6 to 15 (10 for varnish 6) pixels behind the surface pixel were taken. The pixel values recovered, from the 3D data sets, were presented as a histogram of their dB intensities. One thousands bins were used for each histogram. The amplitude within each bin was divided the total number of returned pixels. This was to give normalised results for all samples, *i.e.* the bin values are directly comparable between samples. To give the noise and artefact intensities for each measure, the pixel intensities from above the surface were also taken. The modulus distances from the surface were the same as for the internal volume measurements. These pixels from outside the varnish volume were processed in the same manner as the pixels from within the volume. This selection of pixels is free from scattering signal from within the varnish, but they will still have approximately the same noise/artefact levels. Any dust/dirt above the surface will increase the noise. The increase of the intensities of the pixels within the volume of the varnish, over the pixel intensities from outside of the volume, provides a quantifiable measurement of volume scattering.

### 7.4.2 Results

Varnish 1, where boiled linseed mixed with mastic had been applied, had not produced a transparent coating. Figure 7.4.2.1 shows an averaged OCT image for this coating. Scattering signal from the volume of the varnish is clearly evident. The mixture of Mastic and Linseed oil is known as meglip and is well known for unstable results<sup>10</sup>. OCT shows that the instabilities, of this particular mixture, must result in structural features within the varnish at near optical wavelength scales or bigger. This is required in order for these significant reflections to be possible. This is a good example of a coating, with a poor choice of combined ingredients, which gives a non-transparent finish.

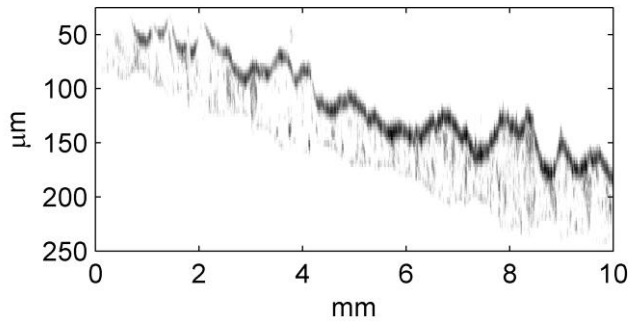


Figure 7.4.2.1  
OCT cross-sectional  
image of aged varnish 1  
(Meglip).

Figure 7.4.2.2 (a) shows the averaged OCT image of varnish 3, known as burgundy pitch<sup>11</sup>. The coating was extremely rough and uneven in thickness. Unlike varnish 1 there is little evidence from the OCT data of substantial light scattering from within the volume of the varnish. Scattering is evident from the particular substrate this coating was applied to. Figure 7.4.2.2 (b) shows the averaged OCT image of varnish 5 (terpene), the labelling of the coating as terpene is fairly ambiguous but will be derived from a tree resin similar to burgundy pitch. This terpene coating has a relatively rough surface, but less than the burgundy pitch. Points of high signal do exist, in the OCT data, from within the volume of the coating, but some of these maybe image artefacts (see the dammar results below for explanation).

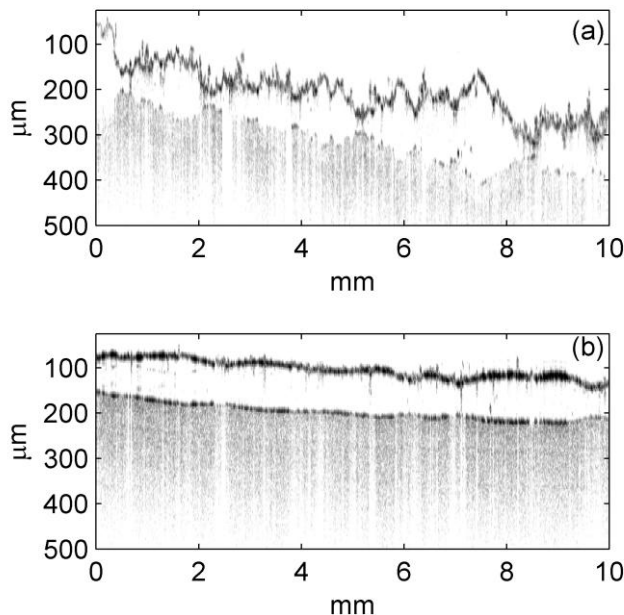


Figure 7.4.2.2  
OCT cross-sectional images  
of aged  
(a) varnish 3 (burgundy  
pitch)  
(b) varnish 5 (terpene).

Dammar and mastic are the two common natural resins used for art conservation presently. The degradation of both resins is well known, with mastic suffering worst (see chapter 1.1.2 for references and discussion). Figure 7.4.2.3 shows the averaged

OCT images of (a) varnish 2 (Dammar), (b) varnish 6 (aged mastic) and (c) varnish 7 (fresher mastic). The surface of the dammar coating is smooth and glossy but contaminated with dust and dirt. This contamination leads to image artefacts within the varnish volume. Other artefacts such as common path interference and harmonic ghost images are also visible. There appears little evidence for volume scattering above these image artefacts. The volume of the aged mastic coating does appear to show some evidence of point signals from within the volume of the varnish, though again these being image artefacts cannot be ruled out. The relatively fresh mastic sample (1998) is distributed more like a droplet, with the smooth surface reflecting the light away from the OCT instrument. There was no evidence for significant volume scattering in this image.

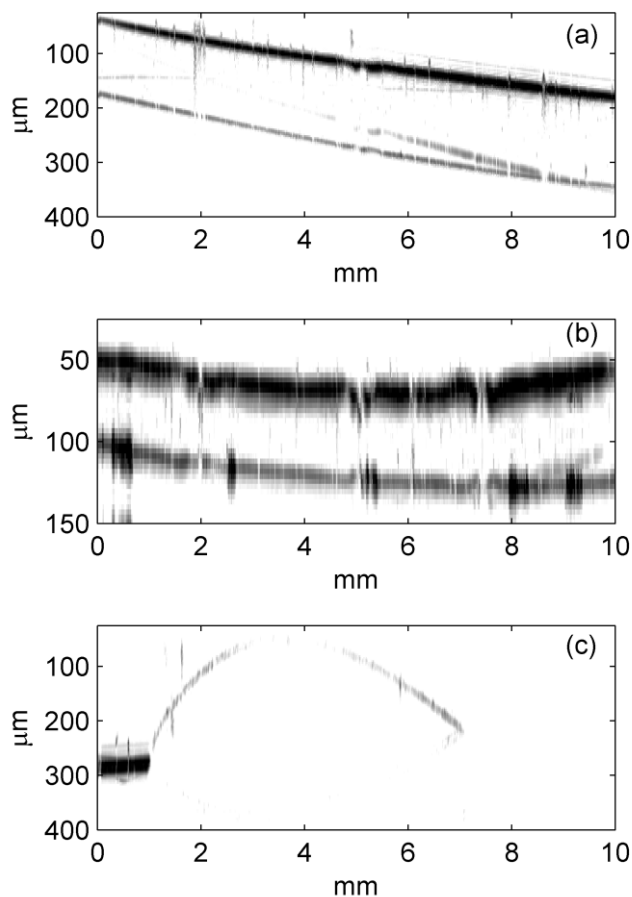


Figure 7.4.2.3  
 OCT cross-sectional images  
 of aged  
 (a) varnish 2 (Dammar)  
 (b) varnish 6 (Aged Mastic)  
 (c) varnish 7 (Fresher  
 Mastic)

The only aged synthetic varnish measured was varnish 4 (AW2 applied in 1952). The thickness of this coating was insufficient to use the volume method to analyse the volume scattering. Figure 7.4.2.4 shows the averaged OCT image across the

edge of the coating. At the edge of the coating it was thicker and had decreased signal from the varnish surface. This allowed visual assessment of the varnish volume signal of the OCT measurement. The small area of the cross section shows no internal scattering from the AW2 varnish.

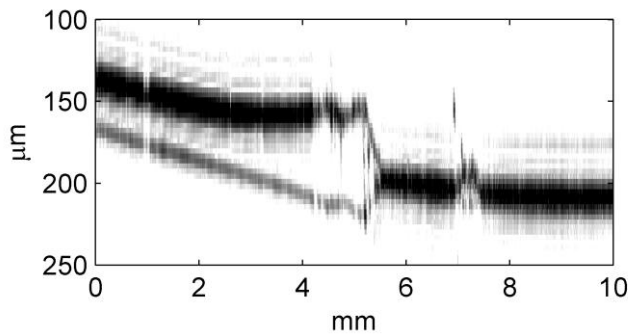


Figure 7.4.2.4  
OCT cross-sectional  
images of aged  
varnish 4 (AW2).

Figure 7.4.2.5 shows the results of the volume scattering measurements, carried out on the meglip, dammar, terpene and aged mastic samples. The increase of OCT signal due to scattering within the meglip sample is clear. The dammar sample, with the large amounts of artefacts identified within the image data (previous figure 7.4.2.3 (a)), does not have a clear increase in the amount of higher scattering pixels, within the varnish. The effect of the artefacts within this data set means that no increase in scattering could be shown. The differences in the shape of the histogram curve for the points above and below the surface show differences in the “noise” of the measurements here. In particular the increase in the amount of pixels between 60 and 70 dB, above the surface, is probably due to signal from dust and dirt. The terpene and aged mastic do show an increase in the amount of higher scattering pixels, though the magnitude of this increase is much smaller compared to meglip. There is again some increase in the pixels above the surface with intensities between 60 and 70 dB, this is consistent with dust on the surface.

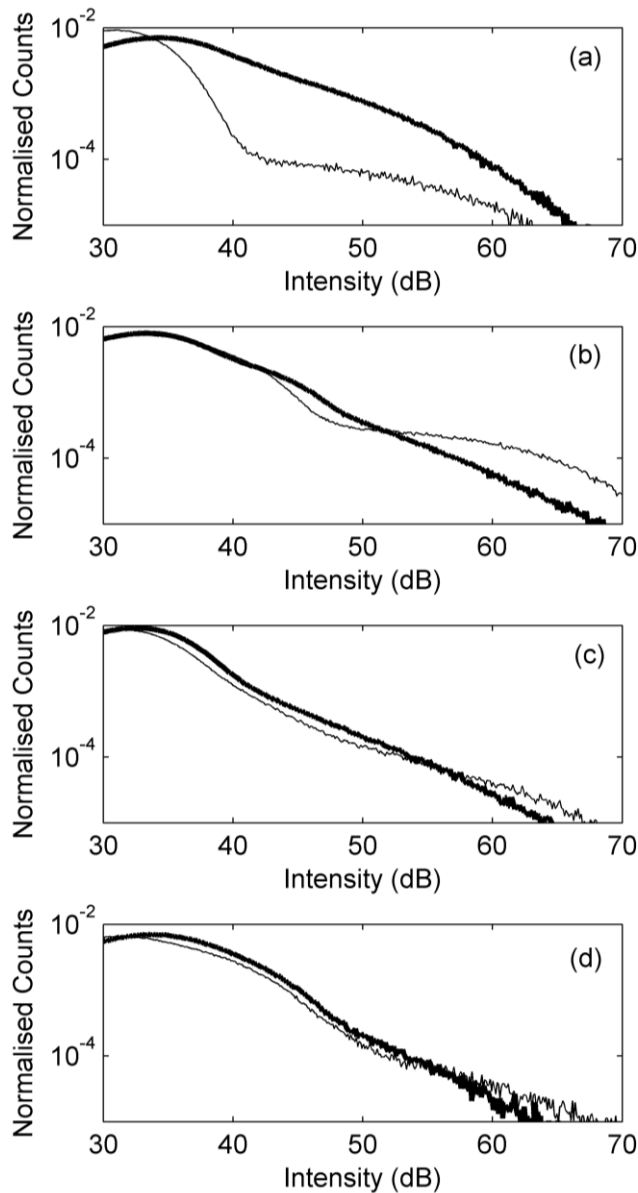


Figure 7.4.2.5  
 Histograms of pixel intensities below (i.e. within varnish volume) (thick line) and above (i.e. outside varnish volume) varnish surface for (a) Varnish 1 (meglip) (b) Varnish 2 (dammar) (c) Varnish 5 (terpene) (d) Varnish 6 (aged mastic).

### 7.4.3 Discussion

OCT can be used to quantify the scattering with the volume of a varnish material. The scattering from the volume of a meglip (known to be a problem) coating was immediately obvious. For such a coating volume scattering is one of the factors that will give it a poor appearance. Though evidence of volume scattering within other aged natural varnishes was found, the magnitude of such scattering was small. For a degraded natural solvent varnish coating, scattering is not likely to be a significant factor in its appearance compared to discoloration.

## 7.5 Conclusion

Recent studies, into the appearances of varnish coatings for paintings, have focused on surface levelling as the main influence on appearance. Previously in the thesis this process has been measured and modelled. From this work predictions can be made about the relative roughness and appearance of different conservator applied coatings. Polymer varnishes, due to their much higher viscosity giving poorer levelling properties, were expected to produce more matte surfaces than low molecular weight resins. This chapter showed for conservator applied brush coatings of Paraloid B72, Dammar, MS2A and Regalrez 1094, the Paraloid (polymer) coating did indeed produce the more matte surface. The reduced gloss of a Paraloid varnish was also measured on a real paint surface as well as ground glass substrates. However the sprayed coatings of MS2A produce a more matte finish than the brushed polymer. This is likely due to much less of the MS2A being applied in the spray coating. In contrast, the sprayed coating of Dammar seemed to be a much heavier coating and produced smoother results than the brushed dammar only. For the sprayed dammar coating a diluted solution, unlike for MS2A, was not used. Decreasing the application concentration is likely to decrease the final thickness of a coating applied by a conservator. There are two reasons for this. Firstly a film with the same applied thickness but higher applied concentration will give a thicker dry film. Secondly, the thickness of any applied film is likely to be dependent on viscosity (hence concentration), analogous to the Landau-Levich-Derjaguin model<sup>5</sup> for coatings on plates drawn out of a liquid bath.

Where a spray coating had been applied on top of a brushed coating, the results were generally glossier. However, with the case of sprayed MS2A coatings this did not necessarily correspond with a decrease in the measured surface roughness. The spraying process may increase the surface roughness at lower spatial frequency scales.

The most important result from the glass plates was not the surface state of the varnish but the differences in the amount of subsurface scattering present in the OCT measurements. The increased presence of subsurface scattering in the Paraloid,

and to a lesser extent MS2A, coatings showed evidence that the behaviour at the varnish-substrate interface may be significant in the final appearance. The presence of scattering voids in the optical system would contribute diffusely scattered white light. This process had been dismissed, as a significant factor in appearance, in recent studies. These results show it may not have been right to do so.

The comparison of the subsurface scattering results, of the varnished plates to an uncoated plate, showed that the source of the voids was fractures beneath the surface glass, which were not filled by the dry varnish coatings. The probable cause of this was that the varnish did not penetrate these voids during application. However the initial filling of the fractures and then the partial withdrawal of the varnish (as it shrinks) during drying is proposed as an alternative mechanism.

The use of OCT to measure the magnitude of volume scattering of several aged varnish coatings, showed that some low magnitude scattering was apparent. For conservator applied varnishes, of thickness in the few micron ranges, this minimal magnitude of scattering is unlikely to be a significant factor in the appearance. The exception to this was a coating of the highly unstable mixture meglip, which was significantly scattering. The structural changes within the volume of this coating as it ages are important to its poor appearance.

## 7.6 References

---

<sup>1</sup> Feller Robert L., "Factors Affecting the Appearance of Picture Varnish", *Science*, 125, pp. 1143-1144 (1957).

<sup>2</sup> van de Hulst H. C., *Light Scattering by Small Particles*, Dover Publications (1981).

<sup>3</sup> Thomson Garry, "Some Picture Varnishes", *Studies in Conservation*, 3 (2), pp 64 - 67 (1957).

<sup>4</sup> De la Rie E. Rene, "The Influence of Varnishes on the Appearance of Paintings", *Studies in Conservation*, 32 (1), 1-13 (1987).

<sup>5</sup> de Gennes Pierre-Gilles, Brochard-Wyart Françoise and Quéré David, *Capillarity and Wetting Phenomena*, Springer (2004).

---

<sup>6</sup> Burley R. and Kenedy B. S., “Dynamic Wetting and Air Entrainment at a Liquid-Solid-Gas Junction”, Ed. Padday J.F., *Wetting, Spreading and Adhesion*, pp 327-360, Academic Press (1978).

<sup>7</sup> Prykäri Tuukka, Czajkowski Jakub, Alarousu Erkki and Myllylä Risto, “Optical coherence tomography as an accurate inspection and quality evaluation technique in paper industry”, *Optical Review*, 17 (3), pp. 218-222 (2010).

<sup>8</sup> Piena Hans, “Regalrez in Furniture Conservation”, *Journal of the American Institute for Conservation*, 40 (1) pp 59-68 (2001).

<sup>9</sup> American Institute for Conservation of Historic and Artistic Works and Samet Wendy, *Painting Conservation Catalog: Varnishes and surface coatings*, AIC (1998).

<sup>10</sup> Mayer Ralf, *The Artists Handbook of Materials and Techniques*, Fourth Edition, faber and faber, 1987.

<sup>11</sup> Coxe John Redman, *The American Dispensatory*, Carey & Lea, 1830.

## 8. Conclusion

There are several factors that have previously been proposed to explain differences in the effect that different varnish coatings have on appearance. Previous studies have shown that the effect of differences in refractive index are negligible. Incomplete wetting of the paint by some varnish coatings has previously been suggested and dismissed. Here substantial differences in the penetration, of different dried conservator applied varnish coatings, into substrates have been shown. Wetting should not be dismissed as a factor in the appearance of different coatings. Scattering within aged varnish samples was detectable with OCT, though this small magnitude is unlikely to have significant impact on the appearance of conservator applied coatings. An exception to this was found for a coating of a known unstable mixture (meglip). However, the factor currently regarded as the most important to appearance is the differences in the surface roughnesses of applied coatings. These differences were shown in conservator applied coatings.

This project has developed the understanding of how the material properties of varnish solutions determine the surface roughnesses of coatings of them. The process that is important to the difference in the surface roughness, of different varnish coatings, is levelling. For conservator varnish solutions the molecular, material and levelling properties, and the relationships between them, have been studied. This provides deeper understanding of how the choice of the components of a varnish solution determines the final appearance.

The measurement of the levelling process required a technique that could measure the varnish-air and varnish-substrate profiles simultaneously (multi-interface profilometry). It had to be sensitive enough to measure a matte interface with only a small (0.027%) total Fresnel reflection coefficient. To do this, the extraction of the interface profiles from OCT images was utilised. The high sensitivity of OCT enabled it to detect the low amounts of returned reflection from a ground glass-varnish interface. The fitting of Gaussian functions, to the OCT axial image data (around the interface), provides positional accuracies that can be (dependent on the surface profile being measured) orders of magnitude better than the axial imaging resolution of the system. It was shown that the limitations for OCT profilometry

were the same as other broadband interferometry techniques. Future instruments maybe designed and developed to fulfil the roles of both OCT and broadband interferometry profilometers. This would remove the need for two separate instruments and provide more capabilities. For smooth interfaces, the largest source of error for the OCT multi-interface profilometry method was vibration within the system. With the averaging of data sets, before the fitting of profile positions, the error in the measurement of smooth interfaces was typically ~50nm (the error was ~125nm without the averaging of image data sets). For rough surfaces, the accuracy of the technique is limited by speckle/diffraction effects.

To correct for refractive index distortions of the OCT measured interfaces, the OCT multi-interface profilometry technique was used to dynamically measure the group refractive index of droplets of varnish. Highly accurate interface positions are important to the accuracy of group refractive index measurements. In the centre of the droplets the measurement accuracy was 0.002. Away from the centre of the droplet, the refractive index measurement was biased towards a lower value. The reason for this distortion is likely to be due to refraction but may also be due to diffraction dependent profile errors.

When a conservator is applying a varnish coating, they have control of the varnish ingredients (and application method) in order to get the desired appearance. There is a series of dependencies between the choice of ingredients of the solution and the final appearance of the coating. The material properties of a varnish solution are dependent on the molecular interactions of the ingredients.

A NMR MOUSE was used to measure the self-diffusion coefficients within two varnish solutions of different resins, one of low molecular weight and one (a polymer) of high molecular weight, over a selection of concentrations. The diffusion of the large polymer resin molecules was very slow, highlighting the difficulty that these molecules have moving past each other. The self-diffusion of the low molecular weight resin molecules was closer in magnitude to the rapid diffusion of the solvent molecules of the solution, than it was the polymer resin molecules at similar concentrations.

NMR relaxometry provides information on the interactions between molecules at different concentrations. The differences in the relaxation times between the two, very different, solutions were minimal. The differences, in the macroscopic behaviour of the coatings of the two varnish resins, are explained by the resin molecules' physical size rather than any differences in inter-monomer/molecule interactions.

For real drying varnish coatings, the potential use of the NMR MOUSE to non-invasively measure remaining solvent content was evaluated. The measurement of coatings was limited in concentration range. As the amount of solvent remaining became small, and the inter-molecular interactions tended to a solid state, the  $T_2$  relaxation times became lower than the instruments capability. The use of a solid-state capable NMR instrument may overcome this limit.

The rheology of varnish solutions were shown to be highly Newtonian over measurable concentrations. Well sampled viscosity-concentration functions were measured for a range of varnish solutions. These functions are essential for modelling (and understanding) the levelling induced roughnesses of different coatings. Viscosity does correlate with molecular weight, especially for high molecular weight resins. The viscosity differences between low molecular weight resins were less substantial and less well correlated with molecular weight averages. For these resins, factors other than just molecular weight will also have a significant influence on viscosity. The use of different solvents has the ability to change the viscosity functions, by magnitudes similar to the differences between low molecular weight resins.

Knowledge of the levelling of films, from outside of the art conservation varnish field, was applied to predict the development of roughness of varnish films from their material properties only. A numerical differential lubrication approximation was used to directly model the surface profile of drying varnish films. These modelled profiles were then compared directly with the experimentally measured profiles. For the polymer varnishes and the high spatial frequency roughness components for low molecular weight varnish coatings, there was a good agreement between modelled and experimental results. For the low molecular weight resins, a

separate mechanism (either Benard-Marangoni or uneven application related) producing low frequency roughness, independent of substrate, was identified. The low frequency range of this additional mechanism is not significant to the surface gloss and appearance of conservator applied coatings.

There are several pieces of future work that can be suggested to continue the work of this project. The differences in the penetration of varnishes coatings into porous substrates needs further investigation. The continued testing of different varnish coatings on ground glass substrates should provide the information on what factors determine whether a coating penetrates the fractures or not. The measurement of penetration of different varnish solutions on porous paint substrates has yet to be achieved. This is needed to confirm that incomplete wetting/penetration does occur for real varnish coatings. The impact of this incomplete penetration on the final appearance of a varnish coating needs to be determined and compared to the effect of surface roughness. This will show which is the most important and where the future focus of research should be. The viscosity-concentration functions measured in this project are invaluable to predicting levelling properties of solutions. The solutions studied can be expanded further to provide a larger resource. In particular, the precise viscosity-concentration functions of the natural varnish solutions, that conservators are trying to mimic (such as mastic and turpentine), will be essential if the modelling method is to be used to predict how they can be mimicked. Likewise, the measurement of evaporation functions for different solutions, different coating thickness and in different conditions, would be a benefit to the use of this model. The modelling method itself can be developed further. The discrepancy of varnish solutions from ideal volume behaviour should be measured, then the effect of this can be included in the models. The effect of including factors such as diffusion, Benard-Marangoni effects and modelling in three dimensions (rather than two) on the model results should also be assessed.

The levelling model developed in this project could be used to predict how the properties of the surface roughness, of a natural varnish coating, can be mimicked precisely using synthetic (*i.e.* more stable) ingredients.

## Appendix 1: Fourier Transform

The Fourier transform<sup>1</sup>

$$\begin{aligned} F(s) &= \int_{-\infty}^{+\infty} f(x)e^{-i2\pi xs} dx \\ f(x) &= \int_{-\infty}^{+\infty} F(s)e^{i2\pi xs} ds \end{aligned} \tag{A1.1}$$

is a mathematical tool that is used throughout this thesis, for a variety of purposes. It is essential to FD OCT, imaging with the MR MOUSE, analysing the properties of a surface's roughness via its Power Spectral Density (PSD) and band passed *rms* roughnesses and finally to previous analytical implementation of the lubrication approximation.

In all these cases the Fourier transform was required numerically on discrete data, hence the discrete form of this transform, the Discrete Fourier Transform (DFT)

$$\begin{aligned} F(s) &= N^{-1} \sum_{x=0}^{N-1} f(x) \exp\left(\frac{-i2\pi xs}{N}\right) \\ f(x) &= \sum_{s=0}^{N-1} F(s) \exp\left(\frac{i2\pi xs}{N}\right) \end{aligned}, \tag{A1.2}$$

was used. To decrease the computation time this is carried out by a Fast Fourier Transform (FFT) algorithm.

Convolution theorem is highly important to the results of the Fourier transformations of the data sets, it states

$$FT(H.J) = FT(H) * FT(J), \tag{A1.3}$$

where FT(I) is the Fourier transform of function I, and H and J are two functions. When taking the Fourier transform of the multiplication of two functions, the result is the same as the convolution of their separate transforms. The importance of this to the OCT is discussed in chapter 2.1.3 and how it is utilised in the measurement in chapter 2.2.2.1. Here the effective spectrum was weighted into a Hann function<sup>2</sup>

$$w(n) = 0.5 \left[ 1 - \cos \left( \frac{2\pi n}{L-1} \right) \right], \quad (\text{A1.4})$$

where  $L$  is the amount of points in the function and  $n$  is the array indices ( $n = 0, 1, \dots, L-1$ ).

Calculating PSD and band passed filtered profiles from raw measured interface profiles produced sectioning artefacts. To reduce these significantly a windowing/weighting function was applied. The function used was

$$w(n) = \frac{L \exp \left[ \frac{16}{L^2} \cdot (n - \bar{n})^2 \right]}{\sum_{j=1}^L \exp \left[ \frac{16}{L^2} \cdot (j - \bar{j})^2 \right]}, \quad (\text{A1.5})$$

where  $n = 1, 2, \dots, L$ . This is a truncated Gaussian function. It is normalised so that it has a mean of 1, which was to reduce the biasing of the PSD and *rms* amplitudes by the application of this window.

---

<sup>1</sup> Bracewell Ronald N., *The Fourier Transform and its Applications*, Third Edition, McGraw-Hill (2000).

<sup>2</sup> Kuo Sen M., Lee Bob H. and Tian Wenshun, *Real-Time Digital Signal Processing Implementations and Applications*, Second Edition, John Wiley & Sons (2006).

## Appendix 2: Additional NMR data

### A2.1 Additional Hahn echo data for molecular liquids

Figures A2.1.1- A2.1.4 provides the Hahn echo data, fits and residual of the fits for cyclohexane, distilled water, dodecane and DMSO from chapter 4.2.2. Figure A2.1.5 provides the partial Hahn echo data and fit used to measure the self diffusion of toluene in table 4.2.4.1.

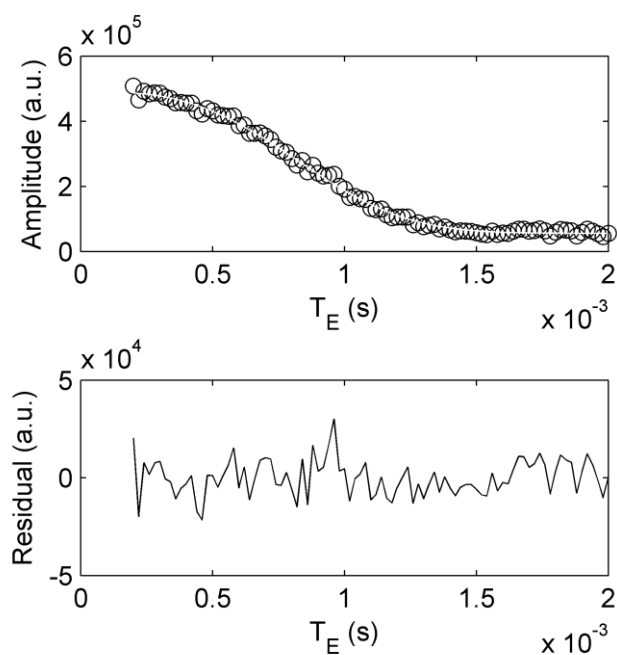


Figure A2.1.1.  
(Top) The Hahn echo amplitude (black circles) measured as a function of  $T_E$  value for cyclohexane and diffusion fit (white line).  
(Bottom) Residual of the data from the fit.

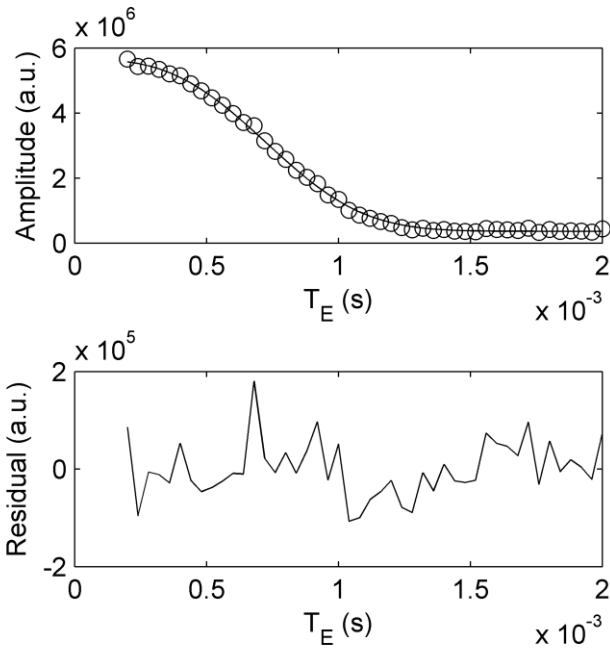


Figure A?.1.2.  
 (Top) The Hahn echo amplitude (black circles) measured as a function of  $T_E$  value for distilled water and diffusion fit (black line).  
 (Bottom) Residual of the data from the fit.

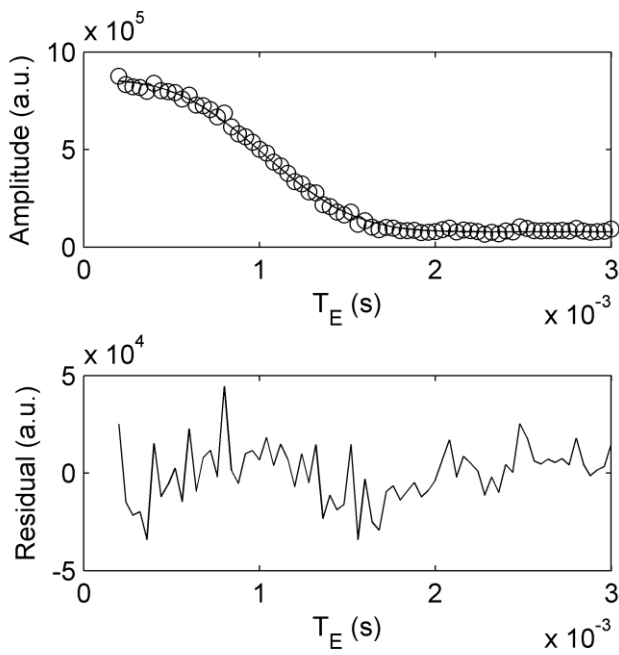


Figure A?.1.3.  
 (Top) The Hahn echo amplitude (black circles) measured as a function of  $T_E$  value for dodecane and diffusion fit (black line).  
 (Bottom) Residual of the data from the fit.

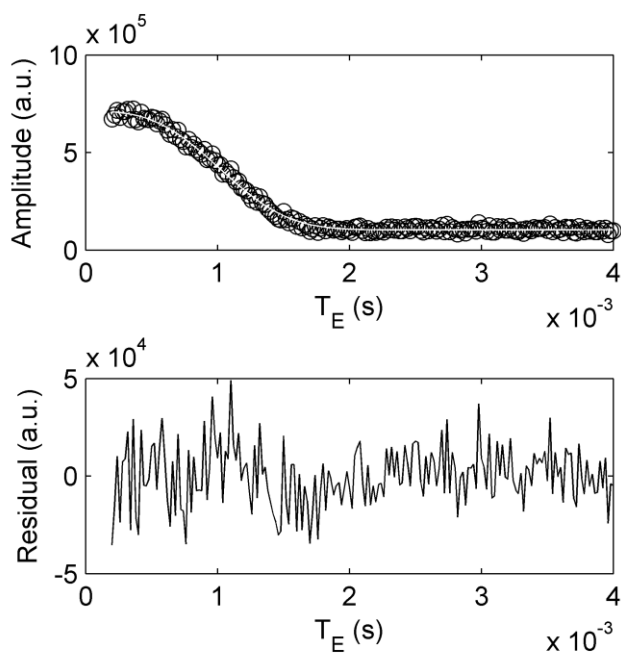


Figure A2.1.4.  
 (Top) The Hahn echo amplitude (black circles) measured as a function of  $T_E$  value for DMSO and diffusion fit (black line).  
 (Bottom) Residual of the data from the fit.

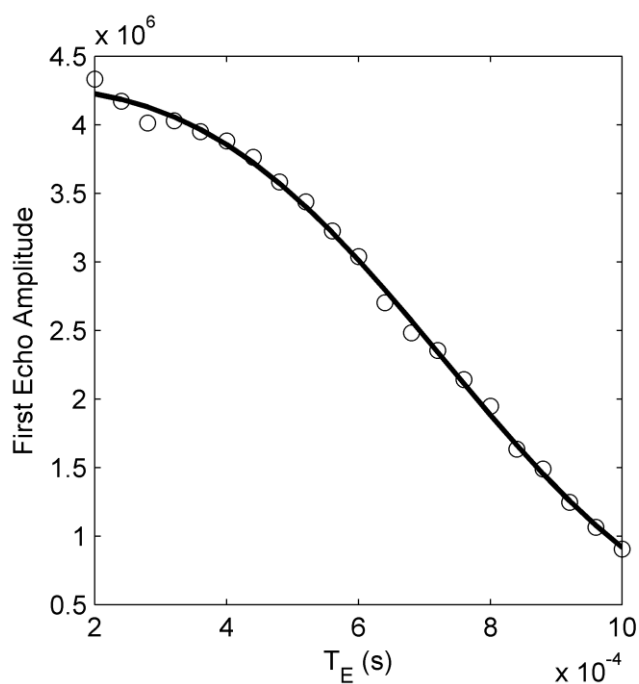


Figure A2.1.5.  
 The Hahn echo amplitude (black circles) measured as a function of  $T_E$  value for toluene and diffusion fit (black line).

## A2.2 Additional CPMG data for molecular liquids

Figures A2.2.1- A2.2.4 provides the example  $T_2^{\text{eff}}$  fits to CPMG train data, the measured  $1/T_2^{\text{eff}}$  as a function of  $T_E^2$  and fitted diffusion relationships, for cyclohexane, distilled water, dodecane and DMSO from chapter 4.2.2.

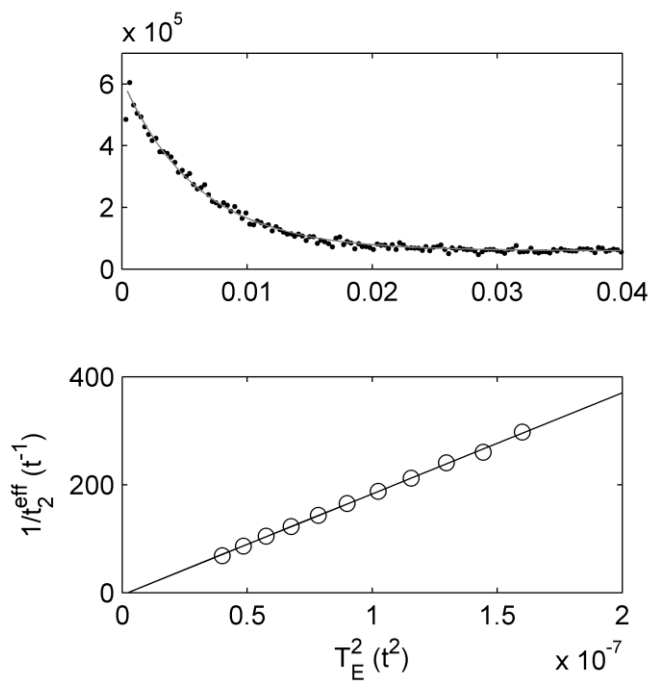


Figure A2.2.1.  
 (Top) Example CPMG train (black dots) and fitted  $T_2^{\text{eff}}$  decay (grey line) for cyclohexane.  
 (Bottom) The measured  $T_2^{\text{eff}}$  times (circles) and fitted diffusion relationship (line).

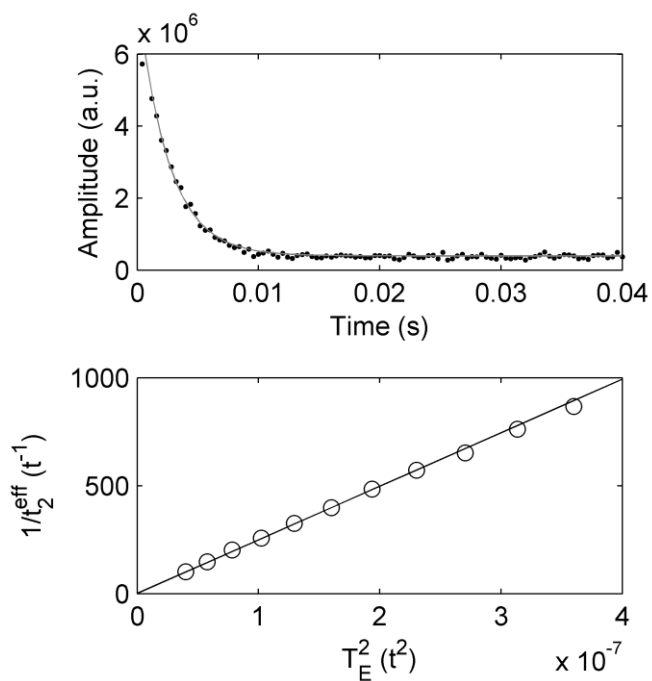


Figure A2.2.2.  
 (Top) Example CPMG train (black dots) and fitted  $T_2^{\text{eff}}$  decay (grey line) for distilled water.  
 (Bottom) The measured  $T_2^{\text{eff}}$  times (circles) and fitted diffusion relationship (line).

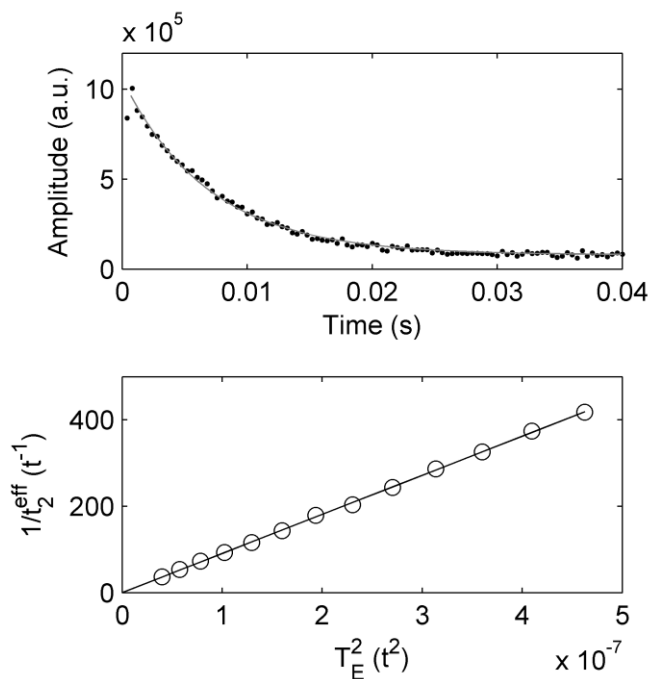


Figure A2.2.3.  
 (Top) Example CPMG train (black dots) and fitted  $T_2^{\text{eff}}$  decay (grey line) for dodecane.  
 (Bottom) The measured  $T_2^{\text{eff}}$  times (circles) and fitted diffusion relationship (line).

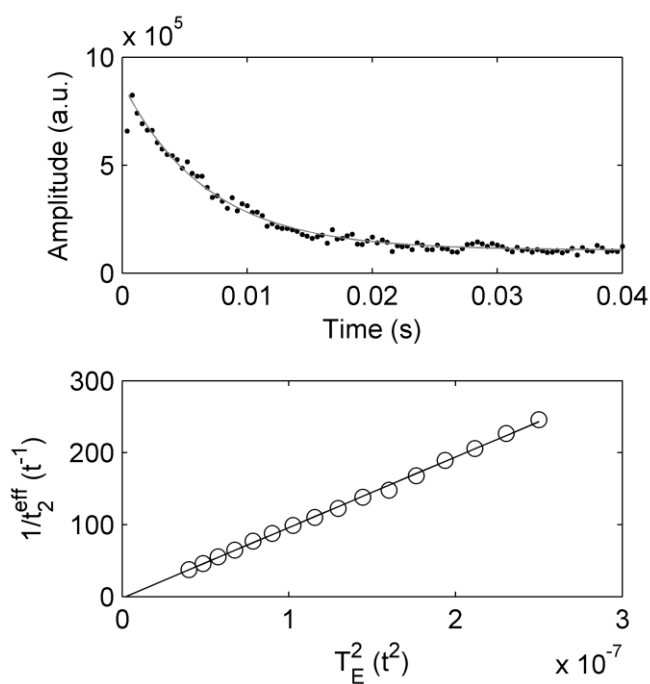


Figure A2.2.4.  
 (Top) Example CPMG train (black dots) and fitted  $T_2^{\text{eff}}$  decay (grey line) for DMSO.  
 (Bottom) The measured  $T_2^{\text{eff}}$  times (circles) and fitted diffusion relationship (line).

### A2.3 Hahn echo data for AYAT and toluene solutions

Figure A2.3.1 to A2.3.4 provide the Hahn echo data and two component diffusion fits for the remaining AYAT and toluene solution in chapter 4.2.3.

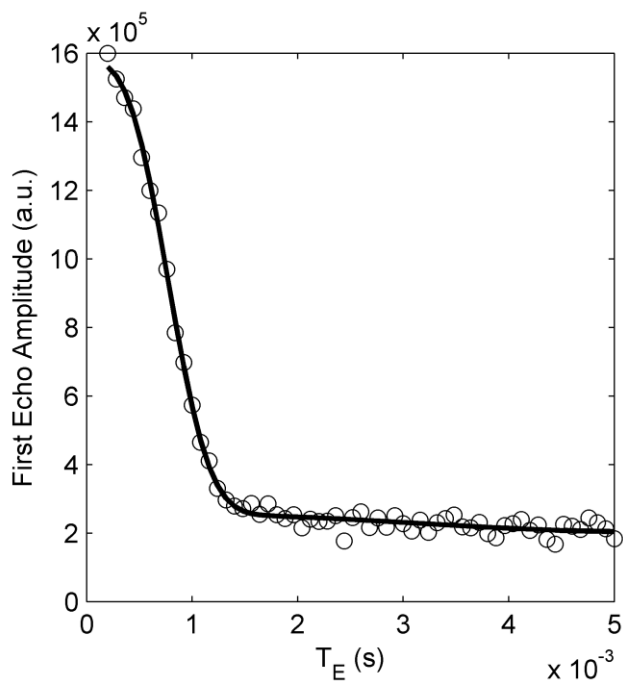


Figure A2.3.1.  
The Hahn echo amplitude (circles) measured as a function of  $T_E$  value for AYAT and toluene, of 1g resin to 13ml solvent, solution and two component diffusion fit (line).

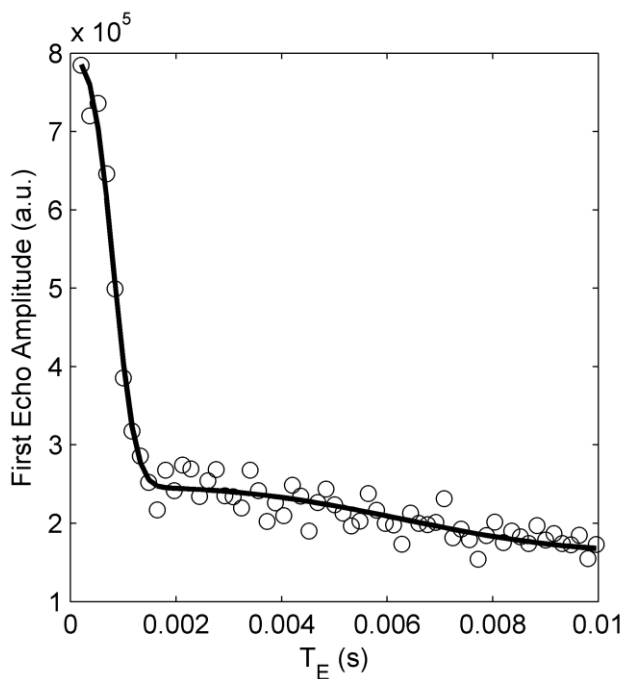


Figure A2.3.2.  
The Hahn echo amplitude (circles) measured as a function of  $T_E$  value for AYAT and toluene, of 2g resin to 12ml solvent, and two component diffusion fit (line).

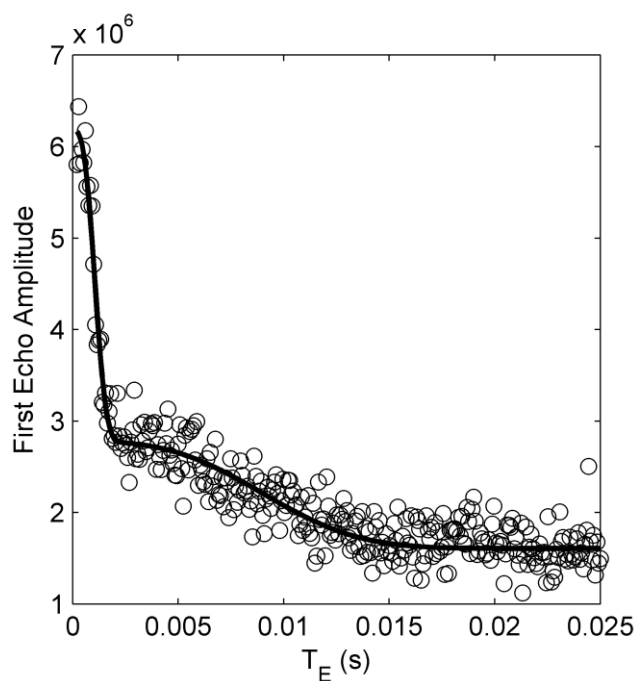


Figure A2.3.3.  
The Hahn echo amplitude (circles) measured as a function of  $T_E$  value for AYAT and toluene, of 4g resin to 10ml solvent, and two component diffusion fit (line).

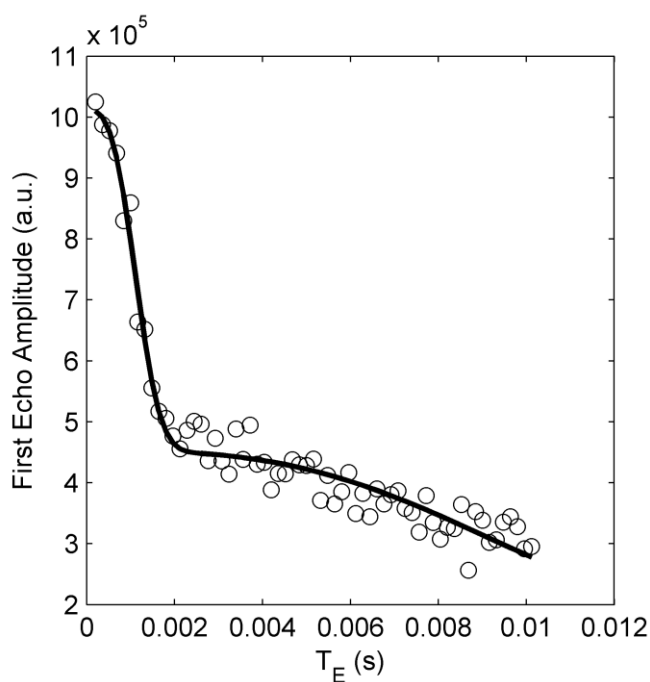


Figure A2.3.4.  
The Hahn echo amplitude (circles) measured as a function of  $T_E$  value for AYAT and toluene, of 4.5g resin to 9.5ml solvent, and two component diffusion fit (line).

## A2.4 AYAT diffusion results comparison between Hahn echo and CPMG method

Table A2.4.1 gives the diffusion measurements for the solvent and resin in AYAT and toluene solutions carried out in chapter 4.2.3 and 4.3.1.2. The CPMG show good agreement for the solvent diffusion apart from the most concentrated sample. The CPMG results show gross overestimation of the diffusion of the resin.

Resin mass (g)	Solvent Volume (ml)	D <sub>S</sub> Hahn 10 <sup>-9</sup> m <sup>2</sup> s <sup>-1</sup>	D <sub>S</sub> CPMG 10 <sup>-9</sup> m <sup>2</sup> s <sup>-1</sup>	D <sub>R</sub> Hahn 10 <sup>-12</sup> m <sup>2</sup> s <sup>-1</sup>	D <sub>R</sub> CPMG 10 <sup>-12</sup> m <sup>2</sup> s <sup>-1</sup>
0.5	13.5	2.28	-	49.0	
1	13	1.85	2.27	28.3	754
2	12	1.59	1.83	3.46	377
3	11	1.13	1.24	1.90	127
4	10	0.736	-	1.17	-
4.5	9.5	0.623	0.667	1.12	-
5	9	0.472	0.828	1.45	240

Table A2.4.1. Self-diffusion coefficient measured values for the solvent and resin in AYAT and toluene solutions, by Hahn echo and CPMG train methods.

### A2.5 AYAT T<sub>2</sub> measurements

From chapter 4.3.1.2, figures A2.5.1 – A2.5.4 provide the measured T<sub>2</sub><sup>eff</sup> values for the resin and solvent of AYAT and toluene solutions of concentrations of 1g resin to 13ml solvent, 3g resin to 11ml solvent, 4.5g resin to 9.5ml solvent and 0.4896g resin to 0.5104g solvent.

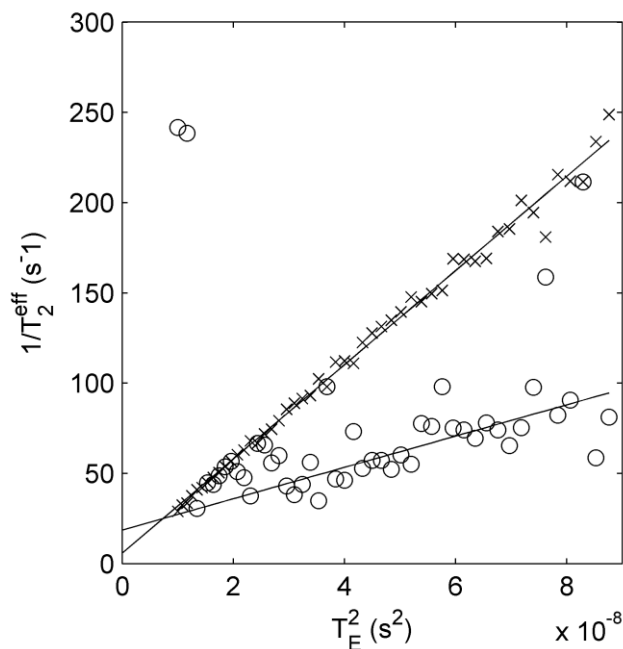


Figure A2.5.1. T<sub>2</sub><sup>eff</sup> measurements and diffusion fits for the resin (circles) and solvent (crosses) in a, 1g resin to 13ml solvent, solution of AYAT and toluene.

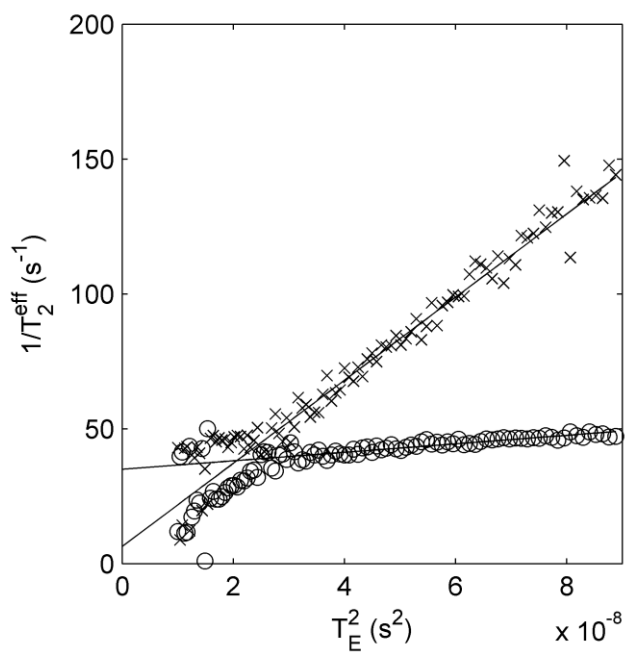


Figure A2.5.2.  
 $T_2^{\text{eff}}$  measurements and diffusion fits for the resin (circles) and solvent (crosses) in a, 3g resin to 11ml solvent, solution of AYAT and toluene.

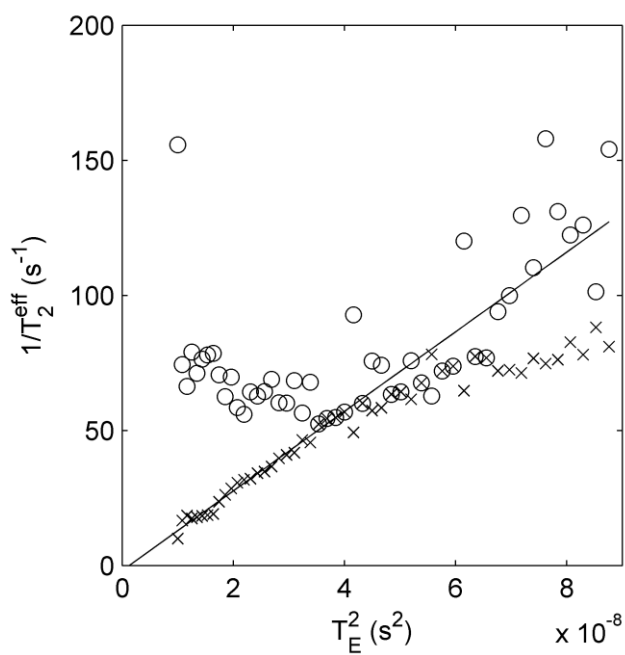


Figure A2.5.3.  
 $T_2^{\text{eff}}$  measurements and diffusion fits for the resin (circles) and solvent (crosses) in a, 4.5g resin to 9.5ml solvent, solution of AYAT and toluene.

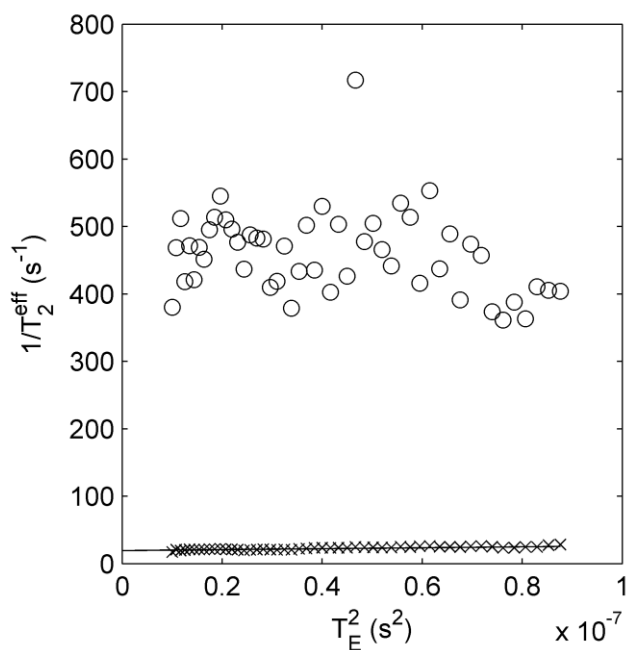


Figure A2.5.4.  
 $T_2^{\text{eff}}$  measurements and diffusion fits for the resin (circles) and solvent (crosses) in a, 0.4896g resin to 0.5104g solvent, solution of AYAT and toluene.

## A2.6 Regalrez $T_2$ measurements

From chapter 4.3.1.3, figures A2.6.1 and A3.5.2 provide the measured  $T_2^{\text{eff}}$  values for the resin and solvent of Regalrez and toluene solutions of concentrations 9g resin to 5ml solvent and 10g resin to 4ml solvent.

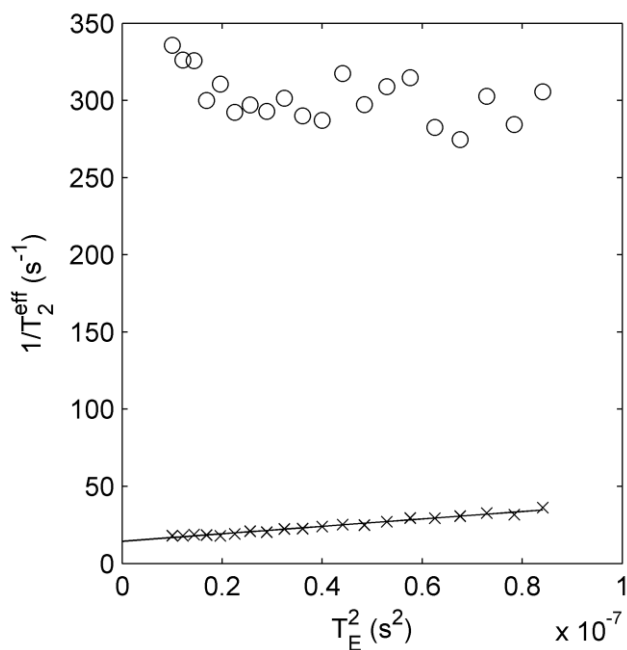


Figure A2.6.1.  
 $T_2^{\text{eff}}$  measurements and diffusion fits for the resin (circles) and solvent (crosses) in a, 9g resin to 5ml solvent, solution of Regalrez and toluene.

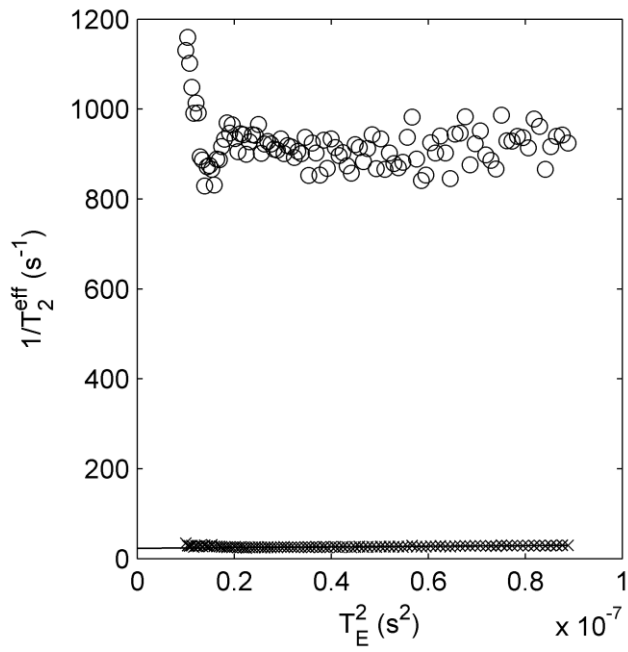


Figure A2.5.4.  
 $T_2^{\text{eff}}$  measurements and  
diffusion fits for the resin  
(circles) and solvent  
(crosses) in a, 10g resin to  
4ml solvent, solution of  
Regalrez and toluene.

### Appendix 3: Flow rheology of various varnish resins dissolved in toluene

In chapter 4.2.1, figure 4.2.1.1 gives the flow results for two concentrations of paraloid B72 and toluene varnish solutions. Here the flow method results for concentrations of 2g of resin dissolved in 12ml of solvent and the highest concentration measured, by the method, are given. These results for the resins Regalrez 1094, Regalrez 1126, Dammar, MS2A, Laropal A81 and AYAT are presented in figure A3.1 to A3.6. All the figures show Newtonian behaviour within experimental error.

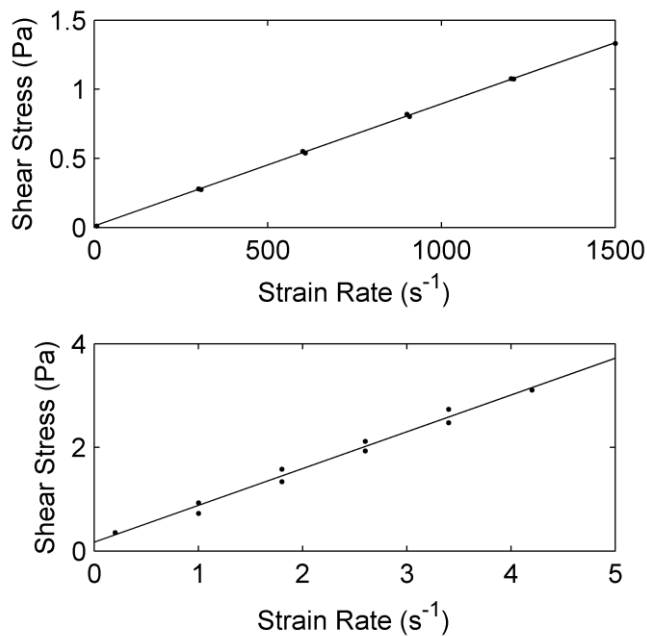


Figure A3.1. Flow rheology of Regalrez 1094 measured at concentrations of (a) 2g resin to 12ml solvent and (b) 10g resin to 4ml solvent.

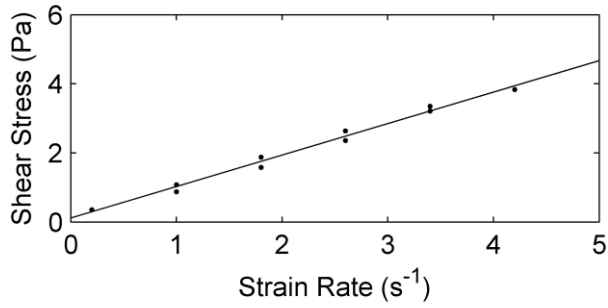
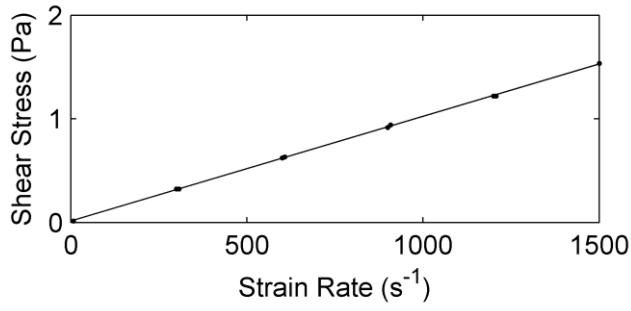


Figure A3.2. Flow rheology of Regalrez 1126 measured at concentrations of (a) 2g resin to 12ml solvent and (b) 9g resin to 5ml solvent.

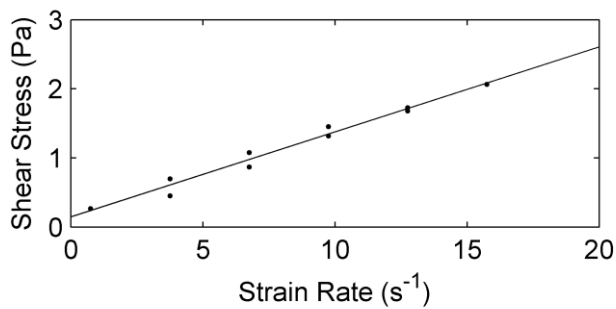
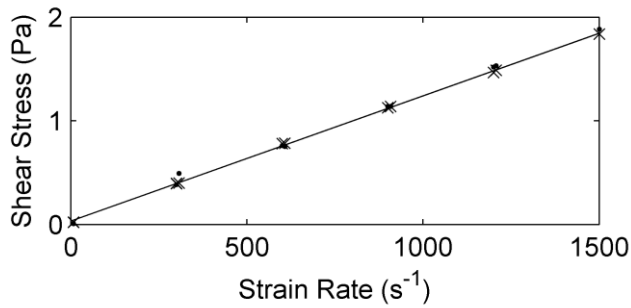


Figure A3.3. Flow rheology of Dammar measured at concentrations of (a) 2g resin to 12ml solvent unfiltered (x) and filtered (.) and (b) 8g resin to 6ml solvent.

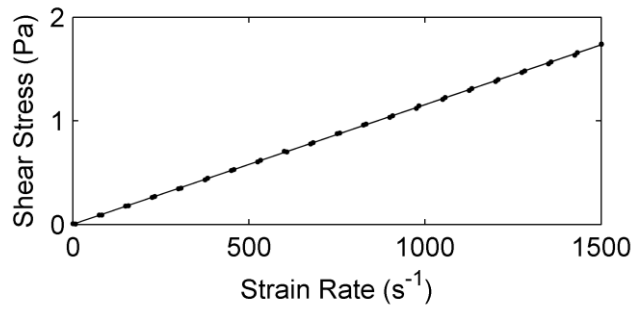


Figure A3.4. Flow rheology of MS2A measured at concentrations of (a) 2g resin to 12ml solvent and (b) 8g resin to 6ml solvent.

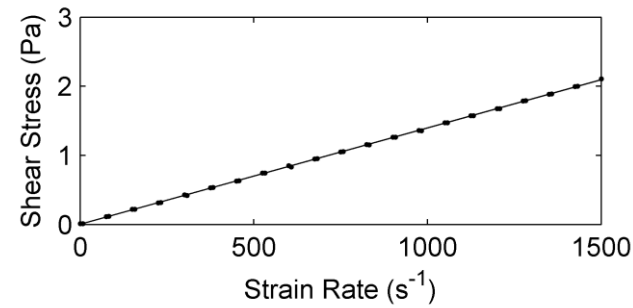
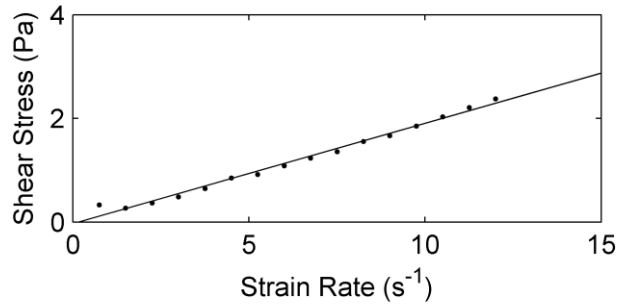
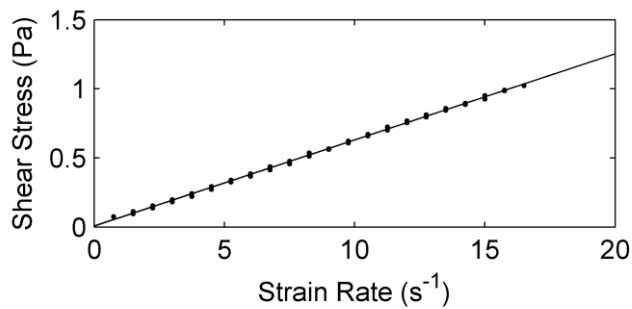


Figure A3.5. Flow rheology of Laropal A81 measured at concentrations of (a) 2g resin to 12ml solvent and (b) 7g resin to 7ml solvent.



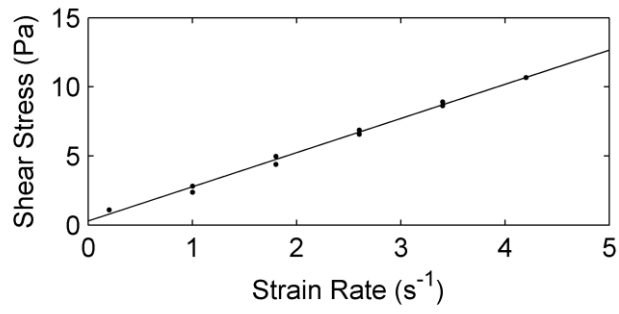
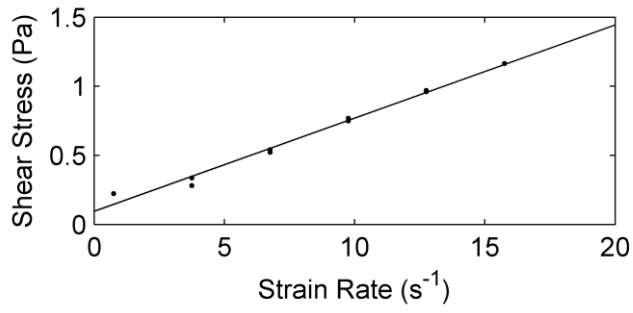


Figure A3.6. Flow rheology of AYAT measured at concentrations of (a) 2g resin to 12ml solvent and (b) 4g resin to 10ml solvent.

## Appendix 4: Substrate preparation

### A4.1 Ground glass

As has been shown in chapter 2.4.2, a coarse rough surface was needed for the substrate measurement with OCT to be representative. The resistance of glass to the solvent and chemical action, of the varnish solution, means that its profile will be constant during measurements and the glass will not alter the varnishes properties. As glass does not scatter light from its volume like a paint surface, the faint signal from the substrate-varnish interface will not be buried by signal originating from behind it. A random rough surface can be made by blasting or grinding the glass with an aggregate, which fractures and removes flakes of the material leaving behind a rough surface. A drawback for this application is that the fracturing of the glass does not always result in the clean break of flakes of glass, leading to subsurface fractures in the final substrate. This substrate fracturing is shown in figure 2.4.2.4 and has a detrimental effect on the recovery of the interface. The grinding method chosen was selected to attempt to minimise this subsurface fracturing.

A manual grinding process was used placing 300 to 355  $\mu\text{m}$  sand between two 6mm A4 glass plates (Figure A4.1.1). The plates were then ground together in a random manner, recycling the sand until it was a fine powder. This was done until the surface material had been removed from the majority of the plates. As the surface roughened the grinding process speeded up and the initial grinding was fastest in the centre of the plate. By the time the surface material had been removed from most of the plate, it was assumed that the central part of the plate will have reached an equilibrium roughness. However, no experimental work was carried out to confirm the development of the roughness during the grinding.

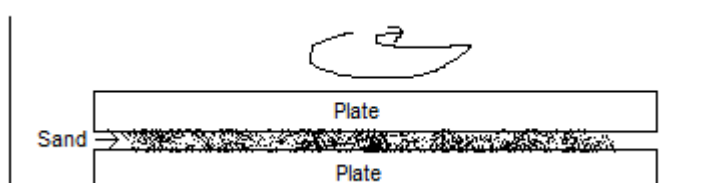


Figure A4.1.1.  
Setup for grinding of  
glass plates.

## A4.2 Laser cut trench

For use as a regular rough substrate, grooved glass substrates were produced. To create regular grooves, with consistent width and depth, laser ablation was considered to produce them. However, the available laser cutter was not able to directly ablate glass, though it was known to cause changes to the glass, allowing a pattern to be engraved or to score glass plates. To determine the effect that the laser cutter had on a glass plate, a long thin rectangle was engraved onto the surface by a raster scan method. This “engraving” was then examined under the OCT, shown in Figure A4.2.1 (a). It is clearly seen that the laser cutter has fractured and deformed the glass. In particular there is a clear boundary in the OCT image between the fractured and un-fractured glass. It was found that, by using a metal point, the fractured glass could be removed leaving a trench in the glass. Figure A4.2.1 (b) shows an OCT image after the fractured glass has been cleared. The OCT data was then be used to measure the surface profiles of the trenches, an example profile is shown in Figure A4.2.1 (c). Ideally the trench would have a rectangular cross section and be smooth. While this is not the case, the regular curved shape could be analytically evaluated and the roughness is smaller than the depth of the trench and of higher spatial frequencies than the width of the trench.

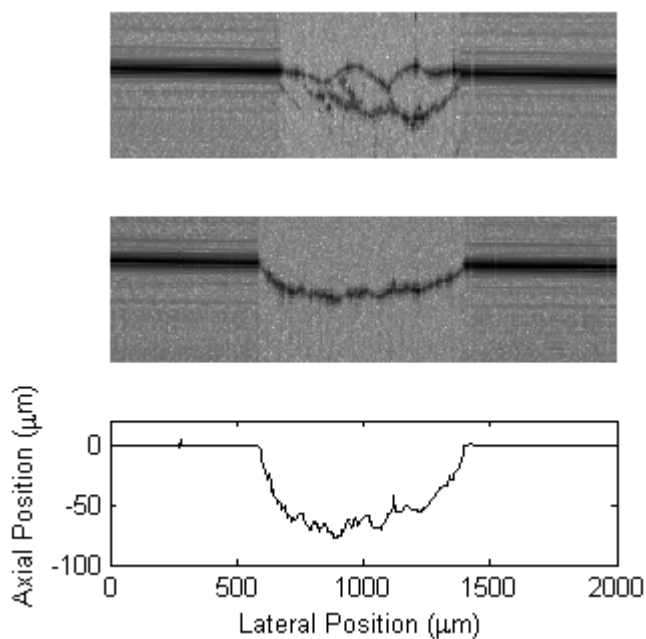


Figure A4.2.1  
(a) OCT cross-sectional image of laser induced fracturing of glass  
(b) OCT cross-sectional image after removal of fractured glass  
(c) OCT measured surface profile of resulting trench.

The depth and roughness of the resulting trench were determined by the operating parameters of the laser cutter. The power to the laser, speed of travel, pulses per unit length of scan and width of thin rectangle could all be controlled. These were varied in the production of a number of trenches. The cross-sectional depth of each trench was measured, with OCT profilometry, at 6 separate locations along the trench. This was carried out as shown in Figure A4.2.1 (c), using a 2mm profile length with 1000 lateral points. The profile was then levelled to the glass surface and the mean and standard deviation of the depth of the points at the bottom (central area not curved sides) of the trench was taken. These results are shown in Table A4.2.1. The depths of the first set of repeats (O and 1 – 5) were too high, being of the magnitude of the thickness of the varnish coating to be applied. The attempt to reduce the produced trench depth resulted in N4 and N5. The reduction of energy transmitted to the surface by lower power and fast speed resulted in the reduction of trench depth. The other difference was the removal of the wet paper towel applied to the glass surface during laser etching. This had been applied on the earlier trenches to help dissipate the energy after heating to prevent breakage of glass. The inclusion of the wet paper towel for low powers was detrimental. The non-homogeneity of the paper towel was evident in the trench etches.

Name	Power (%)	Speed (%)	Pulses per Inch	Width ( $\mu\text{m}$ )	Depth ( $\mu\text{m}$ )
O	100	27	300	500	$64 \pm 10$
1	50	27	300	500	$46 \pm 9$
2	100	27	150	500	$70 \pm 10$
3	100	27	500	500	$69 \pm 10$
4	100	50	300	500	$38 \pm 6$
5	100	20	300	500	$89 \pm 12$
N4 (NWP)	50	100	300	250	$30 \pm 3$
N5 (NWP)	25	100	500	250	$19 \pm 3$

Table A4.2.1. Laser parameters and resulting depth of trench. (NWP – No Wet Paper used as a dissipative cover)

## Appendix 5: viscoelastic models

The deformation of viscoelastic materials, due to the application of shear stresses, can be modelled as a system of mechanical components<sup>1</sup>. Two mechanical component types are used to construct these models. The first of these is a dashpot, which is a viscous damper that produces a resistive force proportional to velocity. The dashpot models viscous drag within the viscoelastic material. The second component is an elastic spring, which deforms with applied stress producing a resistive force proportional to displacement. The spring models the elastic interactions within the material. The deformation against time, of a mechanical system constructed from these two components, can be calculated from an inputted stress (or displacement) function. In order to model the behaviour of a material, these components need to be put into the most appropriate arrangement.

There are two basic arrangements, series and parallel, in which these two components can be combined. Figure A5.1 shows these two arrangements, which are (a) the Maxwell and (b) the Kelvin-Voigt models (or units). More complex models can be constructed by arranging these units in parallel or series to each other (or an individual component).

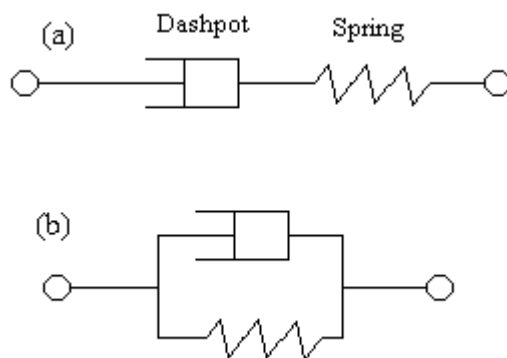


Figure A5.1  
The combination of a dashpot and a spring to form the basic (a) Maxwellian and (b) Kelvin-Voigt mechanical models of viscoelastic materials.

The properties of these two models are very different and generally not applicable to the same materials. A material obeying the Kelvin-Voigt model (Figure A5.1 (b)) will always return to its original shape after the shearing stress is removed, *i.e.* it is not a fluid. This is not suitable for the fluid vanish solutions under investigation, which do not maintain any permanent structure.

If a material obeying the Maxwell model (Figure A5.1 (a)) is placed under a shear stress, it will initially deform by elastic interactions. With time viscous flow can happen, within the material, to try to reduce the applied shear stress. This is a much better description of varnish solutions than the Kelvin-Voigt model. As the experimental results within chapter 5 gave no indication that more complex modelling was needed to account for the results, basic Maxwell behaviour was assumed.

All materials that obey the Maxwell model (Maxwellian) will have their own Maxwell relaxation time,  $\tau$ . Consider a Maxwellian material that is instantaneously shear displaced. This displacement is then kept constant. Initially, the shear stress required for this displacement is due to the elastic component as the viscous dashpot cannot respond instantaneously. The viscous component (dashpot) will start displacing at a rate proportional to the elastic stress within the system. This reduces the elastic stress driving the displacement of the viscous component. As a result the stress,  $S$ , in the system decreases exponentially,

$$S = S_0 \exp\left(-\frac{t}{\tau}\right),$$

where  $S_0$  is the initial elastic stress.

---

<sup>1</sup> Drosdov Aleksey D., Finite elasticity and viscoelasticity a course in non linear mechanics of solids, World Scientific (1996).

Appendix 6: published papers

# Fourier domain optical coherence tomography for high-precision profilometry

Samuel Lawman, Haida Liang

School of Science and Technology, Nottingham Trent University, Clifton Lane, Nottingham, NG11 8NS, United Kingdom

## ABSTRACT

A Fourier domain (FD) optical coherence tomography (OCT) system is shown to be capable of profilometry with two orders of magnitude better accuracy than the axial imaging resolution of the system. High precision OCT profilometry not only achieves similar accuracy as commercial white light interferometry based profilometers but is also capable of profilometry on complex subsurface structures with multiple interfaces of low reflectance. An accuracy of 55nm was achieved with a ThorLabs SROCT on a lab bench without special anti-vibration devices. This technique has the potential for a range of applications, such as high precision refractive index measurements and simultaneous dynamic monitoring of the interface structure of a drying varnish and the substrate.

## 1. INTRODUCTION

Optical Coherence Tomography (OCT)<sup>1,2</sup> is a 3D imaging technique using White Light Interferometry (WLI). It was originally developed in 1991<sup>1</sup> and has found a wide variety of application in biomedicine and beyond<sup>3</sup>, including art conservation<sup>4,5</sup>. The use of high intensity light sources, such as Super Luminescent Diodes (SLD), give this technique high sensitivity which allows the detection of small amounts of scattered light from a sample. The near Gaussian shaped spectrum of SLDs enables high image quality. Axial resolutions of OCT systems at a given wavelength are inversely proportional to the bandwidth of the light source and are typically in the order of 10 $\mu$ m. Lateral resolution is determined by the numerical aperture of the objective lens and the choice of the lens is a trade-off between the desired resolution and the depth of field. Early OCT systems were mostly time domain systems, where depth ranging was achieved by scanning the reference mirror. Later, it was realised that it is also possible to retrieve axial ranging information without any axial motion in the system by dispersing the output of the interferometer using a spectrometer and Fourier transforming the resultant intensity spectrum<sup>6</sup>. Fourier Domain (FD) OCT has become increasingly popular for its improved sensitivity and hence speed. It has the advantage of retrieving axial information without any need for axial scanning in the system. Details on the theory and current developments on OCT can be found in a recent review<sup>2</sup>.

WLI is used as a very popular method for profilometry by measuring the centre of the axial signal response from a surface<sup>7,8</sup>. WLI can measure the position of the surface to accuracies of up to 1nm. Like OCT this can be done in the Fourier domain<sup>9,10</sup>, however such optical profilometry is almost exclusively done in a time domain setup with a scanning reference mirror for the retrieval of the axial information. Since OCT and WLI based optical profilometry both use Michelson interferometry and have very similar setup, they should in principle yield similar precision in profilometry. However, as OCT was developed for *in vivo* tomography, its application for precision profilometry has not been well developed. A common misconception is that the precision of OCT profilometry is of the order of the FWHM of the axial Point Spread Function (PSF). While WLI use thermal sources which have about 3 times the bandwidth of a SLD typically used in OCT, the precision in profilometry commonly quoted for WLI is 3 to 4 orders of magnitude better than that of OCT. In reality, the axial PSF gives the depth resolution, but the position of the surface or the peak of the axial PSF can be determined to much higher accuracy. In the simplest case, it is the strength of the signal or signal to noise ratio that determines the position accuracy. By using high intensity sources, OCT has much higher sensitivity than the common WLI based optical profilometers using thermal sources. In addition, OCT has the advantage of profilometry on multiple interfaces rather than just the top surface.

This paper explores the precision in top surface and subsurface profilometry achievable by OCT and its potential applications.

## 2. EXPERIMENTAL METHOD

### 2.1. The Instrument

The results in this paper are obtained with a Thorlabs SROCT which consists of a Michelson type interferometer, a SLD light source with central wavelength of 930nm and full width half maximum (FWHM) bandwidth of 100nm and a spectrometer. The interferometer and mechanical lateral scanning mechanism are located within a handheld probe and the spectrometer and light source are located in a separate base unit connected to the handheld probe by an optical fibre. The axial resolution of the system is  $6.5\mu\text{m}$  in air; the transverse resolution is  $9\mu\text{m}$  and the maximum depth range is 1.6mm. For the following measurements, the handheld probe is secured to a 3-axes motorised micrometer stage.

The output from the interferometer is dispersed and collected by a linear CCD array. The intensity of light measured by the spectrometer is post-processed to give a 2D cross-section image. First of all, the dark signal from the CCD detector is subtracted from the data. Secondly, due to the finite range of spectrum sampled by the spectrometer, the intensity of the spectra is weighted using a windowing function, to produce a gradual decrease to zero intensity at the edges of the measured spectrum. This is done to reduce ringing in the Fourier transform while trying to limit the effect on the width of the PSF. There are several windowing functions that can be applied depending on preference. The third stage is to convert from  $\lambda$  (wavelength) space to  $k$  (frequency) space. As the spectrometer measures the intensity at equal wavelength spacing but the Fourier transform assumes spacing in equal frequencies, the data needs to be re-sampled in equal  $k$  spacing. After the fast Fourier transform has been carried out and the modulus taken, the last stage is to subtract the DC components of the signal from around the zero path length difference and produce the images for display after converting the intensity values to dB.

### 2.2. Measurements of axial profiles

To obtain an accurate measurement of the axial PSF of the FD-OCT system, increased sampling was undertaken by shifting the probe a fraction of a pixel at a time in the axial direction. The computer controlled micrometer stage was used to move the handheld probe towards or away from the target at a constant velocity to achieve the required sampling density. Figure 1 shows an example of an axial profile taken from a flat interface by this shifting method.

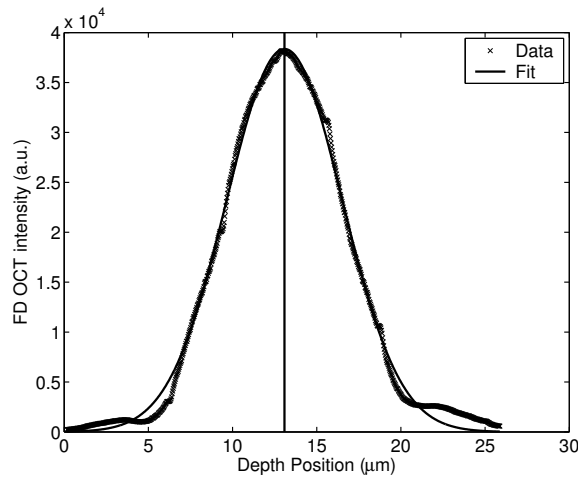


Fig. 1. The system axial point spread function measured by “shifting” the position of the surface by sub pixel amounts between measurements. A Gaussian fit to the data is shown as a solid curve. The vertical line marks the centre of the PSF found by this fit.

As the axial PSF of the FD-OCT closely approximates a Gaussian function (Fig. 1), the axial positions of an interface can be fitted to Gaussian functions using a MatLAB code. The procedure can be repeated to give 2D or 3D surface

profiles. Direct fitting of the axial position of the surface using the measured PSF was carried out, but did not give any improvement in accuracy over a Gaussian fit.

### 2.2.1. Smooth interface performance

The main source of error in the measurement of a smooth surface profile was found to be vibration in the system which can be reduced by taking time domain averages of the cross-section images. To quantify the accuracy of the measurement, a standard flat surface was measured. The surface tilt was removed from the fitted surface profile and the standard deviation of the profile was measured. Fig. 2 shows the decrease in the standard deviation with increasing number of averaged frames. Little further improvement is seen after the averaging of 20 frames. The standard deviation of the surface measurement after averaging is shown to level out at 55nm. The accuracy of the measurement depends on the level of vibration and the value quoted is typical of a measurement during the day on a lab bench without special anti-vibration devices.

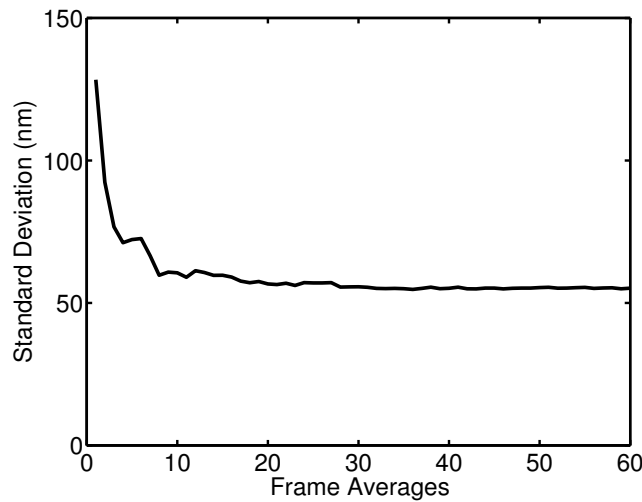


Fig. 2. Standard deviation of the surface profile measured from a standard flat surface as a function of the number of frames averaged.

The high sensitivity and dynamic range of OCT makes it ideal to measure multiple interfaces of complex structures. To evaluate any additional error such as dispersion caused by passing through successive layers in the sample, the first and second interface of a microscope cover slip of approximately 100 $\mu$ m thickness were measured. No decrease in accuracy was found for the second surface in this case.

Verification of the positional reliability of the method was carried out with a standard step surface of 9.932 $\mu$ m in step height. This is a standard surface that is used to calibrate commercial optical profilometers. The OCT cross-section image of the surface is shown in Figure 3a, the surface profile and step height is then extracted from the mean of 60 OCT images (Fig. 3b).

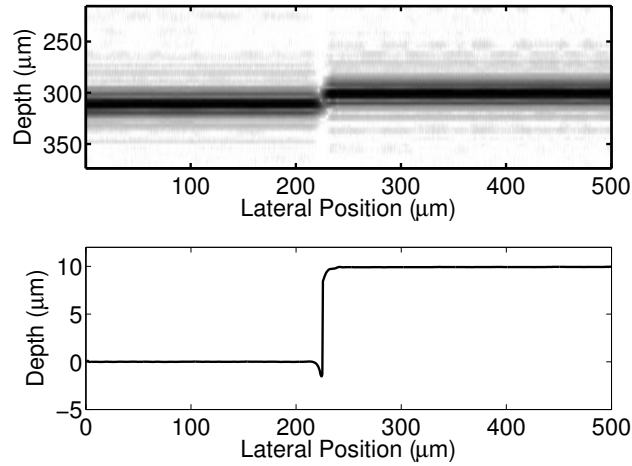


Fig. 3 a) FD-OCT image of a standard step surface in cross-section; b) Surface profile measured from the FD-OCT.

The step height was measured at 6 separate locations on the surface with the FD-OCT which gave a mean of  $9.944 \pm 0.043\mu\text{m}$  consistent with the quoted reference value. The uncertainty in this measurement is similar in magnitude to that of the standard flat surface.

### 2.2.2. Matte surface performance

An important consideration for the accuracy is the roughness of the surface. The coherent nature of all interferometric techniques makes them susceptible to speckle when measuring matte surfaces<sup>8,11</sup>. As a result, the accuracy can deteriorate substantially for these surfaces.

This was demonstrated with a matte surface of a *rms* roughness of order  $1\mu\text{m}$ . FD-OCT was used to measure the surface profile at 4 different axial distances from the sample. The effect of speckle on each measured profile should be de-correlated. In the absence of speckle, the measured profiles should be identical up to measurement errors which were found to be around  $50\text{nm}$  in the previous section. The *rms* roughness of the profiles was found to be  $1.1910 \pm 0.1028\mu\text{m}$ , but the difference between the profiles at different measurement distance was found to be  $1.2818 \pm 0.1458\mu\text{m}$  which is larger than the *rms* roughness of the measured profiles themselves. By assuming random distribution of surface roughness and measurement errors, the effect of speckle and surface roughness can be compared between two profiles. For this data, the estimated surface roughness was found to be  $0.7549 \pm 0.1694\mu\text{m}$ , while the estimated error due to speckle was found to be  $0.9050 \pm 0.0984\mu\text{m}$ . The error due to speckle is comparable to the actual surface roughness for this sample. In comparison, the *rms* surface roughness measured with a Veeco inc. dektak 6M mechanical profilometer with a stylus radius of  $12.5\mu\text{m}$  was found to be  $0.46\mu\text{m}$ . A previous study<sup>19</sup> using a mechanical profilometer with a stylus radius of  $2\mu\text{m}$  to measure the same surface found the *rms* roughness to be  $0.67\mu\text{m}$  consistent with the OCT estimates. The result from the large tip stylus significantly underestimates the surface roughness.

A second coarser rough surface was measured with the OCT at different axial distances from the sample. The measured *rms* roughness of the profiles was  $10.3948 \pm 0.1878\mu\text{m}$  and the *rms* difference between the surface profiles measured at different axial distances was found to be  $4.3809 \pm 0.6494\mu\text{m}$  which was much smaller than the *rms* roughness of the surface profiles themselves. Comparison of profiles gave an estimate of *rms* surface roughness of  $9.9134 \pm 0.1836\mu\text{m}$  and error due to speckle of  $3.0974 \pm 0.4379\mu\text{m}$ . The *rms* roughness measured with the mechanical profilometer with the  $12\mu\text{m}$  radius tip was  $\sim 7\mu\text{m}$  which is, as expected, an underestimate of the roughness compared with the OCT measurements.

The error caused by speckle is dependent on the interface roughness. Measurements of the same profile at different axial positions can be taken and the differences between each result analysed to give an estimation of error due to speckle. The application of standard speckle reduction techniques in the method can be used in reducing some of the speckle error. Typically this involves the averaging of data sets where the speckle pattern is de-correlated.

### 3. APPLICATIONS

#### 3.1. Measurement of Refractive Index

Several methods using OCT have been published to measure group refractive index of materials<sup>12,13,14</sup>. The ability to measure the optical position of interfaces to such a high accuracy as demonstrated in the above section with a FD-OCT will significantly improve the accuracy in the determination of group refractive indices. Group refractive indices are useful in deducing the physical thickness from optical thickness as typically measured with OCT. The simplest method of determining the group refractive index is to take the ratio between optical thickness and the corresponding physical thickness. This can be achieved through taking a FD-OCT cross-section image of a droplet of liquid or homogeneously deposited solid on a flat substrate with no pockets of air or other material between the droplet and the flat substrate. Figure 4a shows such an FD-OCT image of a solution of a polymer resin AYAT dissolved in toluene. The real position of the substrate can be extrapolated under the surface of the droplet and the apparent position of the substrate interface and the height of the material can be measured at the centre of the droplet (Fig. 6b). The physical and optical thicknesses can be measured at each lateral position, and the ratio of these gives the group refractive index.

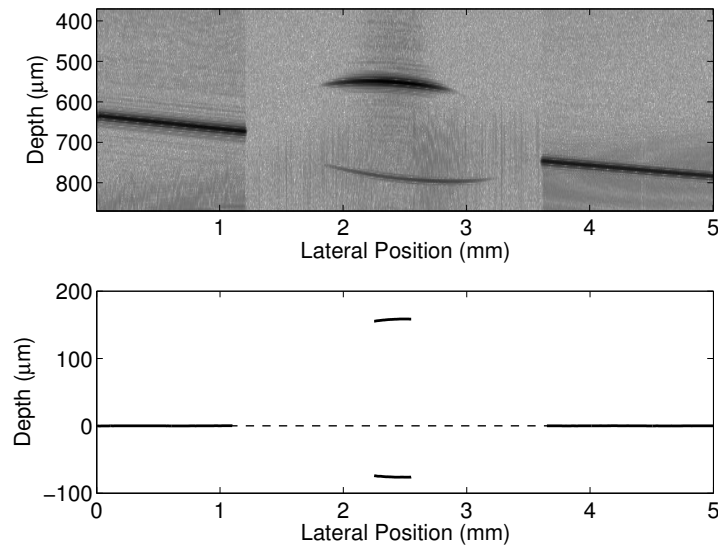


Fig. 4 a) FD-OCT cross-section image of a droplet of a polymer solution on a glass microscope slide; b) High precision fitted interfaces for measuring RI. The distance between the top interface and the dotted line (true surface of the microscope slide) gives the actual physical thickness of the droplet and the distance between the top and bottom interface gives the optical thickness.

To validate the method, the group refractive index of distilled water was measured twice giving consistent results of  $1.3349 \pm 0.0007$  and  $1.3341 \pm 0.0008$  at a wavelength of 930nm. The standard reference value for the phase refractive indices of water at 20°C are 1.32591 at 1.01μm and 1.33211 at 632.8nm<sup>15</sup>. The difference between the group refractive index measured with FD-OCT and the referenced phase refractive index is ~0.009. The group refractive index will be a slightly higher value than the phase refractive index since

$$n_g = n / [1 + \frac{\lambda}{n} \frac{dn}{d\lambda}]$$

where  $n_g$  is the group refractive index,  $n$  is the phase refractive index and  $\lambda$  is the wavelength<sup>16</sup>. Other sources of systematic errors include the assumption in this method of the incident light being collimated and passing through the interfaces of the sample at normal incidence.

This method was also used to measure the change in refractive index of the AYAT varnish as it dries by solvent evaporation. Measurements of the group refractive index with FD-OCT over 40 minutes is shown in Figure 5. The mean  $1\sigma$  error for the measurements at each time is 0.001 which is a better result than has previously been achieved<sup>12,13,14,17</sup> with bulk samples using OCT. The errors quoted in the previous works were for samples at least 3 times thicker than in the current example. The uncertainty in refractive index measurements decreases as the sample thickness increases. Figure 5 shows that the refractive index is found to decrease as the varnish dries. This is consistent with what is expected, since AYAT resin has a lower refractive index than the solvent. As the solvent evaporates the concentration of AYAT increases and hence the refractive index decreases.

The decrease and levelling off of the refractive index as a function of time coincides with the decrease of the thickness of the sample. The thickness of the varnish measured at a single position in the middle of the droplet at the corresponding times was 235.8, 158.0, 145.2, 140.3 and 137.3 $\mu\text{m}$ . The measured thickness versus time gives an indication of the rate of drying of the varnish. The ability of measuring the position of interfaces to a high precision makes FD-OCT ideal for measuring the dynamic change of refractive index of samples such as a drying varnish.

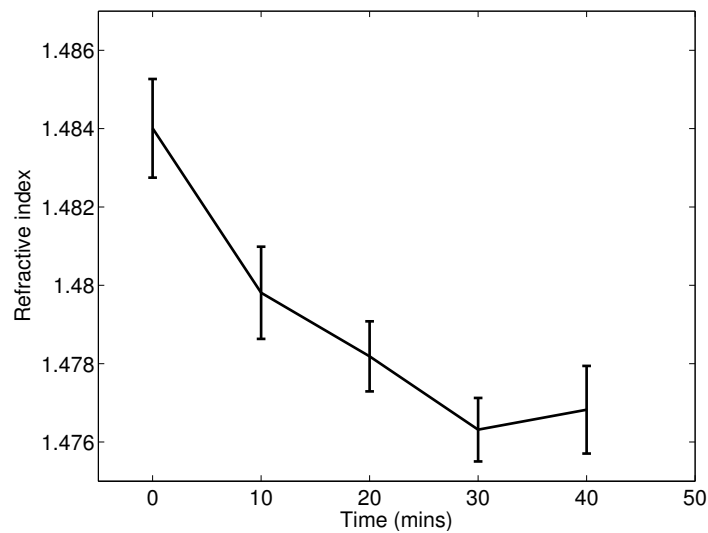


Fig. 5. Measurement of group refractive index of drying AYAT varnish over time. The thickness of the varnish measured at a single position in the middle of the droplet at each time were 235.8, 158.0, 145.2, 140.3 and 137.3 $\mu\text{m}$ .

### 3.2. Direct and dynamic relationship between surface and substrate profiles of a drying varnish

It has long been recognised that different types of varnish give different optical appearances to a painting. Berns and de la Rie<sup>18</sup> first suggested that it was the ability of a varnish at levelling the surface roughness of the underlying paint surface that determines the optical appearance of a painting. Subsequent measurements of the surface roughness of two varnishes, AYAT and Regalrez (a low molecular mass oligomer resin) when applied to substrates of different roughness, was shown to be dependent on the roughness of the substrate and the type of varnish<sup>19</sup>. However, the use of mechanical profilometry and later laser scanning confocal microscopy<sup>20</sup> only allowed the measurement of the top surface, and hence no direct correlation of the varnish surface profile to the substrate underneath could be shown. OCT allows the simultaneous measurement of both the top surface and the substrate profile immediately underneath making it possible to directly correlate the two interface profiles. Preliminary OCT monitoring of a Paraloid B72 varnish drying on a regular rough surface showed that the varnish follows the roughness of the substrate as it dried<sup>21</sup>. Subsequently, OCT imaging of a Ketone varnish and a Paraloid B67 varnish on a painting showed directly that the low molecular weight Ketone varnish

was better at levelling the surface roughness of the painting<sup>4</sup>. However, neither study showed high precision quantitative profiles of the interfaces.

Using the current method of obtaining high precision OCT profilometry, an OCT image of a polymer varnish B72 on a coarse glass substrate was analysed. To reduce the effects of speckle and increase the signal to noise ratio, each axial scan was obtained from spatial averages of 5 axial scans 1 $\mu$ m apart. The FD-OCT cross-section image of the sample is shown in Figure 6 and the extracted interface profiles are shown in Figure 7.

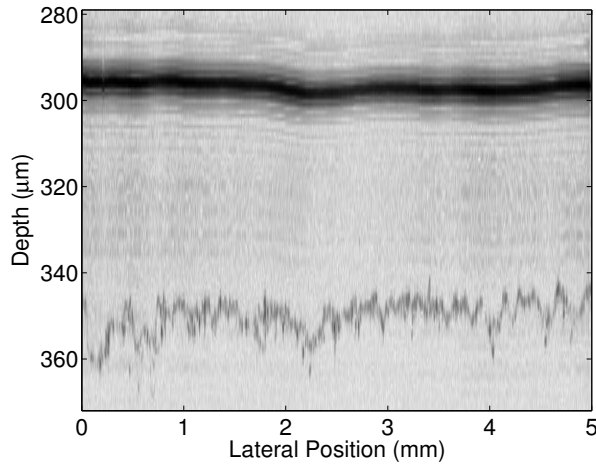


Fig. 6. OCT image of a film of B72 varnish on a rough glass substrate.

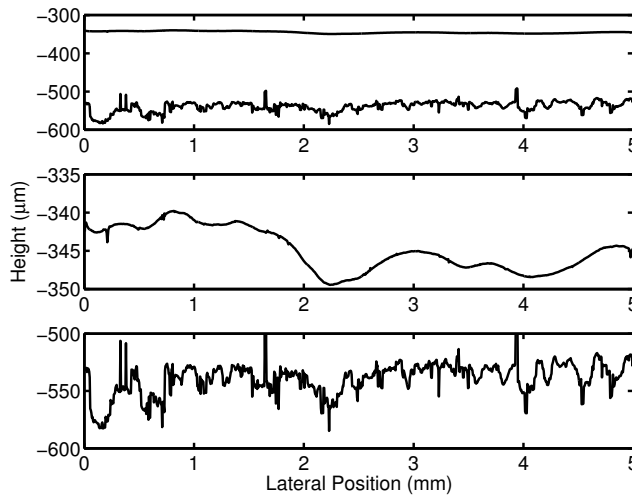


Fig. 7. a) Measured interfaces from the OCT image in Fig. 6; b) A zoomed in version of the air/varnish interface; c) A zoomed in version of the varnish/glass substrate interface.

Both interface profiles are recovered and the roughness of each interface can be characterised. One of the best ways of characterising the roughness scales of a surface is by calculating the power spectrum of the interfaces<sup>22</sup>. Figure 8 shows the power spectrum density of both interfaces.

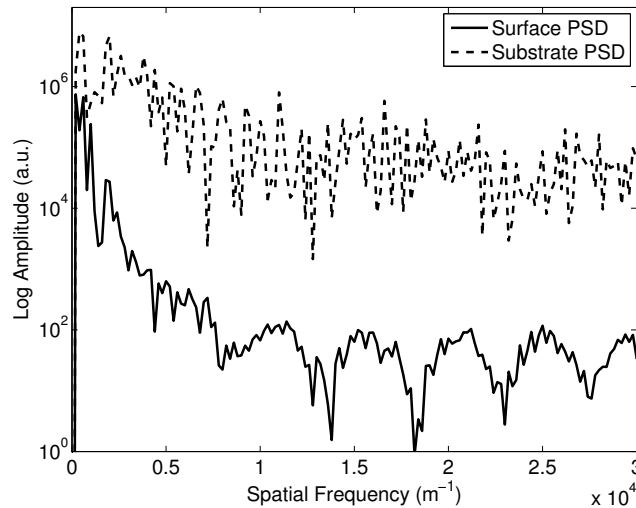


Fig. 8. Power spectrum density of the B72 varnish surface and the rough glass substrate underneath.

The differences in the spatial frequency properties of the roughness of the varnish and substrate are clearly demonstrated. At low spatial frequencies the roughness of the surface is close to the substrate than at higher spatial frequencies. This measurement can be taken a step further to dynamically monitor the surface as the varnish dries. The AYAT varnish solution used for the refractive index measurement was applied to a matte ground glass substrate. Due to the weak signal from the second interface, spatial averaging was again used and points with low signal to noise ratio were discarded. Figure 9a shows part of the cross section profiles measured for the varnish film soon after application. The position of the substrate interface has been adjusted for a refractive index of 1.4840, which is the value measured in Fig. 5 for zero drying time. Figure 9 shows that at this stage in the drying process, the surface profile of the varnish is independent of the substrate as expected.

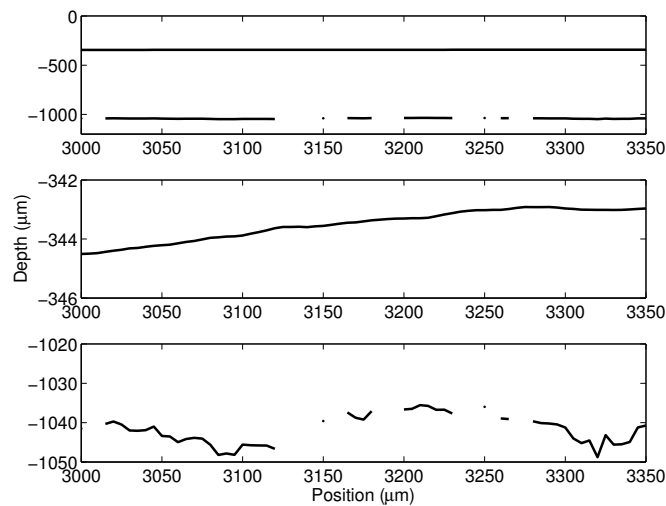


Fig. 9. a) Measured interfaces from an OCT image of a newly applied AYAT varnish film on a rough glass substrate; b) A zoomed in version of the air/varnish interface; c) A zoomed in version of the varnish/substrate interface.

Constant measurement of the varnish was carried out over 25 minutes. Figure 10 shows the same results at the end of the experiment. The adjustment for the second interface was carried out with a refractive index of 1.4763 which is the value measured in Fig. 5 after 30 minutes. The refractive index corrected substrate profiles in Fig. 9c and Fig. 10c are axially displaced. This corresponds to thermal drift over the time the FD OCT system was left on. The rate of this drift is measured to be approximately  $15\mu\text{m}$  in 25 minutes which is consistent with the displacement between the substrate positions in Fig. 9c and Fig. 10c. The cause of this drift in path length is likely to be heating as turning off the instrument and leaving it to cool down reverses this effect.

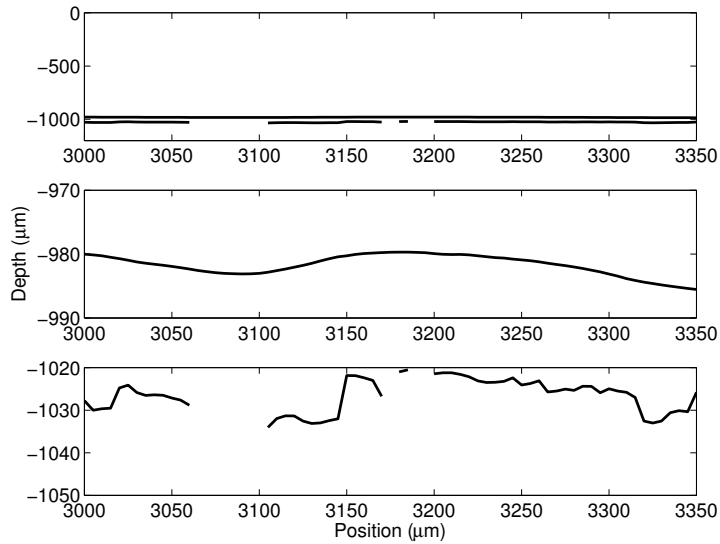


Fig. 10 a) Measured interfaces from an OCT image of a dried AYAT varnish film on a rough glass substrate; b) Air/varnish interface; c) varnish/substrate interface.

Figure 10 shows that after all the solvent has evaporated the thickness of the varnish layer is much thinner than before. The most important thing to note is the profile of the surface now follows the low spatial frequency feature of the substrate profile. To see how the surface profile develops over the drying time, the varnish surface profile is shown over a series of times (Fig. 11).

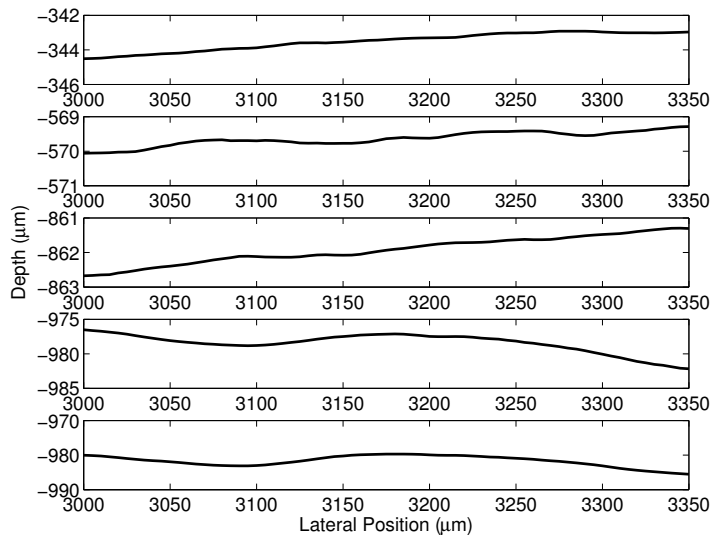


Fig. 11. Varnish surface profile after 0, 4, 8, 11 and 25 minutes drying time.

It can be seen that the main change in the surface profile in this case occurs between 8 and 11 minutes from the initial measurement. The thickness of the varnish at a given position can be calculated from the varnish and substrate profiles by assuming a constant refractive index of 1.484 (Fig. 12). It can be seen that the point at which the surface profile of the varnish settles coincides with the time when the change in thickness levels off.

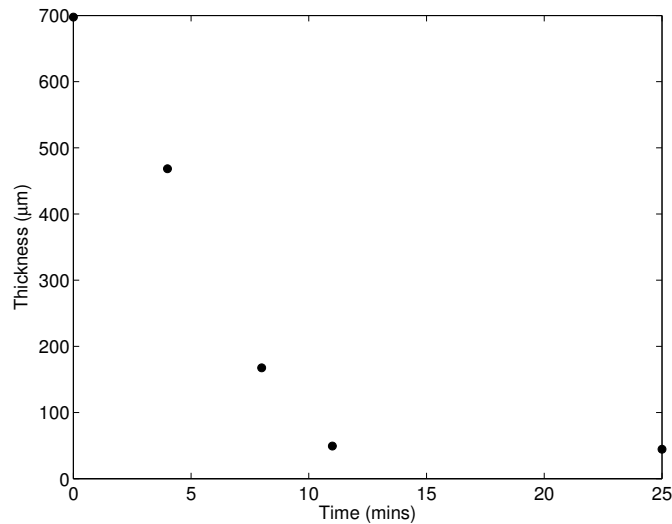


Fig. 12. Thickness of the drying varnish film as a function of time.

High precision profilometry with FD-OCT will be a very powerful technique for measuring the drying of varnishes. It provides the ability to measure refractive index, film thickness and how the surface structure of the varnish follows the substrate during the drying process. This technique will be used as part of a study of the physics of drying varnishes and the relationship between the material and optical properties of varnishes.

#### 4. CONCLUSION

It has been shown that surface profiles can be extracted from FD-OCT data with a precision two orders of magnitude higher than the axial resolution of the instrument when a Gaussian function is fitted to the axial PSF. With a Thorlabs SROCT with an axial resolution of  $6.5\mu\text{m}$ , a precision of 55nm standard deviation was achieved for a smooth surface. The interface profiles can be extracted by post processing of previously collected data without any special measurement procedure. The fundamental limitations of FD-OCT for profilometry are the same as any other WLI profilometry technique.

FD-OCT for multilayer profilometry has shown the potential to be a very useful tool for the study of the relationship between material and optical properties of varnish. The surface roughness of a varnish coating and the profile of the substrate immediately underneath can be measured simultaneously, which allows direct comparison to be made of the surface profile of the varnish and the varnish/substrate interface. It allows measurements of refractive index with OCT at a better accuracy than has previously been possible. The method also enables high precision monitor of the drying of varnish coatings dynamically and non-invasively.

## ACKNOWLEDGEMENTS

S.L. acknowledges a UK Engineering and Physical Sciences Research Council (EPSRC) CASE studentship with additional funding from the National Gallery (London). We would like to thank Marika Spring and colleagues at the National Gallery for helpful discussions and information, Rene de la Rie and colleagues at the National Gallery of Art (Washington D.C.) for discussions and for providing one of the rough samples used in this work.

## REFERENCES

1. Huang, D., Swanson, E. A., Lin, C. P., Schuman, J. S., Stinson, W. G., Chang, W., Hee, M. R., Flotte, T., Gregory, K., Puliafito, C. A. and Fujimoto, J.G, "Optical Coherence Tomography", *Science*, 254 (5035), 1178-1181 (1991).
2. Tomlins, P. H., Wang, R. K., "Theory, developments and applications of optical coherence tomography", *J. Phys. D: Appl. Phys.*, 38, 2519-2535 (2005).
3. Stifter, D., "Beyond biomedicine: a review of alternative applications and developments for optical coherence tomography", *Appl. Phys. B*, 88, 337-357 (2007)
4. Targowski, P., Góra, M., Wojtkowski, M., "Optical Coherence Tomography for Artwork Diagnostics", *Laser Chemistry*, doi:10.1155/2006/35373 (2006)
5. Liang, H., Peric, B., Hughes, M., Podoleanu, A. G., Spring, M., and Roehrs, S., "Optical Coherence Tomography in archaeological and conservation science - a new emerging field", *Proc. SPIE* 7139, 713915 (2008)
6. Fercher, A. F., Hizenberger, C. K., Kamp, G., El-Zaiat, S. Y., "Measurement of intraocular distances by backscattering spectral interferometry", *Optics Communications*, 117, 43-48 (1995).
7. Lee, B. S., Strand, T. C., 1990, "Profilometry with a coherence scanning microscope", *Appl. Opt.* 29, 3784-3788 (1990).
8. Dresel, T., Häusler, G., and Venzke, H., "Three-dimensional sensing of rough surfaces by coherence radar", *Applied Optics*, 31 (7), pp. 919 – 915 (1992).
9. Endo, T., Yasuno, Y., Makita, S., Itoh, M., and Yatagai, T., "Profilometry with line-field Fourier-domain interferometry", *Optics Express*, 13 (3), pp. 695 – 701 (2005).
10. Renlon, D., Jacquot M., Verrier I., Brun G., and Veillas C., "Broadband supercontinuum interferometer for high-resolution profilometry", *Optics Express*, 14 (1), pp. 128 – 137 (2005).
11. Goodman, J. W., [Speckle phenomena in optics, theory and applications], Roberts & Company (2007).
12. Tearney G. J., Brezinski, M. E., Southern, J. F., Bouma, B. E., Hee, M. R., and Fujimoto, J. G., "Determination of the refractive index of highly scattering human tissue by optical coherence tomography", *Opt. Letters*, 20, 2258-2260 (1995)
13. Haruna, M., Ohmi M., Mitsuyama, T., Tajiri, H., Maruyama, H., Hashimoto, M., "Simultaneous measurement of the phase and group indices and the thickness of transparent plates by low-coherence interferometry", *Opt. Letters*, 23, 966-968 (1998)
14. Lin, R., Shure, M., Rollins, A., Izatt, J., Huang, D., "Group index of human cornea at 1.3 $\mu$ m wavelength obtained in vitro by optical coherence domain reflectometry", *Opt. Letters*, 29, 83-85 (2004)
15. [CRC Handbook of chemistry and Physics 87<sup>th</sup> Edition], Ed. Lide, D. R, CRC Press (2006).
16. Born, M. and Wolf, E., [Principles of Optics], Cambridge University Press (1999).
17. Tomlins, P. H., Wooliams, P., Hart, C., Beaumont, A. and Tedaldi, M., "Optical coherence refractometry", *Optics Letters*, 33 (19), 2272 – 2274 (2008).
18. Berns, R. S. and de la Rie E. R., "Exploring the optical properties of Picture varnishes using imaging techniques", *Studies in Conservation*, 48(2), 73-83 (2003)
19. Elias, M., da la Rie, E. R., Delaney, J. K., Charron, E. and Morales, K. M., "Modification of the surface state of rough substrates by two different varnishes and influence on the reflected light", *Optics Communications*, 266, 586-591 (2006).
20. Delaney, J. K., de la Rie, E. R., Elias, M., Sung, L. P. and Morales, K. M., "The role of varnishes in modifying light reflection from rough surfaces", *Studies in conservation*, 53, 170-186 (2008).

21. Liang, H., Cid, M. G., R. Cucu R., Dobre, G., Kudimov, B., Pedro, J., Saunders, D., Cupitt, J., and Podoleanu, A., "Optical coherence tomography: a non-invasive technique applied to conservation of paintings", Proc. SPIE 5857, 261-269 (2005)
22. Bennett, J. M. and Mattson, L., [Introduction to surface roughness and scattering], Optical society of America, Washington (1989).

*To be published in Applied Optics:*

**Title:** High precision dynamic multi-interface profilometry with optical coherence tomography

**Authors:** Haida Liang and Samuel Lawman

**Accepted:** 2 June 2011

**Posted:** 7 June 2011

**Doc. ID:** 141185

Published by

OSA

# High precision dynamic multi-interface profilometry with optical coherence tomography

Samuel Lawman, Haida Liang\*

*School of Science & Technology, Nottingham Trent University, Clifton Lane, Nottingham NG11*

*8NS, UK*

*\*Corresponding author: [haida.liang@ntu.ac.uk](mailto:haida.liang@ntu.ac.uk)*

Optical coherence tomography (OCT) has mostly been used for high speed volume imaging but its profilometry potentials have not been fully exploited. This paper demonstrates high precision (as good as ~50nm) multi-interface profilometry using a Fourier domain OCT system without special anti-vibration devices. The precision is up to two orders of magnitudes better than the depth resolution of the OCT. Detailed analysis of the precision achieved for different surfaces is presented. The multi-interface profiles are obtained as a by-product of the tomography data. OCT has advantage in speed and sensitivity at detecting rough and internal interfaces compared to conventional optical profilometry. An application of the technique to the dynamic monitoring of varnish drying on paint-like substrates is demonstrated, which provides a better understanding of the formation of surface roughness. The technique has potential benefits in the field of art conservation, coatings technology and soft matter physics.

*OCIS codes:* 110.4500 (Optical Coherence Tomography); 120.3180 (Interferometry); 120.6660 (Surface measurements, roughness).

## 1. Introduction

Optical Coherence Tomography (OCT) is an optical interferometric technique that has been developed in the last 20 years with the aim of providing fast, high resolution and high contrast *in vivo* optical sectioning of the eye and other biological tissues [1,2,3,4]. OCT has found a wide variety of applications in biomedicine and its use has been expanded into non-medical fields [5] including art conservation and archaeology [6,7]. There are two modalities of OCT: Time Domain (TD) and Fourier Domain (FD) [8]. In TD OCT, depth ranging is achieved through scanning the mirror in the reference arm of the interferometer. In FD OCT, the reference mirror is fixed and the interference signal is recorded as a function of wavelength using either a spectrometer or a swept source. The spectrum is then Fourier transformed to give the final image.

Profilometry is the measurement of surface profiles and the acquisition of statistical values of roughness from these profiles [9]. It is an important technique in engineering and optics to quantify the quality of surfaces [10]. There are two common classes of profilometry methods: 1) contact mechanical profilometry and 2) a wide variety of non-contact optical techniques including confocal microscopy and interferometry. For smooth continuous surfaces, such as lenses, phase shifting interferometer [11] is a powerful tool that deduces the surface profile from the phase of the interference pattern. However, for surfaces with steep slopes, discontinuities or significant roughness, White Light Interferometry (WLI) [12,13] is better at recording the position of the surface, by measuring the centre of the coherence envelope of the returned signal rather than small relative phase differences.

Both OCT and WLI are broadband Michelson interferometers but with different emphasis. OCT is optimized for high signal-to-noise, rapid tomography with large depth range

and WLI is often optimized for high precision profilometry of relatively smooth material. Commonly in WLI, a time domain setup is used with a broad spectral band thermal source. In contrast, OCT makes use of light sources, such as superluminescent diodes (SLD), with a high intensity and a near Gaussian spectrum to obtain rapid high signal-to-noise images. The Fourier domain method is common in OCT due to benefits in speed and signal-to-noise ratio of measurements, whereas FD modality in WLI profilometry is relatively rare [14,15]. In WLI profilometry, the best possible precision is usually quoted in the nanometers [16], whereas in OCT typical precisions are quoted in microns [17].

Since WLI based optical profilometry and OCT both use broadband Michelson interferometry, they should in principle yield similar precision in profilometry. However, as OCT was developed for *in vivo* tomography, its application in precision profilometry has not been well developed. The axial resolution of both OCT and WLI are inversely proportional to the source bandwidth for the same central wavelength. While WLI use thermal sources which have about 3 times the bandwidth of a SLD typically used in OCT, the precision in profilometry commonly quoted for WLI is 3 to 4 orders of magnitude better than that of OCT. In reality, the position of the surface or the peak of the axial PSF can be determined to much higher accuracy than the depth resolution. The factors that determine the position accuracy are the signal-to-noise ratio of the intensity peak, vibrational stability of the instrument, accuracy of the peak finding algorithm and the nature of the surface roughness. By using high intensity sources such as SLDs, OCT has much higher sensitivity than the common WLI based optical profilometers using thermal sources. This gives OCT the advantage of profilometry on multiple faint interfaces rather than just the top surface.

In this paper, multi-interface OCT profilometry is applied to the dynamic monitoring of varnish coatings on rough substrates. Varnish coatings are used on paintings to serve two purposes: 1) as a protective layer for the paint and 2) as an optical element that changes the appearance of the painting. Raw paint surfaces are generally matte and hence diffusely scatter white light. The observer sees both the diffuse surface scattered white light and the volume scattered colored light from the paint. Since the varnish coating applied on top gives a smoother surface than the paint surface, the light reflected from the varnish surface is dominated more by specular than diffuse reflections. The increased gloss results in an increase in the apparent chroma of the paint when viewed away from the specular direction.

It has long been recognized that different types of varnish give different optical appearances to a painting. Berns and de la Rie [18] showed that it was the ability of a varnish to produce a smooth surface when applied to a rough paint surface, rather than differences in refractive index, that determined their different effect on the optical appearance of a painting. Subsequent measurements of the surface roughness of two varnish resins, AYAT (a high weight PVAc polymer) and Regalrez (a low molecular mass oligomer) when applied to substrates of different roughness, were shown to be dependent on the roughness of the substrate and the type of varnish [19]. However, the use of mechanical profilometry and later laser scanning confocal microscopy [20] only allowed the measurement of the top surface, and hence no direct correlation of the varnish surface profile to the substrate beneath could be shown. Preliminary OCT monitoring of a Paraloid B72 varnish drying on a regular rough surface showed that the varnish follows the roughness of the substrate as it dried [21]. Subsequently, OCT imaging of a Ketone varnish and a Paraloid B67 varnish on a painting showed directly that the low molecular weight Ketone varnish was better at leveling the surface roughness of the painting [6]. However,

neither study showed high precision quantitative profiles of the interfaces. Multi-interface profilometry with OCT allows the simultaneous measurement of both the top surface and the substrate profile beneath making it possible to directly correlate the two interface profiles. Multi-interface OCT profilometry is used in this paper to measure dynamic evolution of the surface profile and the cross-correlation between the surface and substrate profiles for two very different drying varnish coatings. The dynamic development of the surface profile is modeled numerically using the differential lubrication approximation to the Navier-Stokes equation [22,23]. The modeled and experimental surface profiles are compared directly to better understand the relationship between the material properties of a varnish and the formation of the surface roughness of varnish on a rough paint-like substrate..

Previously the authors presented preliminary results on the use of OCT for multiple interface profilometry in a conference proceeding [24]. The evaluation of the accuracy on a standard flat surface gave a standard deviation of 55nm for the positional accuracy. The ranging accuracy was examined using a stepped surface and found to be consistent with the positional accuracy. This study also examined the potential of the technique on random rough surfaces. Important results from the preliminary study will be recapitulated and expanded on in this paper along with new results on applications of the technique. The paper is organized into the following sections. Section 2 describes the detailed characteristics of the OCT used, the necessary instrumental corrections and the processing method for OCT profilometry. Section 3 examines the precision of OCT surface profilometry for smooth surfaces, sinusoidal surfaces and random rough surfaces. Section 4 examines the capabilities of OCT profilometry for multiple interfaces of layered systems, including the determination of the refractive index of the top layer for the correction of optical distortions necessary for the recovery of the internal interface

profiles. Section 5 shows an application of OCT multi-interface profilometry on the dynamic monitoring of the drying of two different types of varnish on a paint-like substrate, as well as a model for the surface roughness formation as a varnish dries. Section 6 gives the conclusions.

## 2. Instrument and methods

The results in this paper are obtained with a Fourier domain Thorlabs SROCT which consists of a Michelson interferometer, a SLD light source (central wavelength of 930nm and bandwidth of 100nm) and a spectrometer. The interferometer and the one axis lateral scanning mechanism are enclosed in a handheld probe. The spectrometer and light source are located in a separate base unit connected to the handheld probe by an optical fiber. The axial resolution of the system is 6.5 $\mu$ m in air, the transverse resolution is 9 $\mu$ m and the maximum depth range is 1.6mm. A Hann window function was used to taper the spectrum. For the following measurements, the handheld probe is secured to a 3-axes motorized micrometer stage.

The optics in the OCT system was telecentric leading to no noticeable “fan beam” distortions [17]. However, the line of equal path length in the 2D image is not flat over the field of view. This is visible in the curvature of the OCT image, and hence the measurement of the surface profile of a standard flat surface can be used to correct any measured surface profile by subtraction. This method was essential for all measurements of profiles greater than 1mm in lateral range.

The axial sample response function of an interface is a  $\delta$ -function because of the refractive index discontinuity. The measured axial intensity profile is the convolution of the sample response function with the axial point spread function (PSF) of the instrument. Figure 1a shows an example of a Gaussian fit to an interface in tomography data of an OCT image. The

fitting of a Gaussian function to this depth intensity profile allows the position of the surface to be found with accuracy much higher than the axial resolution of the system.

Lateral profiles other than the top surface profile are distorted by the optical path length (group refractive index) and refraction (phase refractive index) of the material above. In this paper, group refractive index is assumed to equal phase refractive index. The real position of the second interface is corrected by a 2D Snell's law correction [25]. In this study no data was taken in the other lateral dimension to enable a 3D refraction correction [26].

### **3. Performance of OCT surface profilometry**

#### *3.1 Smooth Surface Performance*

The main source of error in the measurement of a smooth surface profile was found to be vibration in the system which can be reduced by averaging a number of frames. To quantify the accuracy of the measurement, a standard flat surface was measured. Figure 1b shows the decrease in the standard deviation of the surface profile with increasing number of averaged frames. The standard deviation of the surface measurement after averaging is shown to level out at 55nm after 20 averages. The value quoted is typical of a measurement during the day on a lab bench without the use of special anti-vibration devices. Recently, Prykäri et al. [27] used an ultra-high resolution (submicron axial resolution) TD OCT to measure the topography of glossy paper. By measuring the highest intensity point on a highly sampled interferogram, a  $1\sigma$  accuracy of 60nm for the surface profile was quoted, which we have shown to be possible with a much lower resolution OCT without the need to develop expensive ultra-high resolution OCT.

Verification of the positional reliability of the method was carried out with a standard step surface of 9.932 $\mu$ m in step height. This is a standard surface that is used to calibrate

commercial optical profilometers (Veeco). The surface profile and step height is extracted from the mean of 60 OCT images. The step height was measured at 6 separate locations on the surface with the OCT which gave a mean of  $9.94 \pm 0.04\mu\text{m}$  consistent with the quoted reference value. The uncertainty in this measurement is similar in magnitude to that of the standard flat surface.

### *3.2 Sinusoidal surface performance*

Due to the coherent nature of OCT, speckle [28] is a major source of error when measuring profiles of rough/matte surfaces. The simplest case of such a surface is a sinusoid, which can be regarded as a regular rough surface with only one component of spatial frequency.

It is well known that commercial WLI profilometers are susceptible to artifacts when measuring sinusoidal surfaces [16]. To compare the performance of OCT profilometry against a commercial WLI profilometer (Veeco inc. Wyko NT1100), measurements were taken of a sinusoidal surface with peak-to-peak amplitude of  $1.5\mu\text{m}$  and period of  $50\mu\text{m}$ . Figure 2a shows an OCT image of this surface. To measure quantitatively the distortions of each measurement, the expected sinusoid shape was fitted to the profiles. The measured profiles and fits are shown for measurements with the SROCT (Fig. 2b) and the Veeco WLI (Fig 2c). The *rms* of the residual from the fit for the SROCT is  $0.27\mu\text{m}$  and for the Veeco WLI is  $0.26\mu\text{m}$ , showing that the errors are similar.

### *3.3 Random rough surface performance*

The commercial WLI, with its thermal light source, was unable to see the random rough surfaces used in this study. The sensitivity of OCT makes it easy to measure these optically matte surfaces [24,29]. Amaral et al [29] found that with a single profile measurement of random rough surfaces with small *rms* roughness their OCT method significantly overestimated the true

roughness. Here we show that this is due to speckle error dominating the measured surface profile.

The SROCT was used to measure the surface profile at four different axial distances from the sample (100 $\mu\text{m}$  intervals), each with an average of 60 frames. In the absence of speckle, the measured profiles should be identical within measurement errors of 55nm as found in the measurement of the standard flat surface. By assuming Gaussian distribution of surface position and measurement errors, the effect of speckle and surface roughness can be calculated from the difference between two profiles measured from different working distances from the sample. If the effect of speckle in the data of each measured profile is completely de-correlated, the *rms* difference between two axially shifted measurements of the same profile,  $\sigma_D$ , is then given by  $\sigma_D^2 = 2\sigma_S^2 + 2\sigma_V^2$ , where  $\sigma_S$  is the speckle noise and  $\sigma_V$  is the vibration noise. The value of the measured *rms* roughness  $\sigma_M$  of a single profile is then given by  $\sigma_M^2 = \sigma_T^2 + \sigma_D^2 / 2$ , where  $\sigma_T$  is the true surface roughness. The shifting of the axial measurements is also moving the surface in relation to the position of focus of the system. While speckles become more de-correlated with a changing spot size, measurement accuracy for the surface will also decrease with distance from the focus. To reach a compromise, the axial range of measurements was kept within a couple hundred micron range of the focus. Other potential sources of error include alignment errors causing the profiles to be different when measured at different distance from the probe, and hence over-estimating the speckle noise and under-estimating the true roughness. If the speckles are not fully de-correlated, then this method is likely to under-estimate the speckle noise and over-estimate the true roughness.

Performance was evaluated on two random rough surfaces. The first of these has a *rms* roughness of 0.67 $\mu\text{m}$  measured with a mechanical profilometer with a stylus radius of 2 $\mu\text{m}$  in a

previous study [19]. For this surface, the error due to speckle was found to be  $0.90 \pm 0.10\mu\text{m}$  and the *rms* surface roughness was measured to be  $0.76 \pm 0.17\mu\text{m}$  consistent with the roughness measured with the mechanical profilometer. The error in profile measurements due to speckle is larger than the surface roughness for this sample. Therefore it would not be possible to recover the surface profile from a single measurement, even though an accurate estimate for the *rms* roughness is possible.

A second rough surface with *rms* roughness approximately ten times larger was again measured with the SROCT at different axial positions. The *rms* surface roughness was measured to be  $9.91 \pm 0.18\mu\text{m}$  and error due to speckle was  $3.10 \pm 0.44\mu\text{m}$ . In this case, even though the error due to speckle was very high, it was significantly less than the profile *rms* roughness. The speckle noise also gives an indication of the roughness on scales smaller than the lateral resolution. In the above two cases, the speckle noise increases with the larger scale surface roughness.

This simple statistical method for measuring random rough surfaces gives not only the *rms* roughness but also an indication of the uncertainty in the measured surface profile due to speckle.

## **4. Multiple interface profilometry**

OCT is designed for rapid *in vivo* tomographic imaging which ensures high sensitivity. This high sensitivity means that weak reflections from internal interfaces are visible in the image. The OCT profilometry technique can be extended to these internal interfaces to perform multiple interface profilometry.

### **4.1 Refractive index measurement**

In order to correct for optical path length and refraction distortions, the refractive index of the material needs to be known. To determine the refractive index of the varnish to be used in Section 4.2, a droplet of the varnish solution (Regalrez resin dissolved in white spirit) is placed upon a flat microscope slide. An OCT measurement is carried out through the centre of the droplet so that the angle of incidence is normal to the microscope slide and the droplet surface (Fig 3a). Due to the unequal instrumental optical path length across the field of view (Sec. 2), the microscope slide appears to be tilted in the OCT image. The following positions are found with high precision (Fig 3b): 1) the position of the air/droplet interface ( $z_1$ ), 2) the apparent position of the droplet/microscope slide interface beneath ( $z_2$ ), and 3) the real position of the droplet/microscope slide interface obtained by interpolation from the air/microscope slide interface on each side of the droplet ( $z_3$ ). The refractive index is measured by taking the ratio between the optical and real thicknesses of the droplet:  $n = \frac{z_1 - z_2}{z_1 - z_3}$ . The refractive index of the white spirit ( $n=1.41-1.44$ ) is lower than the refractive index of the Regalrez resin ( $n=1.52$ ) [18]. Figure 3c shows that as the concentration increases by evaporation of white spirit, the refractive index of the droplet increases.

A number of papers have been published previously with techniques similar to the above for measuring refractive indices with OCT [30-32]. An increase in position accuracy of determining the interfaces enables better accuracy in refractive index measurements. While the previous studies quoted refractive index accuracies similar to this study, the measurements were obtained from much thicker samples of ~1mm compared with 20 to 150 $\mu$ m in the current study. Given the method of refractive index determination, measurements on thick samples will in general give better accuracy than those on thinner samples. For example, in the refractive index measurements of ~1mm thick fused silica by Wang et al [31] using a similar method, the

thickness accuracy was  $5\mu\text{m}$ , which gave a refractive index error of 0.005. If this had been carried out on a  $29\mu\text{m}$  thick sample, the refractive index error would have been 0.1. Whereas in the refractive index measurements of the drying droplets above, the median  $1\sigma$  refractive index error was 0.003 for a median thickness of  $29\mu\text{m}$ . The much improved position accuracy in the current study enables a potential 30 times improvement in the accuracy of refractive index measurement.

#### 4.2 Measurement of Rough Internal Interfaces

The application of multi-interface OCT profilometry to a drying varnish coating on a rough glass substrate ( $13\mu\text{m}$  *rms* roughness), allows the simultaneous measurement of the smooth varnish surface profile and the substrate profile. To determine the accuracy of recovering the rough substrate profile after correcting for both the optical thickness and refractive effects due to Snell's law, the coarse rough surface was initially measured with the SROCT over a range of 10mm. Without moving the instrument or the substrate, a varnish solution of Regalrez 1094 dissolved in white spirit at a ratio of 1g of resin to 1ml of solvent, was applied by a pipette from the side and left to spread, so that approximately half the surface in the OCT image was covered with the solution.

Due to the massive difference in the intensity of the Fresnel reflection from the air/varnish interface and varnish/glass interface, care needs to be taken in finding the second interface to distinguish it from harmonic and ringing artifacts. In addition, a post processing algorithm for the removal of remaining ringing artifacts and anomalous points was devised and implemented in MATLAB. The 2D Snell's law refractive index correction was then carried out to find the correct second interface. A final result showing the rough substrate profile before and after the application of varnish and the difference between the two are shown in Fig. 4. The

outliers in the difference graph are incorrect identifications of the interface by the automatic routine due to the presence of image artifacts.

To determine the effect of refractive index in the correction of second interface measurements, each measured varnish/substrate profile was corrected for a range of refractive indices. The *rms* of the difference between the measured glass substrate profile before application of the varnish and those of the same substrate profile recovered from below the varnish using various refractive index values are shown in Fig. 5. A minimum occurs at the refractive index value corresponding to that measured in Section 4.1. The minimum *rms* difference approaches the measured speckle error of the substrate surface. Figure 5 shows that for this coarse substrate, a refractive index accuracy of 0.05 is needed to ensure that the error due to refractive index correction is not significant compared to speckle error.

## **5. Dynamic monitoring of surface roughness formation of a drying varnish**

The final roughness of varnish has previously been shown to be dependent on the roughness of the substrate and the type of varnish resin [19]. However, the direct dynamic correlation of the surface profile with the substrate profile had not been studied previously. OCT multi-interface profilometry can measure the correlation of the varnish and substrate profiles directly and dynamically during the drying process. The lubrication approximation to the Navier-Stokes equation can be used to model the formation of the varnish surface profile to compare with the measured time evolution of the varnish surface profiles.

As a varnish coating dries by the evaporation of solvent, its volume decreases. As it shrinks, the surface profile will take the shape of the substrate beneath. This development of surface roughness increases surface area and hence total surface energy. Surface tension acts

against this increase in surface energy by driving a leveling flow to smooth the varnish. This flow can be modeled by the differential of the surface profile  $\Phi(x)$  given by

$$\Delta\Phi(x) = \Delta h(x) = \left\{ \frac{1}{3} \frac{\gamma}{\eta(C(x))} \frac{\Delta}{\Delta x} \left[ \left( \frac{\Delta^3 \Phi(x)}{\Delta x^3} \right) h(x)^3 \right] + E(C(x)) \right\} \Delta t \quad (1)$$

where  $\gamma$  is the surface tension,  $\eta$  is the viscosity of the varnish,  $x$  is lateral position,  $h$  is the varnish thickness,  $C$  is concentration,  $E$  is the change in thickness as a result of evaporation and  $\Delta t$  is the time interval [22,23]. For the model, the surface tension is kept as a constant while the viscosity is determined empirically as a function of concentration from experimental rheology data. The concentration at each lateral position is determined from the initial concentration and the evaporation function as time evolves. The evaporation function is determined empirically from gravimetric measurements of the drying varnish sample. The initial state of the varnish is assumed to be a perfectly flat film of uniform initial concentration.

The dynamic drying of two very different varnish solutions was monitored using the OCT. An AYAT varnish made up of 3g of the polymer AYAT mixed in 11ml of toluene (viscosity of 0.456 Pa.s) was applied to a coarse glass substrate with a bird type applicator (225 $\mu$ m gap or varnish thickness of 145 $\mu$ m). The drying was measured with the SROCT at intervals of approximately 10 seconds. Figure 6 shows the experimental and modeled time evolution of the varnish surface profile during the drying of the varnish with the simultaneously measured substrate profile. Apart from a time delay between the experimental and theoretical starting point expected from the time lapse between the application of varnish and starting the OCT measurements, these direct comparisons of the profiles show that the model produces a close match to the measured surface profile. To compare with the AYAT results, a Regalrez in toluene varnish was applied to a similar rough substrate. It was applied at a concentration of 1g

of Regalrez in 1ml of toluene (viscosity of 0.011 Pa.s) with an applicator gap of 100  $\mu\text{m}$  (or varnish thickness of 70 $\mu\text{m}$ ), to give approximately the same dry varnish thickness as in the AYAT measurement.

The simplest parameter to describe roughness is the *rms* surface roughness. However, this does not contain important spatial information about the surface. Alternatively, Power Spectral Density (PSD) shows the amplitude of roughness as a function of spatial frequency. Figure 7 shows the PSDs of both the modeled and measured final surface profile of the AYAT and Regalrez varnish coatings along with the mean PSD of the two substrate profiles. As has been shown in previous studies [19], both varnishes reduce the higher spatial frequency components of substrate roughness, with Regalrez reducing it more over a larger spatial frequency range than AYAT. The huge difference in viscosity as a function of concentration is the main reason for the difference in the leveling of the two varnishes. AYAT is orders of magnitude more viscous than Regalrez at any concentration. Figure 7 shows that the apparent deviation of the modeled PSD from the measured ones for Regalrez varnish at high frequencies is due to vibration noise.

To compare the development of roughness in different spatial regimes, a high pass and a low pass filter were used to separate the high (above 1  $\text{mm}^{-1}$ ) and low spatial frequencies (below 1  $\text{mm}^{-1}$ ) of the interface profiles. Figure 8a,b show the experimental and modeled development of the *rms* surface roughness in different spatial frequency windows as a function of time for each varnish. For the AYAT varnish, the roughness develops in both spatial regimes during the 15 minutes of drying. There is a time displacement between the model and experimental results which is partly due to the time delay between the application of varnish and the start of OCT monitoring. Both the model and the experimental results show the low frequency surface roughness developing before the high spatial frequency roughness. The sharp glitch in the

roughness measurement is due to a sudden vibration (Fig. 8a). For the Regalrez varnish, the measured roughness in the low spatial frequencies rapidly developed during or immediately after application but before OCT monitoring started. The initial glitch in the low frequency roughness of Regalrez varnish is most likely to be due to the varnish settling since it is still liquid at that point (Fig. 8b). Both the measured and modeled late time roughness for Regalrez varnish is significantly less than that of AYAT varnish on all spatial scales. The model prediction for Regalrez significantly underestimates the surface roughness in the low spatial frequencies. This may be the result of Bénard-Marangoni convection [33] which has not been taken into account by the model.

A key aspect of multi-interface profilometry is the direct measurement of the cross-correlation between the surface and substrate profiles. The time evolution of the experimental and modeled cross-correlation coefficients taking into account the effects of vibration for various spatial frequency windows are shown in Fig. 8c,d, where for AYAT these follow closely the corresponding time evolution in the *rms* roughness. Between 6-7 minutes, there is a rapid increase in correlated roughness which also corresponds to a change in the rate of decrease in thickness as a function of time (Fig. 8e). The trends of the experimental and modeled results show reasonable agreement. Throughout the drying process, the low spatial frequency component show stronger cross-correlation than the high spatial frequency components. For Regalrez varnish, the model predicts higher correlation than the measured values in the low spatial frequencies. The Regalrez and AYAT coatings were also applied to smooth glass substrates where the Regalrez varnish still developed the low spatial frequency roughness while the AYAT did not. The development of the low spatial frequency roughness of the Regalrez varnish was independent of the substrate. The cause of this roughness is likely to be Marangoni

effect [33]. The reduced mobility of AYAT compared to Regalrez may be the reason that it is not susceptible to the same effects.

Comparison of the modeled and measured thickness of the coatings (Fig 8e for AYAT and Fig 8f for Regalrez) enables the accuracy of the evaporation parameters of the model to be assessed. There are some differences between the modeled and experimental results. The final measured thicknesses of the coatings are greater than the model predictions. This is partly due to the model assumption of volume conservation in a resin/solvent mixture which is not always true in reality and would then lead to the over-estimation of the change in volume with evaporation. Future refinements of the model could include a more realistic concentration versus varnish thickness relation as well as exploring different extrapolations of the concentration versus viscosity relation in late times when it is not possible to measure the viscosity directly.

Multi-interface profilometry with OCT is a powerful technique for measuring the drying of varnishes. It has the ability to measure film thickness and how the surface profile of the varnish develops in relation to the substrate profile during the drying process. The rapid dynamic measurements allow detailed studies of the drying process. This technique is being used as part of a study of the physics of drying varnishes to quantify how the material properties of varnish such as surface tension, viscosity and evaporation rate affects the formation of the varnish surface, and hence provide a recipe for varnish mixtures that can produce the desired optical appearance.

## 6. Conclusions

It has been shown that surface profiles can be extracted from OCT data with a precision two orders of magnitude higher than the axial resolution of the instrument when a Gaussian function is fitted to the axial PSF. An *rms* precision of 55nm was achieved for a smooth surface using an

OCT with an axial resolution of  $6.5\mu\text{m}$ . The interface profiles can be extracted by post-processing of previously collected data without any special measurement procedure. With the SROCT used in this study it is also possible to measure the *rms* roughness value of surfaces even when the error due to speckle is higher than this value.

Multi-interface profilometry is ultimately limited by the resolution of the system when dealing with layers thinner than the depth resolution. While improving the resolution of OCT may improve the accuracy in OCT profilometry, orders of magnitude improvements can already be made with a simple post-processing method described in this paper.

The high sensitivity of OCT allows not only the top surface but also the faint internal interfaces to be measured with high accuracy. OCT multi-interface profilometry has the potential to be an invaluable tool for the study of the relationship between material properties of a varnish and the formation of surface roughness which in turn influences its optical properties. The surface roughness of a varnish coating and the profile of the substrate beneath can be measured simultaneously, allowing direct comparison to be made of the surface profile of the varnish and the varnish/substrate interface.

OCT profilometry has the advantage of rapid monitoring compared with conventional profilometry techniques, which is important for applications that require dynamic monitoring. An example of such an application has been demonstrated through the dynamic monitoring of the drying process of a varnish solution on a paint-like interface which has both practical applications in art conservation and importance in theoretical understanding in soft matter physics. A simple lubrication approximation to the Navier-Stokes equation was used to model the dynamic formation of the varnish surfaces for two very different varnish solutions. The modeled surface profiles were compared directly with the measured surface profile during the

drying process, which enables refinement of the model. The parameters of the model can be varied to determine what combination of properties of synthetic varnish solutions can give the desired surface state similar to those given by varnishes based on natural resins, since these are thought to give paintings the preferred optical appearance.

## Acknowledgements

This work was supported by a UK Engineering and Physical Sciences Research Council CASE award, the Leverhulme Trust and the National Gallery. We would like to thank Rene de la Rie and Marika Spring for providing us with samples and for useful discussions about varnishes used in conservation, and Robert Huber for useful discussions.

## References

1. D. Huang, E. A. Swanson, C. P. Lin, J. S. Schuman, W. G. Stinson, W. Chang, M. R. Hee, T. Flotte, K. Gregory, C. A. Puliafito, J. G. Fujimoto, “Optical coherence tomography,” *Science*, 254, 1178-1181 (1991).
2. A. F. Fercher, W. Drexler, C. K. Hitzenberger and T. Lasser, “Optical coherence tomography – principles and applications”, *Rep. Prog. Phys.*, 66, 239-303 (2003).
3. P. H. Tomlins and R. K. Wang, “Theory, developments and applications of optical coherence tomography”, *J. Phys. D: Appl. Phys*, 38, 2519-2535 (2005).
4. W. Drexler and J. G. Fujimoto, *Optical Coherence Tomography Technology and Applications* (Springer, 2008).
5. D. Stifter, “Beyond biomedicine: a review of alternative applications and developments for optical coherence tomography”, *Appl. Phys. B*, 88, 337-357 (2007).

6. P. Targowski, M. Góra and M Wojtkowski, “Optical Coherence Tomography for Artwork Diagnostics”, *Laser Chemistry*, doi:10.1155/2006/35373 (2006)
7. H. Liang, B. Peric, M. Hughes, A. G. Podoleanu, M. Spring, and S. Roehrs, “Optical Coherence Tomography in archaeological and conservation science - a new emerging field”, *Proc. SPIE 7139*, 713915 (2008).
8. A. F. Fercher, C. K. Hizenberger, G. Kamp and S. Y. El-Zaiat, “Measurement of intraocular distances by backscattering spectral interferometry”, *Optics Communications*, 117, 43-48 (1995).
9. K. J. Stout and L. Blunt, *Three Dimensional Surface Topography* (Penton Press, 2000).
10. J. M. Bennett, and L. Mattson, *Introduction to surface roughness and scattering* (Optical society of America, Washington, 1989).
11. H. Schreiber and John H. Bruning, “Phase Shifting Interferometry”, in *Optical Shop Testing*, D. Malacara, ed. Wiley-Interscience (2007), pp. 547-666.
12. B. S. Lee and T. C. Strand, 1990, “Profilometry with a coherence scanning microscope”, *Appl. Opt.* 29, 3784-3788 (1990).
13. T. Dresel, G. Häusler, and H. Venzke, “Three-dimensional sensing of rough surfaces by coherence radar“, *Applied Optics*, 31 (7), 919–915 (1992).
14. T. Endo, Y. Yasuno, S. Makita, M. Itoh, and T. Yatagai, “Profilometry with line-field Fourier-domain interferometry”, *Optics Express*, 13 (3), 695–701 (2005).
15. D. Renlon, M. Jacquot, I. Verrier, G. Brun, and C. Veillas, “Broadband supercontinuum interferometer for high-resolution profilometry”, *Optics Express*, 14 (1), 128–137 (2005).
16. F. Gao, R. K. Leach, J. Petzing, and J. M. Coupland, “Surface measurement errors using commercial scanning white light interferometers”, *Meas. Sci. Technol.*, 19, 015303 (2008).

17. S. Ortiz, D. Siedlecki, L. Remon and S. Marcos, "Optical coherence tomography for quantitative surface topography", *Applied Optics*, 48 (35), 6708-6715 (2009).
18. R. S. Berns and E. R. de la Rie, "The effect of Refractive Index of a Varnish on the Appearance of Oil Paintings", *Studies in Conservation*, 48 (4), 73-83 (2003).
19. M. Elias, E. R. da la Rie, J. K. Delaney, E. Charron and K. M. Morales, "Modification of the surface state of rough substrates by two different varnishes and influence on the reflected light", *Optics Communications*, 266, 586-591 (2006).
20. J. K. Delaney, E. R. de la Rie, M. Elias, L. P. Sung and K. M. Morales, "The role of varnishes in modifying light reflection from rough surfaces", *Studies in conservation*, 53, 170-186 (2008).
21. H. Liang, M. G. Cid, R. Cucu, G. Dobre, B. Kudimov, J. Pedro, D. Saunders, J. Cupitt, and A. Podoleanu, "Optical coherence tomography: a non-invasive technique applied to conservation of paintings", *Proc. SPIE 5857*, 261-269 (2005).
22. L. E. Stillwagon and R. G. Larson, "Fundamentals of topographic substrate leveling", *J. Appl. Phys.*, 63 (11), 5251-5258 (1988).
23. M. D. Bullwinkel, J. Gu and G. A. Campbell, "The effect of drying rate on film leveling over an uneven substrate surface", in *ANTEC '97 - plastics saving planet earth, conference proceedings, vols 1 -3*, (SPE 1997), pp. 2227-2230.
24. S. Lawman and H. Liang, "Fourier domain optical coherence tomography for high-precision profilometry", *Proc. SPIE 7391*, 73910H (2009).
25. A. Podoleanu, I. Charalambous, L. Plesea, A. Dogariu and R. Rosen, "Correction of distortions in optical coherence tomography imaging of the eye", *Phys. Med. Biol.*, 49, 1277-1294 (2004).

26. S. Ortiz, D. Siedlecki, I. Grulkowski, L. Remon, D. Pascual, M. Wojtkowski and S. Marcos, “Optical distortion correction in Optical Coherence Tomography for quantitative ocular anterior segment by three-dimensional imaging”, *Optics Express*, 18 (3), 2782-2796 (2010).
27. T. Prykäri, J. Czajkowski, E. Alarousu and R. Myllylä, “Optical Coherence Tomography as an Accurate Inspection and Quality Evaluation Technique in Paper Industry”, *Optical Review*, 17 (3), 218-222 (2010).
28. J. W. Goodman, *Speckle phenomena in optics, theory and applications* (Roberts & Company, 2007).
29. M. M. Amaral, M. P. Rael, J. P. Caly, R. E. Samad, N. D. Vieira and A. Z. Freitas, *Proc. SPIE 7390, 73900Z* (2009).
30. G. J. Tearney, M. E. Brezinski, J. F Southern, B. E. Bouma, M. R. Hee and J. G. Fujimoto, “Determination of the refractive index of highly scattering human tissue by optical coherence tomography”, *Optics Letters*, 20 (21), 2258-2260 (1995).
31. X. Wang, C. Zhang, L. Zhang, L. Xue and J. Tian, “Simultaneous refractive index and thickness measurements of bio tissue by optical coherence tomography”, *Journal of Biomedical Optics*, 7 (4), pp 628-632 (2002).
32. P. H. Tomlins, P. Wooliams, C. Hart, A. Beaumont and M. Tedaldi, “Optical coherence refractometry”, *Optics Letters*, 33 (19), 2272-2274 (2008).
33. J. V. Koleske, *Paint and Coating Testing Manual: Fourteenth Edition of the Gardner-Sward Handbook* (ASTM, 1995).

## Caption and figure List

1. Fig. 1. (a) A Gaussian fit (solid curve) to the 5 central data points across an air/glass interface. The peak position found by the Gaussian fit is shown by the dashed line; (b) Measured *rms* error of the surface profile of a standard flat surface as a function of the number of frames averaged before fitting.
2. Fig. 2. a) SROCT image of a sinusoidal surface of 1.5  $\mu\text{m}$  peak-to-peak amplitude and 50  $\mu\text{m}$  period; b) Surface profile measured with SROCT (black dots) and a sinusoidal fit to the measurement (solid red curve); c) Surface profile of the same sine surface measured with a Veeco inc. Wyko NT1100 WLI (black dots) and a sinusoidal fit to measurement (solid red curve).
3. Fig. 3. a) SROCT image of a droplet of Regalrez 1094 dissolved in white spirit on a flat microscope slide; b) Positions found from a) including extrapolation of the real position of the microscope slide beneath the droplet; c) Measurement of refractive indices of a drying droplet carried out at 5 minute intervals for 30 minutes, using only data points around the position that the beam is normal to the droplet surface. Error bars of one standard deviation are shown.
4. Fig. 4. (a) Profile of coarse glass substrate measured before (solid black line) and after (red dots) deposition of a varnish solution of Regalrez dissolved in white spirit over half the measured surface profile. The varnish surface is shown by a dashed red curve. The substrate profile below the varnish was recovered by assuming a refractive index of 1.49; (b) Difference between the before and after profiles of the rough glass substrate.
5. Fig. 5. The *rms* difference between the refractive index corrected varnish/substrate interface measurements and the reference measurement before the deposition of the varnish is shown

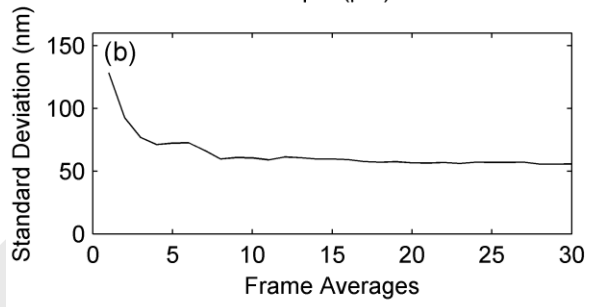
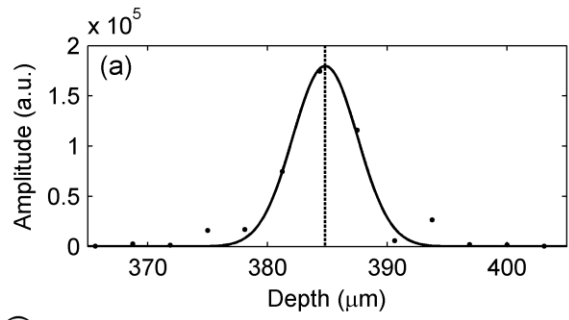
as a function of the assumed refractive index of the varnish for four independent measurements (solid curves). The dotted vertical line shows the measured refractive index of the varnish from Section 4.1. The horizontal solid line shows the measured speckle error of the substrate surface using the method detailed in Section 3.3. The dashed lines represent the  $\pm 1\sigma$  boundaries of this measurement.

6. Fig. 6. Time evolution of the measured surface profile (thick black lines) of a drying AYAT varnish at 10s, 3min 40s, 7min 10s and 14min since the application of the varnish and the profile of the rough glass substrate (thin black line). The corresponding theoretical time evolution of the varnish surface profiles are given in thin green (or gray) curves. (media1)
7. Fig. 7. Power Spectral Densities (PSD) of final surface profile measurements and models of two varnishes applied on similar substrates. The measured PSD of Regalrez varnish surface is shown by the thin solid black line, the modeled PSD is shown by the thin black dashed line and the PSD of vibrational noise is shown by the gray dashed line. The measured PSD of AYAT is shown by the thick red (or black) line and the modeled PSD is shown by the dashed thick magenta (or gray) line. The mean PSD of the two corresponding substrate profiles is shown by the thin light green (or gray) line.
8. Fig. 8. a) The time evolution of the modeled (green or gray lines) and measured (black line) raw *rms* roughness of the surface profile of a drying AYAT varnish coating for the spatial frequencies  $>1\text{mm}^{-1}$  (thin line),  $<1\text{mm}^{-1}$  (thick line) and the full spatial frequency range (medium thickness line) are shown separately; b) The same as part a) for a drying Regalrez coating; c) The time evolution of the measured (black lines) cross-correlation coefficient between the surface and substrate profile of the drying AYAT varnish for the spatial frequencies  $>1\text{mm}^{-1}$  (thin line),  $<1\text{mm}^{-1}$  (thick line) are shown separately; the expected  $\pm 1\sigma$

bounds of the modeled profiles with vibrational noise are shown in thin green (or gray) lines for the spatial frequencies  $>1\text{mm}^{-1}$  and in thick green (or gray) lines for frequencies  $<1\text{mm}^{-1}$ ;

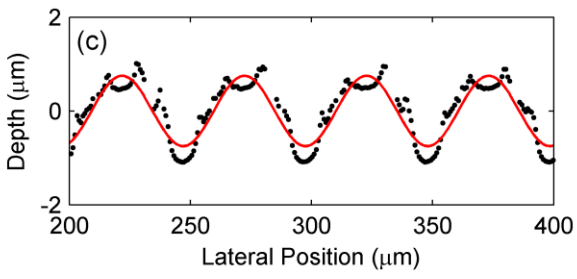
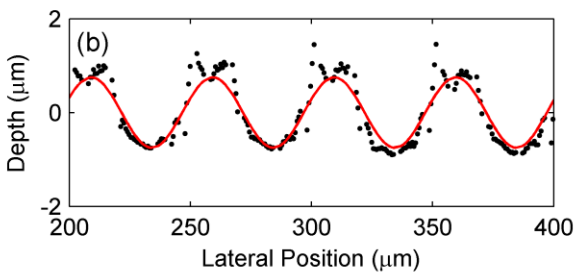
d) The same as part c) for the drying Regalrez coating; e) Measured (black lines) and modeled (green or gray line) varnish thickness versus time for AYAT; f) Varnish thickness versus time for Regalrez.

Published by  
OSA



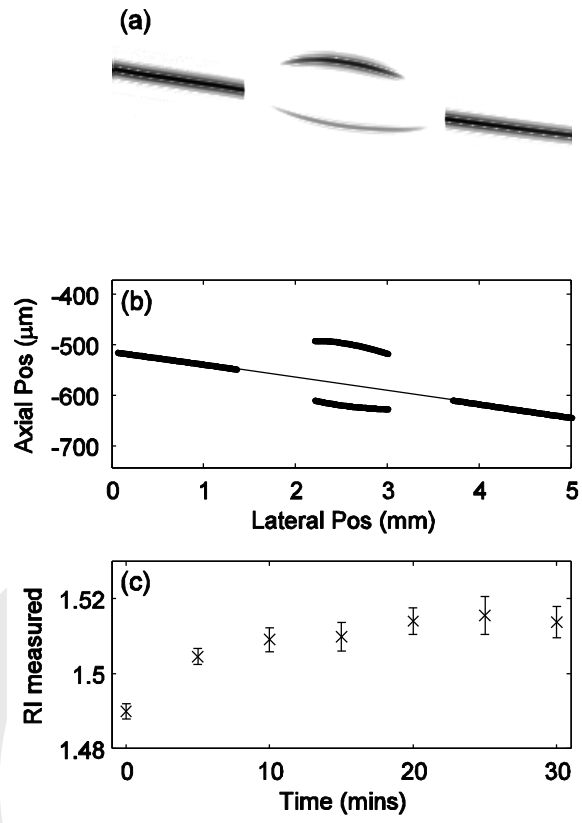
ished by

OSSA



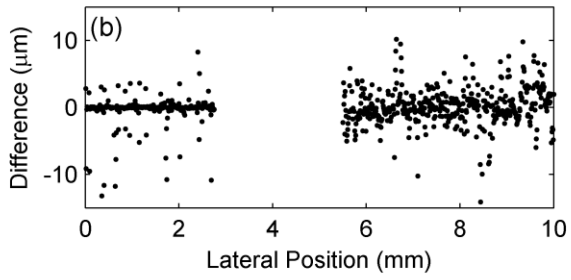
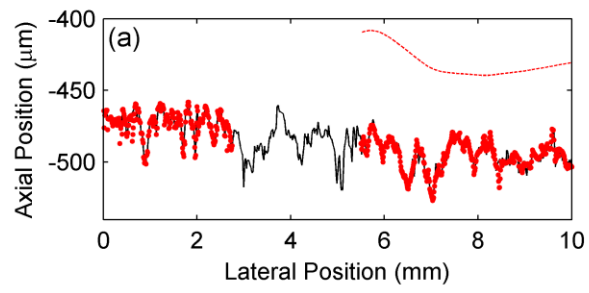
ished by

SA



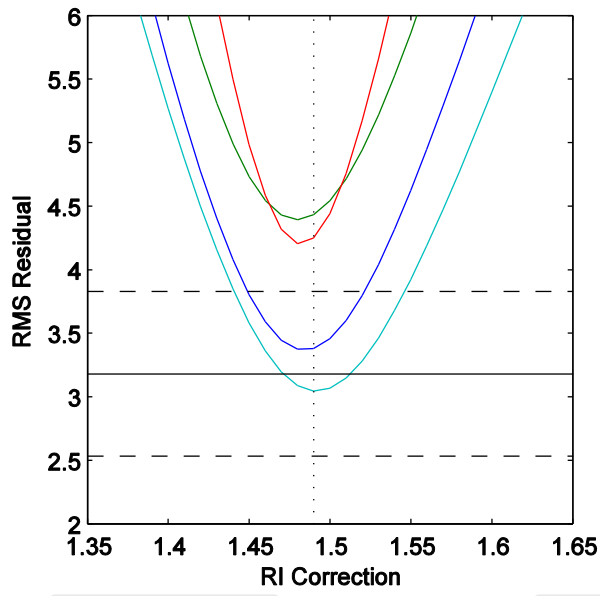
ished by

CSA



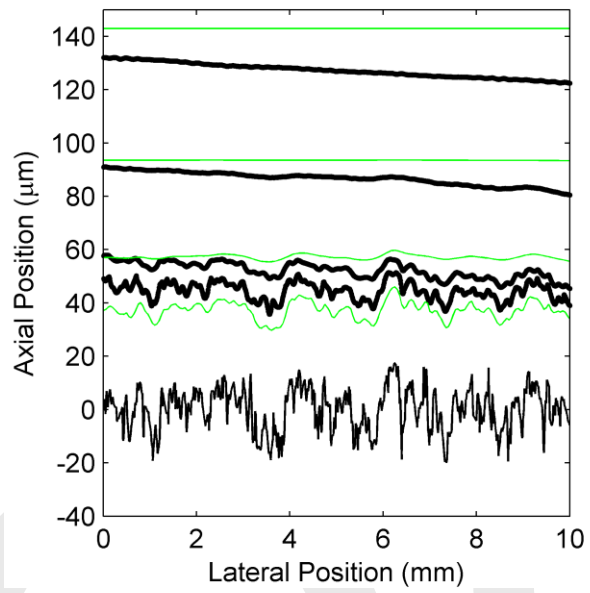
ished by

OSA



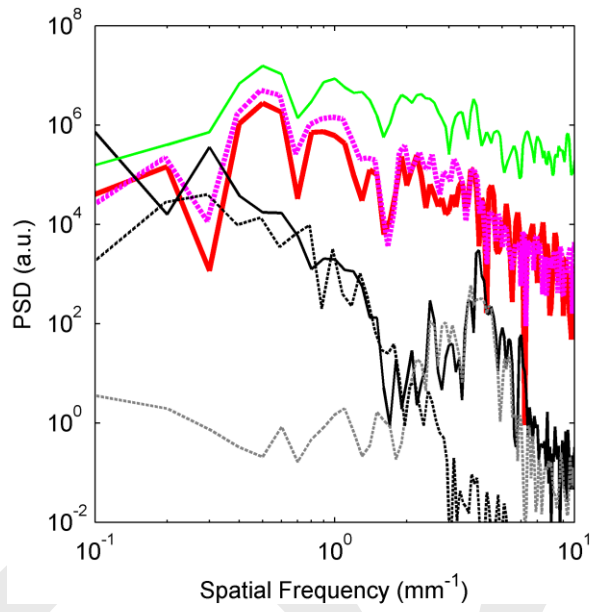
ished by

OSSA



ished by

OSA



ished by

OSSA

